A New Auxiliary Model Approach To Fermionic Criticality: Insights on Mottness in Strongly Correlated Systems

A thesis submitted in partial fulfilment
for the requirements of the degree of

Doctor of Philosophy

by

ABHIRUP MUKHERJEE
(18IP014)

under the supervision of

Prof. Siddhartha Lal

to the

Department of Physical Sciences,
Indian Institute of Science Education and Research Kolkata

August, 2026



Declaration By The Student

Date: August 19, 2026

I, Mr. **Abhirup Mukherjee**, Roll. No. 18IP014, dated August 19 2026, a student of the Department of Physical Sciences of the Integrated PhD Programme of IISER Kolkata, hereby declare that this thesis is my own work and, to the best of my knowledge, it neither contains materials previously published or written by any other person, nor has it been submitted for any degree/diploma or any other academic award anywhere before. I have used the originality checking service to prevent inappropriate copying.

I also declare that all copyrighted material incorporated into this thesis is in compliance with the Indian Copyright Act, 1957 (amended in 2012) and that I have received written permission from the copyright owners for my use of their work. I hereby grant permission to IISER Kolkata to store the thesis in a database which can be accessed by others.

Signature: Abhirup Mukherjee

Name: ABHIRUP MUKHERJEE

Department of Physical Sciences
Indian Institute of Science Education and Research Kolkata
Mohanpur 741246, West Bengal, India

Certificate From The Supervisor

Date: August 19, 2026

This is to certify that the thesis titled "A New Auxiliary Model Approach To Fermionic Criticality:Insights on Mottness in Strongly Correlated Systems" submitted by Mr. **Abhirup Mukherjee**, Roll. No. 18IP014, a student of the Department Physical Sciences of the Integrated PhD Programme of IISER Kolkata, dated August 19 2026, is based upon his own research work under my supervision. I also certify, to the best of my knowledge, that neither the thesis nor any part of it has been submitted for any degree/diploma or any other academic award anywhere before. In my opinion, the thesis fulfils the requirement for the award of the degree of Doctor of Philosophy.

Signature: 

Name: Prof. Siddhartha Lal

Professor
Department of Physical Sciences
Indian Institute of Science Education and Research Kolkata
Mohanpur 741246, West Bengal, India

From You, 5 Years Ago

Acknowledgements

The journey of a PhD is a long endeavour, and I have had the fortune of benefiting from the help and support of many people.

My first note of thanks goes to my supervisor, for helping me, as he often puts it, upgrade from version 1.0 to version 2.0 over the span of five years. Working with him has shaped and matured not only my ideas about how to carry out research, but also my understanding of how best to mentor others.

I have also benefited a lot from interacting with my predecessors Anirban da and Siddhartha da as well as my present group members Debraj, Arnabesh, Sukalyan, Sourav da, Harsha and Ranbir. I am grateful to each of them for the many things I have learnt through our discussions.

My collaborators outside the group have often shared valuable feedback on my work, and provided opportunities to venture outside my usual domain of research. In this regard, I am very thankful to Aashish, Anjan, Prof. A Taraphder, Prof. N S Vidhyadhiraja, Prof. S. R. Hassan, Prof. A Mukherjee, Prof. K Natarajan and Prof. S Pujari.

Thanks are also due to my research progress committee members, Prof. Anandamohan Ghosh and Prof. Ritesh Singh, for ensuring my doctoral work stays on track and for providing regular reviews that often improved the quality of my research.

I would also like to thank IISER Kolkata, SERB (Government of India), and the National Supercomputing Mission for supporting my research and enabling my participation in domestic and international conferences through multiple funding channels.

It's important to have good friends that can support you through difficult periods of your life. I am really blessed in this regard. My friends back home – Shrabona and Anurag – as well as my friends at IISER Kolkata – Biswajit, Debabrata, Sowrabh, Kaustubh, Gourab and Sushrat, among many others, are relations that I deeply value.

Most importantly, I would like to thank my wonderful family – my parents and my *dada* and *boudi* – for having faith in me and for supporting my dreams in every way possible. This thesis is dedicated to my *dimma* – my maternal grandmother – who passed away during the third year of my PhD. She was a woman of remarkable mental fortitude and wisdom, and I have always tried to emulate the dedication she put into everything she did.

List Of Publications

1. *Mott Criticality as the Confinement Transition of a Pseudogap-Mott Metal*.
   Abhirup Mukherjee, S R. Hassan, A Mukherjee, N S. Vidhyadhiraja, A Taraphder, S Lal.
   New J. Phys. 28 013503 (2026)

2. *Holographic entanglement renormalisation for fermionic quantum matter.*.
   Abhirup Mukherjee, S Patra, S Lal.
   J. Phys. A: Math. Theor. 57 275401 (2024)

3. *Kondo frustration via charge fluctuations: a route to Mott localisation.*
   Abhirup Mukherjee, N S Vidhyadhiraja, A Taraphder, S Lal.
   New J. Phys. 25 113011 (2023)

(Not Part of Thesis)

4. *Kondo breakdown as an entanglement transition driven by continuous measurement*.
   D Debata, Abhirup Mukherjee, **Abhirup Mukherjee**, S Lal.
   arXiv:2602.20600 (under review at Phys. Rev. B) (2025)

5. *Revealing the magnetic dimensional crossover in the Heisenberg ferromagnet CrSiTe3 through picosecond strain pulses*.
   A Kumar N M, S Mukherjee, **Abhirup Mukherjee**, A Punjal, S Purwar, T Setti, S Prabhu S., S Lal, N Kamaraju.
   Phys. Rev. B 111, L140414 (2025)

6. *Frustration shapes multi- channel Kondo physics: a star graph perspective*
   S Patra, **Abhirup Mukherjee**, A Mukherjee, N S Vidhyadhiraja, A Taraphder, S Lal.
   J. Phys.: Condens. Matter 35 315601 (2023)

7. *Unveiling the Kondo cloud: Unitary renormalization-group study of the Kondo model*
   A Mukherjee, **Abhirup Mukherjee**, N S Vidhyadhiraja, A Taraphder, S Lal.
   Phys. Rev. B 105, 085119 (2022)

Abstract

This thesis reports (i) the development of a new auxiliary model method for studying translation-invariant models of strongly-interacting electrons, and (ii) an explicit demonstration of the holographic principle in the form of a simple and tractable exact holographic mapping (EHM) for a free fermion system with emphasis on the signatures at a critical Fermi surface. Together, these results shed light on how a system of electrons behaves as it undergoes a correlation-driven metal-insulator transition on a lattice.

The auxiliary model method allows us to create a mapping between a lattice model and an auxiliary impurity model in terms of the Hamiltonian, eigenstates, Greens functions and entanglement measures, among other things. This mapping ensures that such lattice model quantities can be computed indirectly from similar computations within the auxiliary impurity model. In terms of phenomenology, this mapping connects various renormalisation group (RG) fixed points of the impurity model to those of the lattice model. As examples, local Fermi liquid and local moment phases of the impurity site get mapped to Fermi liquid and Mott insulating phases, respectively, on the lattice model. The mapping makes use of translation operators and a many-body version of Bloch's theorem to recreate the lattice model via repeated "tiling" operations on the impurity model. In contrast to other auxiliary model methods such as dynamical mean-field theory (DMFT) and its cluster variants (C-DMFT), this approach does not involve a self-consistency loop, making it more transparent. It also provides significantly more $k-$space resolution which is necessary for studying phenomena such as the pseudogap observed in the copper-oxide high-T_c superconductors.

A short description of the protocol for applying our method is as follows. We first identify the appropriate quantum impurity model corresponding to the lattice model at hand. For example, the impurity model must have a localisation-delocalisation transition on the impurity site in order to capture a metal-insulator transition on the lattice model. As another example, topological features of the band structure can be encoded by working with a topologically non-trivial conduction bath within the impurity model. Having decided upon a quantum impurity model, we solve the model using an impurity solver. In the works described in this thesis, we use the unitary renormalisation group because of its (i) analytical transparency, (ii) ability to deal with weak and strong correlations, (iii) ability to work at zero temperature, and (iv) reduced computational cost. Using the URG, we obtain a hierarchy of Hamiltonians that describe the high-energy and low-energy behaviour of the auxiliary model in various parameter regimes. This requires numerically solving the URG flow equations for various Hamiltonian couplings.

The phases of the impurity model are then characterised by (a) effective Hamiltonians, (b) static equal-time correlations, (c) dynamical correlations such as Greens functions and self-energy, and

(d) entanglement measures. Calculating some of these objects requires carrying out an iterative diagonalisation procedure on the hierarchy of Hamiltonians. Our tiling method then "periodises" these objects into the lattice model, generating required $k-$dependence in the process. Since the conduction bath of the impurity model already inherits the lattice geometry of the parent model, the appropriate symmetries are baked into the quantities. As an example, the lattice $k-$space Greens function G_k obtains contributions from the impurity site Greens function as well as impurity-bath off-diagonal Greens functions. While the former captures the local component of G_k, the latter captures the non-local components. With similar mappings existing for the dynamical correlations and entanglement measures, our method allows us to characterise various phases of the lattice model purely through impurity model computations.

Within our work on the holographic principle, we demonstrate the emergence of a holographic dimension in a system of 2D non-interacting Dirac fermions placed on a torus, by studying the scaling of multipartite entanglement measures under a sequence of renormalisation group (RG) transformations applied in momentum space. Geometric measures defined in this emergent space can be related to the RG beta function of the spectral gap, hence establishing a holographic connection between the spatial geometry of the emergent spatial dimension and the entanglement properties of the boundary quantum theory. We prove, analytically, that changing the boundedness of the holographic space involves a topological transition accompanied by a critical Fermi surface in the boundary theory. We go on to show that this results in the formation of a quantum wormhole geometry that connects the UV and the IR of the emergent dimension. The additional conformal symmetry at the transition also supports a relation between the emergent metric and the stress-energy tensor. In the presence of an Aharonov-Bohm flux, the entanglement gains a geometry-independent piece which is shown to be topological, sensitive to changes in boundary conditions, and related to the Luttinger volume of the system. Upon the insertion of a strong transverse magnetic field, we show that the Luttinger volume is linked to the Chern number of the occupied single-particle Landau levels.

Some Important Questions In this thesis, we have used the auxiliary model tiling method to study three fundamental problems in quantum condensed matter physics: (i) Mott metal-insulator transition on the Bethe lattice in infinite dimensions, (ii) Mott metal-insulator transition on the 2D square lattice, and (ii) quantum criticality in heavy fermion materials in 2D. Towards this, we have applied the method to two paradigmatic models: (a) an extended Hubbard model, and (ii) a bilayer extended Hubbard model. In preparation for applying the tiling approach, we have first analysed the corresponding quantum impurity models.

1. The Mott transition on the Bethe lattice is studied through an extended Anderson impurity model (eSIAM) that hosts local electronic correlation in the conduction bath proximate to the impurity site. Due to the lack of non-local correlations in this limit, it is sufficient to treat the conduction electron in the continuum limit.

2. The Mott transition in 2D is highly sensitive to details of the lattice. This requires us to study a lattice-embedded impurity model, where the impurity site is embedded in a 2D lattice of conduction electrons, and its hybridisation with the bath has the symmetries of the underlying lattice.

3. The heavy fermions problem necessitates a two layer impurity model, each layer acting as a lattice-embedded impurity model and coupled via inter-layer hybridisation.

The tiling approach then translates results from the auxiliary models into appropriate lattice models. In this thesis, we have attempted to answer a number of important open questions in the field:

- *Is there a minimal but effective quantum impurity model Hamiltonian that describes the Mott MIT of the* $1/2-$*filled Hubbard model on the Bethe lattice in infinite dimensions?* Finding such an impurity model would also reduce the considerable computational effort that is presently required in self-consistent approaches. In the same context, is it possible to obtain a low-energy theory for the local gapless excitations precisely at the transition, where the metal is on the brink of destruction?

- For strongly-correlated electronic models, *is it possible to map the renormalisation group fixed points of such lattice models to those of quantum impurity models?* This would provide a firmer theoretical backing to various quantum impurity models, as well as reduce computational costs.

- The phenomenon of Mott insulation involves the localization of itinerant electrons due to strong local repulsion. Upon doping, a pseudogap (PG) phase emerges - marked by selective gapping of the Fermi surface without conventional symmetry breaking in spin or charge channels. *A key challenge is understanding how quasiparticle breakdown in the Fermi liquid gives rise to this enigmatic state, and how it connects to both the Mott insulating and superconducting phases.*

- In heavy-fermion systems, a complete description of the Kondo breakdown class of transitions (that does not rely on spontaneous symmetry breaking within the correlated $f-$layer) is currently missing, especially with regards to capturing both the heavy Fermi liquid and RKKY-dominated phases. *In particular, it would be interesting to place this phenomenology in the context of the Mott transition in low dimensions, and identify the appropriate order parameter for such transitions in the absence of spontaneous symmetry breaking.*

Questions on entanglement and holography become particularly interesting in systems of critical fermions due to the presence of (i) longer-ranged entanglement, (ii) topological features arising from the incompressibility of the Fermi volume and (iii) Fermi surface gapping phase transitions driven by changes in topological quantum numbers. Unlike topologically ordered phases, there is no geometry-independent topological term in the entanglement entropy of free fermionic systems. It is, however, possible to generate such a term even here by placing the system on a multiply connected manifold such as a cylinder, and inserting a magnetic flux through the cylinder. Several questions are therefore pertinent to this discussion:

- Not much is known about the holographic implications of a Fermi surface gapping transition. *What effect does a topological change in a Fermi surface have on the additional dimension generated for the system?* Can the transition be captured by topological invariants defined within the holographic space?

- *What happens to the topological signatures of entanglement entropy across a Fermi surface instability?* If the insulator on the other side has topological features, can we relate topological invariants on either side?

Summary of Main Results

Charge fluctuations in the conduction bath mediate the Mott transition in infinite dimensions driven by strong local correlation. We demonstrate that the Mott-Hubbard transition in the limit of infinite dimensions can be faithfully captured by an effective impurity model transition from a Kondo screened phase into an unscreened local moment phase driven by charge fluctuations in the conduction bath proximate to the impurity. This serves as an explicit construction of the self-consistent impurity model mapping at the heart of the dynamical mean-field approximation. Precisely at the quantum critical point, the local Fermi liquid is replaced by a quasi-local non-Fermi liquid (NFL) that spans the impurity, zeroth and first sites of the conduction bath. The NFL results from a degeneracy between the local moment and singlet states and leads to (i) 'Andreev scattering' of incoming states into orthogonal outgoing states, (ii) anomalous power-law behaviour in the self-energies and two-particle correlations with universal exponents, and (iii) a fractional entanglement entropy of the impurity. This is important as it paves the way for extensions to more realistic studies beyond the limit of infinite dimensions.

Lattice-embedding plus many-body translation operators can be used to compute properties of a lattice model from that an impurity model with local correlations. In order to extend the approach outlined in the previous point to low dimensions and include effects arising from lattice geometries, we have developed a "tiling" approach that relies on a two-dimensional auxiliary model consisting of an Anderson impurity embedded in a minimally-correlated bath. In order to make contact with a lattice model, we construct a translation-invariant Hamiltonian from the impurity model through a many-body tiling procedure: this preserves non-local correlations, as well as allows for momentum-resolved self-energies and renormalised couplings generated from the impurity solution. When employed as an impurity solver, the URG avoids many of the limitations associated with self-consistent many-body schemes and provides direct access to zero-temperature quantum dynamics. Upon tiling the URG analysis, we obtain results for finite-sized two-dimensional square lattices as large as 77×77 sites, offering insights that can be reliably extended toward the thermodynamic limit. The method therefore provides a versatile and economical route for exploring strongly correlated models, particularly in regimes where PG formation, non-Fermi-liquid scaling, and Mott physics intersect.

2D Mott transition as the deconfinement transition of holons and doublons through a Pseudogap-Mott metal. The phenomenon of Mott insulation involves the localisation of itinerant electrons due to strong local repulsion. Upon doping, a pseudogap (PG) phase emerges—marked by selective gapping of the Fermi surface without conventional symmetry breaking in spin or charge channels. In order to explore how the pseudogap emerges from breakdown of quasiparticles, we studied a lattice-embedded impurity model supplemented by the "tiling" approach described in the previous point. At half-filling, the interplay between Kondo screening and bath charge fluctuations

in the impurity model reveals a PG phase characterised by a non-FL (the Mott metal) residing on nodal arcs, gapped antinodal regions of the Fermi surface, and an anomalous scaling of the electronic scattering rate with frequency. The eventual confinement of holon–doublon excitations of this exotic metal obtains a continuous transition into the Mott insulator. Our results identify the PG as a distinct long-range entangled quantum phase, and offer a new route to Mott criticality beyond the paradigm of local quantum criticality. The critical point is mapped to the exactly solvable Hatsugai-Kohmoto model, and we relate our results to an overarching framework for describing such transitions in terms of generalised symmetries and anomalies.

Pseudogapping Transition in A Heavy Fermion Model. As a second application of the tiling framework, we investigate the phase transition in a model of heavy fermion. Instead of the usual approach where one models the correlated $f-$layer in the form of localised spins, we considered essentially a two layer Hubbard model, and we tune the bandwidth of one of the layers to access the highly correlated regime while also being able to study other parameter regimes. We initially study the infinite-dimensional counterpart through a continuum impurity model on a Bethe lattice, and observe several competing phases. Interestingly, the intervening transitions are governed by changes in entanglement patterns within and between the layers. We then extend this to the case of two dimensions by embedding the impurity model on a 2D square lattice. We find that the small to large Fermi surface transition driven by an increasing inter-layer hybridisation displays momentum-space differentiation through partial gapping of the $k-$space spectral function. Presence of long-range entanglement and nodal-antinodal dichotomy in the vicinity of the opening of the hybridisation gap suggests the presence of a variant of the Mott metal phase observed in an earlier work by us. Importantly, this shows a unifying principle governing the metal-insulator transition in the 2D extended Hubbard model considered in the previous point and the bilayer model considered here.

Entanglement holography as a probe for fermionic criticality. This work serves as an alternative perspective on metal-insulator transition, by analysing entanglement renormalisation. In the context of the holographic principle, we demonstrate the emergence of a holographic dimension in a system of 2D non-interacting Dirac fermions placed on a torus, by studying the scaling of multipartite entanglement measures under a sequence of renormalisation group (RG) transformations applied in momentum space. Geometric measures defined in this emergent space can be related to the RG beta function of the spectral gap, hence establishing a holographic connection between the spatial geometry of the emergent spatial dimension and the entanglement properties of the boundary quantum theory. We prove, analytically, that changing the boundedness of the holographic space involves a topological transition accompanied by a critical Fermi surface in the boundary theory. We go on to show that this results in the formation of a quantum wormhole geometry that connects the UV and the IR of the emergent dimension. The additional conformal symmetry at the transition also supports a relation between the emergent metric and the stress-energy tensor. In the presence of an Aharonov–Bohm flux, the entanglement gains a geometry-independent piece which is shown to be topological, sensitive to changes in boundary conditions, and related to the Luttinger volume of the system. Upon the insertion of a strong transverse magnetic field, we show that the Luttinger volume is linked to the Chern number of the occupied single-particle Landau levels.

Contents

1 Introduction **16**
- 1.1 Mott metal-insulator transition: An Introduction . . . 16
- 1.2 Features of Mott metal-insulator transition . . . 19
- 1.3 Models and materials for strong local correlation . . . 23
- 1.4 Phenomenology of Mott transition in lattice models . . . 36
- 1.5 An alternative perspective on metal-insulator transitions: Entanglement renormalisation and holography . . . 44
- 1.6 A New Auxiliary Model Approach Towards Fermionic Criticality . . . 48
- 1.7 Summary Of Chapters . . . 52

2 Methods and Preliminaries **55**
- 2.1 The Unitary renormalisation group method . . . 55
- 2.2 Example: Unitary RG analysis of the Kondo model . . . 64
- 2.3 Some comments on the unitary RG program . . . 67
- 2.4 Comparison of renormalisation group approaches based on canonical transformations 68
- 2.5 Numerical Implementation of Unitary RG Equations . . . 70
- 2.6 Renormalised perturbation theory about fixed points . . . 71
- 2.7 Iterative Diagonalisation of Quantum Impurity Models . . . 77
- 2.8 Optimising Fermi Surface Calculations . . . 80
- 2.9 Measures of entanglement and their computation . . . 83
- 2.10 Wavefunction Renormalisation Group . . . 91
- 2.11 Kondo model spectral function . . . 96
- 2.12 Zero temperature Greens function in frequency domain . . . 100

3 Kondo Frustration via Charge Fluctuations: A Route to Mott Localisation in Infinite Dimensions **105**
- 3.1 Introduction . . . 105
- 3.2 Model Hamiltonian and method . . . 108
- 3.3 Derivation of renormalisation group equations for the extended-SIAM . . . 110
- 3.4 $T = 0$ scaling theory for the e-SIAM . . . 116
- 3.5 Descriptors of the local MIT . . . 121
- 3.6 Universal theory for the local metal-insulator transition . . . 124
- 3.7 Coexistence of local metallic and insulating phases in the e-SIAM . . . 129

3.8 Non-Fermi liquid signatures at the MIT . . . 136
3.9 Discussions and Outlook . . . 143
Appendix 1: Expressing correlation functions in terms of entanglement . . . 145
Appendix 2: One-shot decoupling of impurity from zeroth site . . . 147
Appendix 3: Effective Hamiltonian for the excitations within the Hubbard sidebands 149
Appendix 4: Behaviour of the Kondo scale T_K close to the transition . . . 152
Appendix 5: Effective Hamiltonian for the low-lying excitations at the critical point 153
Appendix 6: Non-Fermi liquid exponents in self-energy and two-particle correlations 159
Appendix 7: Entanglement entropy, magnetisation and phase shift, at the QCP . . . 159
Appendix 8: Additional correlations near the ESQPT and the QCP . . . 163

4 A New Auxiliary Model Approach for Interacting Electrons: Mapping Impurity Models To Lattice Models 165
4.1 What Is The Correct Auxiliary Model For Correlated Electrons on a 2D Square Lattice? . . . 165
4.2 Mapping Auxiliary Model To Lattice Model . . . 167
4.3 Properties of the Bloch states . . . 171
4.4 Mapping Greens Functions from Auxiliary Model to Lattice Model . . . 174
4.5 Entanglement Measures . . . 182
4.6 Some Comments . . . 184
4.7 Discussions . . . 184

5 Mott Criticality as the Confinement Transition of of a Pseudogap-Mott Metal: Insights on Mott Transition and Pseudogap in Two Dimensions 185
5.1 Introduction . . . 185
5.2 Auxiliary Model and URG analysis . . . 188
5.3 Derivation of unitary RG equations for the lattice-embedded impurity model . . . 189
5.4 Reconstructing of lattice model from auxiliary model . . . 196
5.5 Low-energy theory for the lattice-embedded impurity model . . . 197
5.6 Non-Fermi liquid excitations within the Pseudogap . . . 200
5.7 Exactly solvable nodal Non-Fermi liquid at Mott Criticality . . . 203
5.8 Heisenberg Model as a low-energy description of the tiled Mott insulator . . . 210
5.9 Pseudogap as a strongly coupled phase of quantum matter . . . 212
5.10 Conclusions . . . 213
5.11 Appendix: Effective action for the Hubbard-Heisenberg model and the eSIAM . . . 214

6 Competing tendencies In Heavy Fermion Systems: Kondo screening vs. Mott localisation 219
6.1 Introduction . . . 219
6.2 Bilayer extended Hubbard model: Impurity model . . . 220
6.3 Tiling Into Bilayer Extended Hubbard Model . . . 221
6.4 Unitary RG Analysis of The Bilayer Lattice-Embedded ESIAM . . . 224
6.5 Analysis for the simplified case of infinite dimensions . . . 234

6.6 Infinite dimensions: Real-space correlation and phase diagram . . . 235
6.7 Infinite dimensions: Local spectral function . . . 238
6.8 Renormalisation Group Flows For the 2D Lattice-Embedded Impurity Model . . . 240
6.9 Lattice spectral functions . . . 241
6.10 Conclusions . . . 242

7 Holography of Entanglement in 2D Free Fermions: Emergent Geometry and Fermionic Criticality 246
7.1 Introduction . . . 246
7.2 Preliminaries and definitions . . . 248
7.3 Entanglement hierarchy in mixed momentum and real space . . . 253
7.4 EHM, the Ryu-Takayanagi bound and holographic inequalities . . . 257
7.5 Holographic geometry of the RG flow . . . 260
7.6 Curvature of the emergent space . . . 265
7.7 Entanglement Holography and Fermionic Criticality . . . 269
7.8 Extension to the massive case . . . 272
7.9 Topological content of the entanglement spectrum . . . 273
7.10 Conclusions and Outlook . . . 279

8 Summary, Conclusions and Future Work 284
8.1 Revisions . . . 288

Chapter 1

Introduction

In recent years, the term *quantum materials* has come to describe a class of materials that, loosely speaking, display quantum mechanical properties and many-body effects over large length and energy scales. These effects manifest in the form of exotic phenomena, examples of which include unconventional superconductivity and the fractional quantum hall effect. Such materials often involve strong inter-electron interactions, low dimensions and topological properties, making them highly sensitive to small changes in parameters or temperature. This typically means that such materials cannot be described using single-particle or weak-coupling approaches, making the study of such materials more challenging and interesting. Examples of quantum materials include the copper oxide superconductors, heavy fermion materials, Moire materials and quantum spin liquids. The exotic phases that emerge from the interplay of competing tendencies in these materials are often referred to as *quantum matter*. Such phases are usually marked by non-trivial patterns of topology and entanglement. There are several examples of phases of quantum matter, some were already provided: unconventional superconducting states, fractional quantum hall states, strange metals and topologically ordered phases, among others. In this thesis, we are concerned with the study of a specific aspect of quantum matter – correlation-driven metal-insulator transition. In doing so, we will deal with a number of correlated phases such as Mott insulators, strange metals and the pseudogap, all of which will be explained in due course. The phenomenon of Mott insulation is also intimately tied to other exotic effects such as high-T_c superconductivity and spin liquid behaviour; these will not be explored in this thesis.

1.1 Mott metal-insulator transition: An Introduction

The rich physics of Mott metal-insulator transitions in strongly correlated systems has been an active subject of study for quite some time [1–4]. Their appearance in various materials such as the nickelates, cuprates, iridates and manganites, among others, is marked by complex phase diagrams that display dramatic changes in properties across changes in filling and/or bandwidth, even at low temperatures. The physics of Mott transitions is driven by the competition between two energy scales in the system: (i) the scale of itineracy, quantified by the bandwidth, and (ii) the scale of electron-electron repulsion. A Mott insulator arises when the electronic correlations are strong enough that

low-energy electronic excitations become gapped, and the metallic valence band splits into lower and upper bands; for an initially half-filled valence band, the lower band is filled at $T = 0$ while the upper band is vacant. Because of strong electronic repulsion, the electrons in the lower band form local moments which can show a variety of behaviour. This includes various symmetry-broken ground states such as an antiferromagnet [5], or symmetry-preserved states such as quantum spin liquids [6]. The physics of Mottness has been proposed as being responsible for several very interesting phenomena, such as high-temperature superconductivity [5], non-Fermi liquids [7] and the various phases in magic-angle twisted bilayer graphene [8, 9].

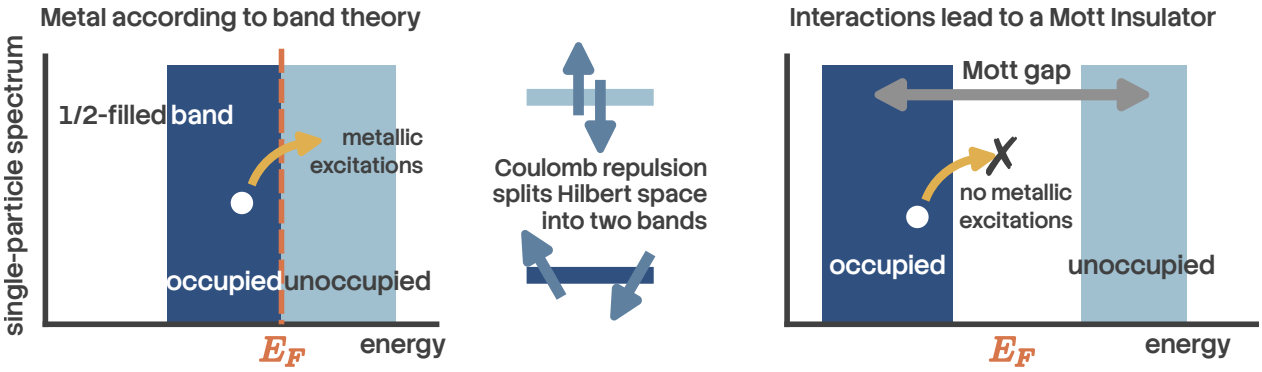

Figure 1.1: *A Mott insulator is an example of strongly correlated phenomena, where inter-electron repulsion leads to insulating behaviour. In the absence of interactions, a half-filled band (left) would result in metallic behaviour according to band theory. Upon including sufficiently strong interactions, the set of states within the band get split into two sub-bands, separated by a spectral gap of the order of the interaction strength. This makes the system metallic, because the lower sub-band remains completely filled while the upper sub-band is empty.*

Initial attempts at explaining metal-insulator transitions were based on a non-interacting picture of electrons (through the work of Bethe, Sommerfeld, Bloch and Wilson among others); in such a picture, electronic bands can arise only from the scattering of electrons off the periodic lattice potential. One then distinguishes between metals and insulators at zero temperature by the position of the Fermi level E_F with respect to the bands: if E_F lies within a band gap, an integer number of bands will be completely filled and the system will be an insulator, whereas if E_F lies within one of the bands, the system will be a metal because there are vacant gapless excitations within the band.

It was first pointed out by Boer and Verwey [10] that certain insulators and semiconductors (such as nickel oxides) have a particle filling that, purely from band theory, would lead to partially filled bands. This poses a challenge because a partially filled band necessarily leads to a metallic phase (see Fig. 1.1 (left)). The insulating behaviour of these materials therefore signals a fundamental limitation of single-particle band theory and points to a qualitatively different mechanism for electron localization—one driven by strong electron–electron interactions rather than by scattering from the lattice potential alone. This realization led to the concept of a Mott insulator, in which charge localization emerges as a genuine many-body effect despite the absence of a band gap in the non-interacting electronic structure. A very simple mechanism for this was put forth by Mott [11–13]: in the presence of a large local Coulomb repulsion cost U on a lattice site, the quantum states $|\Psi_1\rangle$

in which the site is singly occupied get separated in energy from the states $|\Psi_2\rangle$ where the site is doubly occupied by a gap of size U; the former class of states $|\Psi_1\rangle$ form the lower band (LB) while the latter $|\Psi_2\rangle$ form the upper band (UB). If we now have a half-filled system (one electron per site), this electron will completely fill LB and leave UB vacant, leading to an insulating state (see Fig. 1.1 (right)).

Given the above discussion, it is clear that a Mott insulator must involve a gap to charge excitations (excitations that add or remove an electron). It does not however determine the fate of the spin, orbital or other degrees of freedom. One scenario is when the spin or orbital degree of freedom undergoes spontaneous symmetry breaking into an ordered state; in the case of spin, this usually results in a superexchange interaction being generated and leads to an long-range ordered antiferromagnetic Neel state coexisting with the Mott state. Examples of such systems include vanadium sesquioxide V_2O_3 and its derivatives and the high-T_c cuprates (such as La_2CuO_4) [4]. The other scenario is one where the spin degree of freedom retains its symmetry, and we end up with a quantum mechanically non-trivial entangled state (in order to quench the entropy). Examples of such states include quantum spin liquids [14]. Mott insulators without long-range order are of particular interest because of the possibility of topological order, fractional excitations, and novel metallic parent states.

A prototypical model for gaining theoretical understanding of Mott metal-insulator transitions on a lattice is the single-band Hubbard model [1, 15–17]

$$H = -t \sum_{\langle i,j\rangle,\sigma} (c^{\dagger}_{i,\sigma} c_{j,\sigma} + \text{h.c.}) - \frac{U}{2} \sum_{i} (n_{i,\uparrow} - n_{i,\downarrow})^2 - \mu N \ . \tag{1.1}$$

The first term incorporates nearest-neighbour hopping on the lattice, while the second term introduces inter-electron repulsion when two electrons site on the same lattice site; in this way, the model incorporates the two competing tendencies of delocalisation and localisation that are responsible for the Mott MIT. The third term fixes the chemical potential and determines the filling of the lattice. Many of the materials that are studied for Mott MIT involve $d-$electrons that are five-fold degenerate, and these orbitals can hybridise with ligand atoms. The Hubbard model avoids these complexities by focusing on only a single band that lies closest to the Fermi energy, and it is the states of this band that are described by the Hubbard model.

This leaves us with two channels for observing Mott MIT [4]: (i) tuning the bandwidth, and (ii) tuning the filling. The former can be done, in experiments, by applying pressure. Filling is tuned by doping specific elements of a compound with elements of a different valence. The former is referred to as bandwidth-control metal-insulator transition, while the latter is called filling-control metal-insulator transition.

1.2 Features of Mott metal-insulator transition

1.2.1 Two complementary pictures of the Mott transition: Brinkman-Rice vs Mott-Hubbard.

Initial insights into the Mott MIT were obtained by Hubbard [1], thinking along lines similar to Mott. Within this picture, one starts from the insulating large U limit of the Hubbard model (eq. **1.1**) ($U \gg t$. We stay at half-filling for simplicity ($\mu = 0$). The large on-site repulsion leads to the formation of two bands at each site, the lower Hubbard band (LHB) associated with singly-occupied states and the upper Hubbard band (UHB) associated with doubles and holes (states that incur a cost U). In the large U limit, these bands are well-separated, and the dynamics within the bands is a result of the motion of tightly bound holons and doubles (more on this later) that are generated because of the small but non-zero hopping probablity t. As U/t is lowered, the bands come closer and a metal-insulator transition occurs at the critical value of U at which the gap vanishes. For lower U/t, the bands overlap and we get a metal. This picture fails to provide an accurate description of the metal resulting from the melting of such a Mott insulator [18].

An alternative approach to the Mott MIT is due to Brinkman and Rice [19], where the authors applied Gutzwiller's variational method [20] to the half-filled Hubbard model. Gutzwiller's approach involves modifying, through variational factors, the hopping matrix elements that start from doubly occupied states, in order to reflect the electronic correlation at each site. By requiring that the number of doubly-occupied states vanish in the Mott insulating ground state, they obtained a critical value of the interaction strength. In the Brinkman-Rice scenario, therefore, the transition from the metal to the insulating phase occurs when the hopping matrix elements from the doubly-occupied to the singly-occupied states strictly vanishes. Note that in contrast to the Mott-Hubbard picture, this approach starts from a correlated Fermi liquid (renormalised due to the Gutzwiller factors). While it gives a better low-energy description of the correlated metal compared to the Mott-Hubbard picture, it fails to account for the high-energy physics, and treats the Mott insulator as a direct product state of local moments at each state (on account of the strictly zero hopping). This of course means that this method cannot explain antiferromagnetic superexchange processes in the Mott insulator [18].

1.2.2 Holon-doublon unbinding picture of the Mott MIT.

In 1949, Mott proposed a zero temperature explanation for a correlation-driven insulator and a mechanism for its transition into a metal in terms of the motion of holes and doubles in the background of a half-filled lattice (see Fig. 1.2). For $U \ll t$ (strong correlation), the ground state predominantly involves lattice sites with a single electron. Hopping processes between two nearest-neighbour sites transfer an electron between them and create a pair of hole and double, but the pair remains tightly bound to each other. This is because moving the hole independently involves scattering processes that cross the Mott gap, and these processes are not allowed at $T = 0$. But without the independent motion of the hole (or double), there is no current, and the system is an insulator (left, Fig. 1.2).

As U/t is lowered, the gap closes and processes that transport the hole without transporting the double become gapless. This essentially means that the pair becomes deconfined, and the hole can be moved far away from the double (right, Fig. 1.2). Current can then be passed by having the hole

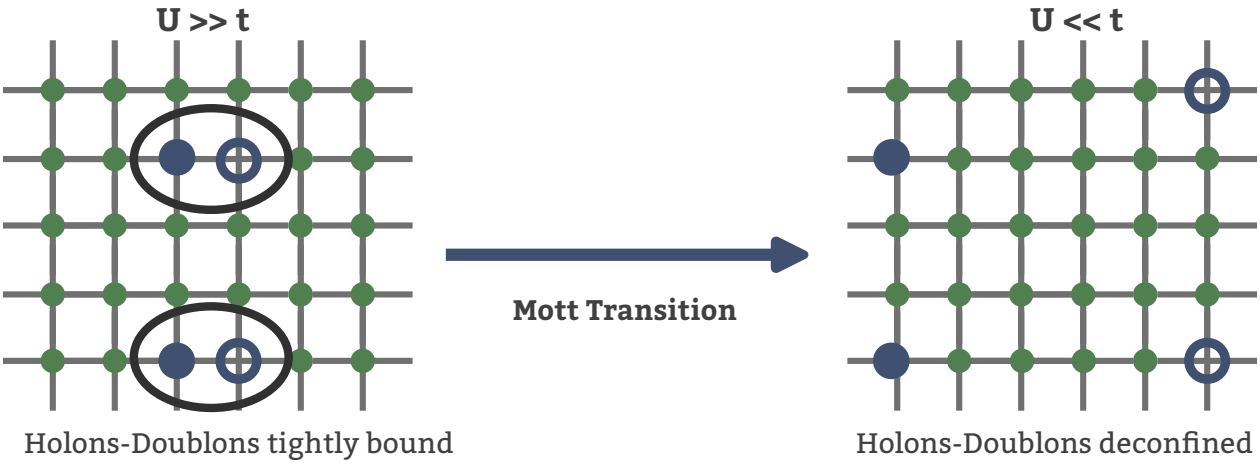

Figure 1.2: *A schematic depiction of Mott's picture of correlation-driven metal-insulator transition. In the insulating state (left), each site is mostly comprised of single spins because of the strong repulsion, but virtual hopping processes can create locally bound pairs of holes and doubles. Because of the gap to charge excitations, these pairs cannot unbind and delocalise. In contrast, in the metallic phase, the presence of gapless excitations means that the hole can move independently of the double, leading to charge transport and metallicity. This frames the Mott MIT as a confiment-deconfinement transition of the holes and doubles.*

move through the lattice, and we get a metallic state. This leads to a picture of the Mott transition into a metal in terms of an unbinding of the hole-double bound states (excitons) that were present in the insulator.

There have been more quantitative studies of this mechanism. I list some of the relatively recent ones here. In [21], Prelovšek et al. studied the motion of holon-doublon pairs in a spin polarised background by rewriting the repulsive Hubbard model in terms of electrons as an attractive Hubbard model of holes and doubles. The model was treated using a BCS-like treatment, and the Mott transition was obtained when the binding energy for the hole-double condensate vanishes. To mark the deconfinement, they show that the approach to the transition from the insulating side is concomitant with an increase in the size of the pairs. This approach however fails to capture the transition for a system away from half-filling. Following a slave-boson treatment of holon-doublon unbinding, Zhou et al. [22] show that the Mott transition from a paramagnetic metal to a Mott insulator on the half-field honeycomb and 2D square lattices occur through an intervening Slater insulator with coherent quasiparticles. In particular, their approach sheds light on the nature of the incoherent excitations in the Hubbard sidebands of the local spectral function. Finally, an older work by Watanabe et al. [23] studies the half-filled Hubbard model on an anisotropic triangular lattice using a Monte carlo method with a variational binding parameter between holons and doublons. Their approach reveals a first order Mott transition, along with robust $d-$wave superconductivity and short-range magnetic order.

1.2.3 Spectral features of the Mott transition.

One of the important diagnostics of the Mott metal-insulator transition is the spectrum for one-particle electron-like excitations, as expressed through the one-particle retarded Greens function $G(\boldsymbol{k},\sigma;t) = -i\theta(t)\langle\{c_{\boldsymbol{k},\sigma}(t), c^{\dagger}_{\boldsymbol{k},\sigma}\}\rangle$. In general, the presence of poles in the Green function at the Fermi energy and in its neighbourhood imply the existence of gapless excitations and hence a metallic phase. It turns out that this statement is equivalent to Luttinger's theorem [24, 25],

$$\frac{N}{V} = 2\int_{G(0,\boldsymbol{k})>0} \frac{d\boldsymbol{k}}{(2\pi)^3}\,, \tag{2.1}$$

which states that the particle density in a metal is equal to the number of states in the Fermi volume. As clarified in the equation, the Fermi volume is defined as the region of $k-$space where the Greens function is positive at $\omega = 0$.

In a Mott insulator, strong correlations lead to the destruction of electronic excitations around $\omega = 0$. This results in the Greens function poles transmuting into zeros. This is also tracked by analogous changes in the electronic self-energy $\Sigma(\boldsymbol{k};\omega)$; Greens function zeros leads to a Mott pole at $\omega = 0$ in $\Sigma(\boldsymbol{k};\omega)$. The points in $k-$space where $\Sigma(\boldsymbol{k};0)$ vanishes is called a Luttinger surface [26]. The Mott metal-insulator transition is therefore about the topological change of a Fermi surface (surface of Greens function poles) into a Luttinger surface (surface of self-energy poles).

As discussed earlier, the appearance of Greens function zeros at $\omega = 0$ leads to the formation of a charge gap that freezes one-particle low-energy excitations. The spectrum gets redistributed into two bands on either side of the gap, the upper and lower Hubbard bands. In the ground state, the lower band is obviously filled while the upper band is empty. Bands of a Mott insulator formed from electronic correlation differ from those formed due to one-particle scattering in a particular way: dynamical spectral weight transfer. Unlike a band insulator, the bands of a Mott insulator are not rigid; tuning the lattice filling results in a continuous transfer of states from one band to another.

The non-rigidity of the bands can be seen most easily from the atomic limit ($t = 0$) of the Hubbard model (eq. 1.1). The local retarded Greens function at an arbitrary site i can be obtained using the equation of motion approach. The final result is [27]

$$G_R(i;\omega) = \frac{1+x}{\omega+\mu+U/2} + \frac{1-x}{\omega+\mu-U/2}\,, \tag{2.2}$$

where $x = 1 - \sum_\sigma \langle n_{i\sigma}\rangle$ is the average number of holes at any site. The spectral weight for the two poles makes it clear that the lower band has $1+x$ number of states while the upper band has $1-x$ states. Changing the number of states in the lower band (by tuning μ and hence x) also changes those in the upper band. For example, by adding 0.1 holes per site to the lower band, the spectral weight in the upper band decreases by the same amount. This is the non-rigidity of the bands mentioned previously.

1.2.4 Preliminary Insights into Mottness From a Toy Model

The Baskaran-Hatsugai-Kohmoto model [28, 29] introduced independently in 1991 and 1992 is an exactly solvable model of electronic correlation that displays a transition from a metallic phase to a

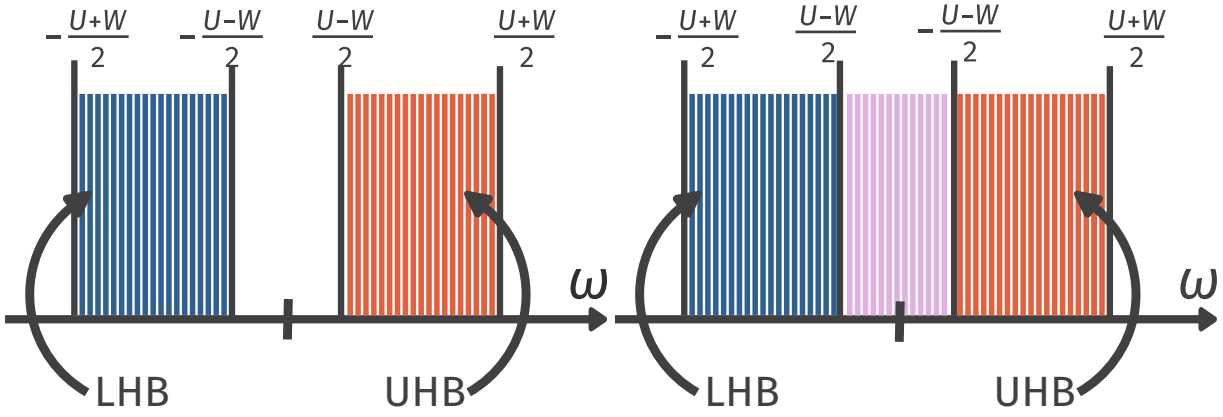

Figure 1.3: *The Mott insulator (left) and non-Fermi liquid (right) phases of the Hatsugai-Kohmoto model. In the Mott insulating phase, each momentum state is singly occupied and the lower (blue) is completely filled, while the upper band consisting of the doubly occupied and empty states is completely empty. There is, thus, a spectral gap to the excitations. In the metallic phase (right), the bands overlap and one can have correlated excitations from singly occupied states to hole and double states. These excitations are non-electronic, and the metal is a non-Fermi liquid.*

Mott insulator. While it's solvability offers an instructive method for studying Mott transition, the infinitely long-ranged nature of its interaction makes it tricky to apply these conclusions to realistic materials.

At half-filling, the model is defined by the following Hamiltonian:

$$H_{\text{BHK}} = \sum_{\mathbf{k},\sigma} \epsilon(\mathbf{k}) n_{\mathbf{k},\sigma} - \frac{U}{2} \sum_{\mathbf{k}} (n_{\mathbf{k},\uparrow} - n_{\mathbf{k},\downarrow})^2 \,. \tag{2.3}$$

Clearly the model is diagonal in momentum-space; the Hamiltonian splits up into commuting 4×4 blocks for every point $\mathbf{k}$:

$$H_{\text{BHK}} = \sum_{\mathbf{k}} H(\mathbf{k}), \quad H(\mathbf{k}) = \epsilon(\mathbf{k}) \sum_{\sigma} n_{\mathbf{k},\sigma} - \frac{U}{2} (n_{\mathbf{k},\uparrow} - n_{\mathbf{k},\downarrow})^2 \,. \tag{2.4}$$

The vacant eigenstate $|0\rangle$ of $H(\mathbf{k})$ has zero energy ($E_0 = 0$), the two singly-occupied states $|\uparrow\rangle$ and $|\downarrow\rangle$ have energy $E_1 = \epsilon(\mathbf{k}) - U/2$ and the doubly-occupied state $|\uparrow,\downarrow\rangle$ has energy $E_2 = 2\epsilon(\mathbf{k})$. This leads to two possible single-particle excitations – one for adding an electron on the vacant state: $\Delta_1 = E_1 - E_0 = \epsilon(\mathbf{k}) - U/2$, the other for adding an additional electron on a singly-occupied state: $\Delta_2 = E_2 - E_1 = \epsilon(\mathbf{k}) + U/2$.

Upon combining states from other $k-$modes, these isolated excitations broaden into bands around $\pm U/2$ because of the continuum of values available to $\epsilon(\mathbf{k})$. For large enough U (compared to the non-interacting bandwidth W), these bands remain well-separated in energy (Fig. 1.3 left), forming lower and upper Hubbard bands. The half-filled system results in the lower band being completely filled and the upper band empty, leading to a Mott insulator. The states within this band are all singly-occupied (per $k-$state). Upon lowering the correlation strength U, the bands touch

each other at the critical value of $U_c = W$ (obtained by equating the top of the lower band to the bottom of the upper band). This mechanism is qualitatively similar to the Mott-Hubbard picture of Mott transition. For lower values of U, the system is a metal due to the presence of gapless excitations within the combined band (Fig. 1.3 right). This therefore provides a simple demonstration of a correlation-driven Mott metal-insulator transition.

1.3 Models and materials for strong local correlation

1.3.1 Introduction to the auxiliary model approach

One of the main results obtained within this thesis is the development of a formalism to study the more realistic case of finite-dimensional interacting models by using appropriately chosen impurity models as auxiliary models. The key to an *auxiliary model method* is to construct an appropriate auxiliary model that while being tractable captures some essential property of the full lattice model [30]. This involves separating the complete degrees of freedom into a system part (H_S) which one treats exactly and the rest of the system (H_R) that one might simplify in order to be able to solve the problem. The non-trivial nature of the problem arises of course from the hybridisation H_{SR} between the system and the bath:

$$H = \begin{bmatrix} H_R & H_{RS} \\ H_{RS}^* & H_S \end{bmatrix} . \tag{3.1}$$

This separation can always be done exactly, if one does not care about tractability. For example, one can take the Hubbard model that describes electrons hopping on a lattice and interacting when two electrons reside on the same lattice site:

$$H_{\text{hub}} = -t \sum_{\langle i,j\rangle,\sigma} (c_{i,\sigma}^\dagger c_{j,\sigma} + \text{h.c.}) + U \sum_i n_{i\uparrow} n_{i\downarrow} , \tag{3.2}$$

and separate this into parts, the system being the local orbitals of a specific site l and the rest of the system being all the other sites:

$$H_S = U n_{l\uparrow} n_{l\downarrow}, \quad H_R = -t \sum_{\langle i,j\rangle,\sigma}{}' (c_{i,\sigma}^\dagger c_{j,\sigma} + \text{h.c.}) + U \sum_i{}' n_{i\uparrow} n_{i\downarrow}, \quad H_{SR} + H_{RS} = -t \sum_{i,\sigma} (c_{l,\sigma}^\dagger c_{i,\sigma} + \text{h.c.}) , \tag{3.3}$$

where the primed summation is carried out over all nearest-neighbour pairs that do not involve l and the summation in $H_{SR} + H_{RS}$ is over all sites adjacent to l.

The smaller system H_S (often called the *cluster*) is typically chosen such that its eigenstates are known exactly. Progress is then made by choosing a simpler form for H_R and its coupling H_{RS} with the smaller system. This combination of the cluster and the simpler bath is then called the *auxiliary system*. A tractable auxiliary system for the Hubbard model is the single-impurity Anderson model (SIAM); the correlated impurity site represents the set of local orbitals of any given site, while the conduction bath represents the rest of the lattice sites in an approximate fashion. Such a construction is shown in fig. 1.4.

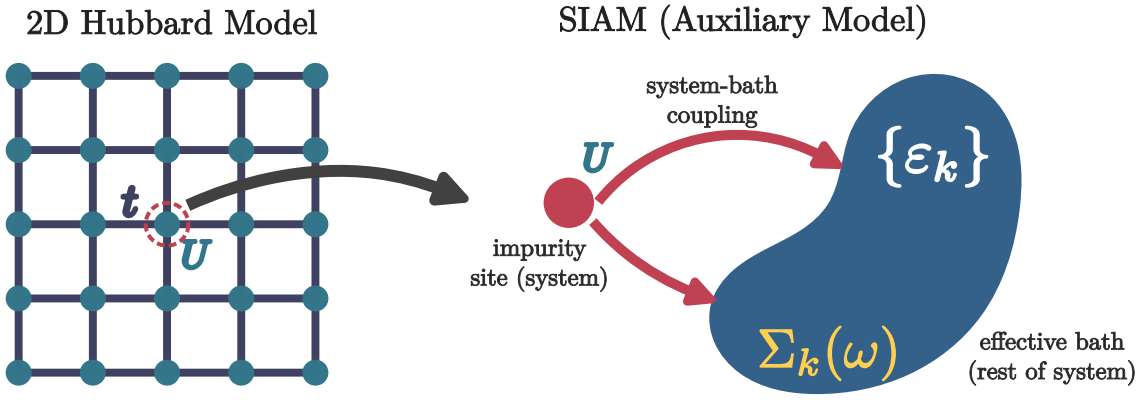

Figure 1.4: *Left: Full Hubbard model lattice with onsite repulsion U^H on all sites and hopping between nearest neighbour sites with strength t^H. Right: Extraction of the auxiliary (cluster+bath) system from the full lattice. The central site on left becomes the impurity site (red) on the right (with an onsite repulsion ϵ_d), while the rest of the $N-1$ sites on the left form a conduction bath (green circles) (with dispersion ϵ_k and correlation modelled by the self-energy $\Sigma_k(\omega)$) that hybridizes with the impurity through the coupling V.*

It should be noted that any reasonable choice of the cluster and bath would break the translational symmetry of the full model: to allow computing quantities, one would need to make the bath (which is a much larger system) simpler than the cluster (which is a single site). This distinction breaks the translational symmetry of the Hubbard model. As a result, calculations that make use of the translation symmetry of the full model (such as $k-$space objects) will require a periodisation operation of an auxiliary model quantity.

1.3.2 Correspondence between $d = \infty$ lattice models and impurity models

Dynamical Mean-Field Theory (DMFT) provides a nonperturbative framework for treating strong local electronic correlations in lattice models by mapping them onto a self-consistent quantum impurity problem [18, 31]. The central idea of DMFT is that in the limit of infinite spatial dimension, or equivalently infinite coordination number, the electronic self-energy becomes purely local while retaining its full dynamical (frequency-dependent) structure. As a result, the many-body lattice problem reduces to an effective single-site problem embedded in a self-consistently determined bath, capturing local quantum fluctuations exactly while neglecting nonlocal correlations. DMFT has become a cornerstone of modern correlated-electron theory, successfully describing Mott metal–insulator transitions, quasiparticle formation, and spectral weight transfer in Hubbard-like models [18, 32].

In order to motivate the impurity model-lattice model mapping inherited by DMFT, we first recall the textbook example of classical mean-field theory. Mean-field theory provides one of the earliest and most instructive examples of controlled approximations in many-body physics. In its

classical incarnation, exemplified by the Ising model,

$$H_{\text{Ising}} = -\sum_{i\neq j} J_{ij} S_i S_j - h \sum_i S_i = -\sum_i S_i (h + \sum_{j\neq i} J_{ij} S_j), \tag{3.4}$$

mean-field theory proceeds by replacing the interaction between a given spin and its neighbors by an *effective static field* proportional to the average magnetization. Writing $S_j = \langle S_j \rangle + \delta S_j$ and neglecting quadratic fluctuations and constant parts, one obtains an *auxiliary problem* in the form of a mean-field Hamiltonian

$$H^{(\text{MF})}_{\text{Ising}} = -\sum_i (h + h_{\text{MF}}(i)) S_i \ , \tag{3.5}$$

where the mean-field h_{MF} comes out to be

$$h_{\text{MF}}(i) = \sum_{j\neq i} 2\langle S_j \rangle J_{ij} \ . \tag{3.6}$$

The above approach assumes two things: (i) the presence of a non-zero *order parameter* $m_j = \langle S_j \rangle$ (in this case, a non-zero magnetisation), and (ii) the smallness of the fluctuations $S_j - \langle S_j \rangle$. The mean-field Hamiltonian can be used to compute the partition function (at inverse temperature β) and hence the magnetisation at a site i of the lattice:

$$m_i = \tanh(\beta(h_{\text{MF}}(i) + h)) = \tanh(\beta \sum_{j\neq i} 2 m_j J_{ij} + \beta h) \ . \tag{3.7}$$

The problem hasn't yet been solved of course; one needs to determine the appropriate value of m_j. We therefore need an additional equation; this is provided by the so-called *self-consistency condition*. The translation invariance of the lattice ensures that the magnetisation must be uniform across sites i and j. This allows us to replace m_j with m_i in the above equation:

$$m_i = \tanh(\beta m_i \sum_{j\neq i} 2 J_{ij} + \beta h) \ . \tag{3.8}$$

This equation can be solved numerically to obtain the uniform magnetisation $m_i = m$. The mean-field approximation becomes exact in the limit of large coordination number, where fluctuations are suppressed and spatial correlations beyond a single site vanish.

An equivalent way of framing the self-consistency equation is to equate the mean-fields on different lattice sites. Combining eqs. 3.7 and 3.6, we have

$$h_{\text{MF}}(i) = \sum_{j\neq i} 2 m_j J_{ij} = \sum_{j\neq i} 2 \tanh(\beta(h_{\text{MF}}(j) + h)) J_{ij} \ . \tag{3.9}$$

The equation in terms of $h_{\text{MF}}(i)$ and $h_{\text{MF}}(j)$ can again be solved numerically by claiming that the mean-field has to be uniform across all the sites owing to translation invariance. This form of the self-consistency requirement (in terms of the field) will be useful to us in the upcoming discussion.

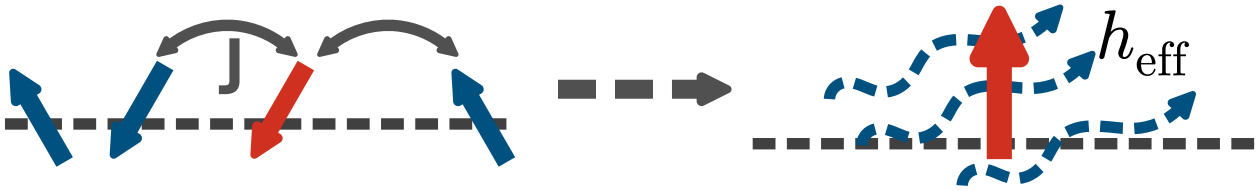

Figure 1.5: *The Ising mode mean-field treatment as an auxiliary model approach. Through the mean-field decoupling followed by the identification of a self-consistent field, the effect of the neighbouring spins is approximated by a magnetic field. This self-consistently determined model of a spin in a magnetic field acts as an auxiliary model for the complete Ising model, representing the local properties of the Ising spins through the properties of the spin subjected to the field.*

The essential feature of classical mean-field theory is therefore the replacement of a many-body problem by an effective *single-site* problem embedded in a self-consistently determined environment. Quantum lattice models admit a closely analogous construction, but with an important conceptual difference: while the classical mean field is static, quantum fluctuations necessarily introduce a tower of excited states that allow for temporal dynamics. This observation underlies the formulation of dynamical mean-field theory (DMFT), which may be viewed as the natural quantum generalization of classical mean-field theory [18, 31].

Similar to the previous case of the Ising model, we will now derive the self-consistency equation for a quantum model. Consider an interacting fermionic lattice Hamiltonian, such as the Hubbard model:

$$H = -\sum_{ij\sigma} t_{ij} c^{\dagger}_{i\sigma} c_{j\sigma} + U \sum_{i} n_{i\uparrow} n_{i\downarrow}, \tag{3.10}$$

defined on a lattice with coordination number z.

The point of this exercise is to calculate the interacting self-energy $\Sigma_k(\omega)$ for the fermions. This therefore acts as an "order parameter" and plays the same role as the local magnetisation in the previous exercise. The self-energy defines the interacting k-space Green's function for a translation-invariant problem:

$$G_{\mathbf{k}}(\omega) = \frac{1}{\omega - \varepsilon_{\mathbf{k}} - \Sigma_{\mathbf{k}}(\omega)}, \tag{3.11}$$

where $\varepsilon_{\mathbf{k}}$ denotes the noninteracting dispersion, and a real-space local Green's function, obtained by summing over momentum:

$$G_{\text{loc}}(\omega) = \sum_{\mathbf{k}} \frac{1}{\omega - \varepsilon_{\mathbf{k}} - \Sigma_{\mathbf{k}}(\omega)}. \tag{3.12}$$

Similar to the earlier exercise, we need to apply a mean-field decoupling to drop certain fluctuations and obtain a similar effective problem. In the context of interacting electrons, such a decoupling is obtained in the limit of infinite dimensionality or coordination number, where the self-energy becomes $k-$independent [31]:

$$\Sigma_{\mathbf{k}}(\omega) = \Sigma_{\text{loc}}(\omega), \text{ or (equivalently) } \Sigma_{ij}(\omega) = \delta_{ij}\Sigma_{\text{loc}}(\omega)\ . \tag{3.13}$$

The mean-field decoupling here therefore corresponds to ignoring spatial fluctuations of the one-particle self-energy, and leads to a local Greens function that is directly connected to the local self-energy:

$$G_{\rm loc}(\omega) = \sum_{\mathbf{k}} \frac{1}{\omega - \varepsilon_{\mathbf{k}} - \Sigma_{\rm loc}(\omega)}. \tag{3.14}$$

It turns out that a local Greens function connected to a local self-energy also defines a quantum impurity problem describing the dynamics of a single correlated site with the other environment sites integrated out:

$$S_{\rm imp} = -\int_0^\beta d\tau d\tau'\, c^\dagger(\tau)\, G^{-1}_{\rm MF}(\tau - \tau')\, c(\tau') + U\int_0^\beta d\tau\, n_\uparrow(\tau) n_\downarrow(\tau). \tag{3.15}$$

This acts as an auxiliary problem for the more complete problem of locally interacting electrons on a lattice. The non-interacting Greens function $G_{\rm MF}$ is as of now unknown, and defines the environment of the impurity site and comprises the dynamics of the sites that have been integrated out. Such an impurity problem is solvable, and the impurity Green's function is given by

$$G_{\rm imp}(\omega) = \frac{1}{G^{-1}_{\rm MF}(\omega) - \Sigma_{\rm imp}(\omega)}, \tag{3.16}$$

The first term in eq. 3.15 is therefore what makes this problem dynamical – it represents the probability of electrons hopping into and out of the impurity site, and leads to fluctuations of its occupancy. We can make the identification of the Greens function $G_{\rm MF}$ as the *mean-field* encountered in the previous example. More specifically, $G_{\rm MF}$ acts as a "field" because it is obtained by integrating out the other sites on the lattice, and it acts on the impurity site by affecting its dynamics.

The complete set of equations for the solving such a dynamical mean-field problem is finally obtained by equating the impurity local Greens function $G_{\rm imp}$ to the lattice local Greens function $G_{\rm loc}$. As discussed earlier, such a solution exists in an exact fashion only in the limit of infinite dimensions, as long as the correct $G_{\rm MF}$ can be found. In order to find the appropriate $G_{\rm MF}$ that allows equating the impurity model Greens function to a lattice mode Greens function, we require an additional equation: the self-consistency condition. Similar to the case of the Ising model, we require that $G_{\rm MF}$ be equal to $G_{\rm loc}$, owing to translation invariance. The full set of coupled DMFT equations is

$$\begin{aligned} G_{\rm MF} &= G_{\rm loc}, \\ \Sigma_{\rm imp}(\omega) &= G^{-1}_{\rm MF}(\omega) - G^{-1}_{\rm imp}(\omega), \\ \Sigma_{\rm loc}(\omega) &= \Sigma_{\rm imp}(\omega), \\ G_{\rm loc}(\omega) &= \sum_{\mathbf{k}} \frac{1}{\omega - \varepsilon_{\mathbf{k}} - \Sigma_{\rm loc}(\omega)}. \end{aligned} \tag{3.17}$$

One can map various features of this self-consistent program with the set of equations obtained above for the Ising model:

- The first equation is equivalent to the feature in the previous exercise where we equated the mean-fields on i and j.

- The second equation is equivalent to computing, in the previous exercise, the magnetisation on the jth site from the partition function.
- The third equation is the essential mean-field approximation, where we equate the self-energy of the simpler decoupled problem to that of the more complete lattice problem and is justified in the limit of infinite dimensions.
- The fourth equation is equivalent, in the previous exercise, to using the computed "magnetisation" of site j in the second step to further compute the mean-field at site i.

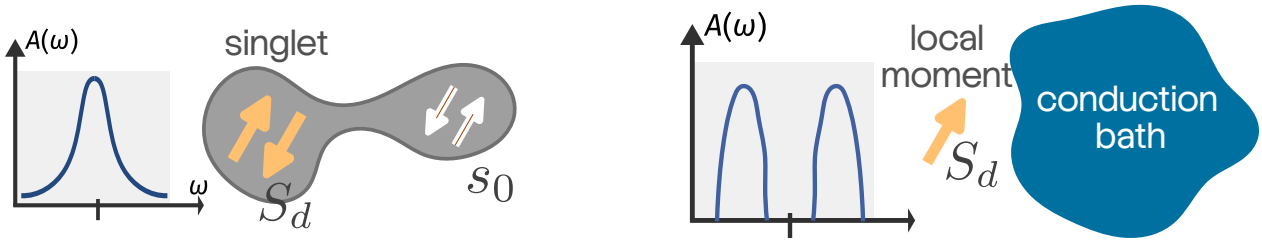

Figure 1.6: *The auxiliary model mapping between interacting lattice models and quantum impurity models involves a dictionary for relating phenomena on either side. For example, Kondo screening and the associated local Fermi liquid excitations on the impurity model (left) map to metallic Fermi liquid behaviour for the lattice model. On the other hand, breakdown in Kondo screening and the presence of a residual unscreened moment at low-energies in the impurity model maps to insulating behaviour in the lattice model.*

In direct analogy with classical mean-field theory, DMFT replaces a lattice model by an effective single-site problem embedded in a self-consistent environment. The crucial distinction is that the mean field is now dynamical rather than static, encoding quantum fluctuations exactly while neglecting spatial correlations. The fact that the correlated self-energy of the impurity site feeds into the impurity-bath hybridisation during the convergence towards self-consistently means that the bath must get correlated in the process. Importantly, this demonstrates the importance of quantum impurity models in investigating correlated lattice models, particularly in the presence of strong local interactions. This is because the effects of local correlations are captured exactly by such an auxiliary model mapping.

1.3.3 Generator of strong local correlations: Quantum impurity models

Within this thesis, we have developed an auxiliary model approach that combines the physics of quantum impurity models with a many-body version of Bloch's theorem to investigate interacting fermionic lattice models. This is motivated by the relative ease in solving impurity models and transparency afforded by such solutions. We now review the phenomenology of some of these impurity models and point out how the various impurity features affect the physics of the lattice models.

The single-impurity Anderson model describes the dynamics of a system of non-interacting itinerant electrons ($c_{k,\sigma}$) hybridising with a localised correlated impurity orbital (d_σ) [15]:

$$H_{\text{AIM}} = \sum_{k,\sigma} \epsilon_k n_{k,\sigma} + \sum_{k,\sigma} V_k (c^\dagger_{k,\sigma} d_\sigma + \text{h.c.}) + \epsilon_d \sum_\sigma n_{d\sigma} + U n_{d\uparrow} n_{d\downarrow} \,. \tag{3.18}$$

V_k controls the hybridisation strength, and ϵ_d and U control the onsite energy and local correlation respectively of the impurity site. In the limit of large U, the impurity dynamics gets projected onto its spin states, and the model then describes the scattering of non-interacting electrons off magnetic impurities, through the Kondo model [33]. Formally, the Kondo model is obtained by carrying out a Schrieffer-Wolff transformation on the Anderson impurity model and then using the condition to $V \ll U$ to drop all contributions beyond second order in the ratio V^2/U [34]:

$$H_{\text{Kondo}} = \sum_{k,\sigma} \epsilon_k n_{k,\sigma} + J \sum_{k_1,k_2} \sum_{\alpha,\beta} \vec{S}_d \cdot \vec{\sigma}_{\alpha,\beta} c^\dagger_{k_1,\alpha} c_{k_2,\beta} \,, \tag{3.19}$$

where $\vec{S}_d$ is the impurity spin formed by projecting the Hilbert space of the impurity to the singly-occupied states.

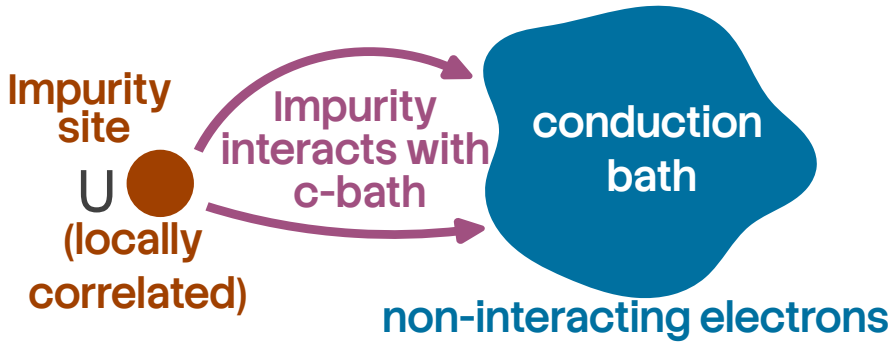

Figure 1.7: *Schematic of a quantum impurity model. The impurity is essentially a locally correlated site that presents a magnetic scattering center for the non-interacting itinerant electrons of the conduction bath. The impurity-bath scattering can appear in multiple forms, such as a one-particle hybridisation through which an electron simply hops between the two regions, or a spin-exchange Kondo interaction that emerges when the impurity site has been reduced to a local moment that can undergo spin-flip scattering with the conduction bath electrons.*

Even though the conduction bath is non-interacting, the presence of local repulsion on the impurity site makes the problem *many-electron* in nature: that is, the "U" term makes it impossible to study the electrons in isolation. This can be seen as follows: imagine two conduction electrons $|k_1 \uparrow\rangle$ and $|k_2 \downarrow\rangle$ trying to hybridise with an empty impurity site. The first electron moves onto the impurity site through a scattering process of the form $c^\dagger_{d\uparrow} c_{k_1\uparrow}$ and makes the impurity site single occupied ($|\uparrow\rangle_d$), but now the second electron k_2 *must pay a cost* of the order of U in order to hybridise with this singly-occupied impurity site through a process of the kind $c^\dagger_{d\downarrow} c_{k_1\downarrow}$. This shows that the conduction electrons *are aware* of the other electrons, and all of them must be treated together.

Another way of seeing this collective behaviour is from the Kondo model. Again imagine two spin-up electrons k_1, k_2 that are about to scatter off the impurity spin (which is presently down) via a *spin-flip* process. The first electron scatters and leaves the impurity spin up while it itself becomes down, but now the second conduction electron cannot spin-flip scatter because the spins cannot be exchanged (both are down!). This is another example of how the conduction electrons can *feel* the presence of the other electrons, and this is what makes the problem many-electron in nature.

Kondo screening Despite the interacting nature of the problem, the problem can be solved in an effectively exact fashion, via Wilson's numerical renormalisation group approach [35, 36], density-matrix renormalisation group approach [37] or the method of *Bethe ansatz* [38, 39]. The former solution is more transparent: for any non-zero value of the hybridisation V (or Kondo coupling J), the low energy physics of the impurity is described by a strong-coupling fixed point ($V = \infty$, or $J = \infty$), where the impurity forms a maximally-entangled singlet state with the local spin density of the conduction bath. The low-energy excitations about such a fixed point can be calculated from renormalised perturbation theory, and describe a local Fermi liquid – one particle excitations in the neighbourhood of the singlet renormalised by a local repulsion term [40, 41]. The crossover from the free local moment at high temperatures to the screened non-magnetic state at low temperatures occurs at an emergent energy scale T_K, the Kondo temperature, which depends exponentially on the strength of the Kondo coupling, and is the only energy scale remaining at low temperatures, so that all thermodynamic quantities must go as a function of T/T_K [35]. Unitary renormalisation group studies show that this crossover is marked by the crystallisation of entanglement between the impurity and the Kondo screening cloud, as well as among the electrons forming the cloud [42]. This entanglement also leads to a non-trivial low-energy theory for the excitations of the Kondo cloud, and it is these excitations that are responsible for the screening mechanism [42].

At half-filling (attained for $\epsilon_d = -U/2$), the only other fixed points of the SIAM are the free orbital fixed point at $V = 0, U = \epsilon_d = 0$ where the impurity site is freely occupied by two independent spins, and the local moment fixed point at $V = 0, U = \infty$, where the impurity site is occupied by a local moment that is decoupled from the bath [36, 43]. Away from half-filling, two other fixed points become available [36, 43]: a valence fluctuation fixed point at $V = 0, \epsilon_d = 0, U = \infty$ where the doubly-occupied state has been projected out from the symmetric free orbital fixed point, and a frozen impurity fixed point at $V = U = 0, \epsilon_d = \infty$ where the impurity site is left completely empty.

The crossover from local moment physics to Kondo screening as the system is tuned from high to low temperatures can also be seen from the impurity spectral function [44–47]. At low frequencies, the spectral function exhibits a sharp resonance around $\omega = 0$ that indicates the presence of gapless single-particle local Fermi liquid excitations (see Fig. 1.6). At higher frequencies, one sees satellite peaks that involve impurity excitations that cost energy of the order of U. The height of the central Kondo resonance is a topological invariant; it is fixed by the impurity occupancy owing to an application of the Friedel sum rule to impurity models [48], and remains unchanged as the interaction U is increased adiabatically while remaining at particle-hole symmetry. The topological nature can also be ascertained by identifying such a sum rule as the impurity model analogue of Luttinger's theorem [24, 25, 49] that relates the total number density of electrons to the number of Greens function poles within the Fermi volume, and which is itself topological [50, 51].

Breakdown of Kondo screening While the Anderson model (or the Kondo model derived from it) only display a strongly-coupled screened phase, it is possible to enhance it in order to introduce Kondo frustration which can eventually lead to a breakdown in the Kondo screening process. Such models are interesting because they provide a means of studying zero temperature *continuous* phase transitions and address experimental signatures of quantum criticality in correlated systems. The canonical example of this is the multichannel Kondo model, involving a single impurity hybridising with multiple independent conduction channels [52]:

$$H_{\mathrm{MCK}} = \sum_{k,\sigma,\alpha} \epsilon_{k,\lambda} n_{k,\sigma,\lambda} + \sum_{k_1,k_2,\lambda} J_\lambda \sum_{\alpha,\beta} \vec{S}_d \cdot \vec{\sigma}_{\alpha,\beta} c^\dagger_{k_1,\alpha,\lambda} c_{k_2,\beta,\lambda} \,, \tag{3.20}$$

here λ is the channel index. In the case of an isotropic Kondo coupling across the channels ($J_\lambda = J$), the strong-coupling $J = \infty$ fixed-point of the single-channel Kondo model is replaced by an intermediate-coupling fixed-point at a finite value J^* [52, 53]. Powerful methods like boundary conformal field theory [54–59], bosonization [60–64], numerical renormalization group [56, 65, 66] and Bethe ansatz [67–71] have shown that the low energy theory of such models exhibit non-Fermi liquid excitations. Further, the system displays anomalous behaviour in thermodynamic properties near $T = 0$ and a fractional zero temperature entropy in the thermodynamic limit (upon ensuring that temperature is taken to zero after the system size is taken to infinity [63, 72]). This anomalous divergent behaviour is a signature of the fact that the MCK system with a single channel-symmetric exchange coupling is quantum critical: the ground state is susceptible to perturbations that introduce channel anisotropy in the exchange couplings [52, 56, 62, 70, 73]. The criticality arises from a degeneracy of the impurity states, and it can be shown that the anomalous features – non-Fermi liquid physics, diverging impurity contributions to thermodynamic quantities and the presence of fractional excitations – that appear at the critical point can be tied to this degeneracy [74].

Another class of models that shows Kondo breakdown is that of pseudogap Anderson and Kondo models, where the impurity hybridises with a conduction bath whose density of states (DOS) varies as $\rho(\omega) \sim |\omega|^r$ with a paramter $r > 0$ that controls how fast the DOS vanishes as the Fermi level is approached. Such behaviour can arise in semi-metals and in long-range ordered systems where the order parameter vanishes at certain points on the Fermi surface (such as $d-$wave superconductors). The pseudogap impurity models exhibit a boundary quantum phase transition between a Kondo-screened strong-coupling phase and an unscreened local-moment phase as a function of interaction strength or exchange coupling [75–78]. At the critical Kondo coupling, the impurity spectral function and spin susceptibility exhibit nontrivial power-law scaling with anomalous exponents determined by r [76, 79–82]. For $0 < r < 1/2$ (in the particle-hole symmetric case), both the local-moment and strong-coupling phases are stable, separated by a critical fixed point characterized by fractional residual entropy and nontrivial hyperscaling relations [76, 83]. For larger exponents, the strong-coupling phase may disappear entirely, and the system remains in the local-moment phase for all couplings [78].

The multi-impurity Anderson and Kondo models furnish another canonical realization of Kondo breakdown, driven by the competition between Kondo screening and inter-impurity interaction. The paradigmatic example is the two-impurity Kondo model (TIKM), in which two localized spins couple both to conduction electrons and to each other via an antiferromagnetic exchange K [84, 85]. In the limit of large $K > 0$, the impurities form a non-magnetic singlet decoupled from the

conduction electrons and suppressing the Kondo resonance. This fixed point is separated from the strong-coupling Kondo screened fixed point through a quantum critical point [84–86] displaying logarithmic or power-law scaling in thermodynamic quantities and fractional residual entropy [87]. A modified version of this model that uses conduction bath-mediated inter-impurity interaction leads to a metallic spin liquid displaying nonlocal impurity-spin entanglement and fractionalized charge excitations [88]. More intricate geometries can be constructed by arranging antiferromagnetically coupled Kondo impurities along a triangle, each hybridising with its own conduction bath; such a model displays a topological phase transition from a symmetry-preserved gapless spin liquid phase with "topological order" to a screened Fermi liquid phase [89]. Indeed, recent experiments have validated such phase diagrams for the case of two impurities by studying pairs of copper atoms in the presence of strong magnetic fields [90].

1.3.4 Examples of materials with strong local correlations

As discussed in the previous section, the route to studying lattice problems via quantum impurity models makes most sense for materials with strong local correlations. Such systems are often referred to as strongly correlated quantum materials, and their phenomenology often lies beyond conventional approaches like density functional theory or perturbative weak-coupling methods. In practise, such materials often involve transition metal elements or rare earth/actinide elements, due to the presence of partially filled $3d-$ or $4f-$orbitals in such elements. This is because these orbitals are more localised around the nucleus than the $s-$ or $p-$orbitals of comparable energy, and hence lead to a reduced itinerant energy scale as well as amplify the effects of local correlations [32].

The localised nature of these orbitals can be understood as follows. For the $3s-$orbital, the $1s$ and $2s$ orbitals have same orbital angular moment l but lower principal quantum number n; since all such wavefunctions must be orthogonal to each other, the $3s-$ orbital must develop nodes in its radial form and extend farther away from the nucleus in order to be orthogonal to these other orbitals. However, for the $3d-$orbital, there is no orbital with same l but lower n; this means that the orthogonality is already enforced by the behaviour of the angular part (the spherical harmonics), and the radial part can remain localised around the nucleus without having to spread out. A similar argument holds for the localised nature of the $4f-$ orbital.

We now discuss the phenomenology of some of these quantum materials in order to identify the challenges in trying to explain them and the kind of models that are likely to be useful in this endeavour.

Transition Metal Oxides (TMOs) Transition Metal Oxides (TMOs) are defined chemically by the presence of partially filled d-shells in transition metals (e.g., Cu^{2+}, Mn^{3+}, V^{4+}) coordinated by oxygen ligands. The physics of TMOs is governed by the competition between the kinetic energy hopping amplitude t and the on-site Coulomb repulsion U; due to the small overlap between the localised $d-$orbitals, the $d-$electrons can delocalise only by hopping onto the ligand atoms. According to the Zaanen-Sawatzky-Allen (ZSA) classification scheme [91], these materials are categorized as either Mott-Hubbard insulators, where the charge gap is determined by the d-d Coulomb interaction ($E_g \approx U$), or Charge-Transfer insulators, where the gap is dictated by the energy difference between

the oxygen p-band and the metal d-band. These derive from considerations of several factors, such as crystal field splitting, arrangement of atoms and lattice symmetries.

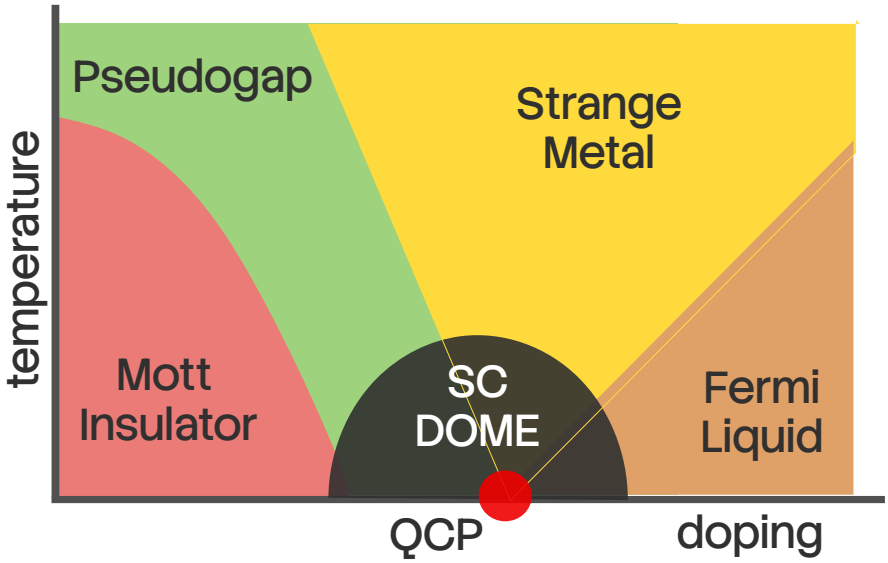

Figure 1.8: *Experimental phase diagram of the high-Tc copper oxide materials. The normal state at half-filling is an antiferromagnetic Mott insulator; doping it leads to a plethora of fascinating phases. Upon (here, hole) doping at low temperatures, the Mott insulator melts and gives rise to a d-wave superconductor with transition temperatures ranging upto 130K at ambient pressures. Further doping the system leads to a correlated Fermi liquid. At higher temperatures, two other regions are observed: the strange metal region with linear-in-temperature resistivity, and the pseudogap with partial gapping of the Fermi surface.*

For example, in the case of octahedral symmetry, repulsion from the surrounding atoms leads to the raising of energy of the $d_{x^2-y^2}$ and $d_{3z^2-r^2}$ orbitals forming the e_g doublet, while the other three orbitals (d_{xy}, d_{yz} and d_{zx}) form the t_{2g} multiplet. For the heavier TMOs (Ti, V, Cr...), the Fermi level lies within e_g. The increased positive nuclear charge (compared to the lighter elements) lowers the energy of the $d-$orbitals and brings them closer to the $p-$orbitals, reducing the charge transfer energy $\Delta = \varepsilon_d - \varepsilon_p$ of transporting an electron from a $d-$state to a $p-$state, compared to the $d-$level repulsion U ($|\Delta| < U$). Geometric reasons (the e_g orbitals point towards the $p-$orbitals) also enhance the hybridisation between $d-$ and $p-$orbitals in such materials. If Δ becomes larger than the bandwidth, we obtain a *charge-transfer insulator*, where the charge gap is decided by Δ. In the lighter TMOs, the Fermi level passes through t_{2g}, and because they point away from the $p-$orbitals, the hybridisation is weaker. Moreover, the reduced positive nuclear charge leads to an increased $\Delta > U$; a U greater than the bandwidth leads to what's called a *Mott-Hubbard insulator*.

Experimental studies of transition metal oxides (TMOs) have established metal–insulator transitions (MITs) as a defining consequence of strong electronic correlations in systems with partially filled (d)-electron shells [92, 93]. Early experiments on vanadates such as V_2O_3 characterised pressure-driven MITs through the pressure- and temperature-dependent conductivity as well as an anomalous enhancement of the optical conductivity [94–96]. Copper oxides constitute the most

extensively studied class of correlated TMOs and provide a canonical example of a doping-driven MIT. Transport measurements on parent compounds such as La_2CuO_4 establish a robust insulating state, while carrier doping leads to anomalous metallic behavior characterized by linear-in-temperature resistivity and unconventional superconductivity [97–99]. Such metal-insulator transition is also reported from angle-resolved photoemission spectroscopy (ARPES) measurements in doped La_2CuO_4 and $Bi_2Sr_2CaCu_2O_8$, along with the emergence of pseudogap near the antinodes at high temperatures and a hole-to-electronlike Fermi surface reconstruction [100–102]. Nickelates ($LaNiO_2$, $La_3Ni_2O_7$, $La_4Ni_3O_{10}$, etc) exhibit related but distinct experimental signatures. With Ni^+ sharing the same $3d^9$ valence configuration as Cu^{2+} in the cuprate superconductors, these materials also display superconductivity, although the mechanism in the nicklelates is different due to the strong coupling between the layers [103, 104]. The optimal doped regime in thin films shows strange metal behaviour, while infinite-layer nickelates show the absence of long-range antiferromagnetic order [105].

Transition Metal Dichalcogenides Transition Metal Dichalcogenides (TMDs) are layered van der Waals materials with the stoichiometry MX_2, where M is a transition metal (e.g., Mo, W) and X is a chalcogen (e.g. S, Se, Te) [106, 107]. Recent interest has focused on the interplay between strong spin-orbit coupling (SOC), electronic correlations and direct bandgap – properties that make them particularly useful for electronic applications, spintronics and DNA sequencing. Layered TMDs have the structure $X - M - X$, with the transition metal sandwiched between two hexagonal planes of chalcogenides. Different combinations of the metals with the chalcogens lead to widely varying structures and electronic properties in TMDs. Experimental studies show that metal–insulator transitions (MITs) in TMDs are commonly intertwined with charge density wave (CDW) formation rather than arising from purely on-site Coulomb localization [108, 109]. In prototypical compounds such as 1T-TaS_2, ARPES and transport measurements reveal fluctuating magnetic order parameters in the Mott state and a transition to superconductivity driven by pressure [110–112]. Scanning tunnelling microscope (STM) pulses have been successfully used to manipulate the metal–insulator transition of 1T-TaS2, demonstrating the macroscopic controllability of the Mott phase [113].

ARPES measurements in 2H-$NbSe_2$ and 2H-$TaSe_2$ exhibit partial gapping of the Fermi surface restricted to nested momentum regions and a temperature-dependent pseudogap similar to the cuprates [114, 115]. This is further supported by optical conductivity experiments that show spectral weight in the midinfrared region along with a low-frequency Drude contribution [116]. Transport measurements on single crystals of $TaSe_2$ reveal that disorder enhances superconductivity by suppressing other competing orders such as CDW [117]. Collectively, these experimental results establish TMDs as a distinct class of correlated materials in which reduced dimensionality, band narrowing, and lattice reconstruction cooperate to produce metal–insulator behavior beyond conventional band theory.

Iron-Based Superconductors The iron-based superconductors (FeSCs), discovered in 2008, constitute a broad family of layered materials that share a common structure: a layer of iron atoms joined by tetrahedrally coordinated pnictogen (P, As) or chalcogen (S, Se, Te) anions arranged in a stacked

sequence; the layers are separated by alkali, alkaline-earth or rare-earth and oxygen/fluorine 'blocking layers' [118–121]. Doping or applying external pressure reveals coupled antiferromagnetic and structural transitions along with superconducting and nematic orders [122–124]. Electrical resistivity measurements in the neighbourhood of the quantum critical point show a crossover from a bad-metal behavior ($T-$linear resistivity) to a Fermi liquid behaviour (T^2-resistivity) [125]. Optical conductivity measurements indicate point to intermediate-to-strong electronic correlations [126].

ARPES measurements reveal a $k-$dependent superconducting gap and de Haas-van Alphen measurements indicate substantial quasiparticle mass enhancements, shedding more light on the correlated nature of the material [127, 128]. Strain-tuning measurements of the nematic susceptibility, and differential elastoresistance measurements have provided compelling evidence for the nematic transition and its surrounding fluctuations being the cause of the structural transition as well as the superconductivity [129, 130]. Neutron scattering and NMR measurements further reveal persistent low-energy spin fluctuations across wide regions of the phase diagram, supporting scenarios in which unconventional superconductivity emerges from the interplay of magnetic, orbital, and nematic degrees of freedom [131, 132].

Heavy-Fermion / Kondo-Lattice Systems Heavy-fermion materials are a class of strongly correlated electron systems typically realized in intermetallic compounds of rare earth metals (such as Ce, Sm and Yb) and actinides (such as U, Np and Pu), where localized f electrons hybridize with itinerant conduction bands [133, 134]. At high temperatures, these systems exhibit local-moment behavior governed by Curie–Weiss susceptibilities and incoherent transport, while at low temperatures the Kondo effect leads to the formation of a coherent many-body state with extremely large quasiparticle effective masses [43]. Experimentally, this crossover is most clearly manifested in transport and thermodynamic measurements: the electrical resistivity shows a characteristic maximum followed by a rapid drop signaling the onset of coherence, while the linear specific heat coefficient $\gamma = C/T$ reaches values orders of magnitude larger than in conventional metals, directly reflecting the heavy quasiparticle mass [135].

A defining feature of heavy-fermion materials is their proximity to magnetic quantum phase transitions, which can be accessed experimentally by pressure, chemical substitution, or magnetic field [136]. Near such quantum critical points (QCPs), transport measurements reveal pronounced non-Fermi-liquid behavior ($T-$linear resistivity) and a vanishing Hall response, along with a divergent effective quasiparticle mass as the transition is approached [137, 138]; these are all indications of the breakdown of electronic excitations near the transition. Neutron scattering experiments provide direct evidence for spin fluctuations down to very low temperatures, interplaying with the itinerant electrons at the QCP and potentially driving the superconducting transition [139, 140]. Quantum oscillation measurements through de Haas–van Alphen experiments further demonstrate Fermi surface reconstruction across the quantum critical point, highlighting the drastic change in Fermi volume [141]. Together, these experimental observations establish heavy-fermion compounds as paradigmatic systems in which strong local correlations, hybridization-driven coherence, and quantum critical fluctuations conspire to produce emergent low-energy quasiparticles and unconventional metallic behavior [142].

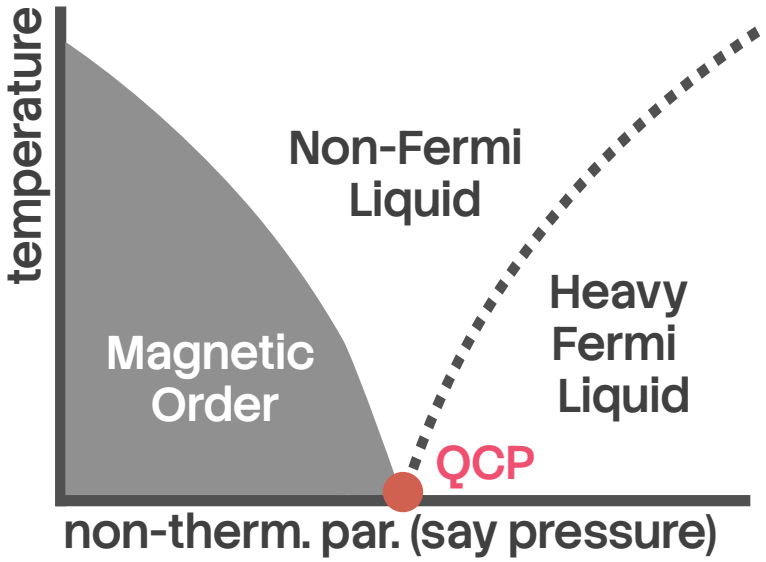

Figure 1.9: *Experimental phase diagram of the Kondo-breakdown class of heavy fermions compounds, as a function of the inter-layer hybridisation. For small hybridisation, the correlated $f-$layer remains decoupled from the itinerant layer in the ground state and undergoes magnetic ordering. For larger values, the $f-$layer undergoes Kondo screening by the itinerant layer, forming inter-layer entangled states. Lying in between these states is a quantum critical point with strange metallic behaviour arising from it at finite temperatures. The transition across the QCP at zero temperature is characterised by a change from a small to a large Fermi volume.*

1.4 Phenomenology of Mott transition in lattice models

1.4.1 The Infinite-Dimensional Hubbard Model

The Hubbard model (introduced in eq. **1.1**) presents one of the most fruitful playgrounds for investigating correlation-driven metal-insulator transitions and its various facets. This model, despite its conceptual simplicity, exhibits a rich variety of phenomena, including antiferromagnetism, superconductivity, and, most notably for our purposes, the correlation-driven Mott metal–insulator transition (MIT) [4, 143–145]. While exact solutions exist in the limits of $d = 1$ [146] and $d = \infty$ [147], the problem remains largely open in more realistic situations such as two and three spatial dimensions.

As discussed earlier, the limit of infinite dimensions presents a drastic simplification for the many-body scattering processes within the problem: the one-particle $k-$space self-energy becomes momentum-independent due to the vanishing of all non-local contributions (they scale as negative powers of the coordination number, which diverges in the limit of $d = \infty$). This simplification lies at the heart of dynamical mean-field theory and its ability to capture the Mott metal–insulator transition at both zero and finite temperatures for this limiting case [18, 147–151]. At half-filling and zero temperature, DMFT predicts a continuous transition as a function of U wherein the quasiparticle weight Z tends to zero at a critical interaction strength U_{c2}, signaling the vanishing of coherent Fermi liquid behavior and the opening of a Mott gap in the single-particle spectral function [18, 149].

The three-peak structure of the interacting spectral function, with a central quasiparticle resonance flanked by incoherent lower and upper Hubbard bands, indicates the presence of highly renormalised Landau quasiparticles [149]. A doping-driven continuous metal-insulator transition also exists for this model at zero temperature, marked by the vanishing of electronic compressibility at a critical value of the chemical potential [152]. The quantum critical point itself (at $T = 0$) is likely to be an exotic state, and important questions about it remain unanswered. *Is it possible to obtain a low-energy theory for the local gapless excitations precisely at the MIT, where the metal is on the brink of destruction? How do these excitations compare with those of the local Fermi liquid, e.g., in terms of self-energies and two-particle correlation functions?*

While the DMFT solution captures the zero temperature transition accurately, the self-consistently determined nature of the conduction bath renders the solution somewhat opaque and makes it difficult to write down an effective Hamiltonian for the low-energy theories. Since the simplest version Anderson impurity model does not contain the mechanism to stabilise a localised phase over a finite-sized parameter regime, an important question arising from the DMFT solution is: *what are the minimal changes that one must implement into the Anderson impurity model in order to capture such a metal-insulator transition (*$1/2$*-filled Hubbard model on the Bethe lattice in* $d = \infty$*), in sufficient accuracy and precision?* Finding such an impurity model would also reduce the considerable computational effort that is presently required in self-consistent approaches.

At finite temperatures, the interaction-driven as well as doping-driven Mott transition become first order, and is characterized by a region of phase coexistence and hysteresis [150, 153]. Two spinodal lines, $U_{c1}(T)$ and $U_{c2}(T)$, emerge; within this region metallic and insulating DMFT solutions coexist, and responses such as resistivity show a significant discontinuity [154]. These lines meet at a finite-temperature critical endpoint (U_c, T_c), above which there is no sharp distinction between metallic and insulating solutions and only a crossover exists between the Mott insulator and the Fermi liquid through a bad-metal regime, as the chemical potential is tuned [150, 152, 155–157]. The coexistence of metallic and insulating phases shows that the insulating solution is present within the many-body spectrum of the metallic phase. This naturally leads to the following question: *since a quantum impurity model lies at the heart of the self-consistency procedure, what does the presence of coexistence region mean for the Hamiltonian dynamics and the spectrum of this impurity model? Can the impurity model Hamiltonian display the emergence of the insulating state prior to the transition, through changes in the eigenstates?* Analytic insight of this kind is particularly important because approaching a coexistence region numerically is often fairly tricky.

The bad metal regime displays anomalous linear-in-temperature resistivity which corresponds to quantum critical ω/T scaling, along the quantum widom line [158, 159]. This is accompanied by the disappearance of the Drude peak in optical conductivity, signalling the loss of quasiparticle transport [158]. Similar quantum critical scaling is also obtained from DMFT solutions at very low temperatures, hinting at a "hidden" quantum criticality that is continuously connected to and responsible for the critical behaviour above the finite temperature endpoint [160]. Luttinger's theorem, which relates the poles of the Greens function within the Fermi volume to the number of electrons in the system at zero temperature, is satisfied within the Fermi liquid phase but is violated in the particle-hole asymmetric Mott insulator by a universal magnitude [161]. The emergence of a quantum critical regime at high temperatures and its connection to similar signatures at low temperatures suggests the presence of quantum fluctuations in the underlying impurity model that modify

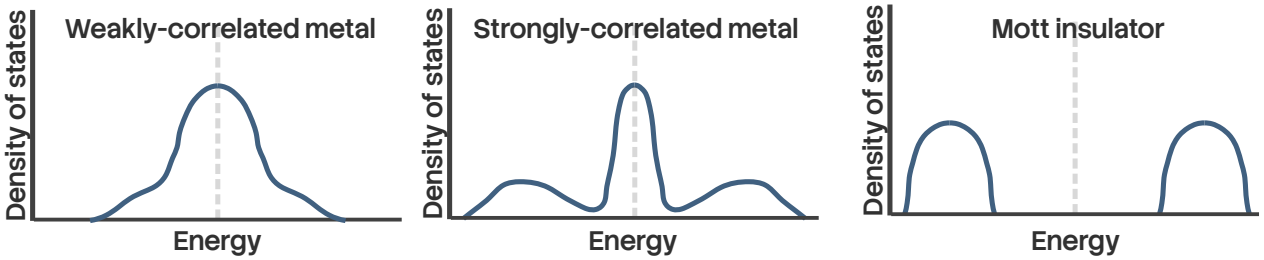

Figure 1.10: *Schematic depiction of the evolution of the local spectral function of the infinite-dimensional Hubbard model as obtained from dynamical mean-field theory (DMFT). At small values of the Hubbard interaction U, the spectral function has a central resonance, indicating good metallic behaviour. For larger values, the central resonance splits and satellite peaks emerge, indicating loss of some spectral weight from zero frequency. Beyond a critical value, the central peak disappears and only the satellite peaks remain, leading to a gapped Mott insulating state.*

the impurity-bath scattering processes and the associated impurity responses. One can therefore ask: *What are the fluctuations that destroy the metal and lead to the insulating phase? Can we obtain a universal theory for these competing tendencies?*

The above studies of single band models describe the Mott transition to be of the Mott-Hubbard kind (described in previous sections), where the size of the gap is determined by the double-occupancy cost U. In order to obtain transition of the charge-transfer kind, one needs to consider at least a two-band model. Indeed, in a non-degenerate two-band Hubbard model with a Charge-Transfer energy Δ for hopping from a $d-$orbital to a $p-$orbital, one sees a Mott-Hubbard transition when $U < \Delta$ and a charge-transfer transition when $U > \Delta$ [162]. The degenerate two-band model with inter-band local correlation shows successive Mott-Hubbard transitions at low temperatures whenever the filling passes through integer values and the interaction strength is intermediate [163].

In the later chapters of this thesis, we will be addressing several of these questions.

1.4.2 The two-dimensional Hubbard model

The 2D Hubbard model is one of the most well-studied models in condensed matter physics, particularly because of its paradigmatic role in Mott metal-insulator transition and its connections to the physics of copper oxide materials and $d-$wave superconductivity. Photoemission experiments reveal the presence of p and d bands close to the Fermi surface in such materials [100]; further work by Zhang and Rice showed that a specific combination of these orbitals governs the low-energy physics, leading to an effective description in terms of a single band Hubbard model [164]. The discovery of high-temperature superconductivity in nickelates and organic charge transfer salts has provided more platforms where the Hubbard model and its extensions can prove to be useful [165, 166].

While simple in appearance, the model has proved to be notoriously hard to solve except in highly specific parameter regimes, despite several decades of computational effort. This is due to several reasons [145]: (i) the presence of closely-lying energy scales arising from competing tendencies, (ii) the inability of several methods to either reach zero temperature or extrapolate to the thermodynamic limit, (iii) the likelihood of approximate/finite-size methods to overestimate tenden-

cies towards spontaneous symmetry breaking, and (iv) the presence of differing phases separated by slow crossovers without any sharp boundaries.

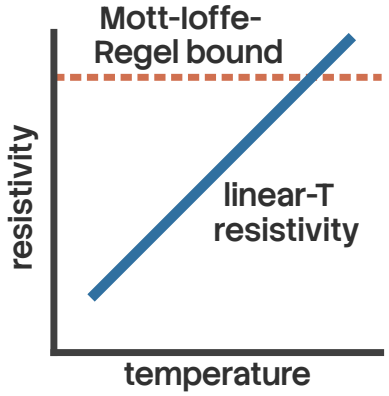

Figure 1.11: *Schematic of resistivity measurement in the strange metal phase of the overdoped cuprates [167]. There are two striking features. The first is the linear dependence of the resistivity on temperature, which cannot be explained from Landau's Fermi liquid theory. The second is the unbounded growth of the resistivity beyond the Mott-Ioffe-Regel (MIR) limit as temperature is increased. For a system of electrons on a lattice, the minimum possible mean-free path for propagating electrons is the lattice spacing, and this sets an upper bound for the resistivity, which is the MIR bound. Resistivity crossing the MIR bound implies that electrons are not the propagating degrees of freedom in such a system.*

At half-filling, the 2D Hubbard model has a spectral gap to charge excitations for any non-zero interaction strength [168–172]. The behaviour below the charge gap is described by a nonlinear sigma model with parameters that depend on the interaction strength U [173]. Upon tuning to finite temperatures, the system goes through a sequence of crossovers from the insulating ordered state to a Fermi liquid state with coherent quasiparticles into a non-Fermi liquid state with partial gapping of the Fermi surface [170, 172, 174]. The excitations of the non-Fermi liquid are described by a marginal Fermi liquid theory, and the Mott insulator displays topological order in the absence of spontaneous symmetry breaking [175]. *Capturing the momentum dependence of static and dynamical quantities in sufficient detail remains an open challenge in such problems, since results from cluster methods suffer from sensitivity to periodisation schemes [176].*

Away from half-filling but at weak coupling, the Neel order is accompanied by incommensurate magnetic orders (also called spiral magnetic state) with wave vectors away from (π, π), as seen from mean-field studies [177, 178]. Functional RG studies indicate that such solutions can exist up to fairly high doping if the superconducting instability is suppressed [179, 180]. Superconductivity with $d-$wave pairing has been achieved from renormalised perturbation studies as well as from diagrammatic Monte Carlo (diagMC), functional RG (fRG) calculations and unitary RG calculations [181–184]. More intricate competition between the superconducting and stripe states is found in three-band Hubbard models from variational Monte Carlo, cluster DMFT and DMRG calculations [185–187]. *Further work is necessary to resolve the closely-lying phases in such models.*

The phenomena of pseudogap (PG), where the Fermi surface acquires a momentum-dependent suppression of spectral weight, has also been observed above a certain temperature from methods

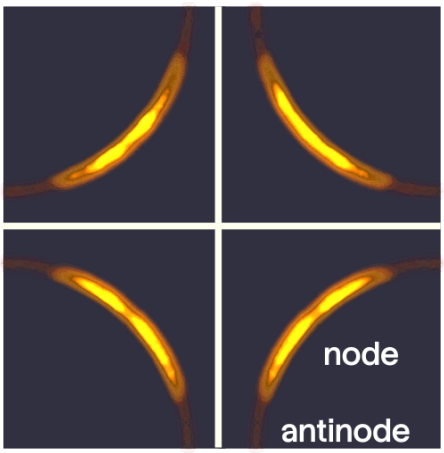

Figure 1.12: *ARPES measurement of the Fermi surface in the pseudogap of underdoped cuprates. The Fermi surface shows partial gapping around the antinodes and gapless behaviour around the nodes. Further doping leads to a reconstruction of the Fermi surface into the strange metal. (Adapted from [188])*

like diagMC and fRG [172, 189]. The gap is seen to open first near the antinodal point $(\pi, 0)$ and spread across the Fermi surface until it reaches the node $(\pi/2, \pi/2)$. The mechanism of the pseudogap at weak to intermediate coupling is found to be long-range antiferromagnetic (AF) correlations [190]. At underdoping, the pseudog is marked by a dominant charge gapping of the antinodes accompanied by strong spin-nematic fluctuations and sub-dominant superconducting phase fluctuations [184]. The pseudogap disappears at large doping when the Fermi surface undergoes a topological transition from hole-like to electron-like. To make matters more complicated, unitary renormalisation group studies find evidence of a shifting character of the pseudogap from spin to charge as the hole doping concentration is increased, and they indicate that the fluctuations present within such regions lead to the variety of ordered states that emerge at low temperatures [184]. Indeed, at strong coupling, the competition between various phases such as $d-$wave superconductivity, antiferromagnetic order and stripe states (spin/charge order modulating in real space) is an active subject of study. Recent studies using various methods like DMRG and iPEPS found that the period 8 charge stripe state is lower in energy than the superconducting state at strong coupling $U/t = 8$ and no next-nearest-neighbour hopping [191]. This was later corroborated by studies from variational Monte Carlo and other DMRG studies [192, 193]. *It is not yet clear whether the stripe period gets lowered as the interaction strength is increased.* At weaker coupling, the above methods report a reduced stability for the stripe state and increased tendency to realise a $d-$wave SC state [182, 194]. *Further investigation is necessary to map the crossovers between stripe and superconducting phases as doping is tuned. Moreover, the precise parameter regime in which the $d-$wave superconducting state becomes more stable than the stripe states is still an open question.*

At strong-coupling, the pseudogap is obtained below optimal doping and has been studied using dynamical methods such as cluster DMFT (DCA, dynamical cluster approximation) and cellular DMFT (CDMFT) [195–198]; in contrast to the weak-coupling feature (where the PG was borne

from long-range AF fluctuations), it is believed that the momentum-space differentiation in this regime is brought about by the proximity to the Mott insulator [197]. Conflicting indications are however provided by a fluctuation analysis that finds that long-lived long-ranged spin-fluctuations at the antinode are responsible for the opening of the PG [199]. The PG is found to be accompanied by non-Fermi liquid behaviour in the one-particle self-energy [196]. The doping value at which the non-Fermi liquid first appears was found to be lower for electron-doping than hole-doping [200]. At half-filling, DCA calculations reveal that the extent of the PG decreases as the next-nearest-neighbour hopping strength is increased [201]. Moreover, while DCA+continuous-time auxiliary field methods do not show any effect of van Hove singularities on the generation of the PG [201], DCA+determinantal Monte Carlo approaches identify the proximity to van Hoves as favouring the formation of a PG [202]. *Methods with better momentum-space resolution is necessary in order to identify the role of nesting and van Hoves on the pseudogap.*

The question of whether superconductivity can arise from repulsion was one of the primary motivations for studying the Hubbard model. DiagMC calculations reveal superconductivity in the ground state at weak-coupling and moderate doping, and with multiple symmetries of the gap [182, 203]. For higher couplings (which is relevant to the cuprates) and moderate doping, stripe states take over. Quantum Monte Carlo and DCA calculations suggest a $d_{x^2-y^2}$ pairing symmetry [169, 204]. DCA calculations on the 2D Hubbard mode suggest low-frequency spin fluctuations as the pairing glue for the superconductivity [205]. Unitary RG studies show the presence of preformed Cooper pairs near the antinodes at finite temperature states above the superconducting dome [184]. *The description of how various parent phases such as the pseudogap and strange metal precipitate superconductivity, in terms of the nature of fluctuations and the appropriate degrees of freedom, is still an open question.* Apart from superconductivity, several strongly correlated materials also exhibit strange metallicity, with transport properties that defy Fermi liquid theory, such as a linear-in-temperature resistivity that extends across large regimes of temperature. Within the Hubbard model, evidence for such $T-$linear resistivity and robustness across temperatures is available from CDMFT and determinantal Monte Carlo calculations [206, 207]. Studies using the unitary renormalisation group method reveal a two electron-one hole composite composite as the dominant excitation within the strange metal [184]. *More reliable methods are needed to access and understand the intermediate temperature regime of strange metals [145, 208].*

In the later chapters of this thesis, we will be addressing several of these questions.

1.4.3 Theories of heavy fermion materials

Heavy fermion materials represent the canonical environment for studying quantum phase transitions in correlated systems, owing to the explicit observation of quantum critical points at the boundary of antiferromagnetic order [209]. These systems involve the coexistence of magnetic moments (arising from localised $4f-$ and $5f-$electrons) and itinerant conduction electrons. The ground state of such a system is dictated by the competition between two kinds of interactions: internal spin-spin interaction J_{RKKY} between localised moments in the $f-$layer, and interaction J_K between $f-$electrons and conduction electrons [210].

Analogous to the screening of a single moment by a conduction bath, the lattice of $f-$moments are prone to undergoing Kondo screening by the conduction electrons through the inter-orbital hy-

bridisation J_K. The local Fermi liquid excitations associated with the spins overlap with each other and become delocalised, leading to a paramagnetic heavy Fermi liquid with highly renormalised quasiparticle mass [211]. Because of the delocalisation of the excitations of the $f-$spin through Kondo screening, the number of carriers increases to $1 + x$ compared to x coming purely from the conduction electrons; this is commonly referred to as the large Fermi surface phase [212]. Indeed, a perturbation theoretic calculation in the on-site interaction strength of the $f-$layer allows one to rewrite the two-orbital model as two decoupled quasiparticle bands with dispersions renormalised by phenomenological parameters like the quasiparticle residue [43]. These phenomenological parameters can be estimated from mean-field approaches [213, 214]. While the temperature T^* at which coherent Landau quasiparticles can proliferate was found to be generically lower than the single impurity Kondo temperature T_K [215], T^* was found to be higher than T_K near half-filling of the conduction layer [216]. At half-filling in both layers, the chemical potential passes through the middle of the gap between the two quasiparticle bands, and the system is a Kondo insulator [217]; for bipartite lattices, the ground state can be generally shown to be unique and a singlet ($S = 0$) [218–220].

Tuning the $f-$layer J_{RKKY} to large values compared to the inter-layer hybridisation can bring forth a quantum phase transition into a different ground state [221]. Experimental evidence suggests that this transition usually falls into one of two classes, depending on the behaviour of the Kondo singlet binding energy E^* in the paramagnetic phase. If E^* remains non-zero as the QCP is approached from the heavy Fermi liquid into the ordered state, the transition is said to fall in the SDW type, because it can be described as an instability of the heavy quasiparticles into a spin-density-wave ordered phase [222–224], in the form of a quantum action that involves the spatial and temporal fluctuations of an order parameter. $CeCu_2Si_2$ is a prototypical material that exhibits quantum criticality of the SDW type [134]. Because of the non-zero binding energy of the singlet state at the QCP, heavy quasiparticles survive across the transition and the Fermi surface is expected to evolve continuously, along with the order parameter [225, 226].

On the other hand, if E^* vanishes at the QCP, the transition belongs to the Kondo breakdown type, which is not compatible with the spin-density-wave scenario [227]. This happens when gapless spin fluctuations within the $f-$layer compete with the Kondo spin-flip processes and lead to the destruction of Kondo screening on the Fermi surface [136]. This is tracked by the vanishing of the quasiparticle residue of the heavy Fermi liquid as one approaches the QCP from the paramagnetic phase [82, 226]; this in turn also implies the critical non-Fermi liquid nature of the large Fermi surface at the transition [228]. *A complete understanding of the Kondo breakdown class of QCP is still missing in the literature.*

Due to the destruction of Kondo screening across the QCP in this class of materials, the localised $f-$spins cease to contribute to the Fermi surface away from the paramagnetic phase, and the Fermi surface shrinks discontinuously from large $(1 + x)$ to small (x) across the QCP [229]. *Such a change in the Fermi volume violates Luttinger's theorem which equates the particles density to the Fermi surface volume, and Oshikawa's topological flux-tuning argument suggests the presence of additional degrees of freedom that respond to the flux while not being part of the Fermi surface. Additional work is needed to identify these degrees of freedom.* Materials like $YbRh_2Si_2$ and $CuCu_{6-x}Au_x$, among others, appear to exhibit behaviour that falls in this class [230, 231]. As mentioned before, several features of this class of experiments are not compatible with the SDW instability transition of the heavy Fermi liquid; these include the jump discontinuous change in

Fermi volume mentioned previously (and an associated discontinuous change in the hall conductivity) [232], vanishing of the scale T_{FL} (associated with the onset of Fermi liquid behaviour) and the divergence of the quasiparticle mass upon approaching the QCP from the paramagnet [227], a universal linear-in-temperature strange metal behaviour of the resistivity in an intermediate finite temperature quantum critical regime above the QCP [230, 233] and the possible lack of magnetic ordering immediately away from the QCP [234, 235]. *At present, the connection of the physics of heavy fermion models like the periodic Anderson model to strange metal behaviour is an open question; the mechanism for generating such behaviour from the QCP remains to be completely understood.*

A fairly comprehensive model for describing the phase transition in heavy fermion systems is the periodic Anderson model (PAM):

$$H_{\mathrm{PAM}} = \varepsilon_f \sum_{i,\sigma} n_{i,f,\sigma} + U_f \sum_i n_{i,f,\uparrow} n_{i,f,\downarrow} + \sum_{k,\sigma} \epsilon_k n_{k,c,\sigma} + V_\perp \sum_{i,\sigma} \left(c^\dagger_{i,f,\sigma} c_{i,c,\sigma} + \mathrm{h.c.} \right) , \tag{4.1}$$

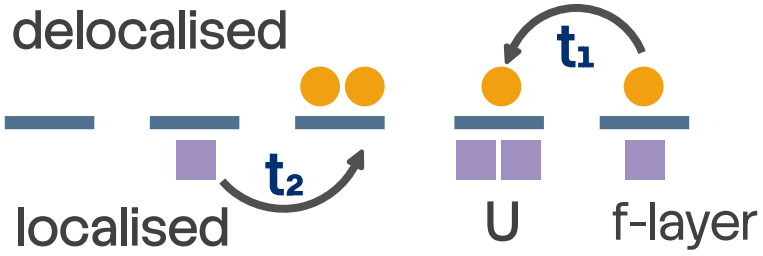

Figure 1.13: *Schematic model of heavy fermions. There are two layers: one uncorrelated delocalised layer (top), and a correlated localised layer (bottom). The delocalised layer has very weak correlation and a large bandwidth, leading to small masses for the carriers. The localised layer has very strong local repulsion leading to extremely narrow bands and highly correlated hopping for the carriers. These two layers hybridise with each other through hopping or spin-exchange processes. This results in a modification of the properties of the weakly correlated layer by the strongly-correlated layer.*

where the subscripts f and c in the operators indicate whether they belong to the $f-$layer or the conduction electron layer. At the Kondo breakdown QCP and in the RKKY-dominated phase, the inter-layer hybridisation is expected to be irrelevant and the $f-$ and conduction electrons fail to bind into a Kondo singlet in the ground state [236, 237]. Several numerical and analytical methods have been applied to investigate various parts of the phase diagram and probe varying aspects of the phenomenology. *However, many of these methods suffer from a lack of predictions of various transport measures like strange metallicity, and they often suffer from insufficient resolution in frequency or momentum space.*

One of the major approaches applied to this problem is that of extended DMFT (EMDFT), in which one maps the PAM to a self-consistently determined Bose-Fermi-Kondo model [82, 238]. One of the smoking gun signatures of quantum criticality is the scaling of dynamical properties as $\omega/k_B T$ due to temperature being the only remaining energy scale in the system; this is captured from EMDFT calculations [226]. Numerically exact unbiased methods like DMRG and auxiliary

field quantum Monte Carlo demonstrate the abrupt change in Fermi surface volume across the transition [239, 240]. Parton methods that implement a slave-particle representation followed by a $1/N$ expansion reveal jump in the conductivity across the transition, with the small Fermi surface arising from a spin-charge separation of the $f-$electrons into a fractionalised Fermi liquid phase [241, 242]. *Currently, a complete description of the Kondo breakdown driven transition that captures the behaviour of both the heavy Fermi liquid and the RKKY-dominated phase is missing.*

In the later chapters of this thesis, we will be addressing several of these questions.

1.5 An alternative perspective on metal-insulator transitions: Entanglement renormalisation and holography

Role of entanglement in fermionic systems The present millennium has seen a rapid surge in the use of quantum entanglement towards the study of quantum and condensed matter systems [243–248]. Being non-local by nature, it is helpful in tracking correlations among particles across both small and large distances, giving valuable insight into the nature of the ground state and the low-energy excitations. Entanglement, in the form of various measures like entanglement entropy and mutual information, is the engine that gives rise to new low-energy degrees of freedom from a renormalisation group (RG) perspective, and is therefore key to understanding and characterising phase transitions and criticality in quantum matter. For instance, entanglement entropy is at the heart of understanding the so-called topological states of matter that can be described in terms of a purely topological effective Lagrangian and have a robust ground state degeneracy and gapless edge states [249–269]. In contrast to systems with local interactions whose subsystem entanglement entropy scales with the area of the subsystem [245, 270, 271], topologically ordered systems have an additional topological term dubbed the topological entanglement entropy [272–290] that quantifies the long-ranged nature of the entanglement in such systems. The non-local nature arises from the fact that the ground state of such a system cannot be made separable (non-entangled) by the application of purely local unitary transformations [247, 291, 292]. Although the topological piece of the entanglement entropy is subdominant compared to the non-topological piece that scales with the subsystem area, it can be isolated by considering the *tripartite information* I_3 of a specific arrangement of subsystems [279, 282]. More generally, all multipartite information I_N beyond mutual information ($N \geq 3$) can be expressed as the product of the topological entanglement entropy and the Euler characteristic of the chosen arrangement of subsystems [293].

More pertinent to the work at hand, however, is the entanglement in free fermionic systems. In this thesis, we will consider relativistic Dirac fermions in two dimensions, both massless and massive. They emerge in several condensed matter systems [294], appearing at the surfaces of three-dimensional topological insulators [295–298], quasi-2D organic materials [299–301] and in arficial materials like cold atoms, molecular and microwave crystals [302–308]. For massless critical systems (or conformal field theories (CFTs)) living in one spatial dimension, the entanglement entropy of a single subsystem of length l scales as $\sim \frac{c}{3} \ln l$ [309–318], where c is the conformal central charge of the CFT. The case of multiple subsystems is more involved, but has been solved [316, 319, 320]. For massive fermions, the entanglement entropy (or rather the entropic $c-$function, which is the spatial derivative of the entropy) can be expressed in the form of differential equations which need to be

solved numerically [319, 321–323]. The solutions lend themselves to small and large mass expansions, reducing to $\frac{1}{3}\ln\frac{l}{\epsilon}-\frac{1}{6}(ml\ln ml)^2+O((ml)^2)$ for the case of small ml, and to $\sim (ml)^{-1/2}e^{-2ml}$ for that of large ml, both for a single interval. The $\ln l$ behaviour is a specific case of the more general $l^{d-1}\ln l$ violation of the area law, as observed in $d-$dimensional fermionic critical systems [319, 324–338]. This violation arises from the non-local nature of the real-space quantum fluctuations that exist in quantum critical fermionic systems.

While there is no geometry-independent subdominant term in the entanglement entropy of free fermionic systems [339, 340], it *is* possible to generate such a term by placing the system on a manifold with a non-trivial topology, say a cylinder, and inserting a magnetic flux through the cylinder [339, 341–344]. For a massless Dirac fermion, if there are ϕ number of electronic flux quanta piercing the system, the additional term that is generated in the entanglement entropy of a subsystem of sufficiently (as defined in Ref. [339]) large length is of the form $\frac{1}{6}\ln\left|2\sin\frac{\phi}{2}\right|$ [339, 342]. There is evidence from numerical computations on discrete models that such a term is a signature of the specific field theory and encodes universality [344–346]. In this thesis, we put this idea on a stronger analytical footing by relating the flux-dependent term to a topological invariant of the field theory, its Luttinger volume [24, 25, 50, 51, 347–349]. Given by the number of $k-$states enclosed by the Fermi surface, Luttinger volume V_L has proved to be one of the most important indicators that distinguish metals from insulating states of matter. In metals, V_L is constrained by the number of particles in the system, following Luttinger's theorem [24, 25, 50]. As shown most prominently in Ref. [50], Luttinger's theorem depends crucially on the presence of extended states in the metal that can respond to flux insertion experiments. We demonstrate in Chapter 7 that indeed it is this subdominant term in the entanglement entropy that carries this dependence and hence encodes Luttinger's theorem. It is known that for strongly-interacting states like Mott insulators or quantum hall states, V_L is modified due to changes in the topology of the Fermi surface [51, 347–349]. In this context, we relate the topological invariant on the metallic side (Luttinger volume) to the topological invariants (the Chern numbers) in the integer quantum hall system that the metal would lead to when placed in a perpendicular magnetic field. Such a relation makes explicit the transmutation of the extended states into the localised states of the insulating phase.

Entanglement hierarchy and the holographic principle The leading geometry-dependent piece is also found to have intriguing properties of its own. The fact that the free fermion Lagrangian is diagonal in momentum space means that the entanglement arises purely from real space quantum fluctuations, and this allows us to study the entanglement of subsystems of varying sizes in momentum space. We find that the entanglement entropy hence obtained has a Russian doll-like nested structure, such that increasing the size of the subsystem in momentum space gradually reveals layers of entanglement. In fact, we argue that such transformations between the subsystems amount to a renormalisation group (RG) flow in the space of the field theories with varying spectral gaps, and the above-mentioned hierarchy in the entanglement entropy then stretches across the RG transformations. The precise prescription for choosing the subsystems is described in Chapter 7. We also show, simultaneously, that the hierarchy holds across multipartite entanglement measures, leading to an onion-like structure where increasing the number of parties in the entanglement measure (mutual information, tripartite information, 4-partite information and so on) leads to additional entanglement that did not exist before. More importantly, we interpret the hierarchy of entanglement

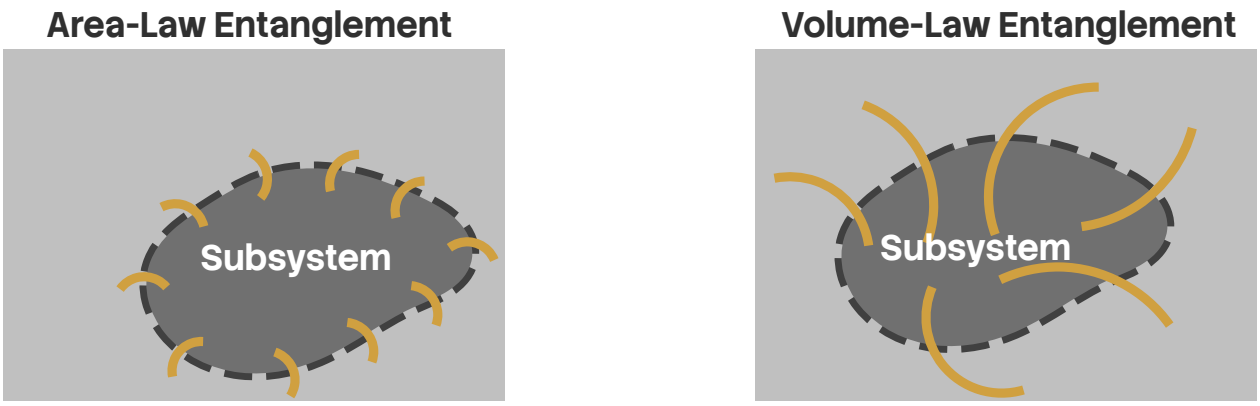

Figure 1.14: *Two classes of entanglement found in quantum systems, grouped by how entanglement measures scale with subsystem size. In systems with a spectral gap (left), correlations decay exponentially with distance, and only the degrees of freedom on the boundary of the subsystem entangle appreciably with the rest of the system. As a result, entanglement entropy of the subsystem scales with the area L^{d-1} of the subsystem: $S_{EE} \propto L^{d-1}$. In contrast, for gapless systems, correlations are more long-ranged and may even span the entire system (for critical states). In such cases, degrees of freedom beyond the proximity of the boundary can entangle with the rest of the system, and such systems can achieve modified area-law $S_{EE} \propto L^{d-1} \ln L$ or even volume-law $S_{EE} \propto L^d$*

.

along the RG flow as the emergence of an additional dimension [350–352], allowing us to define a measure of distance using some non-negative measure of entanglement, like the mutual information [353–356]: the more the entanglement, the less will be the distance between those points. Generation of an additional dimension is, of course, the essence of the AdS/CFT conjecture or, more generally, the holographic principle.

The holographic principle [357–365], also known as the gauge-gravity duality, posits that there exists a duality relation between a quantum field theory with a gauge field, and a gravity theory having one additional spatial dimension [366–369]. The additional dimension can be visualised as a renormalisation group flow that starts from the boundary field theory and extends into the bulk [370–379]. The most popular realisation of the holographic principle is the AdS/CFT correspondence that links a super-symmetric gauge theory with a string theory [380–382]. The essence of holography is that all the information about the bulk gravity theory is already contained within the boundary gauge theory; this idea is very similar to the discovery by Bekenstein and Hawking [383–385] that the entropy of a black hole is determined by its surface area. In fact, Ryu and Takayanagi proposed a generalisation of this result where the entanglement entropy of subsystem region a CFT is determined by the area of the minimal surface that bounds the region in the bulk [386, 387]. The AdS/CFT correspondence happens to be a strong-weak duality - it relates a strongly coupled CFT to a theory of weak classical gravity. This allows physicists to use the holographic principle and convert a problem of strong quantum correlation to one of classical gravity which can be solved using well-known methods [360, 361]. This has led to new insights in various topics of high energy and condensed matter physics, such as the viscosity of the quark-gluon plasma [388], the response functions of the Bose-Hubbard model [389, 390], and the

phenomenology of non-Fermi liquids [391–394], holographic superconductors [395–400], striped phases [401–403] and holographic Fermi liquids [404–408]. An overview of the metallic states (phases that satisfy Luttinger's theorem) and their connections to the gauge-gravity duality have been provided in Refs. [409–411].

Of course, on the flip side, the holographic principle also implies that studying the boundary conformal theory can provide insights into the nature of the bulk quantum gravity theory. This however requires constructing, *ab initio*, the emergent dimension by starting from the field theory, and has proved to be more difficult than the converse, mostly because the field theories are often strongly coupled. Nevertheless, there exist some examples of constructive attempts towards a bulk gravity theory [348, 349, 355, 356, 412–445]. Some well-known approaches include the momentum shell renormalisation approach of Sung-Sik Lee [425–428] and the multi-scale entanglement renormalisation ansatz (MERA) of Vidal [429–433]; both use certain forms of RG flow to generate the extra spatial dimension. The former integrates out high momentum degrees of freedom in favour of generating dynamics for the boundary gauge field, with the RG trajectory variable giving rise to the additional spatial dimension [359]. On the other hand, the MERA works by disentangling degrees of freedom in real space, creating a tensor network in the process [434–436] and leading to a renormalisation in the entanglement. The renormalised entanglement is interpreted as the additional dimension [431]. There exist other approaches that also proceed via entanglement renormalisation, such as the exact holographic mapping [355, 356] (EHM) and the unitary renormalisation group [348, 349, 437] (URG) that operate purely through unitary transformations and have been explicitly shown to lead to a holographic tensor network along the RG flow. Apart from these, there is a body of work due largely to Ki-Seok Kim that provides a geometric description of Wilson's numerical renormalisation group [36,438–440,446], and creates a more general RG framework in terms of an order-parameter field that extends the Ads/CFT correspondence to non-critical theories [441–445].

Questions on entanglement and holography become particularly interesting in systems of critical fermions. As mentioned earlier, such systems differ from bosonic and gapped systems through the presence of longer-ranged entanglement that follows a modified area-law [330, 332] as well as topological features arising from the incompressibility of the Fermi volume [50, 51]. Fermi surface gapping phase transitions in such systems are often driven by changes in topological quantum numbers and the nature of the inter-particle entanglement [136,348,349]. Constructing a framework for fermionic criticality is therefore an active area of research with consequences for important systems such as unconventional superconductors, strange metals and heavy fermions [137,175,184, 447]. Still less is known about the holographic implications of such systems. We extend this body of work by providing an explicit demonstration of the holographic principle in the form of a simple and tractable exact holographic mapping (EHM) for a free fermion system with and without a mass gap. Our program yields analytic relations between the RG flow parameters and their dual bulk quantities such as distances and curvature. This also allows us to study the consequences of a critical Fermi surface (lying precisely at the quantum phase transition) on the nature of the holographic space.

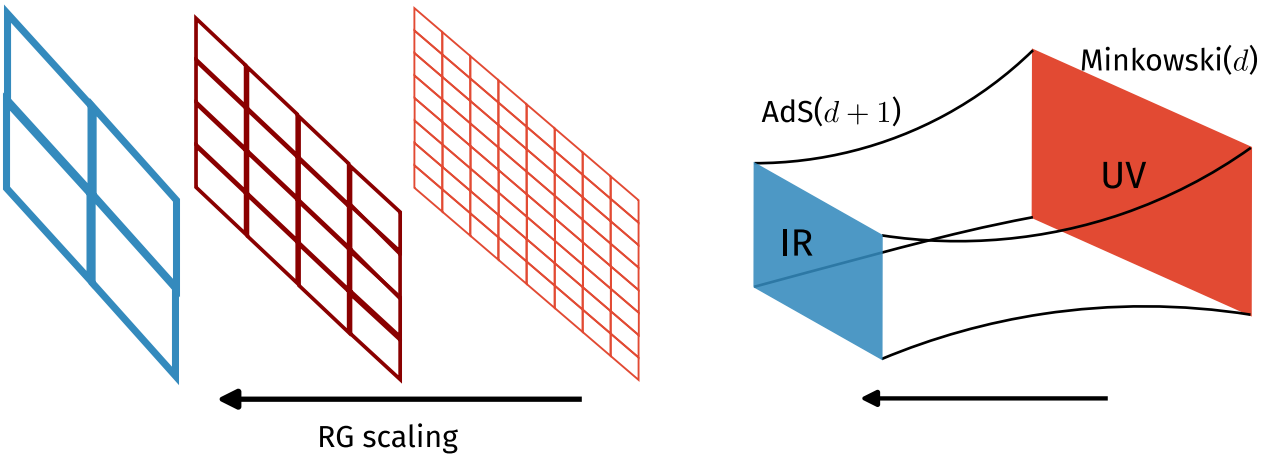

Figure 1.15: *The AdS-CFT correspondence (right), or more generally, the holographic principle maps a quantum field theory in $d-$dimensions to a gravity theory in one extra dimension. The quantum field theory is said to reside at the boundary of this $d+1$-dimensional space. The additional dimension in the gravity theory arises from the hierarchy of quantum fluctuation scales present within the electronic interactions of the quantum field theory, and can be revealed by considering renormalisation group flows (left) of the boundary theory.*

1.6 A New Auxiliary Model Approach Towards Fermionic Criticality

To motivate the construction of a new auxiliary model approach in this thesis, we now write down some important outstanding questions that we will address using our approach.

1. *Can we construct an impurity-based auxiliary model approach that describes interaction-driven electronic phase transitions without imposing self-consistency?* As discussed in the preceding sections, one of the most prominent examples of auxiliary model approaches in the study of correlated fermionic models is dynamical mean-field theory (DMFT). However, solutions arising from DMFT and it's extensions such as cellular DMFT and dynamical cluster approximation suffer from a lack of transparency owing to the numerical approach towards self-consistency. To go beyond such approaches, can we explicitly construct an impurity model that maps to the local physics of some interacting lattice model, and recover the low energy physics of the latter by solving the former? Apart from being much more transparent due to the explicit nature of the construction, such an approach would also be more tractable – because of the simplicity of impurity models – than studying the full lattice model.

2. *Can such an approach map the renormalisation group flows of an auxiliary impurity model to those of a correlated lattice model?* Both impurity and lattice models, due to the presence of many-particle interactions, typically involve a hierarchy of energy scales that are coupled to one another. The framework of renormalisation group (RG) is a powerful approach to identify the "important" physics at various energy scales. In particular, it can be used to identify low-energy effective Hamiltonians that describe the essential physics in the ground state and at

low temperatures, and the microscopic Hamiltonian is said to "flow" into such low-energy fixed-point Hamiltonians. Can our auxiliary model approach map the renormalisation group flows between the impurity and lattice models, at least in terms of the local physics? This would make the underlying mechanism for the RG flows as well as the various fixed-point theories much more transparent.

3. *Does such an auxiliary model approach preserve symmetries of the microscopic/effective theories of the lattice model, and obey various conservation principles such as Luttinger's theorem?* Importantly, an auxiliary model mapping for a lattice model should preserve the symmetries of the full Hamiltonian. It should also, ideally, show the emergence of conservation principles and spectral sum rules. Luttinger's theorem, as an example of such a sum rule, equates the electron density in a system with the Fermi volume in the presence of interactions, as long as the excitations are electronic. Violations in Luttinger's theorem often signal interaction-driven transitions from Fermi liquids to Mott insulators or non-Fermi liquids. Can the above auxiliary model approach capture changes in Luttinger's theorem? An associated question is whether such an approach can show the emergence of Luttinger surfaces through the appearance of zeros in the one-particle Greens function. Such signatures would have topological consequences because the Luttinger sum rule is protected by topological invariants.

4. *Is it possible to describe topological transitions using such an approach?* It is becoming increasingly clear that various materials exhibit phase transitions that are not necessarily tied to the spontaneous breaking of a local symmetry and fall outside the Ginzburg-Landau-Wilson paradigm. Examples include (i) the Mott transition driven by a charge gap but without necessarily a spin gap, (ii) the Kondo breakdown QCP scenario in heavy fermion materials where the large-to-small Fermi surface transition is observed to to be separate from magnetic ordering and (iii) transition from a trivial insulator to a topological insulator driven by changes in band topology. Such transitions do not exhibit the appearance of non-zero local order parameters, and are instead often described by changes in topological invariants and entanglement patterns. One can therefore ask: is such an auxiliary model approach capable of tracking such generalised order parameters?

5. *Can such an auxiliary model approach capture the effects of multiple orbitals and momentum-space differentiation?* One of the primary difficulties with many of the numerical methods typically employed in such problems is the high computational complexity (in time as well as memory) and the inability to resolve momentum-space features to sufficient precision. The increased complexity becomes particularly important in several classes of problems such as multi-band models, which are pertinent to investigations into orbital-selective transitions, heavy fermion physics and twisted bilayer graphene, among many others. The lack of momentum-space resolution is relevant to studies of the pseudogap (PG) phase that is observed in the underdoped high-Tc superconductors; the PG is known to display partial gapping of the Fermi surface around the antinodes while remaining gapless around the nodes. The approach proposed here can benefit in this regard in two ways: the explicit construction might be helpful to avoid the computational cost of a self-consistency loop whilst providing

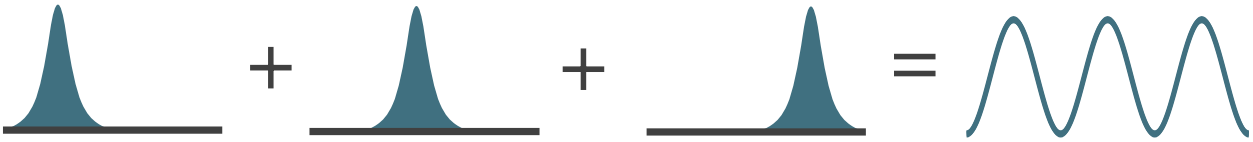

Figure 1.16: *For the problem of a single electron, one can construct the full delocalised translation-invariant eigenstate by taking a superposition of the localised wavefunctions at each site. This is equivalent to repeatedly applying translation operations of varying distances on a single localised wavefunction associated with an arbitrarily chosen lattice site. A similar construction also works for the Hamiltonian, where by applying translation operators on the nearest-neighbour hybridisation processes of a single site, one can reconstruct the full tight-binding model.*

access to a large number of momentum states, and (ii) the mapping to an impurity model makes the analysis much more tractable.

Within the thesis, we have developed a new approach towards studying correlated models with strong local interactions. The strategy goes as follows: We first identify a quantum impurity model that represents faithfully the local physics of the lattice model we are targeting. This is done by solving the impurity and studying it's phenomenology. In order to capture specific aspects of the physics, the impurity model may need to be enhanced by, say, allowing for multiple impurities, or embedding it onto a lattice instead of a continuum, etc. Having identifies the appropriate impurity model, we apply many-body translation operators to the impurity model Hamiltonian in order to restore translation invariance and map it to the target lattice Hamiltonian in the process.

For single-particle wavefunctions $\psi_i(r_i)$, the one-particle momentum operator p_i generates a one-particle translation operator $T_i(\mathbf{a})$ that translates the real-space operators associated with the particle i by the vector $\mathbf{a}$. By applying them to the dynamics of local potential wells at each site, these translation operators can be used to construct a translation-invariant Hamiltonians such as the tight-binding model; a similar application on the local wavefunctions generates delocalised translation-invariant Bloch states. Analogous to the single-particle case, one can construct a many-particle translation operator T [448] that act on an $N-$particle state $\Psi(r_1, r_2, ...r_N)$: $T(\mathbf{a}) = e^{-i\mathbf{a}\cdot\mathbf{P}} = \prod_{i=1}^{N} T_i(\mathbf{a})$, where $\mathbf{P}$ is the total momentum operator. The action of T is to shift all local operators by $\mathbf{a}$ and to multiply all $k-$space operators with a phase shift $e^{i\mathbf{a}\cdot\mathbf{k}}$.

Using such a many-body translation operator, we are able to map both the Hamiltonian as well as eigenstates between the "local" auxiliary impurity model and the translation-invariant lattice model. This leads to specific relations between various observables such as correlations and spectral functions, as well as between entanglement measures. This set of mappings can be used to reconstruct the low-energy physics of the lattice model by starting from that of the auxiliary model.

1.6.1 Important features of the "tiling" auxiliary model approach

Local transition as a diagnostic of lattice transition As mentioned in the preceding paragraphs, the approach developed within this thesis maps the low-energy physics of the lattice model to that of an impurity model with local correlation, hence rendering the problem much more tractable.

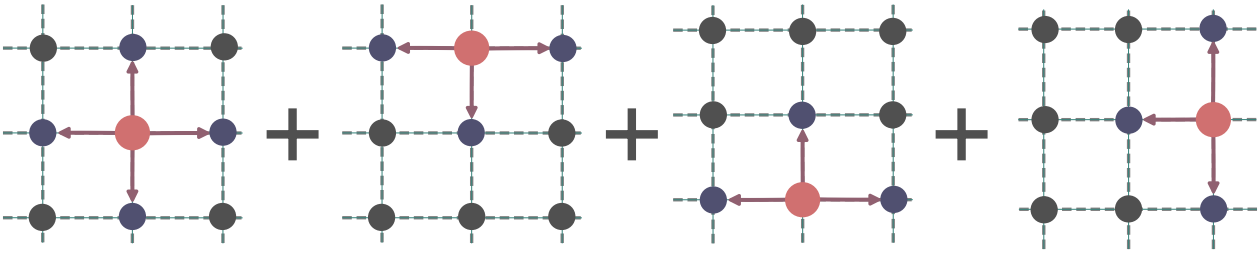

Figure 1.17: *Schematic depiction of the "tiling" step in our auxiliary model approach. In order to restore translation invariance and map our impurity model to a lattice model, we apply many-body translation operators on our impurity model Hamiltonian for all lattice sites; this reconstructs the full lattice model, and leads to relations between the auxiliary model couplings and the lattice model couplings.*

This, for example, means that the presence of local Fermi liquid excitations on the impurity site marked by a broad central Kondo resonance in the local density of states corresponds to a Landau Fermi liquid phase for the lattice model. By inducing a gap in the impurity site density of states and stabilising the local moment states, one can also model a Mott insulator on the lattice model. More exotic phases such as non-Fermi liquids can be engineered by enhancing the impurity model with competing interactions that lead to a pseudogap in the impurity density of states. Taken together, this maps the renormalised groups flows of the impurity model to that of the lattice model.

Restoring translation symmetry using a many-body Blochs' theorem At the heart of the impurity-lattice model mapping are many-body translation operators T. Indeed, they serve to restore translation invariance lost by the introduction of the impurity site into the lattice: $H_{\rm lat} = \sum_i T^\dagger(\mathbf{r}_i) H_{\rm aux} T(\mathbf{r}_i)$. In a similar fashion, the translation operators serve to "extend" the auxiliary model eigenstates into those of the lattice model: $\Psi = \sum_i T^\dagger(\mathbf{r}_i)\psi_{\rm aux}$. This constitutes a many-body version of Bloch's theorem [448, 449], where local impurity model states are superposed to form delocalised wavefunctions that span the lattice. This step plays the role of the self-consistent loop in DMFT by restoring the discrete translational invariance of the lattice model. This is also seen from the fact that translation operation leads to effective renormalised relations for the lattice model couplings in terms of the auxiliary model quantities. These translation operators also introduce non-local inter-auxiliary model contributions into various correlation functions.

Mapping across Greens functions and entanglement measures One of the main results of our tiling approach is the set of mappings between real-space and momentum-space Greens functions of the auxiliary model and the lattice model. This makes it much more tractable to characterise phases on the lattice model. The mappings take into account correlations within a single impurity model as well as contributions from inter-auxiliary model connections, through the translation operators. In the absence of long-range critical fluctuations, these expressions can be truncated to terms up to a few sites away from the impurity complex, and this makes the practical computation possible. Near the transition, it becomes necessary to work with much larger number of sites.

Lattice-embedding as a route to encoding lattice geometry and band topology Another important aspect of the tiling approach is the ability to incorporate lattice effects such as momentum-space differentiation and topological features. We accomplish this by considering an auxiliary model directly on the appropriate lattice. This ensures that the Hamiltonian couplings of the auxiliary model inherit the symmetries of the lattice, and the auxiliary model quantities are then sensitive to lattice effects. This, for example, has allowed us to study a momentum-space anisotropic pseudogap phase in the context of an extended Hubbard model on a 2D square lattice.

1.7 Summary Of Chapters

For the readers' convenience, we now briefly describe the content and layout of the following chapters.

After the introduction, the *Methods and Preliminaries* chapter describes the various techniques and some preliminary ideas employed throughout the thesis. The chapter begins by deriving the unitary renormalisation group formalism and describes it's various properties and a practical protocol for implementing it. That is followed by a demonstration of the implementation of the unitary RG method on a paradigmatic model – the single-channel Kondo model [42]. Through this study of a classic problem, various aspects of the method are clarified. In order to provide more insights, the chapter also details how the unitary RG method is related to other RG-based methods that rely on canonical transformations, such as Poor Man's scaling, Schrieffer-Wolff transformation and CUT (continuous unitary transformation) RG. Apart from the URG, the chapter also describes an iterative diagonalisation method that has been used within this thesis to compute various correlation functions and entanglement measures from the hierarchy of Hamiltonians obtained from the URG. Since various entanglement measures have been used throughout the later chapters, we have also added a section on them here - what they mean, what are their inter-relations, why they are important and how one can compute some of them. The chapter concludes by describing some of the other strategies that have been employed to reduce computational costs in various projects.

In Chapter 3, *Kondo Frustration via Charge Fluctuations: A Route to Mott Localisation in Infinite Dimensions*, we study our first impurity model, the extended Anderson model with local correlation U_b in the conduction bath. We demonstrate that this model hosts a local version of the Mott metal-insulator transition on the Bethe lattice in infinite dimensions, as seen from DMFT. At a critical value of the ratio of U_b and the impurity-bath hybridisation, the effective impurity model shows a transition from a Kondo screened phase into an unscreened local moment phase. For the case of attractive local bath correlations, the model sheds new light on several aspects of the DMFT phase diagram. For example, the $T = 0$ metal-to-insulator quantum phase transition (QPT) is preceded by an excited state QPT (ESQPT) where the local moment eigenstates are emergent in the low-lying spectrum. Long-ranged fluctuations are observed near both the QPT and ESQPT, suggesting that they are the origin of the quantum critical scaling observed recently at high temperatures in DMFT simulations. The $T = 0$ gapless excitations at the quantum critical point display particle-hole interconversion processes, and exhibit power-law behaviour in self-energies and two-particle correlations. These are signatures of non-Fermi liquid behaviour that emerge from the partial breakdown of the Kondo screening. A many-body perturbation theoretic treatment of the Hubbard sidebands

reveals that they are comprised of holon-doublon excitations created by the hybridisation of the impurity site with the conduction bath. These excitations consist of decoupled local Fermi liquids for the holons and doublons at the lowest order, which, at higher orders, become coupled via correlated holon-doublon scattering between impurity and bath.

In Chapter 4, *A New Auxiliary Model Approach for Interacting Electrons: Mapping Impurity Models To Lattice Models*, we lay out the details of the auxiliary model method developed to map impurity models to lattice models. We first motivate the general idea behind auxiliary model methods. This is followed by a construction of the many-body translation operators. We use this, along with a many-body Bloch's theorem, to construct lattice models from quantum impurity models and relate their eigenstates. This then allows us to map correlations functions, self-energies and entanglement measures across models. In particular, we demonstrate how the presence of the conduction bath introduces $k-$space resolution in various quantities.

In Chapter 5, *Mott Criticality as the Confinement Transition of of a Pseudogap-Mott Metal: Insights on Mott Transition and Pseudogap in Two Dimensions*, we apply the auxiliary model tiling method to a lattice-embedded extended SIAM. Applying a many-body tiling scheme to the fixed-point impurity model uncovers a lattice model with electron interactions and Kondo physics. At half-filling, the interplay between Kondo screening and bath charge fluctuations in the impurity model leads to Fermi liquid breakdown. This reveals a pseudogap phase characterized by a non-Fermi liquid (the Mott metal) residing on nodal arcs, gapped antinodal regions of the Fermi surface (Luttinger surfaces), and an anomalous scaling of the electronic scattering rate with frequency. The eventual confinement of holon-doublon excitations of this exotic metal obtains a continuous transition into the Mott insulator. Our results identify the pseudogap as a distinct long-range entangled quantum phase, and offer a new route to Mott criticality beyond the paradigm of local quantum criticality. The phase appears to encode multipartite entanglement, as seen from a large value of the quantum Fisher information. The critical point at the pseudogap-Mott insulator boundary is found to be described by the exactly-solvable Hatsugai-Kohmoto model. The emergence of Luttinger surfaces alters the anomaly structure associated with the generalized symmetry of the FS [44–46]. The corresponding topological charge is defined via the Luttinger–Ward functional. This charge is modified by Green's function zeros, signalling a shift in the underlying anomaly. Within our framework, this reorganization grants topological protection to the RG flows terminating in the PG regime, ensuring the stability of its NFL excitations.

In Chapter 6, *Competing tendencies In Heavy Fermion Systems: Kondo screening vs. Mott localisation*, we study a periodic Anderson model where we treat both the $c-$ and $f-$layers as extended Hubbard models, and analyse it using the tiling approach developed and implemented in the earlier chapters. We first study the case of half-filling and obtain a Kondo insulator at large values of the inter-band hybridisation. We also study the more interesting case of a Mott metal in the $f-$layer hybridising with the $c-$electrons.

In Chapter 7, *Holography of Entanglement in 2D Free Fermions: Emergent Geometry and Fermionic Criticality*, we provide an explicit demonstration of the holographic principle in the form of a simple and tractable exact holographic mapping (EHM) for a free fermion system with and without a mass gap. Our program yields analytic relations between the RG flow parameters and their dual bulk quantities such as distances and curvature. This also allows us to study the consequences of a critical Fermi surface (lying precisely at the quantum phase transition) on the nature

of the holographic space.

We conclude in the final chapter by summarising the main results obtained within the thesis, in terms of the methods developed as well as insights obtained into the behaviour of various models. We describe the impact of these results on the field, the broad conclusions emerging from them and some open questions resulting from the work.

Chapter 2

Methods and Preliminaries

2.1 The Unitary renormalisation group method

The URG method was introduced and formalised in refs. [175,184,348,349]. This section is adapted from those references and expanded wherever required.

Description of the problem

We are given a Hamiltonian $\mathcal{H}$ which is not completely diagonal in the occupation number basis of the electrons, $\hat{n}_k$: $[\mathcal{H}, n_k] \neq 0$. k labels any set of quantum numbers depending on the system. For spin-less Fermions it can be the momentum of the particle, while for spin-full Fermions it can be the set of momentum and spin. There are terms that scatter electrons from one quantum number k to another quantum number k'.

We take a general Hamiltonian,

$$\mathcal{H} = H_e \hat{n}_{q\beta} + H_h \left(1 - \hat{n}_{q\beta}\right) + c^\dagger_{q\beta} T + T^\dagger c_{q\beta} \tag{1.1}$$

Formally, we can decompose the entire Hamiltonian in the subspace of the electron we want to decouple $(q\beta)$.

$$\mathcal{H} = \begin{array}{c} \begin{array}{cc} |1\rangle & |0\rangle \end{array} \\ \begin{pmatrix} H_1 & T \\ T^\dagger & H_0 \end{pmatrix} \end{array} \tag{1.2}$$

The basis in which this matrix is written is $\{|1\rangle, |0\rangle\}$ where $|i\rangle$ is the set of all states where $\hat{n}_{q\beta} = i$. The aim of one step of the URG is to find a unitary transformation U such that the new Hamiltonian $U\mathcal{H}U^\dagger$ is diagonal in this already-chosen basis.

$$\tilde{\mathcal{H}} \equiv U\mathcal{H}U^\dagger = \begin{array}{c} \begin{array}{cc} |1\rangle & |0\rangle \end{array} \\ \begin{pmatrix} \tilde{H}_1 & 0 \\ 0 & \tilde{H}_0 \end{pmatrix} \end{array} \tag{1.3}$$

U_q is defined by

$$\tilde{\mathcal{H}} = U_q \mathcal{H} U_q^\dagger \text{ such that } \left[\tilde{\mathcal{H}}, n_q\right] = 0 \tag{1.4}$$

It is clear that U is the diagonalizing matrix for $\mathcal{H}$. Hence we can frame this problem as an eigenvalue equation as well. Let $|\psi_1\rangle, |\psi_0\rangle$ be the basis in which the original Hamiltonian $\mathcal{H}$ has no off-diagonal terms corresponding to $q\beta$. Hence, we can write

$$\mathcal{H} |\psi_i\rangle = \tilde{H}_i |\psi_i\rangle, i \in \{0, 1\} \tag{1.5}$$

Since $|\psi_i\rangle$ is the set of eigenstates of $\mathcal{H}$ and $|i\rangle$ is the set of eigenstates in which $U\mathcal{H}U^\dagger$ has no off-diagonal terms corresponding to $q\beta$, we can relate $|\psi_i\rangle$ and $|i\rangle$ by the same transformation : $|\psi_i\rangle = U^\dagger |i\rangle$. We can expand the state $|\psi_i\rangle$ in the subspace of $q\beta$:

$$|\psi_i\rangle = \sum_{j=0,1} |j\rangle \langle j| |\psi_i\rangle \equiv |1\rangle |\phi_1^i\rangle + |0\rangle |\phi_0^i\rangle \tag{1.6}$$

where $|\phi_j^i\rangle = \langle j| |\psi_i\rangle$. If we substitute the expansion 1.2 into the eigenvalue equation 1.5, we get

$$\left[H_e \hat{n}_{q\beta} + H_h \left(1 - \hat{n}_{q\beta}\right) + c_{q\beta}^\dagger T + T^\dagger c_{q\beta}\right] |\psi_i\rangle = \tilde{H}_i |\psi_i\rangle \tag{1.7}$$

The diagonal parts $H_e = \text{tr}\left[\mathcal{H}\hat{n}_{q\beta}\right]$ and $H_e = \text{tr}\left[\mathcal{H}\left(1 - \hat{n}_{q\beta}\right)\right]$ can be separated into a purely diagonal part $\mathcal{H}^d$ that contains the single-particle energies and the multi-particle correlation energies or Hartree-like contributions, and an off-diagonal part $\mathcal{H}^i$ that scatters between the remaining degrees of freedom $k\sigma \neq q\beta$. That is,

$$H_e \hat{n}_{q\beta} + H_h \left(1 - \hat{n}_{q\beta}\right) = \mathcal{H}^d + \mathcal{H}^i$$

This gives

$$\left[c_{q\beta}^\dagger T + T^\dagger c_{q\beta}\right] |\psi_i\rangle = \left(\tilde{H}_i - \mathcal{H}^i - \mathcal{H}^d\right) |\psi_i\rangle \tag{1.8}$$

Obtaining the decoupling transformation

We now define a new operator $\hat{\omega}_i = \tilde{H}_i - \mathcal{H}^i$, such that

$$\left[c_{q\beta}^\dagger T + T^\dagger c_{q\beta}\right] |\psi_i\rangle = \left(\hat{\omega}_i - \mathcal{H}^d\right) |\psi_i\rangle \tag{1.9}$$

From the definition of $\hat{\omega}_i$, we can see that it is Hermitian and has no term that scatters in the subspace of $q\beta$, so it is diagonal in $q\beta$ and we can expand it as $\hat{\omega}_i = \hat{\omega}_i^1 \hat{n}_{q\beta} + \hat{\omega}_i^0 \left(1 - \hat{n}_{q\beta}\right)$. Using the expansion 1.6, we can write

$$\hat{\omega}_i |\psi_i\rangle = \hat{\omega}_i^1 |1\rangle |\phi_1^i\rangle + \hat{\omega}_i^0 |0\rangle |\phi_0^i\rangle \tag{1.10}$$

Since the only requirement on $|\psi_i\rangle$ is that it diagonalize the Hamiltonian in the subspace of $q\beta$, there is freedom in the choice of this state. We can exploit this freedom and choose the $|\phi_{0,}^i\rangle$ to be an eigenstates of $\hat{\omega}_i^{1,0}$ corresponding to real eigenvalues $\omega_i^{1,0}$:

$$\left[\mathcal{H}^d + c_{q\beta}^\dagger T + T^\dagger c_{q\beta}\right] |\psi_i(\omega_i)\rangle = \left(\omega_i^1 - \mathcal{H}^d\right) |1\rangle |\phi_1^i\rangle + \left(\omega_i^0 - \mathcal{H}^d\right) |0\rangle |\phi_0^i\rangle \tag{1.11}$$

If we now substitue the expansion 1.6 and gather the terms that result in $\hat{n}_{q\beta} = 1$, we get

$$c^\dagger_{q\beta} T \left|0\right\rangle \left|\phi^i_0\right\rangle = \left(\omega^1_i - \mathcal{H}^d\right) \left|1\right\rangle \left|\phi^i_1\right\rangle \tag{1.12}$$

Similarly, gathering the terms that result in $\hat{n}_{q\beta} = 0$ gives

$$T^\dagger c_{q\beta} \left|1\right\rangle \left|\phi^i_1\right\rangle = \left(\omega^0_i - \mathcal{H}^d\right) \left|0\right\rangle \left|\phi^i_0\right\rangle \tag{1.13}$$

We now define two many-particle transition operators:

$$\begin{aligned} \eta^\dagger(\omega^1_i) &= \frac{1}{\omega^1_i - \mathcal{H}^d} c^\dagger_{q\beta} T \equiv G_1 c^\dagger_{q\beta} T \\ \eta(\omega^0_i) &= \frac{1}{\omega^0_i - \mathcal{H}^d} T^\dagger c_{q\beta} \equiv G_0 T^\dagger c_{q\beta} \end{aligned} \tag{1.14}$$

wher G_j is the propagator $\frac{1}{\omega^j_i - \mathcal{H}^d}$. We can write this compactly as

$$\eta(\hat{\omega}) = G T^\dagger c_{q\beta} = \frac{1}{\hat{\omega}_i - \mathcal{H}^d} T^\dagger c_{q\beta} \tag{1.15}$$

where $\hat{\omega}_i = \omega^0_i \left(1 - \hat{n}_{q\beta}\right) + \omega^1_i \hat{n}_{q\beta} = \begin{pmatrix} \omega^1_i & \\ & \omega^0_i \end{pmatrix}$ is a 2x2 matrix and $\mathcal{H}^d = \mathcal{H}^d_0 \left(1 - \hat{n}_{q\beta}\right) + \mathcal{H}^d_1 \hat{n}_{q\beta}$ and $G = \left(\hat{\omega} - \mathcal{H}^d\right)^{-1}$. It is easy to check that this reproduces the previous forms of $\eta_0(\omega^0_i)$ and $\eta^\dagger_1(\omega^1_i)$. We will later find that it is important to demand that these two be Hermitian conjugates of each other; that constraint is imposed on the denominators:

$$\eta^\dagger(\omega^0_i) = \eta^\dagger(\omega^1_i) \implies \frac{1}{\omega^1_i - \mathcal{H}^d} c^\dagger_{q\beta} T = c^\dagger_{q\beta} T \frac{1}{\omega^0_i - \mathcal{H}^d} \tag{1.16}$$

Henceforth we will assume that this constraint has been imposed.

In terms of these operators, eq. 1.13 becomes

$$\left|1\right\rangle \left|\phi^i_1\right\rangle = \eta^\dagger \left|0\right\rangle \left|\phi^i_0\right\rangle, \quad \left|0\right\rangle \left|\phi^i_0\right\rangle = \eta \left|1\right\rangle \left|\phi^i_1\right\rangle \tag{1.17}$$

These allow us to write

$$\left|\psi_1\right\rangle = \left|1\right\rangle \left|\phi^i_1\right\rangle + \left|0\right\rangle \left|\phi^i_0\right\rangle = (1 + \eta) \left|1\right\rangle \left|\phi^i_1\right\rangle, \quad \left|\psi_0\right\rangle = \left(1 + \eta^\dagger\right) \left|0\right\rangle \left|\phi^i_0\right\rangle \tag{1.18}$$

Recalling that $\left|\psi_i\right\rangle = U^\dagger \left|i\right\rangle$, we can read off the required transformation:

$$U_1 = 1 + \eta \tag{1.19}$$

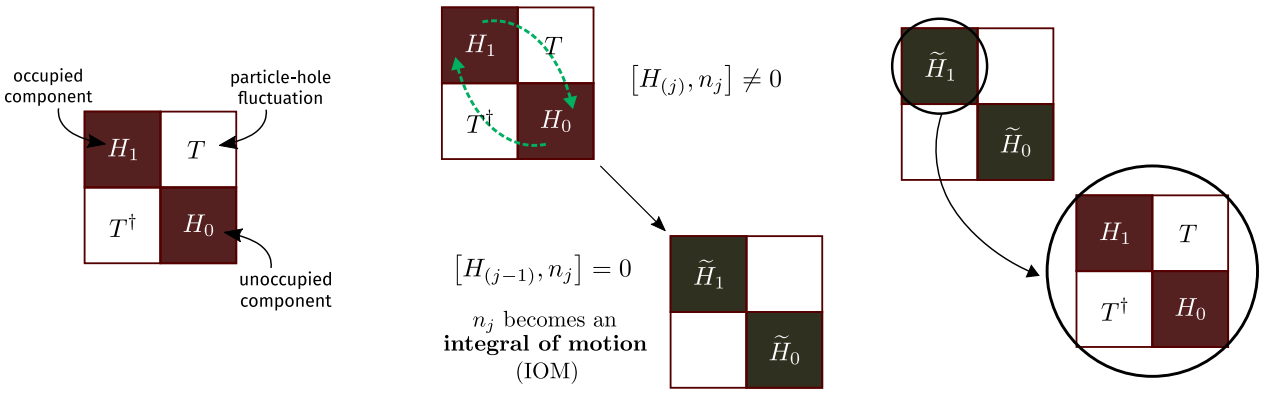

Figure 2.1: *Three steps of the URG: Decompose the Hamiltonian in a 2×2 matrix, apply the unitary operator to rotate it, then repeat these steps with one of the rotated blocks.*

Properties of the many-body transition operators

The operators η have some important properties. First is the Fermionic nature:

$$\eta^2 = \eta^{\dagger 2} = 0 \quad \left[c^{\dagger 2} = c^2 = 0\right] \tag{1.20}$$

Second is:

$$\begin{aligned} |1\rangle |\phi_1^i\rangle = \eta^\dagger |0\rangle |\phi_0^i\rangle = \eta^\dagger \eta |1\rangle |\phi_1^i\rangle \implies \eta^\dagger \eta = \hat{n}_{q\beta} \\ |0\rangle |\phi_0^i\rangle = \eta |1\rangle |\phi_1^i\rangle = \eta\eta^\dagger |\phi_0^i\rangle \implies \eta\eta^\dagger = 1 - \hat{n}_{q\beta} \end{aligned} \tag{1.21}$$

and hence the anticommutator

$$\implies \left\{\eta, \eta^\dagger\right\} = 1 \tag{1.22}$$

Note that the three equations in 1.21 work only when applied on the eigenstate $|\psi_i\rangle$ and not any arbitrary state.

$$\begin{aligned} \eta^\dagger \eta |\psi_i\rangle = |1\rangle |\phi_1^i\rangle = \hat{n}_{q\beta} |\psi_i\rangle \\ \eta\eta^\dagger |\psi_i\rangle = |0\rangle |\phi_0^i\rangle = \left(1 - \hat{n}_{q\beta}\right) |\psi_i\rangle \\ \left\{\eta^\dagger, \eta\right\} |\psi_i\rangle = |\psi_i\rangle \end{aligned}$$

Form of the unitary operators

Although we have found the correct similarity transformations U_i (eqs. 1.19), we need to convert them into a unitary transformation. Say we are trying to rotate the eigenstate $|\psi_1\rangle$ into the state $|1\rangle$. We can then work with the transformation

$$U_1 = 1 + \eta \tag{1.23}$$

In this form, this transformation is not unitary. It can however be written in an exponential form:

$$U_1 = e^\eta \tag{1.24}$$

using the fact that $\eta^2 = 0$. It is shown in ref. [450] that corresponding to a similarity transformation e^{ω},there exists a unitary transformation e^{G} where

$$G = \tanh^{-1}\left(\omega - \omega^{\dagger}\right) \tag{1.25}$$

Applying that to the problem at hand gives

$$U_1^{\dagger} = \exp\left\{\tanh^{-1}\left(\eta - \eta^{\dagger}\right)\right\} \tag{1.26}$$

Let $x = \tanh y$. Then,

$$x = \frac{e^{2y}+1}{e^{2y}-1} \implies y = \frac{1}{2}\log\frac{1+x}{1-x} \implies e^{y} = e^{\tanh^{-1}x} = \sqrt{\frac{1+x}{1-x}} \tag{1.27}$$

Therefore,

$$\exp\left\{\tanh^{-1}\left(\eta - \eta^{\dagger}\right)\right\} = \frac{1+\eta-\eta^{\dagger}}{\sqrt{\left(1+\eta^{\dagger}-\eta\right)\left(1-\eta^{\dagger}+\eta\right)}} = \frac{1+\eta-\eta^{\dagger}}{\sqrt{1+\left\{\eta,\eta^{\dagger}\right\}}} = \frac{1}{\sqrt{2}}\left(1+\eta-\eta^{\dagger}\right) \tag{1.28}$$

The *unitary* operator that transforms the entangled eigenstate $|\psi_1\rangle$ to the state $|1\rangle$ is thus

$$U_1 = \frac{1}{\sqrt{2}}\left(1+\eta^{\dagger}-\eta\right) \tag{1.29}$$

It can also be written as $\exp\left\{\frac{\pi}{4}\left(\eta^{\dagger}-\eta\right)\right\}$ because

$$\begin{aligned}
\exp\left\{\frac{\pi}{4}\left(\eta^{\dagger}-\eta\right)\right\} &= 1 + \left(\eta^{\dagger}-\eta\right)\frac{\pi}{4} + \frac{1}{2!}\left(\eta^{\dagger}-\eta\right)^2\left(\frac{\pi}{4}\right)^2 + \frac{1}{3!}\left(\eta^{\dagger}-\eta\right)^3\left(\frac{\pi}{4}\right)^3 + \ldots \\
&= 1 + \left(\eta^{\dagger}-\eta\right)\frac{\pi}{4} - \frac{1}{2!}\left(\frac{\pi}{4}\right)^2 - \frac{1}{3!}\left(\eta^{\dagger}-\eta\right)\left(\frac{\pi}{4}\right)^3 + \frac{1}{4!}\left(\frac{\pi}{4}\right)^4 + \ldots \\
&= \cos\frac{\pi}{4} + \left(\eta^{\dagger}-\eta\right)\sin\frac{\pi}{4} \\
&= \frac{1}{\sqrt{2}}\left(1+\eta^{\dagger}-\eta\right)
\end{aligned} \tag{1.30}$$

There we used

$$\left(\eta^{\dagger}-\eta\right)^2 = \eta^{\dagger 2} + \eta^2 - \left\{\eta^{\dagger},\eta\right\} = -1 \quad \left[\because \eta^2 = \eta^{\dagger 2} = 0\right] \tag{1.31}$$

and hence

$$\left(\eta^{\dagger}-\eta\right)^3 = -1\left(\eta^{\dagger}-\eta\right) \tag{1.32}$$

and so on.

Effective Hamiltonian

We can now compute the form of the effective Hamiltonian that comes about when we apply U_1 - that is - when we rotate one exact eigenstate $|\psi_1\rangle$ into the occupied Fock space basis $|1\rangle$. From eq. 1.29,

$$\begin{aligned} U_1\mathcal{H}U_1^\dagger &= \frac{1}{2}\left(1+\eta^\dagger-\eta\right)\mathcal{H}\left(1+\eta-\eta^\dagger\right) \\ &= \frac{1}{2}\left(1+\eta^\dagger-\eta\right)\left(\mathcal{H}+\mathcal{H}\eta-\mathcal{H}\eta^\dagger\right) \\ &= \frac{1}{2}\left(\mathcal{H}+\mathcal{H}\eta-\mathcal{H}\eta^\dagger+\eta^\dagger\mathcal{H}+\eta^\dagger\mathcal{H}\eta-\eta^\dagger\mathcal{H}\eta^\dagger-\eta\mathcal{H}-\eta\mathcal{H}\eta+\eta\mathcal{H}\eta^\dagger\right) \\ &= \frac{1}{2}\left(\mathcal{H}^d+\mathcal{H}^i+\mathcal{H}^I+\mathcal{H}\eta-\mathcal{H}\eta^\dagger+\eta^\dagger\mathcal{H}+\eta^\dagger\mathcal{H}\eta-\eta^\dagger\mathcal{H}\eta^\dagger-\eta\mathcal{H}-\eta\mathcal{H}\eta+\eta\mathcal{H}\eta^\dagger\right) \\ &= \frac{1}{2}\left(\mathcal{H}^d+\mathcal{H}^i+\mathcal{H}^I+\left[\eta^\dagger-\eta,\mathcal{H}\right]+\eta^\dagger\mathcal{H}\eta-\eta^\dagger\mathcal{H}\eta^\dagger-\eta\mathcal{H}\eta+\eta\mathcal{H}\eta^\dagger\right) \end{aligned} \tag{1.33}$$

In the last two lines, we expanded the Hamiltonian into the three parts $\mathcal{H}^d, \mathcal{H}^i$ and a third piece $\mathcal{H}^I \equiv c^\dagger_{q\beta}T + T^\dagger c_{q\beta}$.

For reasons that will become apparent, we will split the terms into two groups:

$$\tilde{\mathcal{H}} = \frac{1}{2}\left(\underbrace{\mathcal{H}^d+\mathcal{H}^i+\left[\eta^\dagger-\eta,\mathcal{H}\right]+\eta^\dagger\mathcal{H}\eta+\eta\mathcal{H}\eta^\dagger}_{\text{group 1}}+\overbrace{\mathcal{H}^I-\eta^\dagger\mathcal{H}\eta^\dagger-\eta\mathcal{H}\eta}^{\text{group 2}}\right) \tag{1.34}$$

Group 2 can be easily shown to be 0. Note that terms that have two η or two $\eta^\dagger$ sandwiching a $\mathcal{H}$ can only be nonzero if the intervening $\mathcal{H}$ has an odd number of creation or destruction operators:

$$\eta\mathcal{H}\eta = \eta c_q^\dagger T\eta \tag{1.35}$$

and

$$\eta^\dagger\mathcal{H}\eta^\dagger = \eta^\dagger T^\dagger c_q\eta^\dagger \tag{1.36}$$

Group 2 becomes

$$\text{group 2} = \mathcal{H}^I - \eta^\dagger T^\dagger c_q\eta^\dagger - \eta c_q^\dagger T\eta = c_q^\dagger T + T^\dagger c_q - \eta^\dagger T^\dagger c_q\eta^\dagger - \eta c_q^\dagger T\eta \tag{1.37}$$

To simplify this, we use the relation

$$\begin{aligned} \eta c_q^\dagger T\eta &= \frac{1}{\omega_i^0-\mathcal{H}^d}T^\dagger c_q c_q^\dagger T\eta \\ &= T^\dagger c_q\frac{1}{\omega_i^1-\mathcal{H}^d}c_q^\dagger T\eta \quad \text{[using eq. 1.16]} \\ &= T^\dagger c_q\eta^\dagger\eta \quad \text{[using eq. 1.15]} \\ &= T^\dagger c_q\hat{n}_q \quad \text{[using eq. 1.21]} \end{aligned} \tag{1.38}$$

which gives

$$\eta c_q^\dagger T \eta = T^\dagger c_q \tag{1.39}$$

Taking the Hermitian conjugate of eq. 1.39 gives

$$\eta^\dagger T^\dagger c_q \eta^\dagger = c_q^\dagger T \tag{1.40}$$

Substituting the expressions 1.39 and 1.40 into the expression for group 2, 1.37, shows that is vanishes. This leaves us only with group 1:

$$\widetilde{\mathcal{H}} = \frac{1}{2}\left(\mathcal{H}^d + \mathcal{H}^i + \overbrace{\eta^\dagger \mathcal{H}\eta + \eta\mathcal{H}\eta^\dagger}^{\text{group A}} + \underbrace{\left[\eta^\dagger - \eta, \mathcal{H}\right]}_{groupB}\right) \tag{1.41}$$

Group A simplifies in the following way. First note that $\eta^\dagger \mathcal{H}^I \eta = \eta^\dagger \mathcal{H}^I \eta = 0$ must be 0 because it will involve consecutive $c_{q\beta}$ or consecutive $c_{q\beta}^\dagger$. We are therefore left with the diagonal part of $\mathcal{H}$, which is $H_e \hat{n}_{q\beta} + H_h\left(1 - \hat{n}_{q\beta}\right)$.

$$\eta^\dagger \left[H_e \hat{n}_{q\beta} + H_h\left(1 - \hat{n}_{q\beta}\right)\right]\eta + \eta\left[H_e \hat{n}_{q\beta} + H_h\left(1 - \hat{n}_{q\beta}\right)\right]\eta^\dagger = \eta^\dagger H_h \eta + \eta H_e \eta^\dagger \tag{1.42}$$

This can be shown to be equal to the diagonal part:

$$\text{group A} = \eta^\dagger H_h \eta + \eta H_e \eta^\dagger = H_e \hat{n}_{q\beta} + H_h\left(1 - \hat{n}_{q\beta}\right) = \mathcal{H}^d + \mathcal{H}^i \tag{1.43}$$

It can also be shown that

$$\text{group B} = \left[\eta^\dagger - \eta, \mathcal{H}\right] = 2\left[c_{q\beta}^\dagger T, \eta\right] \tag{1.44}$$

Putting it all together,

$$\tilde{\mathcal{H}} = \mathcal{H}^d + \mathcal{H}^i + \left[c_{q\beta}^\dagger T, \eta\right] \tag{1.45}$$

The renormalizing in the Hamiltonian is

$$\Delta\mathcal{H} = \tilde{\mathcal{H}} - \mathcal{H}^d - \mathcal{H}^i = \left[c_{q\beta}^\dagger T, \eta\right] \tag{1.46}$$

Because of eq. 1.44, it can also be written as

$$\Delta\mathcal{H} = \frac{1}{2}\left[\eta^\dagger - \eta, \mathcal{H}_X\right] = \frac{1}{2}\left[\eta^\dagger - \eta, \mathcal{H}\right] \tag{1.47}$$

This form will be useful later when we make the connection with one-shot Schrieffer-Wolff transformation and CUT RG.

To check that the renormalised Hamiltonian indeed commutes with $\hat{n}_{q\beta}$,

$$\begin{aligned}
\left[\widetilde{\mathcal{H}}, \hat{n}_{q\beta}\right] &= \left[\left[c_{q\beta}^\dagger T, \eta\right], \hat{n}_{q\beta}\right] = \left[c_{q\beta}^\dagger T\eta, \hat{n}_{q\beta}\right] - \left[\eta c_{q\beta}^\dagger T, \hat{n}_{q\beta}\right] \\
&= c_{q\beta}^\dagger T \eta \hat{n}_{q\beta} - \hat{n}_{q\beta} c_{q\beta}^\dagger T\eta \qquad \left[2^{\text{nd}}\ [\ .\ ] \text{ is 0},\ \because c_{q\beta}^\dagger \hat{n}_{q\beta} = \hat{n}_{q\beta}\eta = 0\right] \\
&= c_{q\beta}^\dagger T\eta - c_{q\beta}^\dagger T\eta = 0
\end{aligned} \tag{1.48}$$

Fixed point condition

Within the URG, it is a prescription that the fixed point is reached when the denominator of the RG equation vanishes. This is equivalent to either $\omega_i^1 = \mathcal{H}_1^d$ or $\omega_i^0 = \mathcal{H}_0^d$. This shows that at the fixed point, one of the eigenvalues of $\hat{\omega}_i$ matches the corresponding eigenvalue of the diagonal blocks. This also leads to the vanishing of the off-diagonal block, because eqs. **1.12** and **1.13** gives

$$c_{q\beta}^\dagger T \left|0\right\rangle \left|\phi_0^i\right\rangle = \left(\omega_i^1 - \mathcal{H}_1^d\right) \left|1\right\rangle \left|\phi_1^i\right\rangle = 0 \implies c_{q\beta}^\dagger T = 0 \tag{1.49}$$

Multiple off-diagonal terms

There is a subtle assumption in the definitions eq. **1.14**. In order for η to be the Hermitian conjugate of $\eta^\dagger$, $\mathcal{H}_d$ cannot have any information that relates to the structure of T. To see why, say the total off-diagonal term is composed of two parts: $T = T_1 + T_2$.

$$\begin{aligned} \eta &= \frac{1}{\omega_0 - \mathcal{H}_d}\left(T_1^\dagger + T_2^\dagger\right) c = \left[\frac{1}{\omega^0 - E_1^0} T_1^\dagger c + \frac{1}{\omega^0 - E_2^0} T_2^\dagger c\right] \\ \eta^\dagger &= \frac{1}{\omega^1 - \mathcal{H}_d} c^\dagger \left(T_1 + T_2\right) = \left[\frac{1}{\omega^1 - E_1^1} c^\dagger T_1 + \frac{1}{\omega^1 - E_2^1} c^\dagger T_2\right] \end{aligned} \tag{1.50}$$

where $\mathcal{H}_d T_i^\dagger c = E_i^0 T_i^\dagger c$ and $\mathcal{H}_d c^\dagger T_i = E_i^1 c^\dagger T_i$. We can now see that in order for $\eta = \left(\eta^\dagger\right)^\dagger$ to hold, two conditions must be met:

$$\omega^0 - E_1^0 = \omega^1 - E_1^1, \quad \omega^0 - E_2^0 = \omega^1 - E_2^1 \tag{1.51}$$

This will not hold generally. The correct solution is to realize that each such off-diagonal term T_i will come with its own quantum fluctuation scale ω_i.

$$\begin{aligned} \eta &= \sum_i \frac{1}{\omega_i^0 - E_i^0} T_i^\dagger c \\ \eta^\dagger &= \sum_i \frac{1}{\omega_i^1 - E_1^1} c^\dagger T_i \end{aligned} \tag{1.52}$$

If we now impose the condition that $\eta = \left(\eta^\dagger\right)^\dagger$, we get the relations

$$\omega_i^0 - \omega_i^1 = E_i^0 - E_1^1 \tag{1.53}$$

and so

$$\eta^\dagger - \eta = \sum_i \frac{1}{\omega_i^0 - E_i^0}\left(c^\dagger T_i - T_i^\dagger c\right) \tag{1.54}$$

The expression for the renormalization will not be just $\left[c^\dagger T, \eta\right]$ in this case. That form will be non-Hermitian. The correct form is obtained from the more general form $\left[\eta^\dagger - \eta, \mathcal{H}_X\right]$:

$$\begin{aligned}\Delta\mathcal{H} &= \frac{1}{2}\left[\eta^\dagger - \eta, c^\dagger T + T^\dagger c\right] = \frac{1}{2}\sum_{ij}\frac{1}{\omega_i^0 - E_i^0}\left[c^\dagger T_i - T_i^\dagger c, c^\dagger T_j + T_j^\dagger c\right] \\ &= \frac{1}{2}\sum_{ij}\frac{1}{\omega_i^0 - E_i^0}\left[\hat{n}\left(T_i T_j^\dagger + T_j T_i^\dagger\right) - (1-\hat{n})\left(T_i^\dagger T_j + T_j^\dagger T_i\right)\right] \\ &= \frac{1}{2}\sum_{ij}\left(\frac{1}{\omega_i^0 - E_i^0} + \frac{1}{\omega_j^0 - E_j^0}\right)\left[\hat{n} T_i T_j^\dagger - (1-\hat{n})\, T_i^\dagger T_j\right]\end{aligned} \tag{1.55}$$

Prescription

Given a Hamiltonian

$$\mathcal{H} = \mathcal{H}_1 + \mathcal{H}_0 + c^\dagger T + T^\dagger c \tag{1.56}$$

the goal is to look at the renormalization of the various couplings in the Hamiltonian as we decouple high energy electron states. Typically we have a shell of electrons at some energy D. During the process, we make one simplification. We assume that there is only one electron on that shell at a time, say with quantum numbers q, σ, and calculate the renormalization of the various couplings due to this electron. We then sum the momentum q over the shell and the spin β, and this gives the total renormalization due to decoupling the entire shell.

From eq. 1.45, the first two terms in the rotated Hamiltonian are just the diagonal parts of the bare Hamiltonian; they are unchanged in that part. The renormalization comes from the third term. For one electron $q\beta$ on the shell, the renormalization is

$$\Delta\mathcal{H} = \left[c_{q\beta}^\dagger \mathrm{Tr}\left(\mathcal{H} c_{q\beta}\right), \eta\right] = c_{q\beta}^\dagger \mathrm{Tr}\left(\mathcal{H} c_{q\beta}\right)\eta - \eta c_{q\beta}^\dagger \mathrm{Tr}\left(\mathcal{H} c_{q\beta}\right) \tag{1.57}$$

Since this assumes we have obtained this from U_1, it is fair to tag the η with a suitable label:

$$\Delta\mathcal{H} = c_{q\beta}^\dagger \mathrm{Tr}\left(\mathcal{H} c_{q\beta}\right)\eta_1 - \eta_1 c_{q\beta}^\dagger \mathrm{Tr}\left(\mathcal{H} c_{q\beta}\right)\ . \tag{1.58}$$

It is clear that the first term takes into account virtual excitations that start from a filled state ($\hat{n}_{q\beta} = 1$ initially) - such a term is said to be a part of the *particle sector*:

$$\Delta_1\mathcal{H} = c_{q\beta}^\dagger \mathrm{Tr}\left(\mathcal{H} c_{q\beta}\right)\eta_1\ . \tag{1.59}$$

The second term, on the other hand, considers excitations that start from an empty state. They constitute the *hole sector*:

$$\Delta_0\mathcal{H} = -\eta_1 c_{q\beta}^\dagger \mathrm{Tr}\left(\mathcal{H} c_{q\beta}\right)\ . \tag{1.60}$$

To write the total renormalization in a particle-hole symmetric form, we can use the relation $\eta_0 = -\eta_1$, such that both the terms will now come with a positive sign:

$$\Delta\mathcal{H} = c_{q\beta}^\dagger \mathrm{Tr}\left(\mathcal{H} c_{q\beta}\right)\eta_1 + \eta_0 c_{q\beta}^\dagger \mathrm{Tr}\left(\mathcal{H} c_{q\beta}\right) \tag{1.61}$$

We can make one more manipulation: using eq. 1.16, we get

$$\Delta\mathcal{H} = c^\dagger_{q\beta}\mathrm{Tr}\left(\mathcal{H}c_{q\beta}\right)\eta_1 + \mathrm{Tr}\left(c^\dagger_{q\beta}\mathcal{H}\right)c_{q\beta}\eta^\dagger_0 \tag{1.62}$$

This form of the total renormalization is identical to the one we use in the "Poor Man's scaling"-type of renormalization that was used to get the scaling equations in the Kondo and Anderson models [451, 452]. Writing down the forms of η and $\eta^\dagger$ explicitly, we get

$$\Delta\mathcal{H} = c^\dagger_{q\beta}\mathrm{Tr}\left(\mathcal{H}c_{q\beta}\right)\frac{1}{\omega^0_1 - \mathcal{H}^d_0}\mathrm{Tr}\left(c^\dagger_{q\beta}\mathcal{H}\right)c_{q\beta} + \mathrm{Tr}\left(c^\dagger_{q\beta}\mathcal{H}\right)c_{q\beta}\frac{1}{\omega^1_0 - \mathcal{H}^d_1}c^\dagger_{q\beta}\mathrm{Tr}\left(\mathcal{H}c_{q\beta}\right) \tag{1.63}$$

The renormalization due to the entire shell is obtained by summing over all states on the shell.

$$\Delta\mathcal{H} = \sum_{q\beta}\left[c^\dagger_{q\beta}\mathrm{Tr}\left(\mathcal{H}c_{q\beta}\right)\frac{1}{\omega^0_1 - \mathcal{H}^d_0}\mathrm{Tr}\left(c^\dagger_{q\beta}\mathcal{H}\right)c_{q\beta} + \mathrm{Tr}\left(c^\dagger_{q\beta}\mathcal{H}\right)c_{q\beta}\frac{1}{\omega^1_0 - \mathcal{H}^d_1}c^\dagger_{q\beta}\mathrm{Tr}\left(\mathcal{H}c_{q\beta}\right)\right] \tag{1.64}$$

These equations will now need to be simplified. For example, in the particle sector, we can set $\hat{n}_{q\beta} = 0$ in the numerator, because there is no such excitation in the initial state. Similarly, in the hole sector, we can set $\hat{n}_{q\beta} = 1$ because that state was occupied in the initial state. Another simplification we typically employ is that $\mathcal{H}^d_{0,1}$ will, in general, have the energies of all the electrons. But we consider only the energy of the on-shell electrons in the denominator. After integrating out these electrons, we can rearrange the remaining operators to determine which term in the Hamiltonian it renormalizes and what is the renormalization.

At first sight, one might think that we must evaluate lots of traces to obtain the terms in $\Delta\mathcal{H}$. A little thought reveals that the terms in the numerator are simply the off-diagonal terms in the Hamiltonian: $\mathrm{Tr}\left(c^\dagger_{q\beta}\mathcal{H}\right)c_{q\beta}$ is the off-diagonal term that has $c_{q\beta}$ in it, and $c^\dagger_{q\beta}\mathrm{Tr}\left(\mathcal{H}c_{q\beta}\right)$ is the off-diagonal term that has $c^\dagger_{q\beta}$ in it. Finally, $\mathcal{H}^D$ is just the diagonal part of the Hamiltonian.

2.2 Example: Unitary RG analysis of the Kondo model

We now describe the implementation of the unitary RG method in a simple paradigmatic model, the single-channel Kondo model [42]. It describes the scattering of itinerant non-interacting electrons off a magnetic impurity $\mathbf{S}_d$ [33, 446, 453], and is defined by the Hamiltonian

$$H_K = \sum_{k,\sigma}\epsilon_k n_{k,\sigma} + J\mathbf{S}_d \cdot \frac{1}{2}\sum_{\alpha,\beta}\sigma_{\alpha,\beta}\sum_{k_1,k_2}c^\dagger_{k_1,\alpha}c_{k_2,\beta}\,. \tag{2.1}$$

Note that the Kondo term is effectively of the form $\mathbf{S}_1\cdot\mathbf{S}_2$ with the local spin density of the conduction bath making up the second spin:

$$\frac{1}{2}\sum_{\alpha,\beta}\sigma_{\alpha,\beta}\sum_{k_1,k_2}c^\dagger_{k_1,\alpha}c_{k_2,\beta} = \frac{1}{2}\sum_{\alpha,\beta}\sigma_{\alpha,\beta}c^\dagger_{0,\alpha}c_{0,\beta} = \mathbf{s}_0\,. \tag{2.2}$$

As a result, the Kondo term can be written in the form

$$S_d^z s_0^z + \frac{1}{2} S_d^+ s_0^- + \frac{1}{2} S_d^- s_0^+ \ . \tag{2.3}$$

We will make use of this form.

Because of spin-flip scattering processes, the problem is many-body in nature. In order to obtain the low-energy physics, we will progressively integrate out high-energy modes in the conduction bath and approach the low-energy degrees of freedom. Such an approach is needed because the high and low-energy states interact with each other through the impurity spin and cannot be trivially removed from the problem. The way this works is that the process of integrating out high-energy states generates additional scattering processes within the low-energy states; if these processes already exist in the Hamiltonian, the new contributions *renormalise* the existing couplings, but if the processes don't exist, then the Hamiltonian generates new terms as low energies are approached.

Consider an arbitrary j^{th} step of the process where we wish to integrate out the conduction bath states within a narrow shell about the energies $\pm\epsilon_j$ and retain only the states at $|\epsilon| < |\epsilon_j|$. We designate the states on this shell by the momentum index q, and the states below it by indices k_1 and k_2. We need to first separate the Hamiltonian into diagonal and off-diagonal terms from the perspective of the shell being integrated out:

$$\begin{aligned} H_D &= \sum_{q,\sigma} \epsilon_q n_{q,\sigma} + J\mathbf{S}_d^z \frac{1}{2} \sum_q \left(n_{q,\uparrow} - n_{q,\downarrow} \right) \ , \\ H_X &= J\mathbf{S}_d \cdot \frac{1}{2} \sum_{\alpha,\beta} \sigma_{\alpha,\beta} \sum_{k,q} \left(c_{k,\alpha}^\dagger c_{q,\beta} + c_{q,\alpha}^\dagger c_{k,\beta} \right) \ . \end{aligned} \tag{2.4}$$

In order to make the particle-hole symmetry in the kinetic energy term manifest, we replace the number operators with pseudospin operators $\tau = n - 1/2$ and drop the constant term:

$$\begin{aligned} H_D &= \sum_{q,\sigma} \epsilon_q \tau_{q,\sigma} + J\mathbf{S}_d^z \sum_q \left(n_{q,\uparrow} - n_{q,\downarrow} \right) \ , \\ H_X &= J\mathbf{S}_d \cdot \sum_{\alpha,\beta} \sigma_{\alpha,\beta} \sum_{k,q} \left(c_{k,\alpha}^\dagger c_{q,\beta} + c_{q,\alpha}^\dagger c_{k,\beta} \right) \ . \end{aligned} \tag{2.5}$$

This ensures that particle and hole excitations both cost the same energy. We now describe how to obtain the renormalisation in the Hamiltonian arising from unitarily decoupling the states on the shell. As mentioned earlier, this happens because the process of integrating out the states q generates interactions between the other states $\{k\}$ and this modifies the Hamiltonian couplings.

To keep things brief, we focus on obtaining the renormalisation of the following spin-flip term in the Kondo Hamiltonian:

$$\frac{1}{2} J S_d^+ \sum_{k_1,k_2} c_{k_1,\downarrow}^\dagger c_{k_2,\uparrow} \tag{2.6}$$

For that, we need to figure out which combinations of off-diagonal terms in H_X can result in such terms, when the $q-$states are integrated out. One possibility is

$$\frac{1}{4} \sum_{q,k_1,k_2} J S_d^z c_{q,\uparrow}^\dagger c_{k_2,\uparrow} \frac{1}{\omega - H_D} J S_d^+ c_{k_1,\downarrow}^\dagger c_{q,\uparrow} \ . \tag{2.7}$$

The factor of $1/4$ in front appears due to the two factors of $1/2$ coming from the zz and $+-$ terms in the Kondo terms in H_X.

In order evaluate H_D in the denominator, we note that the hole excitation of $q\uparrow$ at the right (i) indicates that ϵ_q is positive, and the configuration $n_{q,\uparrow}=0$ in the intermediate state means that $\epsilon_q\tau_{q,\uparrow}$ works out to be $|\epsilon_j|/2$, and (ii) the impurity and bath spins are antiparallel in the intermediate state because of the opposite spins of their excitations, and so the $J-$term in the denominator evaluates to $J(1/2)(-1/2)=-J/4$. Substituting these in the expression (and noting the minus sign in front of H_D) gives

$$\frac{1}{4}\sum_{q,k_1,k_2} JS_d^z c_{q,\uparrow}^\dagger c_{k_2,\uparrow}\frac{1}{\omega-|\epsilon_j|/2+J/4}JS_d^+c_{k_1,\downarrow}^\dagger c_{q,\uparrow}=-\frac{J^2/4}{\omega-|\epsilon_j|/2+J/4}\sum_{q,k_1,k_2}\left(\frac{1}{2}S_d^+\right)c_{k_1,\downarrow}^\dagger c_{k_2,\uparrow}n_{q,\uparrow}\,, \tag{2.8}$$

where we used the identity $S_d^zS_d^+=\frac{1}{2}S_d^+$.

In order to truly integrate out the mode q, we set $n_{q,\uparrow}=1$, guided by the fact that the mode was initially occupied. The sum over q then simply evaluates to the number of momentum states available at the energy ϵ_j, which is the density of states $\rho(\epsilon_j)$:

$$-\frac{1}{2}\frac{\rho(\epsilon_j)J^2/4}{\omega-|\epsilon_j|/2+J/4}\sum_{k_1,k_2}S_d^+c_{k_1,\downarrow}^\dagger c_{k_2,\uparrow}\,. \tag{2.9}$$

A partner process can be constructed by exchanging the roles of q and k:

$$-\frac{1}{4}\sum_{q,k_1,k_2} JS_d^z c_{k_1,\downarrow}^\dagger c_{q,\downarrow}\frac{1}{\omega-H_D}JS_d^+c_{q,\downarrow}^\dagger c_{k_2,\uparrow}\,, \tag{2.10}$$

where the minus sign in front arises from the fact that the term before the Greens function is the spin down component of s_0^z. In this case, the intermediate state has a particle excitation of the $q-$ state, which means $\tau_{q.\downarrow}=\frac{1}{2}$, but the energy ϵ_q of the state must also flip sign because the state was initially occupied, so the net contribution again works out to $|E_j|/2$. The $J-$term is also unchanged from the previous process, because the spin orientations are again antiferromagnetic. Together, we get

$$\sum_{q,k_1,k_2} JS_d^z c_{k_1,\downarrow}^\dagger c_{q,\downarrow}\frac{-J^2/4}{\omega-|\epsilon_j|/2+J/4}S_d^+c_{q,\downarrow}^\dagger c_{k_2,\uparrow}=-\frac{1}{2}\frac{\rho(\epsilon_j)J^2/4}{\omega-|\epsilon_j|/2+J/4}\sum_{k_1,k_2}S_d^+c_{k_1,\downarrow}^\dagger c_{k_2,\uparrow}\,. \tag{2.11}$$

Additional contributions are obtained by considering the time-reversed forms of these processes. From the first process above (eq. 2.7), we have:

$$\frac{1}{4}\sum_{q,k_1,k_2} JS_d^+ c_{k_1,\downarrow}^\dagger c_{q,\uparrow}\frac{1}{\omega-H_D}JS_d^zc_{q,\uparrow}^\dagger c_{k_2,\uparrow}\,. \tag{2.12}$$

In this case, the intermediate state has a particle excitation of the $q-$ state, which means $\tau_{q.\uparrow}=\frac{1}{2}$, but the energy ϵ_q of the state must also flip sign because the state was initially occupied, so the

net contribution again works out to $|\epsilon_j|/2$. The $J-$term is also of the same value, because the spin orientations are again antiferromagnetic. Together, we get

$$\frac{1}{4}J\sum_{q,k_1,k_2} S_d^+ c^\dagger_{k_1,\downarrow} c_{q,\uparrow} \frac{1}{\omega - |\epsilon_j|/2 + J/4} J S_d^z c^\dagger_{q,\uparrow} c_{k_2,\uparrow} = \frac{-\frac{1}{2}\rho(\epsilon_j)J^2/4}{\omega - |\epsilon_j|/2 + J/4} \sum_{k_1,k_2} S_d^+ c^\dagger_{k_1,\downarrow} c_{k_2,\uparrow} \,. \quad (2.13)$$

In this case, we used the identity $S_d^+ S_d^z = -\frac{1}{2} S_d^+$.

We finally consider the time-reversed partner of eq. 2.10:

$$\frac{1}{4}\sum_{q,k_1,k_2} J S_d^+ c^\dagger_{k_1,\downarrow} c_{q,\uparrow} \frac{1}{\omega - H_D} J S_d^z c^\dagger_{q,\uparrow} c_{k_2,\uparrow} \,. \quad (2.14)$$

Evaluating this similarly gives

$$\frac{-\frac{1}{2}\rho(\epsilon_j)J^2/4}{\omega - |\epsilon_j|/2 + J/4} \sum_{k_1,k_2} S_d^+ c^\dagger_{k_1,\downarrow} c_{k_2,\uparrow} \quad (2.15)$$

Combining all four contributions, the total renormalisation to the $S_d^+ s_0^-$ term comes out to be

$$-\rho(\epsilon_j)J^2 \frac{1}{\omega - |\epsilon_j|/2 + J/4} \frac{1}{2} \sum_{k_1,k_2} S_d^+ c^\dagger_{k_1,\downarrow} c_{k_2,\uparrow} \,. \quad (2.16)$$

By comparing with the term in the original Hamiltonian (eq. 2.6), we can read off the renormalisation in the coupling J for the jth step:

$$\Delta J^{(j)} = -\frac{\rho(\epsilon_j)J^2}{\omega - |\epsilon_j|/2 + J/4} \,. \quad (2.17)$$

This is the URG equation for the Kondo coupling J. It differs from the perturbative "Poor Man's scaling" equations [453] through the appearance of the Kondo coupling in the denominator. Expanding the URG equation in powers of J/ϵ_j recovers the perturbative form.

2.3 Some comments on the unitary RG program

- In addition to studying the low-energy physics, the unitary RG method can be used to obtain high-energy features as well. This is done by using the renormalised couplings at various points along the RG flow. Renormalised Hamiltonians closer to the UV theory affect the high-frequency spectral features while those closer to the IR fixed point affect the low frequency features. By combining the results from various points along the RG flow, one can reconstruct dynamical quantities like the spectral function and self-energy as well as thermodynamic quantities [454, 455] such as the temperature dependence of the impurity susceptibility [42]. We are currently using such a strategy (as part of a more involved program) to reconstruct the finite temperature phase diagram of the particle-hole symmetric Hubbard model in the limit of infinite dimensions, and the results are quite promising.

  Apart from dynamical quantities, the Hamiltonians along the RG flow have also been used to obtain effective theories at various energies:

  - Close to the IR, the method has allowed us to obtained benchmarks such as the local Fermi liquid and local non-Fermi liquid theories for the single-channel and two-channel Kondo models [42, 74], as well as new results such as the effective theories for the $T = 0$ quantum critical points of the Hubbard model in $D = \infty$ and $D = 2$ [454, 455].
  - Away from the IR, we have obtained an effective theory for charge delocalisation within the Hubbard sidebands for $D = \infty$ [454].

- Coming to the question of a small parameter, the unitary RG involves a hierarchy of contributions arising from a cluster expansion of the renormalised Hamiltonian into scattering vertices of various orders [348]. These describe scattering processes involving four electrons, six electrons and so on; such terms are generated during the RG flow. In practise, one has to truncate the expansion and restrict the RG equation to a finite order of vertices.

2.4 Comparison of renormalisation group approaches based on canonical transformations

We have considered three canonical transformations in this section: the Poor Man's scaling (PMS), the Schrieffer-Wolff transformation (SWT) and the continuous unitary transformation renormalization group (CUT-RG). PMS and SWT are more or less identical; they differ in the context in which they are used. PMS is used when there is an entire spectrum of energies in the model, ranging from a low energy limit to a high energy; it is then employed to decouple the highest energy modes in an iterative fashion. SWT is used when the Hamiltonian can be split into one high and one low energy part, and we need to decouple these two modes. It is clear when seen from this perspective that SWT is like a one-shot PMS; it decouples the UV from the IR in one step, compared to the iterative approach of PMS. However, as has been shown in the previous subsections, both PMS and SWT can be formalized in an identical fashion, so that one can be switched for the other in both contexts.

Now that we have established that PMS and SWT are formally identical, we can relate them to URG. URG is similar in philosophy to PMS in the fact that URG also successively decouples high energy modes from the low energy ones. The difference is that URG takes care of the quantum fluctuations, at least in principle, by introducing a new set of energy scales ω. These ω then parameterise the RG flows of URG, compared to the single RG flow of PMS. Since SWT is formally the same as PMS, these is also a comparison between SWT and URG. Both PMS and SWT trivialize the quantum fluctuation scales of URG by replacing it with the bare energy values.

CUT-RG is philosophically different from the other transformations. Its goal is to gradually reduce the contributions of the off-diagonal terms by making them decay along a certain scale l. Off-diagonal terms that connect states with large energy differences decay faster. In this sense, there is no sequential dropping out of off-diagonal terms; all off-diagonal terms disappear at $l = \infty$. In this sense, it is like a continuous version of SWT. While SWT strives to remove an entire off-diagonal term in one-shot, CUT RG does this gradually by introducing a scale l. This separation of scales is absent in SWT. It does exist in URG and PMS, albeit in a different fashion. There, the separation comes in when we decouple single electron states starting from the Brillouin zone

boundary Λ_N and come down to the Fermi surface Λ_0. Each Λ provides a natural energy scale for separating the high and low energy physics.

If one integrates the continuum generator η over all the scales, one should recover something analogous to the SWT generator. This generator is however necessarily perturbative in the off-diagonal term, since by definition η will only be of first order in $\mathcal{H}_X$. This is in contrast to the non-perturbative generators in URG and, at least in principle, PMS. This non-perturbative form is encapsulated in the presence of a second completely different set of energy scales ω (or E in PMS). This second energy scale is absent in CUT RG because it takes care of at most the second order term.

Another point to note is that since SWT keeps the entire off-diagonal piece in the generator, new terms will almost certainly by generated at every step, and they have to be truncated. This is not the case with URG or PMS, becasue in those methods, we decouple just a single-electron at each step, and so those electrons become integrals of motion at that step, leading to their removal from the off-diagonal piece, and very often the Hamiltonian retains the same form as the bare model. This makes the philosophy of URG and PMS easier to work with. Tied to this is the fact that CUT RG often takes a certain type of interaction in the generator part, and not the entire off-diagonal piece. Hence, at the limit of the flow parameter going to ∞, the chosen off-diagonal piece goes to zero but the remaining off-diagonal pieces still remain. As a result, the Hamiltonian is atmost block diagonal at this stage. On the other hand, URG progressively decouples single electrons, meaning all scattering terms corresponding to that electron vanish at each step.

One last thing to note is that URG, being unitarily implemented with a well-defined generator, does not accomodate for spontaneous symmetry breaking (SSB). In order to see SSB, the symmetry-breaking term has to be added to the bare model explicitly; if this term grows under the RG, then the ground state will be symmetry-broken. CUT RG, however, does allow for SSB through the idea that the generator is not uniquely defined. If the generator commutes with a particular symmetry, then the family of Hamiltonians will also have the symmetry [456]. However, if the generator is replaced by something that is normal ordered w.r.t a particular expectation value, then the CUT RG flow will usually be towards either the symmetry-preserved state or the symmetry-broken state, depending on whichever is stable [457].

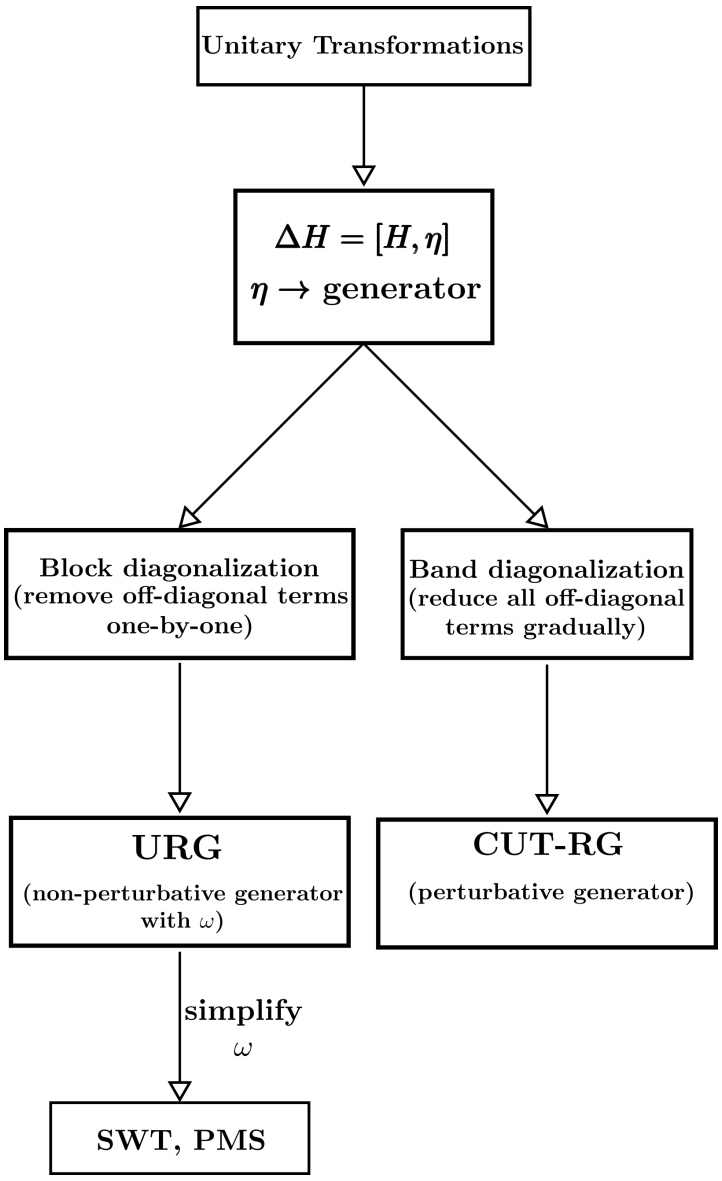

Figure 2.2: *Comparison of the various unitary transformations and their relationships to each other.*

2.5 Numerical Implementation of Unitary RG Equations

The unitary RG equations are usually relatively simple and computationally light to implement. However, in certain models where the number of couplings scales with the system size, a brute force approach might not be feasible for large systems. This occurs, for example, in models that have momentum-differentiated couplings $g_{k,k'}$ that describe the scattering between two scattering states and the renormalisation at each step is not uniform for all choices of (k, k'). In this case, one needs to solve the RG equations for all pairs of (k, k'). One then needs to come up with more

optimal ways of simulating such RG equations. We show here one such approach to this. Different problems might require different approaches to dealing with this.

We consider here an abstract RG equation of the form

$$\Delta g_{k_1,k_2}/\Delta D = -\sum_q \left(g_{k_1,q}g_{q,k_2} - 4g_{q,\bar{q}}W_{k_1,k_2}\right) G_q \ , \tag{5.1}$$

where g is the momentum-dependent coupling we are trying to simulate, W is another coupling that depends on the momenta but itself does not flow, and G is a propagator that depends only the momenta q that are being integrated out at this step. The specific form of G is not necessary for this demonstration. $\bar{q}$ is the particle-hole transformed partner of the state q.

One approach is to "loop" over the couplings g_{k_1,k_2} for every pair k_1, k_2 that lie within the set of states that will renormalise. However, this approach scales very poorly with the number of available $k-$states (which is essentially the number of lattice sites being considered). A more efficient approach is to write the RG equation in a matrix form:

$$\frac{\Delta \bar{g}}{\Delta D} = -\bar{g}\bar{G}\bar{g}^\dagger - 4\bar{W}\mathrm{Tr}\left[\bar{G}'\right] \ , \tag{5.2}$$

where the bars above the couplings indicate that those are matrices. The matrix $\bar{g}$ is defined by the matrix element $\langle k_1|\bar{g}|k_2\rangle = g_{k_1,k_2}$, while $\bar{W}$ is defined as $\langle k_1|\bar{W}|k_2\rangle = W_{k_1,k_2}$. The propagators $\bar{G}$ and $\bar{G}'$ are diagonal matrices defined by the elements $\langle q|\bar{G}|q\rangle = G_q$ and $\langle q|\bar{G}'|q\rangle = G_q g_{q,\bar{q}}$. Importantly, the elements of $\bar{G}$ and $\bar{G}'$ are zero for momenta that are not being integrated out: $\langle k_1|\bar{G}|k_2\rangle = \langle k_1|\bar{G}'|k_2\rangle = 0$; this is important for efficiency.

The simulation of the RG equation has now been reduced to a matrix multiplication. More specifically, one needs to construct two coupling matrices $\bar{g}$ and $\bar{W}$ and two propagator matrices $\bar{G}$ and $\bar{G}'$. At every step, we use eq. 5.2 to update $\bar{g}$, and we redefine $\bar{G}$ and $\bar{G}'$ at every step depending on the states q being integrated out at that step.

2.6 Renormalised perturbation theory about fixed points

In this section, we will describe the technique of carrying out renormalised theory about a gapless fixed point theory towards obtaining a low-energy effective Hamiltonian for the excitations above the ground state. This is useful for characterising metallic phases, and detecting whether the metal is, say, a Landau Fermi liquid or a non-Fermi liquid.

We consider here the case of the single-channel Kondo model. We would like to demonstrate the method by deriving a local Fermi liquid theory for the gapless excitations above the ground state, as obtained by Nozières [40]. In its simplest form, the Kondo model features a spin-1/2 local moment undergoing antiferromagnetic spin-exchange scattering with the local spin-density of a non-interacting electronic conduction bath:

$$H_{\mathrm{K}} = J\mathbf{S}_d \cdot \mathbf{s} + \sum_{k,\sigma} \epsilon_k n_{k,\sigma} \ , \tag{6.1}$$

where S_d and s are the spins of the impurity and the conduction bath. For any non-zero value of the Kondo coupling J (the coupling for the impurity-bath spin exchange processes), it can be shown that

J is relevant under a renormalisation group flow from high energy to low-energy, and the coupling effectively diverges as the fixed point is approached [446]. At the fixed point, the kinetic energy of the conduction bath can be ignored relative to the Kondo coupling, and the ground state is a spin-singlet between the impurity $\mathbf{S}_d$ and the conduction bath local spin density $\mathbf{s}$:

$$|\Psi\rangle_0 = \frac{1}{\sqrt{2}} \left(|\uparrow_d, \Downarrow\rangle - |\downarrow_d, \Uparrow\rangle \right) \ , \tag{6.2}$$

where $\uparrow_d$ represents the configuration of the impurity and the thick arrow is the configuration of the conduction bath spin.

In order to obtain the excitations, we now note that because of the RG-relevance of J, the first term in the Hamiltonian in eq. 6.1 can only have finite energy excitations. Since we are looking for excitations that cost vanishingly small energy, we focus on the second term. With an eye towards developing a perturbation theory over $1/J$, we recast the kinetic energy term in real-space as a tight-binding Hamiltonian connected to the local density that hybridises with the impurity:

$$H_{\text{KE}} = -t^* \sum_{i,\sigma} (c^\dagger_{i,\sigma} c_{i+1,\sigma} + \text{h.c.}) \ . \tag{6.3}$$

Hopping processes from the zeroth site modify the singlet ground state and lead to virtual excitations. in this sense, the zeroth site corresponds to the low-energy electronic excitations with the longest wavelength. We will now obtain the effect of this Hamiltonian by obtaining its renormalisation effects within the ground state subspace.

To better frame the perturbation theory which we will use to obtain the renormalisation effects, we clarify the zeroth Hamiltonian H_0 and perturbation V:

$$\begin{aligned} H_0 &= J^* \mathbf{S}_d \cdot \mathbf{s}, \\ V &= -t^* \sum_{i,\sigma} (c^\dagger_{i,\sigma} c_{i+1,\sigma} + \text{h.c.}) \ . \end{aligned} \tag{6.4}$$

The goal is to obtain the shifts in the energies of H_0 arising from the perturbation term. The eigenstates of H_0 are

$$\begin{aligned} |\Psi\rangle_{0,0,2} &= \frac{1}{\sqrt{2}} \left(|\uparrow_d, \Downarrow\rangle - |\downarrow_d, \Uparrow\rangle \right) : && E = -3J^*/4 \\ |\Psi\rangle_{\frac{1}{2},\frac{\sigma}{2},1} &= |\sigma_d, 0\rangle : && E = 0 \\ |\Psi\rangle_{\frac{1}{2},\frac{\sigma}{2},3} &= |\sigma_d, 2\rangle : && E = 0 \\ |\Psi\rangle_{1,0,2} &= \frac{1}{\sqrt{2}} \left(|\uparrow_d, \Downarrow\rangle + |\downarrow_d, \Uparrow\rangle \right) : && E = J^*/4 \\ |\Psi\rangle_{1,\sigma,2} &= |\sigma_d, \sigma\rangle : && E = J^*/4, \end{aligned} \tag{6.5}$$

where the quantum numbers in the subscript are the total spin $S = S_d + s$, the $z-$component of the total spin $S^z = S^z_d + s^z$, and the total occupancy $N = n_d + n$. The second, third and fifth states are doubly degenerate with σ taking values ± 1. The ground state is of course $|\Psi\rangle_{0,0,2}$. However, this only takes into account the zeroth site in the conduction bath. In order to consider perturbative

processes where an electron hops from the zeroth site to the next (first) site, we need to involve the first site as well. Since the first site does not have any energy in H_0, the eigenstates simply become four-fold degenerate, due to the four possible configurations of the first site. The eigenstates are then labelled as $\Psi_{S,S^z,N,c_1} = |\Psi_{S,S^z,N}\rangle \otimes |c_1\rangle$ where c_1 can be 0, $\uparrow$, $\downarrow$ or 2 depending on the configuration of the first site.

To obtain the excitations, we will calculate the perturbative shifts in the four-fold degenerate ground state subspace spanned by the states $\{\Psi_{0,0,2,0}, \Psi_{0,0,2,\uparrow}, \Psi_{0,0,2,\downarrow}, \Psi_{0,0,2,2}\}$. We will do this order by order, stopping when we obtain the lowest order non-trivial Hamiltonian. At first and third order, the energy shifts are given by

$$\begin{aligned}\Delta E_n^{(1)} &= \langle\Psi_n|V|\Psi_n\rangle \ , \\ \Delta E_n^{(3)} &= \sum_{k_2\neq n, k_3\neq n} \frac{\langle\Psi_n|V|\Psi_{k_3}\rangle\langle\Psi_{k_3}|V|\Psi_{k_2}\rangle\langle\Psi_{k_2}|V|\Psi_n\rangle}{\left(E_n - E_{k_3}\right)\left(E_n - E_{k_2}\right)} - \Delta E_n^{(1)} \sum_{k_3\neq n} \frac{|\langle\Psi_n|V|\Psi_{k_3}\rangle|^2}{\left(E_n - E_{k_3}\right)^2} \ .\end{aligned} \tag{6.6}$$

Both these contributions vanish because of mismatched quantum numbers: upon applying the perturbation Hamiltonian V any odd number of times, the final resultant state will have a different occupancy on the impurity+zeroth site compared to the starting state. Since H_0 conserves the occupancy of the impurity+zeroth site complex, the overlap between such states is zero. More specifically, what this means for the first term of $\Delta E_n^{(3)}$ is the following:

- the excited state k_2 will have either 1 or 3 electrons on the $d+0$ complex (because the ground state hosts 2 electrons there, and V will either add an electron there or remove one electron from it).
- Another application of V means that k_3 will have 0, 2 or 4 electrons.
- A final application of V means that the terminal state will have an odd number of electrons – 1, 3 or 5,

The overlap of this state with the ground state – $\langle\Psi_n|V|\Psi_{k_3}\rangle$ – will therefore vanish.

We therefore focus on the second and fourth order effects. At second order, the renormalisation is given by

$$\Delta E_n^{(2)} = \sum_{k_2\neq n} \frac{|\langle\Psi_n|V|\Psi_{k_2}\rangle|^2}{E_n - E_{k_2}} \ . \tag{6.7}$$

We work with the shifts in the $(0,0,2,0)$ and $(0,0,2,\uparrow)$ states, because the shifts of $(0,0,2)$ and $(0,0,\downarrow)$ can be inferred, respectively, from them using particle-hole symmetry and spin-rotation symmetry. For the state $(0,0,2,0)$, we have

$$V|\Psi_{0,0,2,0}\rangle = -t^*\frac{1}{\sqrt{2}}\left(|\uparrow_d,0,\downarrow_1\rangle - |\downarrow_d,0,\uparrow_1\rangle\right) = \frac{-t^*}{\sqrt{2}}|\Psi\rangle_{\frac{1}{2},\frac{1}{2},1,\downarrow} + \frac{t^*}{\sqrt{2}}|\Psi\rangle_{\frac{1}{2},-\frac{1}{2},1,\uparrow} \ . \tag{6.8}$$

Summing k_2 over the states $\frac{1}{2},\frac{1}{2},1,\downarrow$ and $\frac{1}{2},-\frac{1}{2},1,\uparrow$ with energies $E_n - E_{k_2} = -3J^*/4$, the total shift comes out to be

$$\Delta E^{(2)}_{(0,0,2,0)} = 2\frac{t^{*2}}{2}\times\frac{1}{-3J^*/4} = -\frac{4t^{*2}}{3J^*} \ . \tag{6.9}$$

For the state $(0, 0, 2, \uparrow)$, we have

$$V\,|\Psi_{0,0,2,\uparrow}\rangle = t^* \frac{1}{\sqrt{2}}\left(|\uparrow_d, 0, 2\rangle + |\uparrow_d, 2, 0\rangle\right) = \frac{t^*}{\sqrt{2}}\,|\Psi\rangle_{\frac{1}{2},\frac{1}{2},1,2} + \frac{t^*}{\sqrt{2}}\,|\Psi\rangle_{\frac{1}{2},\frac{1}{2},1,0}\ . \tag{6.10}$$

Summing k_2 over the appropriate eigenstates and using $E_n - E_{k_2} = -3J^*/4$ gives the same shift:

$$\Delta E^{(2)}_{(0,0,2,\uparrow)} = -\frac{4t^{*2}}{3J^*}\ . \tag{6.11}$$

Using symmetries, we also have

$$\Delta E^{(2)}_{(0,0,2,\downarrow)} = \Delta E^{(2)}_{(0,0,2,2)} = -\frac{4t^{*2}}{3J^*}\ . \tag{6.12}$$

W also note that off-diagonal matrix elements are zero in such a setup, because any two states in the ground state subspace will differ by at least one of the two conserved quantum numbers s^z_1 and n_1.

We now need to convert these shifts into a renormalised Hamiltonian that describes the excitations arising from such virtual scattering processes. In the absence of any shift in off-diagonal matrix element, the diagonal shifts will only lead to the generation of number-conserving operators. For example, the shift $\Delta E^{(2)}_{(0,0,2,0)} = -\frac{4t^{*2}}{3J^*}$ means that the energy of the null-occupied state of the first site is lowered by that amount. This can be represented through the operator

$$-\frac{4t^{*2}}{3J^*}(1 - n_{1\uparrow})(1 - n_{1\downarrow})\ . \tag{6.13}$$

Writing down operator forms for the other shifts as well, we get

$$\Delta H^{(2)} = -\frac{4t^{*2}}{3J^*}\left[(1 - n_{1\uparrow})(1 - n_{1\downarrow}) + n_{1\uparrow}(1 - n_{1\downarrow}) + (1 - n_{1\uparrow})n_{1\downarrow} + n_{1\uparrow}n_{1\downarrow}\right]\ . \tag{6.14}$$

However, because the shifts in all the states are identical, adding up all the operators reduces the renormalisation to a constant shift:

$$\Delta H^{(2)} = -\frac{4t^{*2}}{3J^*}\ . \tag{6.15}$$

So we conclude that there's no non-trivial renormalisation at second order.

We now extend the perturbation theory to fourth order. Since the first and third order corrections vanish, and the second order correction only produces a constant shift, the first potentially non-trivial renormalisation arises at fourth order.

For a non-degenerate state, the fourth-order energy shift is

$$\Delta E^{(4)}_n = \sum_{k_1,k_2,k_3\neq n} \frac{\langle\Psi_n|V|\Psi_{k_3}\rangle\,\langle\Psi_{k_3}|V|\Psi_{k_2}\rangle\,\langle\Psi_{k_2}|V|\Psi_{k_1}\rangle\,\langle\Psi_{k_1}|V|\Psi_n\rangle}{(E_n - E_{k_1})(E_n - E_{k_2})(E_n - E_{k_3})} - \Delta E^{(2)}_n \sum_{k_2\neq n} \frac{|\,\langle\Psi_n|V|\Psi_{k_2}\rangle\,|^2}{(E_n - E_{k_2})^2}\ . \tag{6.16}$$

We first calculate it for the state $\Psi_{0,0,2,0}$, where the first site is unoccupied. We initially focus on the first term. One application of V gives

$$V\,|\Psi\rangle_{0,0,2,0} = -\frac{t}{\sqrt{2}}(|\uparrow_d, 0, \downarrow_1\rangle - |\downarrow_d, 0, \uparrow\rangle)\ . \tag{6.17}$$

This allows two possible states in k_2: $|\uparrow_d, 0, \downarrow_1\rangle$ and $|\downarrow_d, 0, \uparrow\rangle$, with overlaps $\pm t/\sqrt{2}$. They are linked by particle-hole symmetry, so we will calculate the subsequent contribution from only the first and then double the result.

With $k_2 = |\uparrow_d, 0, \downarrow_1\rangle$, applying V once more gives

$$V\,|k_2\rangle = -t\,|\uparrow_d, \downarrow, 0_1\rangle\ . \tag{6.18}$$

This has overlap with the triplet state with zero spin, leading to $k_3 = \Psi_{1,0,2,0}$, with an overlap $-t/\sqrt{2}$. A third application of V gives

$$V\,|k_3\rangle = -\frac{t}{\sqrt{2}}(|\uparrow_d, 0, \downarrow_1\rangle + |\downarrow_d, 0, \uparrow_1\rangle)\ . \tag{6.19}$$

The final excited states k_4 are therefore the same as k_2. A final application of V on the two possible k_4 gives

$$\begin{aligned} V\,|\uparrow_d, 0, \downarrow_1\rangle &= -t\,|\uparrow_d, \downarrow, 0_1\rangle\,, \\ V\,|\downarrow_d, 0, \uparrow_1\rangle &= -t\,|\downarrow_d, \uparrow, 0_1\rangle\ . \end{aligned} \tag{6.20}$$

The two final states have overlaps with opposite sign with the ground state. Since the excitation energies in the denominator in the first term of eq. 6.16 are the same for each of the paths, the sum over k_4 reduces to a sum over it's overlap with the ground state. As obtained above, this overlap is of different signs for the two possibilities of k_4, leading to this vanishing of the first term of eq. 6.16.

For the second term, we have already calculated the overlap $\langle\Psi_n|V|k_2\rangle$ as well as the second order shift. Plugging those in gives

$$\Delta E^{(4)}_{0,0,2,0} = -\frac{-4t^{*2}}{3J^*} \times 2\frac{t^{*2}/2}{(-3J^*/4)^2} = \frac{64t^{*4}}{27J^{*3}}\ . \tag{6.21}$$

This is the total fourth order shift for the state $\Psi_{0,0,2,0}$.

We next look at the state $\Psi_{0,0,2,\uparrow}$, starting with the first term. One application of the perturbation Hamiltonian gives

$$V\,|\Psi_{0,0,2,\uparrow}\rangle = \frac{-t^*}{\sqrt{2}}\,(-|\uparrow_d, 0, 2_1\rangle - |\uparrow, 2, 0_1\rangle)\ . \tag{6.22}$$

Proceeding exactly as before, the possible excited states k_2 are $|\uparrow_d, 0, 2_1\rangle$ and $|\uparrow, 2, 0_1\rangle$. The overlaps and denominators for both states are $t^*/\sqrt{2}$ and $-3J^*/4$ respectively. We now focus henceforth on the state $|\uparrow_d, 0, 2_1\rangle$ because the contribution from the other will be identical. Applying the perturbation on this state gives

$$V\,|\uparrow_d, 0, 2_1\rangle = -t^*\,(|\uparrow_d, \uparrow, \downarrow_1\rangle - |\uparrow_d, \downarrow, \uparrow_1\rangle)\ . \tag{6.23}$$

These gives two choices for k_3: the $S^z = 1$ triplet state for $d + 0\ |\uparrow_d, \uparrow, \downarrow_1\rangle$, and the $S^z = 0$ triplet state $\Psi_{1,0,2,\uparrow}$. While the denominators are $-J^*$ for both the states, the overlaps are $-t^*$ and $t^*/\sqrt{2}$ respectively.

Following the first state and applying V on it, we get

$$V\,|\uparrow_d, \uparrow, \downarrow_1\rangle = -t^*\,(|\uparrow, 0, 2_1\rangle + |\uparrow, 2, 0_1\rangle)\ . \tag{6.24}$$

The final set of excited states, k_4, therefore work out to be $|\uparrow, 0, 2_1\rangle$ and $|\uparrow, 2, 0_1\rangle$, giving denominators $-3J^*/4$ and overlaps $-t^*$. The final application of V on either of these states gives $-t^*\left(|\uparrow_d, \uparrow, \downarrow_1\rangle - |\uparrow_d, \downarrow, \uparrow_1\rangle\right)$, and the final overlap with the ground state is $t^*/\sqrt{2}$. The total contribution from the excitation branch $\Psi_{0,0,2,\uparrow} \to |\uparrow_d, 0, 2_1\rangle \to |\uparrow_d, \uparrow, \downarrow_1\rangle \to \ldots$ therefore comes out to be

$$S_1 = 2(t^*/\sqrt{2})(-t^*)^2(t^*/\sqrt{2})/((-3J^*/4)^2(-J^*)) = -\frac{16t^{*4}}{9J^{*3}} \,. \tag{6.25}$$

We now focus on the other excitation branch, $\Psi_{0,0,2,\uparrow} \to |\uparrow_d, 0, 2_1\rangle \to \Psi_{1,0,2,\uparrow} \to \ldots$ Applying V on this excited state gives

$$V\Psi_{1,0,2,\uparrow} = \frac{t^*}{\sqrt{2}}\left(|\uparrow_d, 0, 2_1\rangle + |\uparrow_d, 2, 0_1\rangle\right) \,. \tag{6.26}$$

This gives the same k_3 as the contribution from the other branch, but with a reduced overlap $t^*/\sqrt{2}$ instead of t^*. Since we have already carried out the previous calculation, we can directly write down the result:

$$S_2 = S_1/2 = -\frac{8t^{*4}}{9J^{*3}} \,. \tag{6.27}$$

The factor of $1/2$ arises because the second and third overlaps are suppressed by $1/\sqrt{2}$ compared to the first branch S_1. Combining S_1 and S_2, the total contribution to the first term in the fourth order expression arising from the branch $\Psi_{0,0,2,\uparrow} \to |\uparrow_d, 0, 2_1\rangle \to \ldots$ is

$$-\frac{8t^{*4}}{3J^{*3}} \,. \tag{6.28}$$

By particle-hole symmetry, the contribution from the other branch $\Psi_{0,0,2,\uparrow} \to |\uparrow_d, 2, 0_1\rangle \to \ldots$ is identical. Together, the total fourth order renormalisation from the first term is

$$-\frac{16t^{*4}}{3J^{*3}} \,. \tag{6.29}$$

We now compute the second term in the fourth order expression. Again, the components have already been calculated during the second order calculation, so we just plug them in:

$$-\frac{-4t^{*2}}{3J^*} \times 2\frac{t^{*2}/2}{(-3J^*/4)^2} = \frac{64t^{*4}}{27J^{*3}} \,. \tag{6.30}$$

Adding the two parts, we get for the total fourth order shift:

$$\Delta E^{(4)}_{0,0,2,\uparrow} = -\frac{80t^{*4}}{27J^{*3}} \tag{6.31}$$

Using particle-hole and spin rotation symmetries, we can now write down the fourth order shifts for all four states in the low-energy manifold:

$$\begin{aligned} \Delta E^{(4)}_{0,0,2,0} &= \Delta E^{(4)}_{0,0,2,2} = \frac{64t^{*4}}{27J^{*3}} \\ \Delta E^{(4)}_{0,0,2,\uparrow} &= \Delta E^{(4)}_{0,0,2,\downarrow} = -\frac{80t^{*4}}{27J^{*3}} \,. \end{aligned} \tag{6.32}$$

We can already see that the singly-occupied states experience a lowering of energy due to virtual excitations of the singlet state, while the doubly-occupied state has its energy raised. This effectively means if an electron is already present on the first site, a second incoming electron experiences a repulsion due to it. Replacing each state with the appropriate operator, we can convert this intuition into an effective Hamiltonian for the excitations:

$$\begin{aligned}\Delta H^{(4)} &= \frac{16t^{*4}}{27J^{*3}} \left|\Psi_{0,0,2}\right\rangle \left\langle\Psi_{0,0,2}\right| \left[4(1-n_{1,\uparrow})(1-n_{1,\downarrow}) + 4n_{1,\uparrow})n_{1,\downarrow} - 5n_{1,\uparrow}(1-n_{1,\downarrow}) - 5n_{1,\downarrow}(1-n_{1,\uparrow})\right] \\ &= \frac{16t^{*4}}{27J^{*3}} \left|\Psi_{0,0,2}\right\rangle \left\langle\Psi_{0,0,2}\right| \left[-u\sum_{\sigma} n_{1\sigma} + un_{1\uparrow}n_{1\downarrow}\right] ,\end{aligned} \tag{6.33}$$

where $u = 9$. This is the local Fermi liquid Hamiltonian for excitations above the Kondo screened ground state; the repulsive $n_\uparrow n_\downarrow$ term ensures that the excitations are electronic in nature.

2.7 Iterative Diagonalisation of Quantum Impurity Models

The broad idea is the following. We have a Hamiltonian describing an interacting set of states (in real or momentum space). We can express the total Hamiltonian in an incremental fashion: $H = \sum_i H_i$, where H_{i+1} involves more number of states than H_i. For example, a tight-binding model can be written in that form, with the definition $H_i = c^\dagger_{i+1} c_i + \text{h.c.}$. The iterative diagonalisation method obtains the low-energy spectrum of this problem in the following manner: We first diagonalise the Hamiltonian H for a smaller value of i, small enough such that this can be done exactly. We then truncate the spectrum to a predefined size, and rotate all existing operators to this truncated basis, including the Hamiltonian H. We then consider the "bonding Hamiltonian" ΔH between the existing sites and the new sites, and rotate the same into the truncated basis. Adding the previous rotated Hamiltonian H and the rotated increment Hamiltonian ΔH gives us a truncated but effective Hamiltonian for the increased number of sites. We again diagonalise this, and again retain only a fixed number of states in the spectrum. We keep repeating this until we reach the required number of sites. A similar strategy is employed in numerical renormalisation group [446] and density matrix renormalisation group [458, 459]

Jordan-Wigner Matrix Representation of Fermionic Operators

For a single qubit, the creation/annihilation matrices are

$$c = \begin{pmatrix} 0 & 1 \\ 0 & 0 \end{pmatrix}, c^\dagger = \begin{pmatrix} 0 & 0 \\ 1 & 0 \end{pmatrix} , \tag{7.1}$$

given the convention that $|1\rangle = (0 \;\; 1)$ is the occupied state. For a many-body system, these must be replaced with field operators that have the canonical fermionic algebra. For a system of N 1-particle levels, this can be accomplished through a *Jordan-Wigner*-like transformation

$$c_j = \left(\otimes_1^j \sigma_z\right) \otimes c \otimes \left(\otimes_1^{N-j} \mathbb{I}\right) \;, j \in [0, N-1] \,, \tag{7.2}$$

where $\sigma_z = \begin{pmatrix} 1 & 0 \\ 0 & -1 \end{pmatrix}$ and $\mathbb{I} = \begin{pmatrix} 1 & 0 \\ 0 & 1 \end{pmatrix}$. For example, for spinless electrons on a three-site lattice, we can have three fermionic operators: c_1,c_2, and c_3. Following the above expression, their matrices are

$$c_1 = \begin{bmatrix} 0 & 0 & 1 & 0 & 0 & 0 & 0 & 0 \\ 0 & 0 & 0 & 1 & 0 & 0 & 0 & 0 \\ 0 & 0 & 0 & 0 & 0 & 0 & 0 & 0 \\ 0 & 0 & 0 & 0 & 0 & 0 & 0 & 0 \\ 0 & 0 & 0 & 0 & 0 & 0 & -1 & 0 \\ 0 & 0 & 0 & 0 & 0 & 0 & 0 & -1 \\ 0 & 0 & 0 & 0 & 0 & 0 & 0 & 0 \\ 0 & 0 & 0 & 0 & 0 & 0 & 0 & 0 \end{bmatrix}, c_2 = \begin{bmatrix} 0 & 0 & 1 & 0 & 0 & 0 & 0 & 0 \\ 0 & 0 & 0 & 1 & 0 & 0 & 0 & 0 \\ 0 & 0 & 0 & 0 & 0 & 0 & 0 & 0 \\ 0 & 0 & 0 & 0 & 0 & 0 & 0 & 0 \\ 0 & 0 & 0 & 0 & 0 & 0 & -1 & 0 \\ 0 & 0 & 0 & 0 & 0 & 0 & 0 & -1 \\ 0 & 0 & 0 & 0 & 0 & 0 & 0 & 0 \\ 0 & 0 & 0 & 0 & 0 & 0 & 0 & 0 \end{bmatrix}, c_3 = \begin{bmatrix} 0 & 1 & 0 & 0 & 0 & 0 & 0 & 0 \\ 0 & 0 & 0 & 0 & 0 & 0 & 0 & 0 \\ 0 & 0 & 0 & -1 & 0 & 0 & 0 & 0 \\ 0 & 0 & 0 & 0 & 0 & 0 & 0 & 0 \\ 0 & 0 & 0 & 0 & 0 & -1 & 0 & 0 \\ 0 & 0 & 0 & 0 & 0 & 0 & 0 & 0 \\ 0 & 0 & 0 & 0 & 0 & 0 & 0 & 1 \\ 0 & 0 & 0 & 0 & 0 & 0 & 0 & 0 \end{bmatrix},$$

For later use, we define the *antisymmetriser matrix* $S(j)$ and identity matrix $\mathbb{I}(j)$,

$$\begin{aligned} S(j) &= \otimes_1^j \sigma_z = \sigma_z \otimes \ldots j \text{ times } \ldots \otimes \sigma_z, \\ \mathbb{I}(j) &= \otimes_1^{N-j} \mathbb{I} = \mathbb{I} \otimes \ldots j \text{ times } \ldots \otimes \mathbb{I}\,, \end{aligned} \tag{7.3}$$

to express the fermionic representation compactly:

$$c_j = S(j) \otimes c \otimes \mathbb{I}(N-j)\,. \tag{7.4}$$

Structure of Hamiltonian

We consider a general impurity model, of L number of sites (excluding the impurity site):

$$H_{\text{sys}}(L) = H_{\text{imp}} + H_{\text{imp-bath}} + -t \sum_{\sigma,j=1}^{L-1} \left(c^\dagger_{j,\sigma} c_{j+1,\sigma} + \text{h.c.} \right)\,, \tag{7.5}$$

where H_{imp} is the Hamiltonian for the decoupled impurity site and $H_{\text{imp-bath}}$ is the impurity-bath coupling. Such a system has $2L + 2$ single-particle levels in the full system (2 spin levels for each of the $L + 1$ sites).

Iteration scheme (the initial number of states is L_0):

$$\begin{aligned} H_0(L_0) &= H_{\text{sys}}(L_0)\,, \\ H_{r+1}(L_0) &= H_r(L_0) + \Delta H_r(L_0),\ r \geq 0\,, \\ \Delta H_r(L_0) &= -t \sum_\sigma \left(c^\dagger_{L_0+r,\sigma} c_{L_0+r+1,\sigma} + \text{h.c.} \right). \end{aligned} \tag{7.6}$$

H_0 is the initial Hamiltonian, consisting of L_0 lattice sites in the bath, $H_{r+1}(L_0)$ is the Hamiltonian after $r+1$ iterations having started with L_0 sites, and $\Delta H_r(L_0)$ is the increment term that gets added to $H_r(L_0)$ during the $(r+1)^{\text{th}}$ iteration to give rise to $H_{r+1}(L_0)$.

Iterative Diagonalization

Let the starting Hamiltonian be $H_0(L_0)$, consisting of L_0 single-particle levels (hence a Hilbert space dimension of 2^{L_0}). We start with a single-particle computational basis and construct the L_0 fermionic operators $c_1, c_2, \ldots, c_{L_0}$ in this basis, using eq. 7.4. We also keep track of a large antisymmetriser matrix $S(L_0)$ that will be used to attach new sites when we expand the system. Let M_s be the maximum number of eigenstates we retain in the spectrum at any given step. The value of M_s should be chosen so that a $M_s \times M_s$ matrix can be diagonalised in reasonable time.

S1. Construct the complete Hamiltonian matrix H_0 in our present basis using the field operators $\{c_j\}$. Diagonalise the Hamiltonian (of size $D_0 \times D_0$) and obtain the eigenvalues E_n and eigenstates X_n. Each X_n is a column vector of size D_0.

S2. Retain at most M_s number of eigenstates, preferring the ones with lower energy. The reduced basis for this rotated truncated subspace is constructed by stacking the column vectors X_n horizontally:

$$R = [X_1 X_2 \ldots X_{M_s}]_{D_0 \times M_s} \ . \tag{7.7}$$

This matrix also acts as the transformation to rotates and truncate all operators from the old basis into the new one.

S3. We rotate our Hamiltonian H_0, our fermionic operators $\{c_j\}$ and the large antisymmetrizer matrix $S(L_0)$ into the new reduced basis, using the transformation $O \to R^\dagger O R$.

S4. We now need to expand our system by adding the increment Hamiltonian ΔH_0. Let the number of *new* 1-particle levels in ΔH_0 be L_Δ. These new levels will be indexed as $L_0{+}1, \ldots, L_0{+}L_\Delta$. We need to define antisymmetrized fermionic operators for the new sites:

$$\begin{aligned} c_{L_0+1} &= c \otimes \mathbb{I}(2^{L_\Delta - 1}), \\ c_{L_0+2} &= \sigma_z \otimes c \otimes \mathbb{I}(2^{L_\Delta - 2}), \\ &\ldots \\ c_{L_0+L_\Delta} &= (\otimes_1^{L_\Delta - 1} \sigma) \otimes c \ . \end{aligned} \tag{7.8}$$

These have to be calculated in the local computational basis (of size 2^{L_Δ}) of the new levels.

S5. Combining the new sites with the old sites leads to a combined Hilbert space dimension of $(M_s + 2^{L_\Delta}) \times (M_s + 2^{L_\Delta})$. To allow all operators to act on the enlarged Hilbert space, we expand both sets of operators:

$$\begin{aligned} c_j &= S(L_0) \otimes c_j; \quad j = L_0 + 1, \ldots, L_\Delta \ , \\ c_j &= c_j \otimes \mathbb{I}(2^{L_\Delta}); \quad j = 1, 2, \ldots, L_0 \ , \\ H_0 &\to H_0 \otimes \mathbb{I}(2^{L_\Delta}), \\ S(L_1) &= S(L_0) \otimes \mathbb{I}(2^{L_\Delta}) \ . \end{aligned} \tag{7.9}$$

where $\mathbb{I}(2^{L_\Delta})$ is an identity matrix of dimension $2^{L_\Delta} \times 2^{L_\Delta}$. Note that the operators in the last three equations are the rotated ones (following Step 3).

S6. Using the transformed operators $c_{L_0+1}, \ldots, c_{L_0+L_\Delta}$ for the new sites, construct the difference Hamiltonian matrix ΔH_0 and hence the updated Hamiltonian $H_1 = H_0 + \Delta H_0$ for the next step. Repeat the process starting from step 2 with the new Hamiltonian H_1, the new operators c_j and the new matrix $S(L_1)$ replacing the old counterparts.

2.7.1 Static correlations

We are in general interested in $n-$point correlations of the form $\langle O_1 O_2 \ldots O_n \rangle$, where O_i are operators that act on 1-particle Hilbert spaces. Let the earliest step of the iterative diagonalisation procedure at which all these operators have entered the system be r. At this step r, construct the correlation operator $O_1 O_2 \ldots O_n$ using the fermionic matrices c_j at that step (recall that these matrices will be highly rotated versions of the matrices we started with). Having constructed the operator O, we expand and rotate it after the completion of every future step: $O_{n+1} = (R_n^\dagger O_n R_n) \otimes \mathbb{I}(2^{L_\Delta})$, where R_n is the rotation matrix for the nth step. The last step n^* of the iterative diagonalisation consists of only a diagonalisation and no expansion, resulting in a final set of eigenstates $\{X_i\}$. The form of the correlation operator in this basis is $O_{n^*} = R_{n^*-1}^\dagger O_{n^*-1} R_{n^*}$. The expectation value can now be calculated using the matrix O_{n^*} and the ground state of $\{X_i\}$.

2.7.2 Entanglement measures

In Section 2.9.1, we show how the matrix elements of reduced density matrices can be expressed as expectation values of certain local operators. Using such relations, the computation of reduced density matrix effective boils down to the calculation of specific correlations, which is covered in the previous section.

2.8 Optimising Fermi Surface Calculations

Below, we outline an algorithm for reducing computational cost of carrying out iterative diagonalisation processes focused on the Fermi surface of a quantum impurity model, by rotating the interaction matrix to a sparser form. It is useful when the Hamiltonian has certain symmetry properties arising from specific lattice geometries.

Rotated basis for simplified representation

At the renormalisation group fixed point, we have a renormalised theory for the interaction of the impurity spin S_f with the $f-$layer Fermi surface:

$$H^* = \sum_{\alpha,\beta} \mathbf{S}_f \cdot \boldsymbol{\sigma}_{\alpha,\beta} \sum_{\mathbf{k},\mathbf{q}} J_f^*(\mathbf{k},\mathbf{q}) f_{\mathbf{k},\alpha}^\dagger f_{\mathbf{q},\beta} \,. \tag{8.1}$$

We will now obtain a more minimal representation of this interaction. Each momentum label is summed over all four quadrants Q_1 through Q_4. We assume the lattice structure is such that the

following equation relates Q_1 with Q_3 and Q_2 with Q_4:

$$J_{\mathbf{k},\mathbf{k}'} = -J_{\mathbf{k}+\mathbf{Q},\mathbf{k}'} = -J_{\mathbf{k},\mathbf{k}'+\mathbf{Q}}, \quad \mathbf{Q} = (\pi,\pi). \tag{8.2}$$

With this, we can write

$$\begin{aligned}
\sum_{\mathbf{k},\mathbf{q}} J_f^*(\mathbf{k},\mathbf{q}) f^\dagger_{\mathbf{k},\alpha} f_{\mathbf{q},\beta} &= \sum_{\mathbf{q}} \left[\sum_{\mathbf{k}\in Q_1,Q_2} J_f^*(\mathbf{k},\mathbf{q}) f^\dagger_{\mathbf{k},\alpha} + \sum_{\mathbf{k}\in Q_3,Q_4} J_f^*(\mathbf{k},\mathbf{q}) f^\dagger_{\mathbf{k},\alpha} \right] f_{\mathbf{q},\beta} \\
&= \sum_{\mathbf{q}} \left[\sum_{\mathbf{k}\in Q_1,Q_2} J_f^*(\mathbf{k},\mathbf{q}) f^\dagger_{\mathbf{k},\alpha} + \sum_{\mathbf{k}\in Q_1} J_f^*(\mathbf{k}-\mathbf{Q_1},\mathbf{q}) f^\dagger_{\mathbf{k}-\mathbf{Q_1},\alpha} + \sum_{\mathbf{k}\in Q_2} J_f^*(\mathbf{k}+\mathbf{Q_2},\mathbf{q}) f^\dagger_{\mathbf{k}+\mathbf{Q_2},\alpha} \right] f_{\mathbf{q},\beta} \\
&= \sum_{\mathbf{q}} \left[\sum_{\mathbf{k}\in Q_1} J_f^*(\mathbf{k},\mathbf{q}) \left(f^\dagger_{\mathbf{k},\alpha} - f^\dagger_{\mathbf{k}-\mathbf{Q_1},\alpha} \right) + \sum_{\mathbf{k}\in Q_2} J_f^*(\mathbf{k},\mathbf{q}) \left(f^\dagger_{\mathbf{k},\alpha} - f^\dagger_{\mathbf{k}+\mathbf{Q_2},\alpha} \right) \right] f_{\mathbf{q},\beta} \,.
\end{aligned} \tag{8.3}$$

For ease of notation, we define new fermionic operators $A_{\mathbf{k},\sigma}$:

$$A_{\mathbf{k},\sigma,\pm} = \begin{cases} \frac{1}{\sqrt{2}} \left(f_{\mathbf{k},\sigma} \pm f_{\mathbf{k}-\mathbf{Q_1},\sigma} \right), \mathbf{k} \in Q_1 \,, \\ \frac{1}{\sqrt{2}} \left(f_{\mathbf{k},\sigma} \pm f_{\mathbf{k}+\mathbf{Q_2},\sigma} \right), \mathbf{k} \in Q_2 \,, \end{cases} \tag{8.4}$$

which satisfy the appropriate algebra: $\left\{ A_{\mathbf{k},\sigma,p}, A_{\mathbf{k}',\sigma',p'} \right\} = \delta_{\mathbf{k},\mathbf{k}'} \delta_{\sigma,\sigma'} \delta p, p'$, with $p = \pm$ denoting the flavours of the A fields. Note that only the $p = -1$ flavour enters the Hamiltonian. Henceforth, we drop the label $\pm$ and it is implied that A refers to the $p = -1$ variant.

Decomposing the sum over $\mathbf{q}$ in a similar fashion, we get

$$\sum_{\mathbf{k},\mathbf{q}} J_f^*(\mathbf{k},\mathbf{q}) f^\dagger_{\mathbf{k},\alpha} f_{\mathbf{q},\beta} = 2 \sum_{\mathbf{k},\mathbf{q}\in Q_1,Q_2} J_f^*(\mathbf{k},\mathbf{q}) A^\dagger_{\mathbf{k},\alpha} A_{\mathbf{q},\beta} \,. \tag{8.5}$$

Correlations in truncated representation

In order to calculate equal-time correlations (such as $\langle S_d^+ f^\dagger_{\mathbf{k}\downarrow} f_{\mathbf{k}'\uparrow} \rangle$), we use eq. 8.4 to express the bare fields $f_{\mathbf{k},\sigma}$ in terms of the new fields $A_{\mathbf{k},\sigma,\pm}$ and $B_{\mathbf{k},\sigma,\pm}$:

$$\begin{aligned}
f_{\mathbf{k},\sigma} &= \frac{1}{\sqrt{2}} \left(A_{\mathbf{k},\sigma,+} + A_{\mathbf{k},\sigma,-} \right) \,, \mathbf{k} \in Q_1, Q_2 \\
f_{\mathbf{k}-\mathbf{Q}_1,\sigma} &= \frac{1}{\sqrt{2}} \left(A_{\mathbf{k},\sigma,+} - A_{\mathbf{k},\sigma,-} \right) \,, \mathbf{k} \in Q_1 \\
f_{\mathbf{k}+\mathbf{Q}_2,\sigma} &= \frac{1}{\sqrt{2}} \left(A_{\mathbf{k},\sigma,+} - A_{\mathbf{k},\sigma,-} \right) \,, \mathbf{k} \in Q_2
\end{aligned} \tag{8.6}$$

where the four relations act on operators in four quadrants. These relations allow us to express correlations $F_{k_i,k_j} = \langle S_d^+ c^\dagger_{k_i,\uparrow} c_{k_j,\downarrow} \rangle$ for the bare fields f in terms of the rotated fields. Using the fact

that the Hamiltonian does not couple the fields B_+ and A_+, we have

$$\begin{aligned} F_{k_1,k_1} = F_{k_3,k_3} = -F_{k_1,k_3} &= \frac{1}{2}\langle S_d^+ A^\dagger_{k_1,\downarrow,-} A_{k_1,\uparrow,-})\rangle \ , \\ F_{k_2,k_2} = F_{k_4,k_4} = -F_{k_2,k_4} &= \frac{1}{2}\langle S_d^+ A^\dagger_{k_2,\downarrow,-} A_{k_2,\uparrow,-})\rangle \ , \\ F_{k_1,k_2} = F_{k_3,k_4} = -F_{k_1,k_4} = -F_{k_2,k_3} &= \frac{1}{2}\langle S_d^+ A^\dagger_{k_1,\downarrow,-} A_{k_1,\uparrow,-})\rangle \ , \end{aligned} \tag{8.7}$$

where the momentum state k_i belongs to the quadrant Q_i.

Effective Star Graph Representation of Kondo Interaction

To make computation less intensive, we want to make the Hamiltonian in eq. 8.5 sparser, by going to a star graph representation where each node of the graph couples only with the impurity spin (central node) and not to the other nodes of the graph. We therefore consider a rotated basis of excitations

$$\gamma^\dagger_{i,\sigma} = \sum_k \Lambda_{i,k} A^\dagger_{k,\sigma} \ , \ \text{where} \ \ \sum_k \Lambda^*_{i,k}\Lambda_{j,k} = \delta_{i,j} \ . \tag{8.8}$$

These fermions of course satisfy the appropriate algebra:

$$\left\{\gamma_{i,\sigma}, \gamma^\dagger_{j,\sigma'}\right\} = \sum_{k,q} \Lambda^*_{i,k}\Lambda_{j,q} \left\{A_{k,\sigma}, A^\dagger_{q,\sigma'}\right\} = \delta_{i,j}\delta_{\sigma,\sigma'} \ . \tag{8.9}$$

In order to calculate the coefficients $\Lambda_{i,k}$, we impose the star graph simplification condition described above:

$$\sum_{\mathbf{k},\mathbf{q}} J^*_f(\mathbf{k},\mathbf{q}) A^\dagger_{\mathbf{k},\alpha} A_{\mathbf{q},\beta} = \sum_i K_i \gamma^\dagger_{i,\alpha}\gamma_{i,\beta} \ , \tag{8.10}$$

where K_i are the eigenvalues of the Kondo coupling matrix $J^*_f(\mathbf{k},\mathbf{q})$. Substituting the definition of the γ fields (eq. 8.8) leads to the equation

$$J^*_f(\mathbf{k},\mathbf{q}) = \sum_i \Lambda_{k,i} K_i \Lambda^\dagger_{i,q} \implies \mathcal{J} = \Lambda K \Lambda^\dagger \ , \tag{8.11}$$

where $\mathcal{J}$ is the Kondo coupling matrix with matrix elements $J^*_f(\mathbf{k},\mathbf{q})$, K is a diagonal matrix with the eigenvalues (K_i) of $\mathcal{J}$ along its diagonal, and Λ is the matrix $\Lambda_{i,k}$ (the rotated indices i along the row, and the earlier momentum indices along the column). From eq. 8.11, it is clear that since $\mathcal{J}$ is Hermitian, the matrix Λ is simply the unitary matrix which diagonalises the Kondo matrix $\mathcal{J}$:

$$\Lambda^\dagger \mathcal{J} \Lambda = K \ . \tag{8.12}$$

The prescription is therefore as follows. We compute the unitary transformation Λ that diagonalises $\mathcal{J}$ and obtain the eigenvalues $\{K_i\}$. Using the eigenvalues, we work with the sparser Hamiltonian

$$\vec{S}_f \cdot \sum_{\alpha,\beta} \vec{\sigma}_{\alpha,\beta} \sum_i K_i \gamma^\dagger_{i,\alpha}\gamma_{i,\beta} \ . \tag{8.13}$$

If we have to calculate a certain correlation $C_{k,q}$, we instead calculate the correlation matrix $\tilde{C}_{i,j}$ in the rotated basis, and then transform back using the unitary transformation:

$$C = \Lambda \tilde{C} \Lambda^{\dagger} \ . \tag{8.14}$$

2.9 Measures of entanglement and their computation

The present millennium has seen a rapid surge in the use of quantum entanglement towards the study of quantum and condensed matter systems [243–248]. By tracking quantum correlations among particles across both small and large distances, entanglement measures offer valuable insights into the nature of the ground state and low-energy excitations. This, for example, allows us to distinguish strongly-correlated topologically ordered states characterised by long-ranged entanglement (in the form of a sub-leading topological term in their entanglement entropy [249, 250, 253, 257]) from weakly-interacting topologically trivial phases that have short-ranged area-law entanglement [245, 270, 271].

2.9.1 Reduced density matrix elements as equal-time correlation functions

A density matrix plays the role of a probability density function (PDF) for a quantum system. A classical variable X that can take values $x \in [-X^*, X^*]$ has a PDF $F(X = x)$, which is used, for example, for calculating the average value (expectation value) of the variable:

$$\langle X \rangle = \int_{-X^*}^{X^*} x F(x) dx \ . \tag{9.1}$$

In quantum mechanics, the variables we are interested in are operators O, and a quantum PDF ρ will then give the expectation value of the operator, in a fashion similar to its classical counterpart:

$$\langle O \rangle = \sum_{\phi} \langle \phi | \rho O | \phi \rangle \ ; \tag{9.2}$$

here, the integral over the classical values x is replaced by a sum over the all possible quantum states $|\phi\rangle$ (complete orthonormal basis) of the system. However, we already know that the expectation value of a quantum operator is given by

$$\langle O \rangle = \langle \Psi | O | \Psi \rangle \ . \tag{9.3}$$

To bring this form closer to the one in terms of ρ (eq. 2), we insert an identity resolution: $1 = \sum_{\phi} |\phi\rangle \langle \phi|$:

$$\langle O \rangle = \sum_{\phi} \langle \Psi | O | \phi \rangle \langle \phi | \Psi \rangle = \sum_{\phi} \langle \phi | \Psi \rangle \langle \Psi | O | \phi \rangle \ . \tag{9.4}$$

A comparison of this equation to eq. (2) gives

$$\rho = |\Psi\rangle \langle \Psi| \ ; \tag{9.5}$$

a density matrix (also called density operator) is therefore formally defined as the outer product of the wavefunction with its conjugate. It encodes all information about the state; for example, the probability of measuring the system to be at a position x (hence in a state $|x\rangle$) is given by $P(x) = \langle x|\rho|x\rangle$. From its definition in eq. (5), the DM has the very important property that it has unity trace:

$$\mathrm{Tr}[\rho] = 1 \ , \tag{9.6}$$

where $\mathrm{Tr}[\cdot]$ is the trace of an operator. This is seen very easily be taking the trace in an orthonormal basis in which the state $|\Psi\rangle$ is one of the basis states. For example, consider the DM

$$\rho = \frac{1}{\sqrt{2}} \left[|\Psi_1\rangle \langle\Psi_1| + |\Psi_2\rangle \langle\Psi_2| \right] \ , \tag{9.7}$$

where $|\Psi_{1,2}\rangle$ are orthogonal normalised states. The trace of ρ^2 for such a state is only $1/2$; such states satifying $\mathrm{Tr}[\rho^2] < 1$ are termed *mixed states*; the DM describing such states cannot be written in the form $\rho = |\Psi\rangle \langle\Psi|$ for any wavefunction $|\Psi\rangle$. On the other hand, the DMs that *can* be expressed like that are termed *pure states*, and have $\mathrm{Tr}[\rho^2] = 1$.

One way in which a pure state can be realistically converted into a mixed state is through a measurement process. Consider the zero total spin state formed by two spins:

$$|\Psi\rangle = \frac{1}{2} \left[|\uparrow,\downarrow\rangle + |\downarrow,\uparrow\rangle \right] \ , \rho = |\Psi\rangle \langle\Psi| \ . \tag{9.8}$$

The state $|\uparrow,\downarrow\rangle$ has the first spin pointing up and the second one down, and this is in a superposition with the its flipped counterpart $|\downarrow,\uparrow\rangle$. This is clearly a pure state.

If we now measure the state of the second spin, it will collapse into one of it's two states; the other spin will collapse into the opposite state (given the antiparallel configurations of the spins). What this means is that until one checks what the result of the measurement is, the first spin remains in a statistical superposition of both outcomes (up and down). This is formally expressed through a partial trace operation: the state of the first spin after a measurement of the second spin is obtained by taking the full density matrix ρ and computing its trace over the states $|\sigma_B\rangle$ of the second spin, leaving out the states of the first spin from the trace:

$$\rho_1 = \mathrm{Tr}_2[\rho] = \sum_{\sigma_2} \langle\sigma_2|\rho|\sigma_2\rangle \ ; \tag{9.9}$$

where $|\sigma_2\rangle$ sums over the states $|\uparrow\rangle$ and $|\downarrow\rangle$ of the second spin. this partial tracing operation Tr_2 codifies the measurement process, and the partially traced density matrix ρ_1 is termed a reduced density matrix (RDM) of the first spin, because it only captures information about the first spin (the second spin has been traced out).

To see the connection with mixedness, let us compute the RDM for the first spin explicitly:

$$\rho_1 = \langle\uparrow_2 |\rho| \uparrow_2\rangle + \langle\downarrow_2 |\rho| \downarrow_2\rangle = \frac{1}{2} \left[|\uparrow_1\rangle \langle\uparrow_1| + |\downarrow_1\rangle \langle\downarrow_1| \right] \ , \tag{9.10}$$

where the numbered subscripts on the kets and bras indicate that they only act on the respective Hilbert spaces. To see that ρ_1 describes a mixed state, we adopt a specific representation:

$$\begin{aligned} |\uparrow_1\rangle = \begin{pmatrix} 1 \\ 0 \end{pmatrix}, |\downarrow_1\rangle = \begin{pmatrix} 0 \\ 1 \end{pmatrix}, \\ \implies \rho_1 = \frac{1}{2}\begin{pmatrix} 1 & 0 \\ 0 & 1 \end{pmatrix}, \ \rho_1^2 = \frac{1}{4}\begin{pmatrix} 1 & 0 \\ 0 & 1 \end{pmatrix} . \end{aligned} \tag{9.11}$$

The trace of ρ_1^2 is half, hence it is a mixed state.

The deviation of trace of ρ^2 from its maximum value of unity can be thought of as a measure of the lost information. In the example above, when we traced out the states of the second spin, we lost some information about the state of the first spin as well. This is because the two spins were *entangled*; they had quantum correlations between them. The entanglement arises from the fact that the states of the two spins are anti-correlated.

If instead we had chosen a non-entangled parent state to start from, the reduced density matrix would not have been mixed. For example, consider the state

$$|\Psi\rangle = \frac{1}{2}\left(|\uparrow_1\rangle + |\downarrow_1\rangle\right) \otimes \left(|\uparrow_2\rangle + |\downarrow_2\rangle\right) . \tag{9.12}$$

It is easy to see that this state does not contain any correlations between the two spins - no matter the configuration of the second spin, the first spin is always in the state $|\uparrow_1\rangle + |\downarrow_1\rangle$. The RDM for the first spin comes out to be

$$\rho_1 = \frac{1}{2}\begin{pmatrix} 1 & 1 \\ 1 & 1 \end{pmatrix}, \ \rho_1^2 = \frac{1}{4}\begin{pmatrix} 1 & 1 \\ 1 & 1 \end{pmatrix} , \tag{9.13}$$

revealing that ρ_1 is not mixed.

The above method of calculating an RDM works for simple cases but can fail if (i) we have fermion signs to account for, or (ii) the full basis cannot be expressed as a direct product of local basis sets. The former arises if we are dealing with fermions, and the latter arises if we are working in a rotated basis. We now derive an alternative method for calculating the RDM, one that automatically takes care of the fermion signs and works even if the basis is rotated and complicated to write down. We start by defining the RDM more precisely. Given a state $|\Psi\rangle$ and a bipartition into subsystems S_1 and its complement S_2, the density matrix for the state is $\rho = |\Psi\rangle\langle\Psi|$. A basis state of the full system can be written as $|A, \alpha\rangle = |A\rangle \otimes |\alpha\rangle$, where $\{A\}$ and $\{\alpha\}$ are complete sets of basis states describing S_1 and S_2 respectively. The RDM for S_2 is then defined as

$$\rho_1 = \mathrm{Tr}_\alpha \rho = \sum_\alpha \langle\alpha|\rho|\alpha\rangle . \tag{9.14}$$

The matrix elements of ρ_1 in the basis $\{A\}$ can be expressed as

$$\langle A|\rho_1|B\rangle = \sum_\alpha \langle A, \alpha|\, \rho\, |B, \alpha\rangle . \tag{9.15}$$

We next define an operator $O_{A,B}$ that represents scattering processes between the various states of subsystem S_1: $O_{A,B} = |A\rangle\langle B| \otimes I_2$, but acts as identity on S_2. The expectation value of this operator is

$$\langle O_{A,B}\rangle = \mathrm{Tr}(\rho O_{A,B}) = \sum_{C,\beta} \langle C,\beta|\rho|A\rangle\langle B|C,\beta\rangle = \sum_{\beta} \langle B,\beta|\rho|A,\beta\rangle \ . \tag{9.16}$$

Comparing with eq. 9.15, we obtain the relation

$$\langle A|\rho_1|B\rangle = \langle O_{B,A}\rangle \ . \tag{9.17}$$

This result is significant because it guarantees that in order to calculate the RDM for a subsystem, it is enough to calculate the expectation values of all inter-state off-diagonal transition operators. For example, we take subsystem S_1 to be a two fermion system represented by the operators c_1 and c_2. Assuming a basis $\{|0,0\rangle, |0,1\rangle, |1,0\rangle, |1,1\rangle\}$, where the two entries represent the occupancies of the two fermions, the RDM for this subsystem is determined by the following matrix:

$$\rho_1 = \begin{pmatrix} \langle h_1 h_2\rangle & \langle h_1 c_2^\dagger\rangle & \langle c_1^\dagger h_2\rangle & \langle c_1^\dagger c_2^\dagger\rangle \\ & \langle h_1 n_2\rangle & \langle c_1^\dagger c_2\rangle & \langle c_1^\dagger n_2\rangle \\ & & \langle n_1 h_2\rangle & \langle n_1 c_2^\dagger\rangle \\ & & & \langle n_1 n_2\rangle \end{pmatrix}, \tag{9.18}$$

where the blank entries can be determined from hermiticity. To see how the operators are determined, take the example of the top right element. The two basis states for that matrix element are $|0,0\rangle$ and $|1,1\rangle$.

2.9.2 Quantum Fisher information: a witness of multipartite entanglement

The quantum Fisher information (QFI) F_Q [460,461] quantifies how sensitive a state ρ is to unitary transformations generated by an observable $\hat{O}$. For a pure state $\rho = |\psi\rangle\langle\psi|$, $F_Q(\psi,\hat{O})$ is defined in terms of the variance of the operator $\hat{O}$ (i.e., the connected correlation function):

$$F_Q(\psi,\hat{O}) = 4\Delta(\hat{O})^2 = 4\left(\langle\psi|\hat{O}^2|\psi\rangle - \langle\psi|\hat{O}|\psi\rangle^2\right) \ , \tag{9.19}$$

and it provides an upper bound on the precision that can be achieved in measuring the parameter θ that is dual to the observable $\hat{O}$: $\mathcal{N}(\Delta\theta)^2 \geq F_Q^{-1}$, $\mathcal{N}$ being the number of independent measurements [460,461]. $F_Q(\psi,\hat{O})$ is thus a measure of the entanglement arising from quantum fluctuation content in $|\psi\rangle$ (considered with respect to an eigenstate of $\hat{O}$). This can be made more manifest by considering a traceless operator $\hat{M}$ with eigenstates $\{|m\rangle\}$. Without loss of generality, we can rescale the operator such that $\sum m^2 = 1/2$. If $\varepsilon_m(\psi) \equiv 1 - |\langle m|\psi\rangle|^2$ is the geometric entanglement between a given state $|\psi\rangle$ and the eigenstates of $\hat{M}$, the QFI corresponding to $\hat{M}$ in the state ψ can

be written as

$$F_Q(\psi, \hat{M}) = 4\left[\frac{1}{2} - \sum_m m^2 \varepsilon_m - \left(\sum_m m\varepsilon_m\right)^2\right] . \tag{9.20}$$

The total geometric entanglement $\sum_m \varepsilon_m$ is constrained to be $d_M - 1$, where d_M is the dimension of the operator $\hat{M}$. Because each eigenvalue m has a magnitude of at most $1/\sqrt{2}$ (all m^2 must add up to $1/2$), the maximum magnitude of the last two terms in eq. (9.20) (and hence the minimum value of the QFI) is attained for the case when some of the ε_m are zero. However, because the eigenstates are orthogonal, only one of them can have perfect overlap with the state $|\psi\rangle$ and only one ε_m can be zero at a time. The case of minimum QFI therefore corresponds to $\varepsilon_{m^*} = 0, \varepsilon_{m\neq m^*} = 1$, leading to $F_Q = 0$. The opposite situation arises when all the geometric entanglement measures are non-zero and equal, $\varepsilon_m = 1/d_M$, leading to a maximum QFI value of $F_Q = 2/d_M$. A uniformly spread geometric entanglement distribution, therefore, leads to a larger QFI, while a more focused distribution leads to a smaller QFI. This sums up the relation between the quantum Fisher information and geometric entanglement.

If the operator $\hat{M}$ is such that its eigenstates are separable states from the perspective of a certain party, the vanishing QFI arises when $|\psi\rangle$ has zero geometric entanglement with respect to one of the separable states, and the QFI saturates when $|\psi\rangle$ has a finite geometric entanglement with all of the states. A large QFI can thus be associated with more entanglement. Moreover, if the eigenstates of $\hat{M}$ are symmetry-broken states, a vanishing QFI indicates that $|\psi\rangle$ is very close to such a symmetry-broken state, while a large QFI indicates that $|\psi\rangle$ is a uniform superposition of such symmetry-broken states and therefore preserves the symmetry as a whole. A larger QFI points towards the presence of more quantum fluctuations and a reduced susceptibility towards symmetry-breaking.

We will now relate the QFI to some other measures of correlation. The QFI corresponding to an observable can be directly related to the static lesser Greens functions associated with that observable:

$$F_Q(\psi, \hat{O}_2) = 4\left(\langle \hat{O}_2\hat{O}_1^\dagger\rangle\Big|_{\hat{O}_1^\dagger=\hat{O}_2} - \langle \hat{O}_2\hat{O}_1^\dagger\rangle^2\Big|_{\hat{O}_1=1}\right) = 4\left[G^<_{O_2,O_2}(t\to\infty) - \left(G^<_{1,O_2}(t\to\infty)\right)^2\right] \tag{9.21}$$

Further, the retarded Greens function can very generally be related to the QFI. By using the simplified forms $\frac{i}{2}G^R_{O_2,O_2}(t\to\infty) = \langle (O_2)^2\rangle$ and $\frac{i}{2}G^R_{1,O_2}(t\to\infty) = \langle O_2\rangle$, we get

$$F_Q(\psi, \hat{O}_2) = 2iG^R_{O_2,O_2}(t\to\infty) + \left(G^R_{1,O_2}(t\to\infty)\right)^2 . \tag{9.22}$$

For the sake of completeness, we generalise the above relations to finite temperatures by adopting the approach of Hauke et al. [461]. For a mixed state at inverse temperature β characterised by the density matrix $\rho = \sum_n f_n |n\rangle\langle n|$ where $(E_n, |n\rangle)$ are the eigenvalue-eigenstate pairs and $f_n = e^{-\beta E_n}/\sum_n e^{-\beta E_n}$ are the Boltzmann weights, the FQI can be assigned a spectral representation of the form [461]

$$F_Q(\rho, \hat{O}) = 2\sum_{m,n} \frac{(f_m - f_n)^2}{f_m + f_n} |\langle m|\hat{O}|n\rangle|^2 . \tag{9.23}$$

By using the identity $\frac{f_m - f_n}{f_m + f_n} = \int_{-\infty}^{\infty} d\omega \delta(\omega + E_m - E_n) \tanh(\beta\omega/2)$, the finite temperature FQI can be written in the form

$$F_Q(\rho, \hat{O}) = 2 \int_{-\infty}^{\infty} d\omega \tanh(\beta\omega/2) \sum_{m,n} (f_m - f_n) \delta(\omega + E_m - E_n) |\langle m|\hat{O}|n\rangle|^2 . \quad (9.24)$$

In order to relate this with a correlation function, we now point out that the lesser Greens function $G^<$ and the greater Greens function $G^>$ that we will now define admit spectral representations in terms of the eigenstates $|n\rangle$ of the full problem:

$$G^<_{O^\dagger,O}(t) \equiv i \langle \hat{O}^\dagger \hat{O}(t)\rangle \implies G^<_{O^\dagger,O}(\omega) = 2\pi i \textstyle\sum_{m,n} f_n \delta(\omega + E_m - E_n) |\langle m|\hat{O}^\dagger|n\rangle|^2 , \quad (9.25)$$

$$G^>_{O^\dagger,O}(t) \equiv -i \langle \hat{O}(t)\hat{O}^\dagger\rangle \implies G^>_{O^\dagger,O}(\omega) = -2\pi i \textstyle\sum_{m,n} f_m \delta(\omega + E_m - E_n) |\langle m|\hat{O}|n\rangle|^2 . \quad (9.26)$$

If $\hat{O}$ is a Hermitian operator, eqs. (9.25) can be used to rewrite the QFI in terms of $G^{\lessgtr}_{O^\dagger,O}(\omega)$. Indeed, by combining eqs. (9.25) and eq. (9.24) with the assumption $\hat{O} = \hat{O}^\dagger$, we get

$$F_Q(\rho, \hat{O}) = -\frac{1}{\pi i} \int_{-\infty}^{\infty} d\omega \tanh(\beta\omega/2) \left(G^>_{O,O}(\omega) + G^<_{O,O}(\omega) \right) . \quad (9.27)$$

This constitutes the general relation between the finite temperature QFI for a general Hermitian many-particle operator $\hat{O}$ and the corresponding many-particle correlations at zero and finite frequencies.

The Kubo linear response function associated with the operator $\hat{O}(t)$ due to a perturbation from the same operator is associated with a correlation function/susceptibility $C_{\hat{O}}(t,t') = i\theta(t - t') \left\langle \left[\hat{O}(t), \hat{O}(t')\right]\right\rangle$. By going to the frequency domain, the imaginary part of such a function can be related to the sum of the lesser and greater Greens functions:

$$\begin{aligned} C_{\hat{O}}(\omega) &= i \int_0^{\infty} d(t-t') e^{i\omega(t-t')} \left(\langle \hat{O}(t)\hat{O}(t')\rangle - \langle \hat{O}(t')\hat{O}(t)\rangle \right) \\ \implies C_{\hat{O}}(\omega) - C_{\hat{O}}(\omega)^* &= i \int_0^{\infty} d(t-t') \left(e^{i\omega(t-t')} - e^{-i\omega(t-t')} \right) \left(\langle \hat{O}(t)\hat{O}(t')\rangle - \langle \hat{O}(t')\hat{O}(t)\rangle \right) \\ &= i \int_{-\infty}^{\infty} d(t-t') e^{i\omega(t-t')} \left(\langle \hat{O}(t)\hat{O}(t')\rangle - \langle \hat{O}(t')\hat{O}(t)\rangle \right) \\ &= -\left(G^>_{O,O}(\omega) + G^<_{O,O}(\omega) \right) . \end{aligned}$$

This allows us to connect the QFI with the imaginary part of the Kubo correlation function/susceptibility obtained in Ref. [461]:

$$F_Q(\rho, \hat{O}) = \frac{1}{\pi i} \int_{-\infty}^{\infty} d\omega \tanh(\beta\omega/2) \left(C_{\hat{O}}(\omega) - C_{\hat{O}}(\omega)^* \right) . \quad (9.28)$$

These relations will be useful in Chapter 3 (*Kondo Frustration via Charge Fluctuations: A Route to Mott Localisation in Infinite Dimensions*) and Chapter 5 (*Mott Criticality as the Confinement Transition of of a Pseudogap-Mott Metal: Insights on Mott Transition and Pseudogap in Two Dimensions*) to provide an entanglement-based description of correlation-driven metal-insulator transitions.

2.9.3 Decomposition of entanglement entropy in terms of multipartite information I_n

We first define a partitioning of the entire system into N disjoint regions, $\mathcal{S}_N = \{\nu_1, \nu_2, \ldots \nu_N\}$. Going beyond bipartite mutual information, one can define the $n-$partite information I_n between the members of $\mathcal{S}_n = \{\nu_1, \nu_2, \ldots, \nu_n\}$, which is itself a subset of the exhaustive set of regions $\mathcal{S}_N$:

$$I_n(\nu_1, \ldots, \nu_n) = \sum_{\sigma \in \mathcal{P}(\mathcal{S}_n)} (-1)^{1+|\sigma|} S_{\rm EE}(\sigma) \,, \tag{9.29}$$

where σ is a subset drawn from the power set of $\mathcal{S}_n$, and $|\sigma|$ is the number of members in the subset σ. The 4-partite information can be written as

$$\begin{aligned} & I_4(\nu_1, \nu_2, \nu_3, \nu_4) \\ & = S_{\rm EE}(\nu_1) + S_{\rm EE}(\nu_2) + S_{\rm EE}(\nu_3) + S_{\rm EE}(\nu_4) - S_{\rm EE}(\nu_1 \cup \nu_2) - S_{\rm EE}(\nu_1 \cup \nu_3) \\ & - S_{\rm EE}(\nu_1 \cup \nu_4) - S_{\rm EE}(\nu_2 \cup \nu_3) - S_{\rm EE}(\nu_2 \cup \nu_4) - S_{\rm EE}(\nu_3 \cup \nu_4) + S_{\rm EE}(\nu_1 \cup \nu_2 \cup \nu_3) \\ & + S_{\rm EE}(\nu_1 \cup \nu_2 \cup \nu_4) + S_{\rm EE}(\nu_1 \cup \nu_3 \cup \nu_4) + S_{\rm EE}(\nu_2 \cup \nu_3 \cup \nu_4) + S_{\rm EE}(\nu_1 \cup \nu_2 \cup \nu_3 \cup \nu_4) \,. \end{aligned} \tag{9.30}$$

One can also define the average $n-$partite information $\bar{I}_n$ by considering all sets of n regions:

$$\bar{I}_n = \frac{(N-n)!n!}{N!} \sum_{S_n \in C_n(\mathcal{S}_N)} I_n(S_n) = \frac{(N-n)!n!}{N!} \sum_{S_n \in C_n(\mathcal{S}_N)} \sum_{\sigma \in \mathcal{P}(\mathcal{S}_n)} (-1)^{1+|\sigma|} S_{\rm EE}(\sigma) \,, \tag{9.31}$$

where $C_n(\mathcal{S}_N)$ represents all ways of choosing n distinct elements out of the full set $\mathcal{S}_N$ of subsystems.

The expression for $\bar{I}_n$ can be simplified by splitting the summation over the elements of the power set $\mathcal{P}$ into sets of definite number:

$$\bar{I}_n = \frac{(N-n)!n!}{N!} \sum_{S_n \in C_n(\mathcal{S}_N)} I_n(S_n) = \frac{(N-n)!n!}{N!} \sum_{S_n \in C_n(\mathcal{S}_N)} \sum_{m=1}^{n} \sum_{\sigma_m \in \mathcal{P}_m(\mathcal{S}_n)} (-1)^{1+|\sigma|} S_{\rm EE}(\sigma_m) \,, \tag{9.32}$$

where $\mathcal{P}_m$ represents all subsets of the power set that have m elements. With some combinatorial manipulations, it can be shown that

$$\sum_{S_n \in C_n(\mathcal{S}_N)} \sum_{\sigma_m \in \mathcal{P}_m(\mathcal{S}_n)} = \binom{N-m}{n-m} \sum_{\sigma_m \in C_m(\mathcal{S}_N)} \,. \tag{9.33}$$

To see how this comes about, note that what this equation says is that summing over combinations of subsets of length n of the super set S_N and further summing over all subsets of length $m \leq n$ for each set S_n is equivalent to summing just once over subsets of length m of the super set S_N but now each subset of length m appears with a frequency $f_m = \binom{N-m}{n-m}$. The value for the frequency f_m is simply the number of subsets S_n in which the smaller subset σ_m appears. This can be calculated by allowing m of the n slots in S_n to be filled by the members of σ_m, and the remaining $n-m$ slots

then have to be filled by choosing from the remaining $N-m$ members of the super set S_N; there's obviously $\binom{N-m}{n-m}$ ways of carrying this out.

Implementing this into the expression for $\bar{I}_n$ gives

$$\bar{I}_n = \sum_{m=1}^{n} (-1)^{1+m} \frac{\binom{n}{m}}{\binom{N}{m}} \sum_{\sigma_m \in C_m(\mathcal{S}_N)} S_{\rm EE}(\sigma_m) = \sum_{m=1}^{n} (-1)^{1+m} \binom{n}{m} S_{\rm EE}^{(m)} \ , \tag{9.34}$$

where we have define the average entanglement entropy $S_{\rm EE}^{(m)}$ for all $m-$member sets of regions:

$$S_{\rm EE}^{(m)} = \frac{1}{\binom{N}{m}} \sum_{\sigma_m \in C_m(\mathcal{S}_N)} S_{\rm EE}(\sigma_m) \ . \tag{9.35}$$

With most of the machinery in place, we would now like to express the entanglement entropy $S_{\rm EE}$ purely in terms of multipartite measures I_n. For a system that is invariant under real-space translation (as our lattice model is), the entanglement entropy of any real-space interval should only depend on the extent of the interval. It therefore suffices to calculate the entanglement entropy averaged over all such intervals, and the corresponding measure in our formulation is $S_{\rm EE}^{(1)}$.

We will now express $S_{\rm EE}^{(1)}$ in terms of $\bar{I}_n$, by eliminating $S_{\rm EE}^{(m)} (m > 1)$ from the equations. We adopt the ansatz

$$S_{\rm EE}^{(1)} = \sum_{n=2}^{N} \lambda_n \bar{I}_n = \sum_{n=2}^{N} \lambda_n \binom{n}{m} \sum_{m=1}^{n} (-1)^{1+m} S_{\rm EE}^{(m)} \ . \tag{9.36}$$

In order to separate $S_{\rm EE}^{(1)}$ from the rest of the $S_{\rm EE}^{(m)}$, we exchange the order of summation:

$$S_{\rm EE}^{(1)} = \sum_{m=1}^{N} (-1)^{1+m} S_{\rm EE}^{(m)} \sum_{n=m}^{N} \lambda_n \binom{n}{m} - S_{\rm EE}^{(1)} \lambda_1 = S_{\rm EE}^{(1)} \sum_{n=2}^{N} n\lambda_n - \sum_{m=2}^{N-1} S_{\rm EE}^{(m)} (-1)^m \sum_{n=m}^{N} \binom{n}{m} \lambda_n \ , \tag{9.37}$$

where the constraint of $m \leq n$ in the previous form is now enforced by letting n run from m to N. The $N-1$ coefficients $\{\lambda_n\}$ will be determined by requiring that the $S_{\rm EE}^{(m)} (m > 1)$ vanish on the right-hand side, as well as by matching the coefficients of $S_{\rm EE}^{(1)}$ on both sides. Note that m runs only upto $N-1$ in the second term; this is because, $S_{\rm EE}^{(N)}$ is the entanglement entropy of the full system and hence automatically zero. The equations are

$$\sum_{n=2}^{N} n\lambda_n = 1, \tag{9.38}$$

$$\sum_{n=m}^{N} \binom{n}{m} \lambda_n = 0; \ m = 2, \ldots, N-1 \ . \tag{9.39}$$

We focus on the second equation first, since it is very short for m close to N. For $m = N-1$ and $m = N-2$, we get

$$\begin{aligned} &m = N-1 : \lambda_{N-1} + N\lambda_N = 0 \implies \lambda_{N-1} = -N\lambda_N \\ &m = N-2 : \lambda_{N-2} + (N-1)\,\lambda_{N-1} + \frac{N(N-1)}{2}\lambda_N = 0 \implies \lambda_{N-2} = \frac{N(N-1)}{2}\lambda_N \ . \end{aligned} \tag{9.40}$$

We extrapolate this to the general solution,

$$\lambda_m = (-1)^m \binom{N}{m} \lambda_N, \; m < N \,, \tag{9.41}$$

and then prove that if this is true for λ_{N-m}, it also solves the equation for λ_{N-m-1}, thus amounting to a proof by mathematical induction. The general equation for λ_{N-m-1} is

$$\sum_{n=N-m-1}^{N} \binom{n}{N-m-1} \lambda_n = 0 \implies \lambda_{N-m-1} + \sum_{m'=0}^{m} \binom{N-m'}{N-m-1} \lambda_{N-m'} = 0 \,. \tag{9.42}$$

Substituting the extrapolated solution gives

$$\begin{aligned} \lambda_{N-m-1} = -\sum_{m'=0}^{m} (-1)^{N-m'} \binom{N-m'}{N-m-1} \binom{N}{m'} \lambda_N = \binom{N}{m+1} \lambda_N \sum_{m'=0}^{m} (-1)^{N-m'-1} \binom{m+1}{m'} \\ = (-1)^{N-m-1} \binom{N}{m+1} \lambda_N \,, \end{aligned} \tag{9.43}$$

which is consistent with the general solution eq. 9.41. This determines all coefficients λ_n for $n < N$ in terms of λ_N. To determine λ_N itself, we use eq. 9.38. Substituting eq. 9.41 into it gives

$$\lambda_N \sum_{n=2}^{N} n(-1)^n \binom{N}{n} = 1 \implies \lambda_N = \frac{(-1)^N}{N} \,. \tag{9.44}$$

The decomposition of entanglement entropy into multipartite measures is now complete:

$$\begin{aligned} S_{\mathrm{EE}}^{(1)} &= \frac{1}{N} \sum_{n=2}^{N} (-1)^n \binom{N}{n} \bar{I}_n, \\ \bar{I}_n &= \frac{(N-n)!n!}{N!} \sum_{S_n \in C_n(S_N)} I_n(S_n), \end{aligned} \tag{9.45}$$

where we have assumed N is even in order to drop the global phase factor $(-1)^N$.

We have therefore successfully expressed the entanglement entropy as a hierarchy of multipartite information measures. This will be used in Chapters 4, 5 and 6 within out "tiling" framework, where we map the physics of lattice models to that of quantum impurity models; there, this relation will prove useful in expressing the entanglement entropy of a subsystem of the lattice model in terms of a sum of multipartite information measures involving the impurity site and a collection of bath sites.

2.10 Wavefunction Renormalisation Group

2.10.1 General idea

A reverse URG analysis involves studying the evolution of wavefunctions from the IR to the UV, by implementing inverse renormalisation group transformations. This is made possible by the fact

that the IR fixed point Hamiltonians are often tractable and allow the computation of wavefunctions. Such an analysis gives insight into how states change as high-energy quantum fluctuations are resolved during the Hamiltonian renormalisation from the UV to the IR. It also allows studying the evolution of entanglement measures and correlation functions. This approach was pioneered through applications on the 2D Hubbard model in the form of the momentum-space entanglement renormalisation group (MERG) method, in order to characterise its various phases [447, 462], and has also been used to study a number of quantum impurity models [42, 74].

We will start with a very simple IR ground state wavefunction, and then go back towards the UV ground state by applying the inverse unitary operator $U^\dagger$:

$$U : \underbrace{|1,2,...,N\rangle}_{\text{UV ground state}} \rightarrow |1,2,...,N-1\rangle\,|N\rangle \rightarrow ... \rightarrow \underbrace{|1,2,...,N^*\rangle\,|N^*+1\rangle\,...\,|N\rangle}_{\text{IR ground state}}$$

$$U^\dagger : \underbrace{|1,2,...,N^*\rangle\,|N^*+1\rangle\,...\,|N\rangle}_{\text{IR ground state}} \rightarrow |1,2,...,N^*+1\rangle\,|N^*+2\rangle\,...\,|N\rangle \rightarrow ... \rightarrow \underbrace{|1,,2,...,N\rangle}_{\text{UV ground state}}$$

The first process is the forward RG which we used to obtain the scaling equations. The second process is the reverse RG which we will undertake now. The method has already been applied to study the renormalisation of entanglement in various models of strong correlation. In general, we start with an IR wavefunction that consists a certain number of momentum states n_1 still entangled with the impurity, and the remaining momentum states n_2 disentangled from the impurity. The former are said to be part of the emergent Kondo cloud, while the latter are said to be part of the integrals of motion (IOMs) and appear in direct product with the cloud+impurity system in the ground state wavefunction. Each momentum state is tagged with two conduction bath levels, one above the Fermi surface and one below. These will be represented as $k, \pm$. If we represent the emergent cloud momentum states as $\{k_i\}$ and the IOM states as $\{q_i\}$, the ground state wavefunction can be written as

$$|\Psi\rangle_0 = \left(\otimes_{i=1}^{n_2} |q_i,-,\uparrow\rangle\,|q_i,-,\downarrow\rangle\right) |\Phi\rangle_{\text{cloud}} \left(\otimes_{i=1}^{n_2} |q_i,+,\uparrow\rangle\,|q_i,+,\downarrow\rangle\right) \tag{10.1}$$

Throughout, we have assumed that the IOMs below the Fermi surface are occupied while those above are unoccupied. This means:

$$|\Psi\rangle_0 = \left(\otimes_{i=1}^{n_2} |\hat{n}_{q_i,-,\uparrow}=1\rangle\,|\hat{n}_{q_i,-,\downarrow}=1\rangle\right) |\Phi\rangle_{\text{cloud}} \left(\otimes_{i=1}^{n_2} |\hat{n}_{q_i,+,\uparrow}=0\rangle\,|\hat{n}_{q_i,+,\downarrow}=0\rangle\right) \tag{10.2}$$

$|\Phi\rangle_{\text{cloud}}$ will be obtained by diagonalising a small system of n_1 conduction bath k states. This completes the construction of the IR ground state $|\Psi\rangle_0$. The algorithm of reverse RG then involves applying unitary transformations on this IR wavefunction; the unitary transformations will be the inverse of those that were applied during the forward RG algorithm. Since the forwards RG transformations decoupled k states and transformed them into the IOMS, the inverse transformations will take the momentum states in the IOMs and re-entangle them with the impurity+cloud system, one at a time. This is shown in fig. 2.3.

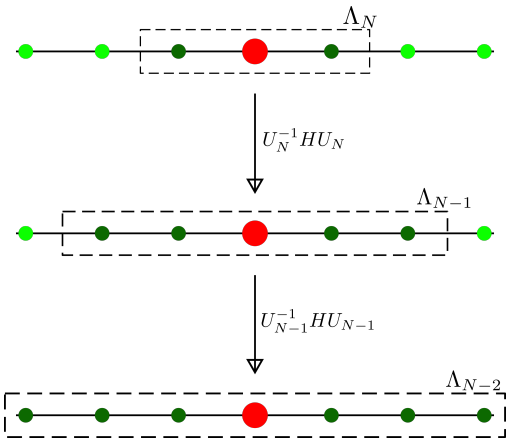

Figure 2.3: *We start with a Hamiltonian with an impurity site (red) coupled with two conduction electrons (dark green), with four other decoupled electrons (bright green). The dotted rectangle represents the emergent window $(-\Lambda_j, \Lambda_j)$ at each step; the electrons inside that rectangle are still entangled with the impurity, while the ones inside have been decoupled. The next step of reverse RG involves applying the inverse transformation on the Hamiltonian, which will couple two more electrons from the IOMS (hence four dark green circles in the second step), leading to an enlargement of the emergent window. The unitary varies for each step, hence the notation U_j.*

The next step is to write down the unitaries that will take us from the IR ground state to the UV ground state. In the forward RG, we used the following unitary for decoupling the shell ϵ_q and spin β is

$$U_{q\beta} = \frac{1}{\sqrt{2}} \left[1 + \eta_{0\beta} + \eta_{1\beta}^{\dagger} \right] . \tag{10.3}$$

Here, the subscripts 0 and 1 indicate it decouples an electron above and below the Fermi surface respectively. The inverse transformation for re-entangling $q\beta$ is

$$U_{q\beta}^{\dagger} = \frac{1}{\sqrt{2}} \left[1 + \eta_{0\beta}^{\dagger} + \eta_{1\beta} \right] . \tag{10.4}$$

The wavefunction after reversing one step of the RG will thus be

$$|\Psi\rangle_1 = U_{q\uparrow}^{\dagger} U_{q\downarrow}^{\dagger} |\Psi\rangle_0 \tag{10.5}$$

Here, q is the first momentum state immediately outside the emergent cloud. Re-entangling further momentum states using their respective unitaries lead to the sequence of wavefunctions $|\Psi\rangle_2, |\Psi\rangle_3$ and so on. A straightforward way of calculating entanglement and correlations across the RG flow is to create a second-quantised prototypical form of the IR state $|\Psi_0\rangle$, and then apply the inverse unitary operators $\{U_i\}$ to this wavefunction in order to generate the family of states $|\Psi_i\rangle = U_i |\Psi_{i-1}\rangle, i > 0$. Quantities like entanglement entropy and correlations can then be calculated by using this family of states. If the unitary is of a specific form, there is instead a more efficient method of doing this, which is what we will describe in the next subsection.

2.10.2 Evolution equation for state tensor coefficients

In the following, we restrict ourselves to the reverse RG analysis of an impurity problem hybridising with the local degree of freedom of a conduction bath. At every step, we allow two states from the IOMS to interact with the already-entangled states (one above the Fermi energy and one below, in order to maintain particle-hole symmetry). After the jth application of the reverse RG transformation, $2j$ number of states are entangled with the impurity site, and the state can be represented as

$$|\Psi_j\rangle = \sum_{\nu_d,\nu_1,\ldots,\nu_{2j}} C^{(j)}_{\nu_d,\nu_1,\ldots,\nu_{2j},I_{2j+1}} |\nu_d\rangle |\nu_1\rangle |\nu_2\rangle \ldots |\nu_{2j}\rangle \otimes |I_{2j+1}\rangle \ , \tag{10.6}$$

where $|\nu_d\rangle$ and $|\nu_i\rangle$ ($i \in [1, 2j]$) sum over the configurations of the impurity site and the effective zeroth site configuration at the jth step. $|I_{2j+1}\rangle$ is the configuration of the integrals of motion from the $(2j+1)^{\text{th}}$ site and beyond. We define the product state $|\psi_{dz}(j)\rangle = |\nu_d\rangle |\nu_1\rangle \ldots |\nu_{2j}\rangle$ for future reference.

We consider a restricted form of RG evolution, where the unitary transformation from IR towards UV can be expressed at any step as

$$U_j^\dagger = 1 + \sum_{i\in[1,2j]} \sum_{\nu_d,\mu_d,\nu_i,\mu_i} \mathcal{T}^{\mu_d}_{\nu_d} (J^{\mu_d,\mu_i}_{\nu_d,\nu_i} c_{2j+1} \mathcal{T}^{\mu_i}_{\nu_i} + K^{\mu_d,\mu_i}_{\nu_d,\nu_i} c^\dagger_{2j+2} \mathcal{T}^{\mu_i}_{\nu_i}) \ , \tag{10.7}$$

where $\mathcal{T}^\nu_\alpha = |\nu\rangle \langle\alpha|$ is a transition operator and sums over all transition operators of the specific subspace (impurity or bath sites). We first obtain the action of the transformation $U_j^\dagger$ on the basis states. We have

$$\begin{aligned}
&\mathcal{T}^{\nu_d}_{\mu_d} c^\dagger_{2j+2} \mathcal{T}^{\nu_i}_{\mu_i} |\mu_d\rangle \ldots |\mu_i\rangle \ldots |2_{2j+1}\rangle |0_{2j+2}\rangle \\
&= \mathcal{T}^{\nu_d}_{\mu_d} c^\dagger_{2j+2} (-1)^{\mu_d + \sum_{k<i} \nu_i} |\mu_d\rangle \ldots |\nu_i\rangle \ldots |2_{2j+1}\rangle |0_{2j+2}\rangle \\
&= \mathcal{T}^{\nu_d}_{\mu_d} (-1)^{\mu_d + \sum_{k<i} \nu_i} (-1)^{\mu_d + \sum_k \nu_i} |\mu_d\rangle \ldots |\nu_i\rangle \ldots |2_{2j+1}\rangle |1_{2j+2}\rangle \\
&= (-1)^{\sum_{k\geq i} \nu_i} |\nu_d\rangle \ldots |\nu_i\rangle \ldots |2_{2j+1}\rangle |1_{2j+2}\rangle \ ,
\end{aligned} \tag{10.8}$$

and

$$\mathcal{T}^{\nu_d}_{\mu_d} c_{2j+1} \mathcal{T}^{\nu_i}_{\mu_i} |\mu_d\rangle \ldots |\mu_i\rangle \ldots |2_{2j+1}\rangle |0_{2j+2}\rangle = (-1)^{\sum_{k\geq i} \nu_i} |\nu_d\rangle \ldots |\nu_i\rangle \ldots |1_{2j+1}\rangle |0_{2j+2}\rangle \ . \tag{10.9}$$

Using these expressions, we construct the state at the $(j+1)^{\text{th}}$ step:

$$\begin{aligned}
|\Psi_{j+1}\rangle = &\sum_{\nu_d,\nu_1,\ldots,\nu_j} C^{(j)}_{\nu_d,\nu_1,\ldots,} |\psi_{dz}(j)\rangle |2_{2j+1}\rangle |0_{2j+2}\rangle |I_{2j+3}\rangle \\
&+ \sum_i \sum_{\mu_d,\mu_i,\nu_d,\nu_i} C^{(j)}_{\mu_d,\ldots,\mu_i,\ldots,} J^{\nu_d,\nu_i}_{\mu_d,\mu_i} (-1)^{\sum_{k\geq i} \nu_k} |\psi_{dz}(j)\rangle |1_{2j+1}\rangle |0_{2j+2}\rangle |I_{2j+3}\rangle \\
&+ \sum_i \sum_{\mu_d,\mu_i,\nu_d,\nu_i} C^{(j)}_{\mu_d,\ldots,\mu_i,\ldots} K^{\nu_d,\nu_i}_{\mu_d,\mu_i} (-1)^{\sum_{k\geq i} \nu_k} |\psi_{dz}(j)\rangle |2_{2j+1}\rangle |1_{2j+2}\rangle |I_{2j+3}\rangle
\end{aligned} \tag{10.10}$$

Gathering similar terms and normalising the state, we can write it as

$$|\Psi_{j+1}\rangle = \frac{1}{L_j}\sum_{\nu_d,\{\nu_i\}} |\psi_{dz}(j)\rangle \Big[C^{(j)}_{\nu_d,\{\nu_i\},1_{2j+1},0_{2j+2},I_{j+1}}|2_{2j+1}\rangle|0_{2j+2}\rangle + C^{(j)}_{+,\nu_d,\{\nu_i\}}|2_{2j+1}\rangle|1_{2j+2}\rangle + C^{(j)}_{-,\nu_d,\{\nu_i\}}|1_{2j+1}\rangle|0_{2j+2}\rangle\Big]|I_{2j+3}\rangle \ , \tag{10.11}$$

where $L_j^2 = \sum_{\nu_d,\{\nu_i\}}\left(C^{(j)}_{\nu_d,\{\nu_i\}}{}^2 + C^{(j)}_{+,\nu_d,\{\nu_i\}}{}^2 + C^{(j)}_{-,\nu_d,\{\nu_i\}}{}^2\right)$ defines the normalisation factor, and

$$\begin{aligned} C_{+,\nu_d,\{\nu_i\}} &= \sum_{i,\mu_d,\mu_i} C^{(j)}_{\mu_d,\ldots,\mu_i,\ldots,\nu_{2j},1_{2j+1},0_{2j+2}} K^{\nu_d,\nu_i}_{\mu_d,\mu_i}(-1)^{\sum_{k\geq i}\nu_k} \\ C_{-,\nu_d,\{\nu_i\}} &= \sum_{i,\mu_d,\mu_i} C^{(j)}_{\mu_d,\ldots,\mu_i,\ldots,\nu_{2j},1_{2j+1},0_{2j+2}} J^{\nu_d,\nu_i}_{\mu_d,\mu_i}(-1)^{\sum_{k\geq i}\nu_k} \ . \end{aligned} \tag{10.12}$$

We can now read off the renormalisation of the state tensor coefficients:

$$\begin{aligned} C^{(j+1)}_{\nu_d,\nu_1,\ldots,\nu_{2j},1_{2j+1},0_{2j+2},I_{2j+3}} &= \frac{1}{L_j}C^{(j)}_{\nu_d,\nu_1,\ldots,\nu_{2j},2_{2j+1},0_{2j+2},I_{2j+3}} \ , \\ C^{(j+1)}_{\nu_d,\nu_1,\ldots,\nu_{2j},2_{2j+1},1_{2j+2},I_{2j+3}} &= \frac{1}{L_j}\sum_i(-1)^{\sum_{k\geq i}\nu_k}\sum_{\mu_d,\mu_i} C^{(j)}_{\mu_d,\ldots,\mu_i,\ldots,\nu_{2j},1_{2j+1},0_{2j+2}} K^{\nu_d,\nu_i}_{\mu_d,\mu_i} \ , \\ C^{(j+1)}_{\nu_d,\nu_1,\ldots,\nu_{2j},1_{2j+1},0_{2j+2},I_{2j+3}} &= \frac{1}{L_j}\sum_i(-1)^{\sum_{k\geq i}\nu_k}\sum_{\mu_d,\mu_i} C^{(j)}_{\mu_d,\ldots,\mu_i,\ldots,\nu_{2j},1_{2j+1},0_{2j+2}} J^{\nu_d,\nu_i}_{\mu_d,\mu_i} \ , \end{aligned} \tag{10.13}$$

We now make an important assumption: the coefficients $K^{\nu_d,\nu_i}_{\mu_d,\mu_i}$ and $J^{\nu_d,\nu_i}_{\mu_d,\mu_i}$ are uniform for the set of states $S(\nu_i)$ and zero for other states. That gives

$$\begin{aligned} C^{(j+1)}_{\nu_d,\nu_1,\ldots,\nu_{2j},1_{2j+1},1_{2j+2},I_{2j+3}} &= \frac{1}{L_j}K\sum_i(-1)^{\sum_{k\geq i}\nu_k}\sum_{\substack{\mu_d\in S(\nu_d),\\ \mu_i\in S(\nu_i)}} C^{(j)}_{\mu_d,\ldots,\mu_i,\ldots,\nu_{2j},1_{2j+1},0_{2j+2}} \ , \\ C^{(j+1)}_{\nu_d,\nu_1,\ldots,\nu_{2j},1_{2j+1},0_{2j+2},I_{2j+3}} &= \frac{1}{L_j}J\sum_i(-1)^{\sum_{k\geq i}\nu_k}\sum_{\substack{\mu_d\in S(\nu_d),\\ \mu_i\in S(\nu_i)}} C^{(j)}_{\mu_d,\ldots,\mu_i,\ldots,\nu_{2j},1_{2j+1},0_{2j+2}} \ , \end{aligned} \tag{10.14}$$

One can also look at renormalisation of expectation values of operators; this is useful for tracking the evolution of correlations and entanglement measures. Consider an operator $O^{\nu_k}_{\mu_k}$ that acts on the kth bath site. The expectation value of this operator at any step can be written as

$$\begin{aligned} \langle O^{\mu_k}_{\nu_k}\rangle_j &= \sum_{\nu_d,\nu_1,\ldots,\nu_{k-1},\nu_{k+1},\ldots,\nu_{2j}} C^{(j)}_{\nu_d,\ldots,\mu_k,\ldots}C^{(j)}_{\nu_d,\ldots,\nu_k,\ldots} \ , \\ \langle O^{\mu_k}_{\nu_k}\rangle_{j+1} &= \sum_{\nu_d,\nu_1,\ldots,\nu_{k-1},\nu_{k+1},\ldots,\nu_{2j+2}} C^{(j+1)}_{\nu_d,\ldots,\mu_k,\ldots}C^{(j+1)}_{\nu_d,\ldots,\nu_k,\ldots} \end{aligned} \tag{10.15}$$

2.11 Kondo model spectral function

We will now obtain forms for spectral functions for the single-channel Kondo model and a two-impurity Kondo model. The former will be used in our work on the extended Anderson impurity model (Chapter 3) and the lattice embedded impurity model (Chapter 5), while the latter will be used in our work on the heavy fermions (Chapter 6).

2.11.1 Single-impurity Kondo model

For the Kondo model defined by the Hamiltonian

$$H_K = \sum_{k,\sigma} \epsilon_k n_{k,\sigma} + J \sum_{k_1,k_2} \mathbf{S}_d \cdot \sigma_{\alpha,\beta} c^\dagger_{k_1,\alpha} c_{k_2,\beta} \ , \tag{11.1}$$

the impurity spin S_d does not have any fermionic operator. In order to define a spectral function for the impurity, we therefore look at the scattering of conduction electrons off it. This is captured by the conduction bath Greens function $G_{k,k'}$, which can be expressed in terms of a $T-$matrix when there are two-particle scattering processes present in the system:

$$G_{k,k'}(\omega) = G^{(0)}_k(\omega) + G^{(0)}_k(\omega) T_{k,k'}(\omega) G^{(0)}_{k'}(\omega) \ , \tag{11.2}$$

where $T_{k,k'}$ is non-zero because of the presence of the impurity spin which scatters momentum states into each other. Because of the local nature of the impurity scattering, the $T-$matrix is also local: $T_{k,k'}(\omega) = T(\omega)$. We therefore use this to define a spectral function:

$$A_{\text{imp}} = -\frac{1}{\pi} \text{Im}\, T(\omega) \ . \tag{11.3}$$

In order to calculate $T(\omega)$, we evaluate $G_{k,k'}$ using the equation of motion method. It is define as

$$G_{k,k'}(t) = -i\theta(t) \langle\langle c_{k,\sigma}(t), c^\dagger_{k',\sigma} \rangle\rangle \ . \tag{11.4}$$

Differentiating against time gives

$$\partial_t G_{k,k'}(t) = -i\delta(t) \langle\langle c_{k,\sigma}, c^\dagger_{k',\sigma} \rangle\rangle - \theta(t) \langle\langle [c_{k,\sigma}(t), H_K], c^\dagger_{k',\sigma} \rangle\rangle \ . \tag{11.5}$$

Evaluating the commutator gives

$$[c_{k,\sigma}(t), H_K] = \epsilon_k c_{k,\sigma} + J \sum_{q,\beta} \mathbf{S}_d \cdot \sigma_{\sigma,\beta} c_{q\beta} \ . \tag{11.6}$$

For convenience we define the local bath operator $c_{0,\beta} = \sum_q c_{q,\beta}$. Substituting the commutator back into the expression gives

$$\partial_t G_{k,k'}(t) = -i\delta(t)\delta_{k,k'} - \theta(t)\epsilon_k \langle\langle c_{k,\sigma}(t), c^\dagger_{k',\sigma} \rangle\rangle - \theta(t) J \sum_\beta \langle\langle \mathbf{S}_d \cdot \sigma_{\sigma,\beta} c_{0,\beta}, c^\dagger_{k',\sigma} \rangle\rangle(t) \ . \tag{11.7}$$

Defining a new Greens function $\tilde{G}$,

$$\tilde{G}_{k'}(t) = -i\theta(t)\sum_{\beta}\langle\langle \mathbf{S}_d \cdot \sigma_{\sigma,\beta} c_{0,\beta}, c^{\dagger}_{k',\sigma}\rangle\rangle \ , \tag{11.8}$$

we have the compact form

$$\partial_t G_{k,k'}(t) = -i\delta(t)\delta_{k,k'} - \theta(t)\epsilon_k\langle\langle c_{k,\sigma}(t), c^{\dagger}_{k',\sigma}\rangle\rangle - i\tilde{G}_{k'}(t) \ . \tag{11.9}$$

We now transform to frequency space, using the definition $f(t) = \int d\omega e^{-i\omega t} g(\omega)$:

$$\omega G_{k,k'}(\omega) = \delta_{k,k'} + \epsilon_k G_{k,k'}(\omega) + J\tilde{G}_{k'}(\omega) \ . \tag{11.10}$$

We setup the equation of motion for $\tilde{G}$ in a similar fashion. We use the Hermitian conjugate $-i\theta(t)\sum_{\beta}\langle\langle c_{k',\sigma}(t), \mathbf{S}_d \cdot \sigma_{\sigma,\beta} c^{\dagger}_{0,\beta}\rangle\rangle$, because it is easier to work with:

$$\begin{aligned}
\partial_t \tilde{G}_{k'}(t) &= -i\delta(t)\sum_{\beta}\delta_{\sigma,\beta}\langle \mathbf{S}_d \cdot \sigma_{\sigma,\beta}\rangle - \theta(t)\langle\langle [c_{k',\sigma}(t), H_K], \sum_{\beta} \mathbf{S}_d \cdot \sigma_{\sigma,\beta} c^{\dagger}_{0,\beta}\rangle\rangle \\
&= -i\delta(t)\langle \mathbf{S}^z_d\rangle - \theta(t)\langle\langle (\epsilon_{k'} c_{k',\sigma}(t) + J\sum_{\alpha} \mathbf{S}_d \cdot \sigma_{\sigma,\alpha} c_{0,\alpha}), \sum_{\beta} \mathbf{S}_d \cdot \sigma_{\sigma,\beta} c^{\dagger}_{0,\beta}\rangle\rangle \\
&= -i\delta(t)\langle \mathbf{S}^z_d\rangle - i\epsilon_{k'} G_{k'}(t) - J\theta(t)\langle\langle \sum_{\alpha} \mathbf{S}_d \cdot \sigma_{\sigma,\alpha} c_{0,\alpha}, \sum_{\beta} \mathbf{S}_d \cdot \sigma_{\sigma,\beta} c^{\dagger}_{0,\beta}\rangle\rangle \ .
\end{aligned} \tag{11.11}$$

At this point, we define a Kondo excitation operator $O_\sigma = J\sum_\alpha \mathbf{S}_d \cdot \sigma_{\sigma,\alpha} c_{0,\alpha}$. Transforming to frequency space gives

$$\omega\tilde{G}_{k'}(\omega) = \langle S^z_d\rangle + \epsilon_{k'} G_{k'}(\omega) + \frac{1}{J}\langle\langle O_\sigma, O^{\dagger}_{\sigma}\rangle\rangle \ , \tag{11.12}$$

which gives an expression for $\tilde{G}_{k'}(\omega)$:

$$(\omega - \epsilon_{k'})\tilde{G}_{k'}(\omega) = \langle S^z_d\rangle + \frac{1}{J}\langle\langle O_\sigma, O^{\dagger}_{\sigma}\rangle\rangle \ . \tag{11.13}$$

Substituting this into eq. 11.10 and noting that the non-interacting Greens function of the conduction bath is $G^{(0)}_k = (\omega - \epsilon_k)^{-1}$, we get

$$(G^{(0)}_k)^{-1} G_{k,k'}(\omega) = \delta_{k,k'} + J\left[\langle S^z_d\rangle + \frac{1}{J}\langle\langle O_\sigma, O^{\dagger}_{\sigma}\rangle\rangle\right] G^{(0)}_{k'} \ , \tag{11.14}$$

which can be finally compared with the general expression in eq. 11.2:

$$G_{k,k'}(\omega) = G^{(0)}_k + G^{(0)}_k\left[J\langle S^z_d\rangle + \langle\langle O_\sigma, O^{\dagger}_{\sigma}\rangle\rangle\right] G^{(0)}_{k'} \ . \tag{11.15}$$

The $T-$matrix for scattering of conduction electrons off the impurity can be read off:

$$T_\sigma(\omega) = J\langle S^z_d\rangle + \langle\langle O_\sigma, O^{\dagger}_{\sigma}\rangle\rangle \ , \tag{11.16}$$

2.11.2 Two-impurity Kondo model

We now generalise this calculation to a two-impurity model S_1, S_2, each with it's own conduction bath:

$$H_{2K} = \sum_{k,\sigma,l} \epsilon_k n_{k,\sigma,l} + J_l \sum_{k_1,k_2,l,\sigma_1,\sigma_2} \mathbf{S}_l \cdot \sigma_{\sigma_1,\sigma_2} c^\dagger_{k_1,\sigma_1,l} c_{k_2,\sigma_2,l} + K \mathbf{S}_1 \cdot \mathbf{S}_2 \ , \tag{11.17}$$

where l sums over the two spins and respective conduction baths, and K is the inter-impurity spin-exchange coupling.

Because of the composite nature of the impurity in this model, we consider a Greens function matrix

$$G = \begin{pmatrix} G_{11} & G_{12} \\ G_{21} & G_{22} \end{pmatrix} \ , \tag{11.18}$$

consisting of the diagonal Greens functions G_{ll} on the two impurities as well as an off-diagonal Greens function G_{12}. This is associated with a similar structure in the $T-$matrices:

$$T(k,k') = \begin{pmatrix} T(k,k')_{11} & T(k,k')_{12} \\ T(k,k')_{21} & T(k,k')_{22} \end{pmatrix} \ , \tag{11.19}$$

where the $T_{l,l'}$ are defined similar to the one-impurity case, but now with the additional index:

$$G_{(k,l),(k',l')}(\omega) = G^{(0)}_{k,l}(\omega) + G^{(0)}_{k,l}(\omega) T_{(k,l),(k',l')}(\omega) G^{(0)}_{k',l'}(\omega) \ . \tag{11.20}$$

The additional physics here is the possibility of scattering from a momentum state k in the bath l to a momentum state k' in the other bath l'.

We can then use the $T-$matrices to define diagonal and off-diagonal spectral functions:

$$A_{\text{imp}}(l,l') = -\frac{1}{\pi} \text{Im}\, T_{l,l'}(\omega) \ . \tag{11.21}$$

In order to calculate $T(\omega)$, we evaluate $G_{(k,l),(k',l')}$ using the equation of motion method. It is define as

$$G(t) = -i\theta(t) \langle\langle c_{k,\sigma,l}(t), c^\dagger_{k',\sigma,l'} \rangle\rangle \ . \tag{11.22}$$

Differentiating against time gives

$$\partial_t G_{k,k'}(t) = -i\delta(t) \langle\langle c_{k,\sigma,l}, c^\dagger_{k',\sigma,l'} \rangle\rangle - \theta(t) \langle\langle [c_{k,\sigma,l}(t), H_{2K}], c^\dagger_{k',\sigma,l'} \rangle\rangle \ . \tag{11.23}$$

Evaluating the commutator gives

$$[c_{k,\sigma,l}(t), H_{2K}] = \epsilon_k c_{k,\sigma,l} + J_l \sum_{q,\beta} \mathbf{S}_l \cdot \sigma_{\sigma,\beta} c_{q,\beta,l} \ . \tag{11.24}$$

For convenience we define the local bath operator $c_{0,\beta,l} = \sum_q c_{q,\beta,l}$. Substituting the commutator back into the expression gives

$$\begin{aligned} \partial_t G_{(k,l),(k',l')}(t) = &-i\delta(t)\delta_{k,k'}\delta_{l,l'} - \theta(t)\epsilon_k \langle\langle c_{k,\sigma,l}(t), c^\dagger_{k',\sigma,l'} \rangle\rangle \\ &-\theta(t) J_l \sum_\beta \langle\langle \mathbf{S}_l \cdot \sigma_{\sigma,\beta} c_{0,\beta,l}, c^\dagger_{k',\sigma,l'} \rangle\rangle(t) \ . \end{aligned} \tag{11.25}$$

Defining a new Greens function $\tilde{G}$,

$$\tilde{G}_{(0,l),(k',l')}(t) = -i\theta(t)\sum_{\beta}\langle\langle \mathbf{S}_l \cdot \sigma_{\sigma,\beta} c_{0,\beta,l}, c^{\dagger}_{k',\sigma,l'}\rangle\rangle \ , \tag{11.26}$$

we have the compact form

$$\partial_t G_{(k,l),(k',l')}(t) = -i\delta(t)\delta_{k,k'}\delta_{l,l'} - \theta(t)\epsilon_k\langle\langle c_{k,\sigma,l}(t), c^{\dagger}_{k',\sigma,l'}\rangle\rangle - i\tilde{G}_{(0,l),(k',l')}(t) \ . \tag{11.27}$$

We now transform to frequency space, using the definition $f(t) = \int d\omega e^{-i\omega t} g(\omega)$:

$$\omega G_{(k,l),(k',l')}(\omega) = \delta_{k,k'}\delta_{l,l'} + \epsilon_k G_{(k,l),(k',l')}(\omega) + J_l \tilde{G}_{(0,l),(k',l')}(\omega) \ . \tag{11.28}$$

We setup the equation of motion for $\tilde{G}$ in a similar fashion. We use the Hermitian conjugate $-i\theta(t)\sum_{\beta}\langle\langle c_{k',\sigma,l'}(t), \mathbf{S}_l \cdot \sigma_{\sigma,\beta} c^{\dagger}_{0,\beta,l}\rangle\rangle$, because it is easier to work with:

$$\begin{aligned}
\partial_t \tilde{G}_{(0,l),(k',l')}(t) &= -i\delta(t)\delta_{l,l'}\sum_{\beta}\delta_{\sigma,\beta}\langle \mathbf{S}_l \cdot \sigma_{\sigma,\beta}\rangle - \theta(t)\langle\langle [c_{k',\sigma,l'}(t), H_{2K}], \sum_{\beta} \mathbf{S}_l \cdot \sigma_{\sigma,\beta} c^{\dagger}_{0,\beta,l}\rangle\rangle \\
&= -i\delta(t)\delta_{l,l'}\langle \mathbf{S}^z_l\rangle - \theta(t)\langle\langle \epsilon_{k'} c_{k',\sigma,l'}(t) + J_{l'}\sum_{\alpha}\mathbf{S}_{l'}\cdot\sigma_{\sigma,\alpha}c_{0,\alpha,l'}, \sum_{\beta}\mathbf{S}_l\cdot\sigma_{\sigma,\beta}c^{\dagger}_{0,\beta,l}\rangle\rangle \\
&= -i\delta(t)\langle \mathbf{S}^z_l\rangle - i\epsilon_{k'}\tilde{G}_{(0,l),(k',l')}(t) - J_{l'}\theta(t)\langle\langle \sum_{\alpha}\mathbf{S}_{l'}\cdot\sigma_{\sigma,\alpha}c_{0,\alpha,l'}, \sum_{\beta}\mathbf{S}_l\cdot\sigma_{\sigma,\beta}c^{\dagger}_{0,\beta,l}\rangle\rangle \ .
\end{aligned} \tag{11.29}$$

At this point, we define a Kondo excitation operator $O_{\sigma,l} = J_l\sum_{\alpha}\mathbf{S}_l\cdot\sigma_{\sigma,\alpha}c_{0,\alpha,l}$. Transforming to frequency space gives

$$\omega\tilde{G}_{(0,l),(k',l')}(\omega) = \delta_{l,l'}\langle S^z_l\rangle + \epsilon_{k'}\tilde{G}_{(0,l),(k',l')}(\omega) + \frac{1}{J_l}\langle\langle O_{\sigma,l'}, O^{\dagger}_{\sigma,l}\rangle\rangle \ , \tag{11.30}$$

which gives an expression for $\tilde{G}_{k'}(\omega)$:

$$(\omega - \epsilon_{k'})\tilde{G}_{(0,l),(k',l')}(\omega) = \delta_{l,l'}\langle S^z_l\rangle + \frac{1}{J_l}\langle\langle O_{\sigma,l'}, O^{\dagger}_{\sigma,l}\rangle\rangle \ . \tag{11.31}$$

Substituting this into eq. 11.10 and noting that the non-interacting Greens function of the conduction bath is $G^{(0)}_k = (\omega - \epsilon_k)^{-1}$, we get

$$(G^{(0)}_k)^{-1}G_{(k,l),(k',l')}(\omega) = \delta_{k,k'}\delta_{l,l'} + J_l\left[\delta_{l,l'}\langle S^z_l\rangle + \frac{1}{J_l}\langle\langle O_{\sigma,l}, O^{\dagger}_{\sigma,l'}\rangle\rangle\right]G^{(0)}_{k'} \ , \tag{11.32}$$

which can be finally compared with the general expression in eq. 11.2:

$$G_{(k,l),(k',l')}(\omega) = \delta_{k,k'}\delta_{l,l'}G^{(0)}_k + G^{(0)}_k\left[\delta_{l,l'}J_l\langle S^z_l\rangle + \langle\langle O_{\sigma,l}, O^{\dagger}_{\sigma,l'}\rangle\rangle\right]G^{(0)}_{k'} \ . \tag{11.33}$$

The $T-$matrix for scattering of conduction electrons off the impurity can be read off:

$$T_{(\sigma,l),(\sigma,l')}(\omega) = \delta_{l,l'}J_l\langle S^z_l\rangle + \langle\langle O_{\sigma,l}, O^{\dagger}_{\sigma,l'}\rangle\rangle \ , \tag{11.34}$$

2.12 Zero temperature Greens function in frequency domain

2.12.1 Spectral representation of Greens function

The impurity retarded Green's function is defined as

$$G_{d\sigma}(t) = -i\theta(t)\left\langle\left\{O_\sigma(t), O_\sigma^\dagger\right\}\right\rangle \tag{12.1}$$

where the average $\langle\rangle$ is over a canonical ensemble at temperature T, and O_σ is the excitation whose spectral function we are interested in. What follows is a standard calculation where we write the Green's function in the spectral representation. The ensemble average for the operator O_σ can be written in terms of the exact eigenstates of the Hamiltonian:

$$H\left|n\right\rangle = E_n\left|n\right\rangle, \quad \left\langle O_\sigma\right\rangle \equiv \frac{1}{Z}\sum_n \left\langle n|O_\sigma|n\right\rangle e^{-\beta E_n} \tag{12.2}$$

where $Z = \sum_n e^{-\beta E_n}$ is the partition function and $\{|n\rangle\}$ is the set of eigenfunctions of the Hamiltonian. We can therefore write

$$\begin{aligned}
&\left\langle\left\{O_\sigma(t), O_\sigma^\dagger\right\}\right\rangle \\
&= \frac{1}{Z}\sum_m e^{-\beta E_m}\left\langle m\right|\left\{O_\sigma(t), O_\sigma^\dagger\right\}\left|m\right\rangle \\
&= \frac{1}{Z}\sum_{m,n} e^{-\beta E_m}\left\langle m\right|\left(O_\sigma(t)\left|n\right\rangle\left\langle n\right|O_\sigma^\dagger + O_\sigma^\dagger\left|n\right\rangle\left\langle n\right|O_\sigma(t)\right)\left|m\right\rangle \qquad \left[\sum_n \left|n\right\rangle\left\langle n\right| = 1\right] \\
&= \frac{1}{Z}\sum_{m,n} e^{-\beta E_m}\left\langle m\right|\left(e^{iH^*t}O_\sigma e^{-iH^*t}\left|n\right\rangle\left\langle n\right|O_\sigma^\dagger + O_\sigma^\dagger\left|n\right\rangle\left\langle n\right|e^{iH^*t}O_\sigma e^{-iH^*t}\right)\left|m\right\rangle \\
&= \frac{1}{Z}\sum_{m,n} e^{-\beta E_m}\left(e^{i(E_m-E_n)t}\left\langle m\right|O_\sigma\left|n\right\rangle\left\langle n\right|O_\sigma^\dagger\left|m\right\rangle + e^{i(E_n-E_m)t}\left\langle m\right|O_\sigma^\dagger\left|n\right\rangle\left\langle n\right|O_\sigma\left|m\right\rangle\right) \\
&= \frac{1}{Z}\sum_{m,n} e^{i(E_m-E_n)t}||\left\langle m\right|O_\sigma\left|n\right\rangle||^2\left(e^{-\beta E_m} + e^{-\beta E_n}\right)
\end{aligned} \tag{12.3}$$

The time-domain impurity Green's function can thus be written as (this is the so-called Lehmann-Kallen representation)

$$G_{d\sigma} = -i\theta(t)\frac{1}{Z}\sum_{m,n} e^{i(E_m-E_n)t}||\left\langle m\right|O_\sigma\left|n\right\rangle||^2\left(e^{-\beta E_m} + e^{-\beta E_n}\right) \tag{12.4}$$

We are interested in the frequency domain form.

$$\begin{aligned}
G_{dd}^\sigma(\omega) &= \int_{-\infty}^{\infty} dt e^{i(\omega)t}G_{dd}^\sigma(t) \\
&= \frac{1}{Z}\sum_{m,n}||\left\langle m\right|O_\sigma\left|n\right\rangle||^2\left(e^{-\beta E_m} + e^{-\beta E_n}\right)(-i)\int_{-\infty}^{\infty} dt\theta(t)e^{i(\omega+E_m-E_n)t}
\end{aligned} \tag{12.5}$$

To evaluate the time-integral, we will use the integral representation of the Heaviside function:

$$\theta(t) = -\frac{1}{2\pi i}\lim_{\eta\to 0^+}\int_{-\infty}^{\infty}\frac{1}{x+i\eta}e^{-ixt}dx \tag{12.6}$$

With this definition, the integral in $G_{d\sigma}(\omega)$ becomes

$$\begin{aligned}(-i)\int_{-\infty}^{\infty}dt\theta(t)e^{i(\omega+i0^+ +E_m-E_n)t} &= (-i)\frac{-1}{2\pi i}\lim_{\eta\to 0^+}\int_{-\infty}^{\infty}dx\frac{1}{x+i\eta}\int_{-\infty}^{\infty}dte^{i(\omega+i0^+ +E_m-E_n-x)t}\\ &= \frac{1}{2\pi}\lim_{\eta\to 0^+}\int_{-\infty}^{\infty}dx\frac{1}{x+i\eta}2\pi\delta\left(\omega+i0^+ +E_m-E_n-x\right)\\ &= \frac{1}{\omega+E_m-E_n+i0^+}\,.\end{aligned} \tag{12.7}$$

The frequency-domain Green's function is thus [463]

$$G^{\sigma}_{dd}(\omega) = \frac{1}{Z}\sum_{m,n}||\langle m|\,O_\sigma\,|n\rangle||^2\left(e^{-\beta E_m}+e^{-\beta E_n}\right)\frac{1}{\omega+E_m-E_n+i0^+} \tag{12.8}$$

The infinitesimally positive imaginary part in the denominator shifts the poles onto the lower half of the complex plane, leaving it analytic in the upper half: this is necessary to make the retarded Greens function causal.

2.12.2 Real and imaginary parts - The Sokhotski-Plemelj theorem

In order to write down the real and imaginary parts of the Greens function, we first prove the *Sokhotski-Plemelj* formula:

$$\lim_{\eta\to 0^+}\frac{1}{x+i\eta} = P\left(\frac{1}{x}\right) - i\pi\delta(x)\,. \tag{12.9}$$

where $P(f(x))$ is the Cauchy principal value, defined as

$$P\left[\int_{-\infty}^{\infty}\frac{dx}{x}\right] = \int_{-\infty}^{0^-}\frac{dx}{x}+\int_{0^+}^{\infty}\frac{dx}{x}\,. \tag{12.10}$$

To prove the above identity, we integrate the left-hand side using a test function $f(x)$:

$$\begin{aligned}\lim_{\eta\to 0^+}\int_{-\infty}^{\infty}\mathrm{dx}\,\frac{f(x)}{x+i\eta} &= \lim_{\eta\to 0^+}\int_{-\infty}^{\infty}\mathrm{dx}\,\frac{f(x)\,(x-i\eta)}{x^2+\eta^2}\\ &= \lim_{\eta\to 0^+}\int_{-\infty}^{\infty}\mathrm{dx}\,f(x)\left[\frac{x}{x^2+\eta^2}-i\eta\frac{1}{x^2+\eta^2}\right]\end{aligned} \tag{12.11}$$

The first integral can be split into three parts:

$$\lim_{\eta\to 0^+}\int_{-\infty}^{\infty}\mathrm{dx}\,f(x)\frac{x}{x^2+\eta^2} = \lim_{\eta\to 0^+}\lim_{\varepsilon\to 0^+}\left[\int_{-\infty}^{-\varepsilon}\mathrm{dx}\,\frac{f(x)x}{x^2+\eta^2}+\int_{\varepsilon}^{\infty}\mathrm{dx}\,\frac{f(x)x}{x^2+\eta^2}+\int_{-\varepsilon}^{\varepsilon}\mathrm{dx}\,\frac{f(x)x}{x^2+\eta^2}\right] \tag{12.12}$$

For the first two parts, it is safe to take the limit of η, because x is always non-vanishing there. For the third part, we can approximate $f(x)$ as $f(0)$ in the neighbourhood $x \in [-\varepsilon, \varepsilon], \varepsilon \to 0$. This leaves an odd function $x/(x^2+\eta^2)$ as the integrand, being integrated over a symmetric range. The third term therefore vanishes. In total, we get

$$\lim_{\eta\to 0^+} \int_{-\infty}^{\infty} \mathrm{dx}\, f(x) \frac{x}{x^2+\eta^2} = \int_{-\infty}^{-\varepsilon} \mathrm{dx}\, \frac{f(x)}{x} + \int_{\varepsilon}^{\infty} \mathrm{dx}\, \frac{f(x)}{x} = P\left(\int_{-\infty}^{\infty} \mathrm{dx}\, \frac{f(x)}{x}\right) . \tag{12.13}$$

To evaluate the second integral of eq. 12.11, we note that the only region in which the integrand is non-zero is when $|x| \simeq 0$; there, we again approximate $f(x)$ as $f(0)$. The remaining integral can then be evaluated easily:

$$-i \lim_{\eta\to 0^+} \eta \int_{-\infty}^{\infty} \mathrm{dx}\, \frac{f(x)}{x^2+\eta^2} = -i \lim_{\eta\to 0^+} \eta f(0) \int_{-\infty}^{\infty} \frac{\mathrm{dx}}{x^2+\eta^2} = -i\pi f(0), \tag{12.14}$$

where we used $\int \frac{dx}{x^2+\eta^2} = \frac{1}{\eta} \arctan(x/\eta)$. Combining eqs. 12.11,12.13 and 12.14, we get

$$\lim_{\eta\to 0^+} \int_{-\infty}^{\infty} \mathrm{dx}\, \frac{f(x)}{x+i\eta} = P\left(\int_{-\infty}^{\infty} \mathrm{dx}\, \frac{f(x)}{x}\right) - i\pi \int_{-\infty}^{\infty} \mathrm{dx}\, f(x)\delta(x) . \tag{12.15}$$

This proves eq. 12.9.

The Sokhotski-Plemelj formula allows us to split the spectral representation into a real and an imaginary part:

$$\begin{aligned} G'_{d\sigma} &= \frac{1}{Z} \sum_{m,n} || \langle m| O_\sigma |n\rangle ||^2 \left(e^{-\beta E_m} + e^{-\beta E_n}\right) P\left(\frac{1}{\omega + E_m - E_n}\right) \\ G''_{d\sigma} &= -\pi \frac{1}{Z} \sum_{m,n} || \langle m| O_\sigma |n\rangle ||^2 \left(e^{-\beta E_m} + e^{-\beta E_n}\right) \delta(\omega + E_m - E_n) . \end{aligned} \tag{12.16}$$

The spectral function, specifically, is defined as follows:

$$A_{d\sigma}(\omega) = -\frac{1}{\pi} G'_{d\sigma} = \frac{1}{Z} \sum_{m,n} || \langle m| O_\sigma |n\rangle ||^2 \left(e^{-\beta E_m} + e^{-\beta E_n}\right) \delta(\omega + E_m - E_n) \tag{12.17}$$

2.12.3 Zero temperature spectral function

We specialise to zero temperature by taking the limit of $\beta \to \infty$. In both the partition function as well as inside the summation, the only term that will survive is the exponential of the ground state energy E_{GS}.

$$Z \equiv \sum_m e^{-\beta E_m} \implies \lim_{\beta\to\infty} Z = d_{\mathrm{GS}} e^{-\beta E_{\mathrm{GS}}}, \quad E_{\mathrm{GS}} \equiv \min\{E_n\}$$

where d_{GS} is the degeneracy of the ground state. The spectral function then simplifies to

$$\begin{aligned} A_{d\sigma} &= \frac{1}{d_{\mathrm{GS}} e^{-\beta E_{\mathrm{GS}}}} \sum_{m,n} || \langle m| O_\sigma |n\rangle ||^2 \left[e^{-\beta E_m} \delta_{E_m, E_{\mathrm{GS}}} + e^{-\beta E_n} \delta_{E_n, E_{\mathrm{GS}}}\right] \delta(\omega + E_m - E_n) \\ &= \frac{1}{d_{\mathrm{GS}}} \sum_{n, n_{\mathrm{GS}}} \left[|| \langle n_{\mathrm{GS}}| O_\sigma |n\rangle ||^2 \delta(\omega + E_{\mathrm{GS}} - E_n) + || \langle n| O_\sigma |n_{\mathrm{GS}}\rangle ||^2 \delta(\omega - E_{\mathrm{GS}} + E_n)\right] \end{aligned} \tag{12.18}$$

The label $n_{\rm GS}$ sums over all states $|n_{\rm GS}\rangle$ with energy $E_{\rm GS}$. In practise, we evaluate this expression by replacing the formal Dirac delta functions with "nascent" ones, such as a Lorentzian function with a sufficiently sharp peak.

2.12.4 Reconstructing full Green function from spectral function: Kramers-Kronig relations

As mentioned earlier, the retarded Greens function $G_R(\omega + i0^+)$ has a complex pole in the lower half of the complex plane. In the following, the frequency ω is assumed to be complex. Consider the integral

$$I(\omega) = \oint_C d\omega' \frac{G_R(\omega')}{\omega' - \omega},\ \omega \in \mathbb{R}\ . \tag{12.19}$$

The contour C encloses the entirety of the upper half of the complex plane as well as almost all points of the real line but avoids the pole at $\omega' = \omega$ by forming a semicircle about that point that extends into the upper half of the plane. Since the integrand is completely analytic in the region enclosed by the contour (recall again that G_R is analytic in the upper half), the integral evaluates to zero (by Cauchy's theorem):

$$I(\omega) = 0\ . \tag{12.20}$$

One can also evaluate the integral along each part of the contour. The semicircular part contributes zero: this is because while the length of the semicircular arc goes as $|\omega'|$, the integrand vanishes faster than $1/|\omega'|$ as $|\omega'| \to \infty$ (this assumes that the Green function vanishes in the limit of $\omega \to \infty$). The part of the contour along the real axis can now be evaluated. The two parts of the contour on either side of the pole contribute

$$\int_{-\infty}^{\omega-0^+} d\omega'\ \frac{G_R(\omega')}{\omega' - \omega} + \int_{\omega+0^+}^{\infty} d\omega'\ \frac{G_R(\omega')}{\omega' - \omega} = P\int_{-\infty}^{\infty} d\omega'\ \frac{G_R(\omega')}{\omega' - \omega} \tag{12.21}$$

To evaluate the part of the integral along the small semicircular around $\omega' = \omega$ (that extends into the upper half), we argue that this contribution should be equal to that obtained by taking the semicircle that goes instead into the lower half but circulates in the opposite direction. Each of these contributions should, in turn, be equal to that obtained from joining these two contours. But joining these contours leads to a closed integral about the pole at $\omega' = \omega$, which is equal to $2\pi G_R(\omega)$.

$$\int_{\rm upper} d\omega'\ \frac{G_R(\omega')}{\omega' - \omega} = \int_{\rm lower} d\omega'\ \frac{G_R(\omega')}{\omega' - \omega} = \frac{1}{2}\oint_{C(\omega)} d\omega'\ \frac{G_R(\omega')}{\omega' - \omega} = i\pi G_R(\omega)\ . \tag{12.22}$$

Combining the last two equations, we get

$$I(\omega) = P\int_{-\infty}^{\infty} d\omega'\ \frac{G_R(\omega')}{\omega' - \omega} + i\pi G_R(\omega)\ . \tag{12.23}$$

Comparing with eq. 12.20 and separating into real part G'_R and imaginary part G''_R gives

$$P\int_{-\infty}^{\infty} d\omega'\ \frac{\left[G'_R(\omega') + iG''_R(\omega')\right]}{\omega' - \omega} + \pi\left[-G''_R(\omega) + iG'_R(\omega)\right] = 0\ . \tag{12.24}$$

Comparing the imaginary parts gives

$$G'_R(\omega) = \frac{1}{\pi} P \int_{-\infty}^{\infty} d\omega' \, \frac{G''_R(\omega')}{\omega' - \omega} = -\mathcal{H}\left[G''_R(\omega)\right] \ , \tag{12.25}$$

where $\mathcal{H}\left[g(\omega)\right] = \frac{1}{\pi} P \int_{-\infty}^{\infty} d\omega' \, \frac{g(\omega')}{\omega - \omega'}$ is the Hilbert transform of the function $g(\omega)$. The spectral function was defined above as $-1/\pi$ times the imaginary part of the Greens function. Exchanging G''_R for A gives

$$G'_R(\omega) = \pi \mathcal{H}\left[A(\omega)\right] \ . \tag{12.26}$$

This provides a method for calculating the real part of a Greens function if the spectral function is already known.

Chapter 3

Kondo Frustration via Charge Fluctuations: A Route to Mott Localisation in Infinite Dimensions

In this chapter, we begin our investigations into Mott criticality by looking into one of the simplest examples: the Mott transition of the Hubbard model in infinite dimensions. In preparation for the development of a new auxiliary model approach, we devote this chapter to identifying the appropriate quantum impurity model for capturing this transition, without employing self-consistency. After identifying the model, we will analyse the model using the unitary RG method and obtain a phase diagram which qualitatively captures the Mott MIT. This sets the stage for extending this approach to low dimensions in later chapters.

3.1 Introduction

The rich physics of metal-insulator transitions in strongly correlated systems has been an active subject of study for quite some time [2–4], yet much still remains to be understood. It involves diverse aspects such as spin and charge fluctuations, quasiparticle renormalisation effects, anomalous metallic phases and unconventional superconductivity, and has been studied using an equally diverse array of methods like mean-field theory, renormalisation group approaches, numerical techniques like exact diagonalisation, quantum Monte Carlo and dynamical mean-field theory, and many others. In particular, dynamical mean-field theory (DMFT) [18, 31, 198, 464–469] obtains an exact solution of the Mott metal-insulator transition (MIT) for the 1/2-filled Hubbard model [1, 11, 16, 17, 19] on the Bethe lattice with infinite coordination number, in terms of an Anderson impurity model with a self-consistently determined bath obtained by requiring, in an iterative manner, that its local Greens function be equal to that of the impurity site. The above-mentioned transition can be captured by the local spectral function through (i) the continuous appearance of a Mott gap, followed by (ii) the sharpening and vanishing of the central Kondo resonance. These two features are often referred to, respectively, as the Mott-Hubbard [1] and Brinkman-Rice [19] scenarios of the Mott MIT. The exact nature of the solution arises from the fact that all non-local contributions to the lattice self-

energy are observed to vanish upon taking the limit of an infinite coordination number for the lattice model. Thus, the simplification is that the dynamics of any local site on the lattice is determined completely by a quantum impurity problem [18, 161]. It must also be noted that this exact solution precludes any long-range order in the system, and corresponds to the case of a maximally frustrated Hubbard model involving long-range and frustrating inter-site hopping such that both the metallic and insulating phases remain paramagnetic [470]. Due to the exact and non-perturbative nature of the DMFT solution for the MIT in $d = \infty$, the method has been extended to models of strongly correlated electrons in finite spatial dimensions [467, 471, 472], as well as the study of the electronic properties of various correlated materials [468, 473, 474].

Despite this progress, a key aspect of the DMFT solution for the Hubbard model in $d = \infty$ remains to be understood. During the search for a self-consistent impurity model, the conduction bath is modified drastically in order to become correlated [475]. The numerical implementation of self-consistency, however, precludes a deeper understanding of the precise nature of the correlations present in the conduction bath of the impurity model, and its implications for the electron dynamics of the associated bulk lattice (Hubbard) model. Indeed, as we demonstrate below, our work paves the way for a more insightful exploration of the physics of the Mott Hubbard transition in strongly correlated electronic systems. Further, it has considerable consequences for the development of functional quantum materials and next-generation quantum technologies. Below, we lay out the specific questions addressed by us, and summarise our results at the end of this section.

i. Is there a minimal but effective quantum impurity model Hamiltonian that describes the Mott MIT of the $1/2$-filled Hubbard model on the Bethe lattice in $d = \infty$? Finding such an impurity model would also reduce the considerable computational effort that is presently required in self-consistent approaches.

ii. What are the fluctuations that destroy the metal and lead to the insulating phase? Can we obtain a universal theory for these competing tendencies?

iii. The coexistence of metallic and insulating phases at $T = 0$ within DMFT shows that the insulating solution is present within the many-body spectrum of the metallic phase. Can an associated impurity model Hamiltonian display the emergence of the insulating state prior to the transition? Analytic insight of this kind is particularly important because approaching a coexistence region numerically is often fairly tricky.

iv. Is it possible to obtain a low-energy theory for the local gapless excitations precisely at the MIT, where the metal is on the brink of destruction? How do these excitations compare with those of the local Fermi liquid, e.g., in terms of self-energies and two-particle correlation functions?

Obtaining answers to these questions would go a long way towards understanding the dominant fluctuations at the heart of the Mott transition and the physical processes that become important as one approaches it. It would also help in understanding the mechanism of DMFT's search for the self-consistent impurity model within the space of Anderson impurity models.

The essence of our approach is to model phenomenologically the lattice self-energy obtained from DMFT in the form of additional bath correlations within an extended Anderson impurity

model. In addition to the usual on-site repulsion (U) and single-particle hybridisation (V) between the impurity and the conduction bath of the Anderson impurity model (eq. (**2.1**)), we introduce (i) an additional on-site correlation (U_b) on the bath site with which the impurity couples, and (ii) an antiferromagnetic Kondo coupling (J) between the impurity and the conduction bath (eq. (**2.2**)). We note that a similar impurity model-based approach was taken towards understanding the physics of the heavy fermions several years ago by Si and Kotliar [476, 477]. We postpone a comparison of our work with theirs to the discussions section. The rest of the work is structured as follows. Sec. (3.2.1) describes the extended model that we will study, and the unitary renormalisation group (URG) method that we employ to study it is presented in Sec. (3.2.2). In Sec. (3.4) and (3.5), we describe the phase diagram and various characteristics of the impurity phase transition. In Sec. (3.7), we use our extended model to explain various features of the coexistence region observed in DMFT. In Sec. (3.8), we describe the effect of the impurity on the low-lying excitations of the bath, near and at the transition. We conclude in Sec. (3.9) with some discussions and possible future directions. For the convenience of readers, we first present below a brief summary of our main results.

Summary of our main results

- *Presence of a local metal-insulator transition*: At a critical value of the parameter $r = -U_b/J$, the effective impurity model shows a transition from a Kondo screened phase into an unscreened local moment phase. The quantum critical point (QCP) involves a degeneration of the Kondo singlet and the local moment states.

- *The physics of Kondo screening and local pairing drives the transition:* The transition involves the frustration of the Kondo screening of the impurity by enhanced local pairing fluctuations in the bath and can be described by a universal theory written in terms of J and U_b.

- *Emergence of insulating solutions in the metallic phase:* Our analysis reveals that at a certain value of the parameter r prior to the transition, the single-particle hybridisation parameter (V) turns irrelevant (in the RG sense), and this leads to the emergence of the local moment solutions within the many-particle spectrum through an excited state quantum phase transition (ESQPT).

- *Critical fluctuations and the coexistence region*: We observe the appearance of long-ranged quantum fluctuations extending into the conduction bath in the vicinity of both the ESQPT at $r = r_{c1}$ and QPT at $r = r_{c2}$. We believe that these are the likely origin of the critical fluctuations observed above the finite temperature second-order critical point in DMFT [470, 478]. The two-step process at $T = 0$ also provides a natural explanation for the coexistence of metallic and insulating features in the phase diagram, in the regime $r_{c1} < r < r_{c2}$.

- *Emergence of non-Fermi liquid excitations at the QCP*: Precisely at the QCP, the local Fermi liquid is replaced by a quasi-local non-Fermi liquid (NFL) that spans the impurity, zeroth and first sites of the conduction bath. The NFL results from a degeneracy between the local moment and singlet states and leads to (i) "Andreev scattering" of incoming states into

orthogonal outgoing states, (ii) anomalous power-law behaviour in the self-energies and two-particle correlations with universal exponents, and (iii) a fractional entanglement entropy of the impurity.

- *Correlated Fermi liquid excitations in the Hubbard sidebands*: A many-body perturbation theoretic treatment of the Hubbard sidebands reveals that they are comprised of the holon-doublon excitations created by the hybridisation of the impurity site with the conduction bath. These excitations consist of decoupled local Fermi liquids for the holons and doublons at the lowest order, which, at higher orders, become coupled via correlated holon-doublon scattering between impurity and bath.

3.2 Model Hamiltonian and method

3.2.1 The extended Anderson impurity model

The single-impurity Anderson model (SIAM) [479, 480] consists of a single impurity site with local repulsive correlation U hybridising with a non-interacting fermionic conduction bath through a (momentum-independent) single-particle transfer whose coupling is V. For the case of a half-filled impurity site, the Hamiltonian of the SIAM is given by

$$\mathcal{H}_{\mathrm{A}} = -\frac{U}{2}\left(\hat{n}_{d\uparrow} - \hat{n}_{d\downarrow}\right)^2 + \sum_{\vec{k},\sigma} \epsilon_{\vec{k}} \tau_{\vec{k},\sigma} + V \sum_{\sigma} \left(c^{\dagger}_{d\sigma} c_{0\sigma} + \mathrm{h.c.}\right), \tag{2.1}$$

where $\tau_{\vec{k},\sigma} \equiv c^{\dagger}_{\vec{k},\sigma} c_{\vec{k},\sigma} - 1/2$ indicate the occupancy of the single-particle momentum state $|\vec{k}\rangle$. Also, $c_{d\sigma}$ and $c_{0\sigma} = \sum_k c_{k\sigma}$ are the fermionic annihilation operators of spin σ for the impurity and conduction bath site to which it couples (henceforth referred to as the *zeroth site*) respectively. The conduction bath is typically considered to possess a constant (i.e., energy-independent) density of states.

The SIAM (along with its $U \to \infty$ limit, the Kondo model) has been studied using several analytical and numerical techniques [36, 38, 39, 42, 446, 451, 452, 481–489]. The general conclusion for the positive U case at $T = 0$ is that on the particle-hole symmetric (that is, half-filled) line, the impurity local moment is always screened by the conduction electrons (referred to as the Kondo cloud [490–501]). Enhanced spin-flip scattering at low-energies leads to the formation of a macroscopic singlet ground state and local Fermi liquid gapless excitations [502, 503]. In order to enhance the SIAM, we introduce two extra two-particle interaction terms into the Hamiltonian:

- a spin-exchange term $J\vec{S}_d \cdot \vec{S}_0$ between the impurity spin $\vec{S}_d$ and the spin $\vec{S}_0$ of the zeroth site, and
- a local particle-hole symmetric correlation term $-U_b\left(\hat{n}_{0\uparrow} - \hat{n}_{0\downarrow}\right)^2$ on the bath zeroth site.

With these additional terms, the Hamiltonian of the *extended single-impurity Anderson model* (henceforth referred to as the e-SIAM) is, at particle-hole symmetry, given by

$$\mathcal{H}_{\text{E-A}} = \mathcal{H}_{\mathrm{A}} + J\vec{S}_d \cdot \vec{S}_0 - \frac{1}{2} U_b \left(\hat{n}_{0\uparrow} - \hat{n}_{0\downarrow}\right)^2 . \tag{2.2}$$

All the terms in the Hamiltonian have been depicted schematically in the left panel of Fig. (3.1). The additional interaction terms J and U_b enjoy particle-hole, SU(2)-spin and U(1)-charge symmetries. The e-SIAM Hamiltonian (eq. (2.2)) therefore preserves all the local symmetries of the half-filled Hubbard model on a lattice, and can potentially serve as an effective auxiliary quantum impurity model (with a correlated bath) describing the local physics of the latter.

3.2.2 The unitary renormalisation group method

In order to obtain the various low-energy phases of the e-SIAM, we perform a scaling analysis of the associated Hamiltonian (eq. (2.2)) using the recently developed unitary renormalisation group (URG) method [348, 349]. The method has been applied successfully on a wide variety of problems of correlated fermions [42, 74, 175, 184, 348, 349, 504–506]. The method proceeds by resolving quantum fluctuations in high-energy degrees of freedom, leading to a low-energy Hamiltonian with renormalised couplings and new emergent degrees of freedom. Typically, for a system with Fermi energy ϵ_F and bandwidth D_0, the sequence of isoenergetic shells $\{D_{(j)}\}, D_{(j)} \in [\epsilon_F, D_0]$ define the states whose quantum fluctuations we sequentially resolve. The momentum states lying on shells $D_{(j)}$ that are far away from the Fermi surface comprise the UV states, while those on shells near the Fermi surface comprise the IR states. This scheme is shown in the right panel of Fig. (3.1).



Figure 3.1: *Left: Schematic 1D representation of the extended SIAM Hamiltonian. The red sphere is the impurity site with on-site Hubbard term U. It is connected via two couplings V and J to the bath zeroth site (large blue sphere) that has its own on-site Hubbard term U_b. The small blue spheres make up the rest of the bath, connected through the single-particle hopping t. Right: High energy - low energy scheme defined and used in the URG method. The states away from the Fermi surface form the UV subspace and are decoupled first, leading to a Hamiltonian which is more block-diagonal and comprised of only the IR states near the Fermi surface.*

As a result of the URG transformations, the Hamiltonian $H_{(j)}$ at a given RG step j involves scattering processes between the $k-$states that have energies lower than $D_{(j+1)}$. The unitary transformation $U_{(j)}$ is then defined so as to remove the number fluctuations of the currently most energetic set of states $D_{(j)}$ [348, 349]:

$$H_{(j-1)} = U_{(j)} H_{(j)} U_{(j)}^\dagger \text{ , such that } \left[H_{(j-1)}, \hat{n}_j\right] = 0 \,. \tag{2.3}$$

The eigenvalue of $\hat{n}_j$ has, thus, been rendered an integral of motion (IOM) under the RG transformation.

The unitary transformations can be expressed in terms of a generator $\eta_{(j)}$ that has fermionic algebra [348, 349]:

$$U_{(j)} = \frac{1}{\sqrt{2}}\left(1 + \eta_{(j)} - \eta^{\dagger}_{(j)}\right) , \qquad \left\{\eta_{(j)}, \eta^{\dagger}_{(j)}\right\} = 1 , \tag{2.4}$$

where $\{\cdot\}$ is the anticommutator. The unitary operator $U_{(j)}$ that appears in Eq. (2.4) can be cast into the well-known general form $U = e^{\mathcal{S}}, \mathcal{S} = \frac{\pi}{4}\left(\eta^{\dagger}_{(j)} - \eta_{(j)}\right)$ that a unitary operator can take, defined by an anti-Hermitian operator $\mathcal{S}$. The generator $\eta_{(j)}$ is given by the expression [348, 349]

$$\eta^{\dagger}_{(j)} = \frac{1}{\hat{\omega}_{(j)} - \mathrm{Tr}\left(H_{(j)}\hat{n}_j\right)} c^{\dagger}_j \mathrm{Tr}\left(H_{(j)} c_j\right) . \tag{2.5}$$

The operators $\eta_{(j)}, \eta^{\dagger}_{(j)}$ behave as the many-particle analogues of the single-particle field operators $c_j, c^{\dagger}_j$ - they change the occupation number of the single-particle Fock space $|n_j\rangle$. The important operator $\hat{\omega}_{(j)}$ originates from the quantum fluctuations that exist in the problem because of the non-commutation of the kinetic energy terms and the interaction terms in the Hamiltonian:

$$\hat{\omega}_{(j)} = H_{(j-1)} - H^{i}_{(j)} . \tag{2.6}$$

$H^{i}_{(j)}$ is the part of $H_{(j)}$ that commutes with $\hat{n}_j$ but does *not* commute with at least one $\hat{n}_l$ for $l < j$. The RG flow continues up to energy D^*, where a fixed point is reached from the vanishing of the RG function. Detailed comparisons of the URG with other methods (e.g., the functional RG, spectrum bifurcation RG etc.) can be found in Refs. [175, 348]. More information on the unitary RG method is provided in Chapter 2.

3.3 Derivation of renormalisation group equations for the extended-SIAM

The Hamiltonian we are working with is the extended Anderson impurity model (described in Section III of the main manuscript):

$$\mathcal{H} = -\frac{1}{2}U\left(\hat{n}_{d\uparrow} - \hat{n}_{d\downarrow}\right)^2 + \sum_{\vec{k},\sigma}\epsilon_{\vec{k}}\tau_{\vec{k},\sigma} + J\vec{S}_d\cdot\vec{S}_0 + V\sum_{\sigma}\left(c^{\dagger}_{d\sigma}c_{0\sigma} + \mathrm{h.c.}\right) - \frac{1}{2}U_b\left(\hat{n}_{0\uparrow} - \hat{n}_{0\downarrow}\right)^2 . \tag{3.1}$$

The renormalisation in the Hamiltonian $H_{(j)}$ at the jth RG step, upon decoupling an electronic state $q\beta$, is given by the expression:

$$\left(\Delta H_{(j)}\right)_{\vec{q},\beta} = H_{(j-1)} - H_{(j)} = c^{\dagger}_{\vec{q},\beta}T_{\vec{q},\beta}\frac{1}{\omega_e - H_D}T^{\dagger}_{\vec{q},\beta}c_{\vec{q},\beta} + T^{\dagger}_{\vec{q},\beta}c_{\vec{q},\beta}\frac{1}{\omega_h - H_D}c^{\dagger}_{\vec{q},\beta}T_{\vec{q},\beta} , \tag{3.2}$$

where $\omega_{e,h}$ are the quantum fluctuation scales for the electron and hole scattering channels, H_D is the part of the Hamiltonian that is diagonal in $k-$space, and $T_{\vec{q},\beta} + T^{\dagger}_{\vec{q},\beta}$ is the part of the Hamiltonian that does not commute with $\hat{n}_{\vec{q},\beta}$ (in short, it is the part that is off-diagonal with respect

to a particular state $\vec{q},\beta$). This off-diagonal part is made up of contributions from V, J and U_b: $T_{\vec{q}\uparrow} = \left[Vc^\dagger_{d\uparrow} + J\sum_{\vec{k}} S^+_d c^\dagger_{\vec{k}\downarrow} + U_b \sum_{\vec{k}_1,\vec{k}_2,\vec{k}_3} c^\dagger_{\vec{k}_1\uparrow} c^\dagger_{\vec{k}_3\downarrow} c_{\vec{k}_4\downarrow}\right] c_{\vec{q}\uparrow}$, while the diagonal part is given by $H_D = \epsilon_{\vec{q}}\tau_{q\uparrow} + \frac{1}{4}JS^z_d\left(\hat{n}_{q\uparrow} - \hat{n}_{q\downarrow}\right) - \frac{1}{2}U_b\left(\tau_{q\uparrow} - \tau_{q\downarrow}\right)^2$. The contribution from U_b is obtained by taking the Hartree contributions corresponding to the states $|q\sigma\rangle$ from the full interacting term in the Hamiltonian. Note that we have ignored potential scattering terms in the off-diagonal part $T_{\vec{q}\beta}$. In order to allow both spin-flip and charge transfer scattering processes, we start from initial states with $\tau_{q\uparrow} = -\tau_{q\downarrow}$. As a result, the contribution to H_D from the kinetic energy is $\epsilon_q\tau_{q\uparrow} = (\pm D)\times\left(\pm\frac{1}{2}\right) = D/2$, while the contribution from U_b is $-\frac{1}{2}U_b\left(\pm\frac{1}{2} - \left(\mp\frac{1}{2}\right)\right)^2 = -U_b/2$.

3.3.1 Renormalisation of U_b

Renormalisation to the bath interaction U_b can arise purely from itself, because of the lack of any impurity operators. We show in Section 5.3 of Chapter 5 that this coupling is in fact marginal.

3.3.2 Renormalisation of the impurity correlation U

The coupling U is renormalised by two kinds of vertices: V^2 and J^2. We will consider these processes one at a time. For convenience, we define $\epsilon_d = -U/2$.

The renormalisation arising from the first kind of terms, in the particle sector, is

$$\begin{aligned}\sum_{q\beta} c^\dagger_{q\beta}c_{d\beta}\frac{V^2}{\omega - H_D}c^\dagger_{d\beta}c_{q\beta} &= \textstyle\sum_{q\beta} V^2\hat{n}_{q\beta}\left(1-\hat{n}_{d\beta}\right)\left(\frac{1-\hat{n}_{d\bar{\beta}}}{\omega_0 - E_0} + \frac{\hat{n}_{d\bar{\beta}}}{\omega_1 - E_1}\right)\\ &= V^2 n_j \textstyle\sum_\beta \left(1-\hat{n}_{d\beta}\right)\left(\frac{1-\hat{n}_{d\bar{\beta}}}{\omega_0 - E_0} + \frac{\hat{n}_{d\bar{\beta}}}{\omega_1 - E_1}\right).\end{aligned} \tag{3.3}$$

q runs over the momentum states that are being decoupled at this RG step: $|q| = \Lambda_j$. $E_{1,0}$ are the diagonal parts of the Hamiltonian at $\hat{n}_{d\bar{\beta}} = 1, 0$ respectively: $E_1 = \frac{D}{2}$ and $E_0 = \frac{D}{2} + \epsilon_d - \frac{J}{4}$. In order to relate ω_0 and ω_1 with the common fluctuation scale ω for the conduction electrons, we will replace these quantum fluctuation scales with the current renormalised values of the single-particle self-energy for the initial state from which we started scattering. For $\hat{n}_{d\bar{\beta}} = 0$, there is no additional self-energy because the impurity does not have any spin: $\omega_0 = \omega$. For $\hat{n}_{d\bar{\beta}} = 1$, we have an additional self-energy of ϵ_d arising from the correlation on the impurity: $\omega_1 = \omega + \epsilon_d$. Substituting the values of $E_{0,1}$ and $\omega_{0,1}$, we get

$$V^2 n_j \sum_\beta \left(1-\hat{n}_{d\beta}\right)\left(\frac{1-\hat{n}_{d\bar{\beta}}}{\omega - \frac{D}{2} - \epsilon_d + \frac{J}{4}} + \frac{\hat{n}_{d\bar{\beta}}}{\omega - \frac{D}{2} + \epsilon_d}\right). \tag{3.4}$$

Performing a similar calculation for the hole sector gives the contribution:

$$V^2 n_j \sum_\beta \hat{n}_{d\beta}\left(\frac{1-\hat{n}_{d\bar{\beta}}}{\omega - \frac{D}{2} + \epsilon_d} + \frac{\hat{n}_{d\bar{\beta}}}{\omega - \frac{D}{2} - \epsilon_d + \frac{J}{4}}\right). \tag{3.5}$$

We now come to the second class of terms: spin-spin. We first look at the particle sector:

$$\frac{J^2}{4}\sum_{q\beta} c^\dagger_{d\bar{\beta}} c_{d\beta} c^\dagger_{q\beta} c_{-q\bar{\beta}} \frac{1}{\omega - H_D} c^\dagger_{d\beta} c_{d\bar{\beta}} c^\dagger_{q\bar{\beta}} c_{q\beta} = \frac{J^2}{4} n_j \frac{1}{\omega - \frac{D}{2} + \frac{J}{4}} \sum_\beta \hat{n}_{d\bar{\beta}} \left(1 - \hat{n}_{d\beta}\right) \ . \tag{3.6}$$

The diagonal part in the denominator was simple to deduce in this case because the nature of the scattering requires the spins S^z_d and $\frac{\beta}{2}\left(\hat{n}_{q\beta} - \hat{n}_{q\bar{\beta}}\right)$ to be anti-parallel. This ensures that the intermediate state has an energy of $E = \frac{D}{2} + \epsilon_d - \frac{J}{4}$, and the quantum fluctuation scale is $\omega' = \omega + \epsilon_d$, such that $\omega' - E = \omega - \frac{D}{2} + \frac{J}{4}$. In the hole sector, we have

$$\frac{J^2}{4} n_j \frac{1}{\omega - \frac{D}{2} + \frac{J}{4}} \sum_\beta \hat{n}_{d\beta}\left(1 - \hat{n}_{d\bar{\beta}}\right) \ . \tag{3.7}$$

From eqs. (3.4), (3.5), (3.6) and (3.7), we write

$$\begin{aligned} \Delta U &= \Delta\epsilon_2 + \Delta\epsilon_0 - 2\Delta\epsilon_1 \\ &= -\frac{4V^2 n_j}{\omega + \frac{U_b}{2} - \frac{D}{2} - U/2} + \frac{4V^2 n_j}{\omega + \frac{U_b}{2} - \frac{D}{2} + U/2 + \frac{J}{4}} - \frac{J^2 n_j}{\omega + \frac{U_b}{2} - \frac{D}{2} + \frac{J}{4}} \ , \end{aligned} \tag{3.8}$$

where we have restored the contribution from U_b in the denominator.

3.3.3 Renormalisation of the hybridisation V

Renormalisation of V happens through two kinds of processes: VJ and VU_b. Within the first kind, the scattering can be either via S^z_d or through $S^\pm_d$. For the first kind, we have the following contribution in the particle sector:

$$\begin{aligned} &\sum_{q\beta} V c^\dagger_{q\beta} c_{d\beta} \frac{1}{\omega - H_D} \frac{1}{4} J \sum_k \left(\hat{n}_{d\beta} - \hat{n}_{d\bar{\beta}}\right) c^\dagger_{k\beta} c_{q\beta} \\ &= \frac{1}{4} V J n_j \frac{1}{2}\left(\frac{1}{\omega'_1 - E} + \frac{1}{\omega'_2 - E}\right) \sum_{k\beta} \left(1 - \hat{n}_{d\bar{\beta}}\right) c_{d\beta} c^\dagger_{k\beta} \ . \end{aligned} \tag{3.9}$$

The transformation from $\frac{1}{\omega - H_D}$ to $\frac{1}{2}\left(\frac{1}{\omega'_1 - E} + \frac{1}{\omega'_2 - E}\right)$ is made so that we can account for both the initial state and the final state energies through the two fluctuation scales ω'_1 and ω'_2 respectively; we calculate the denominators for both the initial and final states and then take the mean of the two (hence the factor of half in front). This was not required previously because, in the earlier scattering processes, the impurity returned to its initial state at the end, at least in terms of $\epsilon_d\left(\hat{n}_{d\uparrow} - \hat{n}_{d\downarrow}\right)^2$, and so we had $\omega'_1 = \omega'_2 = \omega'$. Substituting the energies and the $\omega-$scales, we get

$$-\left(\frac{\frac{n_j}{4} V J \frac{1}{2}}{\omega - \frac{D}{2} + \frac{J}{4}} + \frac{\frac{n_j}{4} V J \frac{1}{2}}{\omega - \frac{D}{2} - \epsilon_d + \frac{J}{4}}\right) \sum_{k\beta} \left(1 - \hat{n}_{d\bar{\beta}}\right) c^\dagger_{k\beta} c_{d\beta} \ . \tag{3.10}$$

One can generate another such process by exchanging the single-particle process and the spin-exchange process:

$$\sum_{q\beta}\frac{1}{4}J\sum_{k}\left(\hat{n}_{d\beta}-\hat{n}_{d\bar{\beta}}\right)c^{\dagger}_{q\beta}c_{k\beta}\frac{1}{\omega-H_D}Vc^{\dagger}_{d\beta}c_{q\beta}\ . \tag{3.11}$$

This is simply the Hermitian conjugate of the previous contribution. Combining this with the previous then gives

$$-\frac{n_j}{8}VJ\left(\frac{1}{\omega-\frac{D}{2}+\frac{J}{4}}+\frac{1}{\omega-\frac{D}{2}-\epsilon_d+\frac{J}{4}}\right)\sum_{k\beta}\left(1-\hat{n}_{d\bar{\beta}}\right)\times\left(c^{\dagger}_{d\beta}c_{k\beta}+\text{h.c.}\right)\ . \tag{3.12}$$

If we similarly calculate the contributions from the spin-exchange processes involving $S^{\pm}_d$, we get

$$-\frac{1}{4}VJn_j\left(\frac{1}{\omega-\frac{D}{2}+\frac{J}{4}}+\frac{1}{\omega-\frac{D}{2}-\epsilon_d+\frac{J}{4}}\right)\sum_{k\beta}\left(1-\hat{n}_{d\beta}\right)\left(c^{\dagger}_{k\bar{\beta}}c_{d\bar{\beta}}+\text{h.c.}\right)\ . \tag{3.13}$$

The contributions from the hole sector are obtained by making the transformation $\hat{n}_{d\bar{\beta}}\to 1-\hat{n}_{d\bar{\beta}}$ on the particle sector contributions. The total renormalisation to V from VJ processes are

$$-\frac{3n_j}{8}VJ\left(\frac{1}{\omega+U_b/4-\frac{D}{2}+\frac{J}{4}}+\frac{1}{\omega+U_b/4-\frac{D}{2}+U/2+\frac{J}{4}}\right)\sum_{k\beta}\left(c^{\dagger}_{d\beta}c_{k\beta}+\text{h.c.}\right)\ . \tag{3.14}$$

The renormalisation in V from U_b arises through terms of VU_b and U_bV kind. We now show that this contribution vanishes entirely.

One particular scattering process in this category involves adding an electron on the impurity site:

$$\sum_{k,q,\beta}Vc^{\dagger}_{d\beta}c_{q\beta}\frac{1}{\omega-H_D}U_b\left[\beta\beta c^{\dagger}_{q\beta}c_{k\beta}n_{q',\beta}+\beta\beta n_{q',\beta}c^{\dagger}_{q\beta}c_{k\beta}+\beta\bar{\beta}c^{\dagger}_{q\beta}c_{k\beta}n_{q',\bar{\beta}}+\beta\bar{\beta}n_{q',\bar{\beta}}c^{\dagger}_{q\beta}c_{k\beta}\right]\ . \tag{3.15}$$

We set $\beta\beta=1$ and $\beta\bar{\beta}=-1$. For $q'\neq q$, the right hand side simplifies into the difference in densities of the two spin components of q':

$$\sum_{k,q,\beta}Vc^{\dagger}_{d\beta}c_{q\beta}\frac{1}{\omega-H_D}U_b\left[2c^{\dagger}_{q\beta}c_{k\beta}n_{q',\beta}-2c^{\dagger}_{q\beta}c_{k\beta}n_{q',\bar{\beta}}\right]=\sum_{k,q,\beta}Vc^{\dagger}_{d\beta}c_{q\beta}\frac{1}{\omega-H_D}4U_b\beta c^{\dagger}_{q\beta}c_{k\beta}s^{z}_{q'}\ . \tag{3.16}$$

In the presence of time-reversal symmetry, we expect the magnetisation $s^z_{q'}=\frac{1}{2}\sum_\beta\beta n_{q',\beta}$ to vanish in the initial state.

The case of $q=q'$ is allowed only in the second term, which leaves us with

$$\sum_{k,q,\beta}Vc^{\dagger}_{d\beta}c_{q\beta}\frac{1}{\omega-H_D}U_bn_{q,\beta}c^{\dagger}_{q\beta}c_{k\beta}=\sum_{k,q,\beta}Vc^{\dagger}_{d\beta}c_{q\beta}\frac{1}{\omega-H_D}U_bc^{\dagger}_{q\beta}c_{k\beta}\ . \tag{3.17}$$

We can resolve this expression into various parts depending on the intermediate energies and terminal energies:

$$\sum_{k,q,\beta} V c^\dagger_{d\beta} c_{q\beta} \frac{1}{2}\left[n_{d\bar{\beta}} \left(\frac{1}{\omega_1 - E_1} + \frac{1}{\omega_2 - E_1} \right) + (1 - n_{d\bar{\beta}}) \left(\frac{1}{\omega_0 - E_0} + \frac{1}{\omega_1 - E_0} \right) \right] U_b c^\dagger_{q\beta} c_{k\beta} \,. \tag{3.18}$$

A second class of processes is generated by reversing the sequence of operations:

$$\sum_{k,q,\beta} U_b \left[\beta\beta c^\dagger_{q\beta} c_{k\beta} n_{q',\beta} + \beta\beta n_{q',\beta} c^\dagger_{q\beta} c_{k\beta} + \beta\bar{\beta} c^\dagger_{q\beta} c_{k\beta} n_{q',\bar{\beta}} + \beta\bar{\beta} n_{q',\bar{\beta}} c^\dagger_{q\beta} c_{k\beta} \right] \frac{1}{\omega - H_D} V c^\dagger_{d\beta} c_{q\beta} \,. \tag{3.19}$$

The left hand side simplifies in the same fashion as did the right hand side in the previous class. Again considering the residual $q = q'$ contribution, we get

$$\sum_{k,q,\beta} U_b n_{q',\beta} c^\dagger_{q\beta} c_{k\beta} \frac{1}{\omega - H_D} V c^\dagger_{d\beta} c_{q\beta} = \sum_{k,q,\beta} U_b c^\dagger_{q\beta} c_{k\beta} \frac{1}{\omega - H_D} V c^\dagger_{d\beta} c_{q\beta} \,. \tag{3.20}$$

Resolving this expression into intermediate and terminal state energies gives

$$\sum_{k,q,\beta} U_b c^\dagger_{q\beta} c_{k\beta} \frac{1}{2}\left[n_{d\bar{\beta}} \left(\frac{1}{\omega_1 - E_2} + \frac{1}{\omega_2 - E_2} \right) + (1 - n_{d\bar{\beta}}) \left(\frac{1}{\omega_0 - E_1} + \frac{1}{\omega_1 - E_1} \right) \right] V c^\dagger_{d\beta} c_{q\beta} \,. \tag{3.21}$$

For a particle-hole symmetric system (as is the case here), we have $\omega_2 = \omega_0$ and $E_2 = E_0$. Moreover, assuming the energies enter linearly, we have $\omega_0 - E_0 = \omega_1 - E_1$. Substituting these, we get

$$\sum_{k,q,\beta} U_b c^\dagger_{q\beta} c_{k\beta} \frac{1}{2}\left[n_{d\bar{\beta}} \left(\frac{1}{\omega_1 - E_0} + \frac{1}{\omega_1 - E_1} \right) + (1 - n_{d\bar{\beta}}) \left(\frac{1}{\omega_0 - E_1} + \frac{1}{\omega_1 - E_1} \right) \right] V c^\dagger_{d\beta} c_{q\beta} \,. \tag{3.22}$$

Taken together with eq. 3.18, the contribution reduces to the anticommutator of $c^\dagger + d\beta$ and $c_{k\beta}$, which vanishes. A similar calculation shows that the contribution from the processes involving the destruction of the impurity electron ($c_{d\beta}$) also vanishes.

3.3.4 Renormalisation of the spin-exchange coupling J

The term $J\vec{S}_d \cdot \vec{S}_0$ can be split into three parts: $J^z S^z_d$, $\frac{1}{2} J^+ S^+_d S^-_0$ and $\frac{1}{2} J^- S^-_d S^+_0$. We will only calculate the renormalisation in J^+, which will be equal to that of J^-, J^z due to spin-rotation symmetry. The terms that renormalise J^+ are of the form $S^+_d S^z_d$ and $S^z_d S^+_d$. In the particle sector, we have

$$\begin{aligned}
-\sum_q \sum_{kk'} \frac{1}{4} J^2 S^+_d c^\dagger_{q\downarrow} c_{k'\uparrow} \frac{1}{\omega - H_D} S^z_d c^\dagger_{k\downarrow} c_{q\downarrow} &= n_j \frac{1}{4} J^2 \left(-\frac{1}{2} S^+_d \right) \sum_{kk'} c^\dagger_{k\downarrow} c_{k'\uparrow} \frac{1}{\omega + \frac{U_b}{2} - \frac{D}{2} + \frac{J}{4}} \,, \\
\sum_q \sum_{kk'} \frac{1}{4} J^2 S^z_d c^\dagger_{q\uparrow} c_{k'\uparrow} \frac{1}{\omega - H_D} S^+_d c^\dagger_{k\downarrow} c_{q\uparrow} &= -n_j \frac{1}{4} J^2 \left(\frac{1}{2} S^+_d \right) \sum_{kk'} c^\dagger_{k\downarrow} c_{k'\uparrow} \frac{1}{\omega + \frac{U_b}{2} - \frac{D}{2} + \frac{J}{4}} \,.
\end{aligned} \tag{3.23}$$

The denominator is determined using $E = \frac{D}{2} + \epsilon_d - \frac{J}{4}$ and $\omega' = \omega + \epsilon_d$. In the hole sector, we similarly have

$$\sum_q \sum_{kk'} \frac{1}{4} J^2 S_d^+ c_{k\downarrow}^\dagger c_{q\uparrow} \frac{1}{\omega - H_D} S_d^z c_{q\uparrow}^\dagger c_{k'\uparrow} = n_j \frac{1}{4} J^2 \left(-\frac{1}{2} S_d^+\right) \sum_{kk'} c_{k\downarrow}^\dagger c_{k'\uparrow} \frac{1}{\omega + \frac{U_b}{2} - \frac{D}{2} + \frac{J}{4}} ,$$
$$- \sum_q \sum_{kk'} \frac{1}{4} J^2 S_d^z c_{k\downarrow}^\dagger c_{q\downarrow} \frac{1}{\omega - H_D} S_d^+ c_{q\downarrow}^\dagger c_{k'\uparrow} = -n_j \frac{1}{4} J^2 \left(\frac{1}{2} S_d^+\right) \sum_{kk'} c_{k\downarrow}^\dagger c_{k'\uparrow} \frac{1}{\omega + \frac{U_b}{2} - \frac{D}{2} + \frac{J}{4}} . \quad (3.24)$$

The renormalisation due to U_b also happens through multiple terms. One of the terms is

$$\frac{1}{2} J U_b \sum_q \sum_{k,k'} S_d^+ c_{q\downarrow}^\dagger c_{k\uparrow} \frac{1}{\omega - H_D} \hat{n}_{q\uparrow} c_{k'\downarrow}^\dagger c_{q\downarrow} = -\frac{1}{2} \frac{J U_b n_j}{\omega - \frac{D}{2} + \frac{U_b}{2} + \frac{J}{4}} \sum_{k,k'} S_d^+ c_{k'\downarrow}^\dagger c_{k\uparrow} . \quad (3.25)$$

The factor of half in front is the same half factor that appears in front of the $S_1^+ S_2^-, S_1^- S_2^+$ terms when we rewrite $\vec{S}_1 \cdot \vec{S}_2$ in terms of $S^z, S^\pm$. Another term is obtained by switching J and U_b:

$$\frac{1}{2} J U_b \sum_q \sum_{k,k'} \hat{n}_{q\downarrow} c_{q\uparrow}^\dagger c_{k\uparrow} \frac{1}{\omega - H_D} S_d^+ c_{k'\downarrow}^\dagger c_{q\uparrow} = -\frac{1}{2} \frac{J U_b n_j}{\omega - \frac{D}{2} + \frac{U_b}{2} + \frac{J}{4}} \sum_{k,k'} S_d^+ c_{k'\downarrow}^\dagger c_{k\uparrow} . \quad (3.26)$$

The corresponding terms in the hole sector are

$$-\frac{1}{2} \frac{J U_b n_j}{\omega - \frac{D}{2} + \frac{U_b}{2} + \frac{J}{4}} \sum_{k,k'} S_d^+ c_{k'\downarrow}^\dagger c_{k\uparrow} , -\frac{1}{2} \frac{J U_b n_j}{\omega - \frac{D}{2} + \frac{U_b}{2} + \frac{J}{4}} \sum_{k,k'} S_d^+ c_{k'\downarrow}^\dagger c_{k\uparrow} . \quad (3.27)$$

3.3.5 Final URG equations

In summary, the renormalisation in the couplings takes the form:

$$\begin{aligned} \Delta U &= 4V^2 n_j \left(\tfrac{1}{d_1} - \tfrac{1}{d_0}\right) - n_j \tfrac{J^2}{d_2}, & \Delta V &= -\frac{3 n_j V J}{8} \left(\frac{1}{d_2} + \frac{1}{d_1}\right), \\ \Delta J &= -\tfrac{n_j J (J + 4U_b)}{d_2} , & \Delta U_b &= 0 , \end{aligned} \quad (3.28)$$

where the denominators d_i are given by

$$d_0 = \omega - \frac{D}{2} + \frac{U_b}{2} - \frac{U}{2}, \; d_1 = \omega - \frac{D}{2} + \frac{U_b}{2} + \frac{U}{2} + \frac{J}{4} , \quad (3.29)$$

$$d_2 = \omega - \frac{D}{2} + \frac{U_b}{2} + \frac{J}{4} , d_3 = \omega - \frac{D}{2} + \frac{U_b}{2} . \quad (3.30)$$

For the sake of completeness, we present the RG equation for a charge isospin Kondo coupling K between the impurity and the bath:

$$\Delta K = -\frac{n_j K (K + 4U_b)}{\omega - \frac{D}{2} + \frac{U_b}{2} + \frac{K}{4}} . \quad (3.31)$$

While the usual Kondo effect describes the screening of an impurity magnetic moment by the local spin density of the conduction bath, one can also envisage a scenario where it is the charge degrees of freedom of the impurity that is screened by the bath [507]. This can happen, for example, if the local correlation on the impurity site is negative. That makes the $n = 0$ and $n = 2$ configurations (unoccupied and doubly occupied) lower in energy. One can then define an *isospin* from this doublet of states, as well as a similar isospin for the doublet of states in the bath. Isospin-flip fluctuations will then involve transitions where an unoccupied state on the impurity scatters to a double occupied state while the bath simultaneously scatters in the opposite manner. It is worth noting that during the Schrieffer-Wolff transformation from the Anderson impurity model to the Kondo model, such charge Kondo terms are also generated but they reside in the high-energy part of the effective theory [27].

The RG equation for K is observed to be identical in form to that for the spin Kondo coupling J, obtained through the transformation $J \to K$. This indicates that charge fluctuations between the bath zeroth and first sites (that are incited by an attractive interaction U_b) lead to the RG irrelevance of $K(> 0)$, and thereby a destabilisation of the charge Kondo effect similar to that presented in the main manuscript for J.

3.4 $T = 0$ scaling theory for the e-SIAM

3.4.1 URG equations for the e-SIAM

The bath coupling U_b is marginal. The RG equations of the remaining couplings for a given quantum fluctuation scale ω are:

$$\begin{aligned}
\Delta U &= 4V^2 n_j \left(\frac{1}{d_1} - \frac{1}{d_0}\right) - n_j \frac{J^2}{d_2}, \\
\Delta V &= -\frac{3 n_j V J}{8}\left(\frac{1}{d_2} + \frac{1}{d_1}\right), \\
\Delta J &= -\frac{n_j J\,(J + 4U_b)}{d_2}\,,
\end{aligned} \tag{4.1}$$

where the denominators d_i are given by

$$d_0 = \omega - \frac{D}{2} + \frac{U_b}{2} - \frac{U}{2},\; d_1 = \omega - \frac{D}{2} + \frac{U_b}{2} + \frac{U}{2} + \frac{J}{4}\,, \tag{4.2}$$

$$d_2 = \omega - \frac{D}{2} + \frac{U_b}{2} + \frac{J}{4}\,, d_3 = \omega - \frac{D}{2} + \frac{U_b}{2}\,. \tag{4.3}$$

The symbols used in the RG equations have the following meanings: ΔU represents the renormalisation of the coupling U in going from the jth Hamiltonian to the $(j-1)^{\text{th}}$ Hamiltonian by decoupling the isoenergetic shell at energy $D_{(j)}$ (see right panel of Fig.(3.1)). n_j is the number of electronic states on the shell $D_{(j)}$. We note that the labels U_0, J_0, V_0 that appear in various figures (and elsewhere in the text) represent the bare values of the associated couplings U, J and V. The RG equations reduce, in the perturbative regime of the couplings U, V and J, to the well-known

"poor man's" scaling forms obtained for the SIAM [452] and the single-channel Kondo model [451] respectively.

The RG fixed point Hamiltonian describes the low-energy phase of the system. In general, if the RG fixed point is reached at an energy scale D^*, the fixed point Hamiltonian $\mathcal{H}^*$ is obtained simply from the fixed point values of the couplings (and by noting that the states above D^* are now part of the IOMs):

$$\mathcal{H}^* = \sum_{\sigma,\vec{k}}^{|\epsilon_{\vec{k}}|<D^*} \epsilon_{\vec{k}} \tau_{\vec{k},\sigma} + V^* \sum_{\sigma} \left(c^{\dagger}_{d\sigma} c_{0\sigma} + \text{h.c.} \right) + J^* \vec{S}_d \cdot \vec{S}_0 - \frac{1}{2} U^* \left(\hat{n}_{d\uparrow} - \hat{n}_{d\downarrow} \right)^2 - \frac{1}{2} U_b \left(\hat{n}_{0\uparrow} - \hat{n}_{0\downarrow} \right)^2 .$$

The fixed point values of the couplings are obtained by solving the RG equations numerically.

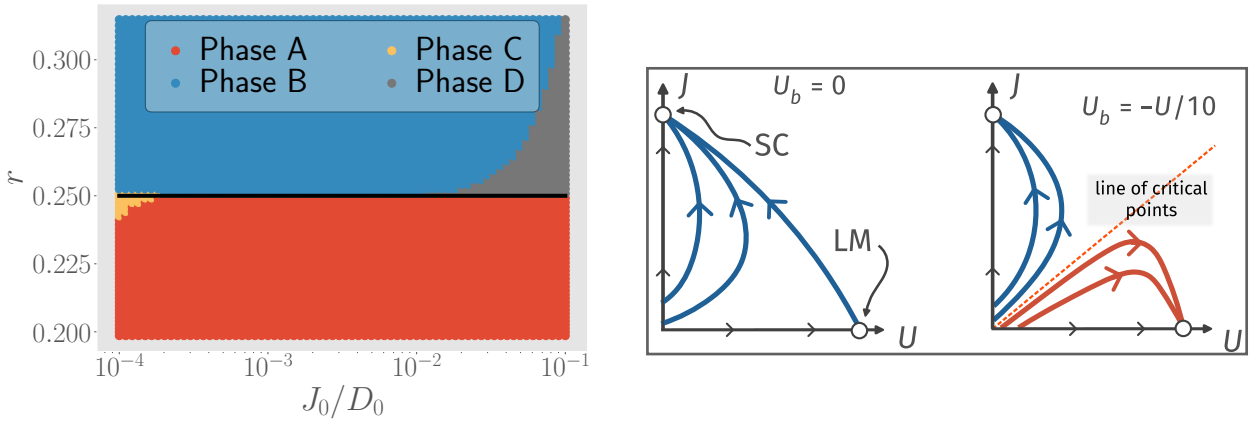

Figure 3.2: *Left: Phase diagram of the e-SIAM, in the space of r and J_0/D_0. U_b is set to $-U_0/10$. The various phases are described in the text. Right: Schematic nature of RG flows for $U_b = 0$ and $U_b = -U/10$. Blue curves represent RG flows towards the strong-coupling (SC) fixed point, while red curves represent RG flows towards the local moment (LM) fixed point.*

3.4.2 Phase diagram

We will work in the low-energy regime where the quantum fluctuation scale ω is such that all the denominators are negative: $d_i < 0 \; \forall \; i$. Moreover, we constrain the impurity and local bath correlations (U and U_b respectively) through the relation $U_b = -U/10$. While the precise value of the factor of $1/10$ is unimportant, we have chosen a factor considerably smaller than 1 in order to demonstrate that an interesting body of results can be obtained with a value of $|U_b|$ that is much smaller than that of U. Further, the negative sign in the above relation is significant, as we shall see below that the MIT is obtained for the case of U_b being negative (i.e., attractive on-site correlations on the zeroth site of the bath). The relation between U_b and U is motivated on phenomenological grounds such that the MIT occurring in the bulk lattice model (obtained upon increasing the on-site Hubbard repulsion to large values) corresponds, in the auxiliary model mapping within DMFT, to the local MIT observed upon tuning the impurity correlation U (and the related bath correlation U_b)

within the proposed effective impurity model Hamiltonian. The physical significance of attractive on-site correlations in the bath lies in providing a mechanism for the frustration of Kondo screening (in the RG equation for an antiferromagnetic Kondo coupling $J(> 0)$, eq. (**4.1**)) within an Anderson impurity coupled to a single channel of conduction electrons. We provide a detailed discussion of this point in the concluding section of our work.

Regime	Low-energy effective Hamiltonian	impurity ground-state
1. $0 < r < r_{c1}$	$\text{K.E}^* + V^* \sum_\sigma \left(c^\dagger_{d\sigma} c_{0\sigma} + \text{h.c.} \right) + J^* \vec{S}_d \cdot \vec{S}_0$	$\frac{1}{\sqrt{2}} \left(\lvert\uparrow_d\rangle \lvert\downarrow_0\rangle - \lvert\downarrow_d\rangle \lvert\uparrow_0\rangle + \lvert 2_d\rangle \lvert 0_0\rangle + \lvert 0_d\rangle \lvert 2_0\rangle \right)$
2. $r_{c1} < r < r_{c2}$	$\text{K.E}^* + J^* \vec{S}_d \cdot \vec{S}_0 - \frac{1}{2} U_b \left(\hat{n}_{0\uparrow} - \hat{n}_{0\downarrow} \right)^2$	$\frac{1}{\sqrt{2}} \left(\lvert\uparrow_d\rangle \lvert\downarrow_0\rangle - \lvert\downarrow_d\rangle \lvert\uparrow_0\rangle \right)$
3. $r_{c2} < r$	$\text{K.E}^* - \frac{U^*}{2} \left(\hat{n}_{d\uparrow} - \hat{n}_{d\downarrow} \right)^2 - \frac{U_b}{2} \left(\hat{n}_{0\uparrow} - \hat{n}_{0\downarrow} \right)^2$	$\{ \lvert\uparrow_d\rangle , \lvert\downarrow_d\rangle \}$

Table 3.1: *Effective Hamiltonians and ground-states of the three important parts of the phase diagram in Fig.* (3.2)*. The ground-state is simplified to capture only the configuration of the impurity site and at most the bath zeroth site. K.E.* represents the kinetic energy of the conduction electron states residing within the fixed point window D^*.*

The phase diagram is shown in the left panel of Fig. (3.2) in terms of the parameter $r = |U_b|/J$ (y-axis) and the ratio of the bare Kondo coupling (J_0) to the bare conduction bath bandwidth (D_0) (x-axis), we first define two important points in the space of couplings. These are values of the parameter r where there is a qualitative change in the nature of RG flows, and hence in the low-energy physics of the model

- $r = r_{c1} \left(= -\left(\frac{U_b}{J}\right)_{c1} = \frac{3}{20} = \left(\frac{U}{10J}\right)_{c1} > 0 \right)$: At this point, the coupling V becomes irrelevant,
- $r = r_{c2} \left(= -\left(\frac{U_b}{J}\right)_{c2} = \frac{1}{4} = \left(\frac{U}{10J}\right)_{c2} \right)$: At this point, the coupling J also turns irrelevant. Note that $r_{c2} > r_{c1}$.

We will use these two values of the parameter r as checkpoints around which we can describe the low-energy physics. There are three important parts in Fig. (3.2):

- red region, $0 < r < r_{c1}$: the $J - V$ model; *V and J are both relevant, but U is irrelevant*; spin and charge delocalisation on the impurity; spin-charge mixing in ground-state
- blue region, $r_{c1} < r < r_{c2}$: the $J - U_b$ model; *J is relevant, but V and U are both irrelevant*; charge localisation and spin delocalisation on the impurity; singlet ground-state
- violet region, $r_{c2} < r$: the $U - U_b$ model; *U is relevant, but V and J are both irrelevant*; spin and charge localisation on the impurity; local moment ground-state. This phase describes a local Mott insulator on the impurity site, characterised by vanishing local double occupancy in ground state (black curve in left panel of Fig. 3.4).

Typical RG flows that lead to these phases are shown in Fig. (3.3). We also note that the grey region shown in the top right corner of Fig.(3.2) corresponds to a model in which all three couplings (J, U and V) are RG irrelevant. We find, however, that this phase is an artefact of solving the RG equations for an impurity coupled to a finite-sized conduction bath, and it gradually disappears upon increasing the bath size.

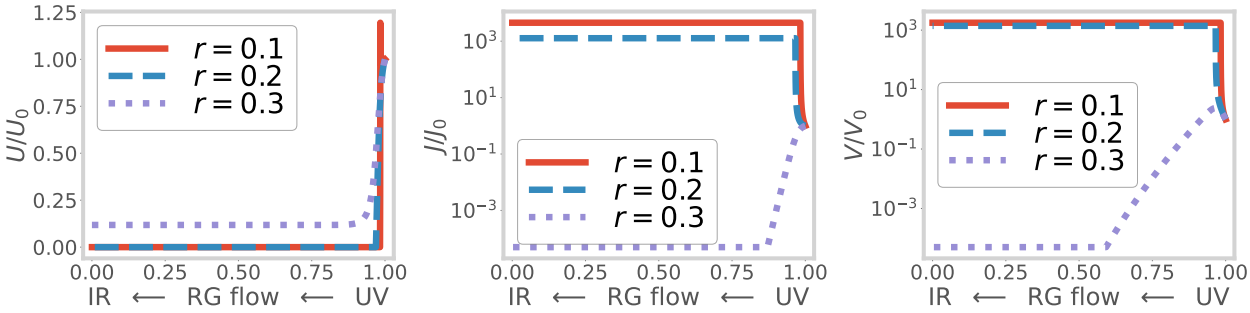

Figure 3.3: *Variation of couplings U, V and J along the RG transformations, for three values of the transition-tuning ratio $r = -U_b/J_0$. The x-axis represents the distance of the running cutoff from the Fermi surface; the rightmost point is the first RG step (UV) and the leftmost point is the final RG step (IR). The red curves represent the flows for $r < r_{c1}$, where both V and J are relevant. The blue curves represent the RG flows for $r_{c1} < r < r_{c2}$, where J is relevant but V is irrelevant. The violet curves represent RG flows for $r > r_{c2}$, where both V and J are irrelevant but U flows to a finite value.*

3.4.3 Phase transition at r_{c2}

The effective Hamiltonians and corresponding impurity ground-states for various phases have been listed in table (3.1). The variation in the ground state has been checked by numerically solving the fixed point Hamiltonian for various bare values of the couplings and is shown in the left panel of Fig. (3.4). A sharp change in the ground state from spin-singlet to local moment shows that the blue and violet phases are separated by an *impurity delocalisation-localisation transition* (black line in Fig. (3.2)). The transition occurs at finite values of the correlations: $r_{c2} = -\left(\frac{U_b}{J}\right)_{c2} = \frac{1}{4} = \left(\frac{U}{10J}\right)_{c2}$. This is a stark contrast from the standard SIAM, where the transition can happen only at on-site correlation $U \to \infty$. Therefore, the presence of the critical point at finite values of the various couplings transforms the landscape of RG phase diagram shown schematically in the right panel of Fig. (3.2) (right panel): the RG flows split into two classes - those that flow towards the strong-coupling Kondo screened fixed point and those that flow towards the local moment fixed point.

By a simple rewriting of the RG equation for J (eq. (**4.1**)), the impurity transition can be seen to arise from a competition between the Kondo screening physics of J and the local pairing physics

of U_b:

$$\Delta J = \overbrace{\frac{(J+2U_b)^2 n_j}{|d_2|}}^{\text{usual Kondo physics}} - \overbrace{\frac{(2U_b)^2 n_j}{|d_2|}}^{\text{competing pairing physics}} , \tag{4.4}$$

where $d_2 = \omega - D/2 + U_b/2 + J/4$. The competition between the effective Kondo term $(J+2U_b)^2$ and the competing pairing term $-4U_b^2$ leads to the presence of two stable phases - one that is Kondo screened and one that remains unscreened.

In the DMFT treatment of the $1/2$-filled Hubbard model on the Bethe lattice in infinite dimensions, the vanishing of non-local contributions to the lattice self-energy means that the lattice Greens function can be computed self-consistently by solving a local quantum impurity problem [18]. In the rest of the work, we provide extensive evidence that the local transition observed in the e-SIAM is very similar to the Mott MIT observed in DMFT. We conclude thereby that the e-SIAM models faithfully the round-trip excursions of an electron on the Bethe lattice, and that the impurity phase transition observed in the e-SIAM offers a local description of the Mott MIT in the bulk Hubbard model. With this evidence in mind, we will henceforth refer to the transition at r_{c2} as a *local metal-insulator transition*.

At this point, a comment is due on the interpretation of an attractive correlation U_b arising in the auxiliary model description of a purely repulsive model Hubbard-like model. We believe that the attractive bath interaction is best not understood as a microscopic coupling, but rather as an emergent effective coupling in the strong coupling limit of the local repulsion U. It captures the tendency of the conduction electrons to favour unoccupied or double occupied states (relative to the singly-occupied states). Perhaps in a more illuminating sense, just as the Coulomb repulsion U represents the tendency that competes with the hopping processes in the simple Hubbard model, the bath correlation W represents the tendency for local charge fluctuations that competes with the local Fermi liquid excitations that propagate out of the impurity site arising from Kondo screening. In this sense, it is a proxy for the hubbard U in the neighbourhood of the impurity site; both compete against delocalisation processes. In this regard, we note that similar emergent nonlocal nearest-neighbor attraction was obtained in the half-filled 2D Hubbard model for low temperatures at sufficiently large values of the local repulsion [508].

3.4.4 The case of repulsive U_b

Henceforth, we will only consider the case of attractive U_b ($U_b > 0$), because that is the regime in which an impurity phase transition is realised at finite values of the couplings. However, before moving on, we will comment briefly on the effects of a repulsive U_b ($U_b > 0$). From the RG equation for J in eq. 4.1, we see that ΔJ is always positive for $U_b > 0$. Moreover, something similar happens in the RG equation for V, where the two terms in the square brackets now enforce each other (J and U_b now have the same sign). Together, they indicate that there will not be any Kondo destruction in the case of $U_b > 0$, and the only fixed points are the weak-coupling one ($J^* = 0$) and the strong coupling one ($J^* = \infty$); there is no local moment phase. This case is therefore adiabatically connected to the case of $U_b = 0$.

3.5 Descriptors of the local MIT

The present section gives more clarity on the nature of the impurity phase transition in the form of additional descriptors of the transition such as impurity spectral function and measures of entanglement, computed from the e-SIAM Hamiltonian. Throughout the rest of the work, we have set the value of the coupling V equal to the Kondo coupling J while generating the quantitative plots.

3.5.1 Evolution of the impurity spectral function

The impurity spectral function of the standard SIAM (eq. (2.1)) always displays a central peak at finite values of U (along with Hubbard sidebands at sufficiently large U), indicating the presence of gapless local Fermi liquid excitations on the impurity site [40,44,446]. To demonstrate the impurity localisation transition, we compute the impurity local spectral function of the e-SIAM (eq. (2.2)). This involves numerically diagonalising the effective Hamiltonian at various energy scales along the RG flow and computing the spectral weight at a range of frequencies from UV to IR. We find that the spectral function (shown in the right panel of Fig. (3.4)) displays three notable features, in agreement with DMFT results [18]:

- The appearance of a *preformed gap* (flattening of spectral function between the central peak and sidebands) as r crosses r_{c1} $\left(= -\left(\frac{U_b}{J}\right)_{c1} = \frac{3}{20} = \left(\frac{U}{10J}\right)_{c1}\right)$: The preformed optical gap simply indicates the separation of the spin (central peak) and charge (sidebands) degrees of freedom beyond r_{c1}. This separation is brought about by the irrelevance of V. We note that the consequences of an irrelevant hybridisation V can be accounted for in many-body perturbation theory, leading to "in-gap" processes within the optical gap of the impurity spectral function [153]. However, we expect that such contributions will be small, and cannot fill in the optical gap observed in Fig.3.4 completely.

- The sharpening of the central peak, and concomitant increase in the preformed gap, as r is increased in the range $r_{c1} < r < r_{c2}$.

- The vanishing of the central peak and appearance of a *hard gap* as r crosses r_{c2}: The irrelevance of J beyond r_{c2} destroys the Kondo screening and localises the impurity moment. This involves the destabilisation of the singlet ground state, and the stabilisation of the local moment states in its place.

These features are also reflected in ground-state correlation measures like spin-flip and charge isospin-flip correlations (see left panel of Fig. (3.5)), which are defined as follows:

$$\frac{1}{2}\left(\langle S_i^+ S_j^-\rangle + \text{h.c.}\right) = \frac{1}{2}\left(\langle c_{i\uparrow}^\dagger c_{i\downarrow} c_{j\downarrow}^\dagger c_{j\uparrow}\rangle + \text{h.c.}\right) \ , \ \frac{1}{2}\left(\langle C_i^+ C_j^-\rangle + \text{h.c.}\right) = \frac{1}{2}\left(\langle c_{i\uparrow}^\dagger c_{i\downarrow}^\dagger c_{j\downarrow} c_{j\uparrow}\rangle + \text{h.c.}\right) \ . \quad (5.1)$$

At small values of r, both the correlations are large as the ground-state has both spin and charge content (row 1 of table (3.1)). The subsequent decrease in the impurity-bath charge flip correlation (violet points of Fig. (3.5)), and the simultaneous increase in the impurity-bath spin-flip correlation (red points of Fig. (3.5)), can be attributed to the irrelevance of V at $r \simeq r_{c1}$ and the appearance

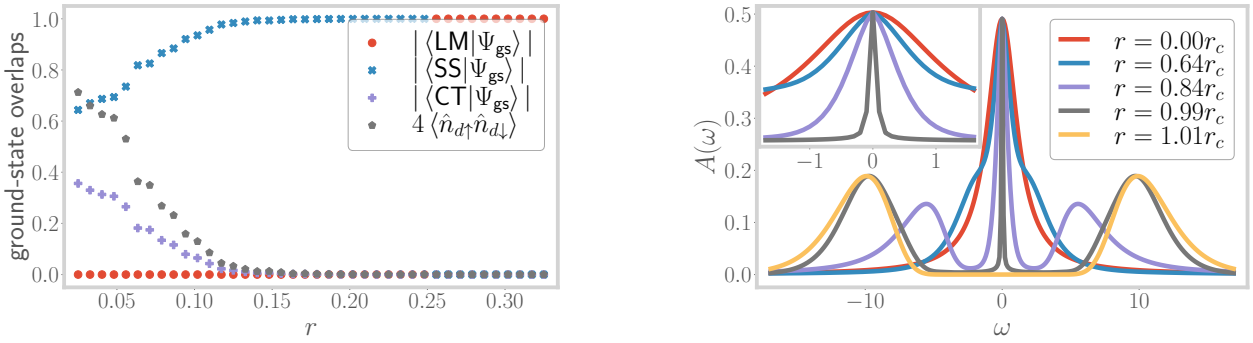

Figure 3.4: *Left: Overlap of the RG fixed point ground state $|\Psi\rangle_{gs}$ with the spin-singlet state $|SS\rangle$, the zero charge member of the charge triplet states $|CT\rangle$ and the local moment states $|LM\rangle$, for all three regimes of the model. The black curve corresponds to the double occupancy on the impurity site and is observed to be strongly suppressed beyond r_{c1}. Beyond the critical point $r_{c2} = 0.25$, the overlaps with the entangled states vanish, indicating the transition to a decoupled local moment. Right: Variation of the impurity spectral function from $r = 0$ to $r > r_{c2}$. At small r, the central peak is broad, but at larger r, it sharpens, and the difference in spectral weight is used in creating the Hubbard sidebands. For $r > r_{c2}$, the central peak vanishes.*

of the preformed gap in the spectral function. Beyond r_{c2}, the spin-flip correlation sharply drops to zero due to the irrelevance of J. They are replaced by intra-bath correlations like the charge isospin-flip correlation between the zeroth site and the first site (blue points of Fig. (3.5)). Such intra-bath correlations are promoted by the bath on-site term U_b. The sudden change in the nature of the ground state, and resulting correlations, at r_{c2} indicates the presence of a quantum critical point whose nature will be analysed further in subsequent sections.

3.5.2 Using entanglement to track correlations across the transition

We will now show that a certain measure of entanglement behaves as an order parameter for the transition. We can define a geometric measure of entanglement in terms of wavefunctions $|\psi_1\rangle$ and $|\psi_2\rangle$ [244, 509, 510]:

$$\varepsilon\left(\psi_1, \psi_2\right) = 1 - |\left\langle \psi_1 | \psi_2 \right\rangle|^2 . \tag{5.2}$$

From this definition, if $|\psi_1\rangle$ corresponds to a separable state, the entanglement content of the state $|\psi_2\rangle$ is small if it's overlap with $|\psi_1\rangle$ is large. For brevity, we will use the notation $\varepsilon_{ss} \equiv \varepsilon\left(\psi_{ss}, \psi_{gs}^{(2)}\right), \varepsilon_{ct} \equiv \varepsilon\left(\psi_{ct}, \psi_{gs}^{(2)}\right)$ to represent the geometric entanglement between the e-SIAM ground-state $|\psi_{gs}\rangle$ and the singlet state $|\psi_{ss}\rangle$ or the charge triplet zero state $|\psi_{ct}\rangle$. The latter two states are shown in Table (3.1). The entanglement measures ε_{ss} and ε_{ct} can be related to the impurity Greens function through the following equation (details can be found in Appendix 1 of this

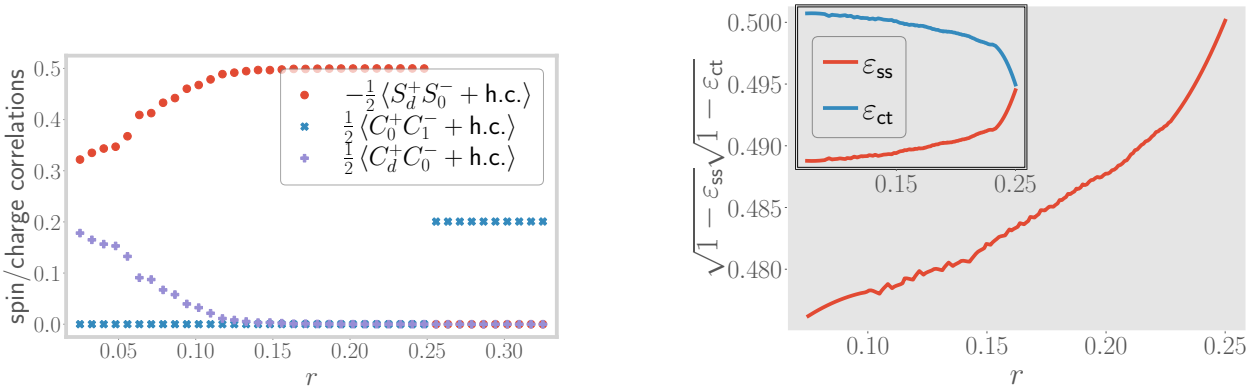

Figure 3.5: *Left: Variation of impurity-bath spin-flip correlation (red) and charge isospin-flip correlation (violet), as well as intra-bath charge isospin-flip correlation (blue), from $r \sim 0$ to $r > r_{c2}$. The imp.-bath isospin correlation vanishes at r_{c1}, indicating the change in RG relevance of V. The imp.-bath spin correlation vanishes at r_{c2}, indicating the marginality of J at that point. The intra-bath correlation picks up after the transition, showing the decoupling of the impurity from the bath. Right: Variation of the geometric entanglement ε_{ss} (blue) w.r.t. the singlet state and that w.r.t the charge triplet zero state, ε_{ct} (red), with r. The former becomes maximum (unity) at r_{c1}, showing that the true ground state has no charge content. The latter discontinuously jumps to unity at r_{c2}, therefore acting as an order parameter for the transition.*

chapter):

$$G_d(\omega) = \sum_n \Big[(1-\varepsilon_{\rm ss})\, G_{\Phi_{\rm ss},\Phi_{\rm ss}}(\omega,n) + (1-\varepsilon_{\rm ct})\, G_{\Phi_{\rm ct},\Phi_{\rm ct}}(\omega,n) + 2\sqrt{(1-\varepsilon_{\rm ss})}\sqrt{(1-\varepsilon_{\rm ct})} G_{\Phi_{\rm ss},\Phi_{\rm ct}}(\omega,n)\Big] , \tag{5.3}$$

where

$$G_{\psi_1,\psi_2}(\omega,n) = \frac{1}{2}\frac{\langle\psi_1|c_{d\sigma}|\Psi_n\rangle\langle\Psi_n|c^\dagger_{d\sigma}|\psi_2\rangle + \text{h.c.}}{\omega + E_{\rm gs} - E_n} + \frac{1}{2}\frac{\langle\psi_1|c^\dagger_{d\sigma}|\Psi_n\rangle\langle\Psi_n|c_{d\sigma}|\psi_2\rangle + \text{h.c.}}{\omega - E_{\rm gs} + E_n} . \tag{5.4}$$

This expression displays that the evolution of the impurity Greens function G_d with r (and related correlation functions shown in the left panel of Fig.(3.5)) is dependent on that of the entanglement measures $\varepsilon_{\rm ss}$ and $\varepsilon_{\rm ct}$ (shown in the right panel of Fig. (3.5)). Indeed, we find that the geometric entanglement $\varepsilon_{\rm ct}$ with the charge sector increases towards unity as the transition at r_{c2} is approached, and remains unity after the transition. A more sensitive measure is the singlet entanglement $\varepsilon_{\rm ss}$: it initially decreases to zero at r_{c1} owing to the irrelevance of V, but rises discontinuously to unity at the transition and becomes equal to the charge entanglement in the local moment phase. Therefore, $\varepsilon_{\rm ss}$ *acts as an order parameter* for the local MIT at r_{c2}. We find that the cross-term $\sqrt{(1-\varepsilon_{\rm ss})}\sqrt{(1-\varepsilon_{\rm ct})}$ decreases monotonically to zero with increasing r (not shown), displaying a continual decrease in the mixing of the spin and charge sectors and the *immobilisation of the doublons and holons on the impurity site*.

In general, any one-particle or two-particle fluctuation $\left\langle O_1 O_2^\dagger \right\rangle$ that acts on the combined Hilbert space of the impurity and the zeroth site can be expressed in terms of these entanglement measures $\varepsilon_{ss}, \varepsilon_{ct}$. The detailed derivations and expressions are given in Appendix 1. As a demonstration, consider the spin-spin correlation $\langle S_d^+ S_0^- \rangle$ between the impurity and the zeroth site shown in the left panel of Fig. (3.5). The general expression given in Appendix 1:

$$\begin{aligned}\langle S_d^+ S_0^- \rangle = \quad & (1-\varepsilon_{ss}) \langle \Phi_{ss} | S_d^+ S_0^- | \Phi_{ss} \rangle + (1-\varepsilon_{ct}) \langle \Phi_{ct} | S_d^+ S_0^- | \Phi_{ct} \rangle \\ & + \sqrt{1-\varepsilon_{ss}} \sqrt{1-\varepsilon_{ct}} \left(\langle \Phi_{ss} | S_d^+ S_0^- | \Phi_{ct} \rangle + \langle \Phi_{ct} | S_d^+ S_0^- | \Phi_{s} \rangle \right) . \end{aligned} \tag{5.5}$$

From the expression given, we find that only the singlet overlap is non-zero, such that $\langle S_d^+ S_0^- \rangle$ is directly proportional to the quantity $1-\varepsilon_{ss}$. As the entanglement measure ε_{ss} increases towards the transition (right panel of Fig. (3.5)), the quantity $1-\varepsilon_{ss}$ decreases, in turn leading to the decrease in the magnitude of the correlation observed in the left panel of Fig. (3.5). For another explicit connection between correlations and entanglement measures, we present relations between the quantum Fisher information (QFI) [461] and many-particle Greens functions in Appendix 1. There, we also plot the QFI for a number of two-particle operators as a function of r, notably the ones corresponding to the degree of compensation for the impurity ($\langle \vec{S}_d \cdot \vec{S}_0 \rangle$) and the impurity magnetisation ($\langle S_d^z \rangle$). These two quantities (and hence the corresponding QFI) are important because they track the local MIT and act as order parameters for the transition, and the QFI corresponding to these two operators quantify the quantum fluctuations present in the system corresponding to these order parameters. We show in Appendix 1 that the two phases on either side of the transition are characterised by distinct values of this pair of QFI: while the QFI corresponding to the degree of compensation is zero in the Kondo screened phase, it becomes non-zero in the local moment phase, and the opposite is true for the QFI arising from the impurity magnetisation. The phase precisely at the transition is distinct from those on either side because it displays a non-zero value for both of the QFI. While it is expected that a critical point would show enhanced fluctuations of multiple kinds (giving rise to universality), it is enlightening to find that this is also reflected in a measure of many-particle entanglement.

3.6 Universal theory for the local metal-insulator transition

In order to identify the competing tendencies near the transition at r_{c2}, we will now obtain the minimal effective Hamiltonian that displays the same transition. This involves integrating out the degrees of freedom that do not affect the low-energy physics near r_{c2}. We note that, due to the irrelevance of V, there is no scattering between the spin and charge states on the impurity at low energies. Further, the impurity charge states $|0\rangle$ and $|\uparrow_d \downarrow_d\rangle$ have been pushed to the high energy Hubbard sidebands because of the large value of U close to r_{c2}. As a result, the impurity charge states can be safely decoupled from the spin states through a Schrieffer-Wolff transformation. Up to second order in V^2/U, this transformation accounts for the effects of U and V by generating an additional (Kondo) spin-exchange term $\delta J \left(\sim \frac{V^2}{U+U_b} \right)$, as well as an additional on-site correlation $\delta U_b \left(\sim \frac{2V^2}{U+U_b+J/2} - \frac{8V^2}{U-U_b} \right)$ on the zeroth site of the conduction bath. In this way, we obtain the

following renormalised effective Hamiltonian:

$$H_{\rm MIT} = \mathcal{J}\vec{S}_d \cdot \vec{S}_0 - \frac{1}{2}\mathcal{U}_b \left(\hat{n}_{0\uparrow} - \hat{n}_{0\downarrow}\right)^2 + H_{\rm K.E.} \,, \tag{6.1}$$

where $\mathcal{J} = J + \delta J$ is the renormalised s-d interaction and $\mathcal{U}_b = U_b + \delta U_b$ is the renormalised local correlation on the bath zeroth site. A schematic 1D construction of the effective Hamiltonian is shown in the left panel of Fig. (3.6). We note that a similar approach towards extracting an effective theory for the Mott MIT has been employed in the past ([511, 512]). However, those works essentially led to renormalised Kondo models that do not possess any frustration of the Kondo screening. Thus, they cannot display an impurity transition in the absence of the requirement of self-consistency and can describe only the physics of the metallic regime. Importantly, the effective $\mathcal{J} - \mathcal{U}_b$ model (eq. (6.1)) is consistent with the IR fixed point Hamiltonian obtained in the appropriate regime $r_{c1} < r < r_{c2}$ (row 2 of table (3.1)).

The RG equations for $\mathcal{J}$ and $\mathcal{U}_b$ of the simplified effective impurity model eq. (6.1) can be obtained by setting $U = V = 0$ in the RG equations (4.1):

$$\Delta\mathcal{J} = -\frac{n_j \mathcal{J}\,(\mathcal{J} + 4\mathcal{U}_b)}{d_2} \quad , \quad \Delta\mathcal{U}_b = 0 \,. \tag{6.2}$$

For $\mathcal{J} + 4\mathcal{U}_b > 0$, the Kondo coupling is relevant and the low-energy phase is a paramagnetic local Fermi liquid with gapless excitations. But for $\mathcal{J} + 4\mathcal{U}_b < 0$, the Kondo coupling becomes irrelevant and the ground state is a decoupled local moment that is isolated from the bath. Such an effective picture of the transition can be understood if one notes that a straightforward way to destroy the Kondo screening is to inhibit the coordinated spin fluctuations between the impurity and the bath. Such frustration of Kondo screening is precisely the effect of the $\mathcal{U}_b$ term: it promotes charge fluctuations on the bath site coupled directly to the impurity, reducing thereby the spectral weight for spin-flip scatterings between the impurity and bath.



Figure 3.6: *Left: Schematic 1D construction of universal theory for the metal-insulator transition, obtained by integrating out the charge states of the impurity near the transition. Right: Zero bandwidth limit of the low-energy effective Hamiltonian for r between r_{c1} and r_{c2} (second row in table (3.1)). The bath is reduced to just a single degree of freedom - the zeroth site that is directly coupled to the impurity site.*

Indeed, the local correlation $\mathcal{U}_b$ encourages entanglement between the sites of the bath and makes the formation of the impurity-bath singlet difficult. In other words, the $\mathcal{J}-\mathcal{U}_b$ model displays the destabilisation of the singlet by redistributing the entanglement from the impurity+bath system to purely within the bath (see left panel of Fig. (3.7)). Given the simplicity of these arguments, our analysis makes the case that local pairing fluctuations of the bath in eq. (6.1) offer a universal mechanism by which to frustrate the Kondo effect and lead thereby to an impurity transition that is

the local counterpart of the Mott MIT obtained by auxiliary model approaches such as DMFT. We note that similar conclusions were reached in Refs. [476,477,486] for the emergence of non-Fermi liquid phases at critical points in the mixed valence regime of the periodic Anderson model.

Further insight into the destabilisation of the singlet can be obtained from a zero-bandwidth approximation of the bath. Under such an approximation, the IR effective Hamiltonian obtained from the RG flow (row 2 of Fig. (3.1) takes the form of a two-site model with modified couplings (shown in the right panel of Fig. (3.6)):

$$\tilde{\mathcal{J}}\vec{S}_d \cdot \vec{S}_0 - \frac{1}{2}\tilde{\mathcal{U}}_b \left(\hat{n}_{0\uparrow} - \hat{n}_{0\downarrow}\right)^2 \ . \tag{6.3}$$

The spectrum of this model is shown in the right panel of Fig. (3.7). For $|\tilde{\mathcal{U}}_b|/\tilde{\mathcal{J}} < 3/2$, the singlet ground-state (red) is separated from the excited local moment states (blue) by a gap of $\frac{-3\tilde{\mathcal{J}}}{4} - \frac{\tilde{\mathcal{U}}_b}{2}$. As we tune r towards r_{c2}, $|\tilde{\mathcal{U}}_b|$ increases and the fixed point value $\tilde{\mathcal{J}}$ decreases, leading to an overall reduction in the gap. At the critical point, the gap closes and the states become degenerate at zero energy; this is the equivalent of the quantum critical point at r_{c2} of the full impurity model that was discussed earlier. We note that the vanishing of the energy of the metallic state was also observed by Brinkman and Rice from a Gutzwiller-type variational calculation of the Hubbard model at half-filling [19].

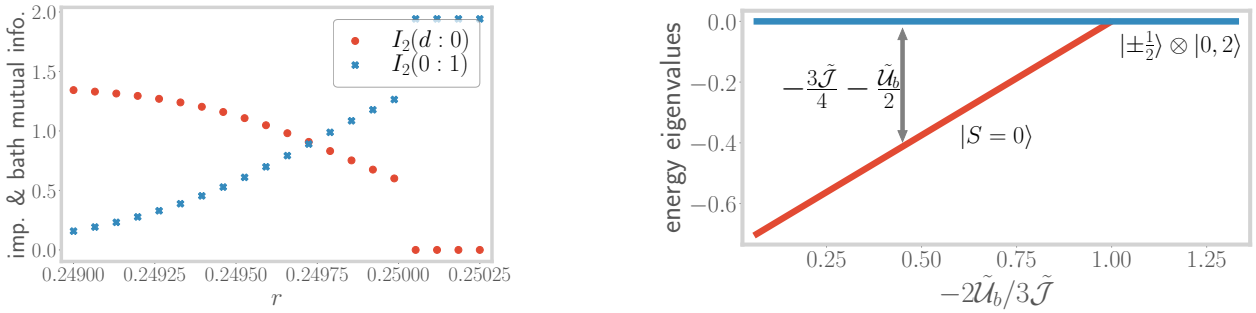

Figure 3.7: *Left: Very close to the transition, the mutual information $I_2(d:0)$ (red curve) between impurity and the zeroth site reduces, while that between the zeroth and the first site ($I_2(0:1)$, blue curve) increases, showing the redistribution of entanglement. Right: Spectrum of the zero bandwidth Hamiltonian of the right panel of Fig. (3.6). The blue line represents the local moment states at zero energy, while the red line represents the singlet state at an energy that continuously increases upon increasing r.*

3.6.1 Local pairing and the destruction of Kondo screening

Very close to the transition at r_{c2}, we find signatures of the breakdown of the Kondo cloud in terms of decaying impurity-zeroth site correlations (blue curve in the left panel of Fig. (3.8)) and enhanced intra-bath correlations. Remarkably, we find an *increase in pairing correlations* between the bath zeroth site and first site (red curve in the left panel of Fig. (3.8)). As discussed above, these are observed to be responsible for the destruction of the Kondo screening: spin and charge degrees

of freedom are mutually exclusive, and the increased charge fluctuations on the bath zeroth site suppress the spin-flip scattering processes between the impurity and the zeroth site. We will show later that these fluctuations lead to the destruction of the local Fermi liquid excitations in our model, and replace them with non-Fermi local excitations in the neighbourhood of r_{c2}. We believe that the observed growth in non-local pairing correlations near the transition at r_{c2} is likely tied to a putative low-energy divergence of the local pairing susceptibility. A similar observation was made in Ref. [476] from an auxiliary model-based analysis of a hole-doped extended Hubbard model in infinite dimensions that is pertinent to the physics of the heavy fermions. Similar to the conclusions of Ref. [476], we expect the pairing fluctuations of the bath to become dominant upon tuning the e-SIAM away from half-filling, signalling an instability towards a superconducting state.

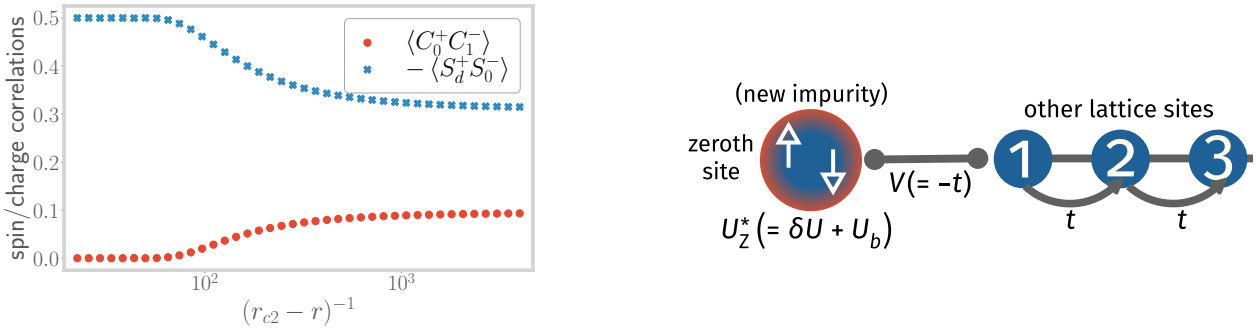

Figure 3.8: *Left: Spin-flip correlation between the impurity and the bath (blue), and charge isospin-flip correlation between the bath zeroth and first sites (red), both as a function of the tuning parameter r, very close to the transition. The operators are defined as* $S_i^+ = c_{i\uparrow}^\dagger c_{i\downarrow}$ *and* $C_i^+ = c_{i\uparrow}^\dagger c_{i\downarrow}^\dagger$. *Right: New effective SIAM Hamiltonian generated upon integrating out the coupling between the impurity and the bath zeroth site. In the new SIAM, the zeroth site acts as the new impurity site with a renormalised on-site correlation* $U_Z^* = U_b + \delta U_Z^*$.

3.6.2 Emergent self-consistency in the e-SIAM

As is well-established, the DMFT self-consistency equation is equivalent to requiring that the impurity Greens function become equal to the local Greens function in the bath [18]. Such a condition is also used in the projective self-consistent technique of Moeller et al. [511] for the states within the central Kondo resonance. We will now show that our model displays a qualitatively similar emergent feature. To proceed, by employing a one-step URG transformation, we integrate out the impurity site from the rest of the fixed-point Hamiltonian of eq. (**4.4**). The details are shown in Appendix 2. The essential idea is similar to that of the Schrieffer-Wolff transformation: removing the impurity-bath couplings J and V generates an additional repulsive correlation δU_z^* on the zeroth site. The new low-energy model H_Z is therefore an Anderson impurity model with a net local correlation $U_Z^* = \delta U_Z^* + U_b$ on the zeroth site (which is now the "new impurity site"), and a single-particle hybridisation $V_Z^* = -t$ coupling with a conduction bath formed by the remaining sites. This new

impurity model is depicted schematically in the right panel of Fig. (3.8).

$$H_Z^* = \underbrace{-\frac{1}{2}U_Z^*\left(\hat{n}_{0\uparrow}-\hat{n}_{0\downarrow}\right)^2}_{\text{new impurity = 0}^{\text{th}}\text{ site}} + \underbrace{V_Z^*\sum_{\langle j,0\rangle}\left(c_{0\sigma}^\dagger c_{j\sigma}+\text{h.c.}\right)}_{\text{hopping between 0}^{\text{th}}\text{ site \& new bath}} + \underbrace{(-t)\sum_{\langle i,j\rangle}\left(c_{i\sigma}^\dagger c_{j\sigma}+\text{h.c.}\right)}_{\text{K.E. of new bath}} . \tag{6.4}$$

Since, for $r < r_{c2}$, the model always flows to strong coupling at low energies, the largest energy scales are J^* and V^*. Using this, the effective correlation U_Z^* on the zeroth site can be expressed to leading order as

$$U_Z^* \simeq \frac{J^*}{4}\frac{1}{1+2\gamma} - V^*\frac{\gamma}{\gamma^2-\frac{1}{4}}, \quad \text{where } \gamma \equiv V^*/J^* . \tag{6.5}$$

From $r = 0$ to $r = r_{c1}$, the factor γ decreases due to the gradual removal of single-particle hopping from the impurity site (irrelevance of V), leading to an increase in the correlation U_Z^*. This is simply a restatement of the fact that the scattering processes that create the central impurity resonance induce a repulsive correlation on the bath zeroth site. The fact that we end up with a standard SIAM on the zeroth site once the impurity site has been integrated out means that the spectral function of this new impurity will again go undergo a sharpening of the central peak (and the appearance of the Hubbard sidebands) upon increasing the parameter r of the original e-SIAM. This ensures that the impurity and zeroth site spectral functions look qualitatively similar up to r_{c1}. One can now repeat iteratively this process - decoupling the zeroth site generates a standard SIAM with a repulsive correlation on the first site, and so on. The fact that excursions starting from any point along the bath can be described by a positive U SIAM is, therefore, the emergent self-consistency in our model. Similar indications of a correlated spectral function on lattice sites far away from the impurity were also observed in Ref. [494] from finite-U slave boson calculations of the SIAM. Beyond r_{c1}, the irrelevance of V means that U_Z^* reduces to just $J^*/4$. As r is now increased towards r_{c2}, the correlation decreases because J is moving towards its critical point, indicating that the bath zeroth site is moving away from its local moment regime. This is another reflection of the increase in pairing fluctuations of the bath, as well as the lowering of spin-flip fluctuations between the impurity and the bath.

For $r > r_{c2}$, the impurity site decouples from the bath in the impurity model. This impurity model can be promoted to a bulk model as follows. Recall that in the auxiliary model mapping, any lattice site $\vec{r}_i$ of the bulk lattice can act as the impurity, and one can think of the impurity model with the impurity at $\vec{r}_i$ as a representation of the excursion of an electron from any such site $\vec{r}_i$ into the rest of the bath. When all such impurity models undergo the transition at $r = r_{c2}$ simultaneously, the result is the decoupling of all sites from their respective baths and a paramagnetic bulk insulator is obtained.

3.7 Coexistence of local metallic and insulating phases in the e-SIAM

The DMFT solution of the Hubbard model on the Bethe lattice exhibits a coexistence region of metallic and insulating solutions between two spinodal lines $U_{c1}(T)$ and $U_{c2}(T)$ [18], with the metallic solution having lower internal energy and the insulating solution being a metastable state at a higher energy [18,32,511,513,514]. The $T = 0$ transition is observed to be second order in nature and occurs through a merging of the metallic and insulating solutions at U_{c2} [511,515]. On the other hand, at $T > 0$, the MIT happens along the first-order line $U_c(T)$ ($U_{c1} < U_c < U_{c2}$) where the free energies of the two solutions become equal, and the two spinodal lines merge into a second order critical point at a sufficiently high temperature T_c. We will now show that our Hamiltonian-based approach gives a clear zero temperature picture of various aspects that can lead to the emergence of the metal-insulator coexistence at $T > 0$.

3.7.1 Excited state quantum phase transition at r_{c1}: the Mott-Hubbard scenario

We have already discussed in detail the nature of the phase transition at r_{c2}: the zero-bandwidth picture provided (around eq. (**6.3**)) shows the merging of the metallic and insulating solutions at that point, enabling identification of r_{c2} with the $T = 0$ continuous phase transition observed at U_{c2} in the DMFT phase diagram. The focus of this subsection is the physics of the other important point r_{c1}. As has been mentioned before, this point marks the RG irrelevance of the single-particle hybridisation amplitude V, and leads to the exclusion of the charge states from the ground-state (see left panel of Fig. (3.4)). This exclusion means that there is now one fewer scattering channel by which the impurity electron can hybridise with the bath. In turn, this leads to a *partial localisation of the impurity*, and can be thought of as the first step towards the more complete localisation that occurs at r_{c2}.

Apart from the change in the ground state, the physics at r_{c1} also involves a phase transition in certain excited states of the spectrum. To expose this, we consider the following states in the zero-bandwidth spectrum of the impurity model given in eq. (**2.2**):

$$|1,\sigma,\pm\rangle = \alpha_\pm |\sigma_d\rangle |0_0\rangle \mp \sqrt{1-\alpha_\pm^2}\, |0_d\rangle |\sigma_0\rangle\,,\ |3,\sigma,\pm\rangle = \alpha_\pm |\sigma_d\rangle |2_0\rangle \mp \sqrt{1-\alpha_\pm^2}\, |2_d\rangle |\sigma_0\rangle\ ,$$
$$E_+ = -\frac{U_0}{4} + \sqrt{V_0^2 + \frac{U_0^2}{16}},\ \ E_- = -\frac{U_{\rm im}}{4} - \sqrt{V_{\rm im}^2 + \frac{U_{\rm im}^2}{16}},$$
$$\alpha_+(U_0,V_0) = \frac{V_0}{\sqrt{V_0^2 + \left(E_+ + \frac{U_0}{2}\right)^2}},\ \ \alpha_- = \frac{E_- + \frac{U_{\rm im}}{2}}{\sqrt{V_{\rm im}^2 + \left(E_- + \frac{U_{\rm im}}{2}\right)^2}}\,. \tag{7.1}$$

where ($\sigma = \uparrow, \downarrow$) and $E_\pm$ is the energy of the states $|1(3),\sigma,\pm\rangle$ and the subscripts d and 0 refer to the impurity and bath zeroth site respectively. The states $|1(3),\sigma,+\rangle$ are high-energy states, so their energy E_+ and coefficient α_+ involve the bare single-particle hybridisation V_0 and impurity on-site

repulsion U_0. On the other hand, the other states $|1(3), \sigma, -\rangle$ are closer to the IR energy scale and involve renormalised intermediate-scale couplings $V_{\rm im}$ and $U_{\rm im}$. Both E_+ and E_- are four-fold degenerate because of the SU(2) spin ($\uparrow \leftrightarrow \downarrow$) and particle-hole ($|0\rangle \leftrightarrow |2\rangle$) symmetries. For example, the degenerate subspace corresponding to E_+ is the set of states $\{|1,\uparrow,+\rangle, |1,\downarrow,+\rangle, |3,\uparrow,+\rangle, |3,\downarrow,+\rangle\}$.

All these states are in general delocalised - they involve the impurity hybridising with the bath via V. At $r = r_{c1}$, however, the coupling V becomes irrelevant and $V_{\rm im} \to 0$, so that the coefficient α_- of the low-energy state becomes unity beyond that point. The low-energy states $|1(3), \sigma, -\rangle$ thus become localised at r_{c1} and give rise to a set of excited and *degenerate local moment states*, i.e., $\alpha_- \to 0$ as $r \to r_{c1}$ leads to

$$|1(3), \sigma, -\rangle \to \begin{cases} |\uparrow_d\rangle |0_0\rangle, |\downarrow_d\rangle |0_0\rangle \\ |\uparrow_d\rangle |2_0\rangle, |\downarrow_d\rangle |2_0\rangle \end{cases} . \tag{7.2}$$

The other coefficient α_+ remains non-zero because, as mentioned earlier, V is non-zero in the UV scales of the RG flow. As a result, the high-energy states $|1(3), \sigma, +\rangle$ remain delocalised, and are separated from the localised states by an energy-scale

$$\lim_{r \to r_{c1}^-} (E_+ - E_-) \simeq \sqrt{V_0^2 + \left(\frac{U_0}{4}\right)^2} + \sqrt{V_{\rm im}^2 + \left(\frac{U_{\rm im}}{4}\right)^2} + \frac{U_{\rm im} - U_0}{4} . \tag{7.3}$$

This is shown schematically in the left panel of Fig. (3.9), and corresponds to the preformed gap in the zero mode spectrum. The point r_{c1} therefore represents *a delocalisation-localisation excited state quantum phase transition* (ESQPT) where degenerate local moment states are emergent as excited states in the many-body spectrum. This localisation of the impurity at r_{c1} is shown in the form of excited state mutual information in the right panel of Fig. (3.9). This ESQPT acts as a precursor to the QPT at r_{c2}, where the local moment states become degenerate with the spin-singlet ground state. The local moment states are stabilised as ground states in the insulating phase for $r > r_{c2}$.

3.7.2 Theory for the charge excitations in the Hubbard sidebands

Beyond r_{c1}, excitations into *the local moment states* $|1, \sigma, -\rangle$ *and* $|3, \sigma, -\rangle$ *reside at the edge of the central peak* in the impurity spectral function (purple curve in the right panel of Fig.(3.4)) but provide no spectral weight due to the lack of electron mobility. This explains the development of a preformed gap in the impurity spectral function. That these local moment states have to reside at the edge of the central peak becomes clear when we note that as the width of the central peak shrinks continuously, the local moment states must also recede towards zero frequency and finally replace the zero frequency peak at $r = r_{c2}$ in order to give rise to the insulating local moment phase for $r > r_{c2}$. On the other hand, the *still-delocalised high-energy states* $|1, \sigma, +\rangle$ *and* $|3, \sigma, +\rangle$ *are pushed into the Hubbard sidebands*, and their hybridisation with the bath through V and t is responsible for the broadening of the sidebands.

This isolation of the delocalised states into the sidebands means that charge delocalisation processes are now excluded from the physics at low energies. As accessing the sidebands involves

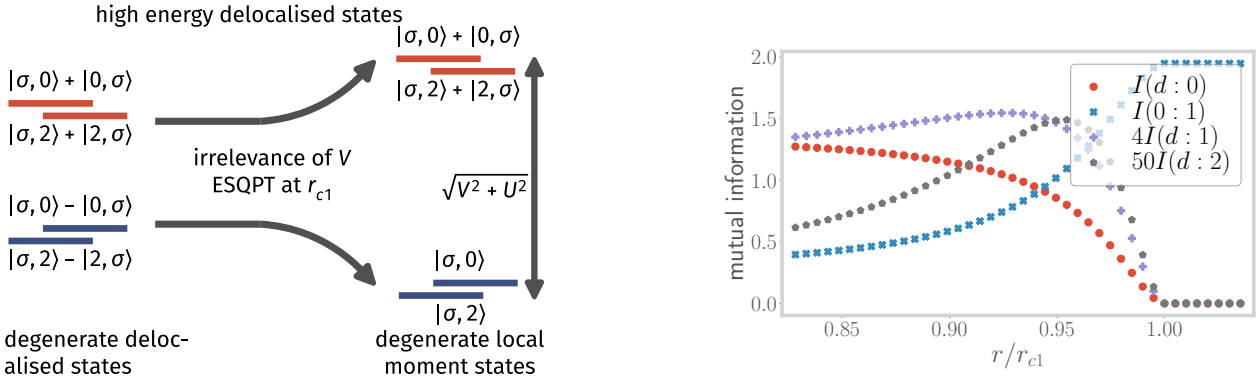

Figure 3.9: *Left: Evolution of the excited states mentioned in Eqs. (7.1) as r is tuned through r_{c1}. The high-energy states (red) retain their impurity-bath coupling, while their low-energy counterparts (blue) become disentangled and form a degenerate set of local moment states. The high-energy states allow delocalisation into the bath and lead to the broad Hubbard sidebands. Right: Variation of mutual information (MI) between various parties, across the ESQPT at r_{c1}. The MI (red) between the impurity and the zeroth site vanishes at r_{c1}, showing the localisation of the impurity. The same between the bath zeroth site and the next site becomes maximum at r_{c1}. The MI between the impurity and the other sites (purple and gray) of the bath show an initial rise near r_{c1}, indicating that entanglement is becoming long-ranged near the ESQPT.*

excitations at exorbitantly high energy scales, such processes can only happen virtually and involve very short time scales. The central Kondo resonance observed at low energies, therefore, does not support any charge delocalisation, and metallic excitations propagate only through spin-flip scattering processes of the impurity. This reveals that the Mott insulator comes about through a local binding of doublons and holons [11, 516, 517]. Closely related to this is the Mott-Hubbard scenario of the MIT, which is equivalent to our observation of the appearance of an optical gap in the spectrum after r_{c1}.

The fact that the sidebands are broad indicates that there are gapless excitations propagating from the impurity site into the conduction bath, but whose energy lies outside the Mott gap. These can also be viewed as metallic excitations of the bath that are induced by the coupled impurity. In order to expose the nature of these excitations, we perform a calculation similar to the local Fermi liquid calculation of Nozières [40]. This involves considering the states at $\omega \sim \pm U/2$ as the ground-states of the Hubbard sidebands, and then computing how excitations into the bath renormalise the ground-state subspace. Up to the second order in the hopping strength t, the effective Hamiltonian for the excitations of the bath can be expressed as

$$H^{(2)}_{\text{eff}} = \frac{4t^2(1-\alpha_+^2)}{E_+ - E_{\text{gs}}} C^z_{\text{tot}} C^z_1 - t \sum_{i>0,\sigma} \left(c^\dagger_{i\sigma} c_{i+1\sigma} + \text{h.c.} \right) , \tag{7.4}$$

where E_+ and α_+ have been defined in eq. (7.1), $C^z_i |2(0)\rangle = +(-)\frac{1}{2} |2(0)\rangle$ is the z-component of the charge isospin operator at a particular site i, and $\vec{C}_{\text{tot}} = \vec{C}_d + \vec{C}_0$ is the total isospin for the impurity and zeroth sites. $E_{\text{gs}} = U/2$ is the two-site energy of the ground-state subspace within the sideband.

These excitations are of the local Fermi liquid kind - the absence of any isospin-flip scattering term promotes the independent delocalisation of the doublon and holon states into the bath. The second-order effective Hamiltonian can therefore be written as the sum of two decoupled parts corresponding to holon and doublon propagation respectively, and suggesting adiabatic continuity with the $U = 0$ Hubbard model [518].

However, fourth-order corrections lead to the appearance of scattering processes that convert holon and doublons into one another, resulting in the local Fermi liquid becoming correlated

$$H_{\text{eff}}^{(4)} = \frac{\gamma^4 \alpha_+^2 \beta^2}{\left(1-\alpha_+^2\right)\left(E'_+ - E_{\text{gs}}\right)} \left[-C^z_{\text{tot}} C^2_{\text{tot}} C^z_1 + \sqrt{2}\mathcal{P}^4_{\text{tot}} \left(C^+_0 - C^+_d\right) C^-_1 + \text{h.c.} \right] , \tag{7.5}$$

where $E'_+ = \frac{U}{4} - \frac{3J}{8} + \sqrt{4V^2 + \left(\frac{U}{4} + \frac{3J}{8}\right)^2}$ is the energy of the state containing the charge isospin triplet zero, and $\beta = \frac{2V}{\sqrt{4V^2+(U+3J/4)^2}}$. $\mathcal{P}^4_{\text{tot}}$ projects on to the $n_d + n_0 = 4$ subspace. The scattering processes in eq. (7.5) are clearly non-Fermi liquid in nature as they allow the inter-conversion of the charge isospin eigenstates, and therefore reduce the lifetime of the quasiparticle excitations of the local Fermi liquid obtained in eq. (7.5). Additional details pertaining to the calculation of this effective Hamiltonian are present in Appendix 3.

3.7.3 Hysteresis and the first-order line

As discussed above, the localisation of charge in the emergent local moment states $|1, \sigma, -\rangle$ and $|3, \sigma, -\rangle$ for $r > r_{c1}$ means they do not contribute any spectral weight to the impurity spectral function. Instead, they lead to an emergent preformed/optical gap between the central Kondo resonance and the Hubbard sidebands on each side. This *optical gap* finally becomes the true Mott gap at $r = r_{c2}$ when the central peak disappears. On the other hand, upon starting from $r > r_{c2}$ and reducing r, the system is initially in the (doubly degenerate) local moment ground states, and the impurity DOS is of course gapped. In the rest of the subsection, we will show that the presence of these two transitions leads to finite temperature behaviour for the e-SIAM that is qualitatively similar to that of the Hubbard model as seen from DMFT (that was described at the beginning of this section, and can also be seen in Fig. 3.10).

At non-zero temperatures, the system is described by not only the ground-state but also the excitations. The metallic and insulating solutions become temperature dependent, with energies $E_M(r,T)$ and $E_I(r,T)$ respectively. The curve $r_{c1}(T)$ at a given temperature again represents the values of the parameter r at which the local moment states enter the spectrum as excited eigenstates, while $r_{c2}(T)$ marks the point where the metallic ground-state leaves the spectrum: $E_M(r_{c2}(T),T) = E_I(r_{c2}(T),T)$. As a result, within the parameter range $r_{c1}(T) < r(T) < r_{c2}(T)$ at a finite temperature T, the low-energy part of the spectrum (states within the central Kondo resonance) involves both the metallic and insulating solutions. These two low-lying solutions then govern the partition function and hence the free energy:

$$Z(r,T) \simeq Z_M(r,T) + Z_I(r,T), \quad F(r,T) \simeq -k_B T \ln\left(Z_M(r,T) + Z_I(r,T)\right), \tag{7.6}$$

where $Z_M(r,T) = \exp\left(-\beta\mathcal{V}\left(E_M(r,T) - TS_M(r,T)\right)\right)$ is the partition function corresponding to the metallic state with energy $E_M(r,T)$ and entropy $S_M(r,T)$ per unit volume $\mathcal{V}$, and

$$Z_I = \exp\left(-\beta\mathcal{V}\left(E_I(r,T) - TS_I(r,T)\right)\right), \tag{7.7}$$

is similarly the partition function corresponding to the local moment states.

In the thermodynamic limit, only the larger of Z_M and Z_I contributes to the partition function $Z(r,T)$. Given a temperature T, there exists a value $r_c(T)$ lying in the range $r_{c1}(T) < r_c(T) < r_{c2}(T)$ at which the partition functions $Z_M(T)$ and $Z_I(T)$ become equal: $Z_M(r_c(T),T) = Z_I(r_c(T),T)$. This condition defines a curve $\{(T, r_c(T))\}$ at which the system undergoes a first-order transition between the metallic and insulating states:

$$\lim_{\mathcal{V}\to\infty} F(r,T) = \begin{cases} -k_B T \ln Z_M(r,T) \text{ if } r < r_c \ (Z_M > Z_I) \\ -k_B T \ln Z_I(r,T) \text{ if } r > r_c \ (Z_M < Z_I) \end{cases} . \tag{7.8}$$

The first-order curve $r_c(T)$ is determined from the partition function equality (or equivalently, the free energy equality) condition between the metal and the insulator:

$$T = \frac{E_M(r_c,T) - E_I(r_c,T)}{S_M(r_c,T) - S_I(r_c,T)} . \tag{7.9}$$

At $T = 0$, the first-order line $r_c(T)$ becomes identical to the critical point r_{c2}, as $E_M(r_c) = E_I(r_c)$ at $T = 0$. This simply means that the thermal entropy plays no role at zero temperature, and the transition is purely quantum-mechanical in nature. As temperature is now increased, the large entropy S_I of the doubly degenerate local moment states comes into play and the insulating state is able to take over at a smaller value of r. This suggests that a first-order transition can take place in the thermodynamic limit at $r_c(T) < r_{c2}(T)$. This has been shown schematically in Fig. (3.10).

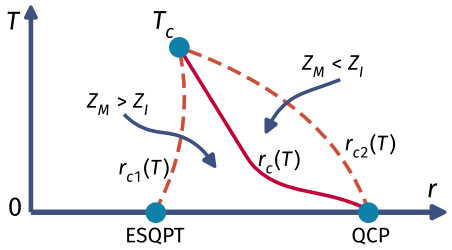

Figure 3.10: *Qualitative structure of the finite temperature coexistence region of the $J - U_b$ model. The dotted lines on the left and the right represent the spinodals r_{c1} and r_{c2} where the insulating and metallic solutions become unstable, respectively. The solid red line represents the first-order line where the free energies and the partition functions of the two solutions become equal, $Z_M = Z_I$.*

Further, away from the thermodynamic limit, the free energy in eq. (7.6) admits contributions from the stable metallic state as well as the metastable insulating state, and results in the coexistence of the two phases. This is because, depending on whether we are approaching from r_{c2}^+ or r_{c1}^-, the system will remain mostly in the minimum of either Z_I or Z_M respectively. There exist finite

activation barriers in the free energy for passage into the other minimum, leading to hysteresis. The transition is observed only at $r_{c1}(T)$ or $r_{c2}(T)$ where the insulating and metallic solutions, respectively, become unstable. These two lines, therefore, mark the spinodals of the coexistence region. At a sufficiently high temperature T_c, the metallic and insulating solutions become indistinguishable at the first spinodal r_{c1}: $E_M(r_{c1}, T_c) = E_I(r_{c1}, T_c), S_M(r_{c1}, T_c) = S_I(r_{c1}, T_c)$. We recall that of these two equalities, the first ($E_M = E_I$) also corresponds to the locus of the second spinodal (corresponding to r_{c2}). Moreover, combining the two equalities (energy and entropy) leads to the free energy equality condition, marking the locus of the first-order line $r_c(T)$. This has the consequence that the two spinodals and the first-order line merge into a second order critical point $r_c(T_c)$ at temperature T_c. This concludes our discussion of the finite temperature behaviour of the extended SIAM model and its qualitative similarities with the DMFT phase diagram for the half-filled Hubbard model on the Bethe lattice.

3.7.4 Zero temperature origin of critical fluctuations above the second order point

Above the second order point $r_c(T_c)$, the DMFT phase diagram shows a rapid crossover from the paramagnetic metallic solution to the paramagnetic insulating solution [18, 519]. Remarkably, signatures of quantum critical scaling in this crossover region have been recently predicted from theoretical analyses [470, 478], as well as detected experimentally in transport measurements of several organic compounds [520, 521]. In Refs. [470, 478], this has been ascribed to the existence of a *hidden quantum criticality* in the maximally frustrated $1/2$-filled Hubbard model on the Bethe lattice with infinite coordination number. In order to locate the zero temperature origin of these signatures of quantum criticality, we inspect carefully the quantum-mechanical fluctuations near the two important points r_{c1} and r_{c2} in our model.

Close to r_{c1}, we compute correlations in the state $|1, \sigma, -\rangle$. As shown in the top panel of Fig. (3.11), we find that while the one-particle correlation between the impurity and the bath vanishes, the same between the zeroth and first sites of the bath picks up. Importantly, these correlations extend beyond the immediate neighbourhood of the impurity. This is observed in, for example, the one-particle correlation between the zeroth site and the second site (purple curve in the top panel of Fig. (3.11)). Some other signatures of correlations in the bath are shown in Fig. (3.11): while the left panel displays increased spin-flip and charge isospin-flip correlations between the zeroth and first sites of the bath, a similar phenomenon is observed between the zeroth and second sites of the bath in the right panel. Our findings are consistent with the presence of scale-invariant solutions obtained from recent NRG-DMFT calculations [160] that correspond to the metastable insulating solutions in the coexistence region.

The growth of similar long-ranged correlations within the bath (and leading away from the immediate neighbourhood of the impurity) near r_{c2} as well. We recall that correlations between the impurity and the zeroth site are observed to decrease (see left panel of Fig.(3.5)). Instead, as shown in Fig. (3.12), non-trivial two-particle correlations arise between the impurity and bath zeroth sites with bath sites that are farther away. The spreading of the spin-spin correlations shown in the left panel of Fig. (3.12) indicates a "stretching" of the Kondo singlet state prior to its destruction. We will show later that these enhanced correlations also result in a diverging quasiparticle mass at r_{c2},

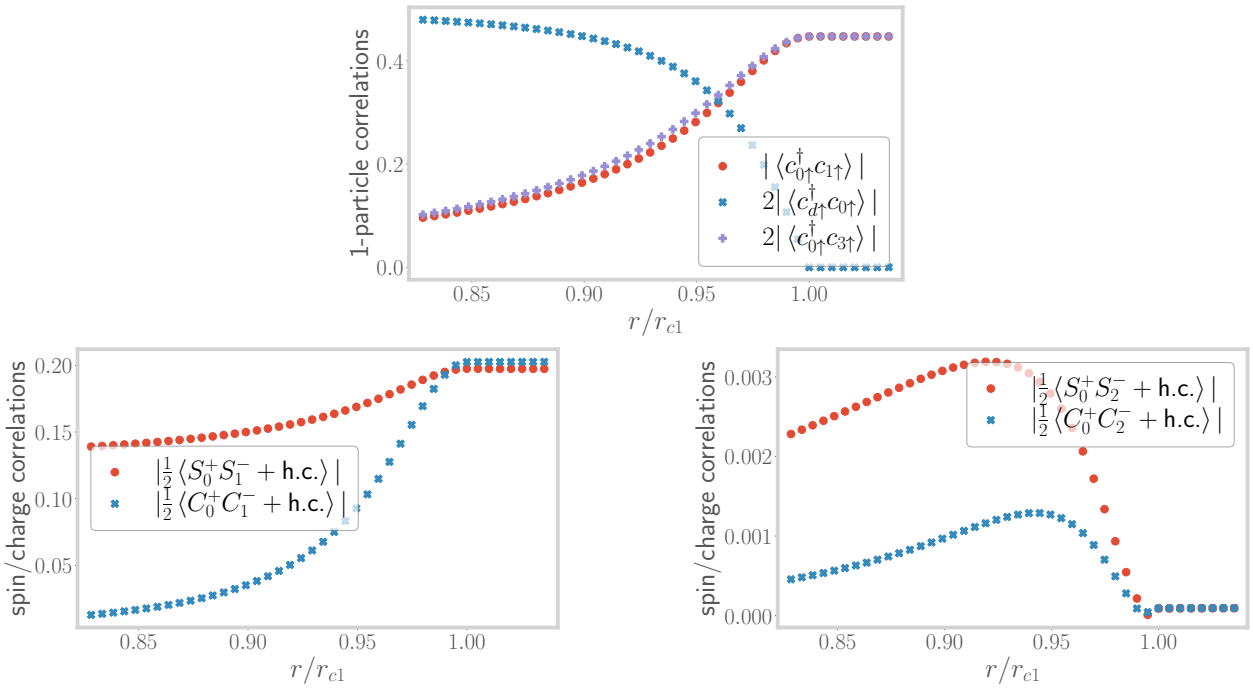

Figure 3.11: *Top: Variation of the one particle correlations in the state $|1,\sigma,-\rangle$ between impurity and bath zeroth site(blue), as well as within the bath (red and violet). The former vanishes, depicting the excited state localisation transition at r_{c1}. Left: Variation of the spin-flip (red) and charge isospin-flip (blue) correlations between impurity and bath, close to r_{c1}. They both increase, indicating that the impurity is now less strongly coupled with the bath. Right: Variation of the spin-flip (red) and charge isospin-flip (blue) correlations between the zeroth and second sites of the bath, close to r_{c1}. Both show an initial increase, leading to the propagation of relatively long-range correlations into the bath.*

indicating a breakdown of the local Fermi liquid metal. Further, the right panel of Fig. (3.12) indicates that longer-ranged pairing correlations develop between the bath zeroth site and bath sites farther away upon approaching the transition.

In general, within the metallic phase and away from r_{c1} or r_{c2}, the impurity is strongly coupled to the bath zeroth site and the impurity-bath entanglement follows an area law characteristic of the local nature of the impurity problem. However, near the excited state and ground state transitions at r_{c1} or r_{c2} respectively, these results indicate a spreading of entanglement into the bath: more and more bath sites beyond the zeroth site get correlated with the impurity site as the ESQPT or the QCP is approached. This is corroborated in Fig. 3 of the Appendices. This suggests a significant enhancement of the entanglement beyond the area law and is consistent with the critical quantum fluctuations observed in the various two-particle correlations.

The results of this subsection indicate that it might be possible to experimentally detect the signatures of such critical quantum fluctuations around the spinodals of the DMFT phase diagram even at $T > 0$. We note that signatures of second-order criticality have been indeed observed recently in vanadium sesquioxide, in the form of critical slowing down and critical opalescence [522]. It is, therefore, tempting to speculate that these signatures arise from the presence of critical quantum fluctuations.

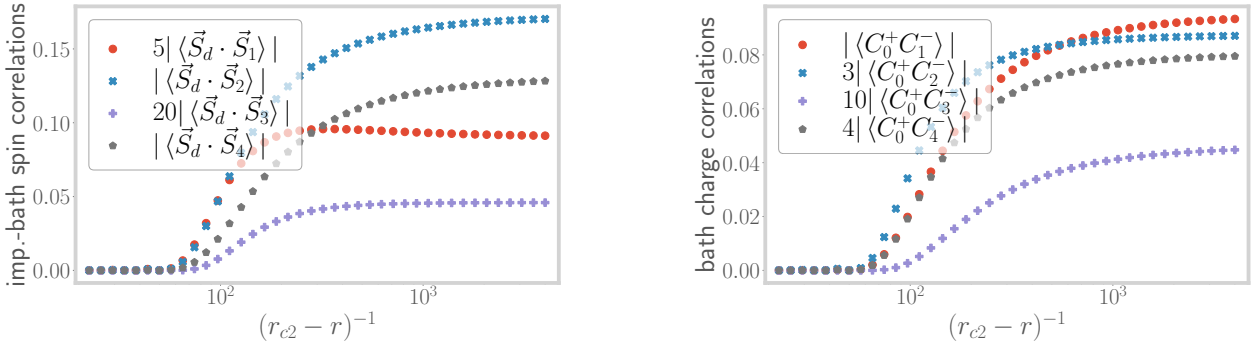

Figure 3.12: *Left: Variation of the spin-spin correlations between the impurity and bath sites 1 through 4, close to r_{c2}. They show an increase, revealing the distribution of entanglement into the bath. Right: Variation of pairing correlations within the bath. These correlations show an increase, because of the weakening of the Kondo singlet.*

3.8 Non-Fermi liquid signatures at the MIT

3.8.1 Death of the local Fermi liquid: the Brinkman-Rice scenario

The low-lying metallic excitations of the bath can be obtained by considering the singlet ground-state of the model (of energy $\sim -3\tilde{\mathcal{J}}/4$) in the metallic phase, and then studying the effect of an electron hopping term (with coupling t) between the singlet and the rest of the bath as a perturbation (see left panel of Fig. (3.13)). Such a strong-coupling expansion in powers of $t^2/\tilde{\mathcal{J}}$ leads to the usual

local Fermi liquid effective Hamiltonian in the Kondo model [40, 42, 52, 446]:

$$H_{\rm LFL} = \mathcal{F}\hat{n}_{1\uparrow}\hat{n}_{1\downarrow} + H_{\rm KE}\ ,\quad \mathcal{F} \sim t^4/\tilde{\mathcal{J}}^3\ , \tag{8.1}$$

where $\hat{n}_{1\sigma}$ are the number operators for the first site (site adjacent to the zeroth site of the conduction bath), $H_{\rm KE}$ is the kinetic energy arising from the nearest-neighbour hopping among all sites in the bath apart from the zeroth site, and $\mathcal{F}$ is the local Fermi liquid correlation strength. The Kondo singlet (formed between the impurity spin and the bath zeroth site) has decoupled from the rest of the lattice, and eq. (8.1) describes the effective Hamiltonian for the rest of the bath beyond the zeroth site.

Following an identical approach, we find that the effective Hamiltonian for the low-lying excitations in the metallic phase is given by

$$H_{\rm LFL} = \mathcal{F}\left[\hat{n}_{1\uparrow}\hat{n}_{1\downarrow} + \left(1-\hat{n}_{1\uparrow}\right)\left(1-\hat{n}_{1\downarrow}\right)\right] + H_{\rm KE},\qquad \text{where } \mathcal{F} = \frac{2t^4}{\tilde{\mathcal{J}}\left(3\tilde{\mathcal{J}}/4+\tilde{\mathcal{U}}_b\right)^2}\ . \tag{8.2}$$

We note that for our extended SIAM, the local Fermi liquid correlation $\mathcal{F}$ diverges as the transition is approached at $3\tilde{\mathcal{J}}/4+\tilde{\mathcal{U}}_b \to 0$. The divergence of $\mathcal{F}$ leads to the divergence of the renormalised mass of the quasiparticles, and can also be obtained from a Gutzwiller variational calculation as shown by Brinkman and Rice [19]. This shows the breakdown of perturbation theory and is indicative of the fact that the ground state is about to change at the metal-insulator transition.

The death of the local Fermi liquid is also seen from the vanishing of the dynamically generated low-energy Kondo screening scale T_K. Towards obtaining T_K close to the transition, we follow the approach used by Moeller et al. 1995 [511] and Held et al. 2013 [512]. Near the transition, they obtained a Kondo model from the SIAM by applying a Schrieffer-Wolff transition that removes the charge fluctuations of the impurity site and retains the physics of only the Kondo coupling J. This amounts to removing the side peaks from the impurity spectral function and focusing on the low-energy central peak (right panel of Fig. (3.13)). Held et al. then integrated the RG equation for this Kondo model by using a Lorentzian DOS $\rho(D)$ in the bath: $\rho(D) = \frac{\rho_0\Gamma^2}{D^2+\Gamma^2}$. This is motivated by the fact that the central peak of the impurity spectral function is a Lorentzian, and the bath becomes equivalent to the impurity site under self-consistency.

We implement the same approach on the e-SIAM, such that the Schrieffer-Wolff transformation leads to a $J-U_b$ model with a Lorentzian electronic DOS in the bath. The expression of the Kondo temperature for such a system has been derived in Appendix 4. Very close to the transition, we have $r \to 0.25^-$, and the Kondo temperature is given by

$$T_K = \frac{D_0}{k_B}\exp\left[-\frac{\ln\left(r_{c2}-r\right)}{4U_b\rho_0}\right]\ , \tag{8.3}$$

where $r_{c2} = 0.25$ and D_0 is the bare bandwidth. Note that the pre-factor of the logarithm is positive as U_b is negative: $-4U_b\rho_0 = |4U_b\rho_0|$. As we approach the transition, the parameter r takes the limit $r \to r_{c2}^-$, and the Kondo temperature scale vanishes:

$$\lim_{r\to r_{c2}^-} T_K = \frac{D_0}{k_B}\lim_{r\to r_{c2}^-}\left(r_{c2}-r\right)^{4|U_b\rho_0|} \to 0\ . \tag{8.4}$$



Figure 3.13: *Left: Setup for obtaining the low-energy excitations above the strong-coupling ground state. The effects of the rest of the bath is included by treating the hopping between the zeroth site (blue sphere on the left) and the first site (sphere labelled 1) as a perturbation on top of the singlet ground state formed by the impurity (red sphere) and the zeroth site. Right: At r_{c1}, the Hubbard sidebands have become isolated from the central peak in the local spectral function because of the finite optical gap. Removing the UV excitations that couple the low-energy and high-energy bands then leads to a theory of the Kondo model with a Lorentzian DOS.*

Following the renormalised perturbation theory approach of Hewson [43, 523], the imaginary part of the self-energy of the local Fermi liquid quasiparticles is given by

$$\mathrm{Im}\left[\Sigma(\omega)\right] \sim \frac{\mathcal{F}^2}{D_0}\frac{\omega^2}{T_K^2}\,, \tag{8.5}$$

while the quasiparticle residue is given by $Z \sim T_K$. The divergence of $\mathrm{Im}\left[\Sigma(\omega)\right]$ at the transition and the vanishing of T_K and the quasiparticle residue are important indicators of the loss of the local Fermi liquid excitations and the breakdown of Kondo screening.

The vanishing of the Kondo temperature scale also leads to the divergence of thermodynamic quantities such as the impurity contribution to local spin susceptibility χ_{imp} and the specific heat coefficient γ_{imp}. As the low-energy theory is a local Fermi liquid, χ_{imp} and γ_{imp} retain their Fermi liquid forms but involve the highly renormalised Kondo temperature scale [446, 524]:

$$\begin{aligned}
\chi_{\mathrm{imp}} &= \frac{w}{4k_B T_K}, \quad \lim_{r\to r_{c2}^-}\chi_{\mathrm{imp}} = \frac{w}{4k_B}\left(r_{c2}-r\right)^{-4|U_b\rho_0|}, \\
\gamma_{\mathrm{imp}} &= \frac{\pi^2 k_B^2 w}{6T_K}, \quad \lim_{r\to r_{c2}^-}\gamma_{\mathrm{imp}} = \frac{\pi^2 k_B^2 w}{6}\left(r_{c2}-r\right)^{-4|U_b\rho_0|},
\end{aligned} \tag{8.6}$$

where $w \sim 0.4128$ is the Wilson number for the Kondo model [42, 446]. These results also show that the ratio of χ_{imp} and γ_{imp}, referred to as the Wilson ratio $R \equiv \frac{4\pi^2 k_B^2 \chi_{\mathrm{imp}}}{3\gamma_{\mathrm{imp}}}$, remains pinned at the single-channel Kondo value of $R_{\mathrm{LFL}} = 2$ for $r \to r_{c2}-$. This shows that the low-frequency Landau quasiparticles are able to survive until very close to the QCP. As we will show in the next subsection, the metallic excitations precisely at the QCP acquire non-Fermi liquid character and involve additional correlations between holons and doublons. These additional correlations are expected to lead to an enhancement of the Wilson ratio. Evidence for this can be found in the DMFT calculation of a local Wilson ratio very close to the Brinkman-Rice transition, $R_{\mathrm{loc}} = 2.9 \pm 0.2$ [18].

3.8.2 Emergence of non-Fermi liquid excitations at the transition

In order to obtain an effective Hamiltonian for the excitations precisely at the critical point $r = 1/4$, we first note that the ground-state subspace of the zero bandwidth $J - U_b$ effective model (eq. (6.3)) becomes degenerate at this point:

$$\frac{1}{\sqrt{2}}\left(|\uparrow\rangle_d\,|\downarrow\rangle_0 - |\downarrow\rangle_d\,|\uparrow\rangle_0\right)\ ,\ |\sigma\rangle_d\,|0\rangle_0\ ,\ |\sigma\rangle\,|2\rangle_0\ ,\quad (\sigma = \uparrow, \downarrow)\ , \tag{8.7}$$

with all the states lying at zero energy. Here, the first ket (with subscript d) represents the impurity spin configuration while the second ket (with subscript 0) represents the configuration of the bath zeroth site). We now diagonalise these states in the presence of the electron hopping t into the rest of the conduction bath, and obtain the effective Hamiltonian for the low-lying excitations mediated by t. This is described in detail in Appendix 5. We note that the ground state is four-fold degenerate at energy $-t$ in the presence of the hopping, and comprises the following states:

$$|N_{\rm tot} = 2, S^z_{\rm tot} = 0\rangle\ ,\ |N_{\rm tot} = 4, S^z_{\rm tot} = 0\rangle\ ,\ |N_{\rm tot} = 3, S^z_{\rm tot} = \frac{1}{2}\rangle\ ,\ |N_{\rm tot} = 3, S^z_{\rm tot} = -\frac{1}{2}\rangle\ , \tag{8.8}$$

where $N_{\rm tot} = \hat{n}_d + \hat{n}_0 + \hat{n}_1$ and $S^z_{\rm tot} = S^z_d + S^z_0 + S^z_1$ are the total number operator and total magnetisation operator respectively for the impurity, bath zeroth and first sites taken together. It is worth observing that

- the presence of the unscreened states $|N_{\rm tot} = 3, S^z_{\rm tot} = \pm\frac{1}{2}\rangle$ in the ground-state subspace is a result of the inexact screening at the critical point, and
- the presence of a degenerate ground-state manifold indicates that these excitations of the bath will likely be of the non-Fermi liquid (NFL) kind [476, 525, 526].

The precise form of the effective Hamiltonian for this non-Fermi liquid, as well as the behaviour of various correlation functions, is obtained by considering the ground-state manifold in conjunction with the excited states at energy $-t$.

Since the total Hamiltonian conserves the total spin $S^z_{\rm tot}$, the effective Hamiltonian separates into two sectors, $S^z_{\rm tot} = 0$ and $|S^z_{\rm tot}| = \frac{1}{2}$. Detailed calculations on obtaining this effective Hamiltonian from the RG fixed point theory are shown in Appendix 5. In order to highlight certain distinct features, we present simplified effective Hamiltonians only for the $S^z_{\rm tot} = 0$ and $S^z_{\rm tot} = \frac{1}{2}$ sectors. We first take a look at the $S^z_{\rm tot} = 0$ sector:

$$H_{\rm eff}^{S^z_{\rm tot}=0} = t\vec{S}_d \cdot \left(\vec{\mathcal{S}}_{1,-} + \vec{\mathcal{S}}_{3,-}\right)\ . \tag{8.9}$$

The effective spin-1/2 ladder operators $\vec{\mathcal{S}}_{1,\pm}$ act on the positive and negative parity sectors (labelled by $\pm$) of the $\hat{n}_0 + \hat{n}_1 = 1$ subspace spanned by the states

$$|\Uparrow\rangle_{1,\pm} = |\uparrow\rangle_0\,|0\rangle_1 \pm |0\rangle_0\,|\uparrow\rangle_1\,,\quad |\Downarrow\rangle_{1,\pm} = |\downarrow\rangle_0\,|0\rangle_1 \pm |0\rangle_0\,|\downarrow\rangle_1\ , \tag{8.10}$$

leading to a Pauli matrix representation of $\vec{\mathcal{S}}_{1,\pm}$ in that basis. The Pauli matrix operators $\vec{\mathcal{S}}_{3,\pm}$ similarly act on the $\hat{n}_0 + \hat{n}_1 = 3$ subspace spanned by the states $|\Uparrow\rangle_{3,\pm} = |\uparrow\rangle_0\,|2\rangle_1 \pm |2\rangle_0\,|\uparrow\rangle_1$ and

$|\Downarrow\rangle_{3,\pm} = |\downarrow\rangle_0 |2\rangle_1 \pm |2\rangle_0 |\downarrow\rangle_1$, obtained by applying the transformation $|0\rangle \rightarrow 2$ on the $\hat{n}_0 + \hat{n}_1 = 1$ counterparts. We now point out two interesting features of this simplified effective Hamiltonian in eq. (8.9).

- The fact that the impurity is now interacting with emergent spins $\vec{\mathcal{S}}_1$ and $\vec{\mathcal{S}}_3$ that span over two lattice sites (0 and 1) instead of just the zeroth site indicates that the entanglement between the impurity and bath is now extended beyond the bath zeroth site, and that *the singlet is being stretched*.
- The presence of two spins that are trying to simultaneously screen the impurity spin introduces frustration in the dynamics of the impurity. This is reminiscent of the 2-channel Kondo effect, and the connection is made more precise in the concluding section of our work.

Both these features are precursors to the ultimate and complete destruction of screening in the local moment regime, and reflect the fact that the impurity-bath system *is now in an over-screened state*.

We now focus on the effective Hamiltonian of the $S^z_{\text{tot}} \neq 0$ subspace:

$$H_{\text{eff}}^{S^z_{\text{tot}}\neq 0} = -\frac{1}{2}t\left(S_d^- \mathcal{B}_\uparrow^+ + \text{h.c.}\right) . \tag{8.11}$$

The Pauli matrix operators $\mathcal{B}_\uparrow^+$ and $\mathcal{B}_\uparrow^-$ flip between the doublet of states $|\uparrow\rangle_0 |\uparrow\rangle_1$ and $\frac{1}{\sqrt{2}}(|2\rangle_0 |0\rangle_1 + |0\rangle_0 |2\rangle_1)$:

$$\begin{aligned} \mathcal{B}_\uparrow^- |\uparrow\rangle_0 |\uparrow\rangle_1 &= \frac{1}{\sqrt{2}}(|2\rangle_0 |0\rangle_1 + |0\rangle_0 |2\rangle_1) , \\ \mathcal{B}_\uparrow^+ \frac{1}{\sqrt{2}}(|2\rangle_0 |0\rangle_1 + |0\rangle_0 |2\rangle_1) &= |\uparrow\rangle_0 |\uparrow\rangle_1 . \end{aligned} \tag{8.12}$$

The structure of the effective Hamiltonian in eq. (8.11) leads to another drastic difference from the behaviour of the local Fermi liquid: it allows for the electrons to be "Andreev scattered" into an orthogonal state by hopping from the first site into the zeroth site. This is easily seen by considering the scattering processes in eq. (8.12): a state $|\uparrow\rangle_0 |\uparrow\rangle_1$ (i.e., with site 1 in $\uparrow$ configuration) has a finite probability of being flipped into the $|\downarrow\rangle_0 |2\rangle_1$ state (i.e., with site 1 in the doublon configuration). *An incident electron $c^\dagger_{1\uparrow}$ can therefore emerge as a doublon $c^\dagger_{1\uparrow}c^\dagger_{1\downarrow}$ or a hole $c_{1\uparrow}$ upon scattering from the zeroth site*. This is a direct consequence of the entanglement between the singlet and the first site at the critical point that was absent in the metallic regime of the e-SIAM. We note that similar orthogonal scattering processes also occur in a two-channel Kondo problem between effective pseudo-particles and pseudo-holes [527].

At this point, it is worth noting that the polarised ground-state $|S^z_{\text{tot}} = \frac{1}{2}\rangle$ can be written as an equal superposition of the singlet state $|\text{SS}\rangle_{d0}\otimes|\uparrow\rangle_1$ and the local moment states $\frac{1}{\sqrt{2}}(|\uparrow, 0, 2\rangle - |\uparrow, 2, 0\rangle)$. This symmetry-broken ground state, along with its counterpart $|S^z_{\text{tot}} = -\frac{1}{2}\rangle$, act as a bridge between the ground states of the metallic and insulating phases. They are thus important in displaying the breakdown of the Kondo cloud at the QCP, and the consequences arising from it. We will hence consider these states in the next subsection and demonstrate some exotic non-Fermi liquid properties of these states, e.g., inexact screening of the impurity, fractional impurity magnetisation and fractional impurity entanglement entropy.

Finally, by mapping the quantum impurity problem of the e-SIAM onto that of a classical Coulomb gas [476, 481], it can be shown that the local self-energies $\Sigma_{dd}(\omega)$ and $\Sigma_{00}(\omega)$ of the impurity and zeroth sites respectively and certain two-particle correlation functions have power-law behaviours in the frequency domain:

$$\mathrm{Re}\left[\Sigma_{dd}\right](\omega) \sim |\omega|^{\gamma_{dd}}, \quad \mathrm{Re}\left[\Sigma_{00}\right](\omega) \sim |\omega|^{\gamma_{00}} , \tag{8.13}$$

$$\left\langle S_d^+ \right\rangle \sim |\omega|^{(\alpha_1-1)/2}, \quad \left\langle c_{0\uparrow}^\dagger c_{0\downarrow}^\dagger \right\rangle \sim |\omega|^{(\alpha_3-1)/2} . \tag{8.14}$$

The precise forms of the exponents in terms of the conduction electron scattering phase shifts, as well as several other technical details of the calculation, are provided in Appendix 6. While the various exponents are found to be non-universal functions of the fixed point value of J and the coupling U_b for $r \longrightarrow r_{c2}-$, we argue in subsection (3.8.4) that they assume universal values precisely at the QCP ($r = r_{c2}$). The algebraic behaviour of these local correlations is reminiscent of critical behaviour ascribed to the class of local quantum criticality [82, 528].

3.8.3 Impurity magnetisation and entanglement entropy

More indications of non-Fermi liquid behaviour at the QCP is obtained from a calculation of the impurity magnetisation and the impurity entanglement entropy ($S_{\mathrm{EE}}(d)$) (shown in Appendix 7) for the symmetry-broken states $|S^z_{\mathrm{tot}} = \sigma/2\rangle$. This leads to a fractional entanglement entropy (in units of $\log 2$) for each of the two states:

$$\begin{aligned} \rho_{\mathrm{imp}} &= \begin{pmatrix} \frac{1}{2} + m^z_{\mathrm{imp}} & 0 \\ 0 & \frac{1}{2} - m^z_{\mathrm{imp}} \end{pmatrix} = \begin{pmatrix} \frac{3}{4} & 0 \\ 0 & \frac{1}{4} \end{pmatrix} , \\ S_{\mathrm{EE}}(d) &= -\mathrm{Tr}\left(\rho_{\mathrm{imp}} \ln \rho_{\mathrm{imp}}\right) \simeq 0.81 \log 2 , \end{aligned} \tag{8.15}$$

where the impurity magnetisation m^z_{imp} takes the value $m^z_{\mathrm{imp}} = 1/4$ at the QCP (i.e., half the value for a local moment). Further, $S_{\mathrm{EE}}(d)$ can be written in terms of an effective impurity degeneracy g_{imp}, which we define using the impurity magnetisation: $g_{\mathrm{imp}} \equiv 1+2|m^z_{\mathrm{imp}}|$, such that it takes the expected values of 1 and 2 in the local Fermi liquid and local moment phases (with m^z_{imp} having values 0 and $\frac{1}{2}$ respectively). The effective degeneracy in the polarised subspace $S^z_{\mathrm{tot}} = \pm 1/2$ at the QCP then turns out to be $3/2$, which is half-way between a unique state and a doublet. This corresponds to partial screening of the impurity degrees of freedom at the QCP, in contrast to complete screening in the metallic phase ($g_{\mathrm{imp}} = 1$) and the absence of screening in the insulating phase ($g_{\mathrm{imp}} = 2$).

In Appendix 7, we show that the incomplete magnetisation (and hence the fractional value of S_{EE}) arises from the mixing of the local Fermi liquid ground-state $|\phi\rangle = \otimes_{k<=k_F} |k\uparrow\rangle |k\downarrow\rangle$ and the gapless excitations above it, $|e\rangle_\sigma = e^\dagger_\sigma |\phi\rangle , e \equiv \sum_{k\in FS} c^\dagger_{k\sigma}$, leading to the decay of the local Fermi liquid quasiparticles [525]. This is captured by the modified ground-state $|-\rangle$ and lowest-lying excited states $|+\rangle$ at the QCP:

$$|\pm\rangle = \frac{1}{\sqrt{2}} \left(|SS\rangle \otimes |e\rangle_\sigma \pm |LM\rangle_\sigma \otimes |\phi\rangle \right) . \tag{8.16}$$

The spin-singlet state $|SS\rangle \sim \sum_\sigma \sigma |\sigma\rangle_d |\bar{\sigma}\rangle_0$ and the local moment state $|LM\rangle_\sigma = |\sigma\rangle_d |2\rangle_0$ represent the configurations of the impurity and the bath zeroth sites. Such a ground-state $|-\rangle$ should be contrasted with the local Fermi liquid ground-state $|SS\rangle \otimes |\phi\rangle$ that is stable in the metallic phase for $r_{c1} < r < r_{c2}$. This change in the ground-state manifests in the vanishing of the quasiparticle residue of the local Fermi liquid excitations: $Z = |\langle +|e^\dagger_\sigma|-\rangle|^2 = |\langle +| (|LM\rangle_\sigma \otimes |e\rangle_\sigma)|^2 = 0$, consistent with the orthogonality catastrophe [529] described below eq. (**8.5**). As the local Fermi liquid quasiparticles are rendered unstable, they are replaced by stable composite three-site excitations of the form, $S^-_d c_{0\bar{\sigma}} e^\dagger_\sigma$. This is further reflected in the fact that the corresponding residue for such three-site composite excitation is non-zero at the QCP: $|\langle +|S^-_d c_{0\bar{\sigma}} e^\dagger_\sigma|-\rangle|^2 > 0$.

3.8.4 Friedel scattering phase shift and fractional excess charge

The orthogonality catastrophe faced by the infrared excitations of the conduction bath at the QCP points towards the presence of an "unrenormalised" phase shift [530] of the scattering $k-$states. Indeed, using the Friedel sum rule [48,531,532], we obtain a $\pi/2$ phase shift for the extended states at the Fermi surface for the QCP, which is only half the unitary limit. This can be seen by recalling that the ground state in eq. (**8.16**) is an equal admixture of a decoupled local moment state and a singlet state. Through the singlet state, the impurity contributes an excess charge of unity to the Fermi surface of the conduction bath (because of the presence of gapless spin-flip fluctuations). The local moment state does not contribute any excess charge, because the impurity is decoupled from the bath. The net excess charge then comes out to be $n_{\text{exc}} = \frac{1}{2}(1+0) = \frac{1}{2}$. From the Friedel sum rule, the phase shift at the fixed point is $\delta^* = \pi n_{\text{exc}} = \pi/2$, as mentioned above. Expectedly, n_{exc} is zero in the local moment phase. Also, as the exponents of the algebraic form for the local quantities shown in eq. (**8.13**) are functions of the scattering phase shift, we find that these exponents take universal values precisely at the QCP.

The values of the excess charge at the QCP and in the local moment phase lead to important corollaries. Firstly, the jump in the excess charge by unity in going from $r < r_{c2}$ to $r > r_{c2}$ is in fact a reduction in the Luttinger volume V_L of the conduction bath [24, 533]. V_L counts the number of extended states present at and below the Fermi volume, and corresponds to a topological quantum number [50, 51, 348, 534]. Since the excess charge n_{exc} calculated above is simply the impurity contribution to V_L at the Fermi surface, the difference in the excess charge across the transition implies that the two phases acquire different values for the invariant V_L. Thus, n_{exc} tracks the change (ΔV_L) in the Luttinger volume, and the transition is topological in nature. Secondly, in a recent work, Sen et al. [535] have shown that the Mott MIT of the infinite-dimensional Hubbard model proceeds through the dissociation of domain walls in a fictitious Su-Schrieffer-Heeger chain connected to the physical lattice sites. If one couples their observation with the fact that the two dissociated domain walls at the ends of the SSH chain are together known to host a single charge [536, 537], it becomes evident that the fractional excess charge we obtain at the QCP corresponds to the state that is localised in the SSH chain near the physical lattice site as obtained by Sen et al. The well-known bulk-boundary correspondence of the SSH model (see, e.g., [538]) suggests that the excess charge n_{exc} and the change ΔV_L in the Luttinger volume are the respective topological invariants of the boundary and bulk in the e-SIAM that are tied to one another. Further, the appearance of a half-quantised n_{exc} at the MIT of the e-SIAM corresponds, in the SSH model, to the dissociation of

a domain wall-anti domain wall pair with each carrying a half charge [536, 537].

We show in Appendix 7 that it is in fact possible to connect the scattering phase shift (δ^*), impurity magnetisation ($m^z_{\rm imp}$), effective degeneracy ($\tilde{g}$) and excess charge ($n_{\rm exc}$) in a single relation:

$$\delta^* = \pi n_{\rm exc} = \left[1 + \left(\frac{2-\tilde{g}}{\tilde{g}-1}\right)^2\right]^{-1} = \frac{4{m^z_{\rm imp}}^2}{1 - 4|m^z_{\rm imp}| + 8{m^z_{\rm imp}}^2} \,. \tag{8.17}$$

As we now discuss, this provides a unified picture of the effect of frustration on the impurity spin. As we have seen earlier, the presence of U_b in the Hamiltonian of the e-SIAM introduces local moment states into the spectrum and leads to states with non-vanishing impurity magnetisation at the QCP. This non-zero magnetisation can be interpreted as a partial screening of the impurity spin, in turn resulting in an effective impurity degeneracy ($1 < \tilde{g} < 2$ between that of a unique screened state and an unscreened local moment. The partial screening also manifests in only half the excess charge being contributed to the conduction bath. This reduction in the excess charge acts as a change in the boundary conditions felt by the conduction electrons coupled to the impurity and manifests as a phase shift that is less than the unitarity limit of π.

3.9 Discussions and Outlook

In summary, we have shown that an attractive correlation on the bath zeroth site is enough to frustrate the Kondo effect and stabilise the local moment phase. The destruction of the Kondo cloud, and the associated local Fermi liquid, occurs through *pairing fluctuations in the bath and proximate to the impurity* (left panel of Fig. (3.8)). This is reminiscent of a subdominant superconducting tendency that was observed in the half-filled Hubbard model at $T = 0$ from a unitary RG treatment in Refs. [175, 437]. We also note the finding of non-local attractive effective interactions in a recent theoretical study of the 2D Hubbard model [508] . We find that the critical point displays non-Fermi liquid behaviour with a vanishing quasiparticle residue Z. The strong agreement of our results with several aspects of DMFT suggests that the local self-energy obtained self-consistently in that method can be represented quite faithfully through the e-SIAM. It will, thus, be important to test the predictions offered by our approach directly within the DMFT method. We note that the non-Fermi liquid at the critical point displays a *partial correlation of doublons and holons* that is distinct from not only the correlated Fermi liquid metal (unbound holons and doublons), but also the paramagnetic insulator (comprised of bound holons and doublons). The excitations that propagate through the two unscreened states in the ground-state subspace (Eq. (8.8)) involve the simultaneous creation of a doublon and a holon: in these channels, the doublons and holons cannot propagate in the absence of each other. Such an incomplete correlation is an intermediate step towards complete confinement in the local moment phase. It appears interesting to experimentally test some of these ideas on a mesoscopic quantum dot [539, 540] which is, apart from the usual electron tunnel coupling to an electronic reservoir, additionally coupled through the proximity effect to a superconducting lead.

We stress here that the e-SIAM analysed in this work represents an impurity model that (i) has a single correlated channel of conduction electrons, (ii) is consistent with the symmetries of a half-filled Hubbard model (SU(2)-spin, U(1)-charge and particle-hole), and (iii) shows a local

metal-insulator transition. The model, therefore, provides a minimal route towards obtaining a Hamiltonian-based understanding of DMFT. Further, at the level of the renormalisation group flows that involve the frustration of Kondo screening, the effect of the attractive on-site interaction U_b introduced by us is equivalent to that of additional bath correlations that have been introduced in related impurity models. These include a single impurity Anderson model with multiple anisotropic conduction channels studied by Giamarchi et al. [541], and a periodic Anderson model enhanced with explicit s-d coupling (as well as a density-density interaction) between the conduction and impurity bands, studied by Si and Kotliar [476, 486, 542] as well as by Ruckenstein et al., [543]. In the former $K-$channel model of Ref. [541], the $z-$component ($V_l,\ l \in [1, K-1]$) of the Kondo interaction term in the $K-1$ additional conduction channels acts a source of frustration for the spin-flip term γ_0 of the Kondo interaction in the original $l = 0$ channel, leading to a breakdown of Kondo screening. The U_b coupling in the e-SIAM acts as a similar source of frustration: the equivalence lies at the level of the renormalisation group equations, such that both V_l and U_b oppose the RG relevance of γ_0 and J respectively. This can be made more precise by comparing the RG equations of our work (eqs.(**4.1**)) and that of Giamarchi et al. [541]: the mapping between the two frustration terms U_b and V_l is found to be of the form $U_b \sim \sum_{l=1}^{K-1} V_l^2 \rho$, where ρ is the conduction bath DOS. A similar relationship can be found between the RG equations obtained by us and those for the extended periodic Anderson model studied by Si and Kotliar [476]. In this sense, our analysis applies to a wide variety of models where the Kondo effect is stable in a certain regime of parameters but is destroyed in other parameter regimes by some form of quantum-mechanical frustration of the impurity spin degree of freedom.

Extensions of the present work involve analysing the mixed valence regime of the impurity site (i.e., away from half-filling) within the e-SIAM auxiliary model. This allows the possibility that the finite-temperature critical end-point of the DMFT first-order transition could turn into a quantum critical point from the merging of the $T = 0$ ESQPT and QPT observed in the present work. Recent DMFT calculations [158] show a shrinking of the coexistence region with hole doping but fall short of revealing a QCP. If such a QCP does exist, can it harbour pair fluctuations between the impurity and zeroth bath sites that become dominant upon doping, signalling thereby a putative superconducting instability of a related bulk model? We recall that a superconducting state of matter was indeed observed to be emergent from a QCP in the hole-doped Hubbard model at $T = 0$ via a unitary RG treatment in Refs. [184, 437]. The phenomenon of electronic differentiation in $k-$space can perhaps be captured by considering cluster variants of the e-SIAM, i.e., multiple impurities connected to one another through single-particle hopping and/or RKKY-like interactions [544, 545]. In general, the presence of multiple and varied classes of correlations in the auxiliary model - localisation from Mott physics, delocalisation from spin and charge fluctuations, and pairing from local attractive correlations - makes this a strong candidate for an auxiliary model that carries the potential for describing the emergence of a variety of novel phases of correlated quantum matter.

Appendix 1: Expressing correlation functions in terms of entanglement

We will first relate the impurity Greens function to the geometric entanglement. Given a ground state $|\Psi\rangle_{\rm gs}$ and a spectrum of energies $\{E_n\}$, the retarded impurity Greens function (in time domain) is defined as $G_{d\sigma}(t) = -i\theta(t)\,\langle\left\{c_{d\sigma}(t), c^{\dagger}_{d\sigma}\right\}\rangle$. It can be given a spectral representation in terms of the eigenstates $\{|\Psi\rangle_n\}$ of the e-SIAM:

$$G_{d\sigma}(\omega) = \frac{1}{Z}\sum_n \left[\frac{|\langle\Psi_{\rm gs}|c_{d\sigma}|\Psi_n\rangle|^2}{\omega + E_{\rm gs} - E_n} + \frac{|\langle\Psi_n|c_{d\sigma}|\Psi_{\rm gs}\rangle|^2}{\omega - E_{\rm gs} + E_n}\right] , \tag{9.1}$$

where $Z \equiv \sum_n e^{-\beta E_n}$ is the partition function. We will now insert a complete basis into the expression. The basis will be the set of eigenstates of the Hamiltonian $H = H_1 + H_2$, where H_1 is the two-site $J - U_b$ Hamiltonian formed by the impurity and zeroth sites, and H_2 is a tight-binding Hamiltonian formed by the remaining sites. Since the Hamiltonians are decoupled, the eigenstates $|\Psi\rangle_{m,n}$ will be direct product states formed by combining the eigenstates $|\phi\rangle_m, |\psi\rangle_n$ of the individual Hamiltonians H_1 and H_2 respectively: $|\Phi\rangle_{m,n} = |\phi\rangle_m \otimes |\psi\rangle_n$. Inserting this basis leads to the expression:

$$|\Psi\rangle_{\rm gs} = \sum_{m,n} |\Phi\rangle_{m,n}\,(\langle\phi_m| \otimes \langle\psi_n|)\,|\Psi_{\rm gs}\rangle \ . \tag{9.2}$$

The ground state of H_1 is the spin-singlet: $|\phi\rangle_0 = |{\rm ss}\rangle$. We denote the ground state of the tight-binding Hamiltonian H_2 by $|\psi\rangle_0$. Because of the highly renormalised couplings V and J, the impurity site is almost maximally entangled with the zeroth site, such that the ground state $|\Psi\rangle_{\rm gs}$ in the $r < 0.25$ regime can be thought of as a direct product of the two-site ground state, $c\,|{\rm ss}\rangle + \sqrt{1-c^2}\,|{\rm ct}\rangle$, in direct product with the tight-binding ground state:

$$|\Psi\rangle_{\rm gs} \simeq \left(c\,|{\rm ss}\rangle + \sqrt{1-c^2}\,|{\rm ct}\rangle\right) \otimes |\psi\rangle_0 = |\Phi\rangle_{\rm ss} + |\Phi\rangle_{\rm ct} \ , \tag{9.3}$$

where $|\Phi\rangle_{\rm ss(ct)} = |{\rm ss\,(ct)}\rangle \otimes |\psi\rangle_0$. This suggests that not all terms in the summation of eq. (9.2) contribute; out of all $\{|\psi\rangle_n\}$, only the ground state $n = 0$ contributes, while only $|ss\rangle$ and $|ct\rangle$ contribute from the set $\{|\phi\rangle_m\}$. The summation then simplifies to

$$|\Psi\rangle_{\rm gs} = |\Phi\rangle_{ss}\,\langle{\rm ss}|\Psi^{(2)}_{\rm gs}\rangle + |\Phi\rangle_{ct}\,\langle{\rm ct}|\Psi^{(2)}_{\rm gs}\rangle \ , \tag{9.4}$$

where $|\Psi^{(2)}_{\rm gs}\rangle$ is the two-site part of the ground state and can be obtained by starting with the full ground state $|\Psi\rangle_{\rm gs}$ and tracing over the other lattice sites of the system.

We assume that the global phases of the wavefunctions are real, and since the internal weights of the wavefunctions are real as well, the overlaps $\langle{\rm ss}|\Psi^{(2)}_{\rm gs}\rangle, \langle{\rm ct}|\Psi^{(2)}_{\rm gs}\rangle$ are also real. We can use these overlaps to define a geometric measure of entanglement [244, 509, 510]:

$$\varepsilon\,(\psi_1, \psi_2) = 1 - |\langle\psi_1|\psi_2\rangle|^2 \ . \tag{9.5}$$

If $|\psi_1\rangle$ is thought of as a separable state, then $|\psi_2\rangle$ should be less entangled if its overlap with $|\psi_1\rangle$ is large, which is indeed borne out by the definition. The overlaps then become $\langle \mathrm{ss}|\Psi_{\mathrm{gs}}^{(2)}\rangle = \sqrt{1-\varepsilon\left(ss,\Psi_{\mathrm{gs}}^{(2)}\right)}$, and similarly for the state $|\mathrm{ct}\rangle$. For brevity, we will use the notation $\varepsilon_{\mathrm{ss}} \equiv \varepsilon\left(ss,\Psi_{\mathrm{gs}}^{(2)}\right), \varepsilon_{\mathrm{ct}} \equiv \varepsilon\left(ct,\Psi_{\mathrm{gs}}^{(2)}\right)$. The retarded impurity Greens function for spin σ can now be written in terms of these measures:

$$\begin{aligned} G_{d\sigma}(\omega) = \frac{1}{Z}\sum_n \Bigg[& (1-\varepsilon_{\mathrm{ss}})\left(\frac{|\langle\Phi_{\mathrm{ss}}|c_{d\sigma}|\Psi_n\rangle|^2}{\omega+E_{\mathrm{gs}}-E_n} + \frac{|\langle\Psi_n|c_{d\sigma}|\Phi_{\mathrm{ss}}\rangle|^2}{\omega-E_{\mathrm{gs}}+E_n}\right) + (1-\varepsilon_{\mathrm{ct}})\,\frac{|\langle\Phi_{\mathrm{ct}}|c_{d\sigma}|\Psi_n\rangle|^2}{\omega+E_{\mathrm{gs}}-E_n} \\ & + (1-\varepsilon_{\mathrm{ct}})\,\frac{|\langle\Psi_n|c_{d\sigma}|\Phi_{\mathrm{ct}}\rangle|^2}{\omega-E_{\mathrm{gs}}+E_n} + \sqrt{(1-\varepsilon_{\mathrm{ss}})}\sqrt{(1-\varepsilon_{\mathrm{ct}})}\frac{\langle\Phi_{\mathrm{ss}}|c_{d\sigma}|\Psi_n\rangle\langle\Psi_n|c^\dagger_{d\sigma}|\Phi_{\mathrm{ct}}\rangle+\mathrm{h.c.}}{\omega+E_{\mathrm{gs}}-E_n} \\ & + \sqrt{(1-\varepsilon_{\mathrm{ss}})}\sqrt{(1-\varepsilon_{\mathrm{ct}})}\frac{\langle\Phi_{\mathrm{ct}}|c_{d\sigma}|\Psi_n\rangle\langle\Psi_n|c^\dagger_{d\sigma}|\Phi_{\mathrm{ss}}\rangle+\mathrm{h.c.}}{\omega-E_{\mathrm{gs}}+E_n}\Bigg] . \end{aligned} \tag{9.6}$$

We now generalise this to any real-space two-particle correlation involving operators O_1, O_2 that are at most two-particle operators and act on the combined Hilbert space of the impurity site and the zeroth site. The so-called lesser Greens function corresponding to these operators is defined as

$$G^<_{O_1^\dagger,O_2}(t) \equiv i\,\langle O_1^\dagger O_2(t)\rangle\,, \quad G^<_{O_1^\dagger,O_2}(t\to\infty) = i\,\langle\Psi_{\mathrm{gs}}|O_1^\dagger O_2|\Psi_{\mathrm{gs}}\rangle\ . \tag{9.7}$$

We focus on the static case ($t\to\infty$) here. Following eq. (9.4), we can rewrite the ground states in terms of the entanglement measures mentioned above.

$$|\Psi\rangle_{\mathrm{gs}} = |\Phi\rangle_{ss}\sqrt{1-\varepsilon_{\mathrm{ss}}} + |\Phi\rangle_{ct}\sqrt{1-\varepsilon_{\mathrm{ss}}}\,, \tag{9.8}$$

where $|\Phi\rangle_{\mathrm{ss(ct)}}$ are the zero spin and zero charge isospin eigenstates of the Hamiltonian $H = H_1 + H_2$ defined below eq. (9.1). Substituting this in the static lesser Greens function gives

$$\begin{aligned} \frac{1}{i}G^<_{O_1^\dagger,O_2}(t\to\infty) = \ & (1-\varepsilon_{\mathrm{ss}})\,\langle\Phi_{\mathrm{ss}}|O_2O_1^\dagger|\Phi_{\mathrm{ss}}\rangle + (1-\varepsilon_{\mathrm{ct}})\,\langle\Phi_{\mathrm{ct}}|O_2O_1^\dagger|\Phi_{\mathrm{ct}}\rangle \\ & + \sqrt{1-\varepsilon_{\mathrm{ss}}}\sqrt{1-\varepsilon_{\mathrm{ct}}}\left(\langle\Phi_{\mathrm{ss}}|O_2O_1^\dagger|\Phi_{\mathrm{ct}}\rangle + \langle\Phi_{\mathrm{ct}}|O_2O_1^\dagger|\Phi_{\mathrm{s}}\rangle\right)\ . \end{aligned} \tag{9.9}$$

This can be extended to generalised retarded Greens functions $G^R_{O_1^\dagger,O_2}(t) \equiv -i\theta(t)\,\langle\left\{O_1^\dagger(t), O_2\right\}\rangle$, whose spectral representation is of the form

$$G^R_{O_1^\dagger,O_2}(\omega) = \frac{1}{Z}\sum_n\left[\frac{\langle\Psi_{\mathrm{gs}}|O_2|\Psi_n\rangle\,\langle\Psi_n|O_1^\dagger|\Psi_{\mathrm{gs}}\rangle}{\omega+E_{\mathrm{gs}}-E_n} + \frac{\langle\Psi_n|O_2|\Psi_{\mathrm{gs}}\rangle\,\langle\Psi_{\mathrm{gs}}|O_1^\dagger|\Psi_n\rangle}{\omega-E_{\mathrm{gs}}+E_n}\right]\ . \tag{9.10}$$

Following an approach very similar to the one that led to eq. (9.6), we can cast the generalised Greens function in terms of the geometric entanglement measures:

$$\begin{aligned} G^R_{O_1^\dagger,O_2}(\omega) = \frac{1}{Z}\sum_n \Bigg[& (1-\varepsilon_{\mathrm{ss}})\left(\frac{(O_1)^*_{\mathrm{ss},n}(O_2)_{\mathrm{ss},n}}{\omega+E_{\mathrm{gs}}-E_n} + \frac{(O_1)^*_{n,\mathrm{ss}}(O_2)_{n,\mathrm{ss}}}{\omega-E_{\mathrm{gs}}+E_n}\right) + (1-\varepsilon_{\mathrm{ct}})\,\frac{(O_1)^*_{\mathrm{ct},n}(O_2)_{\mathrm{ct},n}}{\omega+E_{\mathrm{gs}}-E_n} \\ & + (1-\varepsilon_{\mathrm{ct}})\,\frac{(O_1)^*_{n,\mathrm{ct}}(O_2)_{n,\mathrm{ct}}}{\omega-E_{\mathrm{gs}}+E_n} + \sqrt{(1-\varepsilon_{\mathrm{ss}})}\sqrt{(1-\varepsilon_{\mathrm{ct}})}\frac{(O_2)_{\mathrm{ss},n}(O_1)^*_{\mathrm{ct},n}+\mathrm{h.c.}}{\omega+E_{\mathrm{gs}}-E_n} \\ & + \sqrt{(1-\varepsilon_{\mathrm{ss}})}\sqrt{(1-\varepsilon_{\mathrm{ct}})}\frac{(O_2)_{\mathrm{ct},n}(O_1)^*_{\mathrm{ss},n}+\mathrm{h.c.}}{\omega-E_{\mathrm{gs}}+E_n}\Bigg]\ , \end{aligned} \tag{9.11}$$

where $(O_2)_{\mathrm{ss},n}$ is the matrix element $\langle\Phi_{\mathrm{ss}}|O_2|\Psi_n\rangle$, and similar definitions exist for $(O_1)_{\mathrm{ss},n}$ and its $|\Phi_{\mathrm{ct}}\rangle$ counterparts.

Appendix 2: One-shot decoupling of impurity from zeroth site

We will decouple the impurity states from the fixed point Hamiltonian using a single URG transformation. This will, of course, generate correlations on the zeroth site. The resulting Hamiltonian will be an AIM with the hopping between the zeroth site and the rest of the chain acting as the effective hybridisation. Schematically, we will have

$$H^* = H_{\mathrm{imp}} + V_{\text{imp-0}} + H_0 + H_{\text{0-1}} + H_{\mathrm{rest}} \xrightarrow{\text{decouple imp.}} \begin{aligned} &E_{\mathrm{imp}} + \tilde{H}_0 + H_{\text{0-1}} + H_{\mathrm{rest}} \\ &= H_{\text{new imp}} + V_{\text{new imp - rest}} + H_{\mathrm{rest}} \end{aligned} . \quad (9.12)$$

Since the impurity is not coupled with any site beyond the zeroth site, the parts of the Hamiltonian that involve "rest" will not change in the process. This also means that the decoupling can be performed by looking at the smaller Hamiltonian

$$\begin{aligned} H_{\text{imp+0}} = H_{\mathrm{imp}} + H_0 + V_{\text{imp-0}} = \quad & -\tfrac{U^*}{2}\left(\hat{n}_{d\uparrow} - \hat{n}_{d\downarrow}\right)^2 - U_b\left(\hat{n}_{0\uparrow} - \hat{n}_{0\downarrow}\right)^2 + J^* S^z_d S^z_0 \\ & + V^* \textstyle\sum_\sigma \left(c^\dagger_{d\sigma} c_{0\sigma} + \text{h.c.}\right) + \tfrac{J^*}{2}\left(c^\dagger_{d\uparrow} c_{d\downarrow} c^\dagger_{0\downarrow} c_{0\uparrow} + \text{h.c.}\right) . \quad (9.13) \end{aligned}$$

3.9.1 Renormalisation from V^*

From the off-diagonal term involving V^*, we generate the following term, in the particle sector for 0:

$$\sum_\sigma c^\dagger_{0\sigma} c_{d\sigma} \frac{V^{*2}}{\tilde{\omega} - H_d} c^\dagger_{d\sigma} c_{0\sigma} = \sum_\sigma c^\dagger_{0\sigma} c_{d\sigma} \frac{V^{*2}}{\tilde{\omega} + \frac{U^*}{2}\left(1 - \hat{n}_{d\bar{\sigma}}\right)^2 + U_b \hat{n}_{0\bar{\sigma}} + \frac{J^*}{4}\left(1 - \hat{n}_{d\bar{\sigma}}\right)\hat{n}_{0\bar{\sigma}}} c^\dagger_{d\sigma} c_{0\sigma} \quad (9.14)$$

where $\tilde{\omega}$ is the quantum fluctuation operator for the impurity site and $H_d = -\frac{U^*}{2}\left(\hat{n}_{d\uparrow} - \hat{n}_{d\downarrow}\right)^2 - U_b\left(\hat{n}_{0\uparrow} - \hat{n}_{0\downarrow}\right)^2 + J^* S^z_d S^z_0$, is the diagonal part of the Hamiltonian for the imp+0 system. In order to resolve the operators in the denominator, we expand the unity in the numerator using the identity $1 = \hat{n}_{d\bar{\sigma}}\hat{n}_{0\bar{\sigma}} + \hat{n}_{d\bar{\sigma}}\hat{h}_{0\bar{\sigma}} + \hat{h}_{d\bar{\sigma}}\hat{n}_{0\bar{\sigma}} + \hat{h}_{d\bar{\sigma}}\hat{h}_{0\bar{\sigma}}$, where $\hat{h} = 1 - \hat{n}$ is hole operator. On Substituting this, we get

$$\begin{aligned} \sum_\sigma c^\dagger_{0\sigma} c_{d\sigma} \frac{V^{*2}}{\tilde{\omega} - H_d} c^\dagger_{d\sigma} c_{0\sigma} \quad & = V^{*2} \textstyle\sum_\sigma c^\dagger_{0\sigma} c_{d\sigma} \frac{\hat{h}_{d\bar{\sigma}}\hat{h}_{0\bar{\sigma}} + \hat{h}_{d\bar{\sigma}}\hat{n}_{0\bar{\sigma}} + \hat{n}_{d\bar{\sigma}}\hat{h}_{0\bar{\sigma}} + \hat{n}_{d\bar{\sigma}}\hat{n}_{0\bar{\sigma}}}{\tilde{\omega} + \frac{U^*}{2}\hat{h}_{d\bar{\sigma}} + U_b\hat{n}_{0\bar{\sigma}} + \frac{J^*}{4}\hat{h}_{d\bar{\sigma}}\hat{n}_{0\bar{\sigma}}} c^\dagger_{d\sigma} c_{0\sigma} \\ & = V^{*2} \textstyle\sum_\sigma \hat{h}_{d\sigma}\hat{n}_{0\sigma}\left[\frac{\hat{h}_{d\bar{\sigma}}\hat{h}_{0\bar{\sigma}}}{\tilde{\omega}_{00} + \frac{U^*}{2}} + \frac{\hat{h}_{d\bar{\sigma}}\hat{n}_{0\bar{\sigma}}}{\tilde{\omega}_{01} + \frac{U^*}{2} + U_b + \frac{J^*}{4}} + \frac{\hat{n}_{d\bar{\sigma}}\hat{h}_{0\bar{\sigma}}}{\tilde{\omega}_{10}} + \frac{\hat{n}_{d\bar{\sigma}}\hat{n}_{0\bar{\sigma}}}{\tilde{\omega}_{11} + U_b}\right] . \quad (9.15) \end{aligned}$$

$\tilde{\omega}_{(0,1),(0,1)}$ represents the quantum fluctuation scale corresponding to the configuration in the numerator.

In order to "freeze" the impurity dynamics, we will substitute $\hat{n}_{d\sigma} = \hat{n}_{d\bar{\sigma}} = \frac{1}{2}$, because of the Z_2 symmetry and the particle-hole symmetry of the impurity levels. This gives

$$\frac{1}{4}V^{*2}\sum_{\sigma}\hat{n}_{0\sigma}\left[\frac{\hat{h}_{0\bar{\sigma}}}{\tilde{\omega}_{00}+\frac{U^*}{2}}+\frac{\hat{n}_{0\bar{\sigma}}}{\tilde{\omega}_{01}+\frac{U^*}{2}+U_b+\frac{J^*}{4}}+\frac{\hat{h}_{0\bar{\sigma}}}{\tilde{\omega}_{10}}+\frac{\hat{n}_{0\bar{\sigma}}}{\tilde{\omega}_{11}+U_b}\right] . \tag{9.16}$$

The state that most closely represents the metallic ground state is $\bar{\omega}_{10}$, we take that as the reference quantum fluctuation scale $\bar{\omega}$. It is of the order of $\bar{\omega} \sim -\frac{J^*}{4} - \frac{U^*}{2} - U_b$. We will now relate the other scales to $\bar{\omega}$ by expressing them in terms of the energy of the initial state:

$$\tilde{\omega}_{00} \sim -U_b = \bar{\omega} + \frac{J^*}{4} + \frac{U^*}{2},\ \tilde{\omega}_{01} \sim 0 = \bar{\omega} + \frac{J^*}{4} + \frac{U^*}{2} + U_b,\ \tilde{\omega}_{11} \sim -\frac{U^*}{2} = \bar{\omega} + \frac{J^*}{4} + U_b\ . \tag{9.17}$$

Substituting these gives

$$\frac{1}{4}V^{*2}\sum_{\sigma}\hat{n}_{0\sigma}\left[\hat{h}_{0\bar{\sigma}}\alpha_1 + \hat{n}_{0\bar{\sigma}}\alpha_2\right] , \tag{9.18}$$

where $\alpha_1 = \left(\bar{\omega} + U^* + \frac{J^*}{4}\right)^{-1} + (\bar{\omega})^{-1}$ and $\alpha_2 = \left(\bar{\omega} + U^* + 2U_b + \frac{J^*}{2}\right)^{-1} + \left(\bar{\omega} + 2U_b + \frac{J^*}{4}\right)^{-1}$.

Because of the particle-hole symmetry on the impurity as well as in the bath, the renormalisation from the hole sector is obtained simply by transforming $\hat{n} \leftrightarrow \hat{h}$:

$$\frac{1}{4}V^{*2}\sum_{\sigma}\hat{h}_{0\sigma}\left[\hat{n}_{0\bar{\sigma}}\alpha_1 + \hat{h}_{0\bar{\sigma}}\alpha_2\right] . \tag{9.19}$$

The total renormalisation arising from V is therefore

$$\frac{1}{4}V^{*2}\sum_{\sigma}\left[\alpha_1\left(\hat{n}_{0\sigma}\hat{h}_{0\bar{\sigma}} + \hat{h}_{0\sigma}\hat{n}_{0\bar{\sigma}}\right) + \alpha_2\left(\hat{n}_{0\sigma}\hat{n}_{0\bar{\sigma}} + \hat{h}_{0\sigma}\hat{h}_{0\bar{\sigma}}\right)\right] = \frac{1}{2}V^{*2}\left(\alpha_1 - \alpha_2\right)\left(\hat{n}_{0\uparrow} - \hat{n}_{0\downarrow}\right)^2 + \text{constant} . \tag{9.20}$$

3.9.2 Renormalisation from J^*

The renormalisation arising from decoupling the Kondo coupling has two terms. The first term arises when the spin of the zeroth site is initially up:

$$\begin{aligned}\frac{J^{*2}}{4}c^{\dagger}_{d\downarrow}c_{d\uparrow}c^{\dagger}_{0\uparrow}c_{0\downarrow}\frac{1}{\tilde{\omega}-H_d}c^{\dagger}_{0\downarrow}c_{0\uparrow}c^{\dagger}_{d\uparrow}c_{d\downarrow} &= c^{\dagger}_{d\downarrow}c_{d\uparrow}c^{\dagger}_{0\uparrow}c_{0\downarrow}\frac{J^{*2}/4}{\tilde{\omega}+\frac{U^*}{2}+U_b+\frac{J^*}{4}}c^{\dagger}_{0\downarrow}c_{0\uparrow}c^{\dagger}_{d\uparrow}c_{d\downarrow} \\ &= \frac{J^{*2}}{4}\frac{\hat{n}_{d\downarrow}\hat{h}_{d\uparrow}\hat{n}_{0\uparrow}\hat{h}_{0\downarrow}}{\tilde{\omega}+\frac{U^*}{2}+U_b+\frac{J^*}{4}} .\end{aligned} \tag{9.21}$$

The quantum fluctuation scale $\tilde{\omega}$ for this process can be similarly related to $\bar{\omega}$: $\tilde{\omega} \sim -\frac{U^*}{2} - U_b - \frac{J^*}{4} = \bar{\omega}$. This gives

$$\frac{J^{*2}}{4}\frac{\hat{n}_{d\downarrow}\hat{h}_{d\uparrow}\hat{n}_{0\uparrow}\hat{h}_{0\downarrow}}{\bar{\omega}+\frac{U^*}{2}+U_b+\frac{3J^*}{4}} = \frac{J^{*2}}{16}\frac{\hat{n}_{0\uparrow}\hat{h}_{0\downarrow}}{\bar{\omega}+\frac{U^*}{2}+U_b+\frac{J^*}{4}} , \tag{9.22}$$

as the renormalisation for this configuration. At the final step, we substituted $\hat{n}_{d\sigma} = \hat{h}_{d\sigma} = \frac{1}{2}$. For the other configuration where the spin of the zeroth site is down, we get

$$\frac{J^{*2}}{16}\frac{\hat{n}_{0\downarrow}\hat{h}_{0\uparrow}}{\bar{\omega}+\frac{U^*}{2}+U_b+\frac{J^*}{4}} \ . \tag{9.23}$$

Adding both sectors, we get

$$\frac{J^{*2}}{16}\frac{1}{\bar{\omega}+\frac{U^*}{2}+U_b+\frac{J^*}{4}}\left(\hat{n}_{0\uparrow}-\hat{n}_{0\downarrow}\right)^2 \ . \tag{9.24}$$

3.9.3 Total renormalisation

Adding the contributions from both V^* and J^*, the net renormalisation is the generation of a local correlation term $-U'\left(\hat{n}_{0\uparrow}-\hat{n}_{0\downarrow}\right)^2$ on the zeroth site, where U' is given by

$$U' = \frac{-J^{*2}/16}{\bar{\omega}+\frac{U^*}{2}+U_b+\frac{J^*}{4}} - \frac{1}{2}V^{*2}\left(\frac{1}{\bar{\omega}+U^*+\frac{J^*}{4}}+\frac{1}{\bar{\omega}}-\frac{1}{\bar{\omega}+U^*+2U_b+\frac{J^*}{2}}-\frac{1}{\bar{\omega}+2U_b+\frac{J^*}{4}}\right) \tag{9.25}$$

The effective Hamiltonian for the zeroth site is therefore

$$H_{0+\text{rest}} = \underbrace{-\left(U'+U_b\right)\left(\hat{n}_{0\uparrow}-\hat{n}_{0\downarrow}\right)^2}_{\text{new correlated impurity}} \quad \underbrace{-t\sum_{\substack{j\in\text{n.n. of 0},\\ \sigma}}\left(c^\dagger_{0\sigma}c_{j\sigma}+\text{h.c.}\right)}_{\text{hopping between new impurity \& new bath}} \quad \underbrace{-t\sum_{\langle i,j\rangle}\left(c^\dagger_{i\sigma}c_{j\sigma}+\text{h.c.}\right)}_{\text{K.E. of new bath}} \ . \tag{9.26}$$

Appendix 3: Effective Hamiltonian for the excitations within the Hubbard sidebands

Beyond r_{c1}, the Hubbard sidebands can be seen to separate from the central Kondo resonance in the impurity spectral function. These sidebands are broad, indicating that the impurity site is hybridising with the bath from within the sidebands, at high energies $\omega \sim U/2$. These processes lead to the presence of gapless excitations within the rest of the bath, outside the Mott gap. To find the effective Hamiltonian for the rest of the bath (sites 1 and onwards), we will take the eigenstates of the two-site Hamiltonian Hthat reside within the sideband as our ground-states, and treat the hopping from the zeroth site to the rest of the bath as a perturbation. The two-site Hamiltonian is

$$H_{\text{two site}} = V\sum_\sigma\left(c^\dagger_{d\sigma}c_{0\sigma}+\text{h.c}\right)+J\vec{S}_d\cdot\vec{S}_0-\frac{U}{2}\left(\hat{n}_{d\uparrow}-\hat{n}_{d\downarrow}\right)^2+\frac{U}{2} \ . \tag{9.27}$$

In order to align the doubly-occupied impurity level at the more conventional value of $U/2$, we have shifted the Hamiltonian by the same constant value. The effect of U_b has been ignored because it

is small compared to U at the frequencies pertinent to the physics of the sidebands. The two-site states that reside within the Hubbard sidebands are

$$\begin{aligned} |\Psi_{cc}\rangle \equiv |c\rangle_d |c\rangle_0 \,;\;\; c \in \{0,2\} \,;\;\; |\Psi_{\rm CS}\rangle \equiv \frac{1}{\sqrt{2}} \left(|2\rangle_d |0\rangle_0 - |0\rangle_d |2\rangle_0\right) ; \\ |\Psi_{\sigma,c}\rangle = \alpha |\sigma\rangle_d |c\rangle_0 + \sqrt{1-\alpha^2} |c\rangle_d |\sigma\rangle_0 \,;\; \sigma \in \{\uparrow,\downarrow\} \,; \\ |\Psi_{\rm CT}\rangle = \beta \frac{1}{\sqrt{2}} \left(|\uparrow\rangle_d |\downarrow\rangle_0 - |\downarrow\rangle_d |\uparrow\rangle_0\right) + \sqrt{1-\beta^2} \frac{1}{\sqrt{2}} \left(|2\rangle_d |0\rangle_0 + |0\rangle_d |2\rangle_0\right), \end{aligned} \tag{9.28}$$

where the coefficients of the eigenstates are given by

$$\alpha \simeq \frac{V}{\sqrt{V^2 + \left(E_{\rm X1} + \frac{U}{2}\right)^2}}, \; \beta = \frac{2V}{\sqrt{4V^2 + \left(E_{\rm CS} + \frac{U}{2} + \frac{3J}{4}\right)^2}} \,. \tag{9.29}$$

The energies of the states are

$$\begin{aligned} E_{\rm gs} \equiv E_{00} = E_{22} = E_{CS} = \frac{U}{2}, E_{\rm X1} \equiv E_{\sigma,c} = \frac{U}{4} + \sqrt{V^2 + \frac{U^2}{16}} \,, \\ E_{\rm X2} \equiv E_{\rm CS} = \frac{U}{4} - \frac{3J}{8} + \sqrt{4V^2 + \left(\frac{U}{4} + \frac{3J}{8}\right)^2} \,. \end{aligned} \tag{9.30}$$

The ground state (comprising the states shown in eq. (9.28)) is triply degenerate. In order to study the dynamics of the bath, we now introduce the perturbation $H_I = -t \sum_\sigma \left(c^\dagger_{0\sigma} c_{1\sigma} + \text{h.c.}\right)$. We also take an expanded set of eigenstates $\{|\Psi_n\rangle \otimes |a\rangle\}$, where $\{|\Psi_n\rangle\}$ is the set of eigenstates of $H_{\text{two site}}$, and $|a\rangle \in \{|0\rangle, |\uparrow\rangle, |\downarrow\rangle, |2\rangle\}$ represents the configuration of the first site. The eigenstates of $H_{\text{two site}}$ are also eigenstates the total number operator $\hat{n}_d + \hat{n}_0 + \hat{n}_1$, and since H_I does not conserve the total number, all odd order shifts are zero: $\langle\Psi_n|H_I^b|\Psi_n\rangle, b = 1, 3, \ldots$, is zero for all the eigenstates.

For the second order shift, we need to calculate the overlaps $\langle\Psi_m|H_I|\Psi_n\rangle, m \neq n$ for n in the ground state. Since all three ground-states involve the impurity and zeroth sites in charge configuration (0 or 2), $H_I |\Psi\rangle_n$ will result in states of the form $|0(2)\rangle_d |\sigma\rangle_0 |a\rangle_1$. This resulting state has non-zero overlap only with the part $\sqrt{1-\alpha^2} |c\rangle_d |\sigma\rangle_0 |a\rangle$ of the expanded state $|\Psi_{\sigma,c}\rangle |a\rangle$. The square of each such overlap is, therefore, $t^2 \left(1-\alpha^2\right)$.

- Excitations from the ground-states $|\Psi_{00}\rangle |0\rangle$ and $|\Psi_{22}\rangle |2\rangle$ have zero overlap with any other state, such that the second order shifts in these states is zero.

- Excitations from the ground-states $|\Psi_{00}\rangle |\sigma\rangle$ and $|\Psi_{22}\rangle |\sigma\rangle$ have non zero overlap with one excited state each, such that the second order shift in these states are $\gamma^2 \equiv t^2 \left(1-\alpha^2\right) / \left(E_{\rm X1} - E_{\rm gs}\right)$.

- Excitations from the remaining ground states have non-zero overlaps with two excited states each, such that the second order shift in these states are $2\gamma^2$.

Upon dropping the zeroth order part (because it has no dynamics for the rest of the bath), the effective Hamiltonian at second order in t takes the form

$$H_{\rm eff}^{(2)} = \gamma^2 \left[\left(|\Psi_{00}\rangle \langle\Psi_{00}| + |\Psi_{22}\rangle \langle\Psi_{22}| + 2\,|\Psi_{\rm CS}\rangle \langle\Psi_{\rm CS}| \right) \left(\sum_\sigma |\sigma\rangle_1 \langle\sigma|_1 \right) \right. \\ \left. + 2\left(|\Psi_{22}\rangle \langle\Psi_{22}| + |\Psi_{\rm CS}\rangle \langle\Psi_{\rm CS}| \right) |0\rangle_1 \langle 0|_1 + 2\left(|\Psi_{00}\rangle \langle\Psi_{00}| + |\Psi_{\rm CS}\rangle \langle\Psi_{\rm CS}| \right) |2\rangle_1 \langle 2|_1 \right] \quad (9.31)$$

By using the completeness relation $1 = \sum_\sigma |\sigma\rangle_1 \langle\sigma|_1 + |0\rangle_1 \langle 0|_1 + |2\rangle_1 \langle 2|_1$ of the Hilbert space of the first site, this evaluates to

$$H_{\rm eff}^{(2)} = \text{constant} + \gamma^2 \left(|\Psi_{22}\rangle \langle\Psi_{22}| - |\Psi_{00}\rangle \langle\Psi_{00}| \right) \left(|2\rangle_1 \langle 2|_1 - |0\rangle_1 \langle 0|_1 \right) \,, \quad (9.32)$$

where the "constant" term refers to operators that do not depend on the dynamics of the rest of the bath. By defining the charge isospin operator $C^z\,|2(0)\rangle = +(-)\frac{1}{2}\,|2(0)\rangle$, the effective Hamiltonian can be written as (dropping the non-dynamical part)

$$H_{\rm eff}^{(2)} = 4\gamma^2 C_{\rm tot}^z C_1^z \,, \quad (9.33)$$

where C_i^z is the charge isospin for site i and $C_{\rm tot}^z \equiv C_d^z + C_0^z$ is the z-component of the total charge isospin for the impurity and the zeroth sites.

The fourth order shift in the energy of the eigenstate $|\Psi_n\rangle$ will be given by

$$E_n^{(4)} = \sum_{j,k,l} \frac{(H_I)_{nl}\,(H_I)_{lk}\,(H_I)_{kj}\,(H_I)_{jn}}{(E_l - E_n)\,(E_k - E_n)\,(E_j - E_n)} - E_n^{(2)} \left[\frac{(H_I)_{kn}}{E_k - E_n} \right]^2 \,, \quad (9.34)$$

where the matrix elements $(H_I)_{in}$ are defined as $\langle i|H_I|n\rangle$. This fourth-order shift vanishes for almost all the ground-states. For the remaining states, it becomes important to treat their degeneracy. The "appropriate" combinations of states that provide non-zero fourth order contribution are

$$|+\rangle = \sqrt{\frac{2}{3}}\,|\Psi_{22}\rangle\,|0\rangle_1 + \sqrt{\frac{1}{3}}\,|\Psi_{\rm CS}\rangle\,|2\rangle_1 \,, \quad |-\rangle = -\sqrt{\frac{2}{3}}\,|\Psi_{00}\rangle\,|2\rangle_1 + \sqrt{\frac{1}{3}}\,|\Psi_{\rm CS}\rangle\,|0\rangle_1 \,. \quad (9.35)$$

Corresponding to these ground states, the fourth-order shift in the eigenvalue is

$$E^{(4)} = \frac{3\gamma^4\alpha^2\beta^2}{(1-\alpha^2)\,(E_{\rm X2} - E_{\rm gs})} \,, \quad (9.36)$$

such that the fourth-order contribution to the effective Hamiltonian is

$$H_{\rm eff}^{(4)} = E^{(4)} \left(|+\rangle \langle +| + |-\rangle \langle -| \right) \\ = \frac{\gamma^4\alpha^2\beta^2}{(1-\alpha^2)(E_{\rm X2}-E_{\rm gs})} \left[-C_{\rm tot}^z C_{\rm tot}^2 C_1^z + \sqrt{2}\mathcal{P}_{\rm tot}^4 \left(C_0^+ - C_d^+ \right) C_1^- + \text{h.c.} \right] \,. \quad (9.37)$$

The operator $\mathcal{P}_{\rm tot}^4$ acts on states belonging to the combined $d + 0$ Hilbert space and projects on to the $\hat{n}_d + \hat{n}_0 = 4$ subspace.

Appendix 4: Behaviour of the Kondo scale T_K close to the transition

Towards obtaining the emergent Kondo temperature scale T_K close to the transition, we follow the approach used by Moeller et al. 1995 [511] and Held et al. 2013 [512]. Near the transition, they obtained a Kondo model from the full AIM by applying a Schrieffer-Wolff transition that removes the charge fluctuations of the impurity site and retains the physics of only the s-d coupling J. This amounts to removing the side peaks from the impurity spectral function and focusing on the low-energy central peak. Held et al. then integrated the RG equation for this Kondo model by using a Lorentzian DOS in the bath. This is motivated by the fact that the central peak of the impurity spectral function is a Lorentzian, and the bath becomes equivalent to the impurity site under self-consistency. We implement the same approach but on our extended impurity model, such that the transformation then leads to a $J - U_b$ model. The relevant RG equations are mentioned in Section IV of the main manuscript:

$$\Delta J = -\frac{n_j J\,(J + 4U_b)}{\omega - D/2 + U_b/2 + J/4}, \quad \Delta U_b = 0\,, \tag{9.38}$$

where $n_j = \rho(D)|\Delta D|$ is proportional to the bath density of states. In Section VII of the main manuscript, we show that the spectral function of the zeroth site is tracked by that on the impurity site through the coherent spin-flip fluctuations, and this shows that the appropriate density of states for the bath in this regime is of the Lorentzian kind (same as the shape of the central peak of the impurity spectral function). We therefore set

$$\rho(D) = \frac{\rho_0 \Gamma^2}{D^2 + \Gamma^2}\,, \tag{9.39}$$

where Γ represents the half-width of the Lorentzian. A similar line of arguments was presented by Held et al. [512]. Close to the transition, the RG flow of the Kondo coupling J is stunted by the competing pairing term, and the RG equation can be simplified into the Poor man's scaling $1-$loop form:

$$\frac{dJ}{dD} \simeq -2\rho_0\Gamma^2 \frac{J\,(J + 4U_b)}{\left(\Gamma^2 + D^2\right) D}\,. \tag{9.40}$$

We now integrate this RG equation over the range $D \in [D_0, D^*]$, where D_0 is the bare bandwidth, and D^* is the fixed-point bandwidth. D^* represents the energy scale for the conduction electrons in the IR.

$$\int_{J_0}^{J^*} \frac{dJ}{J\,(J + 4U_b)} = -\int_{D_0}^{D^*} \frac{2\rho_0\Gamma^2 dD}{\left(\Gamma^2 + D^2\right) D}$$

$$\implies \frac{1}{4U_b\rho_0}\left(\ln\frac{J^*}{J_0} - \ln\frac{J^* + 4U_b}{J_0 + 4U_b}\right) = \ln\frac{D^* + \Gamma^2}{D_0 + \Gamma^2} - \ln\frac{D^*}{D_0}\,. \tag{9.41}$$

We will now take the limit of $J_0 + 4U_b \to 0^-$ and *equate the singular terms on both sides* of the equation:

$$\ln\frac{D^*}{D_0} = -\frac{1}{4U_b\rho_0}\ln\frac{J_0 + 4U_b}{J_0} = -\frac{1}{4U_b\rho_0}\ln\left(r_{c2} - r\right) + \text{non-singular part}\,. \tag{9.42}$$

We have replaced the couplings J and U_b with the dimensionless parameters $r = -U_b/J_0$ and $r_{c2} = 1/4$. Dropping the non-singular part and solving for D^* then gives the IR energy scale:

$$D^* = D_0 \exp\left[-\frac{\ln(r_{c2} - r)}{4U_b\rho_0}\right] . \tag{9.43}$$

The dynamically generated Kondo temperature scale is then obtained as

$$T_K = \frac{D^*}{k_B} = \frac{D_0}{k_B} \exp\left[-\frac{\ln(r_{c2} - r)}{4U_b\rho_0}\right] . \tag{9.44}$$

Note that the prefactor of the logarithm is positive because U_b is negative: $-4U_b\rho_0 = |4U_b\rho_0|$. As we approach the transition, the parameter r takes the limit $r \to r_{c2}^-$, and the Kondo temperature scale vanishes:

$$\lim_{r\to r_{c2}^-} T_K = \frac{D_0}{k_B} \lim_{r\to r_{c2}^-} (r_{c2} - r)^{4|U_b\rho_0|} \to 0 . \tag{9.45}$$

Appendix 5: Effective Hamiltonian for the low-lying excitations at the critical point

In order to obtain an effective Hamiltonian for the low-lying excitations in the bath, we will introduce a hopping term V between the zeroth site and the first site into the two-site Hamiltonian H_0, and treat that term perturbatively.

$$H = \underbrace{J\vec{S}_d \cdot \vec{S}_0 - U_b\left(\hat{n}_{0\uparrow} - \hat{n}_{0\downarrow}\right)^2}_{H_0} \underbrace{-t\sum_\sigma \left(c^\dagger_{0\sigma}c_{1\sigma} + \text{h.c.}\right)}_{V} . \tag{9.46}$$

As mentioned before, H_0 is our zeroth Hamiltonian, while V is the perturbation. At the critical point, the zeroth Hamiltonian has a 20−fold degenerate ground-state manifold, and we will show later that it is this degeneracy that leads to NFL excitations. The ground-states are

$$\{|S = S^z = 0\rangle, |\uparrow, 0\rangle, |\uparrow, 2\rangle, |\downarrow, 0\rangle, |\downarrow, 2\rangle\} \otimes \{|0\rangle, |\uparrow\rangle, |\downarrow\rangle, |\uparrow\downarrow\rangle\} . \tag{9.47}$$

The ket to the left of $\otimes$ describes the configuration of the impurity and zeroth sites; $S = S^z = 0$ represents the singlet, while the remaining four states $|\sigma, 0\rangle, |\sigma, 2\rangle$ are local moment states. The ket to the right of $\otimes$ represents the configuration of the first site. Eight of these states have zero matrix elements within the ground-state subspace, even in the presence of the perturbation, so we drop these states. Since the full Hamiltonian conserves the total number of particles $N_{\text{tot}} = \sum_\sigma (\hat{n}_{d\sigma} + \hat{n}_{0\sigma} + \hat{n}_{1\sigma})$ and the total spin $S^z_{\text{tot}} = S^z_d + S^z_0 + S^z_1$, the remaining 12 states can be split into decoupled blocks based on the values of these two operators:

$$\begin{aligned} N_{\text{tot}} = c + 2, S^z_{\text{tot}} = 0 \quad &: |S = S^z = 0\rangle |c\rangle, |\uparrow, c, \downarrow\rangle, |\downarrow, c, \uparrow\rangle ; \; c = 0, 2, \\ N_{\text{tot}} = 3, S^z_{\text{tot}} = \pm\frac{1}{2} \quad &: |S = S^z = 0\rangle |\sigma\rangle, |\sigma, 0, 2\rangle, |\sigma, 2, 0\rangle ; \sigma = \uparrow, \downarrow . \end{aligned} \tag{9.48}$$

The perturbation V will lift the degeneracy in each block; to calculate the modified spectrum, we diagonalise each block in the presence of V. We will first write down the action of the perturbation on the singlet ground-states: this will make it easier to identify the true eigenstates.

$$\begin{aligned} N_{\rm tot} = c+2, S^z_{\rm tot} = 0 \qquad &: V\left|{\rm SS}_c\right\rangle = \tfrac{t}{\sqrt{2}}\left(\left|\downarrow, c, \uparrow\right\rangle - \left|\uparrow, c, \downarrow\right\rangle\right), \; c = 0, 2, \\ N_{\rm tot} = 3, S^z_{\rm tot} = \frac{\sigma}{2} \quad &: V\left|{\rm SS}_\sigma\right\rangle = \tfrac{t}{\sqrt{2}}\left|\sigma\right\rangle \otimes \left(\left|0,2\right\rangle + \left|2,0\right\rangle\right), \; \sigma = \uparrow (1), \downarrow (-1) , \end{aligned} \tag{9.49}$$

where we have introduced the notation $\left|{\rm SS}_\alpha\right\rangle = \left|S = S^z = 0\right\rangle \otimes \left|\alpha\right\rangle, \alpha = 0, \uparrow, \downarrow, 2$. This shows that the action of the perturbation on the singlet state is to create linear combinations of the local moment states in the respective blocks. We therefore define the two possible linear combinations $\left|{\rm LM}^{N_{\rm tot}, S^z_{\rm tot}}_{\pm}\right\rangle$ within each block:

$$\begin{aligned} N_{\rm tot} = c+2, S^z_{\rm tot} = 0 \qquad &: \left|{\rm LM}^{c+2,0}_{\pm}\right\rangle = \tfrac{1}{\sqrt{2}}\left(\left|\uparrow, c, \downarrow\right\rangle \pm \left|\downarrow, c, \uparrow\right\rangle\right), \; c = 0, 2, \\ N_{\rm tot} = 3, S^z_{\rm tot} = \frac{\sigma}{2} \quad &: \left|{\rm LM}^{3,\frac{1}{2}}_{\sigma}\right\rangle = \tfrac{1}{\sqrt{2}}\left(\left|\sigma, 0, 2\right\rangle \pm \left|\sigma, 2, 0\right\rangle\right), \; \sigma = \uparrow (1), \downarrow (-1) . \end{aligned} \tag{9.50}$$

In terms of these linear combinations, we then get

$$\begin{aligned} &V\left|{\rm SS}_0\right\rangle = t\left|{\rm LM}^{2,0}_{-}\right\rangle, \;\; V\left|{\rm LM}^{2,0}_{-}\right\rangle = t\left|{\rm SS}_0\right\rangle, \;\; V\left|{\rm LM}^{2,0}_{+}\right\rangle = 0; \quad V\left|{\rm SS}_\uparrow\right\rangle = t\left|{\rm LM}^{3,\uparrow}_{+}\right\rangle, \\ &V\left|{\rm LM}^{3,\uparrow}_{+}\right\rangle = t\left|{\rm SS}_\uparrow\right\rangle, \;\; V\left|{\rm LM}^{3,\uparrow}_{-}\right\rangle = 0, \;\; V\left|{\rm SS}_\downarrow\right\rangle = t\left|{\rm LM}^{3,\downarrow}_{+}\right\rangle, \;\; V\left|{\rm LM}^{3,\downarrow}_{+}\right\rangle = t\left|{\rm SS}_\downarrow\right\rangle, \\ &V\left|{\rm LM}^{3,\downarrow}_{-}\right\rangle = 0; \quad V\left|{\rm SS}_2\right\rangle = t\left|{\rm LM}^{4,0}_{-}\right\rangle, \;\; V\left|{\rm LM}^{4,0}_{-}\right\rangle = t\left|{\rm SS}_2\right\rangle, \;\; V\left|{\rm LM}^{4,0}_{+}\right\rangle = 0 . \end{aligned} \tag{9.51}$$

The zero matrix elements at the far right of each line should be understood as the fact that V takes those states out of the ground-state subspace. For e.g., the state $V\left|{\rm LM}^{2,0}_{-}\right\rangle$ is not really zero, but the overlap of $V\left|{\rm LM}^{2,0}_{-}\right\rangle$ with any other state in the ground-state subspace spanned by the 20 degenerate states is zero. We now see that each of the 3×3 blocks decouples into a 2×2 block $\begin{pmatrix} 0 & t \\ t & 0 \end{pmatrix}$ and a 1×1 block $\begin{pmatrix} 0 \end{pmatrix}$ when written in terms of the linear combinations $\left|{\rm LM}_{\pm}\right\rangle$. The state in the final block is therefore already an eigenstate, but with zero energy, so that will drop out from the effective Hamiltonian. The remaining 2×2 block has eigenstates $\left|\pm^{N_{\rm tot}, S^z_{\rm tot}}\right\rangle$ that are linear combinations of the singlet states and the surviving local moment combination, with eigenvalues $\pm t$:

$$\begin{aligned} N_{\rm tot} = 2, S^z_{\rm tot} = 0 : \left|\pm^{2,0}\right\rangle &= \frac{1}{\sqrt{2}}\left(\left|{\rm SS}_0\right\rangle \pm \left|{\rm LM}^{2,0}_{-}\right\rangle\right), \\ N_{\rm tot} = 3, S^z_{\rm tot} = \frac{1}{2} : \left|\pm^{3,\frac{1}{2}}\right\rangle &= \frac{1}{\sqrt{2}}\left(\left|{\rm SS}_\uparrow\right\rangle \pm \left|{\rm LM}^{3,\frac{1}{2}}_{+}\right\rangle\right), \\ N_{\rm tot} = 3, S^z_{\rm tot} = -\frac{1}{2} : \left|\pm^{3,-\frac{1}{2}}\right\rangle &= \frac{1}{\sqrt{2}}\left(\left|{\rm SS}_\downarrow\right\rangle \pm \left|{\rm LM}^{3,-\frac{1}{2}}_{+}\right\rangle\right), \\ N_{\rm tot} = 4, S^z_{\rm tot} = 0 : \left|\pm^{4,0}\right\rangle &= \frac{1}{\sqrt{2}}\left(\left|{\rm SS}_2\right\rangle \pm \left|{\rm LM}^{4,0}_{-}\right\rangle\right) . \end{aligned} \tag{9.52}$$

At this point, it is worth noting that the polarised ground-states $\left|S^z_{\rm tot} = \sigma\frac{1}{2}\right\rangle, \sigma = \pm 1$ can be written as an equal superposition of the singlet states $\left|{\rm SS}\right\rangle_{d0} \otimes \left|\sigma\right\rangle_1$ and the local moment states $\frac{1}{\sqrt{2}}\left(\left|\sigma, 0, 2\right\rangle - \left|\sigma, 2, 0\right\rangle\right)$.

The polarised symmetry-broken states therefore act as a bridge between the ground states of the two phases and are important in displaying the breakdown of the Kondo cloud at the QCP and the consequences arising from it (like inexact screening of the impurity and fractional magnetisation and entanglement entropy, which will be discussed in the next section).

By combining the two eigenstates $|\pm\rangle$ for each block, one can then reconstruct the effective Hamiltonian $\mathcal{H}_{\rm eff}^{N_{\rm tot},S^z_{\rm tot}}$ that describes the dynamics of the first site from within the ground-state subspace of the zeroth Hamiltonian. Formally, this is written as

$$\begin{aligned}\mathcal{H}_{\rm eff}^{N_{\rm tot},S^z_{\rm tot}} &= t\,|+^{N_{\rm tot},S^z_{\rm tot}}\rangle\langle+^{N_{\rm tot},S^z_{\rm tot}}| - t\,|-^{N_{\rm tot},S^z_{\rm tot}}\rangle\langle-^{N_{\rm tot},S^z_{\rm tot}}|\ ,\\ &= \begin{cases} t\left[|{\rm SS}_\alpha\rangle\langle{\rm LM}_-^{N_{\rm tot},S^z_{\rm tot}}| + |{\rm LM}_-^{N_{\rm tot},S^z_{\rm tot}}\rangle\langle{\rm SS}_\alpha|\right], & \alpha = 0,2\ ,\\ t\left[|{\rm SS}_\alpha\rangle\langle{\rm LM}_+^{N_{\rm tot},S^z_{\rm tot}}| + |{\rm LM}_+^{N_{\rm tot},S^z_{\rm tot}}\rangle\langle{\rm SS}_\alpha|\right], & \alpha =\uparrow,\downarrow\ .\end{cases}\end{aligned} \tag{9.53}$$

We first write down the effective Hamiltonian for $\alpha = 0$ which corresponds to $N_{\rm tot} = 2, S^z_{\rm tot} = 0$:

$$\mathcal{H}_{\rm eff}^{2,0} = t\left[|{\rm SS}_0\rangle\langle{\rm LM}_-^{2,0}| + |{\rm LM}_-^{2,0}\rangle\langle{\rm SS}_0|\right]\ . \tag{9.54}$$

In order to convert this into a second-quantised form, we will use the following identities:

$$|{\rm SS}_0\rangle = \tfrac{1}{\sqrt{2}}\left(P_d^\uparrow c_{0\downarrow}^\dagger - P_d^\downarrow c_{0\uparrow}^\dagger\right)P_0^{(0)}P_1^{(0)}\,|0\rangle\ ;\quad |{\rm LM}_-^{2,0}\rangle = \frac{1}{\sqrt{2}}\left(P_d^\uparrow c_{1\downarrow}^\dagger - P_d^\downarrow c_{1\uparrow}^\dagger\right)P_0^{(0)}P_1^{(0)}\,|0\rangle \tag{9.55}$$

where $P_i^{(m)}(m = 0,1,2)$ projects onto the $\hat{n}_i = m$ subspace on the i$^{\rm th}$ site, and P_d^σ projects the impurity spin into $|\sigma\rangle\,;\sigma =\uparrow,\downarrow$ configuration. We then have

$$\begin{aligned}|{\rm SS}_0\rangle\langle{\rm LM}_-^{2,0}| &= \tfrac{1}{2}\left(P_d^\uparrow c_{0\downarrow}^\dagger - P_d^\downarrow c_{0\uparrow}^\dagger\right)P_0^{(0)}P_1^{(0)}\left(P_d^\uparrow c_{1\downarrow} - P_d^\downarrow c_{1\uparrow}\right)\\ &= P_1^{(0)}\tfrac{1}{2}\left(P_d^\uparrow c_{0\downarrow}^\dagger c_{1\downarrow} + P_d^\downarrow c_{0\uparrow}^\dagger c_{1\uparrow} - S_d^+ c_{0\downarrow}^\dagger c_{1\uparrow} - S_d^- c_{0\uparrow}^\dagger c_{1\downarrow}\right)P_0^{(0)}\ ,\end{aligned} \tag{9.56}$$

where we have used $P^2 = P$ if P is a projector, and that $P_d^\uparrow P_d^\downarrow = S_d^+$. Substituting these into the effective Hamiltonian and recognising that $P_d^\uparrow = \frac{1}{2} + S_d^z, P_d^\downarrow = \frac{1}{2} - S_d^z$ gives

$$\begin{aligned}\mathcal{H}_{\rm eff}^{2,0} = \frac{t}{2}\ \Big[&\left(\tfrac{1}{2}+S_d^z\right)c_{0\downarrow}^\dagger P_0^{(0)}P_1^{(0)}c_{1\downarrow} - S_d^+c_{0\downarrow}^\dagger P_0^{(0)}P_1^{(0)}c_{1\uparrow} - S_d^-c_{0\uparrow}^\dagger P_0^{(0)}P_1^{(0)}c_{1\downarrow}\\ &+\left(\tfrac{1}{2}-S_d^z\right)c_{0\uparrow}^\dagger P_0^{(0)}P_1^{(0)}c_{1\uparrow}\Big] + {\rm h.c.}\ .\end{aligned} \tag{9.57}$$

In order to make this more illuminating, we define the holon excitation operators $h_{i\sigma}^\dagger = c_{i\sigma}^\dagger P_i^{(0)}$. In terms of these operators, the effective Hamiltonian becomes

$$\begin{aligned}\mathcal{H}_{\rm eff}^{2,0} &= \frac{t}{2}\Big[\left(\frac{1}{2}+S_d^z\right)\left(h_{0\downarrow}^\dagger h_{1\downarrow} + h_{1\downarrow}^\dagger h_{0\downarrow}\right) - S_d^+\left(h_{0\downarrow}^\dagger h_{1\uparrow} + h_{1\downarrow}^\dagger h_{0\uparrow}\right) - S_d^-\left(h_{0\uparrow}^\dagger h_{1\downarrow} + h_{1\uparrow}^\dagger h_{0\downarrow}\right) +\\ &\quad \left(\frac{1}{2}-S_d^z\right)\left(h_{0\uparrow}^\dagger h_{1\uparrow} + h_{1\uparrow}^\dagger h_{0\uparrow}\right)\Big]\\ &= -t\Big[S_d^z\frac{1}{2}\left(h_{0\uparrow}^\dagger h_{1\uparrow} + h_{1\uparrow}^\dagger h_{0\uparrow} - h_{0\downarrow}^\dagger h_{1\downarrow} - h_{1\downarrow}^\dagger h_{0\downarrow}\right) + \frac{1}{2}S_d^+\left(h_{0\downarrow}^\dagger h_{1\uparrow} + h_{1\downarrow}^\dagger h_{0\uparrow}\right)\\ &+ \frac{1}{2}S_d^-\left(h_{0\uparrow}^\dagger h_{1\downarrow} + h_{1\uparrow}^\dagger h_{0\downarrow}\right)\Big] + \frac{t}{4}\left(h_{0\uparrow}^\dagger h_{1\uparrow} + h_{1\uparrow}^\dagger h_{0\uparrow} + h_{0\downarrow}^\dagger h_{1\downarrow} + h_{1\downarrow}^\dagger h_{0\downarrow}\right)\ .\end{aligned} \tag{9.58}$$

The first part of the Hamiltonian (with a $-t$ factor in front) is reminiscent of a two-spin Heisenberg Hamiltonian. To investigate this, we write down the potential second spin:

$$\mathcal{S}_1^z \equiv \frac{1}{2}\left(h_{0\uparrow}^\dagger h_{1\uparrow} + h_{1\uparrow}^\dagger h_{0\uparrow} - h_{0\downarrow}^\dagger h_{1\downarrow} - h_{1\downarrow}^\dagger h_{0\downarrow}\right) . \tag{9.59}$$

Note that each term that comprises the full operator $\mathcal{S}_1^z$ has a combined projector $P_{01}^{(0)} = P_0^{(0)} P_1^{(0)} = P_1^{(0)} P_0^{(0)}$ in the middle with a single annihilation operator to the right. This means that $\mathcal{S}^z$ projects onto the smaller set of only those states that satisfy $\hat{n}_0 + \hat{n}_1 = 1$. That is also the meaning of the subscript 1 in $\mathcal{S}_1^z$. There are four such states: $|\uparrow, 0\rangle$, $|\downarrow, 0\rangle$, $|0, \uparrow\rangle$, $|0, \downarrow\rangle$. In fact, it is easy to see that the eigenstates of $\mathcal{S}^z$ are

$$|\Uparrow\rangle_{1,\pm} = \tfrac{1}{\sqrt{2}}\left(|\uparrow, 0\rangle \pm |0, \uparrow\rangle\right), \quad \mathcal{S}_1^z |\Uparrow\rangle_{1,\pm} = \pm\tfrac{1}{2} |\Uparrow\rangle_{1,\pm}, \tag{9.60}$$

$$|\Downarrow\rangle_{1,\pm} = \tfrac{1}{\sqrt{2}}\left(|\downarrow, 0\rangle \pm |0, \downarrow\rangle\right), \quad \mathcal{S}_1^z |\Downarrow\rangle_{1,\pm} = \mp\tfrac{1}{2} |\Downarrow\rangle_{1,\pm} . \tag{9.61}$$

The label $\pm$ on top of the eigenstates indicates that these are also eigenstates of the parity operator $\mathcal{P}_{01}$ that switches the site labels 0 and 1:

$$\mathcal{P}_{01} |\alpha, \alpha'\rangle = |\alpha', \alpha\rangle ; \;\; \alpha, \alpha' \in \{0, \uparrow, \downarrow, 2\} . \tag{9.62}$$

In fact, the eigenstates $|\Uparrow\rangle_{1,+1}$ and $|\Downarrow\rangle_{1,-1}$ both have $\mathcal{S}^z = \frac{1}{2}$, but are orthogonal because they have different parities. Analogous to the $\mathcal{S}_1^z$ operator, we can also read off the potential $\mathcal{S}_1^\pm$ ladder operators from the effective Hamiltonian:

$$\mathcal{S}_1^+ = h_{0\uparrow}^\dagger h_{1\downarrow} + h_{1\uparrow}^\dagger h_{0\downarrow}, \quad \mathcal{S}_1^- = \left(\mathcal{S}_1^+\right)^\dagger . \tag{9.63}$$

Applying these ladder operators on the eigenstates of $\mathcal{S}_1^z$ gives

$$\mathcal{S}_1^+ |\Downarrow\rangle_{1,\pm} = \pm |\Uparrow\rangle_{1,\pm} ; \quad \mathcal{S}_1^- |\Uparrow\rangle_{1,\pm} = \pm |\Downarrow\rangle_{1,\pm} ; \quad \mathcal{S}_1^+ |\Uparrow\rangle_{1,\pm} = \mathcal{S}_1^- |\Downarrow\rangle_{1,\pm} = 0 . \tag{9.64}$$

This makes it clear that the pair of states $|\Uparrow\rangle_1^+$ and $|\Downarrow\rangle_1^+$ form a spin-half doublet, as does the other pair $|\Uparrow\rangle_1^-$ and $|\Downarrow\rangle_1^-$. We can define new spin operators that act only on a single parity subspace:

$$\mathcal{S}_{1,\pm}^a = \pm \mathcal{S}^a \, \frac{1}{2}\left(1 \pm \mathcal{P}_{01}\right) ; \;\; a = x, y, z . \tag{9.65}$$

The operator $\frac{1}{2}\left(1 \pm \mathcal{P}_{01}\right)$ projects on to the subspace with ± 1 parity. In the notation $\mathcal{S}_{1,\pm}^a$, the label $\pm$ indicates the parity sector to which the operator applies, while 1 indicates that we are operating in the subspace with $\hat{n}_0 + \hat{n}_1 = 1$. Two operators corresponding to different parity subspaces will commute because they act on disjoint Hilbert spaces: $\left[\mathcal{S}_{+1}^a, \mathcal{S}_{-1}^b\right] = 0$. In terms of these projected spin operators, we recover the usual spin-half SU(2) algebra:

$$\begin{aligned} \mathcal{S}_{1,\pm}^z |\Uparrow\rangle_{1,\pm} &= \frac{1}{2} |\Uparrow\rangle_{1,\pm} ; \quad \mathcal{S}_{1,\pm}^z |\Downarrow\rangle_{1,\pm} = -\frac{1}{2} |\Downarrow\rangle_{1,\pm} ; \\ \mathcal{S}_{1,\pm}^+ |\Downarrow\rangle_{1,\pm} &= |\Uparrow\rangle_{1,\pm} ; \quad \mathcal{S}_{1,\pm}^- |\Uparrow\rangle_{1,\pm} = |\Downarrow\rangle_{1,\pm} . \end{aligned} \tag{9.66}$$

The part of the effective Hamiltonian that involves the impurity can now be written in terms of these new spin operators:

$$t\left(\vec{S}_d \cdot \vec{\mathcal{S}}_{-,1} - \vec{S}_d \cdot \vec{\mathcal{S}}_{+,1}\right); \;\; \vec{\mathcal{S}}_\pm = \left(\mathcal{S}^x_\pm \;\; \mathcal{S}^y_\pm \;\; \mathcal{S}^z_\pm\right) \; . \tag{9.67}$$

The last term in eq. (9.58) (with a prefactor of $\frac{t}{4}$) can now be identified as the parity operator $\mathcal{P}_{01}$ acting within the subspace $\hat{n}_0 + \hat{n}_1 = 1$, because it has eigenstates $|\uparrow, 0\rangle \pm |0, \uparrow\rangle$ and $|\downarrow, 0\rangle \pm |0, \downarrow\rangle$ with eigenvalues ± 1. The full effective Hamiltonian in the $N_{\rm tot} = 2$ subspace then takes the compact form

$$\mathcal{H}^{2,0}_{\rm eff} = t\left(\vec{S}_d \cdot \vec{\mathcal{S}}_{1,-1} - \vec{S}_d \cdot \vec{\mathcal{S}}_{1,+}\right) + \frac{t}{4}\mathcal{P}_{01}P^{(1)}_{01} \; , \tag{9.68}$$

where $P^{(1)}_{01} = P^{(1)}_0 P^{(0)}_1 + P^{(0)}_0 P^{(1)}_1$ projects on to the $\hat{n}_0 + \hat{n}_1 = 1$ subspace. In light of these new spin operators, the original eigenstates $|\pm^{2,0}\rangle$ can be written in terms of these emergent spins $|\Uparrow\rangle_{1,\pm}$ and $|\Downarrow\rangle_{1,\pm}$:

$$\begin{aligned} |\pm^{2,0}\rangle &= \frac{1}{2}\left(|\uparrow,\downarrow,0\rangle - |\downarrow,\uparrow,0\rangle \pm |\uparrow,0,\downarrow\rangle \mp |\downarrow,0,\uparrow\rangle\right) = \frac{1}{2}\left[|\uparrow\rangle\left(|\downarrow,0\rangle \pm |0,\downarrow\rangle\right) - |\downarrow\rangle\left(|\uparrow,0\rangle \pm |0,\uparrow\rangle\right)\right] \\ &= \frac{1}{\sqrt{2}}\left(|\uparrow\rangle\,|\Downarrow\rangle_{1,\pm} - |\downarrow\rangle\,|\Uparrow\rangle_{1,\pm}\right) \; . \end{aligned} \tag{9.69}$$

Both the ground and excited states are therefore spin-singlet states, but they belong to the negative and positive parity sectors respectively.

We now proceed to the $N_{\rm tot} = 4$ sector, which is equivalent to $\alpha = 2$ and $\hat{n}_0 + \hat{n}_1 = 3$. From eq. (9.53), we note that the effective Hamiltonian of the $\alpha = 2$ sector is obtained from that of the $\alpha = 0$ sector by replacing the holons with doublons, $|0\rangle \rightarrow |2\rangle$. This allows us to use the results of the $N_{\rm tot} = 2$ sector simply by making the above-mentioned holon-doublon transformation. Accordingly, the composite up and down spins of the 0 + 1-site system become

$$|\Uparrow\rangle_{3,\pm} = \frac{1}{\sqrt{2}}\left(|\uparrow,2\rangle \pm |2,\uparrow\rangle\right), \;\; |\Downarrow\rangle_{3,\pm} = \frac{1}{\sqrt{2}}\left(|\downarrow,2\rangle \pm |2,\downarrow\rangle\right) \; , \tag{9.70}$$

which then allow us to define spin operators for the positive and negative parity sectors:

$$\mathcal{S}^z_\pm = \frac{1}{2}\left(|\Uparrow\rangle_{3,\pm} - |\Downarrow\rangle_{3,\pm}\right), \;\; \mathcal{S}^+_\pm = |\Uparrow\rangle_{3,\pm}\langle\Downarrow|_{3,\pm} \; , \tag{9.71}$$

analogous to those of the $N_{\rm tot} = 2$ sector in eqs. (9.60) and (9.63). These definitions then allow us to rewrite the effective Hamiltonian in terms of the eigenstates of $\mathcal{S}^z_\pm$, and hence in terms of the spin operators $\vec{\mathcal{S}}_{3,\pm}$. The eigenstates $|\pm^{4,0}\rangle$ and the effective Hamiltonian $H^{4,0}_{\rm eff}$ for this sector can be written as

$$|\pm^{4,0}\rangle = \tfrac{1}{\sqrt{2}}\left(|\uparrow\rangle_d\,|\Downarrow\rangle_{3,\pm} - |\downarrow\rangle_d\,|\Uparrow\rangle_{3,\pm}\right) \; . \tag{9.72}$$

The effective Hamiltonian can then be written in terms of these emergent spins

$$\begin{aligned} H^{4,0}_{\rm eff} = \frac{t}{2} \quad & \left[\left(|\uparrow\rangle_d\,|\Downarrow\rangle_{3,+} - |\downarrow\rangle_d\,|\Uparrow\rangle_{3,+}\right)\left(\langle\uparrow|_d\,\langle\Downarrow|_{3,+} - \langle\downarrow|_d\,\langle\Uparrow|_{3,+}\right)\right. \\ & \left. - \left(|\uparrow\rangle_d\,|\Downarrow\rangle_{3,-} - |\downarrow\rangle_d\,|\Uparrow\rangle_{3,-}\right)\left(\langle\uparrow|_d\,\langle\Downarrow|_{3,-} - \langle\downarrow|_d\,\langle\Uparrow|_{3,-}\right)\right] \; . \end{aligned} \tag{9.73}$$

By replacing the emergent spins with the spin operators $\vec{\mathcal{S}}_{3,\pm}$, we get the final form of the Hamiltonian

$$H_{\text{eff}}^{4,0} = t\left(\vec{S}_d \cdot \vec{\mathcal{S}}_{3,-} - \vec{S}_d \cdot \vec{\mathcal{S}}_{3,+}\right) + \frac{t}{4}\mathcal{P}_{01}P_{01}^{(3)} , \tag{9.74}$$

where $\mathcal{P}_{01}$ is the parity transformation operator defined in eq. (9.62) and $P_{01}^{(3)}$ projects on to the $\hat{n}_0 + \hat{n}_1 = 3$ subspace. This completes the effective Hamiltonian for the $S^z_{\text{tot}} = 0$ sector.

We now come to the $S^z_{\text{tot}} = +1/2$ sector. From eq. (9.53), the effective Hamiltonian for this sector is

$$H_{\text{eff}}^{3,\frac{1}{2}} = t\left[|\text{SS}_\uparrow\rangle\langle\text{LM}_-^{3,\frac{1}{2}}| + |\text{LM}_-^{3,\frac{1}{2}}\rangle\langle\text{SS}_\uparrow|\right] , \tag{9.75}$$

where

$$|\text{SS}_\uparrow\rangle = \frac{1}{\sqrt{2}}\left(P_d^\uparrow c_{0\downarrow}^\dagger - P_d^\downarrow c_{0\uparrow}^\dagger\right)c_{1\uparrow}^\dagger|0\rangle ; \quad |\text{LM}_-^{3,\frac{1}{2}}\rangle = \frac{1}{\sqrt{2}}P_d^\uparrow\left(c_{0\uparrow}^\dagger c_{0\downarrow}^\dagger + c_{1\uparrow}^\dagger c_{1\downarrow}^\dagger\right)|0\rangle , \tag{9.76}$$

such that

$$|\text{SS}_\uparrow\rangle\langle\text{LAM}_-^{3,\frac{1}{2}}| = \frac{1}{2}\left(P_d^\uparrow c_{0\downarrow}^\dagger - P_d^\downarrow c_{0\uparrow}^\dagger\right)c_{1\uparrow}^\dagger\left(c_{0\downarrow}c_{0\uparrow} + c_{1\downarrow}c_{1\uparrow}\right)P_d^\uparrow \tag{9.77}$$

$$= -\frac{1}{2}\left[P_d^\uparrow\left(c_{1\uparrow}^\dagger c_{0\uparrow}\hat{n}_{0\downarrow} + c_{0\downarrow}^\dagger c_{1\downarrow}\hat{n}_{1\uparrow}\right) + S_d^-\left(c_{1\uparrow}^\dagger c_{0\downarrow}\hat{n}_{0\uparrow} - c_{0\uparrow}^\dagger c_{1\downarrow}\hat{n}_{1\uparrow}\right)\right] . \tag{9.78}$$

The full effective Hamiltonian then becomes

$$\begin{aligned} H_{\text{eff}}^{3,\frac{1}{2}} &= -\frac{t}{2}\Big[P_d^\uparrow\Big\{\left(c_{1\uparrow}^\dagger c_{0\uparrow} + c_{0\downarrow}^\dagger c_{1\downarrow}\right)\left(P_0^{(2)}P_1^{(0)} + P_0^{(0)}P_1^{(2)}\right) + \left(c_{0\uparrow}^\dagger c_{1\uparrow} + c_{1\downarrow}^\dagger c_{0\downarrow}\right)P_0^{(1)}P_1^{(1)}\Big\} \\ &\quad + S_d^-\left(c_{1\uparrow}^\dagger c_{0\downarrow} - c_{0\uparrow}^\dagger c_{1\downarrow}\right)\left(P_0^{(2)}P_1^{(0)} + P_0^{(0)}P_1^{(2)}\right) + S_d^+\left(c_{0\downarrow}^\dagger c_{1\uparrow} - c_{1\downarrow}^\dagger c_{0\uparrow}\right)P_0^{(1)}P_1^{(1)}\Big] \\ &= t\left[P_d^\uparrow\sqrt{2}\mathcal{A}_{\frac{1}{2}}^z - \frac{1}{2}S_d^+\mathcal{B}_{\frac{1}{2}}^- - \frac{1}{2}S_d^-\mathcal{B}_{\frac{1}{2}}^+\right] , \end{aligned} \tag{9.79}$$

where we have defined

$$\mathcal{A}_{\frac{1}{2}}^z = -\frac{1}{2\sqrt{2}}\left[\left(c_{1\uparrow}^\dagger c_{0\uparrow} + c_{0\downarrow}^\dagger c_{1\downarrow}\right)\left(P_0^{(2)}P_1^{(0)} + P_0^{(0)}P_1^{(2)}\right) + \left(c_{0\uparrow}^\dagger c_{1\uparrow} + c_{1\downarrow}^\dagger c_{0\downarrow}\right)P_0^{(1)}P_1^{(1)}\right] , \tag{9.80}$$

and

$$\mathcal{B}_{\frac{1}{2}}^+ = \left(c_{1\uparrow}^\dagger c_{0\downarrow} - c_{0\uparrow}^\dagger c_{1\downarrow}\right)\left(P_0^{(2)}P_1^{(0)} + P_0^{(0)}P_1^{(2)}\right) ; \quad \mathcal{B}_{\frac{1}{2}}^- = \left(c_{0\downarrow}^\dagger c_{1\uparrow} - c_{1\downarrow}^\dagger c_{0\uparrow}\right)P_0^{(1)}P_1^{(1)} . \tag{9.81}$$

The effective Hamiltonian for the $S^z_{\text{tot}} = -1/2$ sector is obtained by applying the transformations $P_d^\sigma \to P_d^{\bar{\sigma}}, c_{i\sigma} \to c_{i\bar{\sigma}}$ on the Hamiltonian. This is motivated by the fact that applying the same transformations on the $S^z_{\text{tot}} = 1/2$ eigenstates give the $S^z_{\text{tot}} = -1/2$ eigenstates.

$$H_{\text{eff}}^{3,-\frac{1}{2}} = t\left[P_d^\uparrow\sqrt{2}\mathcal{A}_{-\frac{1}{2}}^z - \frac{1}{2}S_d^+\mathcal{B}_{-\frac{1}{2}}^- - \frac{1}{2}S_d^-\mathcal{B}_{-\frac{1}{2}}^+\right] . \tag{9.82}$$

The operators $\mathcal{A}_{-\frac{1}{2}}^z$ and $\mathcal{B}_{-\frac{1}{2}}^\pm$ are obtained by applying the above mentioned transformation on their $S^z_{\text{tot}} = +1/2$ counterparts.

Appendix 6: Non-Fermi liquid exponents in self-energy and two-particle correlations

The one-particle self-energies relating to the impurity and zeroth sites, as well as some relevant two-particle correlation functions, can be shown to follow power-law behaviour close to the Brinkman-Rice transition at r_{c2}, by mapping the impurity model to a classical Coulomb gas, similar to the work of Anderson, Yuval and Hamman for the Kondo model [481] and that of Si and Kotliar for a periodic Anderson model [476]. Indeed, the latter work uses an auxiliary that is similar to our extended Anderson impurity model. In the following, we adapt their results to our model. These non-universal power-laws are signatures of the non-Fermi liquid excitations that emerge at r_{c2}.

Near r_{c2}, extended SIAM can be reduced to a $J-U_b$ model (shown in subsection V.A of the main manuscript). The conduction electrons scattering off the impurity suffer phase shifts because of the presence of the potentials J and U_b. These phase shifts are given by $\delta_{\rm sp} = \arctan(\pi\rho_0 J/2)$ and $\delta_{\rm ch} = \arctan(\pi\rho_0 U_b/2)$ [476, 546], where ρ_0 is the electronic density of states in the conduction bath. The low-energy behaviour of the local impurity and bath self-energies can be expressed in terms of these phase shifts [476]:

$$\begin{aligned} \Sigma_{dd}(\omega) \sim \omega^{\gamma_{dd}},\ \ \Sigma_{d0}(\omega) \sim \omega^{\gamma_{d0}},\ \ \Sigma_{00}(\omega) \sim \omega^{\gamma_{00}}\,, \\ \gamma_{dd} = \frac{5}{4} - \left(\frac{\delta^*_{\rm tot}}{\pi}\right)^2 - \left(\frac{\delta^*_{\rm ch}}{\pi}\right)^2,\ \ \gamma_{d0} = 2\left[\left(\frac{\delta^*_{\rm ch}}{\pi}\right)^2 + \left(\frac{\delta^*_{\rm tot}}{\pi}\right)^2 - \frac{1}{4}\right], \\ \gamma_{00} = \left(\frac{\delta^*_{\rm tot}}{\pi} - \frac{1}{2}\right)^2 + \left(\frac{\delta^*_{\rm ch}}{\pi}\right)^2 - 2\,, \end{aligned} \tag{9.83}$$

where we have defined a total phase shift parameter $\frac{\delta_{\rm tot}}{\pi} \equiv \frac{\delta_{\rm sp}+\delta_{\rm ch}}{\pi} - \frac{1}{2}$. This can be extended to certain correlation functions as well. The impurity spin-flip correlation, the impurity-bath excitonic correlation and the zeroth-site pairing correlation [476]:

$$\begin{aligned} \left\langle S^+_d(\tau) S^-_d(0)\right\rangle \sim \tau^{-\alpha_1} \quad &\Longrightarrow \left\langle S^+_d\right\rangle(\omega) \sim \omega^{(\alpha_1-1)/2}, \\ \left\langle (c^\dagger_{d\uparrow} c_{0\uparrow})(\tau)(c^\dagger_{0\uparrow} c_{d\uparrow})(0)\right\rangle \sim \tau^{-\alpha_2} \quad &\Longrightarrow \left\langle c^\dagger_{d\uparrow} c_{0\uparrow} c^\dagger_{0\uparrow} c_{d\uparrow}\right\rangle(\omega) \sim \omega^{(\alpha_2-1)/2}, \\ \left\langle (c^\dagger_{0\uparrow} c^\dagger_{0\downarrow})(\tau)(c_{0\downarrow} c_{0\uparrow})(0)\right\rangle \sim \tau^{-\alpha_3} \quad &\Longrightarrow \left\langle c^\dagger_{0\uparrow} c^\dagger_{0\downarrow}\right\rangle(\omega) \sim \omega^{(\alpha_3-1)/2}\,, \end{aligned} \tag{9.84}$$

where the exponents are given by

$$\alpha_1 = 2\left(1 - \frac{\delta^*_{\rm sp}}{\pi}\right)^2, \alpha_2 = \left(\tfrac{\delta^*_{\rm tot}}{\pi} - \tfrac{1}{2}\right)^2 + \left(\tfrac{\delta^*_{\rm ch}}{\pi}\right)^2, \alpha_3 = \left(\tfrac{\delta^*_{\rm tot}}{\pi} + \tfrac{1}{2}\right)^2 + \left(1 + \tfrac{\delta^*_{\rm ch}}{\pi}\right)^2\,. \tag{9.85}$$

Appendix 7: Entanglement entropy, magnetisation and phase shift, at the QCP

As mentioned in the previous section, the polarised ground-states $|-\rangle^{3,\pm\frac{1}{2}}$ of eq. (9.52) are special because they involve the strong-coupling ground-state as well as the local moment ground-state.

The overall ground states, therefore, contain both entangled and non-entangled impurity contributions, leading to a departure from maximal entanglement. We will now calculate the impurity entanglement entropy $S_{\rm EE}(d)$ in this polarised ground-state(s) that emerges exactly at the QCP, and show that $S_{\rm EE}(d)$ has a fractional value (in units of $\log 2$). This turns out to be linked to the fact that the impurity is screened partially in these states, leading to an impurity magnetisation that is non-vanishing but only half of that in the local moment phase.

The fractional entropy arises because of the singular scattering of the gapless excitations at the Fermi surface leading to the destruction of the local Fermi liquid. In order to access these processes, we will work with a *semi-continuous* conduction bath beyond the zeroth site (total number of lattice sites $N \to \infty$): $H_{\rm bath} = \sum_{k,\sigma} \epsilon(k) \psi^\dagger_\sigma(k) \psi^\dagger_\sigma(k)$. This conduction bath that is composed of the $k-$states formed from the Hilbert space of the lattice sites beyond the zeroth site will be referred to as the reduced conduction bath. This is in addition to the Hamiltonian for the impurity and zeroth sites: $H_{d0} = J \vec{S}_d \cdot \vec{S}_0 - \frac{U_b}{2} \left(c^\dagger_{0\uparrow} c_{0\uparrow} - c^\dagger_{0\downarrow} c_{0\downarrow} \right)^2$, where $\vec{S}_d$ is the spin operator for the impurity site, and $c^\dagger_{0\sigma}$ creates an electron of spin σ at the zeroth site. The full Hamiltonian also involves a single-particle hopping term that couples these two Hamiltonians: $H = H_{d0} + H_{\rm bath} + H_{\rm int}$, where

$$H_{\rm int} = -t \sum_\sigma \left(c^\dagger_{0\sigma} c_{1\sigma} + \text{h.c.} \right) = -\frac{t}{N} \sum_{k,\sigma} \left[c^\dagger_{0\sigma} \psi_\sigma(k) + \text{h.c.} \right]. \tag{9.86}$$

$c^\dagger_{1\sigma} = \frac{1}{N} \sum_k \psi^\dagger_\sigma(k)$ is the creation operator for the first site of the conduction bath of N sites (but effectively the zeroth site for the reduced conduction bath defined by $H_{\rm bath}$). We will treat $H_{\rm int}$ perturbatively in t/J, in order to obtain the set of renormalised $g-$fold degenerate ground-states $\left\{ |\psi^{(n)}_{\rm gs}\rangle \, ; n = 1, \ldots, g \right\}$.

As mentioned before, the intention here is to calculate magnetisation and entanglement entropy in the non-Fermi liquid ground states. In the case of a degenerate subspace with $S^z_{\rm tot} = \pm 1/2$ where $S^z_{\rm tot} = S^z_d + S^z_0 + S^z_1$ is the total spin operator, the magnetisation m^z_d must be calculated in any *one* of the degenerate states for our problem. This is accomplished by solving the problem in the presence of an infinitesimal magnetic field term $-hS^z_{\rm tot}$ that lifts the degeneracy and chooses one of the symmetry-broken ground-states. This is similar to the "two self-energy description" introduced by David Logan for computing quantities in the local moment phase/Mott insulating phase in terms of different self-energies obtained by inserting positive and negative magnetic fields [161,547,548]. Due to the symmetry of the Hamiltonian under $S^z_{\rm tot} \to -S^z_{\rm tot}$, both the limits $h = 0^+$ and $h = 0^-$ give the same results for the density matrix and the entanglement entropy. We will work with $h = 0^+$. Since the total Hamiltonian H and the perturbation $H_{\rm int}$ preserve the total spin $S^z_{\rm tot} = S^z_d + S^z_0 + \int dk S^z_k$, it is sufficient to solve only for the sector with the most positive value of $S^z_{\rm tot}$, since those are the states that will be selected by the positive magnetic field $h = 0^+$.

In the absence of $H_{\rm int}$, the set of ground-states with a positive $S^z_{\rm tot}$ will contain, to begin with, the local moment states $|\uparrow\rangle_d |0\rangle_0 |\phi\rangle$ and $|\uparrow\rangle_d |2\rangle_0 |\phi\rangle$, where $|\phi\rangle$ represents the filled Fermi sea of the reduced conduction bath, acting as its spinless ground-state. These states have $S^z_{\rm tot} = 1/2$. We can label these states as $|n_{\rm tot}, \mu^z_d\rangle$, using the total number of particles $n_{\rm tot} = n_d + n_0 + n_{\rm bath}$ (which is also conserved, and where we set $n_{\rm bath} = 1$ for the set $|\phi\rangle$), and the average magnetisation μ^z_d of the impurity state: $|2, \frac{1}{2}\rangle \equiv |\uparrow\rangle_d |0\rangle_0 |\phi\rangle$, $|4, \frac{1}{2}\rangle \equiv |\uparrow\rangle_d |2\rangle_0 |\phi\rangle$. Since the singlet state $|SS\rangle_{d0}$ (on the

d and zeroth sites) is degenerate with the local moment states $|\uparrow\rangle_d\,|0(2)\rangle_0$, one can construct other states with $S^z_{\rm tot} = 1/2$ by creating magnetic excitations at the Fermi surface. The fact that we are working with a thermodynamically large bath ($N \to \infty$) means that there will be gapless excitations vanishingly close to the Fermi surface. Such states are of the form $|{\rm SS}\rangle_{d0}\,|e_\uparrow\rangle$ (labeled as $|4,0\rangle$ in the $|n_{\rm tot}, \mu^z_d\rangle$ notation) and $|{\rm SS}\rangle_{d0}\,|h_\downarrow\rangle$ (labeled as $|2,0\rangle$), where $|e_\sigma\rangle$ and $|h_\downarrow\rangle$ are electron and hole states respectively:

$$|e_\sigma\rangle = \sum_k^{\rm FS} \psi^\dagger_\sigma(k)\,|\phi\rangle\,, \quad |h_\sigma\rangle = \sum_k^{\rm FS} \psi_\sigma(k)\,|\phi\rangle\ . \tag{9.87}$$

The sum is over $k-$states on the Fermi surface. The singlet state was set to have zero spin on the impurity site in the state notation, because $\langle S^z_d\rangle$ vanishes in the singlet state. The full set of relevant degenerate ground-states, classified by the total number of particles, is

$$n_{\rm tot} = 4 : |4,0\rangle\,, |4,\frac{1}{2}\rangle\,; \quad n_{\rm tot} = 2 : |2,0\rangle\,, |2,\frac{1}{2}\rangle\ . \tag{9.88}$$

Within each 2×2 block, the interaction matrix $H_{\rm int}$ takes the form (in the basis of the states in eq. (9.88))

$$(H_{\rm int})^{n_{\rm tot}=2}_{\rm gs} = \frac{t}{N}\times\begin{pmatrix} 0 & 1/\sqrt{2} \\ 1/\sqrt{2} & 0 \end{pmatrix} = -\,(H_{\rm int})^{n_{\rm tot}=4}_{\rm gs}\ , \tag{9.89}$$

and the $S^z_{\rm tot} = +\frac{1}{2}$ ground-states are then easily obtained to be of the form $|\psi_{\rm gs}\rangle^{(n_{\rm tot})} = \frac{1}{\sqrt{2}}\left(|n_{\rm tot},0\rangle - |n_{\rm tot},\frac{1}{2}\rangle\right), n_{\rm tot} = 2$ & 4, independent of N. Both ground-states involve an equal superposition of a $\mu^z_d = 1/2$ state and a $\mu^z_d = 0$ state, such that the net impurity magnetisation in either of the renormalised polarised states is

$$m^z_d = \frac{1}{2}\left(0+\frac{1}{2}\right) = \frac{1}{4}\,. \tag{9.90}$$

The reduced density matrix $\rho_{\rm imp} = {\rm Tr}'\left(|\psi_{\rm gs}\rangle^{(n_{\rm tot})}\,\langle\psi_{\rm gs}|^{(n_{\rm tot})}\right)$ (where Tr′ indicates partial trace over all states apart from those of the impurity) for the impurity spin in the polarised states can now be immediately obtained. It is independent of $n_{\rm tot}$, and actually turns out to be halfway between the maximally mixed density matrix $\rho_{\rm MM} = \frac{1}{2}I$ and the non-entangled density matrix $\rho_{\rm NE} = \begin{pmatrix} 1 & 0 \\ 0 & 0 \end{pmatrix}$:

$$\rho_{\rm imp} = \begin{pmatrix} 3/4 & 0 \\ 0 & 1/4 \end{pmatrix} = \frac{1}{2}\left(\rho_{\rm MM}+\rho_{\rm NE}\right), \quad S_{\rm EE}(d) = -{\rm Tr}\left(\rho_{\rm imp}\ln\rho_{\rm imp}\right) \simeq 0.81\log 2\,. \tag{9.91}$$

This fractional value of the entropy in units of $\log 2$ is another signature of the non-Fermi liquid. We can express this in terms of an effective degeneracy $\tilde{g}$ of the impurity degree of freedom. We define

this effective degeneracy as $\tilde{g} = 1 + 2|m_d^z|$, in order to recover the unique ground-state in the local Fermi liquid phase (that has $m_d^z = 0, \tilde{g} = 1$) and the magnetic doublet in the local moment phase (that has $m_d^z = 1/2, \tilde{g} = 2$). The proposed form also results in a non-integer impurity degeneracy for the NFL at the QCP, $\tilde{g}^* = 3/2$. Using the effective degeneracy $\tilde{g}$, one can also write down a general ground-state

$$|\psi_{\rm gs}(g)\rangle = \frac{1}{\sqrt{(2-\tilde{g})^2 + (\tilde{g}-1)^2}} \left[(2-\tilde{g})\,|n_{\rm tot}, 0\rangle - (\tilde{g}-1)\,|n_{\rm tot}, 1/2\rangle\right] , \tag{9.92}$$

that interpolates between the strong-coupling ground-state for $r < r_{c2}$ (therefore $\tilde{g} = 1$) and the weak coupling ground-state $r > r_{c2}$ (therefore $\tilde{g} = 2$), also describing the QCP in between ($\tilde{g} = 3/2$). The entanglement entropy, when written in terms of $\tilde{g}$, takes the form

$$\rho_{\rm imp} = \frac{1}{2}\begin{pmatrix} 2-\tilde{g} & 0 \\ 0 & \tilde{g} \end{pmatrix} = \frac{1}{2} + \begin{pmatrix} m_d^z & 0 \\ 0 & -m_d^z \end{pmatrix}, \tag{9.93}$$

$$S_{\rm EE}(d) = -\left(1 - \frac{\tilde{g}}{2}\right) \ln\left(1 - \frac{\tilde{g}}{2}\right) - \frac{\tilde{g}}{2} \ln \frac{\tilde{g}}{2} . \tag{9.94}$$

The relation between the reduced density matrix $\rho_{\rm imp}$ and the impurity magnetisation m_d^z is consistent with that obtained by Kopp et al., [549].

The general form $|\psi_{\rm gs}(g)\rangle$ of polarised interpolating ground-state also allows us to calculate the excess charge ($n_{\rm exc}$) added, by the impurity, to the conduction bath Fermi surface (through gapless excitations). This then allows the scattering phase shift of the conduction electrons (obtained via the Friedel sum rule, [48, 531, 532]) to be linked with the impurity magnetisation m_d^z. From the definitions of the states $|n_{\rm tot}, 0\rangle$ and $|n_{\rm tot}, 1.2\rangle$, we note that the former state involves an impurity-bath singlet while the latter involves a decoupled local moment. The singlet state contributes an excess charge of unity to the conduction bath: $n_{\rm exc}^{\rm SS} = 1$, because of the impurity-bath entanglement within it. The local state moment does not contribute any excess charge, because the impurity spin is no longer hybridising with the bath in that state: $n_{\rm exc}^{\rm LM} = 0$. Putting these together, the net excess charge contributed by the state in eq. (9.92) is

$$n_{\rm exc} = \frac{1}{(2-\tilde{g})^2 + (\tilde{g}-1)^2} \left[(2-\tilde{g})^2 n_{\rm exc}^{\rm SS} + (\tilde{g}-1)^2 n_{\rm exc}^{\rm LM}\right] = \left[1 + \left(\frac{2-\tilde{g}}{\tilde{g}-1}\right)^2\right]^{-1} . \tag{9.95}$$

At the QCP, the excess charge acquires a fractional value of $1/2$, indicating once more that only half of the impurity remains coupled with the bath at the transition. The Friedel sum rule can be used to equate this excess charge with the phase shift δ^* suffered by conduction electrons as they scatter off the impurity, at the fixed point:

$$\delta^* = \pi n_{\rm exc} = \left[1 + \left(\frac{2-\tilde{g}}{\tilde{g}-1}\right)^2\right]^{-1} = \frac{4 {m_d^z}^2}{1 - 4|m_d^z| + 8 {m_d^z}^2} . \tag{9.96}$$

Equation (9.96) unifies the effect of several important quantities that lead to the frustration of the impurity and the destruction of the Kondo effect. The presence of U_b introduces local moment states

into the spectrum and leads to states with non-vanishing impurity magnetisation m_d^z at the QCP; this non-zero m_d^z can be interpreted as an effective impurity degeneracy $\tilde{g}$ that is only partially screened, resulting in only half the excess charge $n_{\rm exc}$ being contributed to the conduction bath. This reduction in the excess charge acts as a shift in the boundary conditions felt by the conduction electrons and manifests as a phase shift that is less than the unitarity limit of π.

Appendix 8: Additional correlations near the ESQPT and the QCP

We have included some additional correlations for the extended SIAM here to highlight the features that are mentioned in the main manuscript. Left panel of Fig. (3.14) shows the impurity and zeroth site double occupancy. Both vanish at r_{c1}, indicating the emergence of the Kondo model. Very close to r_{c2}, the zeroth site doublon occupancy picks up (see inset), showing the destruction of the Kondo cloud. Right panel of Fig. (3.14) shows various measures of entanglement close to r_{c2}. The impurity-bath mutual information (blue) decreases as the transition is approached, showing the breakdown of impurity screening. The impurity and first site MI (violet), the zeroth site and first site MI (red) and the impurity, zeroth site and first site tripartite information (grey) increase, showing the emergence of long-ranged correlations near the transition. Fig. (3.15) shows the emergence of long-ranged intra-bath mutual information near r_{c1} and r_{c2}, signalling critical behaviour near the ESQPT and QCP respectively. Intra-bath CDW correlations and impurity-bath Ising correlations in Fig. (3.16) also show the previously-mentioned emergence of long-ranged correlations.

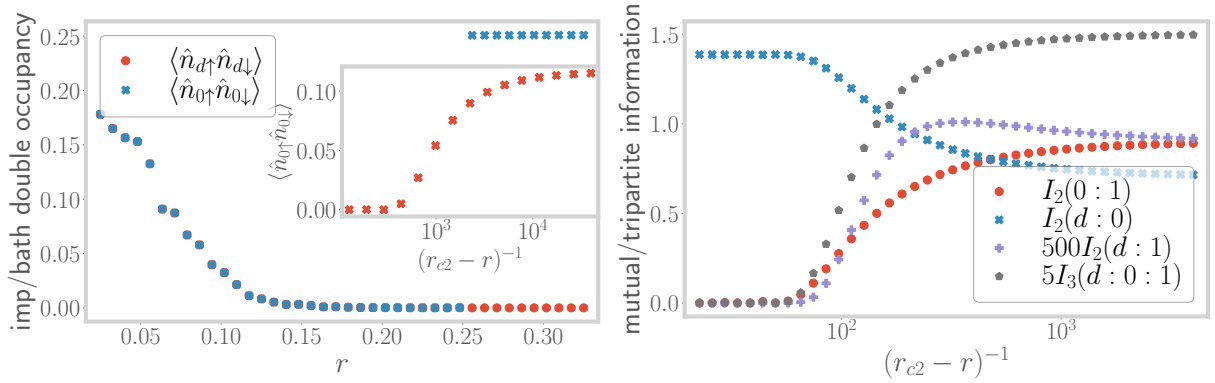

Figure 3.14: *Left: Evolution of the double occupancy of impurity (red) and zeroth sites (blue) ground-state double occupancy, with r. Right: Evolution of various quantum information-theoretic measures, very close to the transition.*

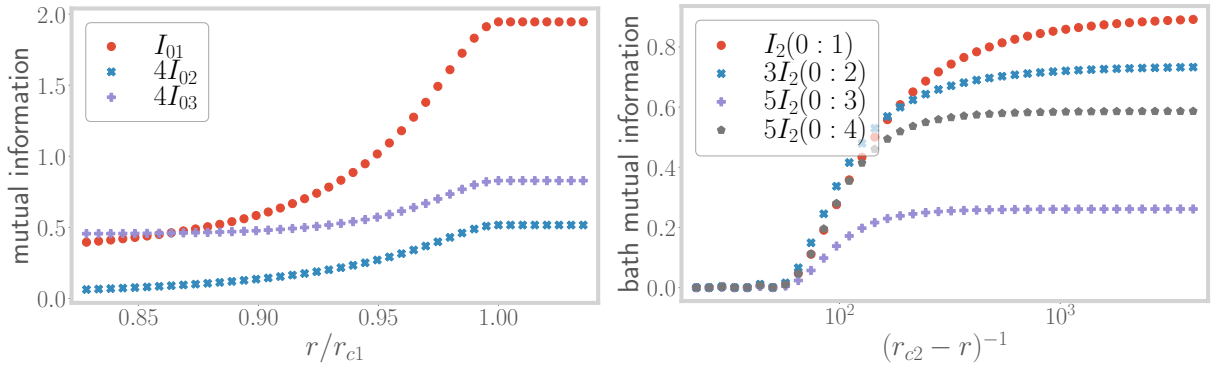

Figure 3.15: *Variation of intra-bath mutual information between zeroth site and sites 1, 2 and 3, near r_{c1} (left) and r_{c2} (right).*

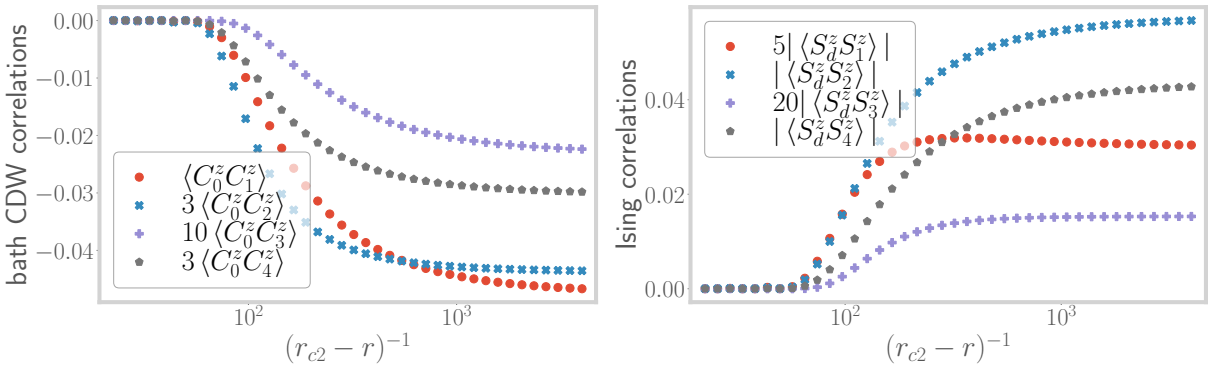

Figure 3.16: *Left: Variation of charge isospin Ising correlations between the zeroth site and bath sites further down the chain. Right: Ising correlations between the impurity site and bath sites beyond the zeroth site. Both sets of correlations show an overall increase as $r \longrightarrow r_{c2}$.*

Chapter 4

A New Auxiliary Model Approach for Interacting Electrons: Mapping Impurity Models To Lattice Models

Having identified the appropriate auxiliary model in the limit of infinite dimensions in the previous chapter, we now focus on extending this approach to the more realistic case of low dimensions. Towards this, develop a "tiling" framework, where we apply manybody translation operators to restore translation invariance and map the impurity model with the lattice model. By embedding the impurity model in well-defined lattices, our method incorporates non-trivial effects such as nesting and momentum-space anisotropy arising from lattice geometries. We leave the application of this method to a concrete problem for the next chapter.

4.1 What Is The Correct Auxiliary Model For Correlated Electrons on a 2D Square Lattice?

As discussed in more detail in the previous chapter, it was necessary to extend the single-impurity Anderson model (SIAM) in order to obtain a phase transition on the impurity site. Without any modification, the standard Anderson model (at particle-hole symmetry) leads to the emergence of an $\omega = 0$ Kondo resonance in the impurity ($d\sigma$) spectral function at any value of the impurity correlation U_d, at sufficiently low temperatures:

$$H_{\mathrm{SIAM}} = \sum_{k,\sigma} \varepsilon_k n_{k,\sigma} - V \sum_{\sigma} (c^{\dagger}_{0,\sigma} c_{d,\sigma} + \mathrm{h.c.}) + \varepsilon_d \sum_{\sigma} n_{d,\sigma} + U_d n_{d,\uparrow} n_{d,\downarrow} \, . \tag{1.1}$$

The operator $c_{0,\sigma}$ acts on the local conduction bath density that couples with the impurity site. The low-energy is one of local Fermi liquid for all parameter regimes. Increasing U_d only serves to reduce the width of the central peak at the cost of the appearance of side bands at energy scales of the order of U_d, but the resonance never disappears. The extended Anderson model that we developed augments the SIAM by allowing for local correlation in the local conduction bath charge

density that couples with the impurity spin:

$$H_{\mathrm{ESIAM}} = H_{\mathrm{SIAM}} + J_K \boldsymbol{S}_d \cdot \boldsymbol{S}_0 - \frac{U_b}{2}\left(n_{0,\uparrow}^2 - n_{0,\downarrow}^2\right); \tag{1.2}$$

tuning this bath correlation to large attractive values (see [508] for some recent findings of non-local effective attractive interactions within the Hubbard model) *does* lead to a localisation transition on the impurity where the local Fermi liquid excitations are replaced by the physics of a gapped local moment on the impurity. We note that the generation of such correlations in the bath is something that occurs in DMFT as well – the conduction bath acquires a *non-trivial self-energy* during the convergence to self-consistency.

While this modified impurity model captures well the Mott metal-insulator transition of the Hubbard model in infinite dimensions, it *lacks any knowledge of the underlying lattice geometry*, and is therefore ill-suited to address the phenomenology of more realistic low-dimensional models. Examples of such phenomenology include the pseudogap phase of the cuprates (with nodal-antinodal dichotomy), strange metal (with $T-$linear resistivity) and high-T_c superconducting phases observed in several families of quantum materials as well as graphene. This leads us to propose the framework of *lattice-embedded quantum impurity models*. Upon embedding the impurity site within the underlying lattice, the coupling between it and its environment must be consistent with the lowered symmetry of the lattice (see Fig. 4.1). Impurity-bath correlations calculated within such an impurity model are sensitive to the lattice geometry, and are much better suited to address the phenomenology mentioned above.

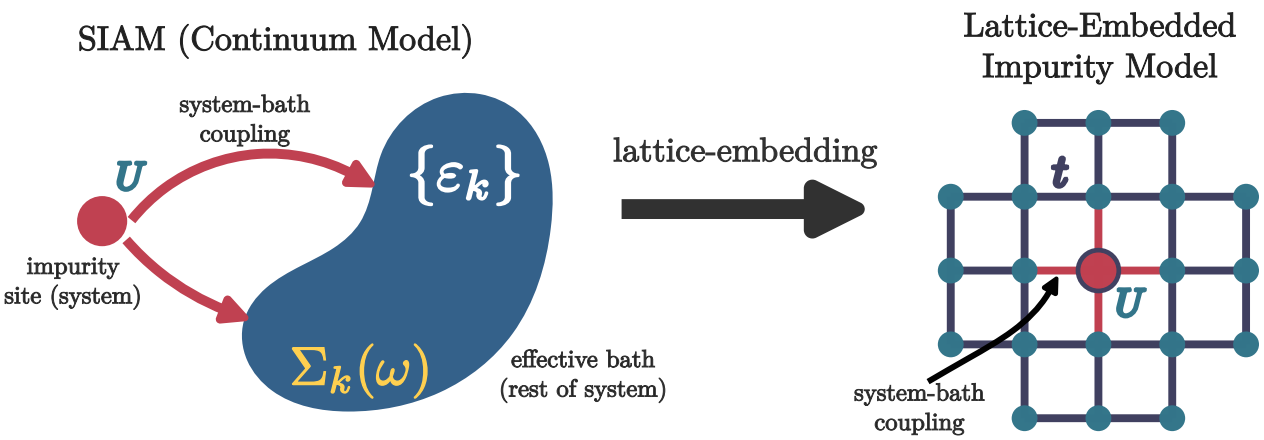

Figure 4.1

As a concrete example, we take the extended SIAM defined in eq. 1.2, and write down its lattice-embedded form on a 2D square lattice, with the impurity placed at the site r_d. This is done by allowing the impurity to hybridise with the four nearest-neighbours, through V and J_K. The same

four sites also carry the local bath interaction. The complete auxiliary model is

$$H = -t \sum_{\langle i,j\rangle,\sigma} (c^{\dagger}_{i,\sigma} c_{j,\sigma} + \text{h.c.}) + \sum_{\langle i,r_d\rangle} \left[-\frac{V}{Z} \sum_{\sigma} (c^{\dagger}_{r_d,\sigma} c_{i,\sigma} + \text{h.c.}) + \frac{J_K}{Z} \boldsymbol{S}_{r_d} \cdot \boldsymbol{S}_i - \frac{W}{2Z} \left(n^2_{i,\uparrow} - n^2_{i,\downarrow} \right) \right] + \varepsilon_d \sum_{\sigma} n_{r_d,\sigma} + U_d n_{r_d,\uparrow} n_{r_d,\downarrow}, \tag{1.3}$$

where Z is the coordination number of the lattice, and the second summation $\sum_{\langle i,r_d\rangle}$ is carried out over all sites i that are nearest-neighbour to the site r_d. Note that the one-particle hybridisation V and the spin-exchange coupling J_K have their *symmetry lowered* from the $s-$wave spherical symmetry of the continuum impurity models to a C_4-symmetry consistent with the underlying lattice. This feature is crucial in explaining the phenomenology of the various low-dimensional materials.

Various enhancements can be applied to such a model. The lattice can be modified to study different materials. More complicated geometries such as a two-layer model can be studied using a two-impurity auxiliary model, where each impurity couples with it's own conduction bath as well as to each other. Such a two-impurity auxiliary model will in fact be utilised during our investigation of the physics of heavy fermion systems in Chapter 6.

4.2 Mapping Auxiliary Model To Lattice Model

In this subsection, we provide an explicit example of constructing a lattice model from a lattice-embedded impurity model. This will involve the use of many-body lattice translation operators, so we begin with a brief discussion of them.

4.2.1 Many-body translation operators

In order to create the bulk model, we need to translate the local auxiliary model over the entire lattice. For this, we define *many-particle global* translation operators $T(\boldsymbol{a})$ that translate all positions by a vector $\boldsymbol{a}$. In terms of many-body states and operators, their action is defined as [448, 449]

$$\begin{aligned} T^{\dagger}(\boldsymbol{a}) \left|\boldsymbol{r}_1, \boldsymbol{r}_2, \ldots\right\rangle &= \left|\boldsymbol{r}_1 + \boldsymbol{a}\right\rangle \otimes \left|\boldsymbol{r}_2 + \boldsymbol{a}\right\rangle \ldots \otimes \left|\boldsymbol{r}_n + \boldsymbol{a}\right\rangle \\ T^{\dagger}(\boldsymbol{a}) O\left(\boldsymbol{r}_1, \boldsymbol{r}_2, \ldots\right) T(\boldsymbol{a}) &= O\left(\boldsymbol{r}_1 + \boldsymbol{a}, \boldsymbol{r}_2 + \boldsymbol{a}, \ldots\right) \ , \end{aligned} \tag{2.1}$$

where $\left|\boldsymbol{r}_1, \boldsymbol{r}_2, \ldots\right\rangle$ is a state in the manyparticle Fock-space basis with the particles localised at the specified positions. For example, for a local fermionic creation operator $c^{\dagger}(\boldsymbol{r})$, we have

$$T^{\dagger}(\boldsymbol{a}) c^{\dagger}(\boldsymbol{r}) T(\boldsymbol{a}) = c^{\dagger}(\boldsymbol{r} + \boldsymbol{a}) \ . \tag{2.2}$$

It acts similarly on the auxiliary model Hamiltonian:

$$T^{\dagger}(\boldsymbol{a}) H_{\text{aux}}(\boldsymbol{r}_d) T(\boldsymbol{a}) = H_{\text{aux}}(\boldsymbol{r}_d + \boldsymbol{a}) \ , \tag{2.3}$$

translating all sites by the vector $\boldsymbol{a}$. By introducing the Fourier transform to momentum space,

$$|\boldsymbol{r}_1, \boldsymbol{r}_2, \ldots\rangle = \otimes_{j=1}^{N} \int d\boldsymbol{k}_j e^{i\boldsymbol{r}_j\cdot\boldsymbol{k}_j} |\boldsymbol{k}_j\rangle \ , \tag{2.4}$$

it is easy to see that the total momentum states are eigenstates of the global translation operators:

$$\begin{aligned} T^{\dagger}(\boldsymbol{a})\,|\boldsymbol{k}_1, \boldsymbol{k}_2, \ldots\rangle &= \otimes_{j=1}^{N} \int d\boldsymbol{r}_j e^{-i\boldsymbol{r}_j\cdot\boldsymbol{k}_j} T^{\dagger}(\boldsymbol{a})\,|\boldsymbol{r}_j\rangle \ , \\ &= \otimes_{j=1}^{N} \int d\boldsymbol{r}_j e^{-i\boldsymbol{r}_j\cdot\boldsymbol{k}_j} |\boldsymbol{r}_j + \boldsymbol{a}\rangle \\ &= \otimes_{j=1}^{N} e^{i\boldsymbol{a}\cdot\boldsymbol{k}_j} \int d\boldsymbol{r}_j e^{-i\boldsymbol{r}_j\cdot\boldsymbol{k}_j} |\boldsymbol{r}_j\rangle \\ &= e^{i\boldsymbol{a}\cdot\boldsymbol{k}_{\text{tot}}} |\boldsymbol{k}_1, \boldsymbol{k}_2, \ldots\rangle \, , \end{aligned} \tag{2.5}$$

where $\boldsymbol{k}_{\text{tot}} = \sum_j \boldsymbol{k}_j$ is the total momentum. This gives a compact form for the translation operator:

$$T^{\dagger}(\boldsymbol{a}) = e^{i\boldsymbol{a}\cdot\hat{\boldsymbol{k}}_{\text{tot}}} \ , \tag{2.6}$$

where $\hat{\boldsymbol{k}}_{\text{tot}}$ is the total momentum operator.

We end this section by calculating the effect of the translation operators on the $k-$space annihilation operators. We have

$$c(\boldsymbol{k}) = \frac{1}{\sqrt{N}} \sum_{\boldsymbol{r}} e^{-i\boldsymbol{k}\cdot\boldsymbol{r}} c(\boldsymbol{r}) \ . \tag{2.7}$$

Applying the translation operator to this decomposition, we get

$$\begin{aligned} T\,(\vec{a})\, c(\boldsymbol{k}) T^{\dagger}\,(\vec{a}) &= \frac{1}{\sqrt{N}} \sum_{\boldsymbol{r}} e^{-i\boldsymbol{k}\cdot\boldsymbol{r}} T\,(\vec{a})\, c(\boldsymbol{r}) T^{\dagger}\,(\vec{a}) \\ &= \frac{1}{\sqrt{N}} \sum_{\boldsymbol{r}} e^{-i\boldsymbol{k}\cdot\boldsymbol{r}} c(\boldsymbol{r} - \vec{a}) \\ &= e^{-i\boldsymbol{k}\cdot\vec{a}} c(\boldsymbol{k}) \ . \end{aligned} \tag{2.8}$$

4.2.2 Periodisation of Auxiliary Model Into Extended Hubbard Model

We recall the lattice-embedded impurity model defined in eq. 1.3. As discussed above, the route to restoring translation symmetry and reconstructing the lattice model is to translate the auxiliary model using many-body translation operators. Accordingly, we identify the "unit cell" of translation. Since we expect the impurity site to capture most of the physics arising from the correlated electrons, a good choice for the unit cell is the impurity site and it's surrounding correlated environment. In order to retain information of the lattice geometry, we convert the hybridisation and bath interaction

terms from real space to $k-$space. The Hamiltonian for the unit cell is therefore

$$H_{\text{clust}}(\boldsymbol{r}_d) = -\sum_{\boldsymbol{k},\sigma} e^{i\boldsymbol{k}\cdot\boldsymbol{r}_d} V(\boldsymbol{k})(c^\dagger_{\boldsymbol{r}_d,\sigma} c_{\boldsymbol{k},\sigma} + \text{h.c.}) + \sum_{\boldsymbol{k}_1,\boldsymbol{k}_2} e^{i(\boldsymbol{k}_1-\boldsymbol{k}_2)\cdot\boldsymbol{r}_d}\, J_K(\boldsymbol{k}_1,\boldsymbol{k}_2)\boldsymbol{S}_{\boldsymbol{r}_d}\cdot\boldsymbol{S}_{\boldsymbol{k}_1,\boldsymbol{k}_2} + \varepsilon_d n_{\boldsymbol{r}_d}$$
$$+ U_d n_{\boldsymbol{r}_d,\uparrow} n_{\boldsymbol{r}_d,\downarrow} - \frac{1}{2}\sum_{\{\boldsymbol{k}_i\},\sigma,\sigma'} \sigma\,\sigma'\, e^{i(\boldsymbol{k}_1-\boldsymbol{k}_2+\boldsymbol{k}_3-\boldsymbol{k}_4)\cdot\boldsymbol{r}_d} W(\{\boldsymbol{k}_i\}) c^\dagger_{\boldsymbol{k}_1,\sigma} c_{\boldsymbol{k}_2,\sigma} c^\dagger_{\boldsymbol{k}_3,\sigma'} c_{\boldsymbol{k}_4,\sigma'}\,, \tag{2.9}$$

where $\boldsymbol{S}_{\boldsymbol{k}_1,\boldsymbol{k}_2} = \sum_{\alpha,\beta} \boldsymbol{\sigma}_{\alpha,\beta} c^\dagger_{\boldsymbol{k}_1,\alpha} c_{\boldsymbol{k}_2,\beta}$, and the Fourier transforms are defined by the following relations:

$$\begin{aligned}
\sum_{\boldsymbol{k}} e^{i\boldsymbol{k}\cdot\boldsymbol{r}_d} V(\boldsymbol{k}) c^\dagger_{\boldsymbol{r}_d,\sigma} c_{\boldsymbol{k},\sigma} &= \frac{V}{Z}\sum_{r\to\text{NN of }\boldsymbol{r}_d} c^\dagger_{\boldsymbol{r}_d,\sigma} c_{\boldsymbol{r},\sigma}\,,\\
\sum_{\boldsymbol{k}_1,\boldsymbol{k}_2} e^{i(\boldsymbol{k}_1-\boldsymbol{k}_2)\cdot\boldsymbol{r}_d}\, J_K(\boldsymbol{k}_1,\boldsymbol{k}_2)\vec{S}_{\boldsymbol{r}_d}\cdot\vec{S}_{\boldsymbol{k}_1,\boldsymbol{k}_2} &= \frac{J_K}{Z}\sum_{r\to\text{NN of }\boldsymbol{r}_d} \boldsymbol{S}_{\boldsymbol{r}_d}\cdot\boldsymbol{S}_{\boldsymbol{r}}\,,\\
\sum_{\boldsymbol{k}_1,\boldsymbol{k}_2,\boldsymbol{q}_1,\boldsymbol{q}_2} e^{i(\boldsymbol{k}_1-\boldsymbol{k}_2+\boldsymbol{k}_3-\boldsymbol{k}_4)\cdot\boldsymbol{r}_d} W(\{\boldsymbol{k}_i\}) c^\dagger_{\boldsymbol{k}_1,\sigma} c_{\boldsymbol{k}_2,\sigma} c^\dagger_{\boldsymbol{k}_3,\sigma'} c_{\boldsymbol{k}_4,\sigma'} &= \frac{W}{2Z}\sum_{r\to\text{NN of }\boldsymbol{r}_d} n_{\boldsymbol{r},\sigma} n_{\boldsymbol{r},\sigma'}\,,
\end{aligned} \tag{2.10}$$

We now translate this unit cell to all sites of the lattice, and reconstruct a translationally-invariant correlated lattice model:

$$H_{\text{latt}} = \sum_{\boldsymbol{r}} T^\dagger(\boldsymbol{r}-\boldsymbol{r}_d) H_{\text{clust}}(\boldsymbol{r}_d) T(\boldsymbol{r}-\boldsymbol{r}_d)\,. \tag{2.11}$$

We consider the effect of the translation operations on each part of the Hamiltonian. The purely local terms translate directly into a chemical potential term and a Hubbard interaction term:

$$\sum_{\boldsymbol{r}} T^\dagger(\boldsymbol{r}-\boldsymbol{r}_d)(\varepsilon_d \sum_\sigma n_{\boldsymbol{r}_d,\sigma} + U_d n_{\boldsymbol{r}_d,\uparrow} n_{\boldsymbol{r}_d,\downarrow}) T(\boldsymbol{r}-\boldsymbol{r}_d) = \varepsilon_d \sum_{\boldsymbol{r},\sigma} n_{\boldsymbol{r},\sigma} + U_d \sum_{\boldsymbol{r}} n_{\boldsymbol{r},\uparrow} n_{\boldsymbol{r},\downarrow}\,. \tag{2.12}$$

The one-particle hybridisation term maps onto a tight-binding hopping term:

$$\begin{aligned}
\sum_{\boldsymbol{r}} T^\dagger(\boldsymbol{r}-\boldsymbol{r}_d)\sum_{\boldsymbol{k}} e^{i\boldsymbol{k}\cdot\boldsymbol{r}_d} V(\boldsymbol{k}) c^\dagger_{\boldsymbol{r}_d,\sigma} c_{\boldsymbol{k},\sigma} T(\boldsymbol{r}-\boldsymbol{r}_d) &= \sum_{\boldsymbol{r}}\sum_{\boldsymbol{k}} e^{i\boldsymbol{k}\cdot\boldsymbol{r}} V(\boldsymbol{k}) c^\dagger_{\boldsymbol{r},\sigma} c_{\boldsymbol{k},\sigma}\\
&= \frac{V}{Z}\sum_{\boldsymbol{r}}\sum_{\boldsymbol{r}'\to\text{NN of }\boldsymbol{r}} c^\dagger_{\boldsymbol{r},\sigma} c_{\boldsymbol{r}',\sigma}\\
&= \frac{2V}{Z}\sum_{\langle\boldsymbol{r},\boldsymbol{r}'\rangle} c^\dagger_{\boldsymbol{r},\sigma} c_{\boldsymbol{r}',\sigma}\,,
\end{aligned} \tag{2.13}$$

where we used eq. 2.8 and the first equation from 2.10, and the fact that each nearest-neighbour pair $\boldsymbol{r},\boldsymbol{r}'$ appears twice in the summation.

The Kondo terms map onto a nearest-neighbour spin-exchange term:

$$\begin{aligned}\sum_{\boldsymbol{r},\boldsymbol{k}_1,\boldsymbol{k}_2} T^\dagger(\boldsymbol{r}-\boldsymbol{r}_d)e^{i(\boldsymbol{k}_1-\boldsymbol{k}_2)\cdot\boldsymbol{r}_d}\, J_K(\boldsymbol{k}_1,\boldsymbol{k}_2)\vec{S}_{\boldsymbol{r}_d}\cdot\vec{S}_{\boldsymbol{k}_1,\boldsymbol{k}_2}T(\boldsymbol{r}-\boldsymbol{r}_d) &= \sum_{\boldsymbol{r},\boldsymbol{k}_1,\boldsymbol{k}_2} e^{i(\boldsymbol{k}_1-\boldsymbol{k}_2)\cdot\boldsymbol{r}}\, J_K(\boldsymbol{k}_1,\boldsymbol{k}_2)\vec{S}_{\boldsymbol{r}}\cdot\vec{S}_{\boldsymbol{k}_1,\boldsymbol{k}_2} \\ &= \frac{J_K}{Z}\sum_{\boldsymbol{r}}\sum_{\boldsymbol{r}'\to\text{NN of }\boldsymbol{r}} \vec{S}_{\boldsymbol{r}}\cdot\vec{S}_{\boldsymbol{r}'}\,, \\ &= \frac{2J_K}{Z}\sum_{\langle\boldsymbol{r},\boldsymbol{r}'\rangle}\vec{S}_{\boldsymbol{r}}\cdot\vec{S}_{\boldsymbol{r}'}\,,\end{aligned} \tag{2.14}$$

where we used the second equation from 2.10. Finally, the bath interaction term W maps onto another Hubbard term

$$\begin{aligned}&\sum_{\boldsymbol{r},\boldsymbol{k}_1,\boldsymbol{k}_2,\boldsymbol{k}_3,\boldsymbol{k}_4} T^\dagger(\boldsymbol{r}-\boldsymbol{r}_d)e^{i(\boldsymbol{k}_1-\boldsymbol{k}_2+\boldsymbol{k}_3-\boldsymbol{k}_4)\cdot\boldsymbol{r}_d}W(\{\boldsymbol{k}_i\})c^\dagger_{\boldsymbol{k}_1,\sigma}c_{\boldsymbol{k}_2,\sigma}c^\dagger_{\boldsymbol{k}_3,\sigma'}c_{\boldsymbol{k}_4,\sigma'}T(\boldsymbol{r}-\boldsymbol{r}_d) \\ &= \sum_{\boldsymbol{r},\boldsymbol{k}_1,\boldsymbol{k}_2,\boldsymbol{k}_3,\boldsymbol{k}_4} e^{i(\boldsymbol{k}_1-\boldsymbol{k}_2+\boldsymbol{k}_3-\boldsymbol{k}_4)\cdot\boldsymbol{r}}W(\{\boldsymbol{k}_i\})c^\dagger_{\boldsymbol{k}_1,\sigma}c_{\boldsymbol{k}_2,\sigma}c^\dagger_{\boldsymbol{k}_3,\sigma'}c_{\boldsymbol{k}_4,\sigma'} \\ &= \frac{W}{2Z}\sum_{\boldsymbol{r}}\sum_{\boldsymbol{r}'\to\text{NN of }\boldsymbol{r}} n_{\boldsymbol{r}',\sigma}n_{\boldsymbol{r}',\sigma'} \\ &= \frac{W}{2}\sum_{\boldsymbol{r}} n_{\boldsymbol{r},\sigma}n_{\boldsymbol{r},\sigma'}\,,\end{aligned} \tag{2.15}$$

where we used the fact that each point $\boldsymbol{r}'$ (which we relabel as r) appears Z times in the summation.

The complete lattice Hamiltonian, after applying the translation operators, is

$$H_{\text{latt}} = \varepsilon_d\sum_{\boldsymbol{r},\sigma} n_{\boldsymbol{r},\sigma} + U_d\sum_{\boldsymbol{r}} n_{\boldsymbol{r},\uparrow}n_{\boldsymbol{r},\downarrow} - \frac{2V}{Z}\sum_{\langle\boldsymbol{r},\boldsymbol{r}'\rangle} c^\dagger_{\boldsymbol{r},\sigma}c_{\boldsymbol{r}',\sigma} + \frac{2J_K}{Z}\sum_{\langle\boldsymbol{r},\boldsymbol{r}'\rangle}\vec{S}_{\boldsymbol{r}}\cdot\vec{S}_{\boldsymbol{r}'} - \frac{W}{2}\sum_{\boldsymbol{r}}\left(n_{\boldsymbol{r},\uparrow}-n_{\boldsymbol{r},\downarrow}\right)^2\,. \tag{2.16}$$

This is clearly an extended Hubbard model, with both 1-particle and spin-exchange nearest-neighbour hybridisation. The general form of the model is

$$H_{\text{ex-Hub}} = -t\sum_{\langle i,j\rangle,\sigma}(c^\dagger_{i,\sigma}c_{j,\sigma}+\text{h.c.}) + J\sum_{\langle i,j\rangle}\boldsymbol{S}_i\cdot\boldsymbol{S}_j + U\sum_i n_{i,\uparrow}n_{i,\downarrow} - \mu\sum_{i,\sigma} n_{i,\sigma}\,, \tag{2.17}$$

such that the effective couplings resulting from the tiling operation is

$$t = \frac{2V}{Z},\; J = \frac{2J_K}{Z},\; U = U_d - W,\; \mu = -\varepsilon_d + \frac{W}{2}\,. \tag{2.18}$$

4.2.3 Form Of The Eigenstates: Bloch's Theorem

The tiled Hamiltonian defined in eq. 2.11 is manifestly symmetric under discrete translation, given that it's expressed in terms of the translation operators. The fact that the Hamiltonian H_{latt} commutes with the many-body translation operator implies that the total crystal momentum is a conserved

quantity. We will now use this to write down a "tiling" relation between the eigenstates of the auxiliary model and those of the lattice model.

In the tight-binding approach to lattice problems, the full Hamiltonian is obtained by translating the dynamics of the localised orbitals at each site over the entire lattice. The full eigenstate $|\Psi\rangle$ is obtained by constructing liner combinations of the eigenstates $|\psi(i)\rangle$ of the local Hamiltonians. According to Bloch's theorem, $|\Psi\rangle$ is of the form $|\Psi_{n,\boldsymbol{K}}\rangle = \sum_i e^{i\boldsymbol{K}\cdot\boldsymbol{r}_i} |\psi_n(i)\rangle$, where $\boldsymbol{K}$ is the single-particle crystal momentum, n is the band-index that labels various states within the local orbital, and $\boldsymbol{r}_i$ sums over the positions of the local Hamiltonians. Bloch's theorem ensures that eigenstates satisfy the following relation under a translation operation by an arbitrary number of lattice spacings $n\boldsymbol{a}$:

$$T^\dagger(l\boldsymbol{a})\,|\Psi_{n,\boldsymbol{K}}\rangle = \sum_i e^{i\boldsymbol{K}\cdot\boldsymbol{r}_i}\,|\psi_n(i+l)\rangle = e^{-il\boldsymbol{K}\cdot\boldsymbol{a}}\,|\Psi_{n,\boldsymbol{K}}\rangle\ . \tag{2.19}$$

As discussed earlier, the eigenstates $|\Psi_{n,\boldsymbol{K}}\rangle$ of the lattice Hamiltonian obtained using eq. 2.11 enjoy the discrete translation symmetry of the lattice, and therefore enjoy a *many-body* Bloch's theorem [448, 449]. This means that the *local* eigenstates $|\psi_n(\boldsymbol{r}_d)\rangle$ (with the impurity located at an arbitrary position $\boldsymbol{r}_d$) of the unit cell auxiliary model Hamiltonian $H_{\text{clust}}(\boldsymbol{r}_d)$ defined in eq. 2.9 can be used to construct eigenstates of the lattice Hamiltonian. The index $n(=0,1,\ldots)$ in the subscript indicates that it is the nth eigenstate of the auxiliary model. The following combination of the auxiliary model eigenstates satisfies a many-particle equivalent of Bloch's theorem [448, 449]:

$$|\Psi_s\rangle \equiv |\Psi_{\boldsymbol{K},n}\rangle = \frac{1}{\sqrt{N}}\sum_{\boldsymbol{r}_d} e^{i\boldsymbol{K}\cdot\boldsymbol{r}_d}\,|\psi_n(\boldsymbol{r}_d)\rangle\ , \tag{2.20}$$

where N is the total number of lattice sites and $\boldsymbol{r}_d$ is summed over all lattice spacings. The set of $n=0$ states form the lowest band in the spectrum of the lattice, while higher values of n produce the more energetic bands.

4.3 Properties of the Bloch states

4.3.1 Translation invariance

It is easy to verify that $\Psi_{\vec{k}}(\{\boldsymbol{r}_k\})$ transforms like Bloch functions under translation by a displacement $\boldsymbol{r}$:

$$\begin{aligned}\Psi_{\vec{k}}(\{\boldsymbol{r}_k+\boldsymbol{r}\}) = \frac{1}{\lambda_{|\vec{k}\rangle}\mathcal{Z}N}\sum_{\boldsymbol{r}_i,\boldsymbol{a}} e^{i\vec{k}\cdot\vec{R}_i}\psi_{\text{aux}}(\boldsymbol{r}_i-\boldsymbol{r},\boldsymbol{a}) = \frac{1}{\lambda_{|\vec{k}\rangle}\mathcal{Z}N}\sum_{\boldsymbol{r}_j,\boldsymbol{a}} e^{i\vec{k}\cdot\left(\vec{R}_j+\boldsymbol{r}\right)}\psi_{\text{aux}}(\boldsymbol{r}_j,\boldsymbol{a}) \\ = e^{i\vec{k}\cdot\vec{R}}\Psi_{\vec{k}}(\{\boldsymbol{r}_k\})\end{aligned} \tag{3.1}$$

In the last equation, we transformed $\boldsymbol{r}_i \to \boldsymbol{r}_j = \boldsymbol{r}_i - \boldsymbol{r}$. Note that the argument $\boldsymbol{a}$ does not change under a translation of the system, because that vector always represents the difference between the impurity lattice position and its nearest neighbours, irrespective of the absolute position of the impurity.

The wavefunction can be even brought into the familiar Bloch function form:

$$\begin{aligned}\Psi^n_{\vec{k}}\left(\{\boldsymbol{r}_k\}\right) &= \sum_{\boldsymbol{r}_i,\boldsymbol{a}} \frac{e^{i\vec{k}\cdot\vec{R}_i}}{\lambda_{|\vec{k}\rangle}\mathcal{Z}N}\psi_{\text{aux}}\left(\{\boldsymbol{r}_d-\boldsymbol{r}_i,\boldsymbol{r}_0-\boldsymbol{r}_i-\boldsymbol{a}\}\right)\\ &= \frac{e^{i\vec{k}\cdot\frac{1}{N}\sum_k \vec{r}_k}}{\lambda_{|\vec{k}\rangle}\mathcal{Z}N}\sum_{\boldsymbol{r}_i,\boldsymbol{a}} e^{-i\vec{k}\cdot\left(\frac{1}{N}\sum_k \boldsymbol{r}_k-\vec{R}_i\right)}\psi_{\text{aux}}\left(\{\boldsymbol{r}_d-\boldsymbol{r}_i,\boldsymbol{r}_0-\boldsymbol{r}_i-\boldsymbol{a}\}\right)\\ &= e^{i\vec{k}\cdot\vec{r}_{\text{COM}}}\eta_{\vec{k}}\left(\{\boldsymbol{r}_k\}\right)\end{aligned} \tag{3.2}$$

where $\boldsymbol{r}_{\text{COM}} = \frac{1}{N}\sum_k \boldsymbol{r}_k$ is the center-of-mass coordinate and

$$\eta_{\vec{k}}\left(\{\boldsymbol{r}_k\}\right) = \frac{1}{\lambda_{|\vec{k}\rangle}\mathcal{Z}N}\sum_{\boldsymbol{r}_i} e^{-i\vec{k}\cdot\left(\frac{1}{N}\sum_k \boldsymbol{r}_k-\vec{R}_i\right)}\psi^n_{\text{aux}}\left(\{\boldsymbol{r}_k-\boldsymbol{r}_i\}\right)\ , \tag{3.3}$$

is the translation symmetric function. This form of the eigenstate allows the interpretation that tuning the Bloch momentum $\vec{k}$ corresponds to a translation of the center of mass of the system (or in this case, of the auxiliary models that comprise the system).

4.3.2 Orthonormality

It is straightforward to show that these states form an orthonormal basis. We start by writing down the inner product of two distinct such states:

$$\begin{aligned}\langle\Psi_{\vec{k}'}|\Psi_{\vec{k}}\rangle &= \frac{1}{\lambda^*_{|\vec{k}'\rangle}\lambda_{|\vec{k}\rangle}\mathcal{Z}^2N^2}\sum_{\boldsymbol{r}_i,\boldsymbol{r}_j,\boldsymbol{a},\boldsymbol{a}'} e^{i\left(\vec{k}\cdot\vec{R}_i-\vec{k}'\cdot\vec{R}_j\right)}\langle\psi_{\text{aux}}\left(\boldsymbol{r}_j,\boldsymbol{a}'\right)|\psi_{\text{aux}}\left(\boldsymbol{r}_i,\boldsymbol{a}\right)\rangle\\ &= \frac{1}{\lambda^*_{|\vec{k}'\rangle}\lambda_{|\vec{k}\rangle}\mathcal{Z}^2N^2}\sum_{\boldsymbol{r}_i,\boldsymbol{r}_j,\boldsymbol{a},\boldsymbol{a}'} e^{i\left(\vec{k}\cdot\vec{R}_i-\vec{k}'\cdot\vec{R}_j\right)}\langle\psi_{\text{aux}}\left(\boldsymbol{r}_0,\boldsymbol{a}'\right)T^\dagger\left(\boldsymbol{r}_0-\boldsymbol{r}_j\right)T\left(\boldsymbol{r}_0-\boldsymbol{r}_i\right)|\psi_{\text{aux}}\left(\boldsymbol{r}_0,\boldsymbol{a}\right)\rangle\end{aligned} \tag{3.4}$$

At this point, we insert a complete basis of momentum eigenkets $1 = \sum_{\vec{q}}|\vec{q}\rangle\langle\vec{q}|$ to resolve the translation operators:

$$\begin{aligned}\langle\Psi_{\vec{k}'}|\Psi_{\vec{k}}\rangle &= \frac{1}{\lambda^*_{|\vec{k}'\rangle}\lambda_{|\vec{k}\rangle}\mathcal{Z}^2N^2}\sum_{\boldsymbol{r}_i,\boldsymbol{r}_j,\boldsymbol{a},\boldsymbol{a}',\vec{q}} e^{i\left(\vec{k}\cdot\vec{R}_i-\vec{k}'\cdot\vec{R}_j\right)}\langle\psi_{\text{aux}}\left(\boldsymbol{r}_0,\boldsymbol{a}'\right)T\left(\boldsymbol{r}_j-\boldsymbol{r}_i\right)|\vec{q}\rangle\langle\vec{q}|\psi_{\text{aux}}\left(\boldsymbol{r}_0,\boldsymbol{a}\right)\rangle\\ &= \frac{1}{\lambda^*_{|\vec{k}'\rangle}\lambda_{|\vec{k}\rangle}\mathcal{Z}^2N^2}\sum_{\boldsymbol{r}_i,\boldsymbol{r}_j,\boldsymbol{a},\boldsymbol{a}',\vec{q}} e^{i\left(\vec{k}\cdot\vec{R}_i-\vec{k}'\cdot\vec{R}_j\right)}\langle\psi_{\text{aux}}\left(\boldsymbol{r}_0,\boldsymbol{a}'\right)e^{i\vec{q}\cdot\left(\boldsymbol{r}_j-\boldsymbol{r}_i\right)}|\vec{q}\rangle\langle\vec{q}|\psi_{\text{aux}}\left(\boldsymbol{r}_0,\boldsymbol{a}\right)\rangle\\ &= \frac{1}{|\lambda_{|\vec{k}\rangle}|^2\mathcal{Z}^2}\delta_{\vec{k},\vec{k}'}\sum_{\boldsymbol{a},\boldsymbol{a}'}\langle\psi_{\text{aux}}\left(\boldsymbol{r}_0,\boldsymbol{a}'\right)|\vec{k}\rangle\langle\vec{k}|\psi_{\text{aux}}\left(\boldsymbol{r}_0,\boldsymbol{a}\right)\rangle\end{aligned} \tag{3.5}$$

At the last step, we used the summation form of the Kronecker delta function: $\sum_{\boldsymbol{r}_i} e^{i\boldsymbol{r}_i\left(\vec{k}-\vec{q}\right)}\sum_{\boldsymbol{r}_j} e^{i\boldsymbol{r}_j\left(\vec{q}-\vec{k}'\right)} = N\delta_{\vec{k},\vec{q}}N\delta_{\vec{k}',\vec{q}}$. The final remaining step is to identify that the inner products inside the summation

are actually independent of the direction $\boldsymbol{a}, \boldsymbol{a}'$ of the connecting vector, and both are equal to the normalisation factor $\lambda_{|\vec{k}\rangle}$:

$$\langle\Psi_{\vec{k}'}|\Psi_{\vec{k}}\rangle = \frac{1}{|\lambda_{|\vec{k}\rangle}|^2\mathcal{Z}^2}\delta_{\vec{k},\vec{k}'}\sum_{\boldsymbol{a},\boldsymbol{a}'}|\lambda_{|\vec{k}\rangle}|^2 = \frac{1}{|\lambda_{|\vec{k}\rangle}|^2\mathcal{Z}^2}\delta_{\vec{k},\vec{k}'}w^2|\lambda_{|\vec{k}\rangle}|^2 = \delta_{\vec{k},\vec{k}'} \tag{3.6}$$

This concludes the proof of orthonormality.

4.3.3 Eigenstates

To demonstrate that these are indeed eigenstates of the bulk Hamiltonian, we will calculate the matrix elements of the full Hamiltonian between these states:

$$\begin{aligned}
\langle\Psi_{\vec{k}'}|\,H_{\text{H-H}}\,|\Psi_{\vec{k}}\rangle &= \frac{1}{\lambda^*_{|\vec{k}'\rangle}\lambda_{|\vec{k}\rangle}\mathcal{Z}^2N^2}\sum_{\boldsymbol{r}_i,\boldsymbol{r}_j,\boldsymbol{r}_k,\boldsymbol{a},\boldsymbol{a}'} e^{i\left(\vec{k}\cdot\vec{R}_i-\vec{k}'\cdot\vec{R}_j\right)}\langle\psi_{\text{aux}}\left(\boldsymbol{r}_j,\boldsymbol{a}'\right)|\,H_{\text{aux}}\left(\boldsymbol{r}_k\right)|\psi_{\text{aux}}\left(\boldsymbol{r}_i,\boldsymbol{a}\right)\rangle \\
&= \frac{1}{\lambda^*_{|\vec{k}'\rangle}\lambda_{|\vec{k}\rangle}\mathcal{Z}^2N^2}\sum_{\boldsymbol{r}_i,\boldsymbol{r}_j,\boldsymbol{r}_k,\boldsymbol{a},\boldsymbol{a}'} e^{i\left(\vec{k}\cdot\vec{R}_i-\vec{k}'\cdot\vec{R}_j\right)}\langle\psi_{\text{aux}}\left(\boldsymbol{r}_0,\boldsymbol{a}'\right)|\,T^\dagger_{\boldsymbol{r}_0-\boldsymbol{r}_j}T_{\boldsymbol{r}_0-\boldsymbol{r}_k}H_{\text{aux}}\left(\boldsymbol{r}_0\right)T^\dagger_{\boldsymbol{r}_0-\boldsymbol{r}_k}T_{\boldsymbol{r}_0-\boldsymbol{r}_i}\,|\psi_{\text{aux}}\left(\boldsymbol{r}_0,\boldsymbol{a}\right)\rangle \\
&= \frac{1}{\lambda^*_{|\vec{k}'\rangle}\lambda_{|\vec{k}\rangle}\mathcal{Z}^2N^2}\sum_{\boldsymbol{r}_i,\boldsymbol{r}_j,\boldsymbol{r}_k,\boldsymbol{a},\boldsymbol{a}'} e^{i\left(\vec{k}\cdot\vec{R}_i-\vec{k}'\cdot\vec{R}_j\right)}\langle\psi_{\text{aux}}\left(\boldsymbol{r}_0,\boldsymbol{a}'\right)|\,T^\dagger_{\boldsymbol{r}_k-\boldsymbol{r}_j}H_{\text{aux}}\left(\boldsymbol{r}_0\right)T_{\boldsymbol{r}_k-\boldsymbol{r}_i}\,|\psi_{\text{aux}}\left(\boldsymbol{r}_0,\boldsymbol{a}\right)\rangle
\end{aligned} \tag{3.7}$$

To resolve the translation operators, we will now insert the momentum eigenstates $|\vec{k}\rangle$ of the full model: $1 = \sum_{\vec{q}}|\vec{q}\rangle\langle\vec{q}|$ in between the operators.

$$\begin{aligned}
\langle\Psi_{\vec{k}'}|\,H_{\text{H-H}}\,|\Psi_{\vec{k}}\rangle &= \sum_{\substack{\boldsymbol{r}_i,\boldsymbol{r}_j,\boldsymbol{r}_k,\\ \boldsymbol{a},\boldsymbol{a}',\vec{q},\vec{q}'}}\frac{e^{i\left(\vec{k}\cdot\vec{R}_i-\vec{k}'\cdot\vec{R}_j\right)}}{\lambda^*_{|\vec{k}'\rangle}\lambda_{|\vec{k}\rangle}\mathcal{Z}^2N^2}\langle\psi_{\text{aux}}\left(\boldsymbol{r}_0,\boldsymbol{a}'\right)|\vec{q}'\rangle\langle\vec{q}'|\,T^\dagger_{\boldsymbol{r}_k-\boldsymbol{r}_j}H_{\text{aux}}\left(\boldsymbol{r}_0\right)T_{\boldsymbol{r}_k-\boldsymbol{r}_i}\,|\vec{q}\rangle\langle\vec{q}|\psi_{\text{aux}}\left(\boldsymbol{r}_0,\boldsymbol{a}\right)\rangle \\
&= \sum_{\substack{\boldsymbol{r}_i,\boldsymbol{r}_j,\boldsymbol{r}_k,\\ \boldsymbol{a},\boldsymbol{a}',\vec{q},\vec{q}'}}\frac{e^{i\left(\vec{k}\cdot\vec{R}_i-\vec{k}'\cdot\vec{R}_j\right)}}{\lambda^*_{|\vec{k}'\rangle}\lambda_{|\vec{k}\rangle}\mathcal{Z}^2N^2}\langle\psi_{\text{aux}}\left(\boldsymbol{r}_0,\boldsymbol{a}'\right)|\vec{q}'\rangle\,e^{-i\vec{q}'\cdot\left(\boldsymbol{r}_k-\boldsymbol{r}_j\right)}e^{i\vec{q}\cdot\left(\boldsymbol{r}_k-\boldsymbol{r}_i\right)}\langle\vec{q}'|H_{\text{aux}}\left(\boldsymbol{r}_0\right)|\vec{q}\rangle\langle\vec{q}|\psi_{\text{aux}}\left(\boldsymbol{r}_0,\boldsymbol{a}\right)\rangle \\
&= \frac{N}{\lambda^*_{|\vec{k}'\rangle}\lambda_{|\vec{k}\rangle}\mathcal{Z}^2}\sum_{\boldsymbol{a},\boldsymbol{a}',\vec{q},\vec{q}'}\delta_{\vec{k},\vec{q}}\delta_{\vec{q},\vec{q}'}\delta_{\vec{q}',\vec{k}}\langle\psi_{\text{aux}}\left(\boldsymbol{r}_0,\boldsymbol{a}'\right)|\vec{q}'\rangle\langle\vec{q}'|H_{\text{aux}}\left(\boldsymbol{r}_0\right)|\vec{q}\rangle\langle\vec{q}|\psi_{\text{aux}}\left(\boldsymbol{r}_0,\boldsymbol{a}\right)\rangle \\
&= \frac{N}{|\lambda_{|\vec{k}\rangle}|^2\mathcal{Z}^2}\delta_{kk'}\sum_{\boldsymbol{a},\boldsymbol{a}'}\langle\psi_{\text{aux}}\left(\boldsymbol{r}_0,\boldsymbol{a}'\right)|\vec{k}\rangle\langle\vec{k}|H_{\text{aux}}\left(\boldsymbol{r}_0\right)|\vec{k}\rangle\langle\vec{k}|\psi_{\text{aux}}\left(\boldsymbol{r}_0,\boldsymbol{a}\right)\rangle \\
&= \frac{N}{|\lambda_{|\vec{k}\rangle}|^2\mathcal{Z}^2}\delta_{kk'}\langle\vec{k}|H_{\text{aux}}\left(\boldsymbol{r}_0\right)|\vec{k}\rangle\underbrace{\sum_{\boldsymbol{a},\boldsymbol{a}'}\langle\psi_{\text{aux}}\left(\boldsymbol{r}_0,\boldsymbol{a}'\right)|\vec{k}\rangle\langle\vec{k}|\psi_{\text{aux}}\left(\boldsymbol{r}_0,\boldsymbol{a}\right)\rangle}_{w^2|\lambda_{|\vec{k}\rangle}|^2} \\
&= N\delta_{kk'}\langle\vec{k}|H_{\text{aux}}\left(\boldsymbol{r}_0\right)|\vec{k}\rangle
\end{aligned} \tag{3.8}$$

The momentum eigenket $|\vec{k}\rangle$ can be expressed as a sum over position eigenkets at varying distances from $\boldsymbol{r}_0$. This form allows a systematic method of improving the energy eigenvalue estimate, because the interacting in the impurity model is extremely localised, so the overlap between two auxiliary models decreases rapidly with distance. The majority of the contribution will come from the state at $\boldsymbol{r}_0$, and improvements are then made by considering auxiliary models at further distances.

4.4 Mapping Greens Functions from Auxiliary Model to Lattice Model

4.4.1 One-particle $k-$space Greens functions

In the previous part, we proposed a form for the eigenstates $|\Psi_s\rangle$ of the bulk Hamiltonian in terms of the ground-states $|\psi_n\rangle$ of the auxiliary models. In this section, we will relate one-particle Greens functions of the lattice model to those of the auxiliary model. We define the retarded time-domain lattice $k-$space Greens function at zero temperature as

$$G(\boldsymbol{k}\sigma;t) = -i\theta(t)\,\langle\Psi_{\rm gs}|\{c_{\boldsymbol{k}\sigma}(t), c^{\dagger}_{\boldsymbol{k}\sigma}\}|\Psi_{\rm gs}\rangle \ . \tag{4.1}$$

where $|\Psi_{\rm gs}\rangle$ is the lattice groundstate. Time evolution of the operators is governed by the lattice Hamiltonian $H_{\rm latt}$:

$$c_{\boldsymbol{k}\sigma}(t) = e^{itH_{\rm latt}} c_{\boldsymbol{k}\sigma} e^{-itH_{\rm latt}} \ . \tag{4.2}$$

By using eq. 2.8 and the fact that the translation operators commute with $H_{\rm latt}$, we have the relation

$$T\,(\vec{a})\,c(\boldsymbol{k})(t)T^{\dagger}\,(\vec{a}) = e^{-i\boldsymbol{k}\cdot\vec{a}}c(\boldsymbol{k})(t)\ , \tag{4.3}$$

which combined with eq. 2.8 gives

$$T\,(\boldsymbol{a})\,c(\boldsymbol{k})(t)c^{\dagger}(\boldsymbol{k})T^{\dagger}\,(\boldsymbol{b}) = e^{i\boldsymbol{k}\cdot(\boldsymbol{b}-\boldsymbol{a})}c(\boldsymbol{k})(t)T^{\dagger}(\boldsymbol{b}-\boldsymbol{a})c^{\dagger}(\boldsymbol{k})\ . \tag{4.4}$$

In order to make use of the mapping between auxiliary model and lattice model Hamiltonians, we would like to express this lattice Greens function in terms of auxiliary model Greens functions – objects that can be computed purely from within a single auxiliary model. This will be a major simplification in our computations, because it is easier to work with a quantum impurity model, as compared to an interacting lattice model.

To make progress towards this, we consider the equivalent object

$$G(\boldsymbol{k}\sigma;t) = -i\theta(t)\frac{1}{2}\left[\langle\Psi_{\rm gs}|\{c_{\boldsymbol{k}\sigma}(t), c^{\dagger}_{\boldsymbol{k}\sigma}\}|\Psi_{\rm gs}\rangle + \langle\Psi_{\rm gs}|\{c_{\boldsymbol{k}\sigma}, c^{\dagger}_{\boldsymbol{k}\sigma}(-t)\}|\Psi_{\rm gs}\rangle\right] \ . \tag{4.5}$$

We consider only the first term for now. We express the lattice groundstate in terms of the auxiliary model groundstates (using eq. 2.20):

$$\langle\Psi_{\rm gs}|\{c_{\boldsymbol{k}\sigma}(t), c^{\dagger}_{\boldsymbol{k}\sigma}\}|\Psi_{\rm gs}\rangle = \frac{1}{N}\sum_{\boldsymbol{r}_1,\boldsymbol{r}_2}\langle\psi_{\rm gs}(\boldsymbol{r}_2)|\{c_{\boldsymbol{k}\sigma}(t), c^{\dagger}_{\boldsymbol{k}\sigma}\}|\psi_{\rm gs}(\boldsymbol{r}_1)\rangle \ . \tag{4.6}$$

We take one of the terms in the anticommutator and proceed to simplify it:

$$\begin{aligned}\sum_{\boldsymbol{r}_1,\boldsymbol{r}_2}\langle\psi_{\rm gs}(\boldsymbol{r}_2)|c_{\boldsymbol{k}\sigma}(t)c^\dagger_{\boldsymbol{k}\sigma}|\psi_{\rm gs}(\boldsymbol{r}_1)\rangle &= \sum_{\boldsymbol{r}_1,\boldsymbol{r}_2}\langle\psi_{\rm gs}(\boldsymbol{r}_d)|T(\boldsymbol{r}_2-\boldsymbol{r}_d)c_{\boldsymbol{k}\sigma}(t)c^\dagger_{\boldsymbol{k}\sigma}T^\dagger(\boldsymbol{r}_1-\boldsymbol{r}_d)|\psi_{\rm gs}(\boldsymbol{r}_d)\rangle\\ &= \sum_{\boldsymbol{r}_1,\boldsymbol{r}_2} e^{i\boldsymbol{k}(\boldsymbol{r}_1-\boldsymbol{r}_2)}\,\langle\psi_{\rm gs}(\boldsymbol{r}_d)|c_{\boldsymbol{k}\sigma}(t)T^\dagger(\boldsymbol{r}_1-\boldsymbol{r}_2)c^\dagger_{\boldsymbol{k}\sigma}|\psi_{\rm gs}(\boldsymbol{r}_d)\rangle\\ &= N\sum_{\boldsymbol{r}} e^{i\boldsymbol{k}\cdot\boldsymbol{r}}\,\langle\psi_{\rm gs}(\boldsymbol{r}_d)|c_{\boldsymbol{k}\sigma}(t)T^\dagger(\boldsymbol{r})c^\dagger_{\boldsymbol{k}\sigma}|\psi_{\rm gs}(\boldsymbol{r}_d)\rangle\ .\end{aligned} \tag{4.7}$$

where $\boldsymbol{r}_d$ is a reference lattice site, and we used eq. 4.4 in the second step. The other term in the anticommutator gives

$$\begin{aligned}\sum_{\boldsymbol{r}_1,\boldsymbol{r}_2}\langle\psi_{\rm gs}(\boldsymbol{r}_2)|c^\dagger_{\boldsymbol{k}\sigma}c_{\boldsymbol{k}\sigma}(t)|\psi_{\rm gs}(\boldsymbol{r}_1)\rangle &= \sum_{\boldsymbol{r}_1,\boldsymbol{r}_2}\langle\psi_{\rm gs}(\boldsymbol{r}_d)|T(\boldsymbol{r}_2-\boldsymbol{r}_d)c^\dagger_{\boldsymbol{k}\sigma}c_{\boldsymbol{k}\sigma}(t)T^\dagger(\boldsymbol{r}_1-\boldsymbol{r}_d)|\psi_{\rm gs}(\boldsymbol{r}_d)\rangle\\ &= \sum_{\boldsymbol{r}_1,\boldsymbol{r}_2} e^{-i\boldsymbol{k}(\boldsymbol{r}_1-\boldsymbol{r}_2)}\,\langle\psi_{\rm gs}(\boldsymbol{r}_d)|c^\dagger_{\boldsymbol{k}\sigma}T^\dagger(\boldsymbol{r}_1-\boldsymbol{r}_2)c_{\boldsymbol{k}\sigma}(t)|\psi_{\rm gs}(\boldsymbol{r}_d)\rangle\\ &= N\sum_{\boldsymbol{r}} e^{-i\boldsymbol{k}\cdot\boldsymbol{r}}\,\langle\psi_{\rm gs}(\boldsymbol{r}_d)|c^\dagger_{\boldsymbol{k}\sigma}T^\dagger(\boldsymbol{r})c_{\boldsymbol{k}\sigma}(t)|\psi_{\rm gs}(\boldsymbol{r}_d)\rangle\ .\end{aligned} \tag{4.8}$$

To resolve the time evolution of the operators, we insert $1=\sum_m|\psi_m(\boldsymbol{r}_d)\rangle\langle\psi_m(\boldsymbol{r}_d)|$ into the equation. We again work with just the first term of the anticommutator for convenience:

$$\begin{aligned}&\sum_{\boldsymbol{r}_1,\boldsymbol{r}_2}\langle\psi_{\rm gs}(\boldsymbol{r}_2)|c_{\boldsymbol{k}\sigma}(t)c^\dagger_{\boldsymbol{k}\sigma}|\psi_{\rm gs}(\boldsymbol{r}_1)\rangle\\ &= N\sum_{\boldsymbol{r},n_1,n_2} e^{i\boldsymbol{k}\cdot\boldsymbol{r}}\,\langle\psi_{\rm gs}(\boldsymbol{r}_d)|c_{\boldsymbol{k}\sigma}(t)\,|\psi_{n_1}(\boldsymbol{r}_d)\rangle\langle\psi_{n_1}(\boldsymbol{r}_d)|\,T^\dagger(\boldsymbol{r})\,|\psi_{n_2}(\boldsymbol{r}_d)\rangle\langle\psi_{n_2}(\boldsymbol{r}_d)|\,c^\dagger_{\boldsymbol{k}\sigma}|\psi_{\rm gs}(\boldsymbol{r}_d)\rangle\\ &= N\sum_{\boldsymbol{r},n_1,n_2} e^{i\boldsymbol{k}\cdot\boldsymbol{r}}\,\langle\psi_{\rm gs}(\boldsymbol{r}_d)|c_{\boldsymbol{k}\sigma}(t)\,|\psi_{n_1}(\boldsymbol{r}_d)\rangle\langle\psi_{n_1}(\boldsymbol{r}_d)|\psi_{n_2}(\boldsymbol{r}_d+\boldsymbol{r})\rangle\langle\psi_{n_2}(\boldsymbol{r}_d)|\,c^\dagger_{\boldsymbol{k}\sigma}|\psi_{\rm gs}(\boldsymbol{r}_d)\rangle\ .\end{aligned} \tag{4.9}$$

The overlap $\langle\psi_{n_1}(\boldsymbol{r}_d)|\psi_{n_2}(\boldsymbol{r}_d+\boldsymbol{r})\rangle$ between the eigenstates of the auxiliary models at $\boldsymbol{r}_d$ and $\boldsymbol{r}_d+\boldsymbol{r}$ are appreciable only for $n_1=n_2$. This is because, for small $\boldsymbol{r}$, the auxiliary models are very similar and the states are therefore almost orthogonal. For large $\boldsymbol{r}$, the overlap is again suppressed because the auxiliary model eigenstates are localised around the impurity. We therefore make the simplifying assumption: $\langle\psi_{n_1}(\boldsymbol{r}_d)|\psi_{n_2}(\boldsymbol{r}_d+\boldsymbol{r})\rangle=\delta_{n_1,n_2}\langle\psi_{n_1}(\boldsymbol{r}_d)|\psi_{n_1}(\boldsymbol{r}_d+\boldsymbol{r})\rangle=\delta_{n_1,n_2}F_{n_1}(\boldsymbol{r})$. Substituting this, we get

$$\sum_{\boldsymbol{r}_1,\boldsymbol{r}_2}\langle\psi_{\rm gs}(\boldsymbol{r}_2)|c_{\boldsymbol{k}\sigma}(t)c^\dagger_{\boldsymbol{k}\sigma}|\psi_{\rm gs}(\boldsymbol{r}_1)\rangle = N\sum_n F_n(\boldsymbol{k})\,\langle\psi_{\rm gs}(\boldsymbol{r}_d)|c_{\boldsymbol{k}\sigma}(t)\,|\psi_n(\boldsymbol{r}_d)\rangle\langle\psi_n(\boldsymbol{r}_d)|\,c^\dagger_{\boldsymbol{k}\sigma}|\psi_{\rm gs}(\boldsymbol{r}_d)\rangle\ , \tag{4.10}$$

where we have defined the Fourier transform $F_n(\boldsymbol{k})=\sum_{\boldsymbol{r}}e^{i\boldsymbol{k}\cdot\boldsymbol{r}}F_n(\boldsymbol{r})$ of the overlap function.

We now consider more carefully the transition operator $c_{\boldsymbol{k}\sigma}$ for the 1-particle excitation giving rise to the above Greens function. Within our auxiliary model approach, gapless excitations within the lattice model are represented by gapless excitations of the impurity site, specifically those that try to screen the impurity site. As a result, the uncoordinated scattering process $c_{\boldsymbol{k}\sigma}$ for the lattice

model must be replaced by a coherent excitation $\mathcal{T}$ within the impurity model that captures those gapless excitations that occur in connection with the impurity, and projects out the uncorrelated excitations that take place even when the impurity site is decoupled from the bath.

In order to construct this auxiliary model $\mathcal{T}-$matrix, we allow for all excitations of the impurity site in conjunction with those of the $k-$state:

$$\mathcal{T}_{k,\sigma} = \left[c^{\dagger}_{r_d\sigma} + S^{\sigma}_{r_d} + C^{+}_{r_d}\right] c_{k\sigma} \ , \tag{4.11}$$

where $S^{+}_{r_d}$ and $C^{+}_{r_d}$ are spin and charge flip operators on the impurity site that cause transition from $|\downarrow\rangle \rightarrow |\uparrow\rangle$ and $|0\rangle \rightarrow |\uparrow\downarrow\rangle$ respectively.

Apart from modifying the excitation operator, we will now simplify the time-evolution as well. The first overlap on the right-hand side of eq. 4.10 expands to

$$\langle\psi_{\rm gs}(\boldsymbol{r}_d)|\mathcal{T}_{\boldsymbol{k},\sigma}(t)|\psi_n(\boldsymbol{r}_d)\rangle = \langle\psi_{\rm gs}(\boldsymbol{r}_d)|e^{i(H_{\rm aux}(\boldsymbol{r}_d)+H_{\rm cav}(\boldsymbol{r}_d))t}\mathcal{T}_{\boldsymbol{k},\sigma}e^{-i(H_{\rm aux}(\boldsymbol{r}_d)+H_{\rm cav}(\boldsymbol{r}_d))t}|\psi_n(\boldsymbol{r}_d)\rangle \ , \tag{4.12}$$

where $H_{\rm aux}(\boldsymbol{r}_d)$ (eq. 1.3) is the auxiliary model Hamiltonian consisting of the cluster Hamiltonian $H_{\rm clust}(\boldsymbol{r}_d)$ along with all one-particle terms $H_{\rm 1p}$ in the Hamiltonian (in a typical lattice model, this will be he tight-binding hopping terms), and $H_{\rm cav}(\boldsymbol{r}_d)$ is the "cavity" Hamiltonian consisting of all interaction (2-particle and beyond) terms in the Hamiltonian. Together, they create the full lattice Hamiltonian: $H_{\rm latt} = H_{\rm aux}(\boldsymbol{r}_d) + H_{\rm cav}(\boldsymbol{r}_d)$. Using the Zassenhaus form of the Baker-Campbell-Hausdorff formula, we have

$$e^{i(H_{\rm aux}(\boldsymbol{r}_d)+H_{\rm cav}(\boldsymbol{r}_d))t} \approx e^{iH_{\rm aux}(\boldsymbol{r}_d)t}e^{iH_{\rm cav}(\boldsymbol{r}_d)t}e^{[H_{\rm aux}(\boldsymbol{r}_d),\, H_{\rm cav}(\boldsymbol{r}_d)]t^2/2} \ , \tag{4.13}$$

where we have dropped the higher-order terms because the commutators involve only the boundary degrees of freedom and become subsequently smaller as the order increases. One can think of the operator $e^{iH_{\rm cav}(\boldsymbol{r}_d)t}e^{[H_{\rm aux}(\boldsymbol{r}_d),\, H_{\rm cav}(\boldsymbol{r}_d)]t^2/2}$ as renormalising the auxiliary model $\mathcal{T}-$matrix through hybridisation with the rest of the system and formally leading to a new $\mathcal{T}-$matrix:

$$\mathcal{T}^{*}_{\boldsymbol{k},\sigma} = e^{iH_{\rm cav}(\boldsymbol{r}_d)t}e^{[H_{\rm aux}(\boldsymbol{r}_d),\, H_{\rm cav}(\boldsymbol{r}_d)]t^2/2}\mathcal{T}_{\boldsymbol{k},\sigma}e^{-[H_{\rm aux}(\boldsymbol{r}_d),\, H_{\rm cav}(\boldsymbol{r}_d)]t^2/2}e^{-iH_{\rm cav}(\boldsymbol{r}_d)t} \ . \tag{4.14}$$

One can also absorb the modulating phase factor $F_n(\boldsymbol{k})$ (defined above and appearing in eq. 4.10) into this renormalisation:

$$\mathcal{T}^{*}_{\boldsymbol{k},\sigma} = e^{iH_{\rm cav}(\boldsymbol{r}_d)t}e^{[H_{\rm aux}(\boldsymbol{r}_d),\, H_{\rm cav}(\boldsymbol{r}_d)]t^2/2}\mathcal{T}_{\boldsymbol{k},\sigma}F_n(\boldsymbol{k})\mathcal{P}_n(\boldsymbol{r}_d)\ e^{-[H_{\rm aux}(\boldsymbol{r}_d),\, H_{\rm cav}(\boldsymbol{r}_d)]t^2/2}e^{-iH_{\rm cav}(\boldsymbol{r}_d)t} \ , \tag{4.15}$$

where $\mathcal{P}_n(\boldsymbol{r}_d)$ projects onto the $n^{\rm th}$ eigenstate $|\psi_n(\boldsymbol{r}_d)\rangle$.

Since the overlap is calculated in the eigenstates of the auxiliary model at $\boldsymbol{r}_d$, we adopt the zeroth order approximation of ignoring this renormalisation. Later, we will specify a prescription of systematically improving our computation. The overlap expression becomes

$$\langle\psi_{\rm gs}(\boldsymbol{r}_d)|\mathcal{T}_{\boldsymbol{k},\sigma}(t)|\psi_n(\boldsymbol{r}_d)\rangle = \langle\psi_{\rm gs}(\boldsymbol{r}_d)|e^{i(H_{\rm clust}(\boldsymbol{r}_d)+H_{\rm 1p})t}\mathcal{T}_{\boldsymbol{k},\sigma}e^{-i(H_{\rm clust}(\boldsymbol{r}_d)+H_{\rm 1p})t}|\psi_n(\boldsymbol{r}_d)\rangle \ . \tag{4.16}$$

To make the problem tractable, we treat the effect of $H_{\rm 1p}$ at the level of an expectation value and note that the effect of the transition operator is to create a hole of momentum $\boldsymbol{k}$ (eq. 4.11). Let the

Hamiltonian H_{1p} be diagonal in certain modes $c_{\nu,\sigma}$ with energies ϵ_ν, and the operator $c_{\boldsymbol{k},\sigma}$ can be expressed in terms of these modes: $c_{\boldsymbol{k},\sigma} = \sum_\nu C_{\nu,\boldsymbol{k}} c_{\nu,\sigma}$. Expanding the $\mathcal{T}-$matrix in this fashion gives

$$\langle\psi_{\rm gs}(\boldsymbol{r}_d)|\mathcal{T}_{\boldsymbol{k},\sigma}(t)|\psi_n(\boldsymbol{r}_d)\rangle = \sum_\nu C_{\nu,\boldsymbol{k}} \langle\psi_{\rm gs}(\boldsymbol{r}_d)|e^{i(H_{\rm clust}(\boldsymbol{r}_d)+H_{1p})t}\mathcal{T}_{\nu,\sigma}e^{-i(H_{\rm clust}(\boldsymbol{r}_d)+H_{1p})t}|\psi_n(\boldsymbol{r}_d)\rangle \ . \tag{4.17}$$

Each excitation $\mathcal{T}_{\nu,\sigma}$ therefore leads to an energy cost $-\epsilon_\nu$. Moreover, $|\psi_n(\boldsymbol{r}_d)\rangle$ and $|\psi_{\rm gs}(\boldsymbol{r}_d)\rangle$ are eigenstates of $H_{\rm clust}(\boldsymbol{r}_d)$ with energies E_n and E_0. This leads to the following simplified expression:

$$\langle\psi_{\rm gs}(\boldsymbol{r}_d)|\mathcal{T}_{\boldsymbol{k},\sigma}(t)|\psi_n(\boldsymbol{r}_d)\rangle = \sum_\nu C_{\nu,\boldsymbol{k}} e^{-i(E_n-E_0+\epsilon_\nu)t} \langle\psi_{\rm gs}(\boldsymbol{r}_d)|\mathcal{T}_{\nu,\sigma}|\psi_n(\boldsymbol{r}_d)\rangle \ . \tag{4.18}$$

Substituting the expression back into 4.10 and then into 4.6, we get an expression for one half of the first part of the retarded Greens function (the full form is in eq. 4.5):

$$\begin{aligned} &-i\theta(t)\,\langle\Psi_{\rm gs}|c_{\boldsymbol{k}\sigma}(t)c^\dagger_{\boldsymbol{k}\sigma}|\Psi_{\rm gs}\rangle \\ &= -i\theta(t)\sum_{\nu,n} C_{\nu,\boldsymbol{k}} e^{-i(E_n-E_0+\epsilon_\nu)t} \langle\psi_{\rm gs}(\boldsymbol{r}_d)|\mathcal{T}_{\nu,\sigma}|\psi_n(\boldsymbol{r}_d)\rangle \langle\psi_n(\boldsymbol{r}_d)|\mathcal{T}^\dagger_{\boldsymbol{k},\sigma}|\psi_{\rm gs}(\boldsymbol{r}_d)\rangle \ . \end{aligned} \tag{4.19}$$

Working through the other term of eq. 4.6 with the same strategy, we get the full expression:

$$\begin{aligned} &-i\theta(t)\,\langle\Psi_{\rm gs}|\{c_{\boldsymbol{k}\sigma}(t), c^\dagger_{\boldsymbol{k}\sigma}\}|\Psi_{\rm gs}\rangle \\ &= -i\theta(t)\sum_{\nu,n} C_{\nu,\boldsymbol{k}} e^{-i(E_n-E_0+\epsilon_\nu)t} \langle\psi_{\rm gs}(\boldsymbol{r}_d)|\mathcal{T}_{\nu,\sigma}|\psi_n(\boldsymbol{r}_d)\rangle \langle\psi_n(\boldsymbol{r}_d)|\mathcal{T}^\dagger_{\boldsymbol{k},\sigma}|\psi_{\rm gs}(\boldsymbol{r}_d)\rangle \\ &\quad -i\theta(t)\sum_{\nu,n} C_{\nu,\boldsymbol{k}} e^{i(E_n-E_0-\epsilon_\nu)t} \langle\psi_{\rm gs}(\boldsymbol{r}_d)|\mathcal{T}^\dagger_{\boldsymbol{k},\sigma}|\psi_n(\boldsymbol{r}_d)\rangle \langle\psi_n(\boldsymbol{r}_d)|\mathcal{T}_{\nu,\sigma}|\psi_{\rm gs}(\boldsymbol{r}_d)\rangle \ . \end{aligned} \tag{4.20}$$

Finally, we consider the other term in eq. 4.5, $-i\theta(t)\,\langle\Psi_{\rm gs}|\{c_{\boldsymbol{k}\sigma}, c^\dagger_{\boldsymbol{k}\sigma}(-t)\}|\Psi_{\rm gs}\rangle$. Proceeding in the same way, eq. 4.18 is replaced by

$$\begin{aligned} \langle\psi_n(\boldsymbol{r}_d)|\mathcal{T}^\dagger_{\boldsymbol{k},\sigma}(-t)|\psi_{\rm gs}(\boldsymbol{r}_d)\rangle &= \langle\psi_{\rm gs}(\boldsymbol{r}_d)|\mathcal{T}_{\boldsymbol{k},\sigma}(-t)|\psi_n(\boldsymbol{r}_d)\rangle^* \\ &= \sum_\nu C^*_{\nu,\boldsymbol{k}} e^{-i(E_n-E_0+\epsilon_\nu)t} \langle\psi_n(\boldsymbol{r}_d)|\mathcal{T}^\dagger_{\nu,\sigma}|\psi_{\rm gs}(\boldsymbol{r}_d)\rangle \ . \end{aligned} \tag{4.21}$$

Evaluating this term exactly as before and changing from time to frequency domain using $g(\omega) = \int dt\, e^{i\omega T} f(t)$ gives

$$\begin{aligned} G(\boldsymbol{k},\sigma;\omega) = \sum_{\nu,n} C_{\nu,\boldsymbol{k}} \Bigg[&\frac{\langle\psi_{\rm gs}(\boldsymbol{r}_d)|\mathcal{T}_{\nu,\sigma}|\psi_n(\boldsymbol{r}_d)\rangle \langle\psi_n(\boldsymbol{r}_d)|\mathcal{T}^\dagger_{\boldsymbol{k},\sigma}|\psi_{\rm gs}(\boldsymbol{r}_d)\rangle}{\omega - (E_n - E_0 + \epsilon_\nu)} \\ &+ \frac{\langle\psi_{\rm gs}(\boldsymbol{r}_d)|\mathcal{T}^\dagger_{\boldsymbol{k},\sigma}|\psi_n(\boldsymbol{r}_d)\rangle \langle\psi_n(\boldsymbol{r}_d)|\mathcal{T}_{\nu,\sigma}|\psi_{\rm gs}(\boldsymbol{r}_d)\rangle}{\omega + (E_n - E_0 - \epsilon_\nu)} \Bigg] + \text{h.c.} \end{aligned} \tag{4.22}$$

We recognise the two parts of the lattice Greens function as a retarded off-diagonal Greens functions calculated within the auxiliary model at $\boldsymbol{r}_d$, but at shifted frequencies $\omega - \epsilon_\nu$:

$$G(\boldsymbol{k},\sigma;\omega) = \sum_\nu \left[C_{\nu,\boldsymbol{k}} \mathcal{G}(\mathcal{T}_{\nu,\sigma}, \mathcal{T}^\dagger_{\boldsymbol{k},\sigma}; \omega - \epsilon_\nu) + C^*_{\nu,\boldsymbol{k}} \mathcal{G}(\mathcal{T}_{\boldsymbol{k},\sigma}, \mathcal{T}^\dagger_{\nu,\sigma}; \omega - \epsilon_\nu) \right] \tag{4.23}$$

We now discuss how to systematically improve this estimate. One way is to include the effect of other auxiliary models in the overlap function $F_n(\boldsymbol{r})$. This will of course require us to calculate an off-diagonal Greens function. As a concrete example, upon including the effects of the auxiliary models nearest to the reference point $\boldsymbol{r}_d$, the expression for the Greens function becomes

$$\begin{aligned} G(\boldsymbol{k},\sigma;\omega) = \sum_{\nu,n} C_{\nu,\boldsymbol{k}} \Bigg[& \frac{\langle \psi_{\rm gs}(\boldsymbol{r}_d)|\mathcal{T}^*_{\nu,\sigma}|\psi_n(\boldsymbol{r}_d)\rangle \langle \psi_n(\boldsymbol{r}_d)|\mathcal{T}^\dagger_{\boldsymbol{k},\sigma}|\psi_{\rm gs}(\boldsymbol{r}_d)\rangle}{\omega - \epsilon_\nu - (E_n - E_0)} \\ & + \frac{\langle \psi_{\rm gs}(\boldsymbol{r}_d)|\mathcal{T}^\dagger_{\boldsymbol{k},\sigma}|\psi_n(\boldsymbol{r}_d)\rangle \langle \psi_n(\boldsymbol{r}_d)|\mathcal{T}^*_{\nu,\sigma}|\psi_{\rm gs}(\boldsymbol{r}_d)\rangle}{\omega - \epsilon_\nu + (E_n - E_0)} \Bigg] , \end{aligned} \tag{4.24}$$

with $\tau^*_{\nu,\sigma} = \mathcal{T}_{\nu,\sigma}(F_n(0) + \sum_{\boldsymbol{a}} F_n(\boldsymbol{a}) e^{i\boldsymbol{k}\cdot\boldsymbol{a}})$ where $\boldsymbol{a}$ sums over the primitive lattice vectors. Another way to include more non-local contributions is by considering the effects of the cavity Hamiltonian in eq. 4.15:

$$\mathcal{T}^*_{\boldsymbol{k},\sigma}(t) = e^{iH_{\rm cav}(\boldsymbol{r}_d)t}(\mathcal{T}_{\boldsymbol{k},\sigma} + t^2/2 \left[[H_{\rm aux}(\boldsymbol{r}_d),\ H_{\rm cav}(\boldsymbol{r}_d)], \mathcal{T}_{\boldsymbol{k},\sigma} \right]) e^{-iH_{\rm cav}(\boldsymbol{r}_d)t} . \tag{4.25}$$

The time-domain Greens function associated with this operator will then need to be calculated, which can then be used to calculate frequency-domain functions.

4.4.2 One-particle real-space Greens functions

We now work with Greens functions for real-space excitations. The retarded Greens function in this case is

$$G(\boldsymbol{r}\sigma;t) = -i\theta(t) \langle \Psi_{\rm gs}|\{c_{\boldsymbol{r}_d+\boldsymbol{r},\sigma}(t), c^\dagger_{\boldsymbol{r}_d,\sigma}\}|\Psi_{\rm gs}\rangle . \tag{4.26}$$

Since our lattice model has discrete translation symmetry, we instead calculate the equivalent quantity

$$G(\boldsymbol{r}\sigma;t) = -i\theta(t)\frac{1}{2}\sum_{\boldsymbol{r}_d} \left[\langle \Psi_{\rm gs}|\{c_{\boldsymbol{r}_d+\boldsymbol{r},\sigma}(t), c^\dagger_{\boldsymbol{r}_d,\sigma}\}|\Psi_{\rm gs}\rangle + \langle \Psi_{\rm gs}|\{c_{\boldsymbol{r}_d+\boldsymbol{r},\sigma}, c^\dagger_{\boldsymbol{r}_d,\sigma}(-t)\}|\Psi_{\rm gs}\rangle \right] . \tag{4.27}$$

Similar to the $k-$space Greens functions, we consider only the first term for now, and express the groundstates as a superposition of auxiliary model Greens functions:

$$\begin{aligned} \sum_{\boldsymbol{r}_d} \langle \Psi_{\rm gs}|c_{\boldsymbol{r}_d+\boldsymbol{r},\sigma}(t)c^\dagger_{\boldsymbol{r}_d,\sigma}|\Psi_{\rm gs}\rangle &= \frac{1}{N}\sum_{\boldsymbol{R},\boldsymbol{\Delta},\boldsymbol{r}_d} \langle \psi_{\rm gs}(\boldsymbol{R}+\boldsymbol{\Delta})|c_{\boldsymbol{r}_d+\boldsymbol{r},\sigma}(t)c^\dagger_{\boldsymbol{r}_d,\sigma}|\psi_{\rm gs}(\boldsymbol{R})\rangle \\ &= \frac{1}{N}\sum_{\boldsymbol{R},\boldsymbol{\Delta}} \langle \psi_{\rm gs}(-\boldsymbol{r}_d)|c_{\boldsymbol{r}-\boldsymbol{R}-\boldsymbol{\Delta},\sigma}(t)T(\boldsymbol{\Delta})c^\dagger_{-\boldsymbol{R},\sigma}|\psi_{\rm gs}(-\boldsymbol{r}_d)\rangle . \end{aligned} \tag{4.28}$$

Local Greens function: $\boldsymbol{r} = 0$

We first consider the case of local Greens function, by setting $\boldsymbol{r} = 0$. We also change the dummy variable $\boldsymbol{r}_d$, $\boldsymbol{R}$ and Δ to $-\boldsymbol{r}_d$, $\boldsymbol{R}$ and $-\boldsymbol{\Delta}$ to make the expressions tidier:

$$\sum_{\boldsymbol{r}_d} \langle \Psi_{\rm gs}| c_{\boldsymbol{r}_d,\sigma}(t) c^{\dagger}_{\boldsymbol{r}_d,\sigma} |\Psi_{\rm gs}\rangle = \frac{1}{N} \sum_{\boldsymbol{R},\boldsymbol{\Delta},\boldsymbol{r}_d} \langle \psi_{\rm gs}(\boldsymbol{r}_d)| c_{\boldsymbol{R}+\boldsymbol{\Delta},\sigma}(t) T^{\dagger}(\boldsymbol{\Delta}) c^{\dagger}_{\boldsymbol{R},\sigma} |\psi_{\rm gs}(\boldsymbol{r}_d)\rangle \ . \tag{4.29}$$

We split the full summation into four parts, based on whether $\boldsymbol{R} = \boldsymbol{r}_d$ and whether $\Delta + \boldsymbol{R} = \boldsymbol{r}_d$:

$$\begin{aligned}\sum_{\boldsymbol{r}_d} \langle \Psi_{\rm gs}| c_{\boldsymbol{r}_d,\sigma}(t) c^{\dagger}_{\boldsymbol{r}_d,\sigma} |\Psi_{\rm gs}\rangle &= \langle \psi_{\rm gs}(\boldsymbol{r}_d)| c_{\boldsymbol{r}_d,\sigma}(t) c^{\dagger}_{\boldsymbol{r}_d,\sigma} |\psi_{\rm gs}(\boldsymbol{r}_d)\rangle \\ &+ \sum_{\boldsymbol{\Delta}\neq 0} \langle \psi_{\rm gs}(\boldsymbol{r}_d)| c_{\boldsymbol{r}_d+\boldsymbol{\Delta},\sigma}(t) T^{\dagger}(\boldsymbol{\Delta}) c^{\dagger}_{\boldsymbol{r}_d,\sigma} |\psi_{\rm gs}(\boldsymbol{r}_d)\rangle \\ &+ \sum_{\boldsymbol{R}\neq \boldsymbol{r}_d} \langle \psi_{\rm gs}(\boldsymbol{r}_d)| c_{\boldsymbol{r}_d,\sigma}(t) T^{\dagger}(\boldsymbol{r}_d - \boldsymbol{R}) c^{\dagger}_{\boldsymbol{R},\sigma} |\psi_{\rm gs}(\boldsymbol{r}_d)\rangle \\ &+ \sum_{\boldsymbol{R}\neq \boldsymbol{r}_d, \boldsymbol{\Delta}\neq \boldsymbol{r}_d} \langle \psi_{\rm gs}(\boldsymbol{r}_d)| c_{\boldsymbol{\Delta},\sigma}(t) T^{\dagger}(\boldsymbol{\Delta} - \boldsymbol{R}) c^{\dagger}_{\boldsymbol{R},\sigma} |\psi_{\rm gs}(\boldsymbol{r}_d)\rangle \ ,\end{aligned} \tag{4.30}$$

where we have used the fact that the location of the auxiliary model does not affect the correlation calculated within the auxiliary model in order to cancel out the summation over $\boldsymbol{r}_d$ with the factor of $1/N$. The reason for splitting the expression into these parts is to explicitly write out which operators act on the impurity site $\boldsymbol{r}_d$ and which act on other real-space sites away from the impurity site. We will now replace the real-space excitation operators away from the impurity site with the associated $T-$matrices, following the discussion above eq. 4.11:

$$\mathcal{T}_{r,\sigma} = \left[\left(\sum_{\sigma'} c^{\dagger}_{\boldsymbol{r}_d\sigma} + \text{h.c.} \right) + \left(S^{+}_{\boldsymbol{r}_d} + \text{h.c.} \right) + \left(C^{+}_{\boldsymbol{r}_d} + \text{h.c.} \right) \right] c_{r\sigma} \ . \tag{4.31}$$

We also insert a complete basis of states of the auxiliary model at $\boldsymbol{r}_d$, $1 = \sum_n |\psi_n(\boldsymbol{r}_d)\rangle \langle \psi_n(\boldsymbol{r}_d)|$, generating an overlap factor F_n as before:

$$\begin{aligned}\sum_{\boldsymbol{r}_d} \langle \Psi_{\rm gs}| c_{\boldsymbol{r}_d,\sigma}(t) c^{\dagger}_{\boldsymbol{r}_d,\sigma} |\Psi_{\rm gs}\rangle &= \langle \psi_{\rm gs}(\boldsymbol{r}_d)| c_{\boldsymbol{r}_d,\sigma}(t) c^{\dagger}_{\boldsymbol{r}_d,\sigma} |\psi_{\rm gs}(\boldsymbol{r}_d)\rangle \\ &+ \sum_{\boldsymbol{r}_1,\boldsymbol{r}_2\neq \boldsymbol{r}_d,n} F_n(\boldsymbol{r}_1 - \boldsymbol{r}_2)^* \langle \psi_{\rm gs}(\boldsymbol{r}_d)| \mathcal{T}_{\boldsymbol{r}_1,\sigma}(t) |\psi_n(\boldsymbol{r}_d)\rangle \langle \psi_n(\boldsymbol{r}_d)| \mathcal{T}^{\dagger}_{\boldsymbol{r}_2,\sigma} |\psi_{\rm gs}(\boldsymbol{r}_d)\rangle \ .\end{aligned} \tag{4.32}$$

Several terms have been dropped because those contributions vanish for systems where the eigenstates conserve total spin S_z.

We next treat the time-evolution of the operators exactly as in the $k-$space Greens function. We replace the one-particle Hamiltonian $H_{\rm 1p}$ with its local component $H_{\rm loc}$ (such as any on-site term of inter-layer hopping, etc). As done previously, we will make use of the eigenstates $\nu(\boldsymbol{r})$ of $H_{\rm loc}$, with energy $\epsilon^{\rm loc}_{\nu}$. Without repeating the details, we state the final result here, for the frequency-domain

real-space local Greens function:

$$\begin{aligned} G_{\rm loc}(\omega) =& \frac{1}{2}\sum_{\nu}\left[C_{\nu,\boldsymbol{r}_d}\mathcal{G}(\nu(r_d)\sigma, c^\dagger_{r_d,\sigma};\tilde{\omega}) + C^*_{\nu,\boldsymbol{r}_d}\mathcal{G}(c_{r_d,\sigma}, \nu^\dagger(r_d)\sigma;\tilde{\omega})\right] \\ &+ \frac{1}{2}\sum_{\boldsymbol{r}\neq r_d,\nu} F_n(\boldsymbol{r}-\boldsymbol{r}_d)^*\left[C_{\boldsymbol{r},\nu}\mathcal{G}(\mathcal{T}_{\nu(r)\sigma}, c^\dagger_{\boldsymbol{r}_d\sigma};\tilde{\omega}) + C^*_{r_d,\nu}\mathcal{G}(\mathcal{T}_{r\sigma}, \nu^\dagger(r_d)\sigma;\tilde{\omega})\right] \\ &+ \frac{1}{2}\sum_{\boldsymbol{r}\neq r_d,\nu} F_n(\boldsymbol{r}-\boldsymbol{r}_d)^*\left[C_{\boldsymbol{r}_d,\nu}\mathcal{G}(\nu(\boldsymbol{r}_d)\sigma, \mathcal{T}^\dagger_{r\sigma};\tilde{\omega}) + C^*_{\boldsymbol{r},\nu}\mathcal{G}(c_{\boldsymbol{r}_d\sigma}, \mathcal{T}^\dagger_{\nu(r)\sigma};\tilde{\omega})\right] \\ &+ \frac{1}{2}\sum_{\boldsymbol{r}_1,\boldsymbol{r}_2\neq r_d,\nu} F_n(\boldsymbol{r}_1-\boldsymbol{r}_2)^*\left[C_{\boldsymbol{r}_1,\nu}\mathcal{G}(\mathcal{T}_{\nu(\boldsymbol{r}_1)\sigma}, \mathcal{T}^\dagger_{\boldsymbol{r}_2\sigma};\tilde{\omega}) + C^*_{\boldsymbol{r}_2,\nu}\mathcal{G}(\mathcal{T}_{\boldsymbol{r}_1\sigma}, \mathcal{T}^\dagger_{\nu(\boldsymbol{r}_2)\sigma};\tilde{\omega})\right] , \end{aligned} \tag{4.33}$$

where the hermitian conjugate in each part comes from considering the second term in eq. 4.27. The shifted frequency $\tilde{\omega} = \omega - \epsilon^{\rm loc}_\nu$ captures the effect of local terms in $H_{\rm 1p}$; the shift is defined as $e^{i\epsilon^{\rm loc}_\nu t}c^\dagger_\nu = e^{iH_{\rm loc}t}c^\dagger_\nu e^{-iH_{\rm loc}t}$. The operator $\nu^\dagger(\boldsymbol{r})$ represents the eigenstates of $H_{\rm loc}$ at any site $\boldsymbol{r}$. The coefficients $C_{\nu,\boldsymbol{r}}$ express the eigenstates in terms of local states: $c_{\boldsymbol{r}} = \sum_\nu C_{\nu,\boldsymbol{r}}c_{\nu(\boldsymbol{r})}$.

Of course, the states ν will differ from the local states $c_{\boldsymbol{r}}$ only if there are multiple local orbitals (say α) that can hybridise among each other. In such a case, one can also think of an inter-orbital Greens function, defined as

$$G_{\rm loc}(\alpha,\alpha';t) = -i\theta(t)\,\langle\Psi_{\rm gs}|\{c_{r_d,\sigma,\alpha}(t), c^\dagger_{\boldsymbol{r}_d,\sigma,\alpha'}\}|\Psi_{\rm gs}\rangle \ . \tag{4.34}$$

Such a Greens function can also be calculated from our approach:

$$\begin{aligned} G_{\rm loc}(\alpha,\alpha';\omega) =& \frac{1}{2}\sum_{\nu}\left[C_{\nu,\alpha}\mathcal{G}(\nu(r_d,\alpha)\sigma, c^\dagger_{r_d,\sigma,\alpha'};\tilde{\omega}) + C^*_{\nu,\alpha'}\mathcal{G}(c_{r_d,\sigma,\alpha}, \nu^\dagger(r_d,\alpha')\sigma;\tilde{\omega})\right] \\ &+ \frac{1}{2}\sum_{\boldsymbol{r}_1,\boldsymbol{r}_2\neq r_d,\nu} F_n(\boldsymbol{r}_1-\boldsymbol{r}_2)^*\left[C_{\alpha,\nu}\mathcal{G}(\mathcal{T}_{\nu(\boldsymbol{r}_1),\sigma,\alpha}, \mathcal{T}^\dagger_{\boldsymbol{r}_2,\sigma,\alpha'};\tilde{\omega}) + C^*_{\alpha',\nu}\mathcal{G}(\mathcal{T}_{\boldsymbol{r}_1,\sigma,\alpha}, \mathcal{T}^\dagger_{\nu(\boldsymbol{r}_2),\sigma,\alpha'};\tilde{\omega})\right] , \end{aligned} \tag{4.35}$$

Non-local Greens function: $\boldsymbol{r} \neq 0$

We next consider the case of non-local Greens function, where the excitations propagate a non-zero distance $\boldsymbol{r}$:

$$\sum_{r_d}\langle\Psi_{\rm gs}|c_{r_d+r,\sigma}(t)c^\dagger_{r_d,\sigma}|\Psi_{\rm gs}\rangle = \frac{1}{N}\sum_{\boldsymbol{R},\boldsymbol{\Delta},\boldsymbol{r}_d}\langle\psi_{\rm gs}(\boldsymbol{r}_d)|c_{\boldsymbol{R}+\boldsymbol{\Delta}+r,\sigma}(t)T^\dagger(\boldsymbol{\Delta})c^\dagger_{\boldsymbol{R},\sigma}|\psi_{\rm gs}(\boldsymbol{r}_d)\rangle \ . \tag{4.36}$$

To bring this expression closer to the one for the local Greens function, we redefine $\Delta + \boldsymbol{r} \to \Delta$:

$$\sum_{r_d}\langle\Psi_{\rm gs}|c_{r_d+r,\sigma}(t)c^\dagger_{r_d,\sigma}|\Psi_{\rm gs}\rangle = \frac{1}{N}\sum_{\boldsymbol{R},\boldsymbol{\Delta},\boldsymbol{r}_d}\langle\psi_{\rm gs}(\boldsymbol{r}_d)|c_{\boldsymbol{R}+\boldsymbol{\Delta},\sigma}(t)T^\dagger(\boldsymbol{\Delta})T(\boldsymbol{r})c^\dagger_{\boldsymbol{R},\sigma}|\psi_{\rm gs}(\boldsymbol{r}_d)\rangle \ . \tag{4.37}$$

This allows to again split the full summation based on whether $\boldsymbol{R} = \boldsymbol{r}_d$ and whether $\Delta + \boldsymbol{R} = \boldsymbol{r}_d$:

$$\begin{aligned}\sum_{\boldsymbol{r}_d} \langle\Psi_{\rm gs}|c_{\boldsymbol{r}_d+\boldsymbol{r},\sigma}(t)c^\dagger_{\boldsymbol{r}_d,\sigma}|\Psi_{\rm gs}\rangle &= \langle\psi_{\rm gs}(\boldsymbol{r}_d)|c_{\boldsymbol{r}_d,\sigma}(t)T(\boldsymbol{r})c^\dagger_{\boldsymbol{r}_d,\sigma}|\psi_{\rm gs}(\boldsymbol{r}_d)\rangle \\ &+ \sum_{\boldsymbol{\Delta}\neq 0}\langle\psi_{\rm gs}(\boldsymbol{r}_d)|c_{\boldsymbol{r}_d+\boldsymbol{\Delta},\sigma}(t)T^\dagger(\boldsymbol{\Delta}-\boldsymbol{r})c^\dagger_{\boldsymbol{r}_d,\sigma}|\psi_{\rm gs}(\boldsymbol{r}_d)\rangle \\ &+ \sum_{\boldsymbol{R}\neq\boldsymbol{r}_d}\langle\psi_{\rm gs}(\boldsymbol{r}_d)|c_{\boldsymbol{r}_d,\sigma}(t)T^\dagger(\boldsymbol{r}_d-\boldsymbol{R}-\boldsymbol{r})c^\dagger_{\boldsymbol{R},\sigma}|\psi_{\rm gs}(\boldsymbol{r}_d)\rangle \\ &+ \sum_{\boldsymbol{R}\neq\boldsymbol{r}_d,\boldsymbol{\Delta}\neq\boldsymbol{r}_d}\langle\psi_{\rm gs}(\boldsymbol{r}_d)|c_{\boldsymbol{\Delta},\sigma}(t)T^\dagger(\boldsymbol{\Delta}-\boldsymbol{R}-\boldsymbol{r})c^\dagger_{\boldsymbol{R},\sigma}|\psi_{\rm gs}(\boldsymbol{r}_d)\rangle\ .\end{aligned} \tag{4.38}$$

Introducing Fourier transforms of the operators and inserting eigenstates of the auxiliary models leads to

$$\begin{aligned}&\sum_{\boldsymbol{r}_d}\langle\Psi_{\rm gs}|c_{\boldsymbol{r}_d+\boldsymbol{r},\sigma}(t)c^\dagger_{\boldsymbol{r}_d,\sigma}|\Psi_{\rm gs}\rangle \\ &= \sum_n F^*_n(\boldsymbol{r})\,\langle\psi_{\rm gs}(\boldsymbol{r}_d)|c_{\boldsymbol{r}_d,\sigma}(t)|\psi_n(\boldsymbol{r}_d)\rangle\,\langle\psi_n(\boldsymbol{r}_d)|c^\dagger_{\boldsymbol{r}_d,\sigma}|\psi_{\rm gs}(\boldsymbol{r}_d)\rangle \\ &+ \sum_{\boldsymbol{k},n} F'_n(\boldsymbol{k})F^*_n(\boldsymbol{r})\,\langle\psi_{\rm gs}(\boldsymbol{r}_d)|\mathcal{T}_{\boldsymbol{k},\sigma}(t)|\psi_n(\boldsymbol{r}_d)\rangle\,\langle\psi_n(\boldsymbol{r}_d)|c^\dagger_{\boldsymbol{r}_d,\sigma}|\psi_{\rm gs}(\boldsymbol{r}_d)\rangle \\ &+ \sum_{\boldsymbol{k},n} F'_n(\boldsymbol{k})^*F^*_n(\boldsymbol{r})\,\langle\psi_{\rm gs}(\boldsymbol{r}_d)|c_{\boldsymbol{r}_d,\sigma}(t)|\psi_n(\boldsymbol{r}_d)\rangle\,\langle\psi_n(\boldsymbol{r}_d)|\mathcal{T}^\dagger_{\boldsymbol{k},\sigma}|\psi_{\rm gs}(\boldsymbol{r}_d)\rangle \\ &+ \sum_{\boldsymbol{k}_1,\boldsymbol{k}_2} F'_n(\boldsymbol{k}_1)F'_n(\boldsymbol{k}_2)^*F^*_n(\boldsymbol{r})\,\langle\psi_{\rm gs}(\boldsymbol{r}_d)|\mathcal{T}_{\boldsymbol{k}_1,\sigma}(t)|\psi_n(\boldsymbol{r}_d)\rangle\,\langle\psi_n(\boldsymbol{r}_d)|\mathcal{T}^\dagger_{\boldsymbol{k}_2,\sigma}|\psi_{\rm gs}(\boldsymbol{r}_d)\rangle\ ,\end{aligned} \tag{4.39}$$

The net difference from the diagonal Greens function is the presence of the overlap factor $F^*_n(\boldsymbol{r})$.

4.4.3 Equal-Time Ground State Correlators

Apart from dynamical correlations such as Greens functions, we would also like to use our approach to calculate static correlation functions in terms of auxiliary model quantities. We first consider a real-space correlation that tracks the propagation of a general excitation described by the operator $O(\boldsymbol{r})$ over a distance $\boldsymbol{\Delta}$:

$$C_O(\boldsymbol{r}) = \langle\Psi_{\rm gs}|O(\boldsymbol{r}_d+\boldsymbol{r})O^\dagger(\boldsymbol{r}_d)|\Psi_{\rm gs}\rangle\ . \tag{4.40}$$

We first consider a local correlation: $\boldsymbol{r} = 0$. To obtain a tractable expression for this, we note that the quantity being computed here is almost identical to the one computed in eq. 4.28, the only difference being the time-evolution of the operator. For the local correlation, we therefore assume the result of eq. 4.31, dropping the time evolution because the correlators in this section are calculated at equal time. We also transform from $k-$space back to real-space because there are no time-evolution

operators which need extended states in order to be resolved. Putting all this together, we get

$$\begin{aligned} C_O^{\text{loc}} &= \langle\psi_{\text{gs}}(\boldsymbol{r}_d)|O(\boldsymbol{r}_d)O^\dagger(\boldsymbol{r}_d)|\psi_{\text{gs}}(\boldsymbol{r}_d)\rangle \\ &+ \sum_{\boldsymbol{r}\neq 0,n} F_n(\boldsymbol{r})\,\langle\psi_{\text{gs}}(\boldsymbol{r}_d)|\mathcal{T}_{O(\boldsymbol{r}+\boldsymbol{r}_d)}|\psi_n(\boldsymbol{r}_d)\rangle\,\langle\psi_n(\boldsymbol{r}_d)|O^\dagger(\boldsymbol{r}_d)|\psi_{\text{gs}}(\boldsymbol{r}_d)\rangle \\ &+ \sum_{\boldsymbol{r}\neq 0,n} F_n(\boldsymbol{r})\,\langle\psi_{\text{gs}}(\boldsymbol{r}_d)|O(\boldsymbol{r}+\boldsymbol{r}_d)|\psi_n(\boldsymbol{r}_d)\rangle\,\langle\psi_n(\boldsymbol{r}_d)|\mathcal{T}^\dagger_{O(\boldsymbol{r}_d)}|\psi_{\text{gs}}(\boldsymbol{r}_d)\rangle \\ &+ \sum_{\boldsymbol{r}_1\neq 0,\boldsymbol{r}_2\neq 0,n} F_n(\boldsymbol{r})\,\langle\psi_{\text{gs}}(\boldsymbol{r}_d)|\mathcal{T}_{O(\boldsymbol{r}_1+\boldsymbol{r}_d)}|\psi_n(\boldsymbol{r}_d)\rangle\,\langle\psi_n(\boldsymbol{r}_d)|\mathcal{T}^\dagger_{O(\boldsymbol{r}_2+\boldsymbol{r}_d)}|\psi_{\text{gs}}(\boldsymbol{r}_d)\rangle\ , \end{aligned} \tag{4.41}$$

where the transition operator $\mathcal{T}_{O(\boldsymbol{r}+\boldsymbol{r}_d)}$ represents impurity-bath correlation:

$$\mathcal{T}_{O(\boldsymbol{r}+\boldsymbol{r}_d),\sigma} = \left[c^\dagger_{\boldsymbol{r}_d\sigma} + S^\sigma_{\boldsymbol{r}_d} + C^+_{\boldsymbol{r}_d}\right] O(\boldsymbol{r}+\boldsymbol{r}_d)\ , \tag{4.42}$$

We next consider non-local correlations over a distance $\boldsymbol{\Delta}$. Adapting eq. 4.39 for the non-local real-space Greens function in the same manner, we get

$$\begin{aligned} C_O(\boldsymbol{\Delta}) &= \sum_n F^*_n(\boldsymbol{\Delta})\,\langle\psi_{\text{gs}}(\boldsymbol{r}_d)|c_{\boldsymbol{r}_d,\sigma}(t)|\psi_n(\boldsymbol{r}_d)\rangle\,\langle\psi_n(\boldsymbol{r}_d)|c^\dagger_{\boldsymbol{r}_d,\sigma}|\psi_{\text{gs}}(\boldsymbol{r}_d)\rangle \\ &+ \sum_{\boldsymbol{r}\neq 0,n} F_n(\boldsymbol{r}+\boldsymbol{\Delta})\,\langle\psi_{\text{gs}}(\boldsymbol{r}_d)|\mathcal{T}_{O(\boldsymbol{r}+\boldsymbol{\Delta}+\boldsymbol{r}_d)}|\psi_n(\boldsymbol{r}_d)\rangle\,\langle\psi_n(\boldsymbol{r}_d)|O^\dagger(\boldsymbol{r}_d)|\psi_{\text{gs}}(\boldsymbol{r}_d)\rangle \\ &+ \sum_{\boldsymbol{r}\neq 0,n} F_n(\boldsymbol{r}+\boldsymbol{\Delta})\,\langle\psi_{\text{gs}}(\boldsymbol{r}_d)|O(\boldsymbol{r}+\boldsymbol{\Delta}+\boldsymbol{r}_d)|\psi_n(\boldsymbol{r}_d)\rangle\,\langle\psi_n(\boldsymbol{r}_d)|\mathcal{T}^\dagger_{O(\boldsymbol{r}_d)}|\psi_{\text{gs}}(\boldsymbol{r}_d)\rangle \\ &+ \sum_{\boldsymbol{r}_1\neq 0,\boldsymbol{r}_2\neq 0,n} F_n(\boldsymbol{r}+\boldsymbol{\Delta})\,\langle\psi_{\text{gs}}(\boldsymbol{r}_d)|\mathcal{T}_{O(\boldsymbol{r}_1+\boldsymbol{\Delta}+\boldsymbol{r}_d)}|\psi_n(\boldsymbol{r}_d)\rangle\,\langle\psi_n(\boldsymbol{r}_d)|\mathcal{T}^\dagger_{O(\boldsymbol{r}_2+\boldsymbol{r}_d)}|\psi_{\text{gs}}(\boldsymbol{r}_d)\rangle\ , \end{aligned} \tag{4.43}$$

4.5 Entanglement Measures

We will now describe the prescription of calculating entanglement measures of the lattice model from within our auxiliary model treatment. In this section, we are interested mainly in two such measures, the entanglement entropy and the mutual information. Given a pure state $|\Psi\rangle$ describing the complete system, the entanglement entropy $S_{\text{EE}}(\nu)$ of a subsystem ν quantifies the entanglement of ν with the rest of the subsystem, and is defined as

$$S_{\text{EE}}(\nu) = -\text{Tr}\left[\rho(\nu)\log\rho(\nu)\right], \quad \rho(\nu) = \text{Tr}_\nu\left[|\Psi\rangle\langle\Psi|\right] \tag{5.1}$$

where Tr $[\cdot]$ is the trace operator, and $\rho(\nu)$ is the reduced density matrix (RDM) for the subsystem ν obtained by taking the partial trace Tr_ν (over the states of ν) of the full density matrix $\rho = |\Psi\rangle\langle\Psi|$. If the subsystem ν describes local regions in real space (or states in $k-$space), we might be interested in the entanglement between two such subsystems ν_1 and ν_2. The correct measure to quantify such entanglement is the mutual information:

$$I_2(\nu_1,\nu_2) = S_{\text{EE}}(\nu_1) + S_{\text{EE}}(\nu_2) - S_{\text{EE}}(\nu_1\cup\nu_2)\ , \tag{5.2}$$

where $\nu_1 \cup \nu_2$ is a larger subsystem formed by combining ν_1 and ν_2.

We start by recalling the decomposition of entanglement entropy in terms of multipartite information as laid out in Section 2.9.3 of Chapter 2. Given a partitioning of the system into mutually exclusive subsystems $\{\nu_i\}$, the average entanglement entropy $S_{\mathrm{EE}}^{(1)}$ over all subsystems can be expressed as

$$\begin{aligned} S_{\mathrm{EE}}^{(1)} &= \frac{1}{N}\sum_{n=2}^{N}(-1)^n\binom{N}{n}\bar{I}_n, \\ \bar{I}_n &= \frac{(N-n)!n!}{N!}\sum_{S_n\in C_n(\mathcal{S}_N)} I_n(S_n), \end{aligned} \tag{5.3}$$

where $\bar{I}_n$ is the average multipartite information I_n over all distinct combinations of n subsystems.

We first take a look at real-space entanglement. Real-space entanglement measures can be used to probe delocalisation-localisation transitions. The simplest such measure is the entanglement of a lattice site in real-space. Since the local entanglement entropy will be uniform at each lattice site for a system with translation invariance, it suffices to calculate the real-space averaged entanglement entropy $S_{\mathrm{EE}}^{(1)}$. The corresponding multipartite measures $\bar{I}_n$ involve collections of lattice sites. We write such a measure as

$$\bar{I}_n = \frac{(N-n)!n!}{N!}\frac{1}{N}\sum_{I(\boldsymbol{r}_d)}\sum_{B^{n-1}(\boldsymbol{r}_d)} I_n(I(\boldsymbol{r}_d); B^{n-1}(\boldsymbol{r}_d)), \tag{5.4}$$

where $I(\boldsymbol{r}_d)$ sums over all lattice sites in the form of an impurity site and $B^{n-1}(\boldsymbol{r}_d)$ considers all possible subsets of size $n-1$ of the remaining bath sites. Together, this choice corresponds to an auxiliary model with the impurity placed at $\boldsymbol{r}_d$. The additional factor of $1/N$ takes care of the overcounting arising from each choice appearing in N auxiliary models. We can therefore write the multipartite information as an average over auxiliary models, each auxiliary model contributing an average I_n over its bath sites:

$$\bar{I}_n = \frac{n}{N^2}\sum_{\boldsymbol{r}_d} I_n^{(\mathrm{tot})}(\boldsymbol{r}_d)\ . \tag{5.5}$$

The quantity $I_n^{(\mathrm{tot})}(\boldsymbol{r}_d)$ is defined as $I_n^{(\mathrm{tot})}(\boldsymbol{r}_d) = \frac{(N-n)!(n-1)!}{(N-1)!}\sum_{B^{n-1}(\boldsymbol{r}_d)} I_n(I(\boldsymbol{r}_d); B^{n-1}(\boldsymbol{r}_d))$. By translation invariance, such a measure will be uniform across auxiliary models and it suffices to calculate the measure for a single auxiliary model located at a reference point $\boldsymbol{r}_d$; the whole expression therefore simplifies to

$$S_{\mathrm{EE}}^{(1)} = \frac{1}{N}\sum_{n=2}^{N}(-1)^n\binom{N-1}{n-1}I_n^{(\mathrm{tot})}(\boldsymbol{r}_d) = \frac{1}{N}\sum_{n=2}^{N}(-1)^n\sum_{B^{n-1}(\boldsymbol{r}_d)} I_n(I(\boldsymbol{r}_d); B^{n-1}(\boldsymbol{r}_d))\ . \tag{5.6}$$

For example, truncating the summation to $n=3$, we have the explicit expression

$$S_{\mathrm{EE}}^{(1)} = \frac{N-1}{N}I_2^{(\mathrm{tot})}(\boldsymbol{r}_d) - \frac{(N-1)(N-2)}{2N}I_3^{(\mathrm{tot})}(\boldsymbol{r}_d) \tag{5.7}$$

4.6 Some Comments

- Strictly speaking, our approach does not pin down a unique impurity model given some lattice model. Nevertheless, a controlled hierarchy can indeed be designed for systematically increasing the accuracy of our procedure, by increasing the number of correlated impurity sites. The cluster beyond 1+4 would be one where there are five impurity sites and the appropriate number of correlated bath sites surrounding them. The complexity of solving such an impurity model is of course higher.

- Given the lack of a unique mapping between the auxiliary model couplings and the lattice model couplings, the program laid out in the thesis does not map a lattice model to a unique impurity model. Nevertheless, we expect the qualitative features of the lattice model (such as the nature of the phases and effective theories) – as reconstructed through our tiling procedure – to be universal to an extent (i.e., independent across the various auxiliary models that can map to that lattice model). In other words, the primary goal of this approach is to discover the broad theories associated with lattice models of a certain kind (the extended Hubbard model, in this case) by mapping them to impurity models of the appropriate kind. We would also add that the appropriate impurity model is also determined by the phenomenology of the lattice model or the material that we are studying.

4.7 Discussions

This chapter was primarily devoted to motivating and developing the "tiling" auxiliary model framework. Using an appropriately-chosen quantum impurity model and many-body translation operators, we demonstrated how one can reconstruct the full lattice model and its low-energy physics. More explicitly, this involves mappings between the two models that leverage the translation operators. The workflow suggested by such an approach is the following. The first step is to identify a quantum impurity model that has the appropriate "local phenomenology" for the lattice model we are targeting. The impurity model needs to be embedded in the appropriate lattice. We then use an impurity solver (in this case, the unitary RG method) to compute various properties of the impurity model. Finally, we use the tiling relations to reconstruct the physics of the lattice model. The embedding step ensures that the lattice effects are encoded in the impurity model couplings and hence in the tiled quantities.

The next step is to apply it to non-trivial problems. We will do that in the next two chapters, by benchmarking the method against existing rigorous results and using it to obtain new insights on such problems.

Chapter 5

Mott Criticality as the Confinement Transition of of a Pseudogap-Mott Metal: Insights on Mott Transition and Pseudogap in Two Dimensions

In the last chapter, we developed a new auxiliary model framework for mapping the low-energy physics of quantum impurity models to that of lattice models. This led to relations between correlation functions, Greens functions and entanglement measures, between the two models. We devote this chapter to applying this method to the problem of Mott transition on the 2D square lattice at half-filling. We first motivate that the appropriate auxiliary model is an extended Anderson impurity model (of the kind studied in Chapter 3) but embedded into a square lattice. This allows encoding the lattice geometry into the impurity model couplings. Through the tiling framework, we reveal that the passage from the Fermi liquid into the Mott insulator involves a distinct intervening pseudogapped phase of matter that has anomalous non-Fermi liquid properties and holon-doublon excitations. This provides a compelling picture of the Mott transition as the confinement of pairs of holes and doubles.

5.1 Introduction

The Landau quasiparticle paradigm [550] underpins our understanding of metallic behaviour, where the screening of long-ranged repulsive interactions between delocalised electrons leads to well-defined excitations that carry the same quantum numbers as free electrons. This remarkable phenomenon - known as adiabatic continuity - is captured by excitations described by poles of the single-particle Greens function of the interacting system. But what defines metallicity when quasiparticles are no longer well-defined [551]? Can a surface of zeros of the Greens function [26], rather than poles forming a Fermi surface, define an entirely new kind of metal? Could such an exotic state serve as the precursor to Mott localisation driven purely by repulsion, and without invoking magnetic order [11]? These questions necessitate a radical departure in understanding conduction in

correlated electron systems beyond the quasiparticle paradigm [167].

The anomalous pseudogap (PG) phase, observed in the cuprates, exhibits nodal-antinodal dichotomy with spectral weight concentrated on Fermi arcs around the nodal regions [552–554]. In the PG phase of such Mott systems [184, 555–583], the single-particle Green's function develops surfaces of zeros, also known as Luttinger surfaces [26, 584], that signals a fundamental obstruction to quasiparticle formation. As interaction strength increases, these zero surfaces proliferate, fragmenting the Fermi surface into nodal arcs [564, 584], violating the Luttinger sum rule by reconfiguring Fermi volume [51], and breaking an emergent $\mathbb{Z}_2$ symmetry associated with the conservation of spin currents in Fermi liquids [585, 586]. Unlike conventional instabilities driven by poles, this phenomenon marks a topological breakdown of Fermi liquid theory [225, 551]. We show that this breakdown arises from a strongly entangled, scale-invariant state of quantum matter, one that serves as the parent metal to the Mott insulator in a half-filled lattice model of strongly correlated electrons. This offers a concrete, controlled framework to understand both the non-quasiparticle character of the pseudogap phase and its continuous evolution into a repulsion-driven insulator, in full alignment with Mott's original vision [11].

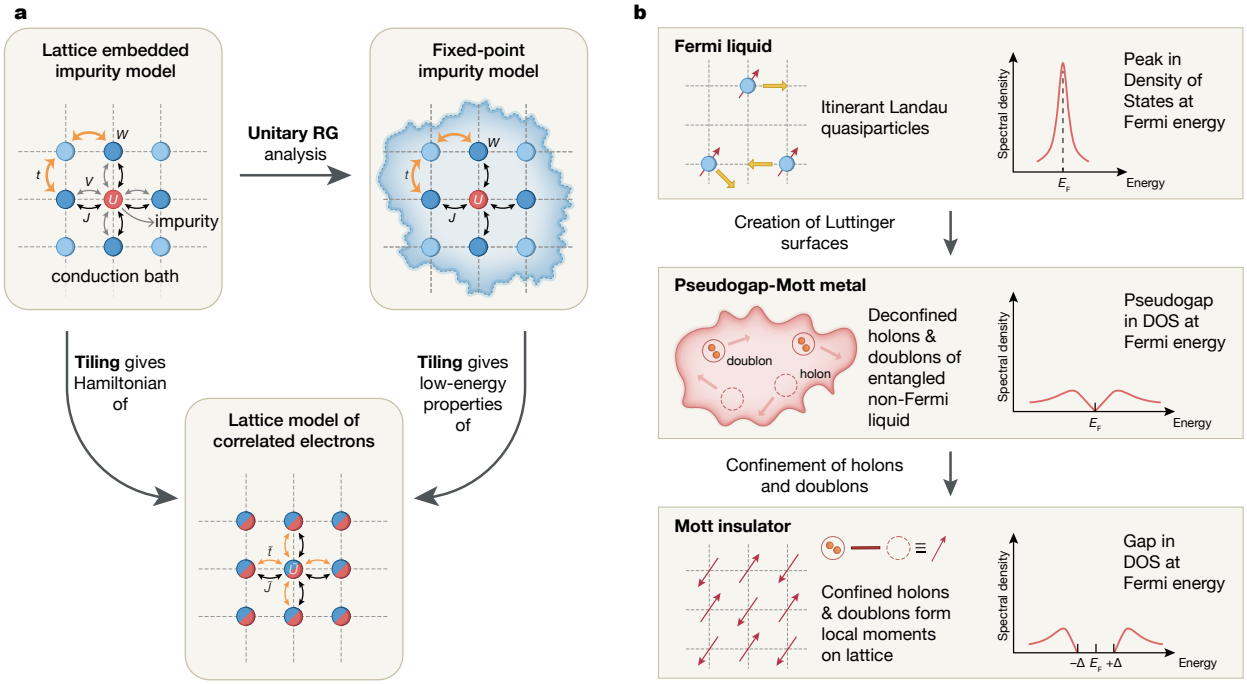

Figure 5.1: *Schematic representation of (a) theoretical framework adopted by us (see main text for explanation of symbols), (b) phases obtained for the extended Hubbard model in two dimensions at $T = 0$, and passage between them.*

Our approach involves developing a renormalization group (RG)-based impurity-to-lattice framework that reconstructs the low-energy physics of a strongly correlated system from the fixed-point structure of a quantum impurity model (Fig. 5.1(a)). Starting from a dynamical Anderson impurity

embedded in a correlated bath, we solve the system using a unitary RG (URG) approach [348, 349]. We then construct a translation-invariant lattice Hamiltonian through a many-body tiling procedure that preserves non-local correlations and inherits momentum-resolved self-energies and renormalized couplings from the impurity solution. The resulting model is an *extended*-Hubbard Hamiltonian on a two-dimensional square lattice at half-filling, with both on-site repulsion and nearest-neighbour spin exchange interactions. These correlations, derived directly from the impurity dynamics, enable tracking the evolution from the FL to the Mott insulator (MI) via an intermediate PG phase.

A central insight of our work is that the PG phase hosts a NFL state governed by Kondo frustration and doublon–holon deconfinement [188] (Fig. 5.1(b)). A correlation scale (W) in the conduction bath suppresses Kondo screening (with coupling J) beyond a critical ratio of W/J, triggering the emergence of Luttinger surfaces in the lattice model. This breakdown of quasiparticles begins at the antinodes and progressively engulfs the nodal regions, driving a continuous transformation into the MI. The resulting NFL exhibits a pseudogapped density of states that vanishes as ω^2 as $\omega \to 0$, multipartite long-range entanglement, and a universal scattering rate of the form $\sim (a + b\,\omega^2)^{-1}$ that grows as $\omega \to 0$. At the critical endpoint of this phase, the URG flow identifies a singular NFL described by the Hatsugai–Kohmoto (HK) model [28, 29, 586], with fully deconfined holon–doublon excitations.

The emergence of Luttinger surfaces alters the anomaly structure associated with the generalized symmetry of the FS [347, 587, 588]. The corresponding topological charge is defined via the Luttinger–Ward functional. This charge is modified by Green's function zeros, signalling a shift in the underlying anomaly. Within our framework, this reorganization grants topological protection to the RG flows terminating in the PG regime, ensuring the stability of its NFL excitations. These are adiabatically connected to the Hatsugai–Kohmoto model [28, 29], reinforcing the interpretation of the PG as a distinct quantum phase. We thus identify the NFL state as a new gapless, long-range entangled phase of correlated matter - the *Mott metal* - whose deconfined holon-doublon excitations are eventually confined across the Mott transition [11].

While we demonstrate our approach for an extended Hubbard model, the underlying framework is broadly applicable to correlated quantum systems. The impurity-plus-tiling construction accommodates multi-orbital degrees of freedom, frustrated geometries, and nontrivial band topology. By deriving lattice Hamiltonians directly from renormalized local dynamics - without relying on mean-field approximations - this method preserves nonlocal correlations and enhances momentum-space resolution. Coupled with the unitary renormalisation group method as the impurity solver, this approach provides access to one-particle as well as two-particle correlations, entanglement measures and several dynamical quantities, making the method very versatile. It thus provides a versatile and controlled route for engineering strongly correlated models, particularly in regimes where PG formation, NFL scaling, and Mott physics intersect.

We now describe the layout of the chapter. In section 5.2, we formulate the lattice-embedded auxiliary quantum impurity model and sketch the unitary renormalisation group (URG) method employed to analyse the impurity model. In Chapter 4, we have already formulated the tiling procedure by which to map the impurity Hamiltonian, eigenstates and observables into a lattice model of strongly correlated electrons via the usage of many-body translation operators. Section 5.5 displays the destruction of the Fermi liquid from the breakdown of Kondo screening, leading to a

pseudogapped non-Fermi liquid phase of matter. The novel properties of this phase are rigorously established in section 5.6. In section 5.7, we demonstrate that the continuous transition between the pseudogap and Mott insulating phases is described by the exactly solvable Hatsugai-Kohmoto model. We demonstrate in section 5.9 the universal organising principle that is responsible for the emergence of the pseudogap non-Fermi liquid phase. This also unveils the pseudogap as the strongly coupled long-range entangled parent metal of the Mott insulator. We conclude in section 5.10.

5.2 Auxiliary Model and URG analysis

To capture the interplay between Kondo physics and Mott localization, our approach relies on a two-dimensional auxiliary model consisting of an Anderson impurity embedded in a minimally-correlated bath, which we solve the system using a unitary RG (URG) approach [348, 349]. The impurity model and URG analysis are laid out in this section. In order to make contact with a lattice model, we construct a translation-invariant Hamiltonian from the impurity model through a many-body tiling procedure: this preserves non-local correlations, as well as allows for momentum-resolved self-energies and renormalized couplings generated from the impurity solution. For the impurity model chosen in this work, tiling results in an *extended*-Hubbard Hamiltonian on a two-dimensional square lattice at particle-hole symmetry (half-filling). The interaction terms within the lattice model are a result of analogous correlations present in the auxiliary model. This is laid out next in Section 5.3.

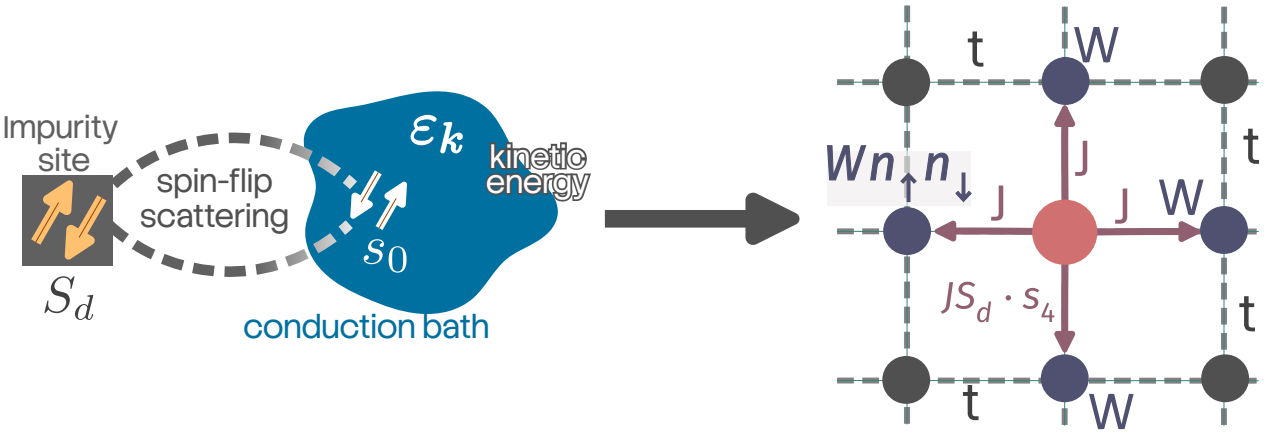

Figure 5.2: *Particle and hole states.*

5.2.1 Lattice-embedded Impurity Model

The auxiliary model consists of a correlated impurity site (with a double occupancy cost U) embedded within a correlated conduction bath defined on a square lattice (see Fig. 5.1(a)). The impurity site hybridises with the conduction bath sites adjacent to it through one-particle hybridisation V as well as a spin-exchange interaction J arising from fluctuations in local spin densities of the elec-

trons. The conduction bath has minimal correlations in the form of a local correlation term W on the sites that are adjacent to the impurity.

The Hamiltonian of the auxiliary model studied here is

$$\mathcal{H}_{\text{aux}} = H_{\text{imp}} + H_{\text{coup}} + H_{\text{cbath}}, \tag{2.1}$$

where the particle-hole symmetric impurity term is

$$H_{\text{imp}} = -\frac{U}{2}\left(\hat{n}_{d\uparrow} - \hat{n}_{d\downarrow}\right)^2, \tag{2.2}$$

describing on-site Coulomb interactions at the impurity. Here, $c^\dagger_{d\sigma}$ creates an electron with spin σ at the impurity site, and $\hat{n}_{d\sigma} = c^\dagger_{d\sigma} c_{d\sigma}$ denotes the corresponding number operator.

The impurity couples to four nearest-neighbour bath sites $c_{Z\sigma}$ through both hybridization and Kondo exchange:

$$H_{\text{coup}} = \frac{J}{2}\sum_{\sigma_1,\sigma_2,Z} \mathbf{S}_d \cdot c^\dagger_{Z\sigma_1} \boldsymbol{\tau}_{\sigma_1\sigma_2} c_{Z\sigma_2} - V\sum_{\sigma,Z}\left(c^\dagger_{Z\sigma} c_{d\sigma} + \text{h.c.}\right), \tag{2.3}$$

where $\boldsymbol{\tau}$ are the Pauli matrices, and Z indexes the four neighbouring bath sites. The half-filled bath includes nearest neighbour hopping and on-site correlations on the site neighbouring the impurity:

$$H_{\text{cbath}} = \sum_{\mathbf{k}} \epsilon_{\mathbf{k}} c^\dagger_{\mathbf{k},\sigma} c_{\mathbf{k},\sigma} - \frac{W}{2}\sum_{Z}\left(\hat{n}_{Z\uparrow} - \hat{n}_{Z\downarrow}\right)^2, \tag{2.4}$$

where $\epsilon_{\mathbf{k}} = -2t(\cos k_x + \cos k_y)$, and W parametrizes local repulsion in the bath that frustrates Kondo screening and drives the system towards local-moment formation. A crucial feature of this construction is that the Kondo coupling acquires a momentum structure upon Fourier transforming:

$$J_{\mathbf{k},\mathbf{k}'} = \frac{J}{2}\left[\cos(k_x - k'_x) + \cos(k_y - k'_y)\right], \tag{2.5}$$

which respects the C_4 symmetry of the square lattice.

5.3 Derivation of unitary RG equations for the lattice-embedded impurity model

In order to obtain the various low-energy phases of our impurity model, we perform a scaling analysis of the associated Hamiltonian using the recently developed unitary renormalisation group (URG) method. The method is described in detail in Chapter 2.

5.3.1 RG scheme

At any given step j of the RG procedure, we decouple the states $\{\mathbf{q}\}$ on the isoenergetic surface of energy ε_j. The diagonal Hamiltonian H_D for this step consists of all terms that do not change the occupancy of the states $\{\mathbf{q}\}$:

$$H_D^{(j)} = \varepsilon_j \sum_{q,\sigma} \tau_{q,\sigma} + \frac{1}{2}\sum_{\mathbf{q}} J_{\mathbf{q},\mathbf{q}} S_d^z \left(\hat{n}_{\mathbf{q},\uparrow} - \hat{n}_{\mathbf{q},\downarrow}\right) - \frac{1}{2}\sum_{\mathbf{q}} W_{\mathbf{q}} \left(\hat{n}_{\mathbf{q},\uparrow} - \hat{n}_{\mathbf{q},\downarrow}\right)^2 , \tag{3.1}$$

where $\tau = \hat{n} - 1/2$ and $W_{\mathbf{q}}$ is a shorthand for $W_{\mathbf{q},\mathbf{q},\mathbf{q},\mathbf{q}}$. The three terms, respectively, are the kinetic energy of the momentum states on the isoenergetic shell that we are decoupling, the spin-correlation energy between the impurity spin and the spins formed by these momentum states and, finally, the local correlation energy associated with these states arising from the W term. The off-diagonal part of the Hamiltonian on the other hand leads to scattering in the states $\{\mathbf{q}\}$. We now list these terms, classified by the coupling they originate from.

Arising from the Kondo spin-exchange term

$$\begin{aligned}
T_{KZ1}^\dagger + T_{KZ1} &= \frac{1}{2}\sum_{\mathbf{k},\mathbf{q},\sigma} \sigma J_{\mathbf{k},\mathbf{q}} S_d^z \left[c_{\mathbf{q}\sigma}^\dagger c_{\mathbf{k},\sigma} + \text{h.c.}\right], \\
T_{KZ2}^\dagger + T_{KZ2} &= \frac{1}{2}\sum_{\mathbf{q},\sigma} \sigma J_{\mathbf{q},\bar{\mathbf{q}}} S_d^z \left[c_{\mathbf{q}\sigma}^\dagger c_{\bar{\mathbf{q}},\sigma} + \text{h.c.}\right], \\
T_{KT1}^\dagger + T_{KT1} &= \frac{1}{2}\sum_{\mathbf{k},\mathbf{q}} J_{\mathbf{k},\mathbf{q}} \left[S_d^+ \left(c_{\mathbf{q}\downarrow}^\dagger c_{\mathbf{k}\uparrow} + c_{\mathbf{k}\downarrow}^\dagger c_{\mathbf{q}\uparrow}\right) + \text{h.c.}\right], \\
T_{KT2}^\dagger + T_{KT2} &= \frac{1}{2}\sum_{\mathbf{q}} J_{\mathbf{q},\bar{\mathbf{q}}} \left[S_d^+ \left(c_{\mathbf{q}\downarrow}^\dagger c_{\bar{\mathbf{q}}\uparrow} + c_{\bar{\mathbf{q}}\downarrow}^\dagger c_{\mathbf{q}\uparrow}\right) + \text{h.c.}\right],
\end{aligned} \tag{3.2}$$

Arising from spin-preserving scattering within conduction bath

$$\begin{aligned}
T_{P1}^\dagger + T_{P1} &= -\sum_{\mathbf{q}\in\varepsilon_j} \sum_{\mathbf{k}_2,\mathbf{k}_3,\mathbf{k}_4<\varepsilon_j} \sum_{\sigma} \left[W_{\mathbf{q},\mathbf{k}_2,\mathbf{k}_3,\mathbf{k}_4} c_{\mathbf{q},\sigma}^\dagger c_{\mathbf{k}_2,\sigma} c_{\mathbf{k}_3,\sigma}^\dagger c_{\mathbf{k}_4,\sigma} + \text{h.c.}\right] \\
T_{P2}^\dagger + T_{P3} &= -\sum_{\mathbf{q}\in\varepsilon_j} \sum_{\mathbf{k}_2<\varepsilon_j} \sum_{\sigma} W_{\mathbf{q},\mathbf{k}_2,\bar{\mathbf{q}},\bar{\mathbf{q}}} c_{\mathbf{q},\sigma}^\dagger c_{\mathbf{k}_2,\sigma} n_{\bar{\mathbf{q}},\sigma} - \sum_{\mathbf{q}\in\varepsilon_j} \sum_{\mathbf{k}_1<\varepsilon_j} \sum_{\sigma} W_{\mathbf{k}_1,\mathbf{q},\mathbf{q},\mathbf{q}} c_{\mathbf{k}_1,\sigma}^\dagger c_{\mathbf{q},\sigma} n_{\mathbf{q},\sigma} \\
T_{P4} &= -\sum_{\mathbf{q}\in\varepsilon_j} \sum_{\mathbf{k}_2,\mathbf{k}_3<\varepsilon_j} \sum_{\sigma} W_{\mathbf{q},\bar{\mathbf{q}},\mathbf{k}_2,\mathbf{k}_3} c_{\mathbf{q},\sigma}^\dagger c_{\bar{\mathbf{q}},\sigma} c_{\mathbf{k}_2,\sigma}^\dagger c_{\mathbf{k}_3,\sigma} \\
T_{P5} &= -\sum_{\mathbf{q}\in\varepsilon_j} \sum_{\mathbf{k}_2,\mathbf{k}_3<\varepsilon_j} \sum_{\sigma} W_{\mathbf{q},\mathbf{k}_2,\mathbf{k}_3,\bar{\mathbf{q}}} c_{\mathbf{q},\sigma}^\dagger c_{\mathbf{k}_2,\sigma} c_{\mathbf{k}_3,\sigma}^\dagger c_{\bar{\mathbf{q}},\sigma} \\
&= +\sum_{\mathbf{q}\in\varepsilon_j} \sum_{\mathbf{k}_2,\mathbf{k}_3<\varepsilon_j} \sum_{\sigma} W_{\mathbf{q},\mathbf{k}_3,\mathbf{k}_2,\bar{\mathbf{q}}} c_{\mathbf{q},\sigma}^\dagger c_{\bar{\mathbf{q}},\sigma} c_{\mathbf{k}_2,\sigma}^\dagger c_{\mathbf{k}_3,\sigma} \\
&= -T_{P4}
\end{aligned} \tag{3.3}$$

Arising from spin-flip scattering within conduction bath

$$\begin{aligned} T_{F1}^{\dagger} + T_{F1} &= \sum_{\mathbf{q}\in\varepsilon_j} \sum_{\mathbf{k}_2,\mathbf{k}_3,\mathbf{k}_4<\varepsilon_j} \sum_{\sigma} \left[W_{\mathbf{q},\mathbf{k}_2,\mathbf{k}_3,\mathbf{k}_4} c^{\dagger}_{\mathbf{q},\sigma} c_{\mathbf{k}_2,\sigma} c^{\dagger}_{\mathbf{k}_3,\bar{\sigma}} c_{\mathbf{k}_4,\bar{\sigma}} + \text{h.c.} \right] \\ T_{F2} &= \sum_{\mathbf{q},\mathbf{q}'\in\varepsilon_j} \sum_{\mathbf{k}_2,\mathbf{k}_3<\varepsilon_j} \sum_{\sigma} W_{\mathbf{q},\mathbf{q}',\mathbf{k}_2,\mathbf{k}_3} c^{\dagger}_{\mathbf{q},\sigma} c_{\mathbf{q}',\sigma} c^{\dagger}_{\mathbf{k}_2,\bar{\sigma}} c_{\mathbf{k}_3,\bar{\sigma}} \\ T_{F3} &= \sum_{\mathbf{q},\mathbf{q}'\in\varepsilon_j} \sum_{\mathbf{k}_2,\mathbf{k}_3<\varepsilon_j} \sum_{\sigma} W_{\mathbf{q},\mathbf{k}_2,\mathbf{k}_3,\mathbf{q}'} c^{\dagger}_{\mathbf{q},\sigma} c_{\mathbf{k}_2,\sigma} c^{\dagger}_{\mathbf{k}_3,\bar{\sigma}} c_{\mathbf{q}',\bar{\sigma}} \\ T_{F4}^{\dagger} + T_{F4} &= \sum_{\mathbf{q},\mathbf{q}',\in\varepsilon_j} \sum_{\mathbf{k}_1<\varepsilon_j} \sum_{\sigma} \left[W_{\mathbf{q},\mathbf{q},\mathbf{q}',\mathbf{k}_1} n_{\mathbf{q},\sigma} c^{\dagger}_{\mathbf{q}',\bar{\sigma}} c_{\mathbf{k}_1,\bar{\sigma}} + \text{h.c.} \right] \end{aligned} \tag{3.4}$$

In all of the terms $T_{P[i]}$ and $T_{F[i]}$, the factor of $1/2$ in front has been cancelled out by a factor of 2 coming from the multiple possibilities of arranging the momentum labels. We will henceforth ignore T_{P4} and T_{P5} because they cancel each other out.

The renormalisation of the Hamiltonian is constructed from the general expression

$$\Delta H^{(j)} = H_X \frac{1}{\omega - H_D} H_X \ . \tag{3.5}$$

The states on the isoenergetic shell $\pm|\varepsilon_j|$ come in particle-hole pairs $(\mathbf{q}, \bar{\mathbf{q}})$ with energies of opposite signs (relative to the Fermi energy). If $\mathbf{q}$ is defined as the hole state (unoccupied in the absence of quantum fluctuations), it will have positive energy, while the particle state $\bar{\mathbf{q}}$ will be of negative energy and hence below the Fermi surface. To be more specific, given a state $\mathbf{q}$ with energy $\pm|\varepsilon_j|$, we define its particle-hole transformed counterpart as the state $\bar{\mathbf{q}} = \boldsymbol{\pi} + \mathbf{q}$, having energy $\mp|\varepsilon_j|$ and residing in the opposite quadrant of the Brillouin zone. Given this definition, we have the important property that

$$\begin{aligned} J_{\mathbf{k},\bar{\mathbf{q}}} &= -J_{\mathbf{k},\mathbf{q}}, \\ W_{\{\mathbf{k}\},\bar{\mathbf{q}}} &= -W_{\{\mathbf{k}\},\mathbf{q}} \ . \end{aligned} \tag{3.6}$$

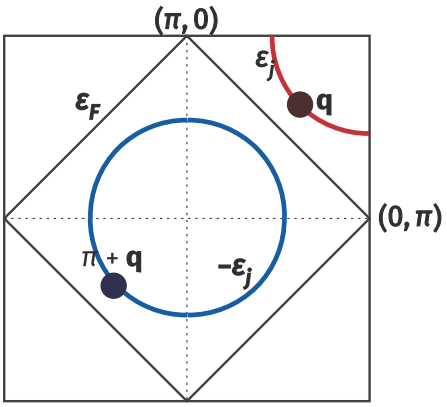

Figure 5.3: *Particle and hole states.*

5.3.2 Renormalisation of the bath correlation term W

The bath correlation term W can undergo renormalisation only via scattering processes arising from itself. Irrespective of whether the state $\mathbf{q}$ being decoupled is in a particle or hole configuration in the initial many-body state, the propagator $G = 1/(\omega - H_D)$ of the intermediate excited state is uniform, and equal to

$$G_W = 1/\big(\omega - |\varepsilon_j|/2 + W_{\mathbf{q}}/2)\big) \ , \tag{3.7}$$

where $W_{\mathbf{q}}$ is the same whether $\mathbf{q}$ is above or below the Fermi surface. The $|\varepsilon_j|/2$ in H_D arises from the excited nature of the state after the initial scattering process.

Scattering arising purely from spin-preserving processes

In this subsection, we calculate the renormalisation to W arising from the terms T_{P1}, T_{P2} and T_{P3}. The first term is

$$\begin{aligned} T_{P1}^\dagger G_W T_{P3} &= \sum_\sigma \sum_{\mathbf{k}_1,\mathbf{k}_2,\mathbf{k}_3,\mathbf{k}_4} \sum_{\mathbf{q}} W_{\mathbf{q},\mathbf{k}_2,\mathbf{k}_3,\mathbf{k}_4} c^\dagger_{\mathbf{q},\sigma} c_{\mathbf{k}_2,\sigma} c^\dagger_{\mathbf{k}_3,\sigma} c_{\mathbf{k}_4,\sigma} G_W W_{\mathbf{k}_1,\mathbf{q},\mathbf{q},\mathbf{q}} c^\dagger_{\mathbf{k}_1,\sigma} c_{\mathbf{q},\sigma} n_{\mathbf{q},\sigma} \\ &= -\sum_\sigma \sum_{\mathbf{k}_1,\mathbf{k}_2,\mathbf{k}_3,\mathbf{k}_4} c^\dagger_{\mathbf{k}_1,\sigma} c_{\mathbf{k}_2,\sigma} c^\dagger_{\mathbf{k}_3,\sigma} c_{\mathbf{k}_4,\sigma} \sum_{\mathbf{q}\in\mathrm{PS}} W_{\mathbf{q},\mathbf{k}_2,\mathbf{k}_3,\mathbf{k}_4} G_W W_{\mathbf{k}_1,\mathbf{q},\mathbf{q},\mathbf{q}} \ . \end{aligned} \tag{3.8}$$

The operators acting on the states being decoupled contract to form a number operator $n_{\mathbf{q},\sigma}$ which projects the sum over $\mathbf{q}$ into the states that are initial occupied (particle sector, PS).

The second such contribution is obtained by flipping the sequence of scattering processes:

$$\begin{aligned} T_{P3} G_W T_{P1}^\dagger &= \sum_\sigma \sum_{\mathbf{k}_1,\mathbf{k}_2,\mathbf{k}_3,\mathbf{k}_4} \sum_{\mathbf{q}} W_{\mathbf{k}_1,\mathbf{q},\mathbf{q},\mathbf{q}} c^\dagger_{\mathbf{k}_1,\sigma} c_{\mathbf{q},\sigma} n_{\mathbf{q},\sigma} G_W W_{\mathbf{q},\mathbf{k}_2,\mathbf{k}_3,\mathbf{k}_4} c^\dagger_{\mathbf{q},\sigma} c_{\mathbf{k}_2,\sigma} c^\dagger_{\mathbf{k}_3,\sigma} c_{\mathbf{k}_4,\sigma} \\ &= \sum_\sigma \sum_{\mathbf{k}_1,\mathbf{k}_2,\mathbf{k}_3,\mathbf{k}_4} c^\dagger_{\mathbf{k}_1,\sigma} c_{\mathbf{k}_2,\sigma} c^\dagger_{\mathbf{k}_3,\sigma} c_{\mathbf{k}_4,\sigma} \sum_{\mathbf{q}\in\mathrm{HS}} W_{\mathbf{q},\mathbf{k}_2,\mathbf{k}_3,\mathbf{k}_4} G_W W_{\mathbf{k}_1,\mathbf{q},\mathbf{q},\mathbf{q}} \ . \end{aligned} \tag{3.9}$$

By virtue of eq. 3.6, the product of couplings $W_{\mathbf{q},\mathbf{k}_2,\mathbf{k}_3,\mathbf{k}_4} G_W W_{\mathbf{k}_1,\mathbf{q},\mathbf{q},\mathbf{q}}$ is the same irrespective of whether $\mathbf{q}$ belongs to the particle or hole sector. The two contributions therefore cancel each other. Moreover, the remaining contributions $T_{P3}^\dagger G_W T_{P1}$ and $T_{P1} G_W T_{P2}^\dagger$ are effectively hermitian conjugates of the two contributions considered above, and therefore also cancel each other.

Scattering arising from spin-flip processes

We now come to the processes that involve spin-flips. Considering T_{F1} and T_{F4} first, we get

$$\begin{aligned} T_{F1}^\dagger G_W T_{F4} &= \sum_\sigma \sum_{\mathbf{k}_1,\mathbf{k}_2,\mathbf{k}_3,\mathbf{k}_4} \sum_{\mathbf{q}} W_{\mathbf{q},\mathbf{k}_2,\mathbf{k}_3,\mathbf{k}_4} c^\dagger_{\mathbf{q},\sigma} c_{\mathbf{k}_2,\sigma} c^\dagger_{\mathbf{k}_3,\bar\sigma} c_{\mathbf{k}_4,\bar\sigma} G_W W_{\mathbf{k}_1,\mathbf{q},\mathbf{q},\mathbf{q}} c^\dagger_{\mathbf{k}_1\sigma} c_{\mathbf{q}\sigma} n_{\mathbf{q}\bar\sigma} \\ &= -\sum_{1,2,3,4} \sum_\sigma c^\dagger_{\mathbf{k}_1\sigma} c_{\mathbf{k}_2\sigma} c^\dagger_{\mathbf{k}_3\bar\sigma} c_{\mathbf{k}_4\bar\sigma} \sum_{\mathbf{q}\in\mathrm{PS}} W_{\mathbf{q},\mathbf{k}_2,\mathbf{k}_4,\mathbf{k}_4} G_W W_{\mathbf{k}_1,\mathbf{q},\mathbf{q},\mathbf{q}} \ , \\ T_{F4} G_W T_{F1}^\dagger &= \sum_\sigma \sum_{\mathbf{k}_1,\mathbf{k}_2,\mathbf{k}_3,\mathbf{k}_4} \sum_{\mathbf{q}} W_{\mathbf{k}_1,\mathbf{q},\mathbf{q},\mathbf{q}} c^\dagger_{\mathbf{k}_1\sigma} c_{\mathbf{q}\sigma} n_{\mathbf{q}\bar\sigma} G_W W_{\mathbf{q},\mathbf{k}_2,\mathbf{k}_3,\mathbf{k}_4} c^\dagger_{\mathbf{q},\sigma} c_{\mathbf{k}_2,\sigma} c^\dagger_{\mathbf{k}_3,\bar\sigma} c_{\mathbf{k}_4,\bar\sigma} \\ &= \sum_{1,2,3,4} \sum_\sigma c^\dagger_{\mathbf{k}_1\sigma} c_{\mathbf{k}_2\sigma} c^\dagger_{\mathbf{k}_3\bar\sigma} c_{\mathbf{k}_4\bar\sigma} \sum_{\mathbf{q}\in\mathrm{HS}} W_{\mathbf{q},\mathbf{k}_2,\mathbf{k}_4,\mathbf{k}_4} G_W W_{\mathbf{k}_1,\mathbf{q},\mathbf{q},\mathbf{q}} \ . \end{aligned} \tag{3.10}$$

By the same arguments as in the previous subsection, these terms cancel each other out. Their hermitian conjugate contributions $T_{F1}G_W T_{F4}^\dagger$ and $T_{F4}^\dagger G_W T_{F1}$ also cancel out. The other two terms are T_{F2} and T_{F3}, and their contributions also cancel out for the same reason:

$$\begin{aligned} T_{F2}G_W T_{F2} &= \sum_\sigma \sum_{\mathbf{k}_1,\mathbf{k}_2,\mathbf{k}_3,\mathbf{k}_4} \sum_{\mathbf{q}} W_{\mathbf{q},\bar{\mathbf{q}},\mathbf{k}_3,\mathbf{k}_4} c^\dagger_{\mathbf{q},\sigma} c_{\bar{\mathbf{q}},\sigma} c^\dagger_{\mathbf{k}_3,\bar{\sigma}} c_{\mathbf{k}_4,\bar{\sigma}} G_W W_{\bar{\mathbf{q}},\mathbf{q},\mathbf{k}_1,\mathbf{k}_2} c^\dagger_{\bar{\mathbf{q}},\sigma} c_{\mathbf{q},\sigma} c^\dagger_{\mathbf{k}_1,\bar{\sigma}} c_{\mathbf{k}_2,\bar{\sigma}} \\ &= \sum_{1,2,3,4} \sum_\sigma c^\dagger_{\mathbf{k}_1\sigma} c_{\mathbf{k}_2\sigma} c^\dagger_{\mathbf{k}_3\bar{\sigma}} c_{\mathbf{k}_4\bar{\sigma}} \sum_{\mathbf{q}\in \mathrm{PS}} W_{\mathbf{q},\bar{\mathbf{q}},\mathbf{k}_3,\mathbf{k}_4} G_W W_{\bar{\mathbf{q}},\mathbf{q},\mathbf{k}_1,\mathbf{k}_2} \,, \\ T_{F3}G_W T_{F3} &= \sum_\sigma \sum_{\mathbf{k}_1,\mathbf{k}_2,\mathbf{k}_3,\mathbf{k}_4} \sum_{\mathbf{q}} W_{\mathbf{q},\mathbf{k}_2,\mathbf{k}_3,\bar{\mathbf{q}}} c^\dagger_{\mathbf{q},\sigma} c_{\mathbf{k}_2,\sigma} c^\dagger_{\mathbf{k}_3,\bar{\sigma}} c_{\bar{\mathbf{q}},\bar{\sigma}} G_W W_{\bar{\mathbf{q}},\mathbf{k}_4,\mathbf{k}_1,\mathbf{q}} c^\dagger_{\bar{\mathbf{q}},\bar{\sigma}} c_{\mathbf{k}_4,\bar{\sigma}} c^\dagger_{\mathbf{k}_1,\sigma} c_{\mathbf{q},\sigma} \\ &= -\sum_{1,2,3,4} \sum_\sigma c^\dagger_{\mathbf{k}_1\sigma} c_{\mathbf{k}_2\sigma} c^\dagger_{\mathbf{k}_3\bar{\sigma}} c_{\mathbf{k}_4\bar{\sigma}} \sum_{\mathbf{q}\in \mathrm{PS}} W_{\mathbf{q},\mathbf{k}_2,\mathbf{k}_3,\bar{\mathbf{q}}} G_W W_{\bar{\mathbf{q}},\mathbf{k}_4,\mathbf{k}_1,\mathbf{q}} \,, \end{aligned} \tag{3.11}$$

Scattering involving both spin-flip and spin-preserving processes

These processes involve the combination of terms like T_{P1} with T_{F4}, and T_{P2} with T_{F1}. These again cancel each other out for the same reasons as outline above.

Net renormalisation for the bath correlation term

Since all the contributions cancel out in pairs, the bath correlation term W is *marginal*.

5.3.3 Renormalisation of the Kondo scattering term J

We focus on the renormalisation of the spin-flip part of the Kondo interaction. For these processes, the intermediate many-body state always involves the impurity spin being anti-correlated with the conduction electron spin, such that the propagator for that state is $G_J = 1/\big(\omega - |\varepsilon_j|/2 + J_{\mathbf{q}}/4 + W_{\mathbf{q}}/2)\big)$.

Impurity-mediated spin-flip scattering purely through Kondo-like processes

The following processes arising from the Kondo term renormalise the spin-flip interaction:

$$\begin{aligned} T^\dagger_{KT1} G_J \left(T_{KZ1} + T^\dagger_{KZ1}\right) &= \frac{1}{4} \sum_{\mathbf{k}_1,\mathbf{k}_1,\mathbf{q}} J_{\mathbf{q},\mathbf{k}_2} S^+_d \left[-c^\dagger_{\mathbf{q}\downarrow} c_{\mathbf{k}_2\uparrow} G_J c^\dagger_{\mathbf{k}_1\downarrow} c_{\mathbf{q}\downarrow} + c^\dagger_{\mathbf{k}_2\downarrow} c_{\mathbf{q}\uparrow} G_J c^\dagger_{\mathbf{q}\uparrow} c_{\mathbf{k}_1\uparrow}\right] J_{\mathbf{k}_1,\mathbf{q}} S^z_d \\ &= -\frac{1}{8} \sum_{\mathbf{k}_1,\mathbf{k}_1,\mathbf{q}} J_{\mathbf{q},\mathbf{k}_2} S^+_d \left[c^\dagger_{\mathbf{k}_1\downarrow} c_{\mathbf{k}_2\uparrow} G_J n_{\mathbf{q}\downarrow} + c^\dagger_{\mathbf{k}_2\downarrow} c_{\mathbf{k}_1\uparrow} (1 - n_{\mathbf{q}\uparrow}) G_J\right] J_{\mathbf{k}_1,\mathbf{q}} \\ &= -\frac{1}{8} \sum_{\mathbf{k}_1,\mathbf{k}_1} S^+_d c^\dagger_{\mathbf{k}_1\downarrow} c_{\mathbf{k}_2\uparrow} \sum_{\mathbf{q}\in \mathrm{PS}} \left[J_{\mathbf{q},\mathbf{k}_2} J_{\mathbf{k}_1,\mathbf{q}} + J_{\bar{\mathbf{q}},\mathbf{k}_1} J_{\mathbf{k}_2,\bar{\mathbf{q}}}\right] G_J \,. \end{aligned} \tag{3.12}$$

In getting the final expression, we used the sigma matrix relation $S^+_d S^z_d = -\frac{1}{2} S^+_d$, and absorbed the projector $1 - n_{\mathbf{q}\uparrow}$ into the sum over the particle sector by replacing q with its particle-hole transformed

counterpart $\bar{q}$. An identical contribution is obtained by switching the sequence of processes:

$$\begin{aligned}\left(T_{KZ1}+T_{KZ1}^{\dagger}\right)G_J T_{KT1}^{\dagger} &= \frac{1}{4}\sum_{\mathbf{k}_1,\mathbf{k}_1,\mathbf{q}} J_{\mathbf{k}_1,\mathbf{q}} S_d^z \left[-c_{\mathbf{k}_1\downarrow}^{\dagger} c_{\mathbf{q}\downarrow} G_J c_{\mathbf{q}\downarrow}^{\dagger} c_{\mathbf{k}_2\uparrow} + c_{\mathbf{q}\uparrow}^{\dagger} c_{\mathbf{k}_1\uparrow} G_J c_{\mathbf{k}_2\downarrow}^{\dagger} c_{\mathbf{q}\uparrow}\right] J_{\mathbf{q},\mathbf{k}_2} S_d^{+} \\ &= -\frac{1}{8}\sum_{\mathbf{k}_1,\mathbf{k}_1} S_d^{+} c_{\mathbf{k}_1\downarrow}^{\dagger} c_{\mathbf{k}_2\uparrow} \sum_{\mathbf{q}\in \mathrm{PS}} \left[J_{\bar{\mathbf{q}},\mathbf{k}_2} J_{\mathbf{k}_1,\bar{\mathbf{q}}} + J_{\mathbf{q},\mathbf{k}_1} J_{\mathbf{k}_2,\mathbf{q}}\right] G_J \ .\end{aligned} \tag{3.13}$$

Scattering processes involving interplay between the Kondo interaction and conduction bath interaction

Looking at $T_{KT1}^{\dagger}$ first, we have

$$T_{KT1}^{\dagger} G_J \left(T_{F4}+T_{F4}^{\dagger}\right) = \frac{1}{2}\sum_{\mathbf{k}_1,\mathbf{k}_2,\mathbf{q}} J_{\mathbf{k}_2,\mathbf{q}} S_d^{+} \left(c_{\mathbf{q}\downarrow}^{\dagger} c_{\mathbf{k}_2\uparrow} G_J W_{\mathbf{q},\mathbf{q},\mathbf{k}_1,\mathbf{q}} n_{q\uparrow} c_{\mathbf{k}_1\downarrow}^{\dagger} c_{\mathbf{q}\downarrow} + c_{\mathbf{k}_2\downarrow}^{\dagger} c_{\mathbf{q}\uparrow} G_J W_{\bar{\mathbf{q}},\bar{\mathbf{q}},\mathbf{q},\mathbf{k}_1} n_{\bar{q}\downarrow} c_{\mathbf{q}\uparrow}^{\dagger} c_{\mathbf{k}_1\uparrow}\right) \ . \tag{3.14}$$

For either of the two choices of the functional form of W, it is easy to show that $W_{\mathbf{q},\mathbf{q},\mathbf{k}_1,\mathbf{q}} = W_{\bar{\mathbf{q}},\bar{\mathbf{q}},\mathbf{q},\mathbf{k}_1}$.

$$T_{KT1}^{\dagger} G_J \left(T_{F4}+T_{F4}^{\dagger}\right) = \frac{1}{2}\sum_{\mathbf{k}_1,\mathbf{k}_2,\mathbf{q}} J_{\mathbf{k}_2,\mathbf{q}} W_{\mathbf{q},\mathbf{q},\mathbf{k}_1,\mathbf{q}} G_J S_d^{+} \left[-c_{\mathbf{k}_1\downarrow}^{\dagger} c_{\mathbf{k}_2\uparrow} n_{\mathbf{q}\downarrow} n_{q\uparrow} + c_{\mathbf{k}_2\downarrow}^{\dagger} c_{\mathbf{k}_1\uparrow} (1-n_{\mathbf{q}\uparrow}) n_{\bar{q}\downarrow}\right] \ . \tag{3.15}$$

Another contribution is obtained by switching the sequence of the scattering processes:

$$\begin{aligned}\left(T_{F4}+T_{F4}^{\dagger}\right) G_J T_{KT1}^{\dagger} &= \frac{1}{2}\sum_{\mathbf{k}_1,\mathbf{k}_2,\mathbf{q}} \left(W_{\mathbf{q},\mathbf{q},\mathbf{k}_1,\mathbf{q}} n_{\bar{q}\uparrow} c_{\mathbf{k}_1\downarrow}^{\dagger} c_{\mathbf{q}\downarrow} G_J c_{\mathbf{q}\downarrow}^{\dagger} c_{\mathbf{k}_2\uparrow} + W_{\bar{\mathbf{q}},\bar{\mathbf{q}},\mathbf{q},\mathbf{k}_1} n_{q\downarrow} c_{\mathbf{q}\uparrow}^{\dagger} c_{\mathbf{k}_1\uparrow} G_J c_{\mathbf{k}_2\downarrow}^{\dagger} c_{\mathbf{q}\uparrow}\right) J_{\mathbf{k}_2,\mathbf{q}} S_d^{+} \\ &= \frac{1}{2}\sum_{\mathbf{k}_1,\mathbf{k}_2,\mathbf{q}} \left(c_{\mathbf{k}_1\downarrow}^{\dagger} c_{\mathbf{k}_2\uparrow} n_{\bar{q}\uparrow}(1-n_{\mathbf{q}\downarrow}) - c_{\mathbf{k}_2\downarrow}^{\dagger} c_{\mathbf{k}_1\uparrow} n_{q\downarrow} n_{\mathbf{q}\uparrow}\right) W_{\mathbf{q},\mathbf{q},\mathbf{k}_1,\mathbf{q}} G_J J_{\mathbf{k}_2,\mathbf{q}} S_d^{+}\end{aligned} \tag{3.16}$$

The two contributions (eqs. 3.15 and 3.16) arising from T_{KT1} cancel each other.

We now consider the other spin-exchange process $T_{KT2}^{\dagger}$. One such contribution is

$$\begin{aligned}T_{KT2}^{\dagger} G_J T_{F3} &= \frac{1}{2}\sum_{\mathbf{k}_1,\mathbf{k}_2,\mathbf{q}} J_{\mathbf{q},\bar{\mathbf{q}}} S_d^{+} \left(c_{\mathbf{q}\downarrow}^{\dagger} c_{\bar{\mathbf{q}}\uparrow} G_J c_{\bar{\mathbf{q}}\uparrow}^{\dagger} c_{\mathbf{k}_2\uparrow} c_{\mathbf{k}_1\downarrow}^{\dagger} c_{\mathbf{q}\downarrow} + c_{\bar{\mathbf{q}}\downarrow}^{\dagger} c_{\mathbf{q}\uparrow} G_J c_{\mathbf{q}\uparrow}^{\dagger} c_{\mathbf{k}_2\uparrow} c_{\mathbf{k}_1\downarrow}^{\dagger} c_{\bar{\mathbf{q}}\downarrow}\right) W_{\bar{\mathbf{q}},\mathbf{k}_2,\mathbf{k}_1,\mathbf{q}} \\ &= -\frac{1}{2}\sum_{\mathbf{k}_1,\mathbf{k}_2,\mathbf{q}} S_d^{+} c_{\mathbf{k}_1\downarrow}^{\dagger} c_{\mathbf{k}_2\uparrow} \left[n_{\mathbf{q}\downarrow}(1-n_{\bar{\mathbf{q}}\uparrow}) + n_{\bar{\mathbf{q}}\downarrow}(1-n_{\mathbf{q}\uparrow})\right] J_{\mathbf{q},\bar{\mathbf{q}}} G_J W_{\bar{\mathbf{q}},\mathbf{k}_2,\mathbf{k}_1,\mathbf{q}} \\ &= -\frac{1}{2}\sum_{\mathbf{k}_1,\mathbf{k}_2} S_d^{+} c_{\mathbf{k}_1\downarrow}^{\dagger} c_{\mathbf{k}_2\uparrow} \sum_{\mathbf{q}\in \mathrm{PS}} \left(J_{\mathbf{q},\bar{\mathbf{q}}} W_{\bar{\mathbf{q}},\mathbf{k}_2,\mathbf{k}_1,\mathbf{q}} + J_{\bar{\mathbf{q}},\mathbf{q}} W_{\mathbf{q},\mathbf{k}_2,\mathbf{k}_1,\bar{\mathbf{q}}}\right) G_J \ .\end{aligned} \tag{3.17}$$

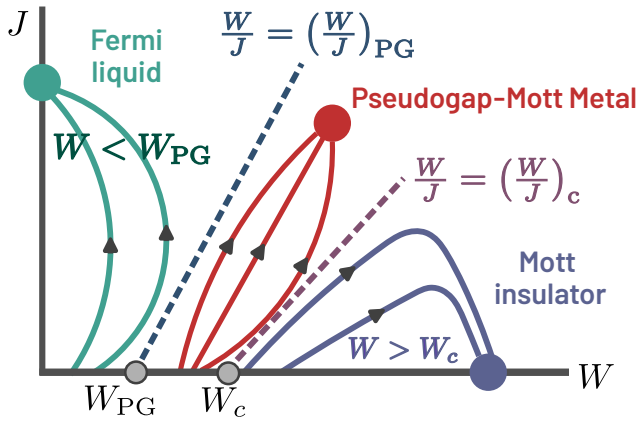

Figure 5.4: *Renormalisation group (RG) flow diagram of the lattice model as obtained from a unitary RG analysis of the lattice-embedded impurity model. For $|W/J| < |W/J|_{PG}$, the flows lead to a Fermi liquid phase, while for $|W/J| < |W/J|_c$, they lead to a Mott insulator. For values in between, the system flows to a Mott metal phase that has a pseudogap in the density of states.*

An identical contribution is obtained from the reversed term:

$$\begin{aligned} T_{F3}G_J T^{\dagger}_{KT2} &= \frac{1}{2}\sum_{\mathbf{k}_1,\mathbf{k}_2,\mathbf{q}} W_{\bar{\mathbf{q}},\mathbf{k}_2,\mathbf{k}_1,\mathbf{q}} \left(c^{\dagger}_{\bar{\mathbf{q}}\uparrow} c_{\mathbf{k}_2\uparrow} c^{\dagger}_{\mathbf{k}_1\downarrow} c_{\mathbf{q}\downarrow} G_J c^{\dagger}_{\mathbf{q}\downarrow} c_{\bar{\mathbf{q}}\uparrow} + c^{\dagger}_{\mathbf{q}\uparrow} c_{\mathbf{k}_2\uparrow} c^{\dagger}_{\mathbf{k}_1\downarrow} c_{\bar{\mathbf{q}}\downarrow} G_J c^{\dagger}_{\bar{\mathbf{q}}\downarrow} c_{\mathbf{q}\uparrow} \right) J_{\mathbf{q},\bar{\mathbf{q}}} S^{+}_d \\ &= -\frac{1}{2}\sum_{\mathbf{k}_1,\mathbf{k}_2} S^{+}_d c^{\dagger}_{\mathbf{k}_1\downarrow} c_{\mathbf{k}_2\uparrow} \sum_{\mathbf{q}\in \mathrm{PS}} \left(J_{\mathbf{q},\bar{\mathbf{q}}} W_{\bar{\mathbf{q}},\mathbf{k}_2,\mathbf{k}_1,\mathbf{q}} + J_{\bar{\mathbf{q}},\mathbf{q}} W_{\mathbf{q},\mathbf{k}_2,\mathbf{k}_1,\bar{\mathbf{q}}} \right) G_J \ . \end{aligned} \tag{3.18}$$

Net renormalisation to the Kondo interaction

Combining the results from eqs. 3.12, 3.13, 3.17 and 3.18, as well as using the properties $J_{\bar{\mathbf{q}},\mathbf{k}_1} J_{\mathbf{k}_2,\bar{\mathbf{q}}} = J_{\mathbf{q},\mathbf{k}_2} J_{\mathbf{k}_1,\mathbf{q}} = J_{\mathbf{k}_2,\mathbf{q}} J_{\mathbf{q},\mathbf{k}_1}$ and $J_{\mathbf{q},\bar{\mathbf{q}}} W_{\bar{\mathbf{q}},\mathbf{k}_2,\mathbf{k}_1,\mathbf{q}} = J_{\bar{\mathbf{q}},\mathbf{q}} W_{\mathbf{q},\mathbf{k}_2,\mathbf{k}_1,\bar{\mathbf{q}}}$, the total renormalisation in the momentum-resolved Kondo coupling $J^{(j)}$ at the jth step amounts to

$$\Delta J^{(j)}_{\mathbf{k}_1,\mathbf{k}_2} = -\sum_{\mathbf{q}\in \mathrm{PS}} \frac{J^{(j)}_{\mathbf{k}_2,\mathbf{q}} J^{(j)}_{\mathbf{q},\mathbf{k}_1} + 4 J^{(j)}_{\mathbf{q},\bar{\mathbf{q}}} W_{\bar{\mathbf{q}},\mathbf{k}_2,\mathbf{k}_1,\mathbf{q}}}{\omega - \frac{1}{2}|\varepsilon_j| + J^{(j)}_{\mathbf{q}}/4 + W_{\mathbf{q}}/2} \tag{3.19}$$

A representation of the RG phase diagram in the $-W/t$ vs. J/t plane of couplings has been provided in Fig.5.5(a) from detailed numerical computations of eq.(3.19). We also provide a schematic representation of RG flows to various fixed point theories in the J vs. W plane of couplings in Fig.5.4. This schematic figure shows the existence of three distinct phases (Fermi liquid metal, Mott Insulator, and Pseudogap-Mott metal) described by distinct fixed point theories of the RG flows. The Fermi liquid metal and Mott Insulator phases are distinguished from the Pseudogap-Mott metal by separatrices of the RG flows.

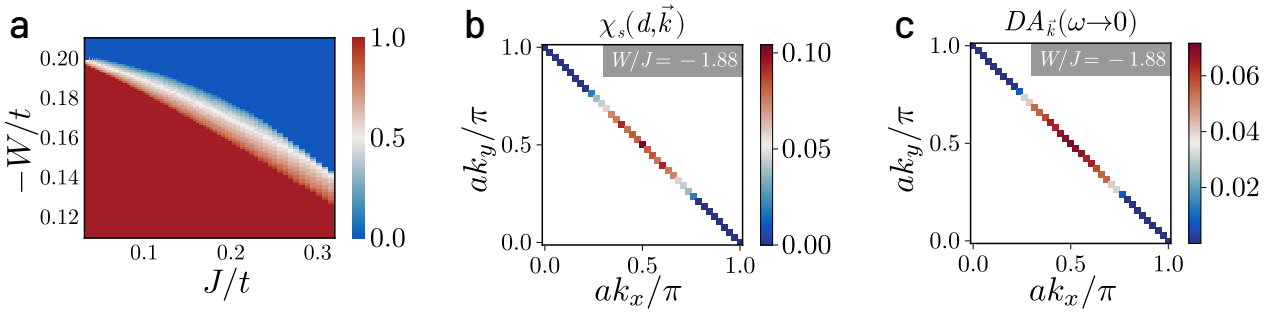

Figure 5.5: *(a) Phase diagram of impurity model at strong coupling in U in terms of competing dimensionless Kondo (J/t) and bath correlation (W/t) couplings. Colourbar represents the fraction of states on the Fermi surface replaced by zeros of the Greens function (Luttinger surface). A pseudogap phase (shaded region) is observed between the local Fermi liquid (red region) and local moment (blue region) phases (b) k-space-resolved spin-spin correlation $\chi_s(d,\mathbf{k}) = \langle \mathbf{S}_d \cdot \mathbf{S}_\mathbf{k} \rangle$ in the pseudogap phase of the impurity model. Antinodal regions are observed to decouple from Kondo screening of the impurity. (c) Upon tiling, this leads to a k-space-resolved antinodal gap in the electronic density of states of the lattice model, corresponding to Luttinger surfaces of zeros.*

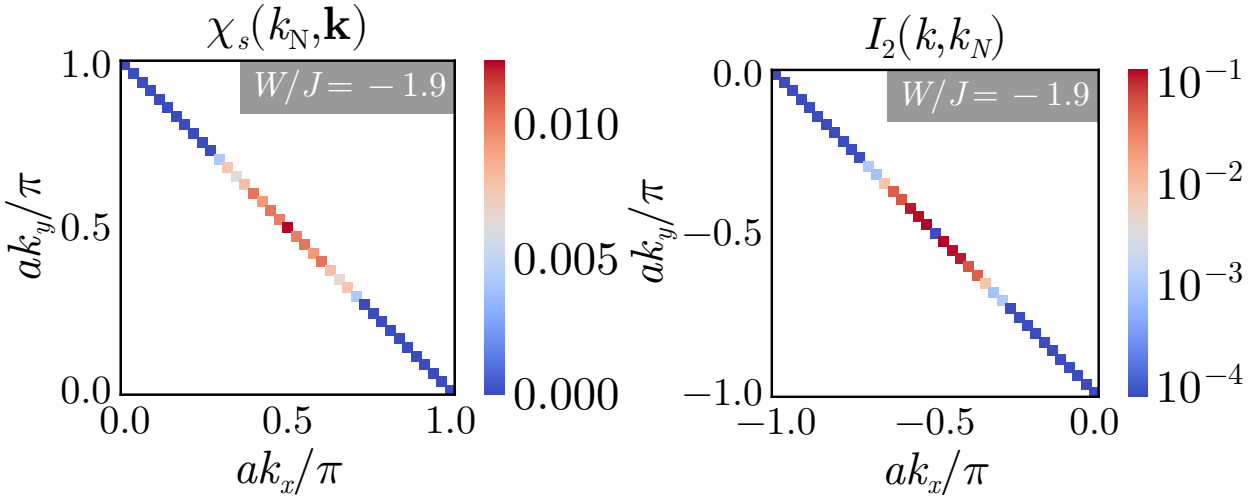

Figure 5.6: *Left: Spin correlations χ_s for the tiled model, between the nodal point $k_N = (-\pi/2,-\pi/2)$ and an arbitrary k−point on the Fermi surface. In the PG, the spin-correlations near the antinode vanish, indicating that they have been removed from the metallic excitations, while the correlations near the nodal point become enhanced because of the increasingly correlated nature of the metal. Right: Mutual information I_2 between an arbitrary k−state and the nodal point. The nodal points remain strongly entangled with each other all the way through the PG.*

5.4 Reconstructing of lattice model from auxiliary model

To reconstruct a translationally invariant lattice Hamiltonian from the impurity model (with Hamiltonian $\mathcal{H}_{\text{aux}}$), we define a many-body tiling prescription that embeds the auxiliary impurity system uniformly across the two-dimensional square lattice. Thus, the tiling process systematically derives

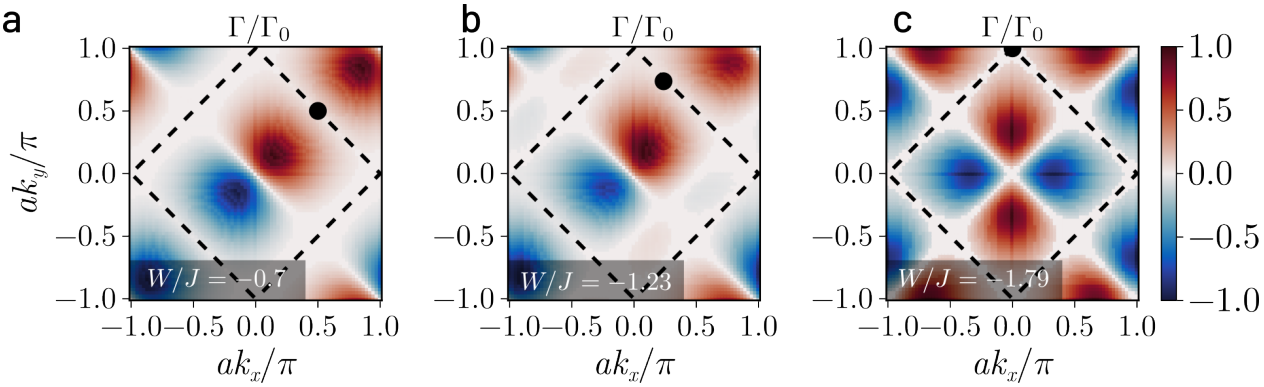

Figure 5.7: *Initiation of the decoupling of $J_{\mathbf{k},\mathbf{k}'}$ (positive, negative and zeros shown in red, blue and white respectively), with $\mathbf{k}$ (black circle) at low-energies for $\mathbf{k}$ corresponding to the node (a), antinode (b) and a point mid-way between them (c) on the top right arm of the FS respectively with tuning W/J. As dictated by the symmetry of $J_{\mathbf{k},\mathbf{k}'}$, the decoupling for a given $\mathbf{k}$ proceeds via the appearance of zeros (white patches) of $J_{\mathbf{k},\mathbf{k}'}$ for $\mathbf{k}'$ initially on the nodal regions of adjacent arms, and progresses gradually towards the antinodes. The decoupling ends with the onset of the pseudogap.*

the full lattice dynamics from the renormalized fixed-point structure of the impurity. As described in Section 5.2, the auxiliary model consists of a single impurity embedded in a correlated bath at the location $\mathbf{r}_d$:

$$H(\mathbf{r}_d) = H_{\text{imp}} + H_{\text{cbath}} + H_{\text{imp-cbath}} \,. \tag{4.1}$$

The form of various terms in eq.(4.1) have been defined in eqs.(2.2), (2.3) and (2.4) in Section 5.2. The tiling procedure is shown in detail in Section 4.2.2 of Chapter 4.

A non-zero chemical potential in the bath and/or the impurity can be included to study the effects of doping. Crucially, the eigenstates of $\mathcal{H}_{\text{tiled}}$ obey a many-body generalization of Bloch's theorem [449], which allows for the exact computation of momentum-resolved observables (presented here for a 77×77 $\mathbf{k}$-space Brillouin zone grid). We shall demonstrate below that the lattice embedding and tiling procedures provide a controlled route to capture low-energy NFL behavior and Mott criticality directly from a quantum impurity model.

5.5 Low-energy theory for the lattice-embedded impurity model

5.5.1 RG Phase Diagram

A detailed picture of the PG in the impurity model is obtained from a momentum-resolved breakdown of Kondo screening in the strong-coupling regime $U \gg t$ phase of H_{aux}. A unitary renormalisation group (URG) scaling analysis [348] obtains a flow equation of the Kondo coupling $J^{(j)}_{\mathbf{k}_1,\mathbf{k}_2}$.

$$\Delta J^{(j)}_{\mathbf{k}_1,\mathbf{k}_2} = -\sum_{\mathbf{q}\in \text{PS}} \frac{J^{(j)}_{\mathbf{k}_2,\mathbf{q}} J^{(j)}_{\mathbf{q},\mathbf{k}_1} + 4 J^{(j)}_{\mathbf{q},\bar{\mathbf{q}}} W_{\bar{\mathbf{q}},\mathbf{k}_2,\mathbf{k}_1,\mathbf{q}}}{\omega - \frac{1}{2}|\varepsilon_j| + J^{(j)}_{\mathbf{q}}/4 + W_{\mathbf{q}}/2} \,, \tag{5.1}$$

where ε_j is the energy of the shell being decoupled at the jth step, the sum is over all occupied momentum states $\mathbf{q}$ of the energy shell ε_j, and $\bar{\mathbf{q}} = \mathbf{q} + \boldsymbol{\pi}$ is the particle-hole transformed state associated with $\mathbf{q}$. The bath interaction coupling $W_{\bar{\mathbf{q}},\mathbf{k}_2,\mathbf{k}_1,\mathbf{q}}$ is found to be marginal under these transformations. While we present a detailed numerical evaluation of the RG equation for $J_{\mathbf{k}_1,\mathbf{k}_2}$ (eq.(**5.1**)) below, it is clear that the frustration of Kondo screening due to charge fluctuations (for attractive bath interactions $W < 0$) leads to the Mott transition [454].

A detailed numerical computation of the URG equation in eq. (**5.1**) leads to the phase diagram shown in Fig. 5.5(a). Upon tuning the ratio of the bath and Kondo interactions (W/J) from zero to negative values, the following phases emerge in the impurity model from the competition between J and W in eq. (**5.1**): (i) for $W/J < (W/J)_{\text{PG}}$, an LFL phase (red region), where the entire FS participates in Kondo screening, (ii) for $\frac{W}{J} \in [(\frac{W}{J})_{\text{PG}}, (\frac{W}{J})_c]$ (shaded region), a local PG phase where disconnected parts of the FS around the node participate in Kondo screening, and (iii) a local moment phase for $\frac{W}{J} > (\frac{W}{J})_c$ (blue region), where the impurity remains unscreened at low-energies. These can be visualised from spin correlations, $\chi_s(d,\mathbf{k}) = \langle \mathbf{S}_d \cdot \mathbf{S}_{\mathbf{k}} \rangle$, as shown in Fig. 5.5(b) for the PG. The values $(W/J)_{\text{PG}}$ and $(W/J)_c$ are therefore the entry into and exit from the PG phase.

Mapping onto the lattice model via tiling, we observe that RG-induced nodal–antinodal dichotomy in $J_{\mathbf{k},\mathbf{k}'}$ in the impurity model is the microscopic origin of the PG in the lattice model: the extinction of Kondo coherence translates into spectral zeros in the lattice Green's function (i.e., Luttinger surfaces) at antinodal momenta (Fig. 5.5(c)). This establishes that the $T = 0$ Mott transition of the 2D *extended*-Hubbard model proceeds from FL to MI through an intervening PG phase. In Fig. 5.6, similar insights obtain from the spin-correlation $\chi_s(\mathbf{k}, k_N) = \langle \mathbf{S}_{\mathbf{k}} \cdot \mathbf{S}_{k_N} \rangle$ in $k-$space (where k_N is the nodal momentum) and mutual information $I_2(\mathbf{k} : k_N)$ between two momentum states: the PG displays Fermi arcs in the nodal regions along with vanishing correlation and entanglement in the antinodal regions.

5.5.2 Unravelling of Kondo Screening

The $\mathbf{k}$-space anisotropy of Kondo breakdown can be visualized in terms of zeros of $J_{\mathbf{k}_N,\mathbf{k}}$, involving spin-flip scattering between the node $\mathbf{k}_N = (\pi/2, \pi/2)$ and a general wavevector $\mathbf{k}$. For any W/J, the C_4 lattice symmetry dictates that $J_{\mathbf{k}_N,\mathbf{k}}$ vanishes if $\mathbf{k}$ belongs to any of the antinodes or adjacent nodes. Tuning W/J towards $(W/J)_{\text{PG}}$ leads to an unravelling of the Kondo screening: $J_{\mathbf{k}_N,\mathbf{k}}$ for $\mathbf{k}$ close to the adjacent nodes turns RG-irrelevant first, and a patch of zeros subsequently appears in $J_{\mathbf{k}_N,\mathbf{k}}$ around this point (Fig. 5.7(a)). Tuning W/J further extends the patch of zeros towards the antinodes (Fig. 5.7(b) and 5.7(c)). Kondo screening thus unravels by a systematic decoupling of all $J_{\mathbf{k}_1,\mathbf{k}_2}$ that connect adjacent quadrants of the Brillouin zone.

Precisely at $W/J = (W/J)_{\text{PG}}$, the antinode joins this connected region of zeros in $J_{\mathbf{k}_1,\mathbf{k}_2}$, marking the decoupling of the antinodes from all other points in the neighbourhood of the FS. This is an interaction-driven Lifshitz transition of the FS, and marks the entry into a PG phase possessing Fermi arcs [190]. Importantly, it coincides with an emergent two-channel Kondo (2CK) impurity model, where each channel corresponds to a pair of Fermi arcs on opposite faces of the conduction bath FS (see Subection 5.5.3). The 2CK nature of the PG is guaranteed by the symmetry of $J_{\mathbf{k},\mathbf{k}'}$:

$$J_{\mathbf{k},\mathbf{k}'} = -J_{\mathbf{k}+\mathbf{Q},\mathbf{k}'} = -J_{\mathbf{k},\mathbf{k}'+\mathbf{Q}}, \quad \mathbf{Q} = (\pi,\pi). \tag{5.2}$$

The PG expands by shrinking these disconnected Fermi arcs towards the respective nodes, leading to nodal metals whose disappearance heralds the Mott transition.

5.5.3 Emergence of a two-channel Kondo Model

As the bath interaction W is tuned through the L-PG phase, the four nodal points in the Brillouin zone are the last to decouple from the impurity. This allows us to write down a simpler Kondo model near the transition, focusing on scattering processes involving the nodal region. Specifically, for the Kondo term $J_{\mathbf{k}_1,\mathbf{k}_2}$), we find that only the following classes of scattering processes survive close to the critical point:

- Both momenta in a neighbourhood around $\mathbf{k}_N$, where $\mathbf{k}_N$ can be any of the four nodal points,
- One momentum from the neighbourhood around $\mathbf{k}_N$, while the other from the neighbourhood around $\mathbf{k}_N + (\pi, \pi)$.

The second class is tied to the first through a symmetry of the Hamiltonian (eq. 5.2). The crucial feature of these processes is that each node only interacts with the other node directly opposite to it across the origin. That is, $(\pi/2, \pi/2)$ and $(-\pi/2, -\pi/2)$ only interact between themselves, while $(\pi/2, -\pi/2)$ and $(-\pi/2, \pi/2)$ form their own pair of connected regions.

Let $S^{\pm}$ be the set of momentum states in a small window around nodes along $k_x = \pm k_y$. As discussed immediately above, the Kondo spin-exchange term close to the transition does not lead to scattering of any $k-$state from S^+ to S^-. This is verified by calculating the ratio $\max\left\{J_{k_1^+,k_2^-}\right\}/\max\left\{J_{k_1^+,k_2^+}\right\}$, where the maximum in the numerator is calculated from all the low-energy (fixed point) Kondo scattering processes that connect the two sets $S^{\pm}$, while the denominator maximum is from within the set S^+. This ratio vanishes (Fig. 5.8) within the local pseudogap regime, indicating that no direct Kondo scattering process persists between the two sectors $S^{\pm}$ at low energies, deep within the pseudogap regime. We call the value of W at which this ratio vanishes W^*.

The decoupling of the $k-$space regions $S^{\pm}$ is captured by the following simplified low-energy Hamiltonian:

$$H_{\text{eff}} = H(S^+) + H(S^-);\ H(S) = \sum_{\mathbf{q}\in S,\sigma} \varepsilon_{\mathbf{q}} c^{\dagger}_{\mathbf{q}\sigma} c_{\mathbf{q}\sigma} + \sum_{\mathbf{q}_1\in S,\mathbf{q}_2\in S} \sum_{\alpha,\beta} J^*(\mathbf{q}_1,\mathbf{q}_2)\mathbf{S}_d \cdot \sigma_{\alpha\beta} c^{\dagger}_{\mathbf{q}_1\alpha} c_{\mathbf{q}_2\beta}\ , \tag{5.3}$$

where $H(S^{\pm})$ represents the dynamics of momentum states residing in regions $S^{\pm}$. The only source of information transfer between the two regions is the fact that they interact with the same impurity local moment. Eq.5.3 tells us that the low-energy dynamics of the embedded eSIAM close to the Kondo-breakdown transition is governed by an emergent **two-channel Kondo model**, with the conduction bath states in the sets $S^{\pm}$ making up the two channels.

The emergence of such two-channel Kondo physics in the pseudogap phase is indicative that the metallic excitations in such a phase are likely to be of the non-Fermi liquid kind. We will elaborate more in this in the coming sections.

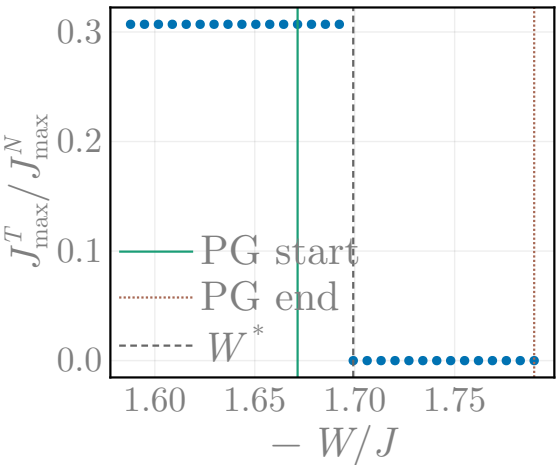

Figure 5.8: *Ratio between the maximum values of the fixed point values of the Kondo couplings for scattering processes between and within the regions S^+ and S^-. The vanishing of the fixed point ratio indicates that the pseudogap regime features a singular low-energy effective theory, where the Fermi surface neighbourhood splits into two disconnected regions with no explicit term in the Hamiltonian connecting them directly.*

5.5.4 Momentum-resolved Dynamical Spectral Weight Transfer

Passage through the PG phase is accompanied by a highly structured transfer of spectral weight across the FS. Strong charge fluctuations develop between the nodal and antinodal regions of the FS in the PG regime of the impurity model (Fig. 5.9(a)), as captured by the correlator:

$$\chi_c(\mathbf{k}_1, \mathbf{k}2) = \left\langle c^\dagger_{\mathbf{k}1\uparrow} c^\dagger_{\mathbf{k}1\downarrow} c_{\mathbf{k}2\downarrow} c_{\mathbf{k}_2\uparrow} + \text{h.c.} \right\rangle . \tag{5.4}$$

These fluctuations dynamically redistribute low-energy spectral weight from the antinodes to higher energies, leading to selective gap formation. Accordingly, the Luttinger surfaces of the PG [26] coincides with the appearance of poles of the lattice model self-energy $\Sigma(\mathbf{k}, \omega = 0)$ near the antinodes; these poles approach the nodes on tuning towards the Mott transition (Fig. 5.9(b)). This mirrors the coalescing of finite-frequency poles of the self-energy poles towards zero frequency in the underlying impurity model (Fig. 5.9(c)).

5.6 Non-Fermi liquid excitations within the Pseudogap

5.6.1 Pseudogapped spectral function and singular self-energy

In the PG regime, the nature of gapless Fermi arcs changes dramatically. We have already argued that the low-energy dynamics of these gapless Fermi arcs are governed by an underlying two-channel Kondo (2CK) impurity model [60, 589]. This is consistent with the rapid fall of the impurity quasiparticle residue Z_{imp} (Fig. 5.10(a)) from finite values in the FL phase to vanishingly small values just before the onset of the PG. Inset shows the simultaneous emergence of increasingly uncompensated

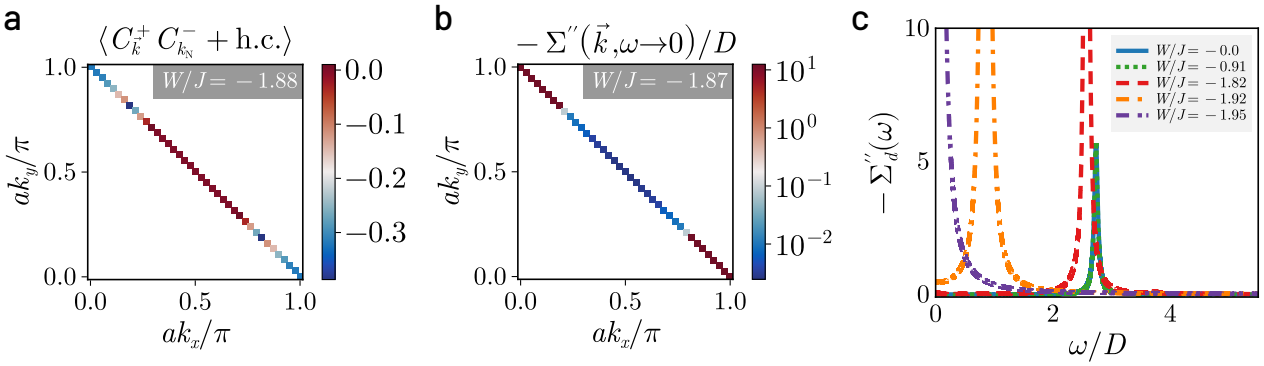

Figure 5.9: *(a) Enhanced charge correlations* $\chi_c(\mathbf{k}_1,\mathbf{k}_2) = \langle c^\dagger_{\mathbf{k}_1\uparrow} c^\dagger_{\mathbf{k}_1\downarrow} c_{\mathbf{k}_2\downarrow} c_{\mathbf{k}_2\uparrow} + h.c.\rangle$ *between the nodal and antinodal regions, signalling Kondo breakdown in the pseudogap phase of the impurity model. (b) In turn, the breakdown leads to the gapping of the antinodal regions in the lattice model, seen from the appearance of poles in the imaginary part of the self-energy. (c) The imaginary part of the impurity self-energy* $\Sigma''(\omega > 0)$ *possesses a pole at non-zero* ω *in the PG that moves towards* $\omega = 0$ *as the Mott transition is approached.*

local magnetic moments upon traversing the PG phase. The accompanying impurity spectral function of the gapless arcs show a pseudogapped behaviour for $\omega \simeq 0$, with a rapid fall in the spectral weight at $\omega = 0$ upon traversing the PG (Fig. 5.10(c)). The collapse of the Kondo resonance into a pseudogapped spectral function is accompanied by the redistribution of spectral weight [26] in the impurity spectral function (Fig. 5.10(b)) from $\omega \sim 0$ to the Hubbard sidebands at finite frequencies $\omega \simeq \pm 3$ (in units of the bandwidth).

Concomitant with this is the emergence of a zero-frequency peak in the imaginary part of the self-energy of the NFL in the PG phase(Fig. 5.11(a)),

$$-1/\Sigma''(\omega) \sim 1/\Sigma''(0) + \omega^\beta \,. \tag{6.1}$$

Remarkably, we find that the exponent $\beta = 2$ characterises the NFL for the entire PG phase (see Fig. 5.11(b)), including the critical end-point. This is in stark contrast with the $\Sigma''(\omega) \sim \omega^2$ for the FL (Fig. 5.11(b)). A similar analysis reveals the power-law scaling for the low-frequency behaviour of the impurity spectral function in Fig.5.12. We observe that $A_d(\omega) \sim A_d(0) + \omega^2$ for the pseudogap phase, while $1/A_d(\omega) \sim 1/A_d(0) + \omega^2$ for the Fermi liquid (inset of Fig. 5.12).

5.6.2 Finite-Frequency Scattering Rate and Optical Response Through the Pseudogap

All $\Sigma''(\omega)$ for the NFL are observed to lie above the Mott-Ioffe-Regel (MIR) bound [590, 591] (dashed blue line in Fig. 5.11(a)), while those for the FL lie below. The MIR bound is the maximum expected scattering rate in metals when the mean free path approaches the lattice spacing:

$$-2\Sigma''_{\text{MIR}} = 1/\tau_{\text{MIR}} \,,\ \tau_{\text{MIR}} = l_{\text{min}}/v_F \,, \tag{6.2}$$

where $l_{\min}$ is the minimum mean free path in metals (equal to one lattice spacing) and $\tau_{\rm MIR}$ is the associated lifetime of quasiparticles close to the FS (with Fermi velocity v_F). The height of the zero-frequency peak rises by almost 4 orders of magnitude from the start of the PG till its end at the Mott transition point (Fig. 5.11(c)); the dramatic growth of the peak height very near the Mott critical point coincides with the coalescing of the finite-frequency poles of the self-energy into a single pole at zero-frequency, signalling the singular nodal NFL present at the Mott quantum critical point.

To further probe the breakdown of coherent transport in the pseudogap (PG) regime, we examine the product of the impurity spectral function $A(\omega)$ and the scattering lifetime $\tau(\omega)$, which approximates the optical conductivity $\sigma(\omega)$ via a Drude-type relation. As shown in the right panel of Fig. 5.12, this quantity exhibits a sharp Drude peak at $\omega = 0$ in the Fermi liquid (FL) regime (blue), consistent with long-lived quasiparticles. In stark contrast, the PG regime (green, red, orange) shows a pronounced suppression of low-frequency conductivity and the emergence of a finite-frequency peak centered near $\omega/D \sim 0.3$–0.4 (where D is the kinetic energy bandwidth).

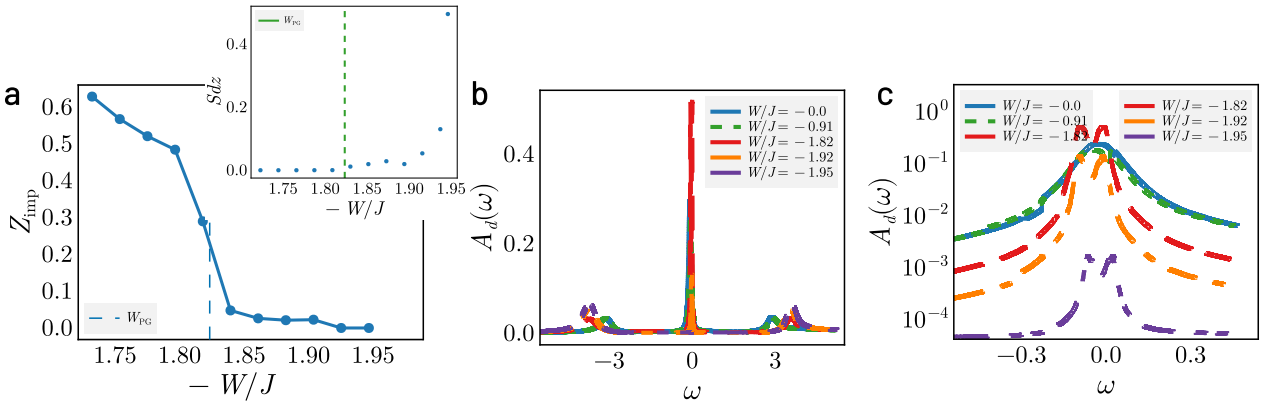

Figure 5.10: *(a) Suppression of quasiparticle residue (Z_{imp}) as the impurity model is tuned towards the Mott transition. An initial drastic fall in Z_{imp} is observed for $W/J \lesssim (W/J)_{PG}$ from 0.3 to around 0.05, signalling the destruction of the FL with unravelling of Kondo screening. A steady decrease in Z_{imp} is observed in passage through the PG, and is vanishingly small close to the Mott transition due to a divergent self-energy. Inset shows the growth of unscreened impurity magnetic moment in the pseudogap phase, signalling the breakdown of Kondo screening. (b) Impurity Spectral function in the FL and PG phases. The evolution of the central peak from Kondo resonance to pseudogap is accompanied by dynamical spectral weight transfer to the Hubbard side bands at finite frequencies $\omega \simeq \pm 3$ (in units of the bandwidth). (c) Zoom-in of the central (Kondo) resonance of the impurity spectral function. While undisturbed in the Fermi liquid phase, it splits into a pseudogap in the PG phase, with its height diminishing rapidly as the Mott transition is approached.*

Strikingly, this peak shifts very little across the PG regime (see inset), despite a deepening spectral gap and diverging self-energy. Its position lies well below the Mott gap ($\sim 2.5D$), suggesting that it represents an emergent mid-infrared (MIR) excitation intrinsic to the Mott metal characterising the PG. This feature closely mirrors the experimentally observed MIR peak in high-T_c cuprates [592–594], which has been variously attributed to excitations of electrons bound to vacancies [595], or the dressing of holes by spin excitations [596]. Here, its robust energy scale and

insensitivity to increasing incoherence imply a universality persisting through the PG, likely rooted in short-range entanglement between deconfined doublons and holons excitations of the Mott metal. This is further evidence that the PG metal is not simply a degraded Fermi liquid, but a distinct phase whose optical response is driven by emergent degrees of freedom.

5.6.3 Non-local correlations in the pseudogap

In Fig. 5.13(a) and 5.13(b), the spin-flip correlations and mutual information between the impurity spin and conduction bath sites respectively are observed to undergo a crossover within the PG, from a short-ranged behaviour at its onset, to a long-ranged behaviour as the Mott transition approaches. The entanglement is also observed to be multipartite in nature: in Fig. 5.13(c), the quantum Fisher information (QFI) [461] computed for the ground state wavefunction using an operator corresponding to the sum of local spin-flip exchange processes shows a jump at the onset of the PG. Further, the FL is observed to possess bi-partite entanglement while the NFL of the PG phase displays pentapartite entanglement [597, 598].

These striking results imply that the Mott transition observed by us lies beyond the local quantum criticality scenario [82]. Instead, we observe the PG phase to be a novel state of strongly interacting quantum matter emergent from the breakdown of local Kondo screening. This state is described by a quantum critical Fermi surface [599] with NFL Fermi arcs that display increasingly critical behaviour, i.e., dynamics described by non-local quantum fluctuations, and excitations that become truly long-ranged close to the transition. It is tempting to conjecture that the long-range entangled critical state captured in Fig. 5.13(b) reflects the existence of a highly efficient scrambler [600–602], i.e., a state in which entanglement spreads among its constituents at the fastest rate permissible by quantum mechanics.

5.7 Exactly solvable nodal Non-Fermi liquid at Mott Criticality

Very close to the transition, the excitations of the nodal NFL correspond to those of a Hatsugai-Kohmoto model [28, 29]. This insight is obtained from a perturbation-theoretic treatment of the RG fixed point Hamiltonian of the impurity model for $W/J \lesssim (W/J)_{\rm PG}$, by considering the effects of a small fixed point Kondo scattering probability J^* in the backdrop of a larger bath interaction parameter $|W|$. This yields the HK model [28, 29] as the singular part of the effective Hamiltonian arising from forward scattering processes.

As the bath interaction W is tuned through the L-PG phase, the nodal region is the last to decouple from the impurity. This allows us to write down a simpler Kondo model near the transition, where only the nodal region is hybridising with the impurity spin through Kondo interactions. This is done by retaining only those scattering processes $\mathbf{k}_1 \rightarrow \mathbf{k}_2$ that originate from and end at $k-$points within a small neighborhood of width $|\mathbf{q}|$ around the four nodal points: $\mathbf{k}_1, \mathbf{k}_2 \in \mathbf{N} + \mathbf{q}, |\mathbf{q}| \ll \pi$, where $\mathbf{N}$ can be any one of the four nodal points $\mathbf{N}_1 = (\pi/2, \pi/2)$, $\mathbf{N}_2 = (-\pi/2, \pi/2)$ and $\mathbf{N}_1 + \mathbf{Q}_1$ and $\mathbf{N}_2 + \mathbf{Q}_2$, where $\mathbf{Q}_1 = (-\pi, -\pi)$ and $\mathbf{Q}_2 = (\pi, -\pi)$ are the two nesting vectors. We have already seen, in Subsection 5.5.3, that the pseudogap regime displays a decoupling of the Brillouin zone into sets of points that have no explicit connecting term in the Hamiltonian. Near the transition, the

neighbourhoods of $\mathbf{N}_1$ and $\mathbf{N}_1 + \mathbf{Q}_1$ form one such connected set, while the other two nodes $\mathbf{N}_2$ and $\mathbf{N}_2 + \mathbf{Q}_2$ form another connected set, but these two sets are disconnected from each other, in the sense of a two-channel model. We also assume that the window of $\mathbf{q}$ is small enough so that the fixed point Kondo coupling values $J^*(\mathbf{q}_1, \mathbf{q}_2)$ for the scattering processes involving $\mathbf{q}_1$ and $\mathbf{q}_2$ can be replaced by an average value J^*.

With these considerations, the simplified low-energy model near the transition describing the Kondo scattering processes can be written as

$$\tilde{H}_{\text{imp-cbath}} = J^* \frac{1}{2} \sum_{l=1,2} \sum_{\mathbf{q}_1,\mathbf{q}_2} \sum_{\alpha,\beta} \mathbf{S}_d \cdot \boldsymbol{\sigma}_{\alpha\beta} \Big(c^\dagger_{\mathbf{N}_l+\mathbf{q}_1,\alpha} c_{\mathbf{N}_l+\mathbf{q}_2,\beta} + c^\dagger_{\mathbf{N}_l+\mathbf{Q}_l+\mathbf{q}_1,\alpha} c_{\mathbf{N}_l+\mathbf{Q}_l+\mathbf{q}_2,\beta} - c^\dagger_{\mathbf{N}_l+\mathbf{Q}_l+\mathbf{q}_1,\alpha} c_{\mathbf{N}_l+\mathbf{q}_2,\beta} - c^\dagger_{\mathbf{N}_l+\mathbf{q}_1,\alpha} c_{\mathbf{N}_l+\mathbf{Q}_l+\mathbf{q}_2,\beta} \Big) \ . \tag{7.1}$$

For scattering processes that involve two opposite nodal points (that is, connected by one of the nesting vectors $\mathbf{Q}_l$, the Kondo coupling is $-J^*$, which explains the negative signs in the third and fourth terms. An explanation of the various dummy indices is in order. The label l can take values 1 or 2, allowing us to consider both the decoupled sets (associated with $\mathbf{N}_1$ and $\mathbf{N}_2$). It also labels the nesting vectors $\mathbf{Q}_l$ associated with the two sets. α and β indicate spin indices, and $\mathbf{q}_1$ and $\mathbf{q}_2$ represent incoming and outgoing momenta in the scattering processes.

Because of the decoupling of the channel $l = 1$ and $l = 2$, we consider only the $l = 1$ channel for the rest of the calculations in this section, and we comment at the end on what the presence of two channels means for the results. In order to simplify the Hamiltonian, we define new fermionic operators

$$\psi_{\mathbf{q},\sigma} = \frac{1}{\sqrt{2}} \left(c_{\mathbf{N}_1+\mathbf{q},\sigma} + c_{\mathbf{N}_1+\mathbf{Q}_1-\mathbf{q},\sigma} \right) \ , \phi_{\mathbf{q},\sigma} = \frac{1}{\sqrt{2}} \left(c_{\mathbf{N}_1+\mathbf{q},\sigma} - c_{\mathbf{N}_1+\mathbf{Q}_1-\mathbf{q},\sigma} \right) \ , \tag{7.2}$$

The operator satisfy fermionic anticommutation relations:

$$\begin{aligned} \left\{ \psi_{\mathbf{q},\sigma}, \psi^\dagger_{\mathbf{q}',\sigma} \right\} &= \left[\delta_{\mathbf{q},\mathbf{q}'} + \frac{1}{2} \left(\delta_{\mathbf{Q}_1-\mathbf{q},\mathbf{q}'} + \delta_{\mathbf{q},\mathbf{Q}_1-\mathbf{q}'} \right) \right] \delta_{\sigma,\sigma'} \\ &= \delta_{\mathbf{q},\mathbf{q}'} \delta_{\sigma,\sigma'} \ , \\ \left\{ \phi_{\mathbf{q},\sigma}, \phi^\dagger_{\mathbf{q}',\sigma} \right\} &= \left[\delta_{\mathbf{q},\mathbf{q}'} - \frac{1}{2} \left(\delta_{\mathbf{Q}_1-\mathbf{q},\mathbf{q}'} + \delta_{\mathbf{q},\mathbf{Q}_1-\mathbf{q}'} \right) \right] \delta_{\sigma,\sigma'} \\ &= \delta_{\mathbf{q},\mathbf{q}'} \delta_{\sigma,\sigma'} \ , \\ \left\{ \psi_{\mathbf{q},\sigma}, \phi^\dagger_{\mathbf{q}',\sigma} \right\} &= \left\{ \phi_{\mathbf{q},\sigma}, \psi^\dagger_{\mathbf{q}',\sigma} \right\} = 0 \ , \end{aligned} \tag{7.3}$$

where both $\mathbf{q}$ and $\mathbf{q}'$ are chosen from a small window around the nodes, so their difference is also small and it is therefore guaranteed that $|\mathbf{q} + \mathbf{q}'| \neq |\mathbf{Q}_1|$, rendering both $\delta_{\mathbf{q},\mathbf{Q}_1-\mathbf{q}'}$ and $\delta_{\mathbf{Q}_1-\mathbf{q},\mathbf{q}'}$ zero. For convenience, we define new number operators for the sum and relative degrees of freedom:

$$s_{\mathbf{q},\sigma} = \psi^\dagger_{\mathbf{q}} \psi_{\mathbf{q}}, \ r_{\mathbf{q},\sigma} = \phi^\dagger_{\mathbf{q}} \phi_{\mathbf{q}} \ . \tag{7.4}$$

We then have the following useful relation between the corresponding number operators $n = c^\dagger c$:

$$n_{\mathbf{N}_1+\mathbf{q},\sigma} + n_{\mathbf{N}_1+\mathbf{Q}_1-\mathbf{q},\sigma} = s_{\mathbf{q},\sigma} + r_{\mathbf{q},\sigma} \ . \tag{7.5}$$

We find that the sum degrees of freedom $s_{\mathbf{q},\sigma}$ do not enter the Kondo scattering Hamiltonian $\tilde{H}_{\text{imp-cbath}}$ (for the single channel $l = 1$), and it is expressed purely in terms of the relative degrees of freedom:

$$\tilde{H}_{\text{imp-cbath}} = J^* \sum_{\mathbf{q}_1,\mathbf{q}_2,\alpha,\beta} \mathbf{S}_d \cdot \boldsymbol{\sigma}_{\alpha\beta} \phi^\dagger_{\mathbf{q}_1\alpha} \phi_{\mathbf{q}_2\beta} \,. \tag{7.6}$$

We now proceed to rewrite the other parts of the Hamiltonian in terms of these new degrees of freedom. The kinetic energy can be written as

$$\begin{aligned} \tilde{H}_{\text{cbath}} &= \sum_{\mathbf{q_1},\mathbf{q_2},\sigma} \varepsilon_{\mathbf{N}_1+\mathbf{q}} \left(n_{\mathbf{N}_1+\mathbf{q},\sigma} + n_{\mathbf{N}_1+\mathbf{Q}_1-\mathbf{q},\sigma} \right) \\ &= \sum_{\mathbf{q},\sigma} \varepsilon_{\mathbf{N}_1+\mathbf{q}} \left(s_{\mathbf{q},\sigma} + r_{\mathbf{q},\sigma} \right) \,, \end{aligned} \tag{7.7}$$

Given that the Kondo coupling acts only on the subspace of the ϕ fields, we consider a simplified form of the bath interaction (for the channel $l = 1$), taking into account scattering processes restricted to the ϕ fields:

$$\tilde{H}_{\text{cbath-int}} = -\frac{1}{2N} \sum_{\mathbf{q}_1,\mathbf{q}_2,\sigma}{}' \frac{W}{2} c^\dagger_{q_1,\sigma} c_{q_2,\sigma} + \frac{1}{4N^2} \sum_{\{\mathbf{q}_i\}}{}' W c^\dagger_{q_1,\uparrow} c_{q_2,\uparrow} c^\dagger_{q_3,\downarrow} c_{q_4,\downarrow} \,, \tag{7.8}$$

where the primed summations indicates each $\{\mathbf{q_i}\}$ in both terms sum over the neighbourhoods of N_1 and $N_1 + Q_1$, and each Fourier transform contributes a factor of $1/\sqrt{2N}$ (if N is the number of points on a single arm of the Fermi surface, the total number of points in $l = 1$ is $2N$). Any single primed summation can be written as

$$\sum_{q}{}' c_{q,\sigma} = \sum_{q} \left(c_{N_1+q,\sigma} - c_{N_1+Q_1-q,\sigma} \right) \,, \tag{7.9}$$

where the unprimed summation only sums over the neighborhood of N_1. The change in sign arises because every transfer of momentum from N_1 to $N_1 + Q_1$ introduces a phase of π within the $k-$dependence of W. Noting that $c_{N_1+q,\sigma} - c_{N_1+Q_1-q,\sigma} = \sqrt{2}\phi^\dagger_q$, we get

$$\tilde{H}_{\text{cbath-int}} = -\frac{W}{2} \sum_{\mathbf{q}_1,\mathbf{q}_2,\sigma} \phi^\dagger_{q_1,\sigma} \phi_{q_2,\sigma} + \frac{W}{N^2} \sum_{\{\mathbf{q}_i\}} \phi^\dagger_{q_1,\uparrow} \phi_{q_2,\uparrow} \phi^\dagger_{q_3,\downarrow} \phi_{q_4,\downarrow} \,. \tag{7.10}$$

We now argue that that the ground state of $\tilde{H}_{\text{cbath-int}}$ is the state

$$|L\rangle = \frac{1}{N} \sum_{\mathbf{q}_1\mathbf{q}_2} \phi^\dagger_{\mathbf{q}_1,\uparrow} \phi^\dagger_{\mathbf{q}_2,\downarrow} |0\rangle \,. \tag{7.11}$$

This can be seen by defining new "local" degrees of freedom $\tilde{\phi}(r)_\sigma) = \frac{1}{\sqrt{N}} \sum_k e^{i\vec{k}\cdot\vec{r}} \phi_{q,\sigma}$. In terms of them, the Hamiltonian takes the form

$$\tilde{H}_{\text{cbath-int}} = -\frac{W}{2} \sum_{\sigma} \phi^\dagger(0)_\sigma \phi(0)_\sigma + W \phi^\dagger(0)_\uparrow \phi(0)_\uparrow \phi^\dagger(0)_\downarrow \phi(0)_\downarrow \,. \tag{7.12}$$

This becomes a four-level problem associated with the two number operators $\phi^\dagger(0)_\sigma\phi(0)_\sigma$ that commute with the Hamiltonian and since $W < 0$, the ground state is doubly degenerate between the completely unoccupied and the doubly occupied states. The state in eq. 7.11 is the doubly occupied state:

$$|L\rangle = \phi^\dagger(0)_\uparrow\phi^\dagger(0)_\downarrow|0\rangle \ . \tag{7.13}$$

This can also be verified by working with the momentum-space ϕ operators.

Since both $\tilde{H}_{\text{imp-cbath}}$ and $\tilde{H}_{\text{cbath-int}}$ commute with $s_{\mathbf{q},\sigma}$, we replace the local objects $\sum_{\mathbf{q}} s_{\mathbf{q},\sigma}$ in $\tilde{H}_{\text{cbath-int}}$ with $\frac{1}{2}$ since the bath is always at half-filling. This results in a simplified Hamiltonian for just the $\phi_{\mathbf{q},\sigma}$ degrees of freedom:

$$\tilde{H} = -\frac{1}{2}W\sum_{\mathbf{q},\sigma} r_{\mathbf{q},\sigma} + W\sum_{\mathbf{q}_1,\mathbf{q}_2} r_{\mathbf{q}_1,\uparrow}r_{\mathbf{q}_2,\downarrow} + \sum_{\mathbf{q}_1,\mathbf{q}_2,\alpha,\beta} J^*\mathbf{S}_d\cdot\boldsymbol{\sigma}_{\alpha\beta}\phi^\dagger_{\mathbf{q}_1\alpha}\phi_{\mathbf{q}_2\beta} \tag{7.14}$$

For bath interaction strength close to the critical value ($W \lesssim W_c$), the fixed point coupling value J^* is much smaller than W. In order to obtain the gapless excitations of the system arising from the presence of the impurity site, we integrate out the impurity dynamics via a Schrieffer-Wolff transformation. The perturbation term $\mathcal{V}$ then consists of Hamiltonian terms that modify the impurity configuration,

$$\mathcal{V} = \sum_{\mathbf{q}_1,\mathbf{q}_2} J^* S^+_d\phi^\dagger_{\mathbf{q}_1\downarrow}\phi_{\mathbf{q}_2\uparrow} + \text{h.c.}\ , \tag{7.15}$$

while the "non-interacting" Hamiltonian is

$$H_D = -\frac{1}{2}W\sum_{\mathbf{q},\sigma} r_{\mathbf{q},\sigma} + W\sum_{\mathbf{q}_1,\mathbf{q}_2} r_{\mathbf{q}_1,\uparrow}r_{\mathbf{q}_2,\downarrow}\ . \tag{7.16}$$

The renormalisation in the dynamics of $b^\dagger_{\vec{k},\sigma}$ are given by

$$\Delta\tilde{H} = \mathcal{P}_L\mathcal{V}\mathcal{P}_H\frac{1}{E_L - H_D}\mathcal{V}\mathcal{P}_L, \tag{7.17}$$

where E_L is the energy of the ground state of H_D, $-(E_L - H_D)$ is the excitation energy of the state generated upon applying the perturbation $\mathcal{V}$, and $\mathcal{P}_{L(H)}$ projects onto the low(high)-energy subspace. For the present Hamiltonian, the low-energy state (associated with E_L) is the one that minimises the bath interaction term $\tilde{H}_{\text{cbath-int}}$; since the coupling W is negative, the minimal configuration is one in which the local operators $\sum_{\mathbf{q}} r_{\mathbf{q},\sigma}$ (for $\sigma = \pm 1$) are unity. This leads to the following low-energy state:

$$|L\rangle = \frac{1}{N}\sum_{\mathbf{q}_1\mathbf{q}_2}\phi^\dagger_{\mathbf{q}_1,\uparrow}\phi^\dagger_{\mathbf{q}_2,\downarrow}|0\rangle \tag{7.18}$$

where $|0\rangle$ is the $r_{\mathbf{q}\uparrow} = r_{\mathbf{q}\downarrow} = 0$ state. The state $|L\rangle$ is at zero energy. High-energy states are obtained by applying, on the state $|L\rangle$, the excitation operator $\phi^\dagger_{\mathbf{q}_1,\sigma}\phi_{\mathbf{q}_2,\bar{\sigma}}$ or its hermitian conjugate. The operator converts a double and a hole to spin states, incurring a total excitation cost of $-W = |W|$.

We now calculate the various terms in $\Delta\tilde{H}$:

$$\begin{aligned}
\mathcal{P}_L\mathcal{V}\mathcal{P}_H\frac{1}{E_L-H_D}\mathcal{V}\mathcal{P}_L &= \left(\frac{1}{2}+S_d^z\right)\sum_{\mathbf{q}_1,\mathbf{q}_2}\frac{J^{*2}}{-4W}\phi^\dagger_{\mathbf{q}_1,\downarrow}\phi_{\mathbf{q}_2,\uparrow}\left(\phi^\dagger_{\mathbf{q}_2,\uparrow}\phi_{\mathbf{q}_1,\downarrow}+(1-\delta_{\mathbf{q}_1,\mathbf{q}_2})\phi^\dagger_{\mathbf{q}_1,\uparrow}\phi_{\mathbf{q}_2,\downarrow}\right)\\
&= -\sum_{\mathbf{q}_1,\mathbf{q}_2}\frac{J^{*2}}{4W}\left[r_{\mathbf{q}_1\downarrow}\left(1-r_{\mathbf{q}_2\uparrow}\right)-(1-\delta_{\mathbf{q}_1,\mathbf{q}_2})\phi^\dagger_{\mathbf{q}_1,\uparrow}\phi^\dagger_{\mathbf{q}_1,\downarrow}\phi_{\mathbf{q}_2,\downarrow}\phi_{\mathbf{q}_2,\uparrow}\right]\\
\mathcal{P}_L\mathcal{V}\mathcal{P}_H\frac{1}{E_L-H_D}\mathcal{V}\mathcal{P}_L &= \sum_{\mathbf{q}_1,\mathbf{q}_2}\frac{J^{*2}}{-4W}\left[r_{\mathbf{q}_1\uparrow}\left(1-r_{\mathbf{q}_2\downarrow}\right)-(1-\delta_{\mathbf{q}_1,\mathbf{q}_2})\phi^\dagger_{\mathbf{q}_1,\downarrow}\phi^\dagger_{\mathbf{q}_1,\uparrow}\phi_{\mathbf{q}_2,\uparrow}\phi_{\mathbf{q}_2,\downarrow}\right]
\end{aligned} \tag{7.19}$$

In both terms, we set $S_d^z = 0$ owing to local SU(2) symmetry on the impurity site. In the same way, we treat the effects of the dispersion term (eq. 7.7) to second order:

$$\begin{aligned}
\mathcal{P}_L\mathcal{V}\mathcal{P}_H\frac{1}{E_L-H_D}\mathcal{V}\mathcal{P}_L &= \sum_{\mathbf{q},\sigma}\frac{\varepsilon^2_{\mathbf{N}_1+\mathbf{q}}}{-W}\left[\psi^\dagger_{\mathbf{q},\sigma}\phi_{\mathbf{q},\sigma}\phi^\dagger_{\mathbf{q},\sigma}\psi_{\mathbf{q},\sigma}+\phi^\dagger_{\mathbf{q},\sigma}\psi_{\mathbf{q},\sigma}\psi^\dagger_{\mathbf{q},\sigma}\phi_{\mathbf{q},\sigma}\right]\\
&= \sum_{\mathbf{q},\sigma}\frac{\varepsilon^2_{\mathbf{N}_1+\mathbf{q}}}{-W}\left[s_{\mathbf{q},\sigma}\left(1-r_{\mathbf{q},\sigma}\right)+r_{\mathbf{q},\sigma}\left(1-s_{\mathbf{q},\sigma}\right)\right]\ .
\end{aligned} \tag{7.20}$$

At the values of $\mathbf{q}$ for which $\varepsilon_{\mathbf{N}_1+\mathbf{q}} > 0$, we can set the number operator $s_{\mathbf{q},\sigma} = 0$ (these positive energy modes are unoccupied in the ground state), while for $\varepsilon_{\mathbf{N}_1+\mathbf{q}} < 0$, we have $s_{\mathbf{q},\sigma} = 1$:

$$\mathcal{P}_L\mathcal{V}\mathcal{P}_H\frac{1}{E_L-H_D}\mathcal{V}\mathcal{P}_L = \sum_{\mathbf{q}(\varepsilon_{\mathbf{N}_1+\mathbf{q}}>0),\sigma}\frac{\varepsilon^2_{\mathbf{N}_1+\mathbf{q}}}{-W}r_{\mathbf{q},\sigma}+\sum_{\mathbf{q}(\varepsilon_{\mathbf{N}_1+\mathbf{q}}<0),\sigma}\frac{\varepsilon^2_{\mathbf{N}_1+\mathbf{q}}}{-W}\left(1-r_{\mathbf{q},\sigma}\right)\ . \tag{7.21}$$

The complete second-order renormalised Hamiltonian is

$$\Delta\tilde{H} = \sum_{\mathbf{q},\sigma}\epsilon_{\mathbf{q}}r_{\mathbf{q},\sigma}+\mathcal{U}\sum_{\mathbf{q},\sigma}r_{\mathbf{q}\sigma}r_{\mathbf{q}\bar{\sigma}}+\mathcal{U}\sum_{\mathbf{q}_1\neq\mathbf{q}_2,\sigma}\left[r_{\mathbf{q}_1\sigma}r_{\mathbf{q}_2\bar{\sigma}}+\phi^\dagger_{\mathbf{q}_1,\bar{\sigma}}\phi^\dagger_{\mathbf{q}_1,\sigma}\phi_{\mathbf{q}_2,\sigma}\phi_{\mathbf{q}_2,\bar{\sigma}}\right]\ . \tag{7.22}$$

where $\epsilon_{\mathbf{q}} = \text{sign}\left(\varepsilon_{\mathbf{N}_1+\mathbf{q}}\right)\frac{\varepsilon^2_{\mathbf{N}_1+\mathbf{q}}}{-W}$ and $\mathcal{U} = \frac{J^{*2}}{4W}$.

The $\mathbf{q}_1 = \mathbf{q}_2$ component of the Hamiltonian shows the emergence of the exactly solvable Hatsugai-Kohmoto model [28, 29] at the critical point. The correlation term $\mathcal{U}\sum_{\mathbf{q},\sigma}r_{\mathbf{q}\sigma}r_{\mathbf{q}\bar{\sigma}}$ leads to a transfer of spectral weight across the Fermi surface and separates the available states into three classes:

$$\langle n_{\mathbf{q}}\rangle = \begin{cases} 2, & \varepsilon_2 = 2\epsilon_{\mathbf{q}}-|\mathcal{U}|\ , \\ 1, & \varepsilon_1 = \epsilon_{\mathbf{q}}\ , \\ 0, & \varepsilon_0 = 0\ , \end{cases} \tag{7.23}$$

In the metallic phase (when $\mathcal{U}$ is less than the bandwidth), the occupancy changes from $n = 2$ to $n = 0$ at $\epsilon_{\mathbf{q}} = |\mathcal{U}|/2$. Across this boundary, the gapless excitations are of the form $\phi^\dagger_{q,\uparrow}\phi^\dagger_{q,\downarrow}$, which are clearly non-Fermi liquid in nature.

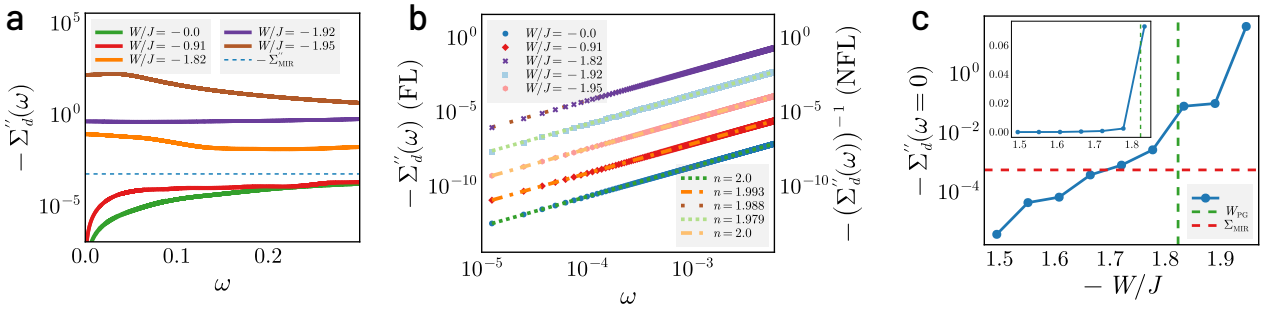

Figure 5.11: *(a) Imaginary part of impurity self-energy $\Sigma''(\omega)$ as a function of frequency ω for Fermi liquid (FL, $|W/J| < 1.79$) and pseudogapped phases (NFL, $|W/J| \geq 1.79$). $\Sigma''(\omega)$ falls to zero as $\omega \to 0$ for the FL, while it attains a peak in the pseudogap. All $\Sigma''(\omega)$ for the NFL are observed to lie above the Mott-Ioffe-Regel (MIR) bound (dashed blue line), while those for the FL lie below. (b) Scaling of $\Sigma''(\omega)$ with frequency for Fermi liquid and pseudogapped phases. The FL self-energy fits to $\Sigma'' \sim \omega^{\alpha}$ with $\alpha \approx 2$, vanishing as $\omega \to 0$, while the NFL self-energy grows as $\Sigma'' \approx a - \omega^{\beta}$ for small ω, with $\beta \approx 2$. Remarkably, the NFL exponent remains mostly unchanged through the entirety of the PG phase. (c) Variation of the zero-frequency imaginary self-energy $-\Sigma''(\omega = 0)$ with ω in the FL and pseudogap phases (entry into the PG is marked by the vertical dashed line). The inset shows the same but in linear scale, in order to display the dramatic rise (by almost 30 times) on entering the PG.*

We now discuss the effects of the $\mathbf{q}_1 \neq \mathbf{q}_2$ component. The first term allows for double excitations that extend across distinct momentum states, and are gapped. The second term also creates gapped excitations involving the regions of zero and double occupancy but these represent subdominant pairing fluctuations of the nodal non-Fermi liquid. We recall that similar fluctuations across the Fermi surface were observed in our calculations of charge correlations in Fig. 5.9 (a), and are consistent with pairing fluctuations observed from quantum Monte Carlo simulations and found to give rise to quantum-critical behavior and PG physics [573].

Consequently, the resulting NFL metal of the lattice model involves long-lived excitations of multiple $\mathbf{k}$-states, and manifest in the form of a divergent one-particle self-energy at the non-interacting FS [603]: $\Sigma_{\mathbf{q}}(\omega) = -\mathcal{U}^2/4(\omega - \epsilon_{\mathbf{q}})$, such that $\Sigma_{\epsilon_{\mathbf{q}}=0}(\omega \to 0) \to \infty$. This zero-frequency self-energy pole presages the transition into a Mott insulating phase, where it marks a hard gap in the spectral function for charge excitations. This is consistent with our findings for the lattice (Fig. 5.9(c)) and impurity self-energies (Fig. 5.11(c)). The nodal Mott metal thus comprises of a Greens function zero at the Fermi energy together with an anistropic massless Dirac dispersion, leading to a non-zero Chern number [604–606]. This topological index survives into the Mott insulator.

For small but non-zero values of $\omega - \epsilon_{\mathbf{k}}$, we obtain a quasiparticle residue that vanishes with ω, $Z_{\rm imp} \sim \omega^2/\mathcal{U}^2$. The scattering rate of this singular NFL possesses a sharp peak at the FS ($\omega = \epsilon_{\mathbf{k}_F}$):

$$\Gamma \sim \mathcal{U}^2 \delta(\omega - \epsilon_{\mathbf{k}}) \,, \tag{7.24}$$

consistent with the sharply peaked Lorentzian $\Sigma''_{\mathbf{k}}(\omega) \sim \omega^{-2}$ captured in Fig. 5.11(a). This quantum critical NFL metal is an example of a strongly coupled scale-invariant form of quantum matter.

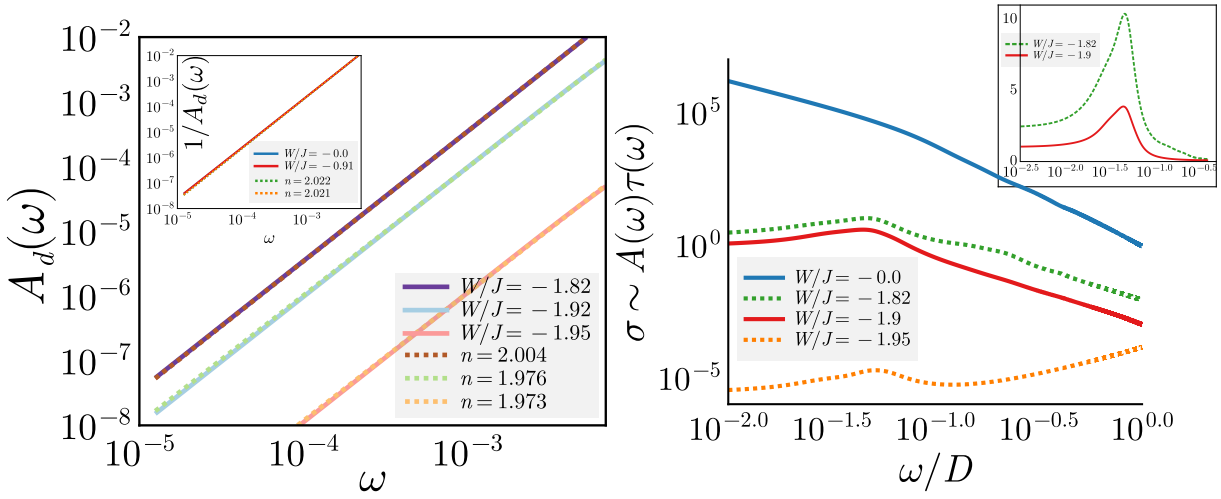

Figure 5.12: *Left: Impurity spectral function $A_d(\omega)$ in the local Fermi liquid (inset) and pseudogap (main). The PG spectral function is fit to a power law (with the $\omega = 0$ contribution subtracted, see Fig. 5.11(c) for the full spectral function). The exponent of the power law comes out to be $n \approx 2$ throughout the PG. The local FL spectral function (inset) is fit to a lorentzian (by fitting the inverse to a power law). Right: Optical conductivity $\sigma(\omega)$ for excitations of the impurity model, approximated through the product of the carrier density (taken from the density of states $A(\omega)$) and the lifetime $\tau(\omega)$ (obtained from the inverse scattering rate $-1/\Sigma''(\omega)$, where Σ'' is the imaginary part of the self-energy). The Fermi liquid (blue) shows a sharp Drude peak at $\omega = 0$ due to the presence of long-lived quasiparticles. The PG (green, red, orange) shows a shifted Drude peak at a non-zero frequency which is reminiscent of the mid-infrared (MIR) peak seen experimentally in the cuprates [592–594]. Inset shows the robustness of the position of the MIR peak through the PG, indicating it as a universal feature of the Mott metal.*

The exact solution for eq.(**7.22**) reveals the presence of low-energy excitations comprised of holons and doublons [29]. These features point to the nodal NFL as a long-ranged and multipartite entangled, strongly interacting scale-invariant state of quantum matter [551, 607–609] that are completely disconnected from the quasiparticles of the FL. Following the arguments laid out in [167], at finite temperatures, such a scale-invariant highly entangled non-Fermi liquid is likely associated with Planckian dissipation (i.e., $\Sigma''(T) \sim k_B T$) and a resistivity that varies linearly with temperature ($\rho \sim T$) [610–612]. This sits well with the possibility that this state is also a highly efficient scrambler [600–602]. Additionally, as mentioned above, we observe that the nodal metal possesses pairing fluctuations that can become dominant upon doping [603].

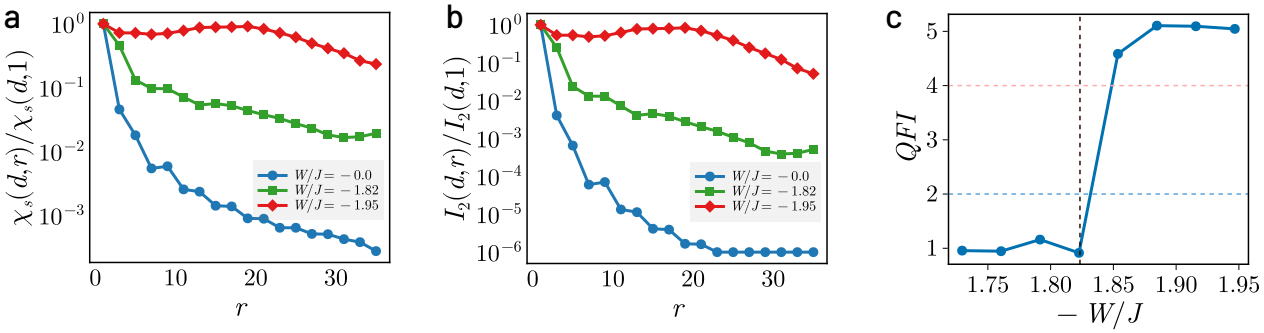

Figure 5.13: *(a) Spin correlation $\langle \mathbf{S}_d \cdot \mathbf{S}_r \rangle$ and (b) mutual information $I_2(d,r)$ between the impurity spin and conduction bath local spin density as a function of the distance* **r** *between them, normalised against the value at $r = 1$. Both decay very quickly in the FL phase (blue), but show long-ranged behaviour in the NFL phase (green and red), extending to the edges of the system at the critical point (red). (c) Evolution of the Quantum Fisher Information F_Q for a nearest-neighbour spin-flip operator $O = \sum_{i \in odd}(S_i^+ S_{i+1}^- + h.c.)$ through the first Lifshitz transition and the pseudogap. The vertical dashed line marks the onset of the PG. To the left of it, the QFI in the Fermi liquid phase shows at most bipartite entanglement ($F_Q < 2$ (below blue dashed line)), while the PG shows the presence of multipartite entanglement upto 5 parties ($F_Q > 4$ (red dashed line)).*

5.8 Heisenberg Model as a low-energy description of the tiled Mott insulator

For simplicity, we consider two impurity sites labelled 1 and 2 associated with two nearest-neighbour auxiliary models. The ground state subspace is four-fold degenerate:

$$|\Psi_L\rangle = \{|\sigma_1, \sigma_2\rangle\} \ , \quad \sigma_i = \pm 1 \ , \tag{8.1}$$

where σ_i is the spin state of site i. This ground state is derived from the following "zeroth order" Hamiltonian that emerges in the local moment phase of the auxiliary models when all scattering processes between the impurity and conduction bath are RG-irrelevant:

$$H_0 = -\frac{U}{2} \sum_{i=1,2} \left(n_{i\uparrow} - n_{i\downarrow}\right)^2 \ ; \tag{8.2}$$

the local correlation on the impurity site becomes the largest scale in the problem in this phase and pushes the $|n_i = 2\rangle$ and $|n_i = 0\rangle$ states to high energies. This then defines the high-energy subspace for our calculation:

$$|\Psi_H\rangle = |C_1, C_2\rangle \ , \tag{8.3}$$

where C_i can take values 0 or 2, indicating that the state i is either empty or full, respectively. Both the double and hole states exist at a charge gap of the order of $U/2$ above the low-energy singly-occupied subspace defined by the states $|\Psi_L\rangle$.

In order to allow virtual fluctuations that can lift the large ground state degeneracy and lower the energy, we consider (perturbatively) the effects of an irrelevant single-particle hybridisation that

connects the nearest-neighbour sites. This perturbation Hamiltonian is therefore of the form

$$H_t = \sum_{\omega} V(\omega)\mathcal{P}(\omega) \sum_{\sigma} \left(c^{\dagger}_{1\sigma} c_{2\sigma} + \text{h.c.} \right) , \tag{8.4}$$

where $V(\omega)$ only acts on states at the energy scale ω; the renormalisation of V is encoded in the fact that $V(\omega)$ is largest for the excited states and vanishes at low-energies: $V(\omega \to 0) = 0$.

In order to obtain a low-energy effective Hamiltonian for the impurity sites arising from this hybridisation, we integrate out H_t via a Schrieffer-Wolff transformation. This leads to the following second-order Hamiltonian:

$$H_{\text{eff}} = \mathcal{P}_L H_t G \mathcal{H}_t \mathcal{P}_L \, . \tag{8.5}$$

The operator $\mathcal{P}_L$ projects onto the low-energy subspace $|\Psi_L\rangle$ - this ensures that we remain in the low-energy subspace at the beginning and at the end of the total process. The Greens function $G = (E_L - H_0)^{-1}$ incorporates the excitation energy to go from the low-energy subspace $|\Psi\rangle_L$ (of energy E_L) to the excited subspace $|\Psi\rangle_H$ of energy $E_L + U/2$. Substituting the form of the perturbation Hamiltonian and the excitation energy into the above expression gives

$$H_{\text{eff}} = \frac{V_H^2}{-U/2} \sum_{\sigma,\sigma'} \left[c^{\dagger}_{1\sigma} c_{2\sigma} c^{\dagger}_{2\sigma'} c_{1\sigma'} + c^{\dagger}_{2\sigma} c_{1\sigma} c^{\dagger}_{1\sigma'} c_{2\sigma'} \right] \, . \tag{8.6}$$

where $V_H \equiv V(\omega \to U/2)$ is the impurity-bath hybridisation at energy scales of the order of the Mott gap, in the sense of an RG flow. Terms with consecutive creation or annihilation operators on the same site are prohibited because each site is singly-occupied in the ground state. It is now easy to cast this Hamiltonian into a more recognizable form. For $\sigma' = \sigma$, we get

$$\sum_{\sigma} \delta_{\sigma,\sigma'} c^{\dagger}_{1\sigma} c_{2\sigma} c^{\dagger}_{2\sigma'} c_{1\sigma'} = \sum_{\sigma} \left(n_{1\sigma} - n_{1\sigma} n_{2\sigma} \right) \, , \tag{8.7}$$

while $\sigma = -\sigma' = \pm 1$ gives

$$\sum_{\sigma} \delta_{\sigma,-\sigma'} c^{\dagger}_{1\sigma} c_{2\sigma} c^{\dagger}_{2\sigma'} c_{1\sigma'} = - \left(S^{+}_1 S^{-}_2 + \text{h.c.} \right) \, . \tag{8.8}$$

For the latter expression, we introduced the local spin-flip operators $S^{\pm}_i$. The expression above it can also be cast into spin variables, using the equations

$$\begin{aligned} \frac{1}{2} \sum_{\sigma} n_{i\sigma} &= \frac{1}{2}, \\ \frac{1}{2} \sum_{\sigma} \sigma n_{i\sigma} &= S^z_i, \end{aligned} \tag{8.9}$$

where the first equation is simply the condition of half-filling at each site, and the second equation is the definition of the local spin operator in $z-$direction. Adding and subtracting the equations gives $n_{i\sigma} = \frac{1}{2} + \sigma S^z_i$.

Substituting everything back into eq. 8.6 and dropping constant terms gives

$$H_{\text{eff}} = 2 \frac{V_H^2}{U/2} \left(2 S^z_1 S^z_2 + S^{+}_1 S^{-}_2 + S^{-}_1 S^{+}_2 \right) = J_{\text{eff}} \mathbf{S}_1 \cdot \mathbf{S}_2 \, , \tag{8.10}$$

where the effective antiferromagnetic Heisenberg coupling is $J_{\text{eff}} = \frac{8V_H^2}{U}$.

5.9 Pseudogap as a strongly coupled phase of quantum matter

We now unveil an organising principle that leads to the remarkable properties observed above for the strongly interacting NFL of the PG phase. The existence of a sharp connected FS at $T = 0$ can be understood as the existence of a topologically protected manifold of gapless chiral excitations in **k**-space at the FS [347]. The FS is characterised by a topological index corresponding to an anomaly in the quantum many-body theory for electrons, and can be understood as a generalised symmetry of such a system [588, 613]. A theorem by Luttinger and Ward [25] shows that a count of the physical charge (known as Luttinger's volume) is identical to the topological index (a so-called homotopy charge known as Luttinger's count) even in the presence of electronic interactions that do not disturb the FS. We will now argue that the emergence of antinodal Luttinger surfaces involve a disconnection of the FS (into Fermi arcs) and that, by following La Nave et al. [588], the accompanying change in its topological properties leads to the existence of gapless NFL excitations that are non-local in nature.

The antinodal Luttinger surfaces arise from the splitting of double poles of the single-particle Greens function on the FS into poles lying on opposite complex half-planes, together with zeros that are pinned at the FS. These changes in the analytic structure of the single-particle Greens function have important consequences. First, the emergent zeros break a $\mathbb{Z}_2$ symmetry of the FS [585, 586, 588]. This symmetry is guaranteed within FL theory because the presence of quasiparticles vanishingly close to the FS allows the interchange of spin and charge degrees of freedom, promoting the separate $SU(2)$ symmetries of spin and charge to the larger symmetry of $O(4) = SU(2) \times SU(2) \times \mathbb{Z}_2$ [585]. The insertion of zeros of the Greens function at the Fermi surface in the PG, and the associated splitting of the Greens function, breaks this $\mathbb{Z}_2$ symmetry by placing the pole for the spin excitation in one half of the complex plane while placing that for the charge excitation in the other half [586, 614].

Second, they signal a divergent electronic self-energy as a function of the wavevector **k**, render ill-behaved the Luttinger-Ward functional of the interacting electronic problem, and violate the generalised symmetry encoded within it. The changes in the pole structure change the Luttinger count topological invariant, while the zeros give rise to an additional topological contribution (linked to the Adler-Bell-Jackiw-type chiral anomaly) [587, 606, 615, 616]. As a consequence of the half-filled particle-hole symmetric nature of the system at hand, Luttinger's volume is preserved upon taking into account topological contributions from both the Luttinger count *and* the zeros [51]. Importantly, La Nave et al. [588] argue, following recent developments in understanding generalised symmetries [617], that the additional anomaly arising from the Luttinger surfaces guarantees the existence of gapless NFL excitations that are non-local in nature.

Thus, the drastic change in nature of the real-space excitations - from locally well-defined Landau quasiparticles of the FL to the increasingly nonlocal excitations of the NFL Fermi arcs in the PG phase - appears to be dictated by a topological principle and, therefore, robust under renormalisation. This signals the NFL Fermi arcs of the PG as an emergent phase of strongly interacting quantum matter - which we dub the *Mott metal* - that is the parent metal of the MI. Such an identification of the pseudogap as a distinct phase is backed up by angle-resolved photoemission spectroscopy (ARPES) experiments [554]; the anomalous momentum, temperature and doping dependence of the gap function observed in the cuprates suggests that the pseudogap maybe described by an or-

der parameter distinct from that of the superconductor [618, 619]. The same topological principle connects the nonlocal unparticle-like gapless excitations [551, 607–609] of the scale-invariant nodal NFL of the HK model observed precisely at the Mott critical point to those of the rest of the PG phase, e.g., a universal scaling of $\Sigma''_{\mathbf{k}}(\omega) \sim (a + \omega^2)^{-1}$ (Fig. 5.11(b)) and local density of states $A_d(\omega) \sim \omega^2$ (Fig. 5.12) of the NFL throughout the PG phase, such that the value of $\Sigma''_{\mathbf{k}}(\omega = 0)$ value continues to grow upon violating the MIR bound (Fig. 5.11(c)).

5.10 Conclusions

Our analysis reveals that the Mott transition proceeds via a continuous evolution through a PG regime characterized by a singular NFL metal - the Mott metal - with deconfined holon–doublon excitations confined to nodal Fermi arcs, and a scaling of it's spectral features with universal power-law exponents. As the system approaches criticality, this metallic phase exhibits increasingly non-local correlations and a divergent self-energy, signalling the breakdown of Landau quasiparticles, formation of local moments and the onset of long-range quantum entanglement. Anchored in two-channel Kondo dynamics at intermediate scales and governed by Hatsugai–Kohmoto physics near the critical endpoint, the Mott metal provides a unified framework for understanding anomalous metallicity in strongly correlated systems. It's fate under finite doping presents a compelling direction for future investigation.

One might ask whether the Mott insulating state obtained here is susceptible to magnetism. Spontaneous symmetry breaking (SSB) has been deliberately excluded within our treatment; this is because the unitary RG method preserves all symmetries of the problem. In an earlier work involving the URG [184], the potential for SSB in the system had been investigated by allowing for a small symmetry breaking field in the microscopic Hamiltonian and then checking its RG flow. Such an investigation has not been carried out in the present set of works. As a result, we only obtain symmetry-preserved insulators. Moreover, similar to [175, 620], we do not find evidence for a Slater transition in the parameter regimes we investigated.

With regards to the pseudogap at half-filling, we note that non-Fermi liquids with partially-gapped Fermi surfaces have been observed within the nearest-neighbour Hubbard model *at half-filling* from DCA [565] and ΣDDMC [172], albeit at finite temperatures above the Mott insulating ground state. Our auxiliary model approach allows us to study the effects of such phases at zero temperature, by tuning additional couplings. Simulating our approach at finite temperatures should presumably lead to similar finite temperature phase diagrams; more work is needed in that regard.

Our finding of metallic phases at half-filling is in contrast to earlier works on the 2D half-filled Hubbard model. Figuring out whether this is because of the extended nature of our model (the additional coupling J) or because of conflicts between the methods will require further investigation. In this context, it is worth noting that a prior work using the URG on the half-filled 2D Hubbard model on the square lattice [175] obtained a Mott insulating ground state at all values of the local repulsion U, and instead obtained a metallic (marginal Fermi liquid) phase at a higher value of the unitary RG *quantum fluctuation scale* ω. The scale ω is roughly tied to the non-commutativity of the delocalisation terms (kinetic energy) and the localisation term (local correlation) within the Hamiltonian, and appears naturally in the formalism due to the presence of multiple energy scales

within a many-body problem. The work [175] investigated the phase diagram as a function of these energy scales, and observed a transition from a metallic phase to a Mott insulating phase, at all values of U. It is therefore tempting to speculate that tuning the ratio W/J within the auxiliary model effectively tunes the quantum fluctuation scale ω for the lattice model. Some support for this idea can be gleaned by thinking of the bath interaction W as the localisation term and the Kondo coupling J as the delocalisation term; their non-commutativity gives rise to multiple energy scales ω which is then being tuned within the auxiliary model. Of course, this requires further investigation to makes things concrete.

More complicated models can be studied by suitably extending the tiling approach and choosing an appropriate auxiliary model. Electron-phonon coupling can be taken into account by studying an Anderson-Holstein model that couples the impurity site to local lattice modes [621]. The effects of disorder can be studied by averaging quantities over various disorder configurations of the conduction bath. The versatility of the unitary RG solver and the impurity model-based construction makes it convenient to explore a large variety of lattice models.

5.11 Appendix: Effective action for the Hubbard-Heisenberg model and the eSIAM

In order to better understand the similarities and differences between the tiling approach outlined here and the approach adopted in dynamical mean-field approximations, we compute the effective action for the local impurity as well as the impurity-zeroth site system, in both the auxiliary and bulk models. This will be done in the limit of infinite coordination number, in order to create a tractable effective theory.

5.11.1 Local theory for the Hubbard-Heisenberg model

We will first work with the Hubbard-Heisenberg model. Let us recall that within the eSIAM, most of the dynamics is governed by the physics of the impurity site and the bath site coupled to the impurity. Accordingly, we will first obtain an effective action within the Hubbard-Heisenberg model for the small system consisting of a local site and all its nearest-neighbours.

We choose a certain local site that we call 0, whose nearest-neighbours will be denoted as $\{\bar{0}\}$. The action for the full Hubbard-Heisenberg model can be formally separated into three parts:

$$S_{\text{H-H}} = S_{0,\bar{0}} + S^{(0,\bar{0})} + S_{\text{int}} \,, \tag{11.1}$$

where $S_{0,\bar{0}}$ represents the part of the action that involves only the sites 0 and $\{\bar{0}\}$, $S^{(0,\bar{0})}$ represents the part that has all the sites apart from 0 and $\{\bar{0}\}$, while S_{int} contains all terms that connect these

two parts. These three parts have the forms

$$\begin{aligned} S_{0,\bar{0}} = &\sum_{i=0,\bar{0}}\sum_{\sigma}\int_0^\beta \mathrm{d}\tau\; c^\dagger_{i\sigma}(\tau)\partial_\tau c_{i\sigma}(\tau) - t\sum_{\bar{0},\sigma}\int_0^\beta \mathrm{d}\tau\;\left[c^\dagger_{0\sigma}(\tau)c_{\bar{0}\sigma}(\tau) + \text{h.c.}\right] \\ &-\frac{U}{2}\sum_{i=0,\bar{0}}\int_0^\beta \mathrm{d}\tau\;\left(n_{i\uparrow}(\tau) - n_{i\downarrow}(\tau)\right)^2 + J\sum_{\bar{0}}\int_0^\beta \mathrm{d}\tau\vec{S}_0(\tau)\cdot\vec{S}_{\bar{0}}(\tau)\,, \end{aligned} \tag{11.2}$$

$$\begin{aligned} S^{(0,\bar{0})} = &\sum_{j\neq(0,\bar{0})}\sum_{\sigma}\int_0^\beta \mathrm{d}\tau\; c^\dagger_{j\sigma}(\tau)\partial_\tau c_{j\sigma}(\tau) - t\sum_{\langle j,l\rangle\neq(0,\bar{0}),\sigma}\int_0^\beta \mathrm{d}\tau\;\left[c^\dagger_{j\sigma}(\tau)c_{l\sigma}(\tau) + \text{h.c.}\right] \\ &-\frac{U}{2}\sum_{j\neq(0,\bar{0})}\int_0^\beta \mathrm{d}\tau\;\left(n_{j\uparrow}(\tau) - n_{j\downarrow}(\tau)\right)^2 + J\sum_{\langle j,l\rangle\neq(0,\bar{0})}\int_0^\beta \mathrm{d}\tau\vec{S}_l(\tau)\cdot\vec{S}_j(\tau)\,, \end{aligned} \tag{11.3}$$

$$\begin{aligned} S_{\text{int}} &= -t\sum_{i\in\bar{0}}\sum_{j\in\text{NN of }i}\sum_{\sigma}\int_0^\beta \mathrm{d}\tau\;\left(c^\dagger_{i\sigma}(\tau)c_{j\sigma}(\tau) + \text{h.c.}\right) + J\sum_{i\in\bar{0}}\sum_{j\in\text{NN of }i}\int_0^\beta \mathrm{d}\tau\vec{S}_i(\tau)\cdot\vec{S}_j(\tau) \\ &= S^{\text{hop}}_{\text{int}} + S^{\text{spin}}_{\text{int}} \end{aligned} \tag{11.4}$$

In order to obtain an effective theory $S^{0,\bar{0}}_{\text{eff}}$ purely for the local system $(0,\bar{0})$, we need to trace over all the other degrees of freedom. This partial trace will be carried out over the states of the so-called "cavity" system $S^{(0,\bar{0})}$. The effective action can be constructed by tracing over scattering processes of all orders that leave the final action diagonal in the system $(0,\bar{0})$. The formal expression can be written as

$$S^{0,\bar{0}}_{\text{eff}} = S_{0,\bar{0}} + \sum_{n=1}^{\infty}\langle\left(S^{\text{hop}}_{\text{int}}\right)^{2n}\rangle_{(0,\bar{0})} + \sum_{n=1}^{\infty}\langle\left(S^{\text{spin}}_{\text{int}}\right)^{2n}\rangle_{(0,\bar{0})} \tag{11.5}$$

where, as mentioned before, the average is carried out in the cavity system $S^{(0,\bar{0})}$. Each hopping term in the expansion is of the form

$$\begin{aligned} &\left(S^{\text{hop}}_{\text{int}}\right)^{2n} \\ &= t^{2n}\sum_{\sigma}\sum_{(i_1,i'_1)\ldots,(i_n,i'_n)}\sum_{(j_1,j'_1)\ldots,(j_n,j'_n)}\int_0^\beta d\tau_1\ldots d\tau_n d\tau'_1\ldots d\tau'_{j_n} \\ &c^\dagger_{i_1\sigma}(\tau_{i_1})c^\dagger_{i_2\sigma}(\tau_2)\ldots c^\dagger_{i_n\sigma}(\tau_n)c_{i'_1\sigma}(\tau'_1)c_{i'_2\sigma}(\tau'_2)\ldots c_{i'_n\sigma}(\tau'_n)\left\langle c_{j_1\sigma}(\tau_1)c_{j_2\sigma}(\tau_2)\ldots c_{j_n\sigma}\,c^\dagger_{j'_1\sigma}(\tau'_1)\ldots c^\dagger_{j'_n\sigma}(\tau'_n)\right\rangle_{(0,\bar{0})} \\ &= t^{2n}\sum_{\sigma}\sum_{(i_1,i'_1)\ldots,(i_n,i'_n)}\sum_{(j_1,j'_1)\ldots,(j_n,j'_n)}\int_0^\beta d\tau_1\ldots d\tau'_{j_n}c^\dagger_{i_1\sigma}(\tau_{i_1})\ldots c^\dagger_{i_n\sigma}(\tau_n)\;c_{i'_1\sigma}(\tau'_1)\ldots c_{i'_n\sigma}(\tau'_n) \\ &G^{(0,\bar{0})}_n\left(\tau_1\ldots\tau_n;\tau'_1\ldots\tau'_n\right)\,, \end{aligned} \tag{11.6}$$

where the indices i_1 through i_n and their primed counterparts run through $\bar{0}$, while j_l ($\in\{j_1,\ldots,j'_n\}$) runs through the nearest-neighbours of the corresponding i_l index. The $n-$particle Greens function

$G_n^{(0,\bar{0})}\left(\tau_1 \dots \tau_n; \tau_1' \dots \tau_n'\right)$ for the cavity system is defined in the usual fashion

$$G_n^{(0,\bar{0})}\left(\tau_1 \dots \tau_n; \tau_1' \dots \tau_n'\right) = \left\langle c_{j_1\sigma}(\tau_1) c_{j_2\sigma}(\tau_2) \dots c_{j_n\sigma}\, c^\dagger_{j_1'\sigma}(\tau_1') \dots c^\dagger_{j_n'\sigma}(\tau_n') \right\rangle_{(0,\bar{0})} \tag{11.7}$$

In the limit of infinite coordination number, only the $n = 1$ term survives:

$$\begin{aligned} \lim_{\mathcal{Z}\to\infty} \sum_{n=1}^{\infty} \langle \left(S_{\text{int}}^{\text{hop}}\right)^{2n} \rangle_{(0,\bar{0})} &= t^2 \sum_\sigma \sum_{i,i'} \int_0^\beta \mathrm{d}\tau \mathrm{d}\tau' c^\dagger_{i\sigma}(\tau) c_{i'\sigma}(\tau') \sum_{j,j'} G_1^{(0,\bar{0})}\left(j\tau; j'\tau'\right) \\ &= \sum_\sigma \sum_{i,i'} \int_0^\beta \mathrm{d}\tau \mathrm{d}\tau'\, \Delta_{ii',\sigma}(\tau-\tau') c^\dagger_{i\sigma}(\tau) c_{i'\sigma}(\tau') \,, \end{aligned} \tag{11.8}$$

where we have defined the bath hybridisation function $\Delta_{ii',\sigma}(\tau - \tau')$ as

$$\Delta_{ii',\sigma}(\tau-\tau') = t^2 \sum_{j\in \text{NN of } i} \sum_{j'\in \text{NN of } i'} G_1^{(0,\bar{0})}\left(j\sigma\tau; j'\sigma\tau'\right) \,. \tag{11.9}$$

Under similar approximations, the spin term in the action reduces to

$$\lim_{\mathcal{Z}\to\infty} \sum_{n=1}^{\infty} \langle \left(S_{\text{int}}^{\text{spin}}\right)^{2n} \rangle_{(0,\bar{0})} = \sum_{i,i'} \int_0^\beta \mathrm{d}\tau \mathrm{d}\tau'\, \chi(\tau-\tau') \vec{S}_i(\tau) \cdot \vec{S}_{i'}(\tau') \,, \tag{11.10}$$

where the susceptibility $\chi_{ii'}(\tau - \tau')$ is defined as

$$\chi_{ii'}(\tau-\tau') = J^2 \sum_{j\in \text{NN of } i} \sum_{j'\in \text{NN of } i'} \vec{S}_j(\tau) \cdot \vec{S}_{j'}(\tau') \,. \tag{11.11}$$

The effective action for the $0, \bar{0}$ system, in the limit of large coordination number, simplifies to

$$\begin{aligned} S_{\text{eff}}^{0,\bar{0}} = &\sum_{i=0,\bar{0}} \sum_\sigma \int_0^\beta \mathrm{d}\tau\, c^\dagger_{i\sigma}(\tau) \partial_\tau c_{i\sigma}(\tau) - t \sum_{\bar{0},\sigma} \int_0^\beta \mathrm{d}\tau \left[c^\dagger_{0\sigma}(\tau) c_{\bar{0}\sigma}(\tau) + \text{h.c.} \right] \\ &- \frac{U}{2} \sum_{i=0,\bar{0}} \int_0^\beta \mathrm{d}\tau \left(n_{i\uparrow}(\tau) - n_{i\downarrow}(\tau)\right)^2 + J \sum_{\bar{0}} \int_0^\beta \mathrm{d}\tau \vec{S}_0(\tau) \cdot \vec{S}_{\bar{0}}(\tau) \\ &+ \sum_{i,i'} \int_0^\beta \mathrm{d}\tau \mathrm{d}\tau' \left[\sum_\sigma \Delta_{ii',\sigma}(\tau-\tau') c^\dagger_{i\sigma}(\tau) c_{i'\sigma}(\tau') + \chi_{ii'}(\tau-\tau') \vec{S}_i(\tau) \cdot \vec{S}_{i'}(\tau') \right] \end{aligned} \tag{11.12}$$

One can also write down an effective action purely for the local site 0. The sites $\bar{0}$ will now be a part of the environment action $S^{(0)}$ instead of the system action, but since the system is thermodynamically large, the cavity action can be assumed to remain the same, such the expectation values are calculated in the same system. As a result, the hybridisation and susceptibility functions remain unchanged. S_{int} is now made of terms that connect 0 and $\bar{0}$, so the transformation from $S^{(0,\bar{0})}$ can be

made by replacing the set $\{j\}$ with the set $\bar{0}$, and the set $\bar{0}$ itself will be replaced by the local site 0. We quote the final form of the local effective action:

$$\begin{aligned} S^0_{\rm eff} = &\sum_\sigma \int_0^\beta d\tau\; c^\dagger_{0\sigma}(\tau)\partial_\tau c_{0\sigma}(\tau) - \frac{U}{2}\int_0^\beta d\tau\;\left(n_{0\uparrow}(\tau) - n_{0\downarrow}(\tau)\right)^2 \\ &+ \int_0^\beta d\tau d\tau'\;\left[\sum_\sigma \Delta_{00,\sigma}(\tau-\tau')c^\dagger_{i\sigma}(\tau)c_{i'\sigma}(\tau') + \chi_{00}(\tau-\tau')\vec{S}_i(\tau)\cdot\vec{S}_{i'}(\tau')\right] \end{aligned} \tag{11.13}$$

5.11.2 Local theory for the extended SIAM

The Hamiltonian for the extended SIAM model is shown in Chapter 3. We will denote the impurity with the label d and the bath sites with the label c. Among the bath sites, we will represent the site coupled to the impurity with z. The full action has the form

$$\begin{aligned} S_{\rm ES} = &\sum_{d,c}\sum_\sigma \int_0^\beta d\tau\; c^\dagger_{i\sigma}(\tau)\partial_\tau c_{i\sigma}(\tau) - t\sum_{\langle i,j\rangle\in c,\sigma}\int_0^\beta d\tau\;\left[c^\dagger_{i\sigma}(\tau)c_{j\sigma}(\tau) + \text{h.c.}\right] \\ &- V\sum_\sigma \int_0^\beta d\tau\;\left[c^\dagger_{d\sigma}(\tau)c_{z\sigma}(\tau) + \text{h.c.}\right] + J\int_0^\beta d\tau \vec{S}_d(\tau)\cdot\vec{S}_z(\tau) \\ &- \frac{U}{2}\int_0^\beta d\tau\;\left(n_{d\uparrow}(\tau) - n_{d\downarrow}(\tau)\right)^2 - \frac{W}{2}\int_0^\beta d\tau\;\left(n_{z\uparrow}(\tau) - n_{z\downarrow}(\tau)\right)^2\;, \end{aligned} \tag{11.14}$$

As in the Hubbard-Heisenberg model, we first obtain an effective action for the pair of sites (d, z). As in the previous calculation, this will again generate a hybridisation function $\Delta_{zz,\sigma}$ for the bath site nearest to the zeroth site. No susceptibility will be generated however, because there is no spin-exchange coupling within the bath. The net result is

$$\begin{aligned} S^{d,z}_{\rm eff} = &\sum_{d,c}\sum_\sigma \int_0^\beta d\tau\; c^\dagger_{i\sigma}(\tau)\partial_\tau c_{i\sigma}(\tau) - V\sum_\sigma \int_0^\beta d\tau\;\left[c^\dagger_{d\sigma}(\tau)c_{z\sigma}(\tau) + \text{h.c.}\right] + J\int_0^\beta d\tau \vec{S}_d(\tau)\cdot\vec{S}_z(\tau) \\ &- \frac{U}{2}\int_0^\beta d\tau\;\left(n_{d\uparrow}(\tau) - n_{d\downarrow}(\tau)\right)^2 - \frac{W}{2}\int_0^\beta d\tau\;\left(n_{z\uparrow}(\tau) - n_{z\downarrow}(\tau)\right)^2 \\ &+ \int_0^\beta d\tau d\tau'\;\sum_\sigma \Delta_{zz,\sigma}(\tau-\tau')c^\dagger_{z\sigma}(\tau)c_{z\sigma}(\tau') \end{aligned} \tag{11.15}$$

This hybridisation $\Delta_{zz,\sigma}$ is calculated in the cavity model of the eSIAM, obtained by removing the impurity and the zeroth site from the full model; it is a completely non-interacting system.

One can go one step further and also remove the zeroth site in order to obtain a theory for the impurity site. With this choice, the cavity model now also includes the zeroth site, and hence contains the correlation term associated with W. The one-particle connection V will lead to a modified hybridisation $\mathcal{F}$ for this effective theory; the Kondo terms will generate a susceptibility. The resultant

action is

$$S^d_{\text{eff}} = \sum_\sigma \int_0^\beta \mathrm{d}\tau\; c^\dagger_{d\sigma}(\tau)\partial_\tau c_{d\sigma}(\tau) - \frac{U}{2}\int_0^\beta \mathrm{d}\tau\;\left(n_{d\uparrow}(\tau) - n_{d\downarrow}(\tau)\right)^2 + \int_0^\beta \mathrm{d}\tau\mathrm{d}\tau'\left[\sum_\sigma \mathcal{F}_\sigma(\tau-\tau')c^\dagger_{i\sigma}(\tau)c_{i'\sigma}(\tau') + \chi_d(\tau-\tau')\vec{S}_i(\tau)\cdot\vec{S}_{i'}(\tau')\right] \tag{11.16}$$

where $\mathcal{F}$ is defined in terms of the local correlator of the zeroth site

$$\mathcal{F}_\sigma(\tau-\tau') = V^2 G^{(d)}_1(z\sigma\tau; z\sigma\tau') = V^2\left\langle c_{z\sigma}(\tau)c^\dagger_{z\sigma}(\tau')\right\rangle_{(d)} \tag{11.17}$$

with the average computed in the interacting cavity model that has the impurity site removed. The interaction arises from the $W-$term. The susceptibility is also calculated in this interacting cavity model, and follows the same definition as in the bulk model:

$$\chi_d(\tau-\tau') = J^2\vec{S}_z(\tau)\cdot\vec{S}_z(\tau')\;. \tag{11.18}$$

This shows that the action of the impurity obtain from the extended Anderson impurity model we are considering (eq. 11.16) is equivalent to the local action of the extended Hubbard model (eq. 11.13) in the limit of infinite coordination number. The approach adopted in the tiling framework developed here is to search for similar equivalences between auxiliary models and lattice models, but in the more complicated case of finite dimensions. This will necessarily introduce non-local correlations into the problem (which can be ignored in $d = \infty$), and the method developed here provides means to incorporate such correlations.

Chapter 6

Competing tendencies In Heavy Fermion Systems: Kondo screening vs. Mott localisation

The previous chapter was devoted to applying our "tiling" approach to the problem of Mott transition on the 2D square lattice. The major result obtained there was that the parent metallic phase of the Mott insulator is a Mott metal-pseudogap phase with deconfined holons and doublons, and it described how the Mott insulator came about through a local binding of these holes and doubles. In this chapter, we turn our attention to the problem of heavy fermions. This is a natural extension of the previous work; while Chapter 5 dealt with competing itinerant and localising tendencies within a single orbital, this work introduces the physics of multiple orbitals and the inter-orbital interaction now acts as another competing tendency.

6.1 Introduction

As another application of the tiling approach, we will tackle the problem of heavy fermions in this chapter. The phenomenology of heavy fermion materials has been discussed in detail in the introduction. They involve localised $f-$electrons from rare earths and actinides hybridising with weakly correlated electrons from s, p or d orbitals. In the phase where this hybridisation is strong and the $f-$electrons are Kondo screened by the conduction layer, the narrow bandwidth of the $f-$electrons leads to highly increased masses for the carriers. Lowering the hybridisation leads to a transition into a small Fermi volume phase where the $f-$electrons do not participate in transport. For systems belonging to the so called Kondo breakdown QCP class, the Kondo screening disappears completely at the transition, leading to a quantum critical point at zero temperature and non-Fermi liquid behaviour emanating from the QCP at finite temperature.

In this regard, we are broadly interested in the following questions:

- *What additional phases emerge upon tuning the correlation of the $f-$layer?* This allows us to investigate a larger parameter regime, and is likely to be important for capturing exotic phenomenology such as symmetry-preserved spin liquid phases in heavy fermion materials.

- *Does the transition from the small to large Fermi surface phases involve changes in entanglement patterns?* Given the proximity of strange metal behaviour to the quantum critical point in such systems, entanglement is likely to be a key characteristic that demarcates various phases and marks the quantum critical nature of the transition.
- *In the presence of a strong correlation on a 2D square lattice, does the heavy fermion transfer display momentum-space anisotropy?* This is an important question not just because of our observation of a momentum-anisotropic Mott metal-pseudogap phase within the extended Hubbard model in a previous work, but also because such a feature would imply an overarching universality of fermionic metal-insulator transitions.

Given the work carried out in the previous chapter, we will approach this problem as follows. In order to model the two orbital nature of the heavy fermion system, we study a bilayer extended Hubbard model. By tuning the correlation strength of one of the layers (the $f-$ layer), we will be able to interpolate between the heavy fermions limit where the $f-$layer is completely localised and other regimes where the $f-$layer has some itineracy. To get a feel for the various competing tendencies, we first study the infinite dimensional limit of the model through a two-impurity Kondo model. We then extend our investigation by considering a lattice-embedded version of the model that incorporates lattice geometries. We will restrict ourselves to the case of half-filling in this work, and investigate the doped case in a future work.

6.2 Bilayer extended Hubbard model: Impurity model

We approach the heavy-fermion problem by starting from a bilayer extended Hubbard model, consisting of two layers (f and c). Towards studying this lattice model, we adopt a two-layer impurity problem (Fig. 6.1) that hosts a correlated impurity site in each layer (S_f and S_d):

$$H_{\text{aux}} = H_{\text{1p}} + H_f + H_d + H_{fd} \,, \tag{2.1}$$

where H_{1p} is the Hamiltonian for the non-interacting itinerant electrons of either layer,

$$H_{\text{1p}} = -t \sum_{\sigma,\alpha} \sum_{\langle i,j \rangle} \left(c^{\dagger}_{i,\sigma,\alpha} c_{j,\sigma,\alpha} + \text{h.c.} \right) - \sum_{i,\sigma,\alpha} \mu_{\alpha} n_{i,\sigma,\alpha} \,, \tag{2.2}$$

such that α sums over the two layers f and d. H_f and H_d describe the dynamics of the correlated impurity sites (and their local neighbourhood) in each layer:

$$\begin{aligned} H_f = -\frac{U_f}{2}(n_{f,\uparrow} - n_{f,\downarrow})^2 + \sum_{Z \in \text{NN}} \Bigg[-V \sum_{\sigma} \left(c^{\dagger}_{f,\sigma} c_{Z,\sigma,f} + \text{h.c.} \right) + \frac{J}{4} \sum_{\alpha,\beta} \mathbf{S}_f \cdot \frac{1}{2} \boldsymbol{\sigma}_{\alpha\beta} c^{\dagger}_{Z,\alpha,f} c_{Z,\beta,f} \\ - \frac{W_f}{4} \left(n_{Z,\uparrow,f} - n_{Z,\downarrow,f} \right)^2 \Bigg] \,, \end{aligned}$$

$$H_d = -\eta_d n_d - \frac{U_d}{2}(n_{d,\uparrow} - n_{d,\downarrow})^2 + \sum_{Z \in \text{NN}} \left[-V \sum_{\sigma} \left(c^{\dagger}_{d,\sigma} c_{Z,\sigma,d} + \text{h.c.} \right) + \frac{J}{4} \sum_{\alpha,\beta} \mathbf{S}_d \cdot \frac{1}{2} \boldsymbol{\sigma}_{\alpha\beta} c^{\dagger}_{Z,\alpha,d} c_{Z,\beta,d} \right] \,, \tag{2.3}$$

where $c^{\dagger}_{\nu,\sigma,\alpha}$ can refer to creation operator for either the $f-$layer. Finally, H_{fd} represents the inter-layer hybridisation:

$$H_{fc} = -V_{\perp} \sum_{\sigma} \left(c^{\dagger}_{d,\sigma} c_{f,\sigma} + \text{h.c.} \right) . \tag{2.4}$$

In the present work, we will restrict ourselves to the case of half-filling in both the layers, by setting

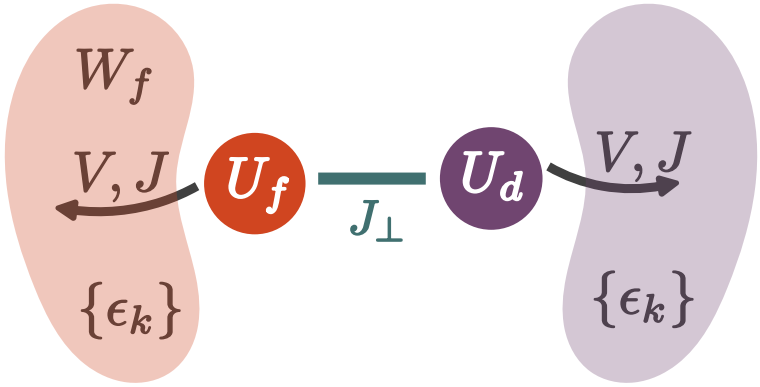

Figure 6.1: *The primary workhorse for this chapter is the two impurity auxiliary model. Each impurity hybridises with its own conduction bath. In order to simulate the correlated nature of the $f-$layer of a lattice model, we will tune the bath correlation W_f to strong values. The impurities interact with each other through the spin-exchange coupling $J_\perp$.*

$\eta_d = 0$.

6.3 Tiling Into Bilayer Extended Hubbard Model

Tiling the impurity model leads to a bilayer extended Hubbard model on the 2D square lattice. In order to tile our auxiliary model to restore translation invariance, we identify the cluster which acts as the "unit" cell of translation. As discussed in the text surrounding eq. 2.9 of Chapter 4, a good choice for the unit cell is the impurity site and it's surrounding correlated environment. Placing the impurity sites at $\boldsymbol{r}_d$ in each layer, we get

$$H_{\text{clust}}(\boldsymbol{r}_d) = H_f(\boldsymbol{r}_d) + H_d(\boldsymbol{r}_d) + H_{fc}(\boldsymbol{r}_d) . \tag{3.1}$$

The details of tiling a cluster Hamiltonian were already shown in Sec. 4.2.2 of Chapter 4; the general idea is to use many-body translation operators (details in Sec. 4.2.1 of Chapter 4) to center the cluster Hamiltonian at various sites of the lattice, such that combining all such terms leads to a periodised

Hamiltonian. we write down the final result here:

$$\begin{aligned} H_{\text{latt}} &= \sum_{r} T^{\dagger}(\boldsymbol{r}) H_{\text{clust}}(\boldsymbol{r}_d) T(\boldsymbol{r}) \\ &= -\frac{2V}{Z} \sum_{\langle i,j\rangle,\sigma} \left(c^{\dagger}_{i,\sigma} c_{j,\sigma} + \text{h.c.} \right) - \sum_{i} \left[\eta_d n_{i,d} + \frac{U_d}{2} (n_{i,\uparrow,d} - n_{i,\downarrow,d})^2 \right] + \frac{2J}{Z} \sum_{\langle i,j\rangle} \boldsymbol{S}_{i,d} \cdot \boldsymbol{S}_{j,d} \\ &\quad - \frac{2V}{Z} \sum_{\langle i,j\rangle,\sigma} \left(f^{\dagger}_{i,\sigma} f_{j,\sigma} + \text{h.c.} \right) - \frac{U_f - W_f}{2} \sum_{i} \left(n_{i,\uparrow,f} - n_{i,\downarrow,f} \right)^2 + \frac{2J}{Z} \sum_{\langle i,j\rangle} \boldsymbol{S}_{i,f} \cdot \boldsymbol{S}_{j,f} \\ &\quad - V_{\perp} \sum_{i,\sigma} (f^{\dagger}_{i,\sigma} c_{i,\sigma} + \text{h.c.}) \end{aligned} \tag{3.2}$$

Tiling the impurity model therefore leads to a bilayer extended Hubbard model (Fig. 6.2), with effective couplings that depend on the auxiliary model couplings. The value of η_d defines the effective chemical potential of the $d-$layer; a non-zero value moves the layer away from half-filling. The $f-$layer is pinned at half-filling.

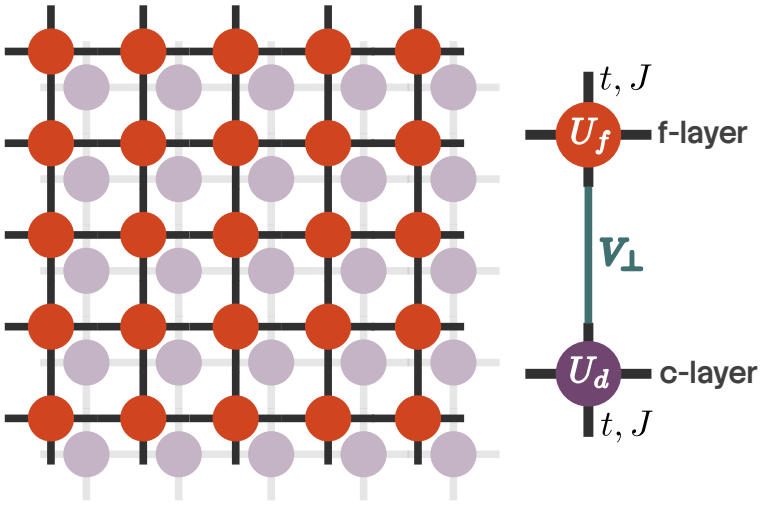

Figure 6.2: *Bilayer Hubbard model reconstructed from tiling the two-impurity auxiliary model. The correlated $f-$layer (orange) hosts a stronger correlation U_f compared to that of the conduction layer (violet) U_d. The two layers are connected by an inter-orbital hybridisation $V_\perp$.*

Following Sec. 4.4.1, the retarded $k-$space Greens function in either layer can be expressed in terms of auxiliary model Greens functions:

$$G(\boldsymbol{k}, \sigma, \alpha; \omega) = \sum_{\nu} C_{\nu,\boldsymbol{k}\alpha} \mathcal{G}(\mathcal{T}_{\nu,\sigma,\alpha}; \omega - \mathcal{E}_{\nu}(\boldsymbol{k})) \tag{3.3}$$

where $\alpha = f, d$ denotes the layer in which the Greens function is being calculated, the modes ν indicate the operators which diagonalise the Hamiltonian $H_{1\text{p}}$, with energies $\mathcal{E}_{\nu}(\boldsymbol{k})$:

$$H_{1\text{p}} = -\frac{2V}{Z} \sum_{\langle i,j\rangle,\sigma} \left(c^{\dagger}_{i,\sigma} c_{j,\sigma} + \text{h.c.} + f^{\dagger}_{i,\sigma} f_{j,\sigma} + \text{h.c.} \right) - V_{\perp} \sum_{i,\sigma} (f^{\dagger}_{i,\sigma} c_{i,\sigma} + \text{h.c.}) - \sum_{i} \eta_d n_{i,d} \,, \tag{3.4}$$

and the $\mathcal{T}-$matrices are defined in eq. 4.11:

$$\mathcal{T}_{\nu,\sigma,\alpha} = \left[\left(\sum_{\sigma'} c^\dagger_{\alpha\sigma} + \text{h.c.}\right) + \left(S^+_\alpha + \text{h.c.}\right) + \left(C^+_\alpha + \text{h.c.}\right)\right] c_{\nu,\sigma} \,, \tag{3.5}$$

In order to calculate $\mathcal{E}_\nu(\boldsymbol{k})$, we introduce the $k-$space modes via a Fourier transform:

$$c^\dagger_{i,\sigma} = \frac{1}{\sqrt{N}} \sum_{\boldsymbol{k}} e^{-i\boldsymbol{k}\cdot\boldsymbol{r}_i} c^\dagger_{\boldsymbol{k},\sigma} \,, \quad f^\dagger_{i,\sigma} = \frac{1}{\sqrt{N}} \sum_{\boldsymbol{k}} e^{-i\boldsymbol{k}\cdot\boldsymbol{r}_i} f^\dagger_{\boldsymbol{k},\sigma} \,. \tag{3.6}$$

In terms of these modes, the 1$-$particle Hamiltonian decouples in $k-$space:

$$H_{1\text{p}} = \sum_{\boldsymbol{k},\sigma} \left[(\epsilon_{\boldsymbol{k}} - \eta_d)(n_{\boldsymbol{k},\sigma,d} + n_{\boldsymbol{k},\sigma,f}) - V_\perp (c^\dagger_{\boldsymbol{k},\sigma} f_{\boldsymbol{k},\sigma} + \text{h.c.})\right] \,. \tag{3.7}$$

The diagonal modes are given by

$$\nu^\dagger_{\boldsymbol{k},\sigma,\pm} = C_{\pm,k} c^\dagger_{\boldsymbol{k},\sigma} + \sqrt{1 - C^2_{\pm,k}} f^\dagger_{\boldsymbol{k},\sigma} \,, \tag{3.8}$$

the coefficients obtained from diagonalising the matrix

$$H_{1\text{p}}(\boldsymbol{k}) = \begin{pmatrix} \epsilon_{\boldsymbol{k}} & -V_\perp \\ -V_\perp & \epsilon_{\boldsymbol{k}} - \eta_d \end{pmatrix} \,. \tag{3.9}$$

The energies are given by $\mathcal{E}_\pm(\boldsymbol{k}) = \epsilon_k - \eta_d/2 \pm \Delta$, with ϵ_k being $-\frac{4V}{Z}(\cos k_x + \cos k_y)$ for a 2D square lattice and $\Delta = \sqrt{V^2_\perp + \eta^2_d/4}$. Substituting into the expression for the lattice Greens function, we get

$$\begin{aligned} G(\boldsymbol{k}, d; \omega) =& C_{+,k}\mathcal{G}(\mathcal{T}_{k+,d}, \mathcal{T}^\dagger_{k,d}; \omega - \mathcal{E}_+(\boldsymbol{k})) + C_{-,k}\mathcal{G}(\mathcal{T}_{k-,d}, \mathcal{T}^\dagger_{k,d}; \omega - \mathcal{E}_-(\boldsymbol{k})) \\ &+ C^*_{+,k}\mathcal{G}(\mathcal{T}_{k,d}, \mathcal{T}^\dagger_{k+,d}; \omega - \mathcal{E}_+(\boldsymbol{k})) + C^*_{-,k}\mathcal{G}(\mathcal{T}_{k,d}, \mathcal{T}^\dagger_{k-,d}; \omega - \mathcal{E}_-(\boldsymbol{k})) \,. \end{aligned} \tag{3.10}$$

Following eq. 4.33, we can similarly write down an expression the local lattice Greens function for the $f-$ and $d-$electrons. For that, we define the local diagonal modes $\nu_\pm$ obtained from the local Hamiltonian

$$H_{\text{loc}} = \begin{pmatrix} 0 & -V_\perp \\ -V_\perp & 0 - \eta_d \end{pmatrix} \,, \tag{3.11}$$

and their associated energies $\varepsilon_\pm$. Within the impurity model, these local bonding/antibonding modes can be constructed on the impurity sites ($\nu_\pm$) or on the neighbouring bath sites, ($\nu^Z_\pm$). The local Greens function can be expressed in terms of these modes:

$$\begin{aligned} G_{dd}(\omega) =& \frac{1}{2}\sum_\nu C_{\nu,d}\left[\mathcal{G}(\nu\sigma, d\sigma; \omega - \varepsilon_\nu) + \mathcal{G}(d\sigma, \nu\sigma; \omega - \varepsilon_\nu)\right] \\ &+ \frac{1}{2}\sum_{\nu^Z} C_{\nu^Z,Z_d}\left[\mathcal{G}(\mathcal{T}_{Z_d,\sigma}, \mathcal{T}_{\nu^Z,\sigma}; \omega - \varepsilon_{\nu^Z}) + \mathcal{G}(\mathcal{T}_{\nu^Z,\sigma}, \mathcal{T}_{Z_d,\sigma}; \omega - \varepsilon_{\nu^Z})\right] \,. \end{aligned} \tag{3.12}$$

The presence of local hybridisation between the $d-$ and $f-$ orbitals makes the inter-orbital Greens function important as well. Following eq. 4.35, we have

$$\begin{aligned} G_{fd}(\omega) =& \frac{1}{2}\sum_{\nu}\left[C_{\nu,f}\mathcal{G}(\nu\sigma, d\sigma;\omega-\varepsilon_{\nu}) + C_{\nu,d}\mathcal{G}(f\sigma,\nu\sigma;\omega-\varepsilon_{\nu})\right] \\ &+ \frac{1}{2}\sum_{\nu^{Z}}\left[C_{\nu^{Z},Z_f}\mathcal{G}(\mathcal{T}_{\nu^{Z},\sigma},\mathcal{T}_{Z_d,\sigma};\omega-\varepsilon_{\nu^{Z}}) + C_{\nu^{Z},Z_d}\mathcal{G}(\mathcal{T}_{Z_f,\sigma},\mathcal{T}_{\nu^{Z},\sigma};\omega-\varepsilon_{\nu^{Z}})\right] . \end{aligned} \tag{3.13}$$

Using these, we can construct the hybridised Greens function associated with the states ν:

$$G_{\nu_+}(\omega) = C^2_{+,d}G_{dd}(\omega) + C^2_{+,f}G_{ff}(\omega) + C_{+,d}C_{+,f}\left[G_{df}(\omega)+G_{fd}(\omega)\right] , \tag{3.14}$$

6.4 Unitary RG Analysis of The Bilayer Lattice-Embedded ES-IAM

In the limit of large U_{α}, we first carry out a Schrieffer-Wolff transformation and work with the following low-energy Hamiltonian:

$$\begin{aligned} H_{\text{aux}} =& \sum_{\mathbf{k},\sigma,\alpha}\epsilon_{\mathbf{k},\alpha}n_{\mathbf{k},\sigma,\alpha} + \sum_{\alpha}\sum_{Z\in\text{NN}}\left[\frac{1}{4}J_{\alpha}\sum_{\sigma,\sigma'}\mathbf{S}_{\alpha}\cdot\frac{1}{2}\boldsymbol{\sigma}_{\sigma\sigma'}c^{\dagger}_{Z,\sigma,\alpha}c_{Z,\sigma',\alpha} - \frac{W_{\alpha}}{4}\left(n_{Z,\uparrow,\alpha}-n_{Z,\downarrow,\alpha}\right)^2\right] \\ &+ J_{\perp}\mathbf{S}_f\cdot\mathbf{S}_d . \end{aligned} \tag{4.1}$$

As we will see, additional terms are generated within the Hamiltonian as we integrate out high-energy degrees of freedom in the conduction baths of the two impurity models. These terms connect the impurity of the $d-(f-)$layer to the nearest-neighbour conduction bath sites of the opposite (i.e. $f-(d-)$)layer, It is therefore necessary to start with an enlarged impurity model Hamiltonian that contains these couplings as well:

$$\begin{aligned} H_{\text{aux}} =& \sum_{\mathbf{k},\sigma,\alpha}\epsilon_{\mathbf{k},\alpha}n_{\mathbf{k},\sigma,\alpha} + \sum_{\alpha}\sum_{Z\in\text{NN}}\left[\frac{1}{4}\sum_{\sigma,\sigma'}\left(J_{\alpha}\mathbf{S}_{\alpha}+K_{\bar{\alpha}}\mathbf{S}_{\bar{\alpha}}\right)\cdot\frac{1}{2}\boldsymbol{\sigma}_{\sigma\sigma'}c^{\dagger}_{Z,\sigma,\alpha}c_{Z,\sigma',\alpha}\right. \\ &\left. -\frac{W_{\alpha}}{4}\left(n_{Z,\uparrow,\alpha}-n_{Z,\downarrow,\alpha}\right)^2\right] + J_{\perp}\mathbf{S}_f\cdot\mathbf{S}_d . \end{aligned} \tag{4.2}$$

Note the additional couplings $K_{\bar{\alpha}}$, where $\bar{\alpha}$ stands for the layer opposite to α.

The two Kondo couplings J and K and the bath interaction W acquire $k-$dependence:

$$\begin{aligned} J(\mathbf{k},\mathbf{q}) &= \frac{J}{2}\left[\cos(\mathbf{k}_x-\mathbf{q}_x)+\cos(\mathbf{k}_y-\mathbf{q}_y)\right] , \\ K(\mathbf{k},\mathbf{q}) &= \frac{K}{2}\left[\cos(\mathbf{k}_x-\mathbf{q}_x)+\cos(\mathbf{k}_y-\mathbf{q}_y)\right] , \\ W(\mathbf{k},\mathbf{q},\mathbf{k}',\mathbf{q}') &= \frac{W}{2}\left[\cos(\mathbf{k}_x-\mathbf{q}_x+\mathbf{k}'_x-\mathbf{q}'_x)+\cos(\mathbf{k}_y-\mathbf{q}_y+\mathbf{k}'_y-\mathbf{q}'_y)\right] . \end{aligned} \tag{4.3}$$

The particle-hole transformed state $\bar{\mathbf{q}}$ associated with $\mathbf{q}$ is defined as $\bar{\mathbf{q}} = \mathbf{q} + (\pi, \pi)$ if $\mathbf{q}$ is in the first or third quadrant and $\mathbf{q} + (\pi, -\pi)$ is in the second or fourth quadrant.

In order to study the low-energy physics of the impurity model, we iteratively integrate out high-energy degrees of freedom using the unitary RG method. Let the momentum states being decoupled from the two layers be $|\mathbf{q}, \sigma, f\rangle$ and $|\mathbf{q}, \sigma, d\rangle$ if they are above the Fermi energy (unoccupied in the low-energy configuration) and $|\bar{\mathbf{q}}, \sigma, f\rangle$ and $|\bar{\mathbf{q}}, \sigma, d\rangle$ if they are below the Fermi energy (occupied in the low-energy configuration) For every shell of conduction bath states of width ΔD integrated out, the Hamiltonian couplings renormalise by folding in the effects of virtual excitations to these states.

The full set of impurity-mediated scattering processes that lead to UV-IR mixing is:

Particle sector excitation These involve excited states above the Fermi energy:

$$\begin{aligned} P_{\text{dir}}(\alpha) &= \frac{1}{2}\sum_{k,q} J_\alpha \mathbf{S}_\alpha \cdot \sigma_{\sigma_1,\sigma_2} c^\dagger_{q,\sigma_1,\alpha} c_{k,\sigma_2,\alpha} \ , \\ P_{\text{ind}}(\alpha) &= \frac{1}{2}\sum_{k,q} K_\alpha \mathbf{S}_\alpha \cdot \sigma_{\sigma_1,\sigma_2} c^\dagger_{q,\sigma_1,\bar{\alpha}} c_{k,\sigma_2,\bar{\alpha}} \ . \end{aligned} \tag{4.4}$$

Hole sector These involve excited states below the Fermi energy:

$$\begin{aligned} H_{\text{dir}}(\alpha) &= \frac{1}{2}\sum_{k,q} J_\alpha \mathbf{S}_\alpha \cdot \sigma_{\sigma_1,\sigma_2} c^\dagger_{k,\sigma_1,\alpha} c_{q,\sigma_2,\alpha} \ , \\ H_{\text{ind}}(\alpha) &= \frac{1}{2}\sum_{k,q} K_\alpha \mathbf{S}_\alpha \cdot \sigma_{\sigma_1,\sigma_2} c^\dagger_{k,\sigma_1,\bar{\alpha}} c_{q,\sigma_2,\bar{\alpha}} \ . \end{aligned} \tag{4.5}$$

Mixed sector These involve simultaneous particle and hole excitations:

$$\begin{aligned} M_{\text{dir}}(\alpha) &= \frac{1}{2}\sum_{q,\bar{q}} J_\alpha \mathbf{S}_\alpha \cdot \sigma_{\sigma_1,\sigma_2} c^\dagger_{q,\sigma_1,\alpha} c_{\bar{q},\sigma_2,\alpha} \ , \\ M_{\text{ind}}(\alpha) &= \frac{1}{2}\sum_{q,\bar{q}} K_{\bar{\alpha}} \mathbf{S}_{\bar{\alpha}} \cdot \sigma_{\sigma_1,\sigma_2} c^\dagger_{q,\sigma_1,\bar{\alpha}} c_{\bar{q},\sigma_2,\bar{\alpha}} \ . \end{aligned} \tag{4.6}$$

6.4.1 Particle/hole scattering processes: direct with direct

We already have the renormalisation group equations for the couplings J_α in the case of $J = K = 0$, arising from P_{dir} and H_{dir}:

$$\frac{\Delta J_f(\mathbf{k}_1, \mathbf{k}_2)}{\Delta D} = -\int_{UV} d\mathbf{q}\, \rho(\mathbf{q}) \left[J_f(\mathbf{k}_1, \mathbf{q}) J_f(\mathbf{q}, \mathbf{k}_2) + 4 J_f(\mathbf{q}, \bar{\mathbf{q}}) W_f(\mathbf{k}_1, \mathbf{q}, \bar{\mathbf{q}}, \mathbf{k}_2) \right] G_f^{(0)}(\mathbf{q}) \ , \tag{4.7}$$

where $\mathbf{q}$ sums over the UV states being integrated out, $\rho(\mathbf{q})$ is the density of states for the momentum states being integrated out and $G_f^{(0)}$ is the propagator for the excited intermediate state (for $J_\perp = 0$):

$$G_\alpha^J(\mathbf{q}) = \frac{1}{\omega - |\epsilon_\alpha(\mathbf{q})|/2 + J_\alpha(\mathbf{q})/4 + W_\alpha(\mathbf{q})/2} \,. \tag{4.8}$$

An identical equations holds for ΔJ_d, with all $f-$quantities replaced with $d-$quantities. Switching on $J_\perp$ modifies the excitation energy in the propagator, while either of the Ks do not enter the denominator because either the impurity or the conduction bath labels do not match the ones fluctuating in this process:

$$G_\alpha(\mathbf{q}) = \frac{1}{1/G_\alpha^J - J_\perp \vec{S}_f \cdot \vec{S}_d} \,. \tag{4.9}$$

This expression can be simplified by noting that the operator in the denominator has only two eigenvalues, $-3/4$ in the singlet sector and $1/4$ in the triplet sector. Defining the projectors $\mathcal{P}_0$ and $\mathcal{P}_1$ for the two sectors, we have

$$\vec{S}_f \cdot \vec{S}_d = \frac{-3}{4}\mathcal{P}_0 + \frac{1}{4}\mathcal{P}_1, \quad \mathcal{P}_0 + \mathcal{P}_1 = \mathbb{I} \,. \tag{4.10}$$

Using these relations, we can write

$$\begin{aligned} G_f(\mathbf{q}) &= \frac{1}{1/G_f^J + 3J_\perp/4}\mathcal{P}_0 + \frac{1}{1/G_f^J - J_\perp/4}\mathcal{P}_1 \\ &= \left(\frac{1/4}{1/G_f^J + 3J_\perp/4} + \frac{3/4}{1/G_f^J - J_\perp/4}\right)\mathbb{I} + \left(\frac{1}{1/G_f^J + 3J_\perp/4} + \frac{1}{1/G_f^J - J_\perp/4}\right)\vec{S}_f \cdot \vec{S}_d \,. \end{aligned} \tag{4.11}$$

Only the first operator renormalises the Kondo interaction:

$$\begin{aligned} \frac{\Delta J_\alpha}{\Delta D} = -\int_{UV} d\mathbf{q}\, \rho(\mathbf{q})\, [J_\alpha(\mathbf{k}_1, \mathbf{q}) J_\alpha(\mathbf{q}, \mathbf{k}_2) + 4 J_\alpha(\mathbf{q}, \bar{\mathbf{q}}) W_\alpha(\mathbf{k}_1, \mathbf{q}, \bar{\mathbf{q}}, \mathbf{k}_2)] \left(\frac{1}{4}\frac{1}{1/G_\alpha^J(\mathbf{q}) + 3J_\perp/4}\right. \\ \left. + \frac{3}{4}\frac{1}{1/G_\alpha^J(\mathbf{q}) - J_\perp/4}\right) \,. \end{aligned} \tag{4.12}$$

We now simplify the second term, in conjunction with the two kinds of processes on either side: J^2 processes and JW processes. We first focus on the J^2 processes.

Effect of inter-layer term $\vec{S}_f \cdot \vec{S}_d$ on J^2 processes

Taking into account the other spin operators on either side of $G_f(\mathbf{q})$ in the full scattering process, we have

$$\frac{1}{2}\sum_{a,b,c}\sum_{\alpha,\beta}\sum_{\gamma,\delta} S_f^a \sigma_{\alpha,\beta}^a S_f^b S_d^b S_f^c \sigma_{\gamma,\delta}^c \left[\delta_{\beta,\gamma} c_{k,\alpha,f}^\dagger c_{q,\beta,f} c_{q,\gamma,f}^\dagger c_{k',\delta,f} + \delta_{\alpha,\delta} c_{\bar{q},\alpha,f}^\dagger c_{k',\beta,f} c_{k,\gamma,f}^\dagger c_{\bar{q},\delta,f}\right] \,. \tag{4.13}$$

Integrating out the UV states using $n_{\bar{q}\beta} = 1 - n_{q\beta} = 1$, we get

$$\frac{1}{2}\sum_{a,b,c}\sum_{\alpha,\beta,\gamma} S^a_f S^b_f S^b_d S^c_f \left[\sigma^a_{\alpha,\beta}\sigma^c_{\beta,\gamma} c^\dagger_{k,\alpha,f} c_{k',\gamma,f} + \sigma^a_{\alpha,\beta}\sigma^c_{\gamma,\alpha} c_{k',\beta,f} c^\dagger_{k,\gamma,f}\right] . \tag{4.14}$$

Using $\sum_\beta \sigma^a_{\alpha,\beta}\sigma^c_{\beta,\gamma} = (\sigma^a\sigma^c)_{\alpha,\gamma} = \delta_{ac}\delta_{\alpha\gamma} + i\epsilon_{acm}\sigma^m_{\alpha,\gamma}$ in the first term and $\sum_\alpha \sigma^c_{\gamma,\alpha}\sigma^a_{\alpha,\beta} = (\sigma^c\sigma^a)_{\gamma,\beta} = \delta_{ca}\delta_{\gamma\beta} - i\epsilon_{acm}\sigma^m_{\gamma,\beta}$ in the second term, relabelling $\beta \to \gamma$ and $\gamma \to \alpha$ there and using $c_{k',\gamma}c^\dagger_{k,\alpha} = \delta_{k,k'}\delta_{\alpha,\gamma} - c^\dagger_{k,\alpha}c_{k',\gamma}$, we get

$$\frac{1}{2}\sum_{a,b,c}\sum_{\alpha,\gamma} S^a_f S^b_f S^b_d S^c_f \left[\delta_{a,c}\delta_{k,k'}\delta_{\alpha,\gamma} + 2i\epsilon_{acm}\sigma^m_{\alpha,\gamma} c^\dagger_{k,\alpha,f} c_{k',\gamma,f}\right] . \tag{4.15}$$

We also use the spin-half identity

$$\begin{aligned}\sigma^a\sigma^b\sigma^c &= (\delta_{ab} + i\epsilon_{abp}\sigma^p)\sigma^c \\ &= \delta_{ab}\sigma^c + i\epsilon_{abp}(\delta_{pc} + i\epsilon_{pcr}\sigma^r) \\ &= \delta_{ab}\sigma^c - \delta_{ac}\sigma^b + \delta_{bc}\sigma^a + i\epsilon_{abc} ,\end{aligned} \tag{4.16}$$

which when contracted with ϵ_{acm} gives

$$\begin{aligned}\sum_{a,c}\epsilon_{acm}\sigma^a\sigma^b\sigma^c &= \sum_{a,c}\epsilon_{acm}(\delta_{ab}\sigma^c + \delta_{bc}\sigma^a + i\epsilon_{abc}) \\ &= \sum_{a,c}(\epsilon_{acm}\delta_{ab}\sigma^c + \epsilon_{cam}\delta_{ba}\sigma^c - i\epsilon_{acm}\epsilon_{acb}) \\ &= -2i\delta_{bm} .\end{aligned} \tag{4.17}$$

For the first term of eq. 4.15, we get

$$\begin{aligned}\frac{1}{2}\sum_{a,b,c}\sum_{\alpha,\gamma} S^a_f S^b_f S^b_d S^c_f \delta_{a,c}\delta_{k,k'}\delta_{\alpha,\gamma} &= \delta_{k,k'}\sum_{a,b} S^a_f S^b_f S^a_f S^b_d \\ &= \frac{1}{4}\delta_{k,k'}\sum_b (S^b_f - 3S^b_f + S^b_f)S^b_d \\ &= -\frac{1}{4}\delta_{k,k'}\sum_b S^b_f S^b_d .\end{aligned} \tag{4.18}$$

For the second term, we obtain

$$\begin{aligned}\frac{1}{2}\sum_{a,b,c}\sum_{\alpha,\gamma} S^a_f S^b_f S^b_d S^c_f 2i\epsilon_{acm}\sigma^m_{\alpha,\gamma} c^\dagger_{k,\alpha,f} c_{k',\gamma,f} &= \frac{1}{4}\sum_b\sum_{\alpha,\gamma}\delta_{bm} S^b_d \sigma^m_{\alpha,\gamma} c^\dagger_{k,\alpha,f} c_{k',\gamma,f} \\ &= \frac{1}{2}\sum_b S^b_d \frac{1}{2}\sum_{\alpha,\gamma}\sigma^b_{\alpha,\gamma} c^\dagger_{k,\alpha,f} c_{k',\gamma,f}\end{aligned} \tag{4.19}$$

Substituting these in the expression for the renormalisation gives

$$\begin{aligned}&\frac{1}{2}\sum_{a,b,c}\sum_{\alpha,\gamma}S^a_f S^b_f S^b_d S^c_f\left[\delta_{a,c}\delta_{k,k'}\delta_{\alpha,\gamma}+2i\epsilon_{acm}\sigma^m_{\alpha,\gamma}c^\dagger_{k,\alpha,f}c_{k',\gamma,f}\right]\\&=-\frac{1}{4}\mathbf{S}_f\cdot\mathbf{S}_d\delta_{k,k'}+\frac{1}{2}\sum_{\alpha,\gamma}\mathbf{S}_d\frac{1}{2}\sigma_{\alpha,\gamma}c^\dagger_{k,\alpha,f}c_{k',\gamma,f}\ .\end{aligned}\tag{4.20}$$

The first term leads to the renormalisation of the inter-layer hybridisation $J_\perp$:

$$\frac{\Delta J_\perp}{\Delta D}=-\frac{1}{4}\int_{UV}d\mathbf{q}\,\rho(\mathbf{q})\int_{IR}d\mathbf{k}\rho(\mathbf{k})\sum_\alpha J_\alpha(\mathbf{k},\mathbf{q})^2\left(\frac{1}{1/G^J_\alpha+3J_\perp/4}+\frac{1}{1/G^J_\alpha-J_\perp/4}\right),\tag{4.21}$$

while the second term gives rise to the indirect impurity-bath inter-layer Kondo couplings K_α mentioned earlier above eq. 4.2:

$$\frac{\Delta K_\alpha}{\Delta D}=\frac{1}{2}\int_{UV}d\mathbf{q}\,\rho(\mathbf{q})J_{\bar\alpha}(\mathbf{k}_1,\mathbf{q})J_{\bar\alpha}(\mathbf{q},\mathbf{k}_2)\left(\frac{1}{1/G^J_{\bar\alpha}+3J_\perp/4}+\frac{1}{1/G^J_{\bar\alpha}-J_\perp/4}\right),\tag{4.22}$$

Effect of inter-layer term $\vec{S}_f\cdot\vec{S}_d$ on JW processes

We now turn to the effect of the $\vec{S}_f\cdot\vec{S}_d$ in eq. 4.11 on processes that involve a Kondo scattering J and a bath scattering W. The non-vanishing processes are of the form

$$\begin{aligned}P_1&=(S^+_f\mathbf{S_f}\cdot\mathbf{S_d}+\mathbf{S_f}\cdot\mathbf{S_d}S^+_f)c^\dagger_{k,\downarrow}c_{k',\uparrow},\\P_2&=P_1^\dagger,\\P_z&=(S^z_f\mathbf{S_f}\cdot\mathbf{S_d}+\mathbf{S_f}\cdot\mathbf{S_d}S^z_f)\sum_\sigma\sigma c^\dagger_{k,\sigma}c_{k',\sigma}\ .\end{aligned}\tag{4.23}$$

In order to evaluate them, we note that for any $a\in x,y,z$, we have

$$S^a_1\mathbf{S_1}\cdot\mathbf{S_2}+\mathbf{S_1}\cdot\mathbf{S_2}S^a_1=\sum_b\{S^a_1,S^b_1\}S^b_2=\frac{1}{4}\sum_b 2\delta_{a,b}S^b_2=\frac{1}{2}S^a_2\ .\tag{4.24}$$

Using this, we obtain

$$\begin{aligned}P_1&=\frac{1}{2}S^+_d c^\dagger_{k,\downarrow}c_{k',\uparrow},\\P_2&=\frac{1}{2}S^-_d c^\dagger_{k,\uparrow}c_{k',\downarrow},\\P_z&=\frac{1}{2}S^z_d\sum_\sigma\sigma c^\dagger_{k,\sigma}c_{k',\sigma}\ .\end{aligned}\tag{4.25}$$

Since the bath sites are in the $f-$layer, these terms again lead to the renormalisation of the indirect couplings K_α. Combining with eq. 4.22, we get

$$\frac{\Delta K_\alpha}{\Delta D} = \frac{1}{2}\int_{UV} d\mathbf{q}\,\rho(\mathbf{q})\,[J_{\bar\alpha}(\mathbf{k}_1,\mathbf{q})J_{\bar\alpha}(\mathbf{q},\mathbf{k}_2) - 4J_{\bar\alpha}(\mathbf{q},\bar{\mathbf{q}})W_{\bar\alpha}(\mathbf{k}_1,\mathbf{q},\bar{\mathbf{q}},\mathbf{k}_2)]\left(\frac{1}{1/G^J_{\bar\alpha}+3J_\perp/4} + \frac{1}{1/G^J_{\bar\alpha}-J_\perp/4}\right), \tag{4.26}$$

6.4.2 Particle/hole scattering processes: indirect with indirect

The processes that apply to this class are very similar to those participating in the direct-direct class; the only difference is that the bath degrees of freedom have to be transferred from $\alpha \to \bar\alpha$, due to the inter-layer nature of this coupling. As a result, we will have straightforward counterparts to the renormalisation equations obtained in the previous section, eqs. 4.12, 4.21 and 4.26. The first equation is for the renormalisation of the indirect coupling through itself,

$$\frac{\Delta K_\alpha}{\Delta D} = -\int_{UV} d\mathbf{q}\,\rho(\mathbf{q})\,[K_\alpha(\mathbf{k}_1,\mathbf{q})K_\alpha(\mathbf{q},\mathbf{k}_2) + 4K_\alpha(\mathbf{q},\bar{\mathbf{q}})W_{\bar\alpha}(\mathbf{k}_1,\mathbf{q},\bar{\mathbf{q}},\mathbf{k}_2)]\left(\frac{1}{4}\frac{1}{1/G^K_{\bar\alpha}(\mathbf{q})+3J_\perp/4} + \frac{3}{4}\frac{1}{1/G^K_{\bar\alpha}(\mathbf{q})-J_\perp/4}\right). \tag{4.27}$$

where the indirect Greens function G^K_α is defined as

$$G^K_{\bar\alpha}(\mathbf{q}) = \frac{1}{\omega - |\epsilon_{\bar\alpha}(\mathbf{q})|/2 + K_\alpha(\mathbf{q})/4 + W_{\bar\alpha}(\mathbf{q})/2}, \tag{4.28}$$

and reflects the fact the excitations are happening on impurity and bath states in opposite layers. The second equation is for the effect of the inter-layer term through the denominator of such processes, leading to a renormalisation of the inter-layer itself:

$$\frac{\Delta J_\perp}{\Delta D} = -\frac{1}{4}\int_{UV} d\mathbf{q}\,\rho(\mathbf{q})\int_{IR} d\mathbf{k}\rho(\mathbf{k})\sum_\alpha K_\alpha(\mathbf{k},\mathbf{q})^2\left(\frac{1}{1/G^K_{\bar\alpha}+3J_\perp/4} + \frac{1}{1/G^K_{\bar\alpha}-J_\perp/4}\right). \tag{4.29}$$

The final equation is for the renormalisation of the direct Kondo coupling arising from indirect processes. Similar to how the direct Kondo coupling renormalised the indirect coupling, this occurs through two routes. The complete equation is

$$\frac{\Delta J_\alpha}{\Delta D} = \frac{1}{2}\int_{UV} d\mathbf{q}\,\rho(\mathbf{q})\,[K_{\bar\alpha}(\mathbf{k}_1,\mathbf{q})K_{\bar\alpha}(\mathbf{q},\mathbf{k}_2) - 4K_{\bar\alpha}(\mathbf{q},\bar{\mathbf{q}})W_\alpha(\mathbf{k}_1,\mathbf{q},\mathbf{q},\mathbf{k}_2)]\left(\frac{1}{1/G^K_\alpha+3J_\perp/4} + \frac{1}{1/G^K_\alpha-J_\perp/4}\right). \tag{4.30}$$

6.4.3 Particle/hole scattering processes: direct with indirect

These processes are composed of a direct Kondo excitation process followed by an indirect Kondo de-excitation process, or vice versa. They can be of the particle excitation or the hole excitation kind. Within the particle or hole sector, we again have two sets of processes depending on whether the initial process is direct or indirect:

a. $P_{\rm dir}(d)\ G_d\ H_{\rm ind}(f)$ + h.c.

b. $P_{\rm dir}(f)\ G_f\ H_{\rm ind}(d)$ + h.c.

c. $H_{\rm ind}(f)\ G_d\ P_{\rm dir}(d)$ + h.c.

d. $H_{\rm ind}(d)\ G_f\ P_{\rm dir}(f)$ + h.c.

As mentioned above, $a(b)$ and $c(d)$ are time-reversed partners of each other. We will now show that the contributions from these processes lead to a renormalisation of the inter-layer Kondo term. We suppress the Greens function since it is the same for all the terms:

$$G_\alpha^{JK} = \frac{1}{\omega - |\epsilon_\alpha(\mathbf{q})|/2 + J_\alpha/4 + K_{\bar\alpha}/4 + W_\alpha(\mathbf{q})/2 - J_\perp/4}\,, \tag{4.31}$$

containing antiferromagnetic contributions from J_α and K_α and ferromagnetic contribution in $J_\perp$. The contribution from the pair is of the form

$$\begin{aligned}
&\sum_\alpha \left[P_{\rm dir}(\alpha)H_{\rm ind}(\bar\alpha) + H_{\rm ind}(\bar\alpha)P_{\rm dir}(\alpha)\right] \\
&= \sum_{\alpha,a,b,\beta,\gamma,\delta} \frac{1}{4}J_\alpha(q,k')K_{\bar\alpha}(k,q)\left[\mathbf{S}^a_\alpha\sigma^a_{\beta,\gamma}c_{k',\gamma,\alpha}\mathbf{S}^b_{\bar\alpha}\sigma^b_{\delta,\beta}c^\dagger_{k,\delta,\alpha} + \mathbf{S}^b_{\bar\alpha}\sigma^b_{\delta,\beta}c^\dagger_{k,\delta,\alpha}\mathbf{S}^a_\alpha\sigma^a_{\beta,\gamma}c_{k',\gamma,\alpha}\right]
\end{aligned} \tag{4.32}$$

The sum over β can be carried out:

$$\begin{aligned}
&\sum_{\alpha,a,b,\beta,\gamma,\delta} \frac{1}{4}J_\alpha(q,k')K_{\bar\alpha}(k,q)\left[\mathbf{S}^a_\alpha\sigma^a_{\beta,\gamma}c_{k',\gamma,\alpha}\mathbf{S}^b_{\bar\alpha}\sigma^b_{\delta,\beta}c^\dagger_{k,\delta,\alpha} + \mathbf{S}^b_{\bar\alpha}\sigma^b_{\delta,\beta}c^\dagger_{k,\delta,\alpha}\mathbf{S}^a_\alpha\sigma^a_{\beta,\gamma}c_{k',\gamma,\alpha}\right] \\
&= \sum_{\alpha,a,b,\gamma,\delta} \frac{1}{4}J_\alpha(q,k')K_{\bar\alpha}(k,q)(\sigma^b\sigma^a)_{\delta,\gamma}\mathbf{S}^a_\alpha\mathbf{S}^b_{\bar\alpha}\left[c_{k',\gamma,\alpha}c^\dagger_{k,\delta,\alpha} + c^\dagger_{k,\delta,\alpha}c_{k',\gamma,\alpha}\right] \\
&= \sum_{\alpha,a,b,\gamma,\delta} \frac{1}{4}J_\alpha(q,k')K_{\bar\alpha}(k,q)(\sigma^b\sigma^a)_{\delta,\gamma}\mathbf{S}^a_\alpha\mathbf{S}^b_{\bar\alpha}\delta_{k,k'}\delta_{\delta,\gamma} \\
&= \sum_{\alpha,a,b} \frac{1}{4}J_\alpha(q,k')K_{\bar\alpha}(k,q)\mathrm{Trace}(\sigma^b\sigma^a)\mathbf{S}^a_\alpha\mathbf{S}^b_{\bar\alpha}\delta_{k,k'}\,.
\end{aligned} \tag{4.33}$$

Adding the contribution from the hermitian conjugate and restoring the Greens function, we get the total contribution as

$$\sum_\alpha \left[P_{\rm dir}(\alpha)H_{\rm ind}(\bar\alpha) + H_{\rm ind}(\bar\alpha)P_{\rm dir}(\alpha)\right] + \text{h.c.} = \frac{1}{2}\mathbf{S}_d\cdot\mathbf{S}_f\sum_{\alpha,q,k}\frac{J_\alpha(q,k)K_{\bar\alpha}(k,q)}{1/G^{JK}_\alpha - J_\perp/4}\,. \tag{4.34}$$

The renormalisation of the inter-layer coupling arising from this process is

$$\frac{\Delta J_\perp}{\Delta D} = \int_{UV} d\mathbf{q}\, \rho(\mathbf{q}) \int_{IR} d\mathbf{k} \rho(\mathbf{k}) \sum_{\alpha,q,k} \frac{J_\alpha(q,k) K_{\bar{\alpha}}(k,q)}{1/G_\alpha^{JK} - J_\perp/4} \,. \tag{4.35}$$

6.4.4 Mixed processes

We now turn to the renormalisation arising from particle-hole mixed processes (designated as M_α above). There are four types of process:

$$\begin{aligned}
P_1 &: \sum_\alpha M_{\rm dir}(\alpha) G M_{\rm dir}(\alpha) \\
P_2 &: \sum_\alpha M_{\rm ind}(\alpha) G M_{\rm ind}(\alpha) \\
P_3 &: \sum_\alpha [M_{\rm dir}(\alpha) G M_{\rm ind}(\bar{\alpha}) + \text{h.c.}] \\
P_4 &: \sum_\alpha [M_{\rm dir}(\alpha) G M_{\rm ind}(\alpha) + \text{h.c.}] \\
P_5 &: \sum_\alpha [M_{\rm dir}(\alpha) G M_{\rm dir}(\bar{\alpha}) + M_{\rm ind}(\alpha) G M_{\rm ind}(\bar{\alpha})] \,.
\end{aligned} \tag{4.36}$$

We first note that P_1 and P_2 are equivalent to the ones considered in the direct-direct and indirect-indirect subsections, specifically the renormalisation of $J_\perp$ in eq. 4.21 and its indirect counterpart, the only difference being that k will now range over the UV subspace instead of IR:

$$\begin{aligned}
\frac{\Delta J_\perp}{\Delta D} = -\frac{1}{4} \int_{UV} d\mathbf{q}\, \rho(\mathbf{q}') \int_{UV} d\mathbf{q}' \rho(\mathbf{q}') \sum_\alpha \Bigg[& J_\alpha(\mathbf{q}', \mathbf{q})^2 \left(\frac{1}{1/G_\alpha^J + 3J_\perp/4} + \frac{1}{1/G_\alpha^J - J_\perp/4} \right) \\
& + K_\alpha(\mathbf{k}, \mathbf{q})^2 \left(\frac{1}{1/G_{\bar{\alpha}}^K + 3J_\perp/4} + \frac{1}{1/G_{\bar{\alpha}}^K - J_\perp/4} \right) \Bigg] \,.
\end{aligned} \tag{4.37}$$

The other equations in the same subsection – the ones pertaining to the renormalisation of J_α or K_α are not relevant here because they require the participation of IR bath operators. Similarly, P_3 and P_4 are equivalent to the ones considered in the previous subsection (eq. 4.35), the only difference being that the dummy variable k in the previous subsection would now have to range only over the UV subspace:

$$\frac{\Delta J_\perp}{\Delta D} = \int_{UV} d\mathbf{q}\, \rho(\mathbf{q}) \int_{UV} d\mathbf{q}' \rho(\mathbf{q}') \sum_\alpha \frac{J_\alpha(q,q') K_{\bar{\alpha}}(q',q)}{1/G_\alpha^{JK} - J_\perp/4} \,. \tag{4.38}$$

We finally evaluate the contribution from processes P_4 and P_5. In order to capture coherent scattering processes between the two layers arising from P_4, we project onto the following rotated basis of excited states:

$$\begin{aligned}
|H\rangle_\pm &= \frac{1}{\sqrt{2}} \left(|H(\mathbf{q})\rangle_f \pm |H(\mathbf{q})\rangle_d \right) \,, \\
\mathcal{P}(\mathbf{q})_H &= |H\rangle_+ \langle H|_+ + |H\rangle_- \langle H|_- \,,
\end{aligned} \tag{4.39}$$

where $|H(\mathbf{q})\rangle_\alpha$ is the state obtained upon exciting both states in the layer α: $|H(q)\rangle_\alpha = c^\dagger_{\mathbf{q},\alpha} c_{\bar{\mathbf{q}},\alpha} |L\rangle_f |L\rangle_d$, and $\mathcal{P}(\mathbf{q})_H$ projects onto this rotated excited basis. We focus on the spin-flip component $J_\perp S^+_f S^-_d$ of the Hamiltonian. There are two kinds of processes that renormalise this coupling. We first consider one that involves a spin-flip of the $d-$layer followed by a spin-flip of the $f-$layer:

$$\Delta H = \frac{1}{N^2} \sum_{\mathbf{q}\in \mathrm{UV}} \langle L| \frac{1}{2} J_f(\bar{\mathbf{q}},\mathbf{q}) S^+_f c^\dagger_{\mathbf{q}-\downarrow,f} c_{\mathbf{q}+\uparrow,f} \mathcal{P}(\mathbf{q})_H G \mathcal{P}(\mathbf{q})_H \frac{1}{2} J_d(\mathbf{q},\bar{\mathbf{q}}) S^-_d c^\dagger_{\mathbf{q}\uparrow,d} c_{\bar{\mathbf{q}}\downarrow,d} |L\rangle \ , \tag{4.40}$$

where $|L\rangle = |L\rangle_f |L\rangle_d$ is the initial configuration for both layers. G is the propagator for the excited state:

$$G = \frac{1}{\omega - H_D} \ , \tag{4.41}$$

where H_D is the diagonal part of the Hamiltonian corresponding to the excited(intermediate) state. The diagonal part consists of the kinetic energy and the Ising part of the Kondo interaction:

$$H_D = \sum_{\mathbf{q},\sigma\in\mathbf{q}_\pm,\alpha} \epsilon_\alpha(\mathbf{q}) \tau_{\mathbf{q},\sigma} + \frac{1}{2} \sum_\alpha J_\alpha S^z_\alpha \sum_{\mathbf{q},\sigma} \sigma n_{\mathbf{q},\sigma,\alpha} + J_\perp \vec{S}_f \cdot \vec{S}_d \ . \tag{4.42}$$

Calculating the matrix elements of the propagator in the rotated basis gives

$$\begin{aligned} \mathcal{P}(\mathbf{q})_H G \mathcal{P}(\mathbf{q})_H =& \frac{1}{2} \left(\frac{1}{1/G^J_{ff} - J_\perp/4} + \frac{1}{1/G^J_{dd} - J_\perp/4} \right) (|H\rangle_+ \langle H|_+ + |H\rangle_- \langle H|_-) \\ &+ \frac{1}{2} \left(\frac{1}{1/G^J_{ff} - J_\perp/4} - \frac{1}{1/G^J_{dd} - J_\perp/4} \right) (|H\rangle_+ \langle H|_- + |H\rangle_- \langle H|_+) \ , \end{aligned} \tag{4.43}$$

where

$$G^J_{\alpha\alpha}(\mathbf{q}) = \frac{1}{\omega - \frac{1}{2}\left[\epsilon_\alpha(\mathbf{q}) - \epsilon_\alpha(\bar{\mathbf{q}})\right] + \frac{1}{2} J_\alpha(\mathbf{q}) + W_\alpha(\mathbf{q})} \ . \tag{4.44}$$

where $\bar{\epsilon}_\alpha(\mathbf{q}) = \epsilon_f(\mathbf{q}) - \epsilon_f(\bar{\mathbf{q}})$ is the total excitation energy for the pair of states $\mathbf{q}, \bar{\mathbf{q}}$.

In eq. 4.40, since the first process is an excitation into a $d-$state and the second process is a de-excitation from an $f-$state, the expression can be simplified into

$$\begin{aligned} \langle L| S^+_f c^\dagger_{\mathbf{q}-\downarrow,f} c_{\mathbf{q}+\uparrow,f} \mathcal{P}(\mathbf{q})_H G \mathcal{P}(\mathbf{q})_H S^-_d c^\dagger_{\mathbf{q}+\uparrow,d} c_{\mathbf{q}-\downarrow,d} |L\rangle &= S^+_f S^-_d \langle H_f| \mathcal{P}(\mathbf{q})_H G \mathcal{P}(\mathbf{q})_H |H_d\rangle \\ &= \frac{1}{2} \left(\frac{1}{1/G^J_{ff} - J_\perp/4} + \frac{1}{1/G^J_{dd} - J_\perp/4} \right) S^+_f S^-_d \ . \end{aligned} \tag{4.45}$$

The net Hamiltonian renormalisation is finally a sum over the contribution from each mode:

$$\Delta H = \frac{1}{8N^2} \sum_{\mathbf{q}\in \mathrm{UV}} J_f(\bar{\mathbf{q}},\mathbf{q}) J_d(\mathbf{q},\bar{\mathbf{q}}) \left(\frac{1}{1/G^J_{ff} - J_\perp/4} + \frac{1}{1/G^J_{dd} - J_\perp/4} \right) S^+_f S^-_d \ . \tag{4.46}$$

Converting the sums to integrals (assuming a density of states $\rho(\mathbf{q})$) gives the final expression

$$\frac{\Delta H}{\Delta D} = \frac{1}{8N} S_f^+ S_d^- \int_{UV} d\mathbf{q}\, \rho(\mathbf{q}) J_f(\bar{\mathbf{q}}, \mathbf{q}) J_d(\mathbf{q}, \bar{\mathbf{q}}) \left(\frac{1}{1/G^J_{ff}(q) - J_\perp/4} + \frac{1}{1/G^J_{dd}(q) - J_\perp/4} \right) . \quad (4.47)$$

The time-reversed partner of this process can be obtained simply by exchanging the $d-$interaction with the $f-$interaction. Since the renormalisation itself is symmetric, the contribution is equal to what we obtained here. The total renormalisation in the coupling for the term $S_f^+ S_d^-$ is therefore

$$\frac{\Delta J_\perp}{\Delta D} = \frac{1}{2} \int_{UV} d\mathbf{q}\, \rho(\mathbf{q}) J_f(\bar{\mathbf{q}}, \mathbf{q}) J_d(\mathbf{q}, \bar{\mathbf{q}}) \left(\frac{1}{1/G^J_{ff}(q) - J_\perp/4} + \frac{1}{1/G^J_{dd}(q) - J_\perp/4} \right) . \quad (4.48)$$

Taking into account P_5 by replacing couplings J_α with K_α and the Greens function $G^J_{\alpha\alpha}$ with

$$G^K_{\alpha\alpha}(\mathbf{q}) = \frac{1}{\omega - \frac{1}{2}\left[\epsilon_\alpha(\mathbf{q}) - \epsilon_\alpha(\bar{\mathbf{q}})\right] + \frac{1}{2} K_{\bar{\alpha}}(\mathbf{q}) + W_\alpha(\mathbf{q})} , \quad (4.49)$$

we have the total renormalisation

$$\begin{aligned} \frac{\Delta J_\perp}{\Delta D} = \frac{1}{2} \int_{UV} d\mathbf{q}\, \rho(\mathbf{q}) \Bigg[& J_f(\bar{\mathbf{q}}, \mathbf{q}) J_d(\mathbf{q}, \bar{\mathbf{q}}) \sum_\alpha \frac{1}{1/G^J_{\alpha\alpha}(\mathbf{q}) - J_\perp/4} \\ & + K_f(\bar{\mathbf{q}}, \mathbf{q}) K_d(\mathbf{q}, \bar{\mathbf{q}}) \sum_\alpha \frac{1}{1/G^K_{\alpha\alpha}(\mathbf{q}) - J_\perp/4} \Bigg] . \end{aligned} \quad (4.50)$$

6.4.5 Complete RG Equations

Inter-layer Kondo coupling $J_\perp$

$$\begin{aligned} \frac{\Delta J_\perp}{\Delta D} = & -\frac{1}{4} \int_{\mathrm{UV}} d\mathbf{q}\, \rho(q) \int_{\mathrm{UV+IR}} d\mathbf{k}\, \rho(k) \sum_\alpha \Bigg[J^2_\alpha(q,k) \left(\frac{1}{1/G^J_\alpha + 3J_\perp/4} + \frac{1}{1/G^J_\alpha - J_\perp/4} \right) \\ & K^2_\alpha(q,k) \left(\frac{1}{1/G^K_{\bar{\alpha}} + 3J_\perp/4} + \frac{1}{1/G^K_{\bar{\alpha}} - J_\perp/4} \right) \Bigg] \\ & + \int_{\mathrm{UV}} d\mathbf{q}\, \rho(q) \int_{\mathrm{UV+IR}} d\mathbf{k}\, \rho(k) \sum_\alpha \frac{J_\alpha(q,k) K_{\bar{\alpha}}(k,q)}{1/G^{JK}_\alpha - J_\perp/4} \\ & + \frac{1}{2} \int_{UV} d\mathbf{q}\, \rho(\mathbf{q}) \sum_\alpha \left[\frac{J_\alpha(\bar{\mathbf{q}}, \mathbf{q}) J_{\bar{\alpha}}(\mathbf{q}, \bar{\mathbf{q}})}{1/G^J_{\alpha\alpha}(\mathbf{q}) - J_\perp/4} + \sum_\alpha \frac{K_\alpha(\bar{\mathbf{q}}, \mathbf{q}) K_{\bar{\alpha}}(\mathbf{q}, \bar{\mathbf{q}})}{1/G^K_{\alpha\alpha}(\mathbf{q}) - J_\perp/4} \right] \end{aligned} \quad (4.51)$$

Direct Kondo coupling J_α

$$\begin{aligned}\frac{\Delta J_\alpha(k_1,k_2)}{\Delta D} = &-\int_{UV} d\mathbf{q}\,\rho(\mathbf{q})\,[J_\alpha(\mathbf{k}_1,\mathbf{q})J_\alpha(\mathbf{q},\mathbf{k}_2)+4J_\alpha(\mathbf{q},\bar{\mathbf{q}})W_\alpha(\mathbf{k}_1,\mathbf{q},\bar{\mathbf{q}},\mathbf{k}_2)]\\ &\left(\frac{1/4}{1/G^J_\alpha(\mathbf{q})+3J/4}+\frac{3/4}{1/G^J_\alpha(\mathbf{q})-J_\perp/4}\right)\\ &+\frac{1}{2}\int_{UV} d\mathbf{q}\,\rho(\mathbf{q})\,[K_{\bar\alpha}(\mathbf{k}_1,\mathbf{q})K_{\bar\alpha}(\mathbf{q},\mathbf{k}_2)-4K_{\bar\alpha}(\mathbf{q},\bar{\mathbf{q}})W_\alpha(\mathbf{k}_1,\mathbf{q},\bar{\mathbf{q}},\mathbf{k}_2)]\\ &\left(\frac{1}{1/G^K_\alpha+3J_\perp/4}+\frac{1}{1/G^K_\alpha-J_\perp/4}\right).\end{aligned} \tag{4.52}$$

Indirect Kondo coupling K_α

$$\begin{aligned}\frac{\Delta K_\alpha(k_1,k_2)}{\Delta D} = &-\int_{UV} d\mathbf{q}\,\rho(\mathbf{q})\,[K_\alpha(\mathbf{k}_1,\mathbf{q})K_\alpha(\mathbf{q},\mathbf{k}_2)+4K_\alpha(\mathbf{q},\bar{\mathbf{q}})W_{\bar\alpha}(\mathbf{k}_1,\mathbf{q},\bar{\mathbf{q}},\mathbf{k}_2)]\\ &\left(\frac{1}{4}\frac{1}{1/G^K_{\bar\alpha}(\mathbf{q})+3J_\perp/4}+\frac{3}{4}\frac{1}{1/G^K_{\bar\alpha}(\mathbf{q})-J_\perp/4}\right)\\ &+\frac{1}{2}\int_{UV} d\mathbf{q}\,\rho(\mathbf{q})\,[J_{\bar\alpha}(\mathbf{k}_1,\mathbf{q})J_{\bar\alpha}(\mathbf{q},\mathbf{k}_2)-4J_{\bar\alpha}(\mathbf{q},\bar{\mathbf{q}})W_{\bar\alpha}(\mathbf{k}_1,\mathbf{q},\bar{\mathbf{q}},\mathbf{k}_2)]\\ &\left(\frac{1}{1/G^J_{\bar\alpha}+3J_\perp/4}+\frac{1}{1/G^J_{\bar\alpha}-J_\perp/4}\right).\end{aligned} \tag{4.53}$$

Propagators

$$\begin{aligned}\text{Intra-layer spin-flip excitation: } G^J_\alpha(\mathbf{q}) &= \frac{1}{\omega-|\epsilon_\alpha(\mathbf{q})|/2+J_\alpha(\mathbf{q})/4+W_\alpha(\mathbf{q})/2},\\ \text{Inter-layer spin-flip excitation: } G^K_\alpha(\mathbf{q}) &= \frac{1}{\omega-|\epsilon_\alpha(\mathbf{q})|/2+K_{\bar\alpha}(\mathbf{q})/4+W_\alpha(\mathbf{q})/2},\\ \text{Both spins, one of the baths: } G^{JK}(\mathbf{q}) &= \frac{1}{\omega-|\epsilon_\alpha(\mathbf{q})|/2+J_\alpha(\mathbf{q})/4+K_{\bar\alpha}(\mathbf{q})/4+W_\alpha(\mathbf{q})/2},\\ \text{Intra-layer spin-flip, two UV excitation: } G^J_{\alpha\alpha}(\mathbf{q}) &= \frac{1}{\omega-\frac{1}{2}[\epsilon_\alpha(\mathbf{q})-\epsilon_\alpha(\bar{\mathbf{q}})]+\frac{1}{2}J_\alpha(\mathbf{q})+W_\alpha(\mathbf{q})},\\ \text{Inter-layer spin-flip, two UV excitation: } G^K_{\alpha\alpha}(\mathbf{q}) &= \frac{1}{\omega-\frac{1}{2}[\epsilon_\alpha(\mathbf{q})-\epsilon_\alpha(\bar{\mathbf{q}})]+\frac{1}{2}K_{\bar\alpha}(\mathbf{q})+W_\alpha(\mathbf{q})}.\end{aligned} \tag{4.54}$$

6.5 Analysis for the simplified case of infinite dimensions

We first investigate the properties of the impurity model in the limit of infinite dimensions, on a Bethe lattice. This limit suppresses any momentum-space differentiation arising from low-dimensional lattices, and allows the study of real-space local properties.

We simulate the RG equations by adding small seed values of K_f and K_d and check whether they grow to non-zero values or remain vanishingly small. We find that positive seed values are irrelevant under RG flow and have no effect. Instead, negative values are relevant and reach non-zero values in the fixed point Hamiltonian. We there simulate the RG equations with small negative seed values for K_f and K_d. We find that The other couplings are set as follows, in units of the conduction electron bandwidth: $J_f = J_d = 0.1, W_d = 0.0$. The results are shown in Fig. 6.3, in the form of the renormalised low-energy fixed point values of the Kondo couplings J_f and J_d and the inter-layer coupling $J_\perp$, all as functions of W_f and $J_\perp$. We find that the $d-$layer Kondo coupling J_d (central panel) undergoes a suppression at larger values of the inter-layer coupling $J_\perp$. This coincides with an increase in the renormalised value of $J_\perp$ (right panel) itself, indicating a transfer of correlations from within the $d-$layer to between the $d-$ and $f-$layers. The couplings J_d is, however, largely unaffected by the bath correlation of the $f-$layer, as seen from the lack of any dependence of the boundary on W_f.

The $f-$layer coupling J_f (left panel) is suppressed with increasing $|W_f|$ as well as increasing $J_\perp$. The phase space for J_f therefore splits, roughly, into four regions. The lower left region involves a dominant J_f coupling and displays local Fermi liquid excitations within the $f-$layer. The upper left region has the in-plane correlation W_f driving J_f to irrelevance and leads to a Mott insulator within the $f-$layer, which can order magnetically if spontaneous symmetry breaking is allowed. The lower right region has the influence of both J_f and $J_\perp$ and therefore involves the hybridisation of the local Fermi liquids in the two layers. Finally, the upper right region has the Mott state of the $f-$layer hybridising with the $d-$layer through $J_\perp$.

6.6 Infinite dimensions: Real-space correlation and phase diagram

In order to characterise the various phases, we compute a set of real-space correlations involving the impurity sites and the conduction bath sites hybridising with them. For small $|W_f|$, the $f-$layer

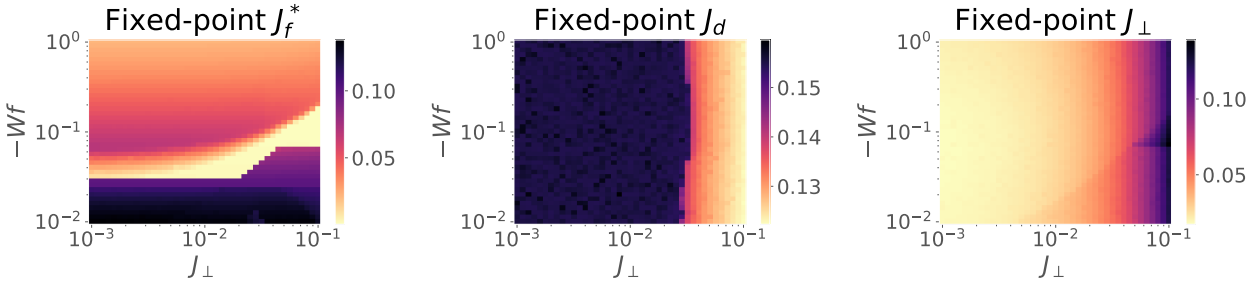

Figure 6.3: *Fixed-point values for the direct Kondo couplings J_α and $J_\perp$. The $f-$layer Kondo coupling is highly suppressed by increasing both $|W_f|$ and $J_\perp$. The conduction layer coupling J_d is mildly suppressed by $J_\perp$. The inter-layer coupling $J_\perp$ itself grows as its bare value is increased. Going from left to right therefore represents a heavy fermion transition from intra-orbital screening at small $J_\perp$ to inter-orbital Kondo screening at large $J_\perp$.*

is highly correlated but still itinerant due to the presence of local Fermi liquid excitations. In order to capture the $J_\perp$-driven transition in this regime, we track the inter-impurity compensation factor $\langle \mathbf{S}_f \cdot \mathbf{S}_d \rangle$ that quantifies the strength of the singlet state between these two sites. As seen from the left panel in Fig. 6.4, the inter-impurity correlation (red curve) grows to large values as $J_\perp$ is increased and eventually saturates close to the maximum value. This marks a transition from a phase in which the two metallic layers are decoupled and participate in transport independently, to one in which the local Fermi liquids hybridise and form local bound states.

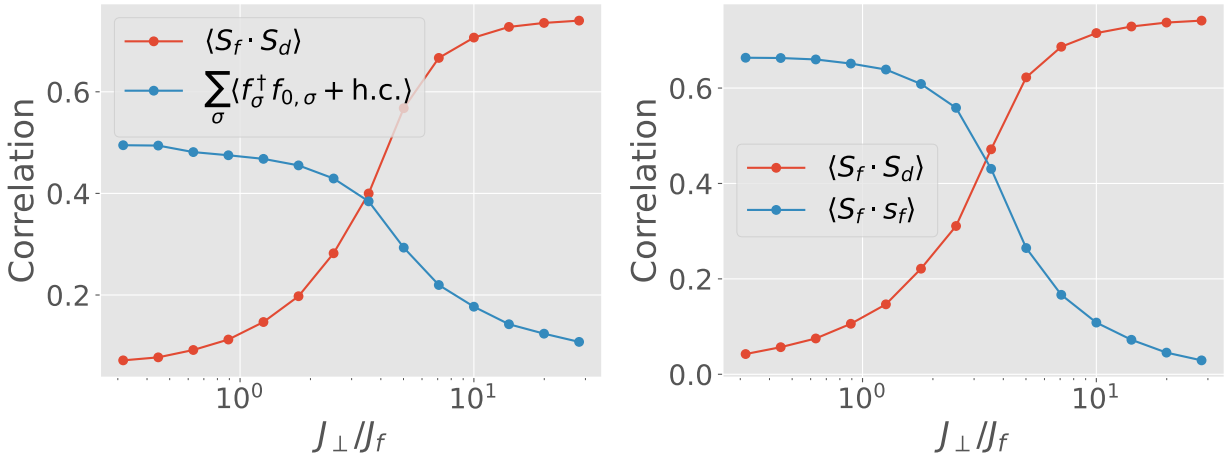

Figure 6.4: *Characterisation of the transition for small and large $|W_f|$ in terms of real-space correlation measures. Left: For small $|W_f|$, the $f-$layer is weakly correlated and Kondo screening involves both spin and charge degrees of freedom. Accordingly, we track the transition using the charge compensation factor (blue) and the inter-layer spin correlation (red). The charge compensation is suppressed as $J_\perp$ is increased and is replaced with the inter-layer correlation, showing the buildup of inter-layer Kondo screening. Right: For large $|W_f|$, the $f-$spins are localised and interact with each other through intra-orbital spin correlation $\langle S_f \cdot s_f \rangle$. As $J_\perp$ is increased, these intra-orbital spin correlations are again replaced by inter-orbital spin correlations. In this way, our analysis shows how the inter-orbital correlations replace intra-orbital correlations for both small and large $|W_f|$.*

A complimentary picture is obtained in the same regime by studying the one-particle hybridisation between the $f-$impurity and its nearest-neighbour site f_0. While this measure is large for small $J_\perp$, indicating the presence of in-plane Kondo screening, and it gets suppressed as $J_\perp$ is increased, revealing that the $f-$impurity is no longer hybridising with its own bath.

For large $|W_f|$, the $f-$layer is sufficiently strongly correlated to form a Mott insulator where the charge excitations are gapped, and the low-energy theory is described by a Heisenberg model. Here, we retain the inter-layer compensation factor as a measure but we replace the one-particle hybridisation with the spin-spin correlation $\langle \mathbf{S}_f \cdot \mathbf{s}_f \rangle$ between the $f-$spin and it's nearest spin; this change is necessitated by the charge gap in the spectrum. We again find that the inter-layer correlation grows as $J_\perp$ is increased, while the intra-layer spin correlation shrinks. This marks a transition between a phase with no Kondo screening between the layers (and where the $f-$layer is potentially

magnetically ordered) to one where the $f-$spin is Kondo screened by the other layer. In the context of heavy fermions, this marks a Kondo breakdown QCP between a magnetically-ordered phase with no (static) Kondo screening versus a heavy Fermi liquid phase where the $f-$spin participates in transport through its hybridisation with the other layer. For the case of a half-filled conduction bath, the strongly coupled $J_\perp$ phase corresponds to a Kondo insulator comprised of tightly bound inter-layer singlets. Mott likened this to an insulating inter-layer excitonic condensate [622].

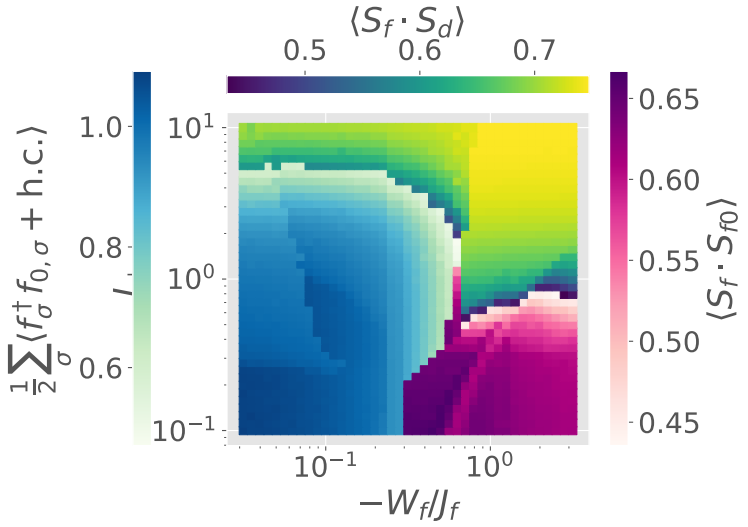

Figure 6.5: *Phase diagram of the infinite dimensional impurity model on the Bethe lattice, derived from real-space correlations. The three colors represent three different correlations, defined through the labels. The left half is mostly dominated by the weakly correlated intra-orbital Kondo screened phase where the one-particle correlation between the $f-$electrons is active (blue colorbar). At small $|W_f|$, this phase transitions into the inter-orbital screened*

These conclusions are crystallised in the phase diagram in Fig. 6.5, computed using the three measures described above. For small $J_\perp$ and $|W_f|$ (lower left region), the two layers are metallic and mostly decoupled. Increasing $J_\perp$ along the $y-$axis leads to a Kondo insulating phase, while increasing $|W_f|$ along the $x-$axis leads to the $f-$layer becoming insulating and decoupled from the other layer.

We have also characterised the transition using entanglement measures. Specifically, the mutual information (left, Fig. 6.6) between the $f-$ and $d-$spins grows during the emergence of the Kondo insulator, as $J_\perp$ is increased. While this holds for both large and small $|W_f|$, there's one difference. Upon lowering $J_\perp$, the I_2 for the case of small $|W_f|$ vanishes much more rapidly compared to the case of large $|W_f|$. We believe the former is due to the gapless excitations present within the $f-$layer at small $|W_f|$ that promote strong entanglement within the layer and hence compete with the inter-layer entanglement. Moreover, the mutual information between the zeroth sites of the two conduction baths (right, Fig. 6.6) is maximised in the vicinity of the transition. This shows that the transition into the Kondo insulator is marked by long-range inter-layer correlations.

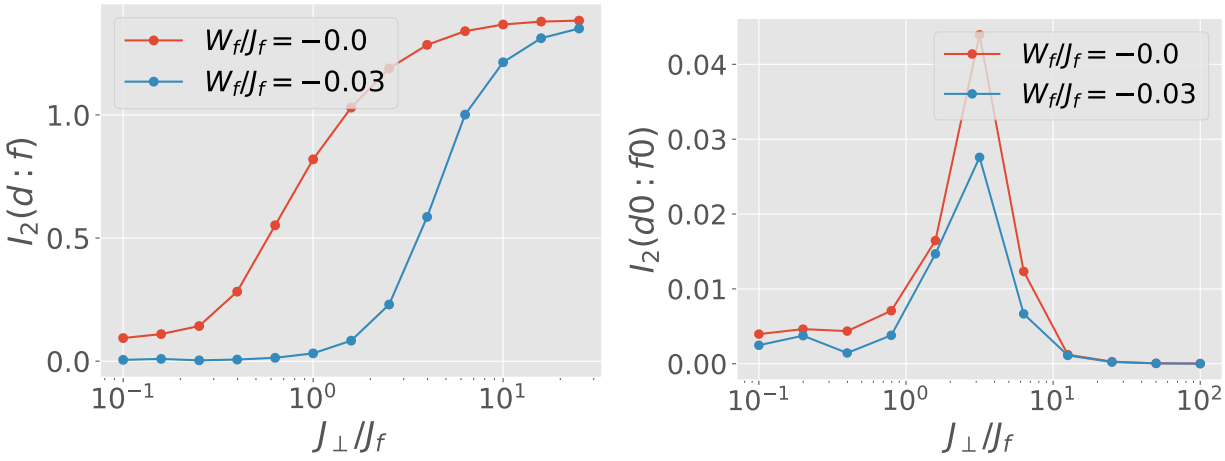

Figure 6.6: *Left: Transfer of entanglement during the transition from intra-orbital screened phase to inter-orbital screened phase. For both small (red) and large (blue) $|W_f|$, the mutual information between the two impurities grows as the inter-orbital screening increases. Right: Close to the transition, we detect an increase in the range of entanglement, through a rise in the value of the mutual information between the zeroth site of the conduction layer and that of the $f-$layer. This suggests that the transition is marked by a critical point.*

6.7 Infinite dimensions: Local spectral function

To further investigate the phases, we compute the local spectral functions of the $f-$ and $d-$impurities, for large (Fig. 6.7) and small (Fig. 6.8) $|W_f|$. From our earlier work on the extended Anderson impurity model [454], we know that the $f-$impurity can support a Kondo resonance only for $|W_f|$ below the critical value, and it displays a Mott gap above it. Our calculations now show how this central resonance hybridises with the resonance of the $d-$layer through the inter-orbital Kondo coupling.

For large $|W_f|$ (Fig. 6.7), we find no effect of the inter-orbital hybridisation $J_\perp$ at small values, because of the hard gap in the spectrum. At larger values of $J_\perp$, fluctuations of the $f-$impurity through the gapless excitations of the $d-$layer lead to some spectral weight near $\omega = 0$. This a pseudogap phase of matter. For larger values, the inter-orbital hybridisation is large enough to open a gap in the spectrum, and we obtain a Kondo insulator.

For weak $|W_f|$, both the $f-$ and $d-$impurities exhibit a central Kondo resonance at small $J_\perp$ (see Fig. 6.8). For larger $J_\perp$, this resonance splits into two bands, in both the layers. At half-filling, the lower bands are filled. These bands correspond to the two hybridised levels formed locally due to the mixing of the $f-$ and $d-$impurities. We therefore again get a Kondo insulator. Similar to the large $|W_f|$ case, the formation of the Kondo insulator again passes through a pseudogap in both the $d-$ and $f-$ spectral functions.

Away from half-filling, if the chemical potential lies in one of the bands, the systems becomes a heavy Fermi liquid. The value of W_f determines the amount of correlation in the heavy Fermi liquid. Larger values of $|W_f|$ lead to narrow bands for the metal.

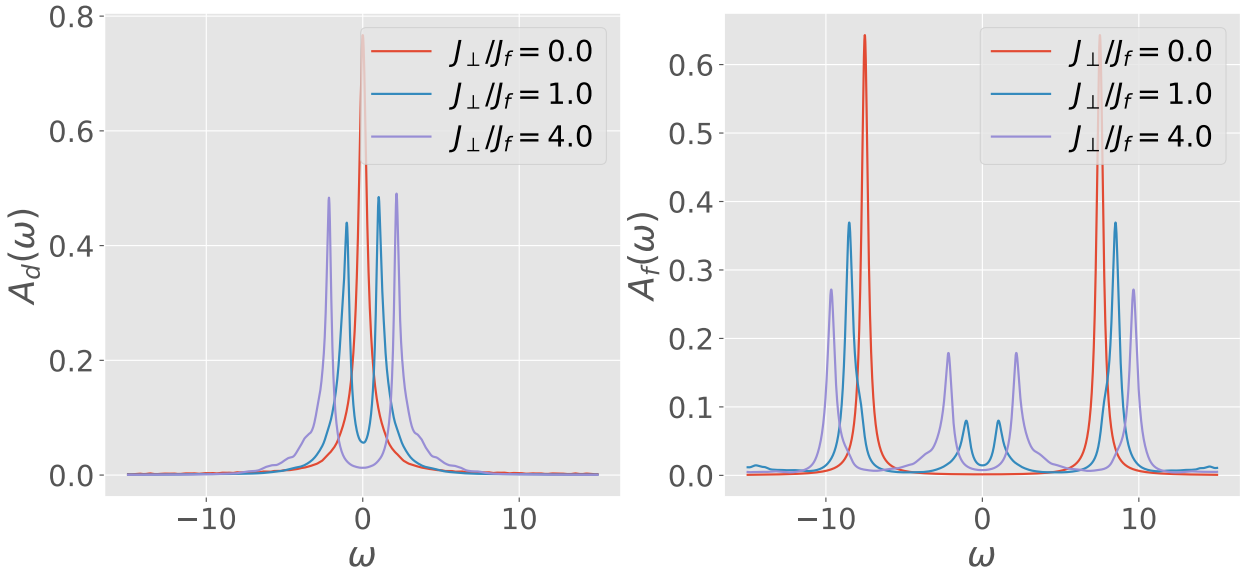

Figure 6.7: *Spectral functions of the $d-$ (left) and $f-$impurity (right), for large $|W_f|$. The $d-$impurity shows a splitting of the central resonance because of spin-flip scattering processes with the $f-$impurity. The f spectral function initially has a Mott gap for small $J_\perp$. At large $J_\perp$, scattering processes with the $d-$layer lead to states at low energies in the form of a pseudogap. Further increasing $J_\perp$ leads to a Kondo insulator.*

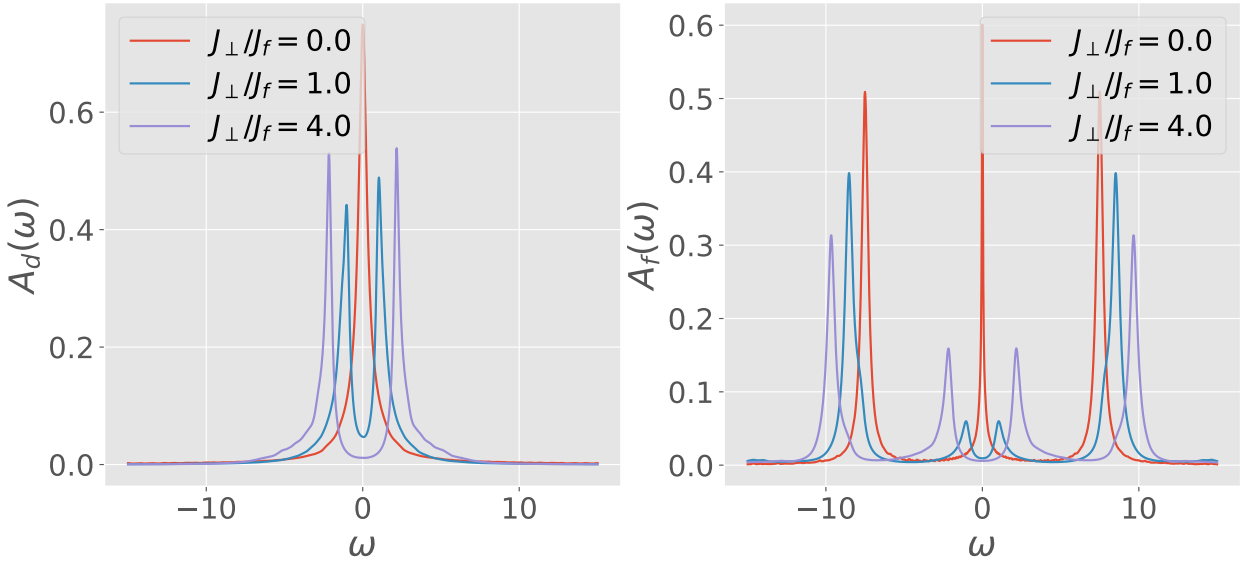

Figure 6.8: *Spectral functions of the $d-$ (left) and $f-$impurity (right), for small $|W_f|$. The $d-$impurity again shows a splitting of the central resonance because of spin-flip scattering processes with the $f-$impurity. In this case, the $f-$resonance is initially gapless because $|W_f|$ is below its critical value, and it shows behaviour to the d impurity. At large $J_\perp$, both the spectral functions acquire a hybridisation gap in the spectrum and a Kondo insulator emerges.*

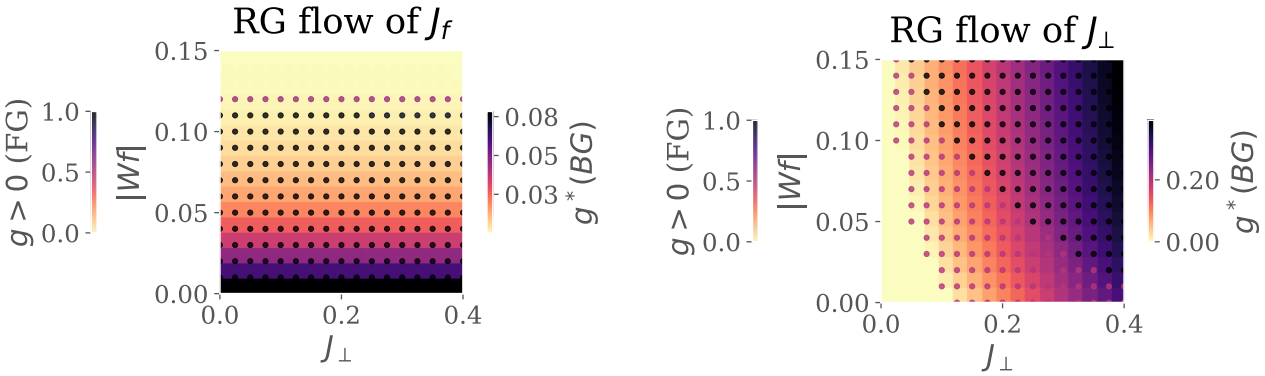

Figure 6.9: *RG phase diagrams for the Kondo couplings J_f (left) and $J_\perp$ (right). For each plot, the background color (quantified by the right colorbar) tracks the fixed point value of the coupling as a function of the inter-layer couplings $J_\perp$ and the $f-$layer bath interaction $|W_f|$. The marker color complements this by tracking whether the coupling is relevant, intermediate-coupling or irrelevant in the RG sense, by taking the values 1, $1/2$ or 0 respectively.*

6.8 Renormalisation Group Flows For the 2D Lattice-Embedded Impurity Model

We now extend our analysis to capture the more realistic case of two dimensions, on a square lattice. We focus on the renormalisation group flows of the couplings.

Fig. 6.9 shows the fixed point values of the couplings J_f and $J_\perp$ under unitary renormalisation group flow. We view these values as a function of the $f-$layer bath interaction W_f and inter-layer Kondo coupling $J_\perp$. In each panel, the right (left) colorbar quantifies the background (marker) color of the plot. The background displays the fixed point value of each coupling whereas the marker color tracks whether the couplings is relevant (1), intermediate coupling (0.5) or irrelevant (0).

The Kondo coupling J_f (left panel) of the $f-$layer becomes RG-irrelevant for larger values of $|W_f|$; this leads to an in-plane Mott transition of the kind observed in our earlier work, where the local Fermi liquid excitations of the $f-$impurity give way to a pseudogapped non-Fermi liquid Mott metal phase which ultimately destabilises into a local moment phase. The RG flow of J_f does not appear to be significantly affected by the variation of $J_\perp$. Concomitant with the irrelevance of J_f under increasing $|W_f|$, the inter-plane coupling $J_\perp$ (right panel) becomes RG-relevant, as seen from the darkening markers as we go to higher $|W_f|$.

These simulations motivate an RG-based phase diagram that appears to be qualitatively similar to the phase diagram (Fig. 6.5) obtained in infinite dimensions in the previous sections: (i) weak $J_\perp$, weak $|W_f|$: decoupled metallic layers, each layer participating in transport independently, (ii) strong $J_\perp$, strong $|W_f|$: Kondo insulator regime, where the local moments of the $f-$layer hybridise with the itinerant electrons of the $d-$layer to form a band insulator with the chemical potential situated in the hybridisation gap, (iii) strong $J_\perp$, weak $|W_f|$: Kondo insulator regime but where the $f-$impurity entangles not only with the $d-$impurity but with other electrons in the $f-$layer as well, and (iv) weak $J_\perp$, strong $|W_f|$: the so-called RKKY regime, where the $f-$layer forms local moments which decouple from the $d-$layer and are then free to interact with one another (and perhaps even order

magnetically).

6.9 Lattice spectral functions

We now compute real-space and $k-$space spectral functions within the lattice model by using our tiling framework.

We first compute the local spectral functions of the $f-$ and $d-$layers in real space (Fig. 6.10). As expected, the $d-$layer spectral function shows a central metallic peak at $J_\perp = 0$ which opens a hybridisation gap at large $J_\perp$, leading to a Kondo insulator. The $f-$spectral function behaves similarly. This clearly shows the transition from an in-plane metal/insualtor (depending on the value of $|W_f|$), to an inter-plane hybridised state.

To further understand the nature of the states that are occupied in the Kondo insulator, we obtain local spectral functions in the bonding and antibonding basis (Fig. 6.11): $c_{i,\sigma,\pm} = c_{i,\sigma,f} \pm c_{i,\sigma,d}$. In the absence of $J_\perp$ (left plots), both are equal to each other, and show metallic behaviour, indicating that they are both half-filled in the ground state. At large $J_\perp$, the central resonance of A_+ and A_- gets shifted to positive and negative frequencies respectively. This clearly shows the formation of the two bands of a Kondo insulator due to the inter-layer hybridisation. In the ground state, only one of them is occupied while the other is empty, and this is what makes it an insulator. Tuning the chemical potential into one of the bands can lead to a heavy Fermi liquid.

We next focus on the $k-$space spectral functions, in order to identify any momentum-space differentiation arising from the inter-layer hybridisation. We have already seen within our earlier work on the extended Hubbard mode in two dimension [455] that tuning the bath correlation $|W|$ leads to a pseudogapping transition that starts with the selecting gapping of the antinodes and ends with the gapping of the nodes. In order to investigate similar phenomena here, we obtain the lattice nodal and antinodal spectral functions, as a function of W_f and $J_\perp$ (Fig. 6.12). Going from the top panel to the bottom panel corresponds to increasing the correlation of the $f-$layer, and within each row, the left and right panels capture the density of states at the node and antinode respectively. Finally, within each panel, we show how the density of states varies as the inter-layer hybridisation $J_\perp$ is increased.

We find that the anisotropy between the two $k-$space points is maximal at small $|W_f|$ as $J_\perp$ is increased, as seen by comparing the purple curves in the two panels. More precisely, we find that the inter-layer hybridisation affects the antinodal point more strongly, leading to the opening of a hybridisation gap at the antinodal point first. In contrast, at larger values of $|W_f|$, the anisotropy is greater at small $J_\perp$, and this anisotropy is due primarily to the bath correlation.

Prompted by this, we calculate the anisotropy between the nodal and antinodal spectral functions at zero frequency, to get a more concrete picture of the $k-$space differentiation in the complete parameter regime. Fig. 6.13 backs up our conclusions from the previous calculation (Fig. 6.12). We find that at small $|W_f|$, the anisotropy increases as $J_\perp$ is increased, which means that hybridisation gap opens at different values of $J_\perp$ for different points on the Fermi surface. The journey from the degenerate decoupled metal at $J_\perp/J_f \ll 1$ to the Kondo insulator at $J_\perp/J_f > 1$ there passes through a pseudogap in terms of the hybridisation gap. In contrast, at large $|W_f|$, the differentiation is suppressed at large $J_\perp$, which suggests that the hybridisation gap there opens uniformly over the

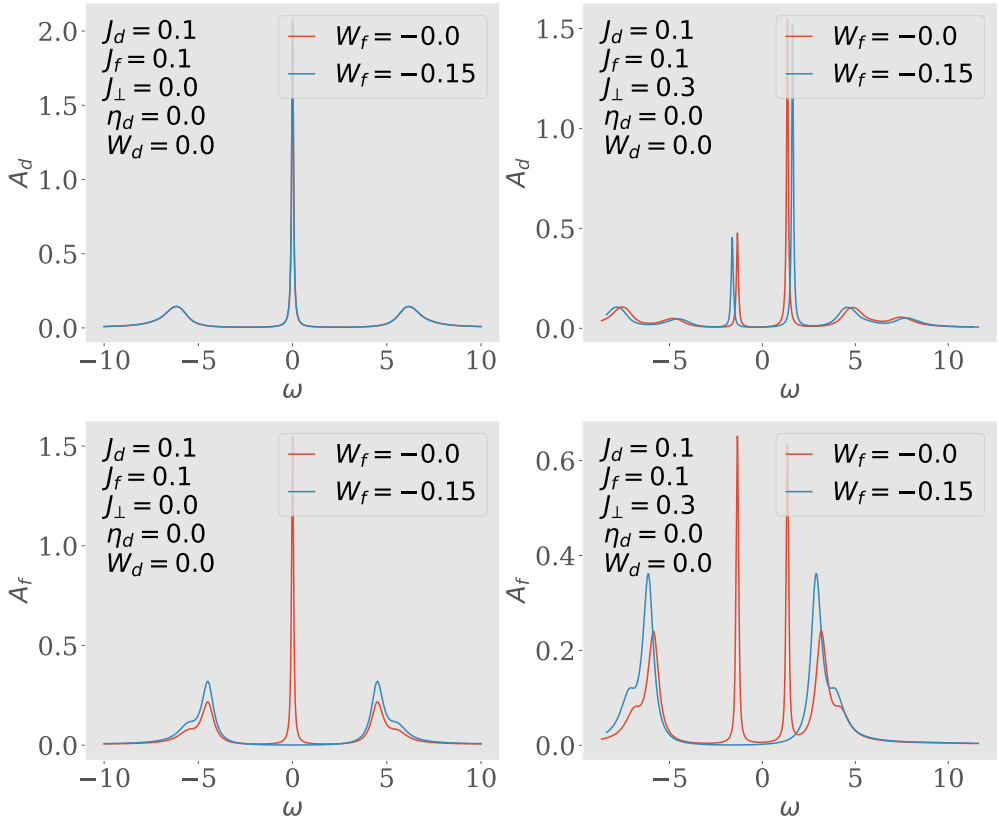

Figure 6.10: *Spectral functions A_d (top) and A_f (bottom) of the lattice model, for excitations in the $d-$ and $f-$layers respectively. Both show a central Kondo resonance for $J_\perp = 0$ which splits into two bands upon adding a non-zero $J_\perp$. Increasing $|W_f|$ to large values gaps out the local Fermi liquid excitations of A_f.*

Fermi surface.

6.10 Conclusions

In this chapter, we have investigated specific aspects of the heavy fermions problem at half-filling by approaching it from a more general model – the two-orbital Hubbard model. We first study the appropriate auxiliary model – a two-impurity Kondo model – and then apply the tiling method developed in the earlier chapters to calculate lattice quantities. We have investigated various properties of the models by varying the bath correlation W_f in the correlated $f-$layer and the inter-orbital hybridisation $J_\perp$. Consolidating all the measures leads to a phase diagram with several competing states.

For large $J_\perp$, the state is always a Kondo insulator due to particle-hole symmetry, but the nature of the Kondo insulator changes depending on the correlation of the $f-$layer. Interestingly, for small W_f, the Kondo insulator displays momentum-space anisotropy in terms of a selective opening of

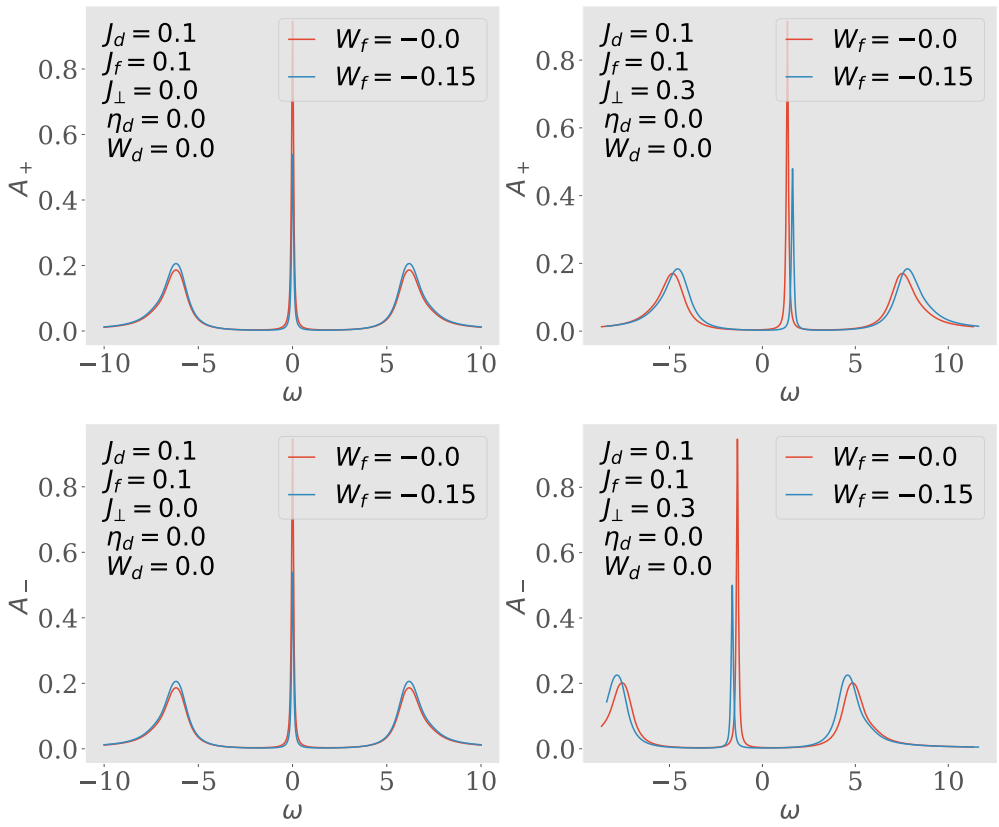

Figure 6.11: *Spectral functions of the tiled model, for excitations in the bonding (two on the left) and antibonding (two on the right) basis, defined by the Greens function $G_{k,\pm} = G(k_d \pm k_f; \omega)$. There is no hybridisation for $J_\perp = 0$ (first and third plots), and the only effect of W_f is to shrink the height of the central resonance. Introducing a non-zero $J_\perp$ splits the central resonance into an upper band (second from left) and a lower band (first from right). This leads to a Kondo insulator, where $\omega = 0$ resides inside the hybridisation gap.*

the hybridisation gap at various parts of the Fermi surface. The transition into the Kondo insulator is marked by an increase in the mutual information between the layers, and we find evidence of long-range entanglement in the vicinity of the transition.

While it is true that our results are all at $T = 0$, it stands to reason that the characteristics of these phases will survive against thermal fluctuations up to some finite temperature. For example, the pseudogap non-Fermi liquid behaviour we see near the transition arises from the quantum critical fluctuations; these fluctuations can survive up to certain temperatures and have finite temperature counterparts. We are presently investigating this in the $D = \infty$ Hubbard model at half-filling, by extending the unitary RG treatment to finite temperatures.

This investigation leads to a number of interesting avenues for further studies. The presence of long-range entanglement at the transition might be relevant to the observation of strange metallic behaviour in heavy-fermion compunds at high temperatures above the quantum critical point. Moreover, the momentum-anisotropic entry into the Kondo insulator observed here is likely to af-

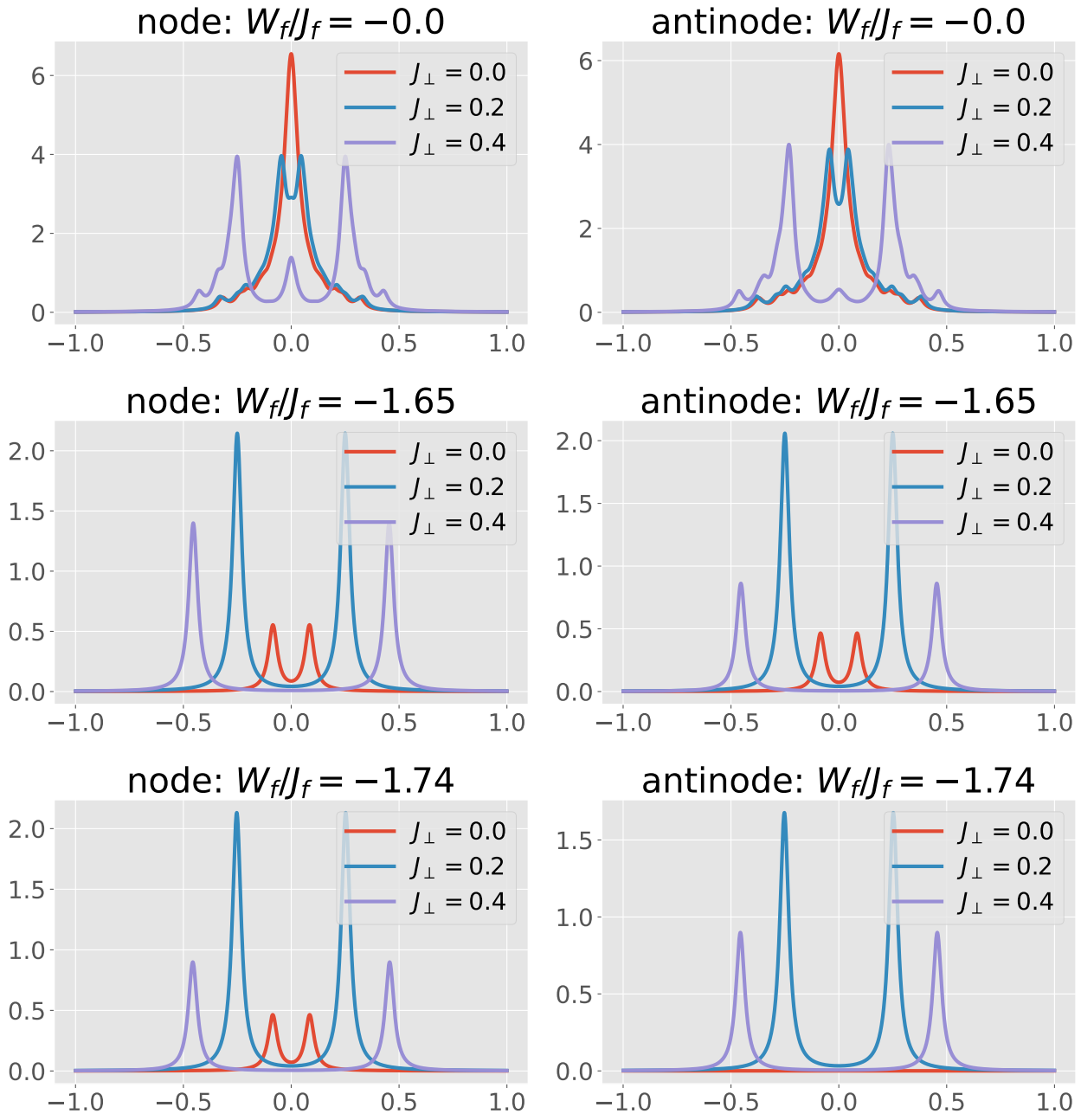

Figure 6.12: *Spectral functions of the nodal (left) and antinodal (right) $k-$space point in the $f-$layer. $|W_f|$ increases from the top panel to the bottom panel, while $J_\perp$ increases within each panel. For small $|W_f$, the effect of $J_\perp$ is to create a hybridisation gap in the central resonance of both layers. For large $|W_f|$, the $f-$layer is a Mott insulator, and introducing $J_\perp$ then leads to weak metallic processes due to virtual tunneling into the $d-$layer. These processes again acquire a hybridisation gap at large $J_\perp$.*

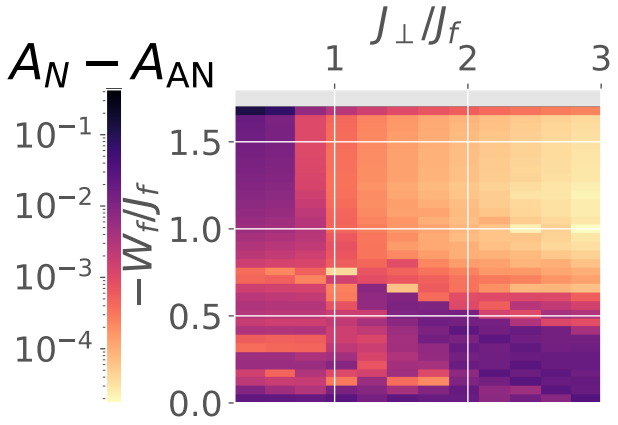

Figure 6.13: *Anisotropy in the $\omega = 0$ values between the nodal and antinodal spectral functions for the lattice model. For small $|W_f|$, we can see an increase in momentum-space differentiation as $J_\perp$ is increased. For large $|W_f|$, it is instead restricted to small $J_\perp$. At larger values of $|W_f|$, the differentiation disappears (gray patch) because both the node and the antinode gap out.*

fect the small to large Fermi surface transition observed in the Kondo breakdown QCP class of heavy fermion systems away from half-filling. Finally, more studies need to be carried out on the small $J_\perp$ region of the phase diagram at small as well as large W_f to identify the possibility of symmetry preserved spin liquid of fractionalised Fermi liquid phases.

Chapter 7

Holography of Entanglement in 2D Free Fermions: Emergent Geometry and Fermionic Criticality

In the final work chapter of this thesis, we tackle the problem of fermionic criticality from an alternative perspective – entanglement holography. In contrast to the rest of the chapters where we have been dealing with interacting many-body problems and renormalisation group flows of Hamiltonians, this chapter deals with the much more simple problem of non-interacting 2D fermions with a tunable mass gap, analysed from the renormalisation group flow of its entanglement. In doing so, we will show that this provides another method of characterising phases arising from fermionic criticality.

7.1 Introduction

The present millennium has seen a rapid surge in the use of quantum entanglement towards the study of quantum and condensed matter systems [243–248]. In this thesis, we will consider relativistic Dirac fermions in two dimensions, both massless and massive. They emerge in several condensed matter systems [294], appearing at the surfaces of three-dimensional topological insulators [295–298], quasi-2D organic materials [299–301] and in arficial materials like cold atoms, molecular and microwave crystals [302–308]. For massless critical systems (or conformal field theories (CFTs)) living in one spatial dimension, the entanglement entropy of a single subsystem of length l scales as $\sim \frac{c}{3} \ln l$ [309–318], where c is the conformal central charge of the CFT. While there is no geometry-independent topological piece in the entanglement entropy of free fermionic systems [339, 340], it *is* possible to generate such a term by placing the system on a manifold with a non-trivial topology, say a cylinder, and inserting a magnetic flux through the cylinder [339, 341–344]. There is evidence from numerical computations on discrete models that such a term is a signature of the specific field theory and encodes universality [344–346]. In this thesis, we put this idea on a stronger analytical footing by relating the flux-dependent term to a topological invariant of the field theory, its Luttinger volume [24, 25, 50, 51, 347–349].

Defined as the number of $k-$states enclosed by the Fermi surface, Luttinger volume V_L has proved to be one of the most important indicators that distinguish metals from insulating states of matter. As shown most prominently in Ref. [50], Luttinger's theorem depends crucially on the presence of extended states in the metal that can respond to flux insertion experiments. We demonstrate here that indeed it is this subdominant term in the entanglement entropy that carries this dependence and hence encodes Luttinger's theorem. Moreover, we relate the topological invariant on the metallic side (Luttinger volume) to the topological invariants (the Chern numbers) in the integer quantum hall system that the metal would lead to when placed in a perpendicular magnetic field. Such a relation makes explicit the transmutation of the extended states into the localised states of the insulating phase.

The leading geometry-dependent piece within the entanglement entropy is also found to have intriguing properties of its own. The fact that the free fermion Lagrangian is diagonal in momentum space means that the entanglement arises purely from real space quantum fluctuations, and this allows us to study the entanglement of subsystems of varying sizes in momentum space. In fact, we argue that such transformations between the subsystems amount to a renormalisation group (RG) flow in the space of the field theories with varying spectral gaps, and the above-mentioned hierarchy in the entanglement entropy then stretches across the RG transformations. More importantly, we interpret the hierarchy of entanglement along the RG flow as the emergence of an additional dimension [350–352], allowing us to define a measure of distance using some non-negative measure of entanglement, like the mutual information [353–356]: the more the entanglement, the less will be the distance between those points. Generation of an additional dimension is, of course, the essence of the AdS/CFT conjecture or, more generally, the holographic principle.

The essence of holography is that all the information about the bulk gravity theory is already contained within the boundary gauge theory; this idea is very similar to the discovery by Bekenstein and Hawking [383–385] that the entropy of a black hole is determined by its surface area. In fact, Ryu and Takayanagi proposed a generalisation of this result where the entanglement entropy of subsystem region a CFT is determined by the area of the minimal surface that bounds the region in the bulk [386, 387]. This allows physicists to use the holographic principle and convert a problem of strong quantum correlation to one of classical gravity which can be solved using well-known methods [360, 361].

Of course, on the flip side, the holographic principle also implies that studying the boundary conformal theory can provide insights into the nature of the bulk quantum gravity theory. This however requires constructing, *ab initio*, the emergent dimension by starting from the field theory, and has proved to be more difficult than the converse, mostly because the field theories are often strongly coupled. One example of this is the MERA; it works by disentangling degrees of freedom in real space, creating a tensor network in the process [434–436] and leading to a renormalisation in the entanglement. The renormalised entanglement is interpreted as the additional dimension [431].

Constructing a framework for fermionic criticality is therefore an active area of research with consequences for important systems such as unconventional superconductors, strange metals and heavy fermions [137, 175, 184, 447]. Still less is known about the holographic implications of such systems. We extend this body of work by providing an explicit demonstration of the holographic principle in the form of a simple and tractable exact holographic mapping (EHM) for a free fermion system with and without a mass gap. Our program yields analytic relations between the RG flow

parameters and their dual bulk quantities such as distances and curvature. This also allows us to study the consequences of a critical Fermi surface (lying precisely at the quantum phase transition) on the nature of the holographic space.

The chapter is structured in the following manner. Sec. 7.2 describes the system we work with and defines certain physical ideas and measures of entanglement that are employed in later sections. In Sec. 7.3, we define the scaling transformations mentioned earlier, and discuss its implications on the scaling of entanglement in the system under study. In Sections 7.4,7.5 and 7.6, we probe the holographic nature of the entanglement, unveiling an emergent spatial dimension in the process and obtain several characteristics of this emergent geometry. Section 7.7 discusses the consequences of a critical Fermi surface on the holographic space, and how the emergent curvature can be linked to a convergence parameter associated with the RG flows. In Section 7.9, we probe the topological aspects of the entanglement, and discuss its implications for the system at hand. We conclude with a discussion of our results in Sec. 7.10 and point out some open questions.

Summary of our main results

For the convenience of the reader, we present below a summary of the main results obtained by us.

1. Quantum information measures (such as entanglement entropy and multipartite information) reveal a hierarchical structure in the nature of entanglement within the system. We relate geometric parameters like distance and curvature of the holographic dimension to an RG beta function of the mass gap, providing thereby an explicit analytic manifestation of the holographic principle. We show that a change in the in the boundedness of the space corresponds to a change in certain topological winding numbers.

2. We go on to argue that this topological transition and the underlying critical Fermi surface coincides with the formation of a quantum wormhole geometry that connects the UV and the IR of the emergent dimension. The additional (conformal) symmetry at the transition links the emergent metric and the stress-energy tensor.

3. We show that the geometry-independent part of the entanglement is invariant under appropriate scaling transformations for a system of fixed number density, and is related to the Luttinger volume of the gapless fermionic system. In the presence of a strong transverse magnetic field, the topological Luttinger volume in the metallic state transforms into the Chern number C of the insulating integer quantum Hall state.

7.2 Preliminaries and definitions

7.2.1 The system

In this work, we focus on the case of Dirac fermions in two spatial dimensions described by the Lagrangian (in natural units $\hbar = c = 1$) $\mathcal{L} = \int \mathrm{d}x\, \mathrm{d}y\, \overline{\psi}(x,y,t)\left(i\gamma^\mu\partial_\mu - m\right)\psi(x,y,t)$. The system is placed on a 2−torus of dimensions $L_x \times L_y$ with periodic boundary conditions, such that $\psi(x,y,t) = \psi(x+L_x,y,t) = \psi(x,y+L_y,t)$. Entanglement measures will be calculated in the presence of a gauge field A that transforms the Lagrangian by shifting the momenta: $i\partial_\mu \longrightarrow i\partial_\mu + eA$.

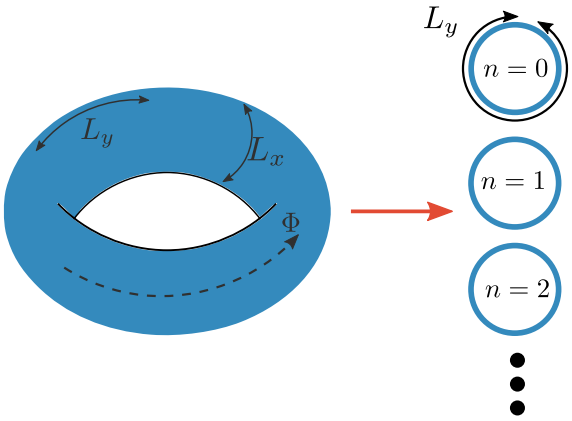

Figure 7.1: *The model on the left consists of a system of non-interacting electrons placed on a torus with a flux threading through it. The model on the right consists of a sum of* $1+1-$*dimensional systems, each consisting of massive electrons placed on a ring; the* $1+1-D$ *systems are decoupled from each other. The mass arises from the flux. These two models can be shown to be equivalent to each other [338, 339, 342, 623].*

We choose the vector potential A such that, in any particular setup, it couples to just one component of the momentum (say, the $x-$component). This results in $\phi = eAL_x/2\pi$ units of flux quantum threading the torus in the $y-$direction. One of our goals is to express the Luttinger volume V_L in terms of multi-partite measures of entanglement $\left(I^g_{\{\mathcal{A}_i\}}(\phi)\right)$ between multiple subsystems $\{\mathcal{A}_i, i = 1, 2, \ldots, g\}$ [293], in the presence of the flux ϕ. The precise definition of I^g and the method of choosing the subsystems will be given later. In order to calculate $I^g_{\{\mathcal{A}_i\}}$, however, we find it convenient to take the thin torus limit: $(L_y/L_x) \to \infty$, keeping l/L_y fixed. Importantly, this operation does not affect quantities such as V_L as long as we keep the number density unchanged.

In order to calculate entanglement measures, we will express the $2+1-$dimensional system as a sum of an infinite number of massive $1+1-$dimensional systems [338, 339, 342, 623]. In the presence of a gauge field $\vec{A} = A\hat{x}$, the complete Lagrangian (in natural units) is

$$\mathcal{L} = \int \mathrm{d}x\, \mathrm{d}y\, \overline{\psi}(x,y) \left[\gamma^\mu \left(i\partial_\mu - eA_\mu\right) - m\right] \psi(x,y)\,, \tag{2.1}$$

where $A_\mu = A\delta_{\mu,x}$ and $\phi = eAL_x/2\pi$. The integral ranges over the surface area of the torus, and the time dependence of the fields has been suppressed. Due to the periodic boundary conditions (PBCs) in the $x-$direction, the momenta k_x are quantised: $k^n_x = \frac{2\pi n}{L_x}, n \in \mathbb{Z}$. We then expand the fields $\psi(x,y)$ in these momenta:

$$\psi(x,y) = \sum_{n=-\infty}^{\infty} e^{ik^n_x x} \psi(k^n_x, y)\,. \tag{2.2}$$

In the absence of the gauge field, the Lagrangian for $2+1-$dimensional massive non-interacting relativistic electrons (in natural units) is

$$\mathcal{L} = \int \mathrm{d}x\, \mathrm{d}y\, \overline{\psi}(x,y) \left[\gamma^\mu (i\partial_\mu - eA_\mu) - m\right] \psi(x,y)\,. \tag{2.3}$$

The integral ranges over the area of the torus on which the electrons reside, and the time dependence of the fields has been suppressed. Each component $\psi^a, a = 0, 1, 2, 3$, of the Dirac spinor $\psi = \begin{pmatrix}\psi^0 & \psi^1 & \psi^2 & \psi^3\end{pmatrix}$ satisfies the Dirac equation

$$\left[\gamma^\mu(i\partial_\mu - eA_\mu) - m\right]\psi^a(x,y) = 0\,, \tag{2.4}$$

which is equivalent to the form

$$\int dx\,\overline{\psi^a}(x,y)\left[\gamma^\nu(i\partial_\nu + eA_\nu) + m\right]\left[\gamma^\mu(i\partial_\mu - eA_\mu) - m\right]\psi^a(x,y) = 0\,. \tag{2.5}$$

Due to the periodic boundary conditions (PBCs) in the $x-$direction, the momenta k_x are quantised: $k_x^n = \frac{2\pi n}{L_x}, n \in \mathbb{Z}$. We expand the fields $\psi^a(x,y)$ in these momenta:

$$\psi^a(x,y) = \sum_{n=-\infty}^{\infty} e^{ik_x^n x}\psi^a(k_x^n, y)\,. \tag{2.6}$$

Writing the Dirac equation in terms of the dual fields $\psi^a(k_x^n, y)$ gives

$$\sum_{m,n}\left(\overline{\psi^a}(k_x^m,y)e^{-ik_x^m x}\right)\left[\gamma^\nu(i\partial_\nu + eA_\nu) + m\right]\left[\gamma^\mu(i\partial_\mu - eA_\mu) - m\right]\left(e^{ik_x^n x}\psi^a(k_x^n,y)\right) = 0\,. \tag{2.7}$$

Evaluating the right operation gives

$$\left[\gamma^\mu(i\partial_\mu - eA_\mu) - m\right]\left(e^{ik_x^n x}\psi^a(k_x^n,y)\right) = e^{ik_x^n x}\left[\gamma^\mu(i\partial_\mu - eA_\mu) - \left(\gamma^x(k_x^n + eA_x) + m\right)\right]\psi^a\,. \tag{2.8}$$

Similarly, the left operation gives

$$\begin{aligned}\left(\overline{\psi^a}(k_x^m,y)e^{-ik_x^m x}\right)\left[\gamma^\nu(i\partial_\nu + eA_\nu) + m\right] &= \left[\left[\gamma^\nu(i\partial_\nu - eA_\nu) + m\right]\left(e^{ik_x^m x}\gamma_0\psi^a\right)\right]^\dagger \\ &= \overline{\psi^a}e^{-ik_x^m x}\left[\gamma_\nu(i\partial^\nu + eA_\nu) - \left(\gamma^x(k_x^n + eA_x) - m\right)\right]\,.\end{aligned} \tag{2.9}$$

Substituting these into the equation eq.(2.7) gives

$$\sum_n \int \mathrm{d}y\,\overline{\psi^a}(k_x^n,y)\left[-(i\partial_\mu + eA_\mu)(i\partial_\mu - eA_\mu) + (k_x^n + eA_x)^2 + m^2\right]\psi^a(k_x^n,y) = 0\,, \tag{2.10}$$

where we have used $\int \mathrm{d}x\, e^{ix\left(k_x^m - k_x^n\right)} = \delta_{m,n}$. In terms of these dual fields, the Lagrangian can be shown to be equivalent to a tower of massive $1+1-$dimensional fermions (see Fig. 7.1):

$$\mathcal{L} = \sum_{k_x^n}\int \mathrm{d}y\,\overline{\psi}(k_x^n,y)\left(\gamma^\mu(i\partial_\mu - eA_\mu) - M(n,\phi)\right)\psi(k_x^n,y)\,, \tag{2.11}$$

with an effective mass $M_{n,\phi}$ given by

$$M_{n,\phi} = \sqrt{m^2 + (k_x^n + eA)^2} = \sqrt{m^2 + \frac{4\pi^2}{L_x^2}(n+\phi)^2}\,. \tag{2.12}$$

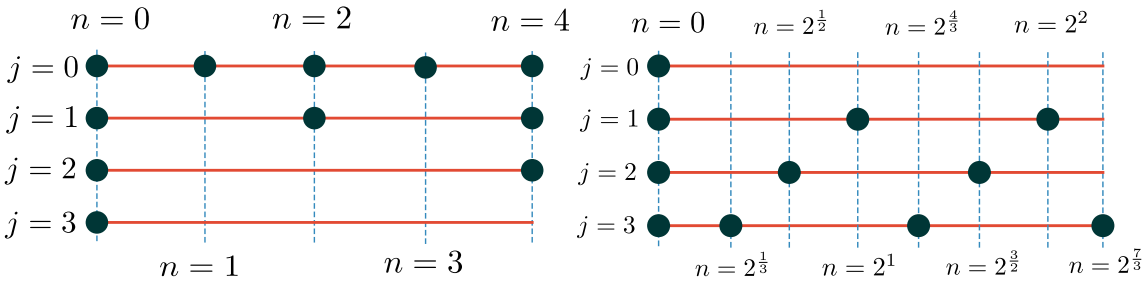

Figure 7.2: *Visual depiction of the subsets $\mathcal{A}_z(j)$ employed by us in this work, for $z = 1$ and $z = -1$. As j is changed by 1, the spacing between the modes in the subset increases by a factor of 2^{jz}. Top: $z = 1$. The initial subset $\mathcal{A}_z(0)$ has $k-$states at the modes $n = 0, 1, 2, 3, 4$. Upon changing j by 1, the new subset obtained has double the spacing between the modes ($2^{jz} = 1/2^j$) of the previous number of modes. That is, if $j = 0$ has $0, 1, 2, 3, 4$, then $j = 1$ has $0, 2, 4$, $j = 2$ has $0, 4$ and $j = 3$ has 0. Bottom: $z = -1$. In this case, the number of modes get double at each state ($2^{-iz} = 2^i$). We start with $k-$modes present only at $n = 0$, but the scaling transformations lead to $j = 1$ having the modes $0, 4$, $j = 2$ having $0, 2, 4$, and so on.*

This decoupling ensures that the various modes $n \in \mathbb{Z}$ are disentangled from one another, such that the total density matrix ρ_{2D} of the $2 + 1-$dimensional system can be written as a product of the density matrices ρ^n_{1D} for each of the modes:

$$\rho_{2D} = \prod_{n=-\infty}^{\infty} \rho^n_{1D} \,. \tag{2.13}$$

We will focus primarily on the case of massless $2 + 1-$dimensional electrons by setting $m = 0$, such that the effective mass is given by $M_{n,\phi} = \frac{2\pi}{L_x}|n + \phi|$. Certain results will, however, be generalised to the case of massive fermions ($m \neq 0$). While the massless case corresponds to the gapless excitations of a Fermi liquid or those at the surface of a topological insulator, the massive case corresponds to gapped or insulating states of matter, e.g., the Bogoliubov-de Gennes quasiparticles above an $s-$wave superconducting gap. Massive Dirac fermions have also been observed experimentally in several materials like ultrathin films [624], topological insulating crystals [625] and van der Waals heterostructures [626]. They are also emergent at low-energies, for instance, in fermionic nonlinear $\sigma-$models [627], and can also be realised near the IR fixed point of the kagome Heisenberg quantum antiferromagnets placed in an external magnetic field along the $z-$direction [504].

7.2.2 Entanglement measures

We will work with two measures of entanglement discussed below. Given the density matrix $\rho = |\Psi\rangle\langle\Psi|$ for the ground state $|\Psi\rangle$ of the complete system, the entanglement entropy (EE) of a set of subsystems $\{\mathcal{A}_i, i = 1, 2, \ldots, g\}$ with the rest of the system is given by:

$$S_{\{\mathcal{A}_i\}} = -\mathrm{Tr}\left[\rho_{\{\mathcal{A}_i\}} \ln \rho_{\{\mathcal{A}_i\}}\right]; \qquad \rho_{\{\mathcal{A}_i\}} = \mathrm{Tr}_{\{\mathcal{A}_i\}}\left[\rho\right] \,. \tag{2.14}$$

$\mathrm{Tr}\,[\cdot]$ is the trace operation over all degrees of freedom, while $\mathrm{Tr}_{\{\mathcal{A}_i\}}\,[\cdot]$ is the partial trace over only the states corresponding to the set of subsystems $\{\mathcal{A}_i\}$. $\rho_{\{\mathcal{A}_i\}}$ is referred to as the reduced density

matrix for the rest of the system (complement of the set $\{\mathcal{A}_i\}$). Using EE, one can define the mutual information $I(\{\mathcal{A}_i\} : \{\mathcal{B}_i\})$ between two subsystems A and B:

$$I_2\left(\{\mathcal{A}_i\} : \{\mathcal{B}_i\}\right) = S(\{\mathcal{A}_i\}) + S(\{\mathcal{B}_i\}) - S(\{\mathcal{A}_i\} \cup \{\mathcal{B}_i\}) \,, \tag{2.15}$$

where $S(\{\mathcal{A}_i\} \cup \{\mathcal{B}_i\})$ is the EE of $\{\mathcal{A}_i\} \cup \{\mathcal{B}_i\}$ with the rest. Higher order measures of information among N subsystems can also be defined similarly (see, e.g., [293]). Such multi-partite measures of quantum information convey the degree of correlations present within the system - the presence of $N-$particle correlations ensures all information measures up to the $N-$partite information will be non-zero.

One final object of interest in this context is the entanglement Hamiltonian $\mathcal{H}(\{\mathcal{A}_i\})$ for a subsystem $\{\mathcal{A}_i\}$, defined through the relation [259, 264]

$$\rho_{\{\mathcal{A}_i\}} = \frac{e^{-\mathcal{H}(\{\mathcal{A}_i\})}}{\mathrm{Tr}\left(e^{-\mathcal{H}(\{\mathcal{A}_i\})}\right)} \,. \tag{2.16}$$

The entanglement Hamiltonian is essentially the spectrum of the reduced density matrix, and contains additional information on the nature of correlations beyond the entanglement entropy. For the system we are considering (described in the previous subsection), the total reduced density matrix can be decomposed into decoupled 1D modes (eq. (2.13)). This implies that the total entanglement Hamiltonian is simply a sum of the individual Hamiltonians for the 1D modes:

$$\rho_{2\mathrm{D}} = \prod_{n=-\infty}^{\infty} \rho_{1\mathrm{D}}^{n} \sim \prod_{n=-\infty}^{\infty} e^{-\mathcal{H}_{1\mathrm{D}}^{n}(\{\mathcal{A}_i\})} = e^{-\mathcal{H}_{2\mathrm{D}}(\{\mathcal{A}_i\})} \,, \tag{2.17}$$

where $\mathcal{H}_{2\mathrm{D}} = \sum_n \mathcal{H}_{1\mathrm{D}}^{n}$.

7.2.3 Luttinger volume

The Luttinger volume V_L is defined as the number of $\vec{k}-$space points inside the Fermi surface [24,25] :

$$V_L = \int_{G_{\vec{k}}(\omega=0)>0} \frac{1}{(2\pi)^d} d\vec{k} = \int_0^{k_F} \frac{1}{(2\pi)^d} d\vec{k} \,. \tag{2.18}$$

The integral (referred to as Luttinger's integral) runs over all $\vec{k}-$space points where the $\omega = 0$ Greens function is positive, and the Fermi momentum k_F is defined as the set of points in $\vec{k}-$space where $G_{\vec{k}}(\omega = 0)$ changes sign. Luttinger's integral can be shown to be topological in nature [50, 51], promoting Luttinger's volume to the status of a topological invariant that characterises the system. For systems with long-lived excitations close to the Fermi surface, V_L is equal to the average number density of electrons in the system, leading to Luttinger's theorem [24, 25, 347]. For systems with gapped excitations in the momentum window $k \leq k^*$ above the ground state, the violation ΔV_L of Luttinger's theorem can be quantified through a count of the bound states [348]:

$$\Delta V_L = \int_0^{k_F} \frac{1}{(2\pi)^d} d\vec{k} - \int_{k^*}^{k_F} \frac{1}{(2\pi)^d} d\vec{k} = \int_0^{k^*} \frac{1}{(2\pi)^d} d\vec{k} \tag{2.19}$$

7.3 Entanglement hierarchy in mixed momentum and real space

Before beginning our calculations of entanglement measures, we define the subsystem(s) whose entanglement we want to obtain. The subsystems we will use in this work are of the following kind:

$$\mathcal{A}_z(i) = \widetilde{A}_z(i) \times A_z(i) \ , \tag{3.1}$$

where i takes integral values starting from zero, z can take all integral values apart from 0 and $\times$ represents the Cartesian product between the set of real space points $\widetilde{A}_z(i) = \{0 \leq y \leq l\}$ and the set of momentum space points

$$\begin{aligned} A_z(i) &= \left\{k_x^n\right\};\ k_x^n = \frac{2\pi}{L_x} n;\ \max(\{k_x^n\}) = \frac{2\pi N}{L_x}\ ; \\ n &\in \{-N, -N + t_z(i), \ldots, -t_z(i), 0, t_z(i), N\}\ ;\ t_z(i) = 2^{i^z}\ , \end{aligned} \tag{3.2}$$

and where $t_z(i) = 2^{i^z}$ is the difference between consecutive values of n. The subset $\mathcal{A}_z(i)$ is therefore a region in mixed momentum and real spaces, spanned by the variables k_x and y respectively. In $y-$space, the region is of length l and bounded by the points $y = 0$ and $y = l$. In k_x-space, $\mathcal{A}_z(i)$ comprises the points $\left\{0, \pm 2^{i^z}\frac{2\pi}{L_x}, \pm 2^{i^z}\frac{4\pi}{L_x}, \ldots\right\}$ such that $|k_x| \leq \frac{2\pi N}{L_x}$. For example, for the case of $z = 1$ and N being a multiple of 4, we have

$$\begin{aligned} A_1(0) &= \left[-\frac{2\pi}{L_x}N, -\frac{2\pi}{L_x}(N-1), \ldots, -\frac{2\pi}{L_x}2, -\frac{2\pi}{L_x}1, 0, \frac{2\pi}{L_x}1, \frac{2\pi}{L_x}2, \ldots, \frac{2\pi}{L_x}(N-1), \frac{2\pi}{L_x}N\right]\ , \\ A_1(1) &= \left[-\frac{2\pi}{L_x}N, -\frac{2\pi}{L_x}(N-2), \ldots, -\frac{2\pi}{L_x}4, -\frac{2\pi}{L_x}2, 0, \frac{2\pi}{L_x}2, \frac{2\pi}{L_x}4, \ldots, \frac{2\pi}{L_x}(N-2), \frac{2\pi}{L_x}N\right]\ , \\ A_1(2) &= \left[-\frac{2\pi}{L_x}N, -\frac{2\pi}{L_x}(N-4), \ldots, -\frac{2\pi}{L_x}8, -\frac{2\pi}{L_x}4, 0, \frac{2\pi}{L_x}4, \frac{2\pi}{L_x}8, \ldots, \frac{2\pi}{L_x}(N-4), \frac{2\pi}{L_x}N\right]\ . \end{aligned} \tag{3.3}$$

Note that N represents the edge of the Brillouin zone, and will be sent to infinity when we calculate quantities in the continuum limit. In Fig. 7.2, we have shown two such families of subsets $\mathcal{A}_z(0), \mathcal{A}_z(1), \mathcal{A}_z(2), \mathcal{A}_z(3), \ldots$, for $z = 1$ and $z = -1$.

We note here that the transformations for $z < 0$ correspond to increasing the density (fine-graining) of k_x-states by adding more momentum states while keeping the bounds fixed. This involves reducing the interval in k_x-space, and hence equivalent to increasing the system size L_x. This is similar to methods such as numerical renormalisation group treatment of the Kondo problem [446] where an increasing number of states are added to the system at increasingly larger distances from the impurity site, such that the system asymptotically goes to the thermodynamic limit. The other case of $z > 0$ is, on the contrary, a decimation process in k_x-space, and equivalent to reducing the system size. Indeed, it will be shown later that the sequence of Hamiltonians generated in the process (for both positive and negative z) are related to one other by renormalisation group transformations.

Within a given set $\mathcal{A}_z(i)$, the distance between adjacent $k-$space points is $\frac{2\pi}{L_x}t_z(i)$ where $t_z(i) = 2^{i^z}$. Choosing $i = 0$ keeps the set of k_x-space points unchanged, such that we recover the entire

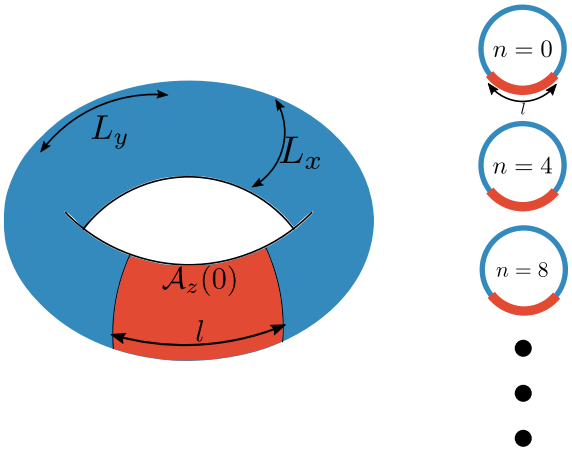

Figure 7.3: *Top: Depiction of the subset $\mathcal{A}_z(i)$ for the choice $i = 0$. Setting $i = 0$ leads to unchanged length L_x along x and the constraint $0 \leq y \leq l$ in the $y-$direction. This creates an annulus (red region) of height l and circumference L_x.*
Bottom: Typical $k-$modes present in the subset $\mathcal{A}_z(i)$ for $z = 1$ and $i = 2$. This is because, if $i = 0$ has the modes $n = 0, 1, 2, 3, 4, \ldots,$ increasing i by 2 increases the spacing between the modes to $2^{2^z} = 4$, so that the mode just after $n = 0$ is $n = 4$, and the one following that is $n = 8$, and so on.

Lagrangian of eq. (2.1) in the $x-$direction for system size L_x, while the $y-$direction is constrained to length l. This means that $\mathcal{A}_z(0)$ is just an annulus that wraps around the $x-$direction of the torus and extends to a length l longitudinally in the $y-$direction (shown in Fig. 7.3). Along with the period $t_z(i)$, one can also define the fraction of maximum points present in the set $\mathcal{A}_z(i)$ as

$$f_z(i) = 1/t_z(i) = 2^{-i^z} \ . \tag{3.4}$$

For example, for $z > 0$, $f_z(i) = 2^{-i^z}$ expresses the fact that in going from the set at $j = 0$ to the set at $j = i$, the number of elements in the set is scaled down by a factor of 2^{i^z} (see Fig. 7.4).

We now define the shorthand notation $S_z(i)(\phi) \equiv S_{\mathcal{A}_z(i)}(\phi)$ to denote the EE of the subsystem $\mathcal{A}_z(i)$ in the presence of the Aharonov-Bohm flux ϕ. In order to calculate $S_z(i)$, we start with $i = 0$. As mentioned earlier, this is essentially the EE between an annulus of length l and the rest of the $2-$torus. Since the density matrices are in product, the total EE is just a sum of the EE arising from each mode:

$$S_{\mathcal{A}_z(0)}(\phi) \equiv S_z(0)(\phi) = \lim_{N\to\infty} \sum_{n=-N}^{N} S^n_{\widetilde{A}_z(0)} \ , \tag{3.5}$$

where $\widetilde{A}_z(0)$ acts as a projection of the annulus on the $k_x - y$ plane, and S^n indicates that the EE is calculated for the nth mode. Each massive fermionic mode has a correlation length-scale $\xi_n = 1/M_{n,\phi}$. We choose l to be much larger than the largest correlation length: $l \gg \max(\{\xi_n, \forall\, n\})$. Using the expression for ϕ and the quantisation of the momenta k^n_x, this condition can be expressed as

$$l \gg \frac{L_x}{2\pi} \times \max\left(\left\{\frac{1}{|n+\phi|}\right\}\right) = \frac{L_x}{2\pi\,\{\phi\}} \ , \tag{3.6}$$

where $\{\phi\} = \phi - \lfloor\phi\rfloor$ is the fractional part of the flux ϕ in units of the flux quantum. Since we are in the thin torus limit, L_x must remain finite, and the maximum correlation can diverge only if $\{\phi\} = 0$. We ensure that l is larger than the correlation lengths by choosing ϕ to be necessarily non-integral, as this guarantees that the correlation lengths remain finite. Then, the EE of the annulus is given by [339, 342]

$$S_z(0)(\phi) = c\left[\alpha\frac{L_x}{\epsilon} - \ln\left|2\sin(\pi\phi)\right|\right], \tag{3.7}$$

where c is the conformal central charge and ϵ is a UV cutoff; c is $1/3$ for a Dirac fermion. The computation of $S_z(0)(\phi)$ uses the EE $S^n_{\widetilde{A}_z(0)}$ of a 1−D chain of fermions with a mass $M_{n,\phi}$ [316,324]: $S^n_{\widetilde{A}_z(0)} = c\ln\frac{L_x}{2\pi\epsilon} - c\ln|n+\phi|$. On summing over n and regularising the UV cutoff, the first term of eq.(3.7) produces the leading area-law term of $S_0(\phi)$ [339]:

$$\sum_{n=-\infty}^{\infty} c\ln\frac{L_x}{2\pi\epsilon} \to c\alpha\frac{L_x}{\epsilon}, \tag{3.8}$$

where α is a cutoff-dependent non-universal constant.The flux-dependent term in $S^n_{\widetilde{A}_z(0)}$ leads to the sub-leading term of $S_z(0)(\phi)$, and requires a regularisation using the Hurwitz zeta function [339]:

$$\sum_{n=-\infty}^{\infty}\ln|n+\phi| = \sum_{n=-\infty}^{\infty}\left[\ln|n+\phi| + \ln|n+(1-\phi)|\right] = -\frac{\partial\zeta(\phi)}{\partial\phi} - \frac{\partial\zeta(1-\phi)}{\partial\phi}, \tag{3.9}$$

where $\zeta(\phi) = \sum_{n=-\infty}^{\infty}(n+\phi)^{-1}$ is the Hurwitz zeta function. The derivative converges to $\frac{\partial\zeta(\phi)}{\partial\phi} = \ln\Gamma(\phi) - \frac{1}{2}\ln 2\pi$, as long as the zero mode $n+\phi = 0$ is excluded from the summation. The latter condition is guaranteed as we have chosen ϕ to be a non-integer. Γ is the Gamma function, satisfying $\Gamma(\phi)\Gamma(1-\phi) = \pi/\sin(\pi\phi)$. Substituting the derivative gives [339, 342, 346]

$$\sum_{n=-\infty}^{\infty}\ln|n+\phi| = \ln 2\pi - \ln\left[\Gamma(\phi)\Gamma(1-\phi)\right] = \ln\left|2\sin(\pi\phi)\right|. \tag{3.10}$$

For a general $\mathcal{A}_z(i)$, there are certain modifications to the expression in eq. (3.7). For the first term in eq.(3.7), we have

$$\lim_{N\to\infty}\sum_{\substack{n=-N,\\ -N+t_z(i),\ldots}}^{N} c\ln\frac{L_x}{2\pi\epsilon} = \lim_{N\to\infty}\sum_{\substack{n'=-\frac{N}{t_z(i)},\\ -\frac{N}{t_z(i)}+1,\ldots}}^{\frac{N}{t_z(i)}} c\ln\frac{L_x}{2\pi\epsilon} = t_z^{-1}(i)\lim_{N\to\infty}\sum_{n=-N}^{N} c\ln\frac{L_x}{2\pi\epsilon} \to c f_z(i)\frac{\alpha L_x}{\epsilon}. \tag{3.11}$$

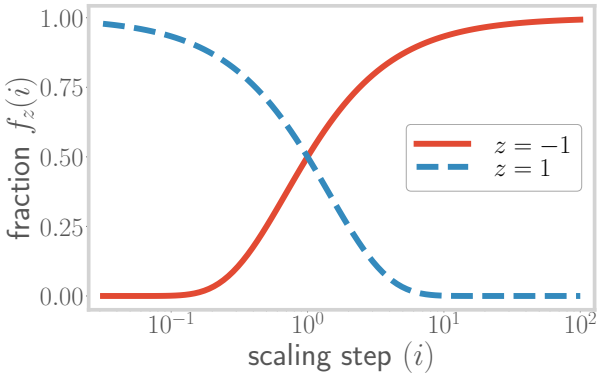

Figure 7.4: *A plot of the fraction of states remaining upon performing i number of transformations on the starting Hamiltonian. Obtained by plotting the expression $f = 2^{-i^z}$, for a range of i, and for two values of z (red and blue). This fraction decreases for $z > 0$ (blue curve), and increases for $z < 0$ (red curve).*

Similarly, for the second term, we have

$$\lim_{N\to\infty} \sum_{\substack{n=-N,\\ -N+t_z(i),\ldots}}^{N} \ln|n+\phi| = \lim_{N\to\infty} \sum_{\substack{n'=-\frac{N}{t_z(i)},\\ -\frac{N}{t_z(i)}+1,\ldots}}^{\frac{N}{t_z(i)}} \ln|n' t_z(i)+\phi| = \lim_{N\to\infty} \sum_{\substack{n'=-\frac{N}{t_z(i)},\\ -\frac{N}{t_z(i)}+1,\ldots}}^{\frac{N}{t_z(i)}} \ln\left(f_z(i)|n'+f_z(i)\phi|\right)$$
$$= \sum_{n'=-\infty}^{\infty} \ln|n'+f_z(i)\phi|\,, \tag{3.12}$$

where we have assumed that $t_z(i)$ is finite, and dropped the constant part $\ln f_z(i)$ (which can be absorbed into the UV cutoff ϵ in eq. (3.11)). Following eq. (3.10), this gives

$$\lim_{N\to\infty} \sum_{\substack{n=-N,\\ -N+t_z(i),\ldots}}^{N} \ln|n+\phi| = \ln\left|2\sin\left(\pi f_z(i)\phi\right)\right|\,. \tag{3.13}$$

Combining both parts, we obtain the expression for the EE that will be employed in what lies ahead:

$$S_z(i)(\phi) = c f_z(i)\frac{\alpha L_x}{\epsilon} - c\ln\left|2\sin\left(\pi f_z(i)\phi\right)\right|\,. \tag{3.14}$$

It is evident from the expression in eq. (3.14) that, as modes are added into the subsystem, the L_x-dependent geometric part of the EE increases, leading to a *hierarchical structure* in the entanglement. A similar result was previously shown to hold for geometric measures of entanglement of quantum-mechanical systems with eigenstates such as the W and GHZ states and their symmetric superpositions [628]. The variation of the geometric part with the subsystem index j is shown in Fig. 7.4.

The above-mentioned hierarchy in entanglement measures leads to an interesting property for the entanglement: the combined entanglement entropy of any number of systems $\{\mathcal{A}_z(i)\}$ is equal to

the entanglement entropy of the most dense system among them. For $z > 0$, the sets become smaller as the RG index increases, while for $z < 0$, the sets become larger as the RG index increases. Thus, we may write

$$S_{\{\mathcal{A}_z(i)\}} = \theta(z) S_{\min\{i\},z} + \theta(-z) S_{\max\{i\},z}, \ . \tag{3.15}$$

The mutual information $I^2(i,j)$ between the systems at two RG steps i and j can then be computed:

$$I^2(i,j) \equiv S_z(i) + S_{j,z} - S_{i\cup j,z} = \theta(-z) S_{\min(i,j),z} + \theta(z) S_{\max(i,j),z} \ . \tag{3.16}$$

In light of this subsystem-based hierarchical structure, we can also consider the $g-$partite information $I^g_{\{\mathcal{A}_z(i)\}}$ among g sets $\{\mathcal{A}_z(i)\}$. I^g is defined as [293]

$$I^g_{\{\mathcal{A}_z(i)\}} = \sum_{r=1}^{g} (-1)^{r+1} \sum_{\substack{\beta \in \mathcal{P}(\{\mathcal{A}_z(i)\}) \\ |\beta| = r}} S_\beta \ , \tag{3.17}$$

where $\mathcal{P}(\{\mathcal{A}_z(i)\})$ is the power set of $\{\mathcal{A}_z(i)\}$, and $|\beta| = r$ indicates that the sum is carried out only over those sets β that have r number of elements in them. For example, for $g = 3$, we have

$$I^3 = S_{\mathcal{A}_z(0)} + S_{\mathcal{A}_z(1)} + S_{\mathcal{A}_z(2)} - S_{\mathcal{A}_z(0)\cup\mathcal{A}_z(1)} - S_{\mathcal{A}_z(1)\cup\mathcal{A}_z(2)} - S_{\mathcal{A}_z(2)\cup\mathcal{A}_z(0)} + S_{\mathcal{A}_z(0)\cup\mathcal{A}_z(1)\cup\mathcal{A}_z(2)} \ . \tag{3.18}$$

For our choice of subsystems, the $g-$partite information can be shown to be equal to the EE of the *intersection set* of the concerned $g-$sets (details in Appendix A). For the case of $z > 0$, this takes the form

$$I^g_{\{\mathcal{A}_z(i)\}}(\phi) = S_g(\phi) = c f_{g,z} \alpha \frac{L_x}{\epsilon} - c \ln \left| 2 \sin\left(\pi f_{g,z} \phi\right) \right| \ . \tag{3.19}$$

Since the $g-$partite information is simply the EE of the gth subsystem, the hierarchy in the EE can thus be seen to lead to multiple levels of correlation in the system, corresponding to an increasing number of parties entering the set.

Finally, we note that the geometric (L_x-dependent) part of the EE in eq. (3.14), as well as any of the information measures I^g (eq. (3.19)), has the same form even if we start with a non-zero mass $m > 0$ [339]. This ensures that the above observations regarding the hierarchical structure of the entanglement hold even for gapped electronic systems.

7.4 EHM, the Ryu-Takayanagi bound and holographic inequalities

As we will now show, the approach laid out above to the creation of subsystems amounts essentially to performing a sequence of renormalisation group (RG) transformations on the momentum modes of the Hamiltonian in the $x-$ direction. We consider here the general case of massive Dirac electrons $M_{n,\phi} = \sqrt{m^2 + \frac{\pi^2}{L_x^2}(n+\phi)^2}$. Further, we define the superset $\mathcal{A}_z^{(0)}$ of k_x-states: $\mathcal{A}_z^{(0)} = \bigcup_{i=0}^{\infty} \mathcal{A}_z(i)$, such that all k_x-states that can appear at any point of the sequence $\{\mathcal{A}_z(i); i = 0, 1, 2, \ldots\}$ are

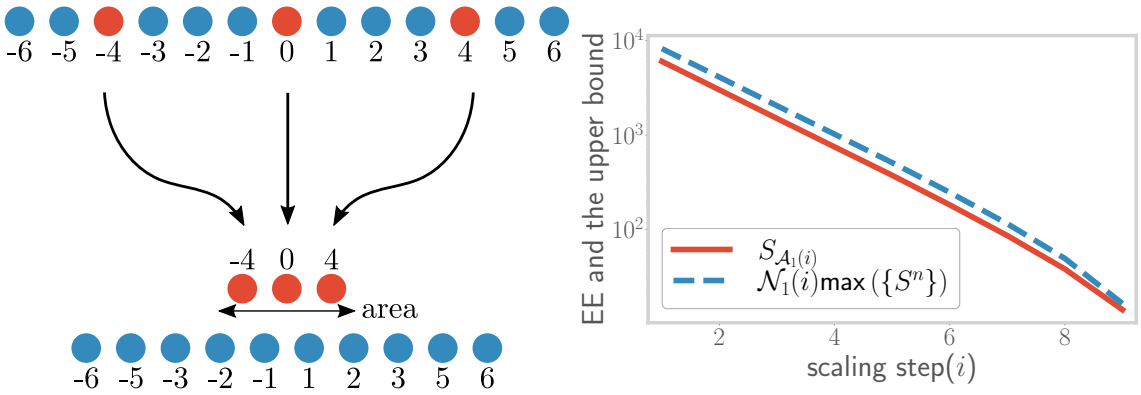

Figure 7.5: *Top: Modes forming the subsystem $\mathcal{A}_z(i)$ (red circles) form the boundary between $\mathcal{A}_z(i)$ and its complement (blue circles). Bottom: Scaling of the subsystem entanglement entropy (red), and its upper bound (blue), as the RG transformations are performed (denoted by increasing index i). The bound is saturated at large i.*

present within it. This superset can now be used to define a parent Hamiltonian $H(0)$ that consists of all the modes in the $x-$direction:

$$H(0) = \sum_{k_x \in \mathcal{A}_z^{(0)}} H(k_x) \,, \tag{4.1}$$

where $H(k_x)$ is the Hamiltonian for a massive Dirac fermion that extends over a length L_y in the single spatial dimension, and having mass $M_{n,\phi}$. The Hamiltonian at any given step of the RG is then obtained by projecting onto appropriate sets of momenta. The set of momentum at step j is given by $\mathcal{A}_{j,z} = \frac{2\pi}{L_x} \times \{0, \pm t_z(j), \pm, 2t_z(j), \ldots\}$ with $t_z(j) = 2^{jz}$. The projector onto this set is given by

$$P_{j,z} = \sum_{k_x^1=0,1} \sum_{k_x^2=0,1} \ldots \sum_{k_x^N=0,1} |\hat{n}_{k_x^1} \hat{n}_{k_x^2} \ldots\rangle \langle \hat{n}_{k_x^1} \hat{n}_{k_x^2} \ldots| \,, \quad k_x^j \in \mathcal{A}_{j,z} \,, \tag{4.2}$$

and the Hamiltonian at the corresponding step is then obtained as

$$H_z(i) = P_z(i) H(0) P_z(i) \,. \tag{4.3}$$

In this formulation of the RG, the index i represents the RG step, while the parameter z indicates the *strength of the scaling* mechanism: for $z > 0$, a higher value of z means that the states of the Hamiltonian become rarer as the index i increases, while for $z < 0$, the states become denser with increasing i. Importantly, we will see subsequently that the parameter z corresponds also to the anomalous dimension of the coupling that leads to a spectral gap in the electronic dispersion, dictating its growth or decay under RG evolution (eq.(5.6)).

Since this is a free theory, the $k-$modes are decoupled, and the projection operation preserves the spectrum of the remaining degrees of freedom. The renormalised Hamiltonian (eq. (4.3)) can then be said to constitute an exact holographic mapping (EHM) [355, 356] in the direction of the RG transformations. It is also pertinent to note that the sequence of transformations in eq. (4.3)

can be thought of as a simple and specific example of a unitary renormalisation group (URG) procedure [348, 349] that first disentangles and then projects out a certain set of degrees of freedom. Because the operation is unitary, the URG preserves the spectrum in the process. In the present case, the disentanglement operation is unity. The URG has already been shown to lead to a holographic renormalisation of the Hilbert space geometry which can be seen through the evolution of the Fubini-Study metric under the URG transformations [348]. Our approach differs from MERA implementations like those in refs. [629, 630] in the fact that while those are involve a real space renormalisation scheme, we perform our scaling transformations in momentum space.

More evidence for the holographic nature of the construction comes from the fact that the entanglement entropy for both the massless and massive cases satisfy the bound provided by the Ryu-Takayanagi proposal that relates the entanglement of a conformal field theory (CFT) with the geometry of its gravity dual [386, 387]:

$$S_{\mathcal{A}_z(i)} \leq \mathcal{N}_z(i)\max\left(\{S^n\}\right) \ . \tag{4.4}$$

In the above constraint, $\max\left(\{S^n\}\right)$ is the maximum single entropy of all the modes n residing in $\mathcal{A}_z(i)$, and $\mathcal{N}$ is the area of the minimal surface that separates the subsystem $\mathcal{A}_z(i)$ from the rest. In order to see how this is satisfied in the presence case, we note that since the subsystem $\mathcal{A}_z(i)$ is interspersed among the rest of the system (see left panel of Fig. 7.5), the minimal surface is as large as the subsystem itself. The area of this surface is therefore given by the number of modes in $\mathcal{A}_z(i)$. Using this information, the right hand side of eq. (4.4) can be written as

$$\mathcal{N}_z(i)\max\left(\{S^n\}\right) = \max\left(\{S^n\}\right) N f_z(i) = \max\left(\{S^n\}\right) \sum_{n\in\mathcal{A}_z(i)} \ . \tag{4.5}$$

Following eq. (2.13), the left hand side of eq. (4.4) can, on the other hand, be written as

$$S_{\mathcal{A}_z(i)} = \sum_{n'\in\mathcal{A}_z(i)} S^{n'} \leq \sum_{n'\in\mathcal{A}_z(i)} \max\left(\{S^n\}\right) \ . \tag{4.6}$$

Comparing eqs. (4.5) and (4.6), we recover the Ryu-Takayanagi condition of eq. (4.4). The scaling of both the left and right hand sides of eq. (4.4) has been shown in the right panel of Fig. 7.5.

Entanglement measures like entanglement entropy and mutual information (associated with disjoin intervals) have been shown to satisfy a number of inequalities in quantum field theories with gravity duals. We now consider some of them here, and show that the theory considered by us here also satisfies these inequalities. One such constraint is the monogamy of mutual information, which says that for three disjoint regions A_1, A_2 and A_3, we must have $I_2(A_1 : A_2) + I_2(A_1 : A_3) \leq I_2(A_1 : A_2 \cup A_3)$, where $I_2(A_1 : A_2) = S(A_1) + S(A_2) - S(A_1 \cup A_2)$ [631]. For this, we consider three disjoint regions, all of the kind depicted in the left panel of fig. 7.3, but at different positions $y_i \in [l_i, l_i + L]\,, i = 1, 2, 3$. We assume that the distance $l_i - l_{i+1}$ between adjacent regions is much larger than the correlation length. Calabrese and Cardy have shown that the total entanglement entropy of the union of such disjoint regions is obtained by multiplying the entanglement entropy of any one region with the number of disjoin intervals. Putting all this together, we get

$$\begin{aligned} S(A_1) = S(A_2) = S(A_3), \\ S(A_1 \cup A_2) = S(A_1 \cup A_3) = 2S(A_1), \\ S(A_1 \cup A_2 \cup A_3) = 3S(A_1)\ , \end{aligned} \tag{4.7}$$

leading to the above inequality being satisfied:

$$I_2(A_1 : A_2) + I_2(A_1 : A_3) - I_2(A_1 : A_2 \cup A_3) = 0 \,. \tag{4.8}$$

We next consider a cyclic family of inequalities in terms of conditional entropies, introduced and proved in Ref. [632]: $\sum_{i=1}^{2k+1} S(A_i|A_{i+1}\dots A_{i+k}) \geq S(A_1 \dots A_{2k+1})$, where $S(A_i|A_j) = S(A_i \cup A_j) - S(A_j)$. Using the results of eq. (4.7), we get $\sum_{i=1}^{2k+1} S(A_i|A_{i+1}\dots A_{i+k}) = \sum_{i=1}^{2k+1} S(A_i) = (2k+1)S(A_1)$ and $S(A_1 \dots A_{2k+1}) = (2k+1)S(A_i)$, leading to $\sum_{i=1}^{2k+1} S(A_i|A_{i+1}\dots A_{i+k}) = S(A_1 \dots A_{2k+1})$, which also satisfies the inequality. In both cases, we find that the inequality is satisfied by saturating the bound; this is a consequence of the fact that the intervals are separated by distances larger than the correlation length and the total entanglement entropies are simply a sum of the individual entropies.

7.5 Holographic geometry of the RG flow

7.5.1 RG evolution as the emergent dimension

To obtain a more specific description of the RG flow as the emergence of a geometric space, we introduce a measure of distance. For this, we will employ another bipartite measure of entanglement - the mutual information I^2, as defined in eq. (2.15), due to its non-negative nature. We focus on the massless case $m = 0$ for the time-being. Inspired by Refs. [353, 356, 447, 633], we adopt the following definition for distance:

$$d_z(i,j) \equiv \ln \frac{I^2_{\max}}{I^2_z(i:j)} \,, \tag{5.1}$$

where $I^2_z(i:j) \equiv I^2\left(\mathcal{A}_z(i), \mathcal{A}_{j,z}\right)$ is the mutual information between the two mentioned sets, and $I^2_{\max}$ is the mutual information between two maximally entangled systems. Accordingly, $d_z(j)$ is zero (i.e., the mutual information is maximum) at $j = 0$ if $z > 0$ and $j = \infty$ if $z < 0$, and this distance increases (decreases) with the decrease (increase) in the mutual information as the scaling transformations are performed.

We compute the distance between the points i and j to obtain the scaling of the distance $d_z(j)$. We assume $i < j$ without loss of generality. At each step, we tune the flux ϕ so as to remove the flux-dependent part from the EE. Following eq. (3.16), the mutual information is of the form $\theta(-z)S_i + \theta(z)S_j$, such that the distance is given by

$$d_z(i,j) = \theta(-z) \ln \frac{S_{\max}}{S_z(i)} + \theta(z) \ln \frac{S_{\max}}{S_{j,z}} = \theta(z) j^z \ln 2 + \theta(-z) i^z \ln 2 \,. \tag{5.2}$$

For $z > 0$, the distance increases as j increases (keeping i fixed), as the $k-$space points are made more coarse-grained under the RG transformations. On the other hand, for $z < 0$, the distance decreases as i is increased (keeping j fixed). The rate of increase or decrease depends on the value of z. This scaling of the distance is shown in the left panel of Fig. 7.6.

At any given RG step j, we define two subsystems $\mathcal{B}^1_j$ and $\mathcal{B}^2_j$. The first subsystem $\mathcal{B}^1_j$ is the entire set of states $\mathcal{A}_{j,z}$ available at the jth RG step, while the second subsystem $\mathcal{B}^2_j$ is the set comprising

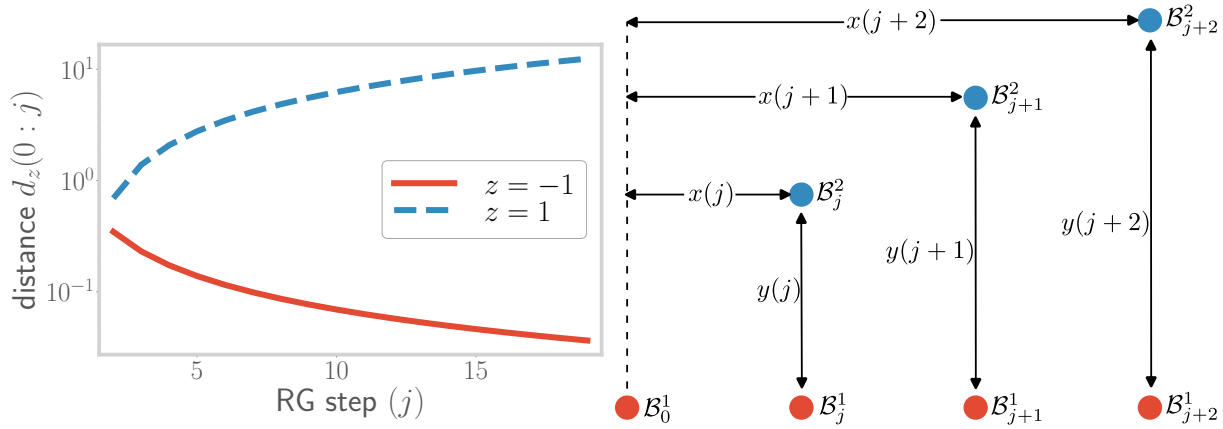

Figure 7.6: *Top: Variation of the information distance $d_z(0:j)$ (defined along the RG direction) under the scaling transformations. Obtained by plotting the expression for the distance, as a function of the number of transformations j, for two values of z. For $z=1$ (blue curve), the distance between two extreme points increases, showing a decrease in entanglement. For $z=-1$ (red curve), the distance decreases, showing an increase in entanglement. Bottom: Geometry of subsystems used for calculating the emergent curvature. The red blobs represent the subsystems generated along the emergent direction, through the scaling transformations: $\mathcal{A}_{\in j} \to \mathcal{B}_{j+1}$. The blue blobs represent subsystems generated within the $1+1-$dimensional field theory, transverse to the emergent direction.*

those modes that remain to be considered at the next RG step if $z>0$, and the set comprising only the modes that were present in the previous step for $z<0$. This scheme is shown in the right panel of Fig. 7.6. The mutual information between these two sets defines a measure of distance y_j at the jth RG step:

$$y_z(j) \equiv \ln \frac{I^2_{\max}}{I^2_z(\mathcal{B}^1_j : \mathcal{B}^2_j)} = \begin{cases} (j+1)^z \ln 2\,, & z>0\,, \\ (j-1)^z \ln 2, & z<0\,. \end{cases} \tag{5.3}$$

The distance along the RG direction ($x_z(j)$) is, on the other hand, defined as the distance between the current RG step and the one with the maximum entanglement entropy:

$$x_z(j) \equiv \theta(z)d(0,j) + \theta(-z)d(j,\infty) = j^z \ln 2\,, \tag{5.4}$$

where $d(i,j)$ was defined in eq. (5.1).

The connection of the $x-$ and $y-$distances to the RG can be made manifest by relating them to the RG beta function. As we have seen above, even though we are working with massless Dirac fermions ($m=0$), the Aharonov-Bohm flux and the dimensional reduction into $1+1-$dimensional modes generate an effective mass $M_{n,\phi} = \frac{2\pi}{L_x}(n+\phi)$ for $n>0$. At a specific RG step j, the nth mode is given by $t_z(j)\times n$ on account of the RG transformations in k_x-space. With these points in mind, we define a coupling $g_z(j)$ that acts as a measure of the gap in the single-particle spectrum

$$g_z(j) \equiv \ln \frac{M_{n+1,\phi}(j) - M_{n,\phi}(j)}{2\pi/L_x} = \ln t_z(j) = j^z \ln 2\,. \tag{5.5}$$

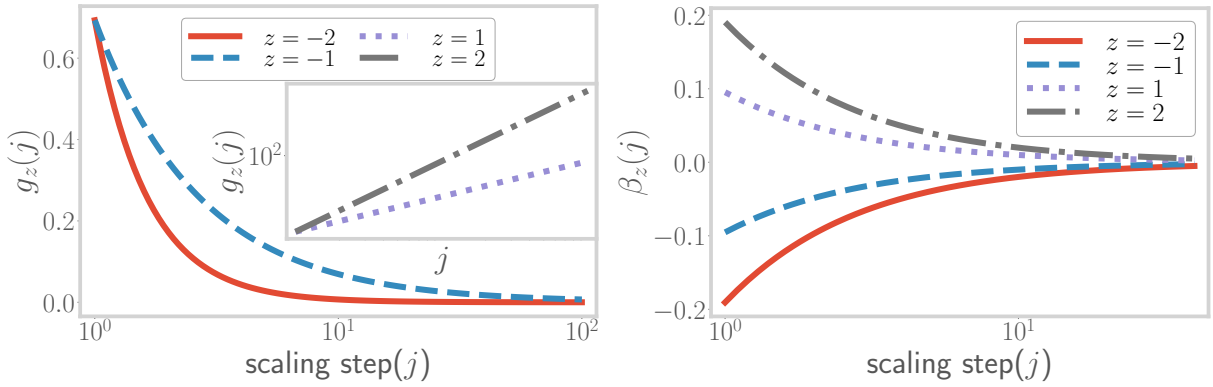

Figure 7.7: *Top: Depiction of the RG flow of the coupling $g_z(j)$. For $z < 0$ (blue and red curves), the coupling is RG-irrelevant and shows a decrease as j is increased. For $z > 0$ (gray and violet curves), the coupling is RG-relevant and shows an increase as j is increased. Bottom: Variation of RG beta function $\beta_z(j)$ for the coupling $g_z(j)$, as a function of step index j. For all values of z, the beta function converges to 0 as $j \to \infty$, indicating a fixed point of the coupling g.*

The RG beta-function for the coupling $g_z(j)$ can then be written as

$$\beta_z(j) \equiv \frac{\Delta \log g_z}{\Delta j} = \log \frac{g_z(j+1)}{g_z(j)} = z \ln\left(1 + \frac{1}{j}\right) , \tag{5.6}$$

where we have substituted $\Delta j = 1$. The beta function is positive for $z > 0$, indicating that the coupling $g_z(j)$ is RG-relevant in this regime (left panel of Fig. 7.7). On the other hand, the beta function is negative for $z < 0$, leading to irrelevant RG flows in this regime. The RG beta-function $\beta_z(j)$ itself decreases monotonically as j increases under the RG transformations (see Fig. 7.7): for a finite z, a fixed point is reached at $j \to \infty$ where the beta function goes to zero.

As we will now see, the flow of the RG beta functions can be related to the extremisation of a potential defined in the space of Hamiltonians. This potential is a function of the mutual information $I_z^2(0:j)$:

$$\beta_z(j) = -\Delta \left[\ln\left(\ln \frac{I_z^2(0:j)}{I_{\max}^2} \right) \right] . \tag{5.7}$$

The potential given within the square brackets above corresponds to an RG monotone whose fixed point corresponds with the fixed point of the RG. For relevant flows, the above equation ensures that the function $\ln\left(\ln \frac{I_z^2(0:j)}{I_{\max}^2}\right)$ is always minimised under the RG flow, with the consequence that the trajectories ultimately lead to minimisation of the mutual information. This indicates that the relevance of the mass coupling leads in turn to the decrease of the correlation length and hence a lowering of entanglement between points that are separated in real space. On the other hand, for irrelevant flows, the above-mentioned function is maximised, implying that the RG trajectories now maximise the entanglement. This reflects the fact that the decreasing mass leads to increased correlation lengths and an approach towards criticality.

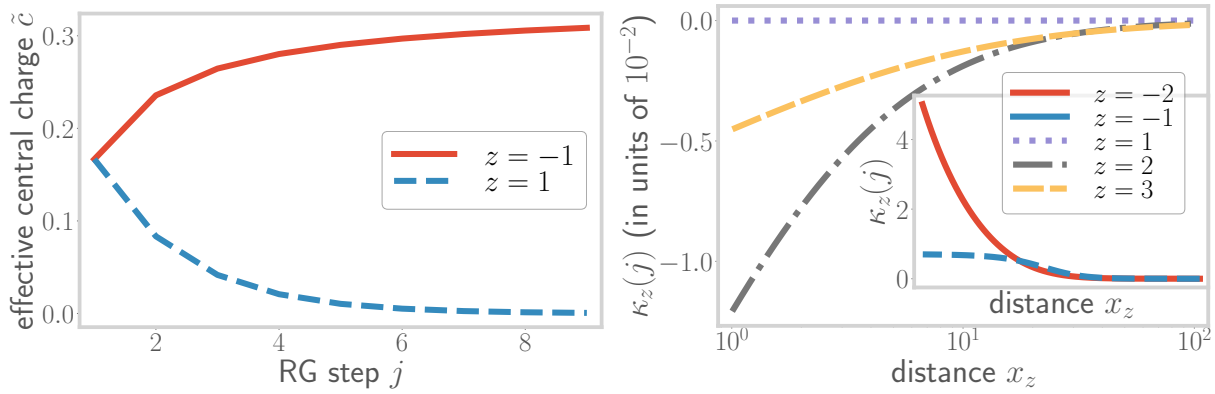

Figure 7.8: *Top: Variation of the effective central charge defined in eq. (5.10), under the RG transformations for relevant ($z = 1$, blue curve) and irrelevant ($z = -1$, red curve) flows. In the former case, the central charge starts from the fermionic gapless value of $1/3$ and vanishes towards the fixed point, indicating the flow to a gapped massive phase. In the latter case, it starts from the gapped value of 0, and increases to $1/3$ at the fixed point, indicating the flow to a gapless phase. Bottom: Variation of the curvature $\kappa_z(j)$ along the RG for multiple values of z. $z = 1$ leads to a flat space with zero curvature, while $z > 1$ and $z < 1$ (inset) lead to negative and positive curvature respectively.*

Given eqs.(5.3), (5.4) and (5.7), we can relate the distances x and y to the beta function β_z:

$$x_z = \left(e^{\frac{\beta_z}{z}} - 1\right)^{-z} \ln 2\,, \tag{5.8}$$

$$y_z = \begin{cases} x_z e^{\beta} & z > 0\,, \\ x_z \left(2 - e^{\frac{\beta}{z}}\right)^{z} & z < 0\,. \end{cases} \tag{5.9}$$

The contrasting behaviour of the beta function depending on the sign of z indicates that it tracks the effective number of degrees of freedom that contribute to the entanglement (eq. (3.14)) at any given RG step. Indeed, we find that the effective number of degrees of freedom is the effective $c-$function (or central charge) $\tilde{c}_z(j)$ of the theory, taking the form $\tilde{c}_z(j) = f_z(i)c$. The beta function is thus related to the $c-$function as

$$\beta_z = \Delta \left[\ln\left(\ln \frac{c}{\tilde{c}_z(j)}\right)\right]\,. \tag{5.10}$$

For RG relevant flows, the $c-$function is found to diminish from the free fermion central charge $c = 1/3$, reaching the value of zero at the fixed point (where only the central $n = 0$ mode remains and the rest have been removed because of the large mass gap). The non-negative, non-increasing nature of the $c-$function, and its flow towards its minimum at the fixed point, leads to speculate that eq.(5.10) can be thought of as a holographic counterpart of Zamalodchikov's $c-$theorem [371,634–636]. For RG irrelevant flows, the behaviour is reversed. The flow of the $c-$function is shown in the left panel of Fig. 7.8.

7.5.2 Embedding the emergent dimension on a metric space

We have shown above that the renormalisation group flow of the Hamiltonian leads to the emergence of an additional direction, quantified by the parameter x_j. This will now be used to construct a metric, in the following way. We already know that the scaling transformations lead to a graph of theories that are connected via edges that represent the mutual information between any two theories. As a result, this "information graph" can be mapped on to a new "distance graph" where the edges now represent the distance between the theories at the nodes. Finally, these distances can be used to define a metric for the distance graph: the metric between any two nodes will be the distance along the shortest path between these two nodes. This approach as well as some of the terminology are inherited from reference [637].

The RG flow can be represented as an "information graph" $G(V, E)$, where the systems $\mathcal{B}_j^1$ (defined above eq. (5.3)) constitute the set of vertices $V = \{V_j\}$ and the mutual information $I_z^2(j : j')$ between the systems $\mathcal{B}_j^1$ and $\mathcal{B}_{j'}^1$ constitute the edges E_{ij} between the vertices. This information graph is characterised by an adjacency matrix whose elements are defined by the mutual information edge weights $I_z^2(j : j')$ [638]. This graph structure is shown in Fig. (7.6), with the red spheres indicating the vertices. In order to define a metric space, we will map the graph G to another graph $\mathcal{G}$ that has the same vertices as G, but whose edges are weighted according to a well-defined notion of distance.

A path $\mathcal{P}$ in $\mathcal{G}$ is defined as a sequence of m vertices: $\mathcal{P}(V_1, V_2, \ldots V_m)$. The distance along the path is defined as the sum of distances along every pair of consecutive vertices: $l(\mathcal{P}) = \sum_{i=1}^{m-1} d(V_i, V_{i+1})$, where $d(V_i, V_{i+1}) = d(i, i+1)$ (see eq. (5.1)). The *geodesic* between two points V_i and V_j is the path $\mathcal{P}$ which minimises the distance $l(P)$, and the distance along the geodesic then defines the *metric* $\tilde{d}(V_i, V_j)$ between two vertices V_i and V_j [637, 638]:

$$\tilde{d}(V_i, V_j) = \min_{\mathcal{P}} \{l(\mathcal{P})\} = \min_{\mathcal{P}} \left\{ \sum_{i=1}^{m-1} d(V_i, V_{i+1}) \right\} , \tag{5.11}$$

where the minimisation is carried out over all possible connected paths $\{\mathcal{P}\}$ between V_i and V_j, and m is the total number of vertices in a particular connected path $\mathcal{P}_m$. Following the expression for the distance $d(i, j)$ obtained in eq. (5.2), the metric takes the form

$$\tilde{d}(V_i, V_j) = \theta(z) j^z \ln 2 + \theta(-z) i^z \ln 2, \quad (i < j) , \tag{5.12}$$

where we have assumed $i < j$, without loss of generality.

Finally, the metric dimension of the emergent space can be determined by finding the set with the lowest possible cardinality that can resolve the metric space [637, 639]. In order for a set to resolve the metric space, we must have $d(i, a) = d(j, a) \implies i = j$ for all points a in the set and for any pair of points i and j in the metric space. In our case, the singleton set $\mathcal{R} = \{0\}$ can resolve the metric space for $z > 0$, as $d(i, 0) = d(j, 0) \implies i^z = j^z \implies i = j$. Similarly, the singleton set $\mathcal{R} = \{\infty\}$ resolves the metric space for $z < 0$. As a result, we conclude that our emergent metric space is one-dimensional in nature.

7.6 Curvature of the emergent space

Further insight on the spatial geometry of the RG flows can be obtained by looking at the curvature generated by the RG transformations. In the plane of the directions x and y generated by the RG flow, the curvature can be written using the ideas of analytic geometry as

$$\kappa_z(j) = \frac{v_z'(j)}{\left[1 + v_z(j)^2\right]^{\frac{3}{2}}}\,, \tag{6.1}$$

where

$$\begin{aligned} v_z(j) &\equiv \frac{\Delta y_z(j)}{\Delta x_z(j)} = \frac{y_z(j+1) - y_z(j)}{x_z(j+1) - x_z(j)} \\ &= \begin{cases} \frac{(j+2)^z - (j+1)^z}{(j+1)^z - j^z} & z > 0\,, \\ \frac{(j)^z - (j-1)^z}{(j+1)^z - j^z} & z < 0\,, \end{cases} \end{aligned} \tag{6.2}$$

and

$$v_z'(j) \equiv \frac{v_z(j+1) - v_z(j)}{x_z(j+1) - x_z(j)}\,. \tag{6.3}$$

The curvature $\kappa_z(j)$ has been plotted against the RG step index j in right panel of Fig. 7.8. For $z = 1$, the first derivative $v_z(j)$ becomes unity, so the second derivative $v_z'(j)$ (and hence the curvature) vanishes, leading to a flat (Minkowski) space. For $z > 1$, the curvature becomes negative, while it is positive for $z < 0$. All the flows lead to an asymptotically flat space (i.e., the curvature vanishes) as $j \to \infty$.

The different signatures of the emergent curvatures can be attributed to the different ways in which the mass of the theory scales under the decimation procedure. For $z > 0$, the curvature defined in eq. (6.1) can be written in terms of the beta function:

$$\kappa_z(j) = \frac{\left[e^{\beta(j)} - 1\right]^{\frac{1}{2}} j^{-z}}{\left[e^{\beta(j)+\beta(j+1)} - 1\right]^{\frac{3}{2}}} \left[\frac{e^{\beta(j+2)} - 1}{1 - e^{-\beta(j+1)}} - \frac{e^{\beta(j+1)} - 1}{1 - e^{-\beta(j)}}\right]\,. \tag{6.4}$$

This equation relates directly a geometric quantity (i.e., the curvature) of the bulk emergent space with the RG beta function for the field theory on the boundary. From Fig. 7.7, as the beta functions flow towards zero, we see from eq. (6.4) that the first fraction inside the square brackets is the first to vanish, followed by the second fraction. The sequential vanishing of these two fractions prior to the vanishing of the denominator $e^{\beta(j)} - 1$ in eq.(6.4) leads to the asymptotic vanishing of the curvature towards the fixed point. Different choices of $z > 0$ can be thought to represent different relevant perturbations that drive the system towards *gapped fixed points*, leading to distinct curvatures of the bulk. By employing the relation $v_z(j) = \Delta S_{j+1,z}/\Delta S_{j,z}$, eq. (6.1) can also be cast in terms of the entanglement entropy $S_{j,z}$, $S_{j+1,z}$ and $S_{j+2,z}$. The resulting non-linear relationship between $\kappa_z(j)$ and $S_{j,z}$ obtained is, however, in contrast to the linear dependence obtained by Cao et al. [637] between entanglement perturbations on the Hilbert space and the curvature of the resultant holographic space.

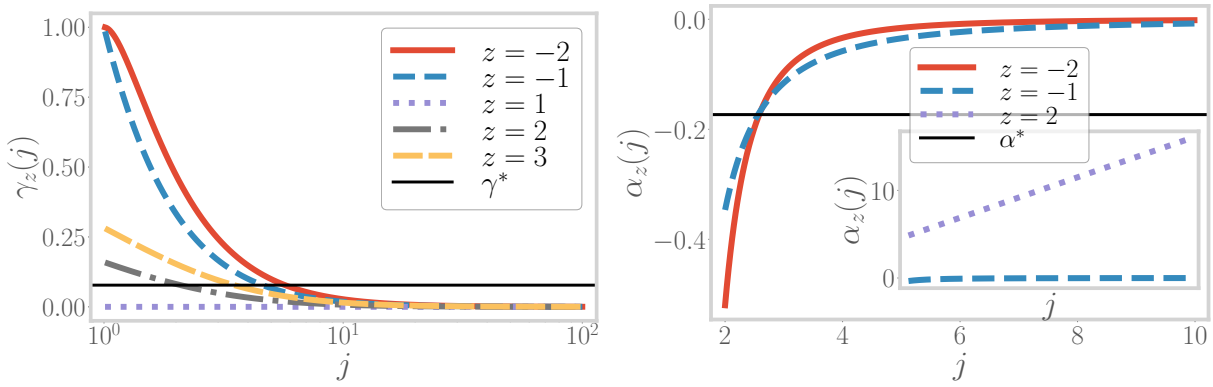

Figure 7.9: *Top: Variation of γ_z along the RG for multiple values of $z > 0$. All trajectories for $z > 1$ intersect the line $y = \gamma^*$. Bottom: Variation of α_z along the RG for multiple values of $z < 0$. All trajectories intersect the line $y = \alpha^*$*

7.6.1 Topological nature of the sign of curvature

We will now argue that the signature of the curvature κ corresponds to a topological quantum number, and that a change in the signature as z is tuned through 1 amounts to a topological translation. For this, we first point out (following eq. (6.1)) that the sign of the curvature is determined purely by the sign of $\gamma_z(j) \equiv 1 - v_z(j+1)/v_z(j)$ and $\alpha_z(j) = y_z(j+1) - y_z(j)$:

$$\begin{aligned} \kappa_z(j) &= \frac{v_z'(j)}{\left[1 + v_z(j)^2\right]^{\frac{3}{2}}} = -\frac{\alpha_z(j)\,\gamma_z(j)}{(\Delta x_z(j))^2\left[1 + v_z(j)^2\right]^{\frac{3}{2}}} \\ \implies \text{sign}\left[\kappa_z(j)\right] &= -\text{sign}\left[\alpha_z(j)\right]\text{sign}\left[\gamma_z(j)\right] \ . \end{aligned} \tag{6.5}$$

We now promote j to a continuous complex variable with the real part being greater than or equal to 1: $\text{Re}\,[j] \geq 1$. The quantities $\alpha_z(j)$ and $\gamma_z(j)$ can be written as

$$\alpha_z(j) = \begin{cases} [(j+2)^z - (j+1)^z]\log 2, & z > 0 \\ [j^z - (j-1)^z]\log 2, & z < 0 \end{cases} \ , \tag{6.6}$$

$$\gamma_z(j) = \begin{cases} 1 - \frac{[(j+3)^z - (j+2)^z][(j+1)^z - j^z]}{[(j+2)^z - (j+1)^z]^2}, & z > 0 \\ 1 - \frac{[(j+1)^z - j^z]^2}{[j^z - (j-1)^z][(j+2)^z - (j+1)^z]}, & z < 0 \ . \end{cases} \tag{6.7}$$

As shown in Fig.7.9(left panel), the function γ_z is positive and monotonically decreasing for $z > 1$ or $z \leq -1$, and vanishes identically for $z = 1$. On the other hand, $\alpha_z(j)$ is positive for $z > 1$, zero at $z = 1$ and negative for $z \leq -1$ (see Fig.7.9(right panel)). Combining this, we find that the sign of the curvature can be written as:

$$\text{sign}\left[\kappa_z\right] = \begin{cases} -1, & z \geq 1 \\ 1, & z \leq -1 \end{cases} = \begin{cases} -\text{sign}\left[\gamma_z(j)\right], & z \geq 1 \\ -\text{sign}\left[\alpha_z(j)\right], & z \leq -1 \ . \end{cases} \tag{6.8}$$

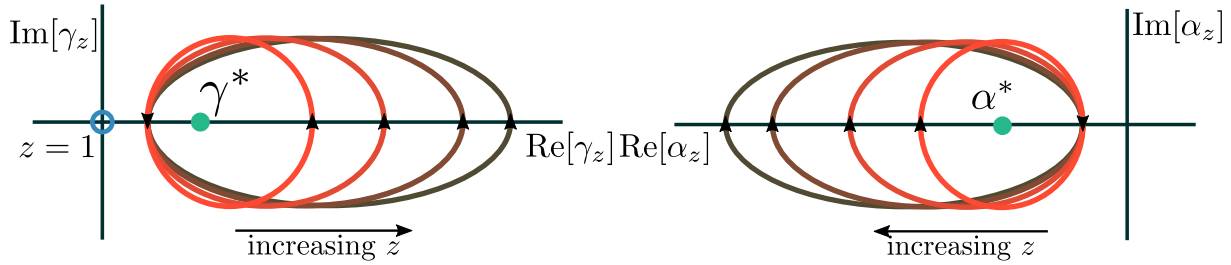

Figure 7.10: *Top: Contours $\gamma_z(C)$ for multiple values of $z > 0$. As z increases, the contours extend in the positive Re $[\gamma_z]$ direction. Bottom: Contours $\alpha_z(C)$ for multiple values of $z > 0$. As z increases, the contours extend in the negative Re $[\gamma_z]$ direction.*

We start by considering the region $z \geq 1$. Since $z = 0$ is excluded by definition, the denominator is always non-zero. This indicates that $\gamma_z(j)$ is continuous and monotonically decreasing in this range: the maximum value of $\{\gamma_z(j), j \in [1, \infty]\}$ occurs at $j = 1$. Further, the maximum value $\gamma_z(1)$ increases with the value of z, ranging between $\gamma_2(2)$ at $z = 2$ and unity at $z \to \infty$. These two features are demonstrated in the left panel of Fig. 7.9, and imply that all curves $\{\gamma_z(j) : j\}$ will take values both greater than and less than the value $\gamma^* \equiv \gamma_2(2)$ (dotted line in left panel of Fig. 7.9). Thus, the plot shows that there always exists a real value j_z^* for any given integer value $z > 1$ such that $\gamma_z(j_z^*) = \gamma^* = \gamma_2(2)$. This is precisely what ceases to happen for $z = 1$, as that is the only curve in the left panel of Fig. 7.9 that does not pass through γ^*.

Indeed, the difference between the curvature for the $z = 1$ and $z > 1$ classes can be captured by expressing the presence of the solution j_z^* in the form of a winding number. For this, we use the fact that the sign of $\gamma_j(z)$ is given by the following integral:

$$\text{sign}\,[\gamma_z(j)]\Big|_{z\geq 1} = \frac{1}{2\pi i}\oint_C \mathrm{d}j\,\frac{\partial}{\partial j}\ln\left[\gamma_z(j) - \gamma^*\right]\,, \tag{6.9}$$

where the contour C extends from $j = 1$ to $j = \infty$, and is shown in the left panel of Fig. 7.12. As the value of z is tuned from 2 to 1, the pole at j_z^* disappears and the integral reduces to zero. As shown in Fig. 7.10, the integral can thus be expressed as the winding number of the curve $\gamma_z(C(j))$ that counts the number of times the contour $\gamma_z(C)$ winds around the singularity at γ^*:

$$\text{sign}\,[\gamma_z(j)] = \frac{1}{2\pi i}\oint_C \mathrm{d}j\,\frac{\partial(\gamma_z(j) - \gamma^*)}{\gamma_z(j) - \gamma^*} = \frac{1}{2\pi i}\oint_{\gamma_z(C)}\frac{\mathrm{d}\gamma_z}{\gamma_z - \gamma^*}\,. \tag{6.10}$$

This is easily seen from the following argument. If we write a general complex variable y in the form $y = re^{i\theta}$ and consider a general contour C that starts from $r = r_0, \theta = 0$ and ends at $r = r_0, \theta = 2w\pi$ (such that the winding number of the curve is w), integrals of the form given above simplify and return the winding number itself:

$$\frac{1}{2\pi i}\oint_C \frac{dy}{y} = \frac{1}{2\pi i}\int_{r_0}^{r_0}\frac{dr}{r} + \frac{1}{2\pi}\int_0^{2w\pi} d\theta = w\,, \tag{6.11}$$

where we used $dy = y\left(\frac{dr}{r} + d\theta\right)$.

The winding numbers take integer values, and are topological in nature: they are robust against geometric deformations, and change only when the curve crosses the singularity at $\gamma = \gamma^*$. Thus, for $z > 1$, the contour $\gamma_z(C)$ encloses the singularity at γ^* exactly once, leading to a winding number of unity. As z is lowered towards $z = 2$, the contours becomes smaller such that, in order to go from $z = 2$ to $z = 1$, the contour has to be moved across the singularity. This constituting a change in the topology of the contour: for $z = 1$, the contour no longer encloses the pole and the winding number is zero. In fact, at $z = 1$, the contour itself (depicted in blue) is of vanishing radius because $\gamma_1(j)$ has a constant value of zero. To complete the connection, we use eq. (6.5) to relate this topological winding number to the sign of the curvature:

$$\text{sign}\left[\kappa_z\right]\Big|_{z\geq 1} = -\mathcal{W}_z(\gamma^*)\,, \tag{6.12}$$

where $\mathcal{W}_z(\gamma^*)$ is the winding number for $\gamma_z(C)$ around γ^*.

One can make a very similar argument for the case of $z \leq -1$. Here, as shown in the right panel of Fig. 3.10, the relevant quantity is $\alpha_z(j)$. For each curve α_z, the minimum value is at $j = 1$. For all z, this minimum starting value is largest for $z = -1$, and all subsequent curves $\alpha_z(j)$ start from even lower values. If we define a value $\alpha^* \equiv \alpha_z(j = 1)/2$, it is then clear that all curves $\alpha_z(j)$ will pass through the value α^* (dotted line in right panel of Fig. 3.10) at some value of j. This is very similar to the situation discussed just above for the case of $z \geq 1$ (with γ^* playing the role of α^*); we, therefore, employ the same technique here. Taking the same contour C as defined above, we write the sign of α_z as the winding number of the curve $\alpha_z(C)$ around the point $\alpha_z = \alpha^*$

$$\text{sign}\left[\alpha_z(j)\right]\Big|_{z\leq -1} = -\mathcal{W}'_z(\alpha^*) = \frac{1}{2\pi i}\oint_{\alpha_z(C)}\frac{\mathrm{d}\alpha_z}{\alpha_z - \alpha^*}\,. \tag{6.13}$$

For $z > 0$, α_z is positive, and the curve $\alpha_z(C)$ encloses points in the positive half of the real axis such that the winding number in the right panel of Fig. 7.10 is then zero. This indicates that the function $1 - 2\mathcal{W}'_z(\alpha^*)$ is unity for $z > 0$, leaving any other function in product with it unchanged. On the other hand, it is -1 for $z < 0$, returning the correct sign of $\alpha_z(j)$ in that range. Combining with eq. (6.12), the sign in the entire range can be expressed as

$$\text{sign}\left[\kappa_z\right] = \mathcal{W}_z\left(\gamma^*\right) \times \left[2\mathcal{W}'_z\left(\alpha^*\right) - 1\right]\,. \tag{6.14}$$

We can now summarise the topological nature of the sign of the curvature. For $z > 0$, the second winding number $\mathcal{W}'$ is 0. As z varies from 2 to 1, the other winding number $\mathcal{W}$ changes from 1 to 0, constituting the first topological change. In contrast, upon varying z from 1 to -1, both winding numbers change: $\mathcal{W}$ from 0 to 1, and $\mathcal{W}'$ from 0 to 1. This constitutes the second topological change. Together, the two changes show that going from an open geometry (negative curvature) to a closed geometry (positive curvature) involves two topological transformations.

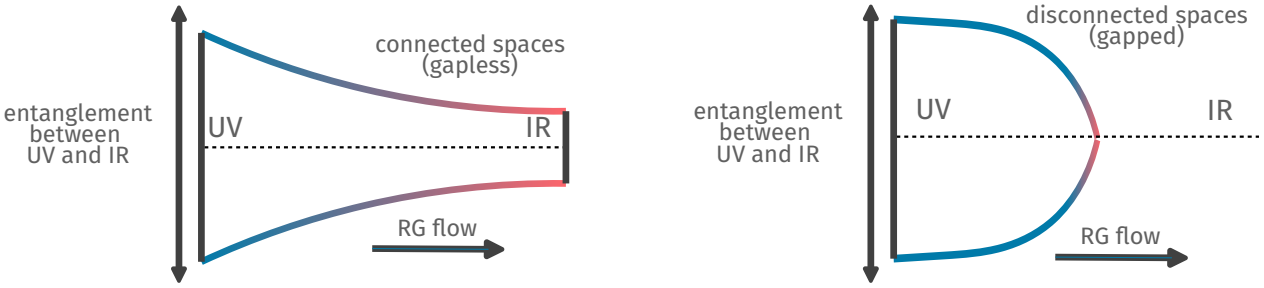

Figure 7.11: *Schematic depiction of the emergent geometries in the cases of gapless (top) and gapped (bottom) RG flows. While the gapless RG flow involves a growth in the entanglement between the UV and IR spaces, the latter leads to the vanishing of UV-IR entanglement. This results in the emergence of connected and disconnected geometries, respectively.*

7.7 Entanglement Holography and Fermionic Criticality

7.7.1 Equivalence between a critical Fermi surface and a holographic wormhole

As mentioned previously under eq. (**4.3**), the quantity z corresponds to the anomalous dimension of the spectral gap g_z in the effective field theory: a change in the sign of z corresponds to a change in the nature of the RG flow from relevance to irrelevance and vice-versa. The holographic nature of the RG flow dictates that such a change arises by a variation in some quantity in the parent interacting theory from which the effective field theory of non-interacting Dirac fermions can be thought to have originated. Indeed, such a change in the RG relevance has drastic consequences: a relevant spectral distance g_z implies a gap in the excitations at the fixed point, while an irrelevant g_z indicates the presence of gapless excitations. The presence or absence of a gap in the low-energy excitations determines the topology of the electronic Fermi surface through the change of a topological invariant, the Luttinger volume of the system [24, 50, 51, 348, 349] (also see eq. (**2.19**)).

At the transition between the gapless (metallic) and gapped (insulating) states, the Fermi surface becomes critical, signalled by the vanishing lifetime of the gapless excitations close to it. Our formulation shows that such a gap-inducing transition and its associated quantum critical Fermi surface has consequences for the space generated along the RG flow. For the gapless case ($z < 0$), the degrees of freedom in the UV and the IR have finite entanglement, indicating that they are part of the same connected holographic space(see Figs. 7.6 and 7.7), while for the gapped case ($z < 0$), the entanglement vanishes into the IR, leading to a decoupling of these two regions and their separation into disconnected spaces [353]. These two scenarios are shown schematically in Fig. 7.11. It is therefore tempting to conclude that at the transition between the gapped and gapless states, a *wormhole geometry* connects the UV and the IR via some minimal entanglement [353, 637]. Our results also suggest that the presence of such a wormhole would then coincide with two topological transitions, the first being the change in the sign of the curvature (as shown in the previous subsection), and the second being the change in the topological Luttinger volume of the underlying quantum field theory (as discussed in the previous paragraph). We end by noting that we have provided, in a later section of this work, additional support for the topological nature

of Luttinger's volume and its connection to the holographically generated space by relating it to multipartite entanglement (see eq. (9.17)).

7.7.2 Connecting modular energy with the metric

The notion of an entanglement Hamiltonian was introduced in eq. (2.16). At the transition between the gapless (metallic) and gapped (insulating) states, the system becomes critical, and the Dirac electrons are described by a CFT. It turns out that for such a CFT, the entanglement Hamiltonian takes a particularly simple form. In this subsection, we will relate the emergent metric to the entanglement Hamiltonian obtained at the IR fixed point, focusing on the theory at the transition.

For a 1D CFT, the entanglement Hamiltonian corresponding to a partition of length l is given by [640, 641]

$$\mathcal{H}_{1D} = \frac{2\pi L}{c} \int_0^l \mathrm{dx}\, \frac{L^2 - x^2}{2L^2} T_{00}(x)\,, \tag{7.1}$$

where $T_{\mu\nu}$ is the stress-energy tensor of the CFT and c is the speed of light. We have already shown in eq. (2.17) that the entanglement Hamiltonian for the 2D theory is simply a sum of the 1D counterparts, owing to the decoupling of 1D modes in the Lagrangian. Working in a region where T_{00} is approximately uniform, the 2D entanglement Hamiltonian can be expressed as

$$\mathcal{H}_{2D} \sim \sum_n \mathcal{H}_{1D} = \frac{2\pi L^2}{3c} \sum_n T_{00}^n\,, \tag{7.2}$$

where T_{00}^n is the average value of T_{00} within the partition for the CFT associated with the nth mode.

In order to make the connection with the emergent geometry, we use the entanglement first law [642], which states that at first order, small variations ΔS of the entanglement entropy can be equated to the associated change in the expectation value of the entanglement Hamiltonian:

$$\Delta S(A) = \Delta I_2(A_0 : A) = \langle \Delta \mathcal{H} \rangle = \frac{2\pi L^2}{3c} \sum_n \left\langle T_{00}^n \right\rangle, \tag{7.3}$$

where $\langle \mathcal{H} \rangle = \mathrm{Tr}\,(\rho \mathcal{H})$ is often referred to as the modular energy, and we have equated $\Delta S(A)$ and $\Delta I_2(A_0 : A)$ following eq. (3.16). Further, since the entanglement at the critical point is expected to be large, we can approximate the expression for the metric between points (i, j) obtained in subsection 7.5.2 as $\tilde{d}(i, j) = -\ln I^2(i : j)/I^2_{\max} \simeq |I^2(i : j)/I^2_{\max} - 1|$. Combining this equation with eq. (7.3) leads to the following interesting relation:

$$\Delta \tilde{d}(i, j) \simeq \frac{2\pi L^2}{3c} \sum_n \left\langle T_{00}^n \right\rangle\,. \tag{7.4}$$

The equation relates the change in a geometric measure (the emergent metric) with a mass/energy term. An analogous relation was obtained for states for which the entropy obeys an area law by Cao et al [637], connecting the spatial curvature and the stress tensor, ultimately leading to a semi-classical Einsteins field equation for gravity. Our formulation does not however lead to a relation involving the curvature, and we speculate that this is due to the violation of the area law in entanglement of fermionic critical systems. Instead, we show in the next section that the curvature in our formulation is related to the rate of convergence of the RG flows.

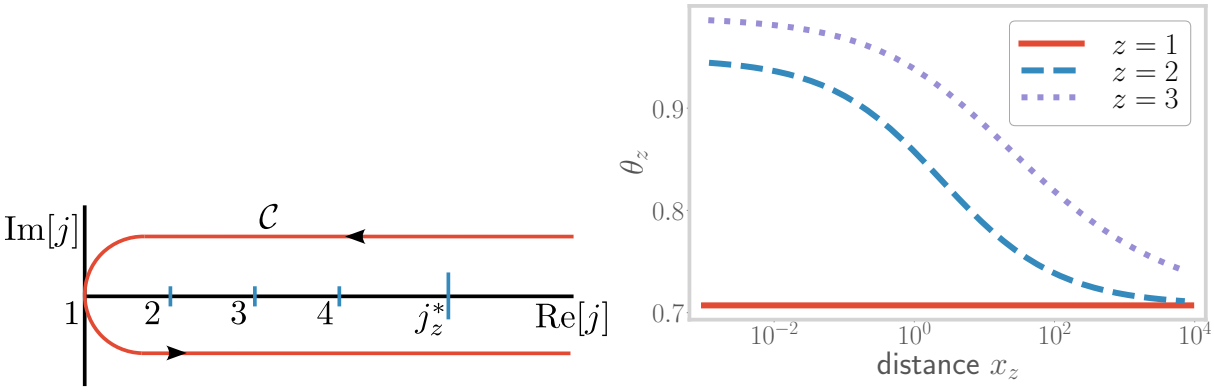

Figure 7.12: *Top: The contour C used in eq. (6.9). It extends across all values of j, and the integral counts the number of poles of the function $1/(\gamma - \gamma^*)$ encircled by the contour. Bottom: Evolution of expansion parameter θ_z with distance x_z, leading to the fixed point at $\theta_z^* = 1/\sqrt{2}$.*

7.7.3 Kinematics of the RG flows

Further statements on the RG flow and the emergent holographic dimension can be made by studying quantities that can serve as candidates for the convergence parameter θ for the RG flows of g_z [643, 644]. We consider the following funcion as a candidate for the convergence parameter for the case of $z > 0$:

$$\theta_z(j) = \frac{1}{\sqrt{v_z^{-2}+1}} = \left[1 + \left\{\frac{1 - e^{-\beta_z(j)}}{e^{\beta_z(j+1)-1}}\right\}^2\right]^{-\frac{1}{2}} . \tag{7.5}$$

The parameter θ_z has been plotted in Fig. 7.12, and the behaviour is observed to be very similar to that of the beta function shown in Fig. 7.7. Indeed, this similarity describes the holographic nature of the RG flow: the emergent geometry (as seen through θ_z) is dictated by the RG flow described by β.

The quantity θ can be interpreted as an estimate of the rate of change of area enclosed by a fixed number of RG trajectories. To see that this is the case, we note that by using $v_j = \Delta y/\Delta x$, the expansion parameter can be written as $\theta = \Delta y(j)/\sqrt{\Delta x^2 + \Delta y^2} \sim \Delta g(j+1)/\sqrt{\Delta x^2 + \Delta y^2}$. Considering RG flows for $g_z(j)$ corresponding to multiple z, the area enclosed by the curves is given by the maximum g_z, and Δg_z is then the change in the area under the RG transformation. The denominator $\sqrt{\Delta x^2 + \Delta y^2}$ is the distance covered in the emergent spacetime, rendering θ as the rate of change of the area.

The equation of motion for this expansion parameter can then be obtained as:

$$\frac{\mathrm{d}\theta_z}{\mathrm{d}x} = \frac{v_z^{-3}}{\left(1 + v_z^{-2}\right)^{\frac{3}{2}}} \frac{\mathrm{d}v_z}{\mathrm{d}x_j} = \kappa_z . \tag{7.6}$$

The simple form of this relation makes it clear that for relevant flows (corresponding to a negative curvature $\kappa_z < 0$), θ_z flows to a minimum. Following Fig. 7.8, this is accompanied by the minimisation of the $c-$function to zero. It is, therefore, tempting to conclude that eq. (7.6) for the spatial

evolution of the convergence parameter θ is dual to eq. (5.10) that controls the flow of the c-function of the quantum theory along the RG flow.

7.8 Extension to the massive case

We will now generalise several of the main results obtained above to the case of two-dimensional electrons with a single-particle mass-gap $M_{n,\phi} = \sqrt{m^2 + \frac{4\pi^2}{L_x^2}(n+\phi)^2}$. Given that they depend only on the geometric part of the entanglement (which remains unchanged on introducing the mass $M_{n,\phi}$), the following set of key qualitative results and observations discussed earlier continue to hold for the case of a dispersion with a mass-gap:

- the hierarchical structure of the entanglement content (e.g., the area-law term in eqns.(3.14) and (3.17)) and the fact that the entanglement satisfies the Ryu-Takayanagi bound (right panel of Fig.7.5),
- the dependence of the emergent distances x and y on the RG flow (Fig.7.6, eqns.(5.2) and (5.3)), and the fact that the RG beta function tracks the central charge (Fig.7.8),
- various qualitative and quantitative properties of the curvature (e.g., eq.(6.1)), including the topological nature of its sign (eq.(6.14)), and
- the existence of a convergence parameter that is related to the RG flow, and the equation that governs the evolution of the convergence parameter (eq.(7.6)).

The functional forms of certain other results do, however, undergo changes. For instance, the coupling $g_z(j)$ is given by the (more general) expression

$$\begin{aligned} g_z(n,j) &= \ln \frac{M_{n+1,\phi}(j) - M_{n,\phi}(j)}{2\pi/L_x} \\ &= \ln \left[\sqrt{\tilde{m}^2 + (t_z(j)(n+1)+\phi)^2} - \sqrt{\tilde{m}^2 + (t_z(j)n+\phi)^2} \right] , \end{aligned} \tag{8.1}$$

where $\tilde{m} = mL_x/2\pi$ is a dimensionless parameter. We will work with the coupling for the mode $n = 0$:

$$g_z(0,j) = \ln \left[\sqrt{\tilde{m}^2 + (t_z(j)+\phi)^2} - \sqrt{\tilde{m}^2 + \phi^2} \right] . \tag{8.2}$$

In order to simplify the analysis, we work in the large mass limit $\frac{t_z+\phi}{\tilde{m}} \to 0$. In this limit, upon expanding the square root and retaining only the lowest order term, we obtain

$$g_z(0,j) = \ln \frac{[t_z(j)+\phi]^2 - \phi^2}{2\tilde{m}} . \tag{8.3}$$

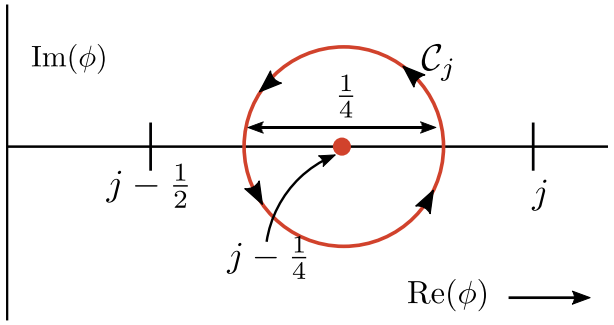

Figure 7.13: *Contour C_j used to integrate eq. (9.3). The contour is chosen so as to encircle the simple pole of $1/Q$ at $\phi = j - 1/4$.*

The RG beta function $\beta = \ln(g_z(j+1)/g_z(j))$ can, in the large mass limit, then be related to the emergent distances x and y in terms of the coupling $g_z(j)$:

$$x_z(j) = \ln t_z(j) = \ln\left[\sqrt{2\tilde{m}\, e^{g_z(0,j)} + \phi^2} - \phi\right], \tag{8.4}$$

$$y_z(j) = \begin{cases} \ln\left[\sqrt{2\tilde{m}\, e^{g_z(0,j+1)} + \phi^2} - \phi\right], & z > 0\,, \\ \ln\left[\sqrt{2\tilde{m}\, e^{g_z(0,j-1)} + \phi^2} - \phi\right], & z < 0\,. \end{cases} \tag{8.5}$$

The quantitative dependence of the $c-$function on the RG beta function can also be expressed more generally as

$$e^{\beta_z(j)} = \left[\ln \frac{\left(\frac{\tilde{c}(j+1)}{c} + \phi\right)^2 - \phi^2}{2\tilde{m}}\right]\left[\ln \frac{\left(\frac{\tilde{c}(j)}{c} + \phi\right)^2 - \phi^2}{2\tilde{m}}\right]^{-1}. \tag{8.6}$$

Quantities such as the curvature κ and the convergence parameter θ can similarly be expressed in terms of the coupling $g_z(j)$.

7.9 Topological content of the entanglement spectrum

7.9.1 Luttinger's volume as a winding number: the massless case

We will now show how to obtain Luttinger's volume (eq.(2.18)) from the g-partite information entanglement measure I^g of a system of massless 2D electrons. The flux-dependent part of the g-partite information I^g can be used to probe the $k-$space volume V_L within the Fermi surface. We define a quantity $Q_g(\phi)$ that is periodic in the flux ϕ and independent of the geometry:

$$Q_g(\phi) = f_{g,z}\left[\frac{1}{\sqrt{2}} - \frac{1}{2}e^{-\frac{1}{c}\left(I^g_{\{\mathcal{A}_z(i)\}}(\phi) - I^g_{\{\mathcal{A}_z(i)\}}(\phi^{(0)} f_{g,z})\right)}\right] = f_{g,z}\left[\frac{1}{\sqrt{2}} - \left|\sin\left(\pi\phi f_{g,z}\right)\right|\right], \tag{9.1}$$

where $\phi^{(0)} = \frac{1}{6}$ is the value at which the flux-dependent part of $S_0(\phi)$ vanishes. Further, from eq.(3.19), we have

$$I^g_{\{\mathcal{A}_z(i)\}}(\phi_g) - I^g_{\{\mathcal{A}_z(i)\}}(\phi_g^{(0)} f_{g,z}) = -c \ln\left(2|\sin\left(\pi\phi f_{g,z}\right)|\right) \ . \tag{9.2}$$

Note that the non-differentiablity of $Q_g(\phi)$ at $\phi f_{g,z} = 0, 1, 2, \ldots$ is not a concern as ϕ is chosen to be non-integral, ensuring that $\phi f_{g,z}$ is also non-integral.

In order to express the number N_L^x of positive k_x-states available inside the Fermi surface in the $x-$direction in terms of $Q_g(\phi)$, we need to establish a relation between the flux ϕ and the Fermi surface. The k_x-states of interest to us are given by $k_x^n = \frac{2\pi n}{L_x}, n \in \mathbb{Z}, 0 \leq k_x^n \leq k_x^F$, where k_x^F is the $x-$component of the Fermi momentum $\vec{k}_F$. Assuming the flux-free Hamiltonian has time-reversal symmetry, there should be an equal number of states with the opposite momenta. Let n^* be the integer for which $k_x^{n^*} \leq k_x^F$ and $k_x^{n^*+1} > k_x^F$. Since the flux couples to the k_x-states as $k_x^n \to k_x^n + eA = \frac{2\pi n + 2\pi\phi}{L_x}$, tuning ϕ by 1 leads to the entire spectrum of k_x-states being shifted by one quantum number: $k_x^n \to \frac{2\pi(n+1)}{L_x} = k_x^{n+1}$. This means that the state $k_x^{n^*}$ moves to $k_x^{n^*+1}$, and hence out of the Fermi volume by crossing k_x^F. This flow of the spectrum is shown in Fig. 7.15.

If we now connect the system to a particle reservoir with the chemical potential set to zero, any k_x-state that moves out of the Fermi volume becomes unoccupied. We continue tuning the flux to a value ϕ^*, where the system becomes entirely devoid of any particles. The number of k_x-states that are below k_x^F can then be said to be given by the number of times ϕ goes through an integer value while changing from 0^+ to $\phi^* + 0^+$. Since we do not set the flux to an integer value, we can equivalently count the number of times ϕ goes through, say, three-quarters of an integer - $j - \frac{1}{4} : j = 1, 2, \ldots$ - in changing from 0^+ to $\phi^* - 0^+$. We will now show that this count can be expressed in terms of Q_g. We begin by considering $Q_0(\phi) = \frac{1}{\sqrt{2}} - |\sin\pi\phi|$. At every three-quarter value of the flux, the quantity $\phi_j = j - \frac{1}{4} : j = 1, 2, \ldots$, $|\sin\pi\phi_j|$ attains the value of $\sin\frac{\pi}{4} = \frac{1}{\sqrt{2}}$, such that $Q_0^{-1}(\phi)$ goes through a simple pole. Each such pole ϕ_j can be picked up via a complex integral around a contour C_j that encloses the pole:

$$-f_j \frac{1}{2\sqrt{2}i} \oint_{C_j} \frac{d\phi}{Q_0(\phi)} = 1 \ , \tag{9.3}$$

where f_j is either $+1$ or -1 and is defined through the equation $|\sin\left(\pi\left(j - \frac{1}{4}\right)\right)| = f_j \sin\left(\pi\left(j - \frac{1}{4}\right)\right)$, and C_j is a circle of diameter $1/4$ centered at $\phi = j - \frac{1}{4}$ (shown in Fig. 7.13). The evaluation of the integral eq.(9.3) is shown in Appendix B. In order to drop the sign prefactor f_j, we reorient those contours for which f_j is $+1$, and such that they wind around in the clockwise direction. The contours are shown in the left panel of Fig. 7.14, and defined as

$$C_j(\phi) = \left\{\phi : \phi = j - \frac{1}{4} + \frac{1}{8}e^{i\theta}, \theta \in \left[0, -2\pi f_j\right]\right\} \ , \tag{9.4}$$

such that they host a singularity at their center. With this redefinition of the contours, we have

$$\frac{1}{2\sqrt{2}i} \oint_{C_j} \frac{d\phi}{Q_0(\phi)} = 1 \ . \tag{9.5}$$

Counting the number of three-quarter values then reduces to counting the number of poles of Q_0^{-1} in the above-mentioned range $\phi \in (0, \phi^*)$. In this way, we can now express the count N_L^x in terms of Q_0:

$$N_L^x = \frac{1}{2}\sum_{j=1}^{\phi^*} \frac{1}{2\sqrt{2}i}\oint_{C_j(\phi)} \frac{d\phi}{Q_0(\phi)} = \frac{1}{2\sqrt{2}}\sum_{j=1}^{\phi^*} \frac{1}{2i}\oint_{C_j(\phi)} \frac{d\phi}{Q_0(\phi)} \,. \tag{9.6}$$

The factor of half in eq.(9.6) is required as we want to count only the number of positive momentum states (and which is equal to the number of negative momentum states).

In going from $Q_0(\phi)$ to a general $Q_g(\phi)$, the only change required is to redefine $\phi \to \phi_g = f_{g,z}\phi$. This implies that while the states in $k-$space have become more coarse-grained, the flux ϕ has become more fine-tuned by the same scaling factor. This is a reflection of the overall conservation of particle number density: keeping the chemical potential fixed, the increased spacing between the k_x-states implies that a smaller number of particles are now occupying an equally smaller volume. As the number density is conserved, so is the Luttinger volume (eq.(2.18)), and this shows that our approach is consistent with the holographic Luttinger theorem [407]. Thus, given that $\phi_g^* = \phi^*$, the expression for N_L^x remains practically unchanged:

$$N_L^x = \frac{1}{2\sqrt{2}}\sum_{j=1}^{\phi^*} \frac{1}{2i}\oint_{C_j(\phi_g)} \frac{d\phi_g}{\frac{1}{\sqrt{2}} - |\sin\pi\phi_g|} \,. \tag{9.7}$$

In order to rewrite N_L^x in terms of the flux ϕ, we start by making the substitution $\phi_g \to f_{g,z}\phi$:

$$N_L^x = \frac{1}{2\sqrt{2}}\sum_{j=1}^{\phi^*} \frac{1}{2i}\oint_{C_j(f_{g,z}\phi)} \frac{f_{g,z}d\phi}{\frac{1}{\sqrt{2}} - |\sin\left(\pi f_{g,z}\phi\right)|} \,. \tag{9.8}$$

In the above equation, we can recognise $\frac{f_{g,z}}{\frac{1}{\sqrt{2}}-|\sin\left(\pi f_{g,z}\phi\right)|}$ as $Q_g^{-1}(\phi)$. Also note that the contour can be written as

$$C_j(f_{g,z}\phi) \equiv C_j^g(\phi) = \left\{\phi : \phi = t_{g,z}\left(j - \frac{1}{4} + \frac{e^{i\theta}}{8}\right),\ \theta \in \left[0, -2\pi f_j\right]\right\} . \tag{9.9}$$

These curves are again circles of radius $1/8$, but centered at $t_{g,z}\times\left(1-\frac{1}{4}\right), t_{g,z}\times\left(2-\frac{1}{4}\right), t_{g,z}\times\left(3-\frac{1}{4}\right)$ and so on. These are simply a generalisation of the curves defined in eq. (9.4); the curves for $t_{g,z} = 2$ are shown in the right panel of Fig. 7.14. Substituting this in eq.(9.8) gives

$$N_L^x = \frac{1}{2\sqrt{2}}\sum_{j=1}^{\phi^*} \frac{1}{2i}\oint_{C_j^g(\phi)} \frac{d\phi}{Q_g} \,. \tag{9.10}$$

For a spatially isotropic system, the Fermi volume is given by

$$V_L = v_2 \times \pi\left(N_L^x\right)^2 = \frac{1}{2}\frac{\pi^3}{V}\left[\sum_{j=1}^{\phi^*} \frac{1}{2i}\oint_{C_j^g(\phi)} \frac{d\phi}{Q_g(\phi)}\right]^2 \,, \tag{9.11}$$

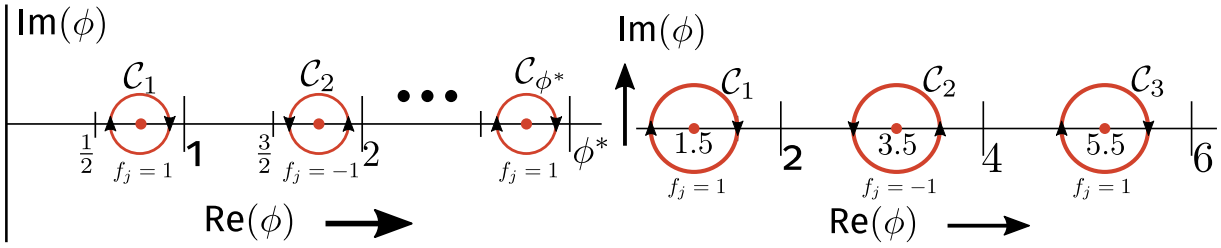

Figure 7.14: *Top: Contours C_j used to integrate over Q_0^{-1} in eq. (9.6). Tall vertical lines represent integer values of $Re(\phi)$. All contour start and end within two adjacent integer values. The final contour C_{ϕ^*} ends just short of $Re(\phi) = \phi^*$. Note the alternating direction of the contours brought about by the alternation of f_j in going from $j = 1$ to $j = 2$, and so on. Bottom: Contours C_j^g for $t_{g,z} = 2$, centered at $2\left(1-\frac{1}{4}\right), 2\left(2-\frac{1}{4}\right)$ and $2\left(3-\frac{1}{4}\right)$. Note the alternating directions of the contours.*

where V is the real space volume of the system, and $v_d = (2\pi)^d / V$ is the volume of the smallest unit in $k-$space. For a generally anisotropic Fermi volume, each direction in the $d-$dimensional $k-$space can be completely specified by an angular coordinate θ with respect to some predefined coordinate system. For each direction $\hat{\theta}$, we can insert a gauge field $\vec{A} = A\hat{\theta}$ and take the thin torus limit in this direction, obtaining thereby the $g-$partite information $I^g(\phi_\theta)$ for length l in the direction perpendicular to $\hat{\theta}$. With the $\theta-$dependent I^g, one can then define the quantity $Q_g(\phi_\theta)$ which counts the number of states N_L^θ in the direction $\hat{\theta}$ inside the Fermi volume. In this way, the total Fermi volume can be obtained by integrating over θ:

$$V_L = \frac{\pi^2}{4V}\int_0^{2\pi} d\theta \left[\sum_{j=1}^{\phi_\theta^*} \frac{1}{2\pi i}\oint_{C_j^g(\phi)} \frac{d\phi}{Q_g(\phi)}\right]^2 . \tag{9.12}$$

It is important to note that the quantity V_L is independent of the RG index g, and is thus identical in value for all g members of the hierarchy at the gth step of the coarse-graining process.

The topological nature of Luttinger volume can be made further manifest by expressing it in terms of winding numbers, following Ref. [51] for the case of interacting electrons. To do so, we point out that the integrand $Q_g^{-1}(\phi)$ can be written as a derivative:

$$\frac{1}{Q_g(\phi)} = \frac{\sqrt{2}}{\pi}\frac{\partial}{\partial\phi}\ln Y_j^g = \frac{\sqrt{2}}{\pi}\frac{1}{Y_j^g}\frac{\partial Y_j^g}{\partial\phi} , \tag{9.13}$$

where

$$\begin{aligned} Y_j^g(\phi) &\equiv \left[\frac{f_j \tan 3\pi/8 - \tan\left(\pi f_{g,z}\phi/2\right)}{\tan\left(\pi f_{g,z}\phi/2\right) - \tan\left(\pi/8\right)}\right]^{f_j} \\ &= \begin{cases} \frac{\tan 3\pi/8 - \tan\left(\pi f_{g,z}\phi/2\right)}{\tan\left(\pi f_{g,z}\phi/2\right) - \tan(\pi/8)}, & \text{when } j = \text{odd, and} \\ \frac{\tan\left(\pi f_{g,z}\phi/2\right) + \tan(\pi/8)}{-\tan 3\pi/8 - \tan\left(\pi f_{g,z}\phi/2\right)}, & \text{when } j = \text{even} . \end{cases} \end{aligned} \tag{9.14}$$

Substituting this into the expression for 2−dimensional isotropic Luttinger volume in eq. (9.11), we obtain

$$V_L = \frac{\pi^3}{V}\left[\sum_{j=1}^{\phi^*}\frac{1}{2\pi i}\oint_{Y_j^g(C_j^g)}\frac{\mathrm{d}Y_j^g}{Y_j^g}\right]^2 . \tag{9.15}$$

As before, the specific integral in the above expression is a winding number that counts the number of times the contour $Y_j^g(C_j^g)$ winds around the singularity at $Y_j^g = 0$. Note that these are the same singularities that exist at the centers of the contours C_j^g and that are picked up in, for example, eq. (9.3). To demonstrate this, we point out that the centers of the contours are given by $\phi = t_{g,z}\left(j-\frac{1}{4}\right), j = 1, 2, \ldots, \phi^*$. At these values, we have

$$\tan\left(\frac{\pi f_{g,z}\phi}{2}\right) = \tan\left(\frac{\pi j}{2}-\frac{\pi}{8}\right) = \begin{cases}\tan\frac{3\pi}{8}, j = 1, 3, \ldots \\ -\tan\frac{\pi}{8}, j = 2, 4, \ldots\end{cases} \tag{9.16}$$

Comparing with eq. (9.14), we can see that the numerators of Y_g^j are zero at these values of ϕ for both even and odd values of j. This leads to $Y_g^j = 0$, and hence a singularity in $\frac{dY_g^j}{Y_g^j}$. These values of the flux are therefore the common singularities that are picked up by the poles of $Q_g^{-1}(\phi)$ as well as the winding numbers.

We now define w_g^j as the winding number for the curve $Y_g^j(C_j^g)$ around $Y_g^j = 0$, and $\mathcal{W}(\phi^*) = \sum_{j=1}^{\phi^*} w_j^g$ as the total winding number for all the curves $\left\{Y_j^g\left(C_j\right), j = 1, 2, \ldots\right\}$. Then, the isotropic Fermi volume takes the compact form

$$V_L = \frac{\pi^3}{V}\mathcal{W}(\phi^*)^2 . \tag{9.17}$$

7.9.2 A relation between the quantum hall Chern numbers and Luttinger's volume

Interestingly, the above method employed in using entanglement measures to extract the Luttinger volume can also be applied (with suitable modifications) to an integer quantum hall system (generated upon placing the system in a strong transverse magnetic field) to obtain the number of filled Landau levels (a Chern number). To begin, we imagine a system of free non-relativistic electrons in a cylinder geometry (fig. 7.16), and placed in a magnetic field $\nabla\times\vec{A} = \vec{B}$ that points radially outwards. The field $\vec{B}$ generates Φ flux quanta through the surface of the cylinder. An Aharonov-Bohm flux $\vec{A}' = -2\pi\phi/L_x\hat{x}$ is also placed in the x−direction (i.e., along the circumference of the cylinder). We divide the cylinder into two subsystems A and B (fig. 7.16), such that tuning the dimensionless flux ϕ by 1 transfers a charge equal to the first Chern number, from A to B. The translation invariance in the x−direction ensures that the momentum k_x are good quantum numbers; for each value of k_x, we can define the matrix elements of the single-particle correlation matrix $G(k_y)$ for the subsystem A as [645, 646]

$$G_{ij}^A(k_x) = \langle\psi_{\mathrm{gs}}|c_{k_x,i}^\dagger c_{k_x,j}|\psi_{\mathrm{gs}}\rangle , \tag{9.18}$$

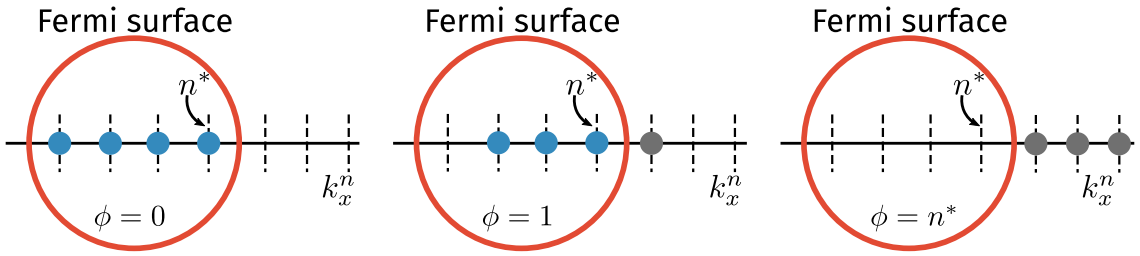

Figure 7.15: *Spectral flow of the states within the Fermi voume. The red curve represents the Fermi surface. Upon tuning the flux ϕ, the $k-$space states (indicated in the form of dotted lines along the k_x-axis) are shifted towards the Fermi surface. The blue circles represent electrons with momenta below k_F, and are part of the ground state. On the other hand, the grey circles represent particles with momenta above k_F: they have moved out of the system, and into the reservoir connected to it (see discussion in main text). Each time ϕ changes by 1, the state nearest to the Fermi surface moves out of the Fermi volume. Tuning ϕ by n^* empties the entire Fermi volume.*

where $|\psi_{\rm gs}\rangle$ is the ground state and i, j represent the degrees of freedom other than k_x. The total matrix G^A is constructed by joining the smaller blocks $G^A(k_x)$. As ϕ is varied, the variation of the trace of the flux-dependent matrix $G^A(\phi)$ is linear in the flux ϕ: $\mathrm{Tr}\left[G^A(\phi)\right] - \mathrm{Tr}\left[G^A(0)\right] = -\frac{1}{e}\sigma_H\phi$. This implies that as long as there are extended states at sufficiently small energies, we will have spectral flow that can be captured through the integral:

$$-\frac{\sigma_H}{2\pi i e}\int_{C_H}\frac{d\phi}{\mathrm{Tr}\left[G^A(\phi)\right] - \mathrm{Tr}\left[G^A(0)\right]}\,, \tag{9.19}$$

where C_H is a circle of radius $1/2$ in the complex plane centered at $\phi = 0$. This integral is zero if there is no spectral flow, i.e., the effect of the gauge field can be removed by a gauge transformation and the trace is insensitive to the flux. In order to count the number of filled Landau levels (essentially, the filling factor ν), we can now vary the flux quanta Φ (due to $\vec{B}$) so as to change the filling from ν to 0:

$$\nu = -\frac{\sigma_H}{2\pi i e}\sum_{\Phi'=\Phi}^{\Phi^{\rm max}}\int_{C_H}\frac{d\phi}{\mathrm{Tr}\left[G^A_{\Phi'}(\phi)\right] - \mathrm{Tr}\left[G^A_{\Phi'}(0)\right]}\,. \tag{9.20}$$

The subscript Φ' on G^A indicates that the correlations depend on the variable magnetic field $\vec{B}'$. The upper limit $\Phi^{\rm max}$ is given by the lowest value of the magnetic field $\vec{B}'$ for which only one Landau level is filled. The magnetic field is varied such that exactly an integer number of Landau levels are filled at any given value. Importantly, the filling factor ν is known to be a Chern number C (Φ) [257,647].

We can also relate eq. (9.20) to the entanglement of the system by introducing the entanglement spectrum [246, 259], which refers to the set of eigenvalues $\left\{\lambda^A_\chi(k_x)\right\}$ of the reduced density matrix $\rho^A(k_x)$ for subsystem A corresponding to the momentum mode k_x in the $x-$direction and χ is a particular configuration of the degrees of freedom $\{i\}$ in the $y-$direction. We have the relation [646]

$$\lambda^A_\chi(k_x) = \mathrm{Det}\left[P_\chi G^A(k_x)\left(1 - P_\chi\right)G^A(k_x)\right]\,, \tag{9.21}$$

where P_χ is an operator that projects on to the subset of states $\{j\}$ in $\{i\}$ that are occupied in the configuration χ. This relation between G^A and the eigenvalues λ then leads to the same conclusion

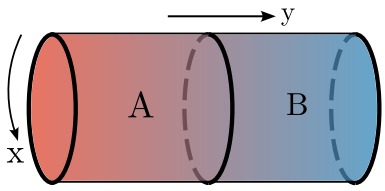

Figure 7.16: *Cylindrical geometry for the integer quantum Hall system, with a magnetic field $\vec{B}$ pointing radially outwards through the surface of the cylinder. An Aharanov-Bohm vector potential acts in the $x-$direction (i.e., along the circumference). The entanglement is calculated between the subsystem A and its compliment B.*

as in the case without the magnetic field: the pole structure of the entanglement spectrum encodes the topological information of the system revealed in eq.(9.20). In the case of zero magnetic field, the topological quantity revealed from the pole structure was a winding number ($\mathcal{W}$), while in the present case it is a Chern number.

Finally, we reveal the connection between the winding numbers $\mathcal{W}$ in the metallic case and the Chern numbers in the integer quantum Hall system. The degeneracy of each Landau level is equal to the number of flux quanta Φ generated by the magnetic field B. Since the total number of particles in the system is fixed, the electronic states of the filled Fermi sea that form the Luttinger volume (in the absence of the external B-field) are redistributed into the Landau levels with the appropriate degeneracy as a strong transverse magnetic field is turned on. Thus, we have the constraint that the total number of occupied states $C \times \Phi$ in the quantum hall system (C being the Chern number and equal to the number of filled Landau levels) must be equal to $\pi \left(N_L^x\right)^2$, the total number of occupied states in the metallic system. Combining eqs. 9.10 and 9.17 with this discussion then allows us to relate C to the winding number $\mathcal{W}(\phi^*)$:

$$C \times \Phi = \left\lfloor \frac{\pi}{4} \mathcal{W}(\phi^*)^2 \right\rfloor = \frac{V_L}{v_2} \,, \tag{9.22}$$

where $v_2 = 4\pi^2/V$ is the volume of the $k-$space unit cell (defined below eq. (9.10)) and $\lfloor \cdot \rfloor$ is the floor function and returns the largest integer less than or equal to the argument.

7.10 Conclusions and Outlook

In summary, we have shown that considering the renormalisation group flows of the spectral gap coupling of a system of non-interacting electrons in $2+1-$dimensional theory leads to hierarchical arrangement of the entanglement with scale, and that the geometrical part of the entanglement can be described as the emergence of an additional spatial dimension, leading to holographic expressions for geometric parameters like distance and curvature. We show that changing the boundedness of the holographic space involves a topological transition with the Fermi surface of the boundary theory turning critical, and involves the generation of a geometric wormhole between the UV and IR degrees of freedom. For the massless case, the presence of an Aharonov-Bohm flux generates a geometry-independent term in the entanglement entropy which can be linked to the Luttinger

volume of the gapless fermionic system. By placing the system of 2 + 1 dimensional electrons in a strong magnetic field, we argue that the Chern number topological invariant for the ground states of the integer quantum Hall ground system are constrained by the value of the Luttinger volume in the underlying metallic system (i.e., prior to the insertion of the field).

How robust are our conclusions towards the inclusion of electronic correlations? Given the adiabatic continuity that links Fermi liquids to the non-interacting Fermi gas, i.e., the preservation of the k-space quantum numbers under adiabatic inclusion of (screened) inter-particle interactions, we expect our results to be equally valid for the many-particle entanglement of the excitations described by the fixed point effective theory for the Fermi liquid. This also suggests that our results for the wormhole geometry and the stress-energy tensor relation at the critical Fermi surface apply very generally to phase transitions that destabilise and gap out the Fermi surface. Specifically, this has profound implications for metal-insulator transitions driven by strong correlations. Non-Fermi liquids are, however, not adiabatically continuous to the Fermi gas. Thus, it should be interesting to adapt our approach to the study of interacting models of electrons that lead to gapless non-Fermi liquids (including those that are known to appear at quantum critical points related to the breakdown of a Fermi liquid). For instance, Ref. [648] reports that the second Renyi entropy of a thin k-space shell proximate to the Fermi surface is related to the quasiparticle residue; how would this change in a non-Fermi liquid? It also appears interesting to identify the effects of electronic correlations on various aspects of the emergent space. The renormalisation group techniques applied in Refs. [462, 648–651] could also be worth investigating towards answering these questions.

It is interesting to note that our results point towards a broader similarity between the gapless fermionic systems considered here and gapped topologically ordered quantum liquids. Recall that the latter are known to possess a ground state degeneracy that is dependent on the topological nature of the interacting electronic system, leading to a subsystem entanglement entropy that has a geometry-independent subleading piece (S_{topo}) referred to as the topological entanglement entropy. It was shown by some of us recently [293] that for a collection of N subsystems (CSS) that form a closed annular structure, the $n-$partite quantum entanglement information measures I^n $(3 \leq n \leq N)$ are a topological invariant equal to the product of S_{topo} and the Euler characteristic of the planar manifold on which the CSS is embedded. This appears to be analogous to our finding of the hierarchical sequence of quantities $\{Q_g\}$ defined at a particular RG step (and arising out of the topological flux-dependent piece of the entanglement entropy), all of whom encode the same Luttinger volume for the gapless systems we have studied (eq. (**9.12**)). Further, the robustness of the n-partite information I^n against small deformations of the CSS in a topologically ordered system can be compared to the invariance of N_L^x to small deformations of the contours $C_1, C_2, \ldots$ (see right panel of Fig. 7.14). It appears tempting to speculate on a possible universal origin underlying these similarities (see also [462] for a recent investigation of the entanglement properties of various quantum liquids).

Our results lead to a number of interesting questions. Firstly, the convergence parameter θ is reminiscent of the expansion rate of congruence flows on Riemannian manifolds in the context of the Raychaudhuri equation [643]. While the evolution equation for θ (eq. (**7.6**)) obtained by us is not of the same form (as there is no time variable, neither is there a θ^2 term in the expansion rate), we do expect such an equation to hold for an appropriately defined expansion parameter [644, 652]. This likely requires the introduction of temporal dynamics of the emergent spatial dimension, and lies well beyond the purview of the present work. Secondly, it remains to be seen how the geometry-

independent part of the entanglement behaves in the presence of a mass ($m > 0$) for the Dirac fermions: a spectral gap is expected to have consequences for Luttinger's theorem [348] (see also eq.(2.19)), as well as for the many-particle entanglement. For instance, Ref. [648] reports that the second Renyi entropy shows the signatures of the condensation of Cooper pairs in the BCS problem.

Finally, we would like to point out an interesting conclusion that emerges from our analysis. As observed by us, the system considered here shows a hierarchy of multipartite entanglement measures beyond just the mutual information. Further, we have shown that the mutual information leads to the emergence of the holographic dimension. However, whether the higher-party measures also have a holographic interpretation remains an open question. We note that studies of the time-variation of tripartite information during an equilibrium process after the injection of energy suggest that it remains negative throughout the process [653–655], indicating that care must be taken in defining geometric measures using it. Nevertheless, our study raises the possibility of obtaining a generalisation of the gauge-gravity duality from the perspective of many-particle entanglement. We speculate that the higher order information measures will lead to a modification of the universal entanglement Hamiltonian obtained at criticality. Further, that these modifications can be visualised as a *hypergraph*: just as a graph contains edges that connect any two nodes, a hypergraph contains *hyperedges* that can connect more than two nodes. The eigenvalues $\epsilon^{(n)}$ (with $n > 2$) of the entanglement Hamiltonian would act as hyperedges connecting the degrees of freedom $\{i, j, \ldots\}$. We leave an investigation of these aspects to future works.

Appendix A: Evaluation of multi-partite information

We define the multipartite information among g sets $\{\mathcal{A}_z(i)\}$ as [293]

$$I^g_{\{\mathcal{A}_z(i)\}} = \sum_{r=1}^{g} (-1)^{r-1} \sum_{\beta\in\mathcal{P}(\{\mathcal{A}_z(i)\})}^{|\beta|=r} S_\beta \,, \tag{10.1}$$

where $\mathcal{P}(\{\mathcal{A}_z(i)\})$ is the power set of $\{\mathcal{A}_z(i)\}$, and $|\beta| = r$ implies that we sum only over those sets β that have r number of elements in them. We will first evaluate the internal sum σ_r over the set β for a general r:

$$\sigma_r = \sum_{\beta\in\mathcal{P}(\{\mathcal{A}_z(i)\})}^{|\beta|=r} S_\beta \,. \tag{10.2}$$

For this, we first note that following eq. (3.15), the entanglement entropy (EE) of the union of a given sequence of sets $\{i\}$ is given by the EE of the set with the highest (lowest) index for a positive (negative) z. As a result, the EE S_β for the set β is simply $S_\beta = \theta(z)S_{\min(\beta)} + \theta(-z)S_{\max(\beta)}$. If $n_j^{(r,+)}$ ($n_j^{(r,-)}$) is the number of sets of cardinality r that have the element $\mathcal{A}_{j,z}$ as the element with the smallest (largest) index j, the internal sum can be written as

$$\sigma_r = \sum_{j=1}^{g-(r-1)} \theta(z) n_j^{(r,+)} S_{j,z} + \sum_{j=r}^{g} \theta(-z) n_j^{(r,-)} S_{j,z} \,. \tag{10.3}$$

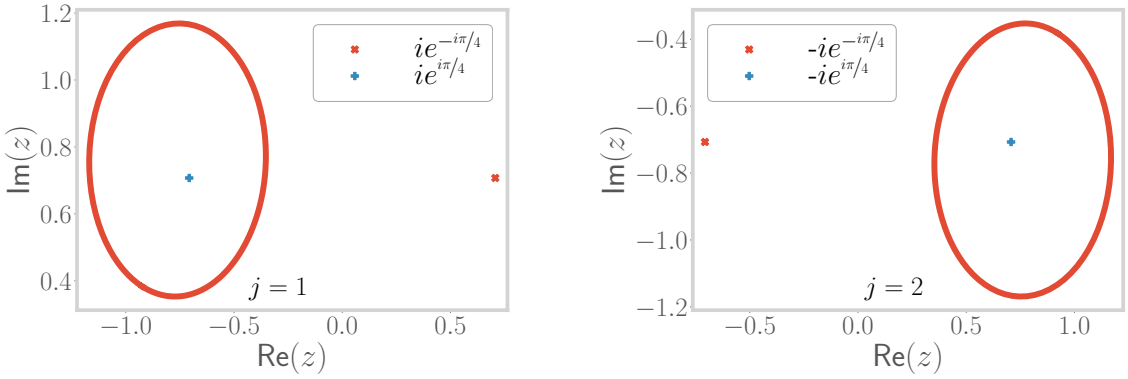

Figure 7.17: *Contours $z(C_j)$ for two values of j employed for evaluating the integral eq.(10.8), and the locations of the poles $z^{\pm}_{\pm}$. For each j, only one pole (shown in blue) contributes, as the other (shown in red) is not enclosed by the contour.*

The number $n_j^{(r,+)}$ corresponds to the number of ways one can pick $r-1$ elements out of a set of $g-j$ elements: $n_j^{(r,+)} = \binom{g-j}{r-1}$. Similarly, $n_j^{(r,-)}$ corresponds to the number of ways one can pick $r-1$ elements out of a set of j elements: $n_j^{(r,-)} = \binom{j}{r-1}$. We can also extend the limits on the two summations by defining $\binom{n}{m} = 0$ for $n < m$. With these considerations, eq. (10.3) takes the form

$$\sigma_r = \sum_{j=1}^{g} \left[\theta(z)\binom{g-j}{r-1} + \theta(-z)\binom{j}{r-1}\right] S_{j,z} \,. \tag{10.4}$$

This can now be substituted into the full expression for the multipartite equation, giving

$$\begin{aligned} & I^g_{\{\mathcal{A}_z(i)\}} \\ &= \sum_{r=1}^{g} (-1)^{r-1} \sum_{j=1}^{g} \left[\theta(z)\binom{g-j}{r-1} + \theta(-z)\binom{j}{r-1}\right] S_{j,z} \\ &= \sum_{j=1}^{g} S_{j,z} \left[\theta(z) \sum_{r=0}^{g-j} (-1)^r \binom{g-j}{r} + \theta(-z) \sum_{r=0}^{j} (-1)^r \binom{j}{r}\right] . \end{aligned} \tag{10.5}$$

From the binomial theorem, we can now recognise each internal sum as over r as a polynomial expansion. That is, upon comparing with $(x-1)^n = \sum_{m=0}^{n} \binom{n}{m} (-1)^m x^{n-m}$, we obtain $\sum_{r=0}^{g-j} (-1)^r \binom{g-j}{r} = \lim_{x\to 1}(x-1)^{g-j} = \delta_{g,j}$. Similarly, the other sum evaluates to $\delta_{j,0}$. Substituting these into the expression for $I^g_{\{\mathcal{A}_z(i)\}}$ gives

$$\begin{aligned} I^g_{\{\mathcal{A}_z(i)\}} &= \sum_{j=1}^{g} S_{j,z} \left[\theta(z)\delta_{g,j} + \theta(-z)\delta_{j,0}\right] \\ &= \theta(z) S_g + \theta(-z) S_0 \,. \end{aligned} \tag{10.6}$$

By noting that S_g and S_0 are, respectively, the EE of the intersection set of $\{\mathcal{S}_z(i)\}$, one can combine the two terms in the previous equation into

$$I^g_{\{\mathcal{A}_z(i)\}} = \theta(z)S_g + \theta(-z)S_0 = S_{\cap\{\mathcal{A}_z(i)\}} \ . \tag{10.7}$$

Appendix B: Evaluation of the contour integral that counts poles

We prove eq. (9.3) in this appendix. The integral in question is given by

$$\mathcal{I} = \oint_{C_j} \frac{d\phi}{Q_0(\phi)} = \oint_{C_j} \frac{d\phi}{\frac{1}{\sqrt{2}} - |\sin \pi\phi|} \ , \tag{10.8}$$

where C_j is the contour shown in Fig. 7.13 and the variable ϕ is given by $\phi = \left\{\phi_j + \frac{1}{8}e^{i\theta} : \theta \in [0, 2\pi]\right\}$, where $\phi_j = j - \frac{1}{4}$ is the center of the contour. In order to evaluate the integral, we make a variable change: $z = e^{i\pi\phi}$, giving $dz = i\pi z\, d\phi$ and $\sin \pi\phi = \frac{1}{2i}\left(z - \frac{1}{z}\right)$. Depending on the value of j, $\sin \pi\phi$ can be either positive or negative. We denote either case by a subscript $\mathcal{I}_\pm$ corresponding to the contour $C_\pm$, giving $|\sin(\pi\phi)| = \pm \sin(\pi\phi)$. Casting the integral in terms of z, we obtain

$$\mathcal{I}_\pm = \frac{1}{i\pi} \oint_{z(C_\pm)} \frac{dz/z}{\frac{1}{\sqrt{2}} \mp \frac{1}{2i}\left(z - \frac{1}{z}\right)} = \oint_{z(C_\pm)} \frac{\mp\frac{2}{\pi}\, dz}{\left(z \mp \frac{i}{\sqrt{2}}\right)^2 - \frac{1}{2}} \ . \tag{10.9}$$

The integrand in $\mathcal{I}_+$ has two simple poles at $z^\pm_+ = +ie^{\mp i\pi/4}$. Similarly, the integrand in $\mathcal{I}_-$ has two simple poles at $z^\pm_- = -z^\pm_+$. We plot the contour and the two poles for two contours of opposite signature in Fig. 7.17; it is clear that only the pole at $z^+_\pm$ contributes to the integral. Using the residue theorem, the integral evaluates to

$$\begin{aligned} \mathcal{I}_\pm &= \oint_{z(C_\pm)} \frac{\mp\frac{2}{\pi}\, dz}{(z - z^+_\pm)(z - z^-_\pm)} \\ &= \mp\frac{2}{\pi} 2\pi i \lim_{z \to z^+_\pm} \frac{1}{z - z^-_\pm} \\ &= \mp 2\sqrt{2} i \ . \end{aligned} \tag{10.10}$$

This proves eq. (9.3).

Chapter 8

Summary, Conclusions and Future Work

In the final chapter, we will summarise the results obtained from the research carried out in the thesis, clarify the major conclusions derived from them, and point out some avenues for further work. In a nutshell, we have applied a two-pronged approach to metal-insulator transitions through this body of work. The first approach tackles the effects of strong local correlation through the development of a new method that maps interacting fermionic models to quantum impurity models. The other complimentary approach involves studying the effects of metal-insulator transition on entanglement renormalisation, and characterising phases through the emergent geometry resulting from such flows.

We began, in the "Abstract", by listing some important questions that we intended to address through this thesis. We will now clarify how this body of work answers those questions.

Is there a minimal but effective quantum impurity model Hamiltonian that describes the Mott MIT of the $1/2$*–filled Hubbard model on the Bethe lattice in infinite dimensions?* In Chapter 3, we show that an extended Anderson impurity model that hosts local attractive correlation in the conduction bath proximate to the impurity site is capable of faithfully capturing the $d = \infty$ Mott MIT, with sufficient detail. Indeed, we show that the attractive correlation promotes charge fluctuations in the conduction bath which ultimately destabilise Kondo screening and introduce a local moment fixed point in the phase diagram of the impurity model. We find that the metallic excitations at such a transition is of the non-Fermi liquid kind; this provides some preliminary understanding of quantum critical scaling observed in DMFT studies of such systems at high temperatures. Our explicit construction of Kondo breakdown in a simple prototypical system is important because it makes possible the extension of such an approach to more complicated problems where tackling the lattice model directly is problematic and an auxiliary model approach is more pragmatic.

Overall, this work underscores the ubiquity of non-Fermi liquid physics, long-range entanglement and topological changes in fermionic criticality. This is especially relevant to several classes of materials that display non-Fermi liquid behaviour and Fermi surface reconstruction at high temperatures above a quantum critical point. In our case, the topology emerged in the form of a change in the excess charge density contributed to transport by the impurity. Often in correlated systems, phase transitions do not involve the crystallisation of local order paramters. Instead, they are marked by changes in entanglement patters. Our demonstration of this in a simple model likely means it is a very universal feature of correlation-driven transitions. In terms of methodological advances, our

approach bypasses the need for a self-consistent treatment of the auxiliary model and in the process provides increased transparency as well as highly reduced computational costs.

Is it possible to map the renormalisation group fixed points of such lattice models to those of quantum impurity models? We have now demonstrated this (in Chapters 4, 5 and 6), in the form of our "tiling" framework. The obvious differences between lattice models and impurity models is that the latter lacks translation invariance and hosts correlations locally. We bridge these differences by using a many-body Bloch's theorem that restores translation invariance and reconstructs the Hamiltonian and wavefunctions of the lattice model from that of the impurity model. We further use these relations to map diagnostics such as correlation functions and entanglement measures that includes inter-auxiliary model contributions that encode non-local correlations and wavefunction coherence.

The workflow for applying the tiling approach is the following. We first use an impurity solver to obtain the low-energy physics of the impurity model; in this thesis, we have used the unitary renormalisation group method. By using our tiling relations, we reconstruct ground state static correlations and dynamical correlations of the lattice model from that of the auxiliary model. This effectively maps the renormalisation group flows of one model to those of the other. In fact, our approach goes beyond and captures relations between wavefunction structures as well, in the form of entanglement measures. One of the most important features of our approach is the flexibility it affords in terms of lattice geometry, band structure, presence of multiple orbitals and other aspects. These features can be easily tuned in the lattice model by tuning the appropriate feature within the impurity model; the relevant change is reflected in the form of updated mappings between the lattice and auxiliary model.

A key challenge in the field of quantum matter is understanding how quasiparticle breakdown in the Fermi liquid gives rise to the strange metal and pseudogap states in the cuprates, and how it connects to both the Mott insulating and superconducting phases. We address this in Chapter 5 of the thesis, by applying our "tiling" framework to the problem of the extended Hubbard model on the 2D square lattice. The primary result obtained is that the parent metallic phase of the Mott insulator is not the Fermi liquid; instead, upon increasing the correlation strength, the Fermi liquid undergoes a transition at $T = 0$ into a Mott metal-pseudogap phase that has deconfined holes and doubles as non-Fermi liquid excitations and displays long-range entanglement and large self-energy at $\omega = 0$. The formation of the Mott insulator then involves the opening of a hard gap in the spectrum that confines these holes and doubles into locally bound pairs. In summary, our work shows how quasiparticles initially morph into holes and doubles which eventually bind together to form the Mott insulator.

One of the major outcomes of our work is the establishment of the pseudogap as a bonafide phase of matter at $T = 0$, characterised by (i) an anomalous self-energy exponent, (ii) unbound holons and doublons as the long-lived excitations, (iii) coexistence of Fermi arcs and "Luttinger arcs" (regions of zeros of Greens function) along the $E = 0$ surface, and (iv) long-range multipartite entanglement that is much more fascinating than the entanglement structure in either the Fermi liquid or the Mott insulator. Our observed evolution of the phases, while at half-filling and at $T = 0$, is quite reminiscent of the phenomenology of the cuprates observed at finite temperatures and as a function of doping. This is very likely not an accident and hints at a convergence of the essential physics of fermionic criticality within our approach. Finally, our work briefly sheds light on the microscopic justification behind a recently proposed overarching framework for Mottness, in terms of the break-

ing of a generalised symmetry involving Luttinger's theorem and the emergence of an anomaly in the low-energy theory for the pseudogap and Mott insulator. Our approach, by demonstrating the emergence of self-energy poles on the erstwhile Fermi surface, motivates why the Luttinger-Ward functional (that depends on the analyticity of the self-energy) becomes singular due to increasing correlations and hence leads to the appearance of the anomaly that is absent in the Fermi liquid phase.

In heavy-fermion systems, a complete description of the Kondo breakdown class of transitions (that does not rely on spontaneous symmetry breaking within the correlated $f-$layer) is currently missing, especially with regards to capturing both the heavy Fermi liquid and RKKY-dominated phases. In particular, it would be interesting to place this phenomenology in the context of the Mott transition in low dimensions, and identify the appropriate order parameter for such transitions in the absence of spontaneous symmetry breaking. In Chapter 6, we investigated these questions from a bilayer Hubbard model, using a two-impurity model as the auxiliary model. Our findings further support some of the broad conclusions derived from the previous chapters. In particular, we find that entanglement measures are useful for tracking the small to large Fermi surface transition. Specifically, a long-range inter-bath mutual information is maximised at the critical point, while the inter-impurity mutual information broadly acts as an order parameter for the transition. This again showcases the key role played by entanglement in the classification and description of such phases.

We have also investigated the presence of pseudogap-like phases in the vicinity of the transition. Indeed, we find that similar to our findings on the extended Hubbard model, the opening of the hybridisation gap is anisotropic along the Fermi surface, appearing initially at the antinode and later at the node. This suggests a partially gapped phase emerging as a result of tuning the inter-layer hybridisation, and has similarities with the phenomenology of the Mott metal phase observed by us in the earlier work.

What effect does a topological change in a Fermi surface have on the additional "entanglement" dimension generated for the system "under evolution through renormalisation"? What happens to the topological signatures of entanglement entropy across a Fermi surface instability? This is addressed in Chapter 7, where we adopt an alternative approach to fermionic criticality – entanglement holography. Within a model of non-interacting fermions in 2D with a tunable mass gap, we investigated the renormalisation of entanglement under scaling transformations, and linked this to the emergence of an additional dimension by mapping mutual information to distance. In other words, we showed that entanglement geometry is equivalent to the geometry of space, in the form of a concrete demonstration of the holographic principle. One of the major outcomes of this exercise was that we were able to show that tuning our model through a gap closing transition leads to a topological change in the emergent additional space: its curvature changes sign, and the transition point in particular displays a wormhole geometry that connects the UV and IR scales of the theory. This, in the spirit of the other chapters as well, highlights the importance of topology in understanding Fermi surface instabilities.

Unlike topologically ordered phases that contain a distinct topological piece in the subsystem entanglement entropy, gapless and symmetry-broken gapped phases do not have a topological component. Nevertheless, in the search for a relation between Fermi surface topology and entanglement, we showed that the subsystem entanglement entropy can be used to define a topological invariant of the metallic phase. Through flux-insertion arguments, we show that this invariant is essentially

equivalent to the Luttinger volume of the system, which is a well known topological invariant. The insulating phase derived from such a metallic phase is ordinarily topologically trivially, but hosts integer quantum hall plateaus in the presence of a strong magnetic field. We go on to show that the topological invariant in the metallic phase can be linked to the topological invariant on the IQHE side – the Chern number of the occupied states. This shows that under suitable conditions, there is a "conservation of topology" across a Fermi surface instability from a metal into an integer quantum hall (bulk) insulator.

I close by discussing some open questions motivated by this research and some avenues for further work. All our results have been obtained at zero temperatures and at half-filling. Some obvious extensions, therefore, include studying these models at finite temperatures and with doping. In the context of the extended Anderson impurity model (Chapter 3), our work does not completely address the origin of quantum critical behaviour above the finite temperature critical point in DMFT studies of the Hubbard mode in infinite dimensions. *Which part of our impurity model phase diagram do those fluctuations emanate from?* Moreover, the Anderson impurity model is known to host additional fixed points when valence fluctuations are allowed. *What additional physics do these fixed points bring in when coupled with the bath correlation which is crucial to our extension?* These are questions that need additional investigation. With regard to the our tiling study on the extended Hubbard model (Chapter 4 and 5), our observation of subdominant pairing fluctuations near the transition is indicative of putative superconductivity. *Can these pairing tendencies condense into Cooper pairs under doping?* Moreover, our non-Fermi liquid does not show strange metal behaviour. *Can finite temperature calculations of the model reveal such behaviour, particularly in the form of linear-T resistivity?* The large scattering rate and multipartite nature of entanglement in the Mott metal phase is certainly indicative of a strong thermalisation of electrons that is often associated with strange metal behaviour.

In the heavy fermions project (Chapter 6), we have already obtained interesting results at half-filling in the form of quantum critical entanglement measures and a phase with partial hybridisation gap on the Fermi surface. *Further studies away from half-filling should clarify how this partial gapping interplays with the Fermi surface reconstruction observed when the heavy Fermi liquid is born from the insulating phase.* Finite temperature studies will be useful in probing the phase diagram above the quantum critical point. A relatively less studied part of the phase diagram is the RKKY-dominated insulating phase. *Investigating this phase for spin liquid signatures is a major problem that deserves attention.* Finally, we note that since Chapter 7 deals with the holographic properties of Dirac fermions particularly, it should be interesting to check whether the results are modified if one replaces Dirac fermions with more general Dirac-Lifshitz fermions ($E(k) \sim k^{\alpha}$, $\alpha \geq 1$).

8.1 Revisions

Bibliography

[1] John Hubbard. Electron correlations in narrow energy bands. In *Proceedings of the royal society of london a: mathematical, physical and engineering sciences*, volume 276, pages 238–257. The Royal Society, 1963.

[2] N. F. Mott. Metal-insulator transition. *Rev. Mod. Phys.*, 40:677–683, Oct 1968.

[3] R F Milligan and G A Thomas. The metal-insulator transition. *Annual Review of Physical Chemistry*, 36(1):139–158, 1985.

[4] Masatoshi Imada, Atsushi Fujimori, and Yoshinori Tokura. Metal-insulator transitions. *Reviews of modern physics*, 70(4):1039, 1998.

[5] Patrick A. Lee, Naoto Nagaosa, and Xiao-Gang Wen. Doping a mott insulator: Physics of high-temperature superconductivity. *Rev. Mod. Phys.*, 78:17–85, Jan 2006.

[6] A. Pustogow, M. Bories, A. Löhle, R. Rösslhuber, E. Zhukova, B. Gorshunov, S. Tomić, J. A. Schlueter, R. Hübner, T. Hiramatsu, Y. Yoshida, G. Saito, R. Kato, T.-H. Lee, V. Dobrosavljević, S. Fratini, and M. Dressel. Quantum spin liquids unveil the genuine mott state. *Nature Materials*, 17(9):773–777, Sep 2018.

[7] G. R. Stewart. Non-fermi-liquid behavior in d- and f-electron metals. *Rev. Mod. Phys.*, 73:797–855, Oct 2001.

[8] Yuan Cao, Valla Fatemi, Ahmet Demir, Shiang Fang, Spencer L. Tomarken, Jason Y. Luo, Javier D. Sanchez-Yamagishi, Kenji Watanabe, Takashi Taniguchi, Efthimios Kaxiras, Ray C. Ashoori, and Pablo Jarillo-Herrero. Correlated insulator behaviour at half-filling in magic-angle graphene superlattices. *Nature*, 556(7699):80–84, Apr 2018.

[9] Yuan Cao, Valla Fatemi, Shiang Fang, Kenji Watanabe, Takashi Taniguchi, Efthimios Kaxiras, and Pablo Jarillo-Herrero. Unconventional superconductivity in magic-angle graphene superlattices. *Nature*, 556(7699):43–50, Apr 2018.

[10] J H de Boer and E J W Verwey. Semi-conductors with partially and with completely filled 3d-lattice bands. *Proceedings of the Physical Society*, 49(4S):59, aug 1937.

[11] N F Mott. The basis of the electron theory of metals, with special reference to the transition metals. *Proceedings of the Physical Society. Section A*, 62(7):416–422, jul 1949.

[12] N. F. Mott. On the transition to metallic conduction in semiconductors. *Canadian Journal of Physics*, 34(12A):1356–1368, 1956.

[13] N. F. Mott. The transition to the metallic state. *The Philosophical Magazine: A Journal of Theoretical Experimental and Applied Physics*, 6(62):287–309, 1961.

[14] Takayuki Isono, Taichi Terashima, Kazuya Miyagawa, Kazushi Kanoda, and Shinya Uji. Quantum criticality in an organic spin-liquid insulator κ-(bedt-ttf)2cu2(cn)3. *Nature Communications*, 7(1):13494, Nov 2016.

[15] P. W. Anderson. New approach to the theory of superexchange interactions. *Phys. Rev.*, 115:2–13, Jul 1959.

[16] Junjiro Kanamori. Electron Correlation and Ferromagnetism of Transition Metals. *Progress of Theoretical Physics*, 30(3):275–289, 09 1963.

[17] Martin C. Gutzwiller. Effect of correlation on the ferromagnetism of transition metals. *Phys. Rev. Lett.*, 10:159–162, Mar 1963.

[18] Antoine Georges, Gabriel Kotliar, Werner Krauth, and Marcelo J Rozenberg. Dynamical mean-field theory of strongly correlated fermion systems and the limit of infinite dimensions. *Reviews of Modern Physics*, 68(1):13, 1996.

[19] W. F. Brinkman and T. M. Rice. Application of gutzwiller's variational method to the metal-insulator transition. *Phys. Rev. B*, 2:4302–4304, Nov 1970.

[20] Martin C. Gutzwiller. Correlation of electrons in a narrow *s* band. *Phys. Rev.*, 137:A1726–A1735, Mar 1965.

[21] Peter Prelovšek, Jure Kokalj, Zala Lenarčič, and Ross H. McKenzie. Holon-doublon binding as the mechanism for the mott transition. *Phys. Rev. B*, 92:235155, Dec 2015.

[22] Sen Zhou, Yupeng Wang, and Ziqiang Wang. Doublon-holon binding, mott transition, and fractionalized antiferromagnet in the hubbard model. *Phys. Rev. B*, 89:195119, May 2014.

[23] Tsutomu Watanabe, Hisatoshi Yokoyama, Yukio Tanaka, and Jun-ichiro Inoue. Superconductivity and a mott transition in a hubbard model on an anisotropic triangular lattice. *Journal of the Physical Society of Japan*, 75(7):074707, 2006.

[24] JM Luttinger. Fermi surface and some simple equilibrium properties of a system of interacting fermions. *Physical Review*, 119(4):1153, 1960.

[25] Joaquin Mazdak Luttinger and John Clive Ward. Ground-state energy of a many-fermion system. ii. *Physical Review*, 118(5):1417, 1960.

[26] Igor Dzyaloshinskii. Some consequences of the luttinger theorem: The luttinger surfaces in non-fermi liquids and mott insulators. *Physical Review B*, 68(8):085113, 2003.

[27] Philip Phillips. *Advanced solid state physics*. Cambridge University Press, 2012. Discussion regarding f-sum rule and dynamical spectral weight transfer in pages 394-395, section 12.4 on Cooper pairs and computation of effective two particle energy.

[28] G. Baskaran. An exactly solvable fermion model: spinons, holons and a non-fermi liquid phase. *Modern Physics Letters B*, 05(09):643–649, 1991.

[29] Yasuhiro Hatsugai and Mahito Kohmoto. Exactly solvable model of correlated lattice electrons in any dimensions. *Journal of the Physical Society of Japan*, 61(6):2056–2069, 1992.

[30] Richard M. Martin, Lucia Reining, and David M. Ceperley. *Interacting Electrons: Theory and Computational Approaches*. Cambridge University Press, 2016.

[31] Walter Metzner and Dieter Vollhardt. Correlated lattice fermions in $d = \infty$ dimensions. *Phys. Rev. Lett.*, 62:324–327, Jan 1989.

[32] Antoine Georges. Strongly correlated electron materials: Dynamical mean-field theory and electronic structure. *AIP Conference Proceedings*, 715(1):3–74, 2004.

[33] Jun Kondo. Resistance minimum in dilute magnetic alloys. *Progress of theoretical physics*, 32(1):37–49, 1964.

[34] JR Schrieffer and P.A.Wolff. Relation between the anderson and kondo hamiltonians. *Phys. Rev.*, 149:491, 1966.

[35] Kenneth G Wilson. The renormalization group: Critical phenomena and the kondo problem. *Reviews of Modern Physics*, 47(4):773, 1975.

[36] H. R. Krishna-murthy, J. W. Wilkins, and K. G. Wilson. Renormalization-group approach to the anderson model of dilute magnetic alloys. i. static properties for the symmetric case. *Phys. Rev. B*, 21:1003–1043, Feb 1980.

[37] S Nishimoto and E Jeckelmann. Density-matrix renormalization group approach to quantum impurity problems. *Journal of Physics: Condensed Matter*, 16(4):613, jan 2004.

[38] N. Andrei. Diagonalization of the kondo hamiltonian. *Phys. Rev. Lett.*, 45:379–382, Aug 1980.

[39] P B Wiegmann. Exact solution of the s-d exchange model (kondo problem). *Journal of Physics C: Solid State Physics*, 14(10):1463–1478, apr 1981.

[40] P Nozieres. A "fermi-liquid" description of the kondo problem at low temperatures. *Journal of Low Temperature Physics*, 17:31, 1974.

[41] Ian Affleck. Conformal field theory approach to the kondo effect. *Acta Phys.Polon.B*, 26(1869), 1995.

[42] Anirban Mukherjee, Abhirup Mukherjee, N. S. Vidhyadhiraja, A. Taraphder, and Siddhartha Lal. Unveiling the kondo cloud: Unitary renormalization-group study of the kondo model. *Phys. Rev. B*, 105:085119, Feb 2022.

[43] A. C. Hewson. *The Kondo Problem to Heavy Fermions*. Cambridge University Press, 1993.

[44] T.A. Costi and A.C. Hewson. A new approach to the calculation of spectra for strongly correlated systems. *Physica B: Condensed Matter*, 163(1):179–181, 1990.

[45] T.A. Costi and A.C. Hewson. Static and dynamic properties of the anderson model with conduction electron screening. *Physica C: Superconductivity*, 185-189:2649–2650, 1991.

[46] Ryu Takayama and Osamu Sakai. Excitation spectra of the anderson model with coulomb interaction between localized and conduction electrons. *Physica B: Condensed Matter*, 186-188:915–917, 1993.

[47] Wanda C. Oliveira and Luiz N. Oliveira. Generalized numerical renormalization-group method to calculate the thermodynamical properties of impurities in metals. *Phys. Rev. B*, 49:11986–11994, May 1994.

[48] David C. Langreth. Friedel sum rule for anderson's model of localized impurity states. *Phys. Rev.*, 150:516–518, Oct 1966.

[49] Richard M Martin. Fermi-surface sum rule and its consequences for periodic kondo and mixed-valence systems. *Physical Review Letters*, 48(5):362, 1982.

[50] Masaki Oshikawa. Topological approach to luttinger's theorem and the fermi surface of a kondo lattice. *Physical Review Letters*, 84(15):3370, 2000.

[51] Kazuhiro Seki and Seiji Yunoki. Topological interpretation of the luttinger theorem. *Physical Review B*, 96(8):085124, 2017.

[52] Nozières, Ph. and Blandin, A. Kondo effect in real metals. *J. Phys. France*, 41(3):"193–211", 1980.

[53] J Gan. On the multichannel kondo model. *Journal of Physics: Condensed Matter*, 6(24):4547, jun 1994.

[54] Ian Affleck and Andreas W.W. Ludwig. Critical theory of overscreened kondo fixed points. *Nuclear Physics B*, 360(2):641–696, 1991.

[55] Andreas W. W. Ludwig and Ian Affleck. Exact, asymptotic, three-dimensional, space- and time-dependent, green's functions in the multichannel kondo effect. *Phys. Rev. Lett.*, 67:3160–3163, Nov 1991.

[56] Ian Affleck, Andreas W. W. Ludwig, H.-B. Pang, and D. L. Cox. Relevance of anisotropy in the multichannel kondo effect: Comparison of conformal field theory and numerical renormalization-group results. *Phys. Rev. B*, 45:7918–7935, Apr 1992.

[57] Ian Affleck and Andreas WW Ludwig. Exact conformal-field-theory results on the multichannel kondo effect: Single-fermion green's function, self-energy, and resistivity. *Physical Review B*, 48(10):7297, 1993.

[58] Olivier Parcollet and Antoine Georges. Transition from overscreening to underscreening in the multichannel kondo model: Exact solution at large N. *Phys. Rev. Lett.*, 79:4665–4668, Dec 1997.

[59] Ian Affleck. Non-fermi liquid behavior in kondo models. *Journal of the Physical Society of Japan*, 74(1):59–66, 2005.

[60] V. J. Emery and S. Kivelson. Mapping of the two-channel kondo problem to a resonant-level model. *Phys. Rev. B*, 46:10812–10817, Nov 1992.

[61] David G. Clarke, Thierry Giamarchi, and Boris I. Shraiman. Curie and non-curie behavior of impurity spins in quantum antiferromagnets. *Phys. Rev. B*, 48:7070–7076, Sep 1993.

[62] Gergely Zaránd and Jan von Delft. Analytical calculation of the finite-size crossover spectrum of the anisotropic two-channel kondo model. *Phys. Rev. B*, 61:6918–6933, Mar 2000.

[63] Jan von Delft, Gergely Zaránd, and Michele Fabrizio. Finite-size bosonization of 2-channel kondo model: A bridge between numerical renormalization group and conformal field theory. *Phys. Rev. Lett.*, 81:196–199, Jul 1998.

[64] A. J. Schofield. Bosonization in the two-channel kondo model. *Phys. Rev. B*, 55:5627–5630, Mar 1997.

[65] R Bulla, T Costi, and T Pruschke. Numerical renormalisation group method for quantum impurity systems. *Rev. Mod. Phys.*, 80:395, 2008.

[66] H. B. Pang and D. L. Cox. Stability of the fixed point of the two-channel kondo hamiltonian. *Phys. Rev. B*, 44:9454–9457, Nov 1991.

[67] N. Andrei and C. Destri. Solution of the multichannel kondo problem. *Phys. Rev. Lett.*, 52:364–367, Jan 1984.

[68] A. M. Tsvelick and P. B. Wiegmann. Solution of then-channel kondo problem (scaling and integrability). *Zeitschrift für Physik B Condensed Matter*, 54(3):201–206, Sep 1984.

[69] A M Tsvelick. The thermodynamics of multichannel kondo problem. *Journal of Physics C: Solid State Physics*, 18(1):159–170, jan 1985.

[70] Natan Andrei and Andrés Jerez. Fermi- and non-fermi-liquid behavior in the anisotropic multichannel kondo model: Bethe ansatz solution. *Phys. Rev. Lett.*, 74:4507–4510, May 1995.

[71] Gergely Zaránd, Theo Costi, Andres Jerez, and Natan Andrei. Thermodynamics of the anisotropic two-channel kondo problem. *Phys. Rev. B*, 65:134416, Mar 2002.

[72] A. V. Rozhkov. Impurity entropy for the two-channel kondo model. *International Journal of Modern Physics B*, 12(32):3457–3463, 1998.

[73] Ru Zheng, Rong-Qiang He, and Zhong-Yi Lu. Order parameter for the multichannel kondo model at quantum criticality. *Phys. Rev. B*, 103:045111, Jan 2021.

[74] Siddhartha Patra, Abhirup Mukherjee, Anirban Mukherjee, N S Vidhyadhiraja, A Taraphder, and Siddhartha Lal. Frustration shapes multi-channel kondo physics: a star graph perspective. *Journal of Physics: Condensed Matter*, 35(31):315601, may 2023.

[75] D. Withoff and E. Fradkin. Phase transitions in gapless fermi systems with magnetic impurities. *Phys. Rev. Lett.*, 64:1835–1838, 1990.

[76] C. Gonzalez-Buxton and K. Ingersent. Renormalization-group study of anderson and kondo impurities in gapless fermi systems. *Phys. Rev. B*, 57:14254–14269, 1998.

[77] R. Bulla, T. Pruschke, and A. C. Hewson. Anderson impurity in pseudogap fermi systems. *J. Phys.: Condens. Matter*, 9:10463–10472, 1997.

[78] K. Ingersent. Behavior of magnetic impurities in gapless fermi systems. *Phys. Rev. B*, 54:11936–11953, 1996.

[79] K. Ingersent and Q. Si. Critical local-moment fluctuations in the pseudogap anderson model. *Phys. Rev. Lett.*, 89:076403, 2002.

[80] L. Fritz and M. Vojta. Phase transitions in the pseudogap anderson and kondo models. *Phys. Rev. B*, 70:214427, 2004.

[81] O. Parcollet and A. Georges. Non-fermi-liquid regime of a doped mott insulator. *Phys. Rev. B*, 59:5341–5360, 1999.

[82] Qimiao Si, Silvio Rabello, Kevin Ingersent, and J. Lleweilun Smith. Locally critical quantum phase transitions in strongly correlated metals. *Nature*, 413(6858):804–808, Oct 2001.

[83] R. Bulla, M. Vojta, and W. Hofstetter. Numerical renormalization group for quantum impurities in a pseudogap. *Phys. Rev. B*, 62:R6115–R6118, 2000.

[84] B. A. Jones and C. M. Varma. Study of two magnetic impurities in a fermi gas. *Phys. Rev. Lett.*, 58:843–846, 1987.

[85] B. A. Jones, C. M. Varma, and J. W. Wilkins. Low-temperature properties of the two-impurity kondo hamiltonian. *Phys. Rev. Lett.*, 61:125–128, 1988.

[86] I. Affleck, A. W. W. Ludwig, and B. A. Jones. Conformal-field-theory approach to the two-impurity kondo problem. *Phys. Rev. B*, 52:9528–9546, 1995.

[87] I. Affleck and A. W. W. Ludwig. Exact conformal-field-theory results on the multichannel kondo effect. *Phys. Rev. B*, 48:7297–7321, 1993.

[88] Krzysztof P. Wójcik and Johann Kroha. Quantum spin liquid in an rkky-coupled two-impurity kondo system. *Phys. Rev. B*, 107:L121111, Mar 2023.

[89] Elio J. König, Piers Coleman, and Yashar Komijani. Frustrated kondo impurity triangle: A simple model of deconfinement. *Phys. Rev. B*, 104:115103, Sep 2021.

[90] A. Spinelli, M. Gerrits, R. Toskovic, B. Bryant, M. Ternes, and A. F. Otte. Exploring the phase diagram of the two-impurity kondo problem. *Nature Communications*, 6(1):10046, Nov 2015.

[91] J. Zaanen, G. A. Sawatzky, and J. W. Allen. Band gaps and electronic structure of transition-metal compounds. *Phys. Rev. Lett.*, 55:418, 1985.

[92] Masatoshi Imada, Atsushi Fujimori, and Yoshinori Tokura. Metal-insulator transitions. *Rev. Mod. Phys.*, 70:1039–1263, 1998.

[93] D. B. McWhan, T. M. Rice, and J. P. Remeika. Mott transition in cr-doped v_2o_3. *Phys. Rev. Lett.*, 23:1384–1387, Dec 1969.

[94] P. Limelette, A. Georges, D. Jérome, P. Wzietek, P. Metcalf, and J. M. Honig. Universality and critical behavior at the mott transition. *Science*, 302(5642):89–92, 2003.

[95] M. J. Rozenberg, G. Kotliar, H. Kajueter, G. A. Thomas, D. H. Rapkine, J. M. Honig, and P. Metcalf. Optical conductivity in mott-hubbard systems. *Phys. Rev. Lett.*, 75:105–108, Jul 1995.

[96] M. M. Qazilbash, M. Brehm, Byung-Gyu Chae, P.-C. Ho, G. O. Andreev, Bong-Jun Kim, Sun Jin Yun, A. V. Balatsky, M. B. Maple, F. Keilmann, Hyun-Tak Kim, and D. N. Basov. Mott transition in vo2 revealed by infrared spectroscopy and nano-imaging. *Science*, 318(5857):1750–1753, 2007.

[97] H. Takagi, B. Batlogg, H. L. Kao, J. Kwo, R. J. Cava, J. J. Krajewski, and W. F. Peck. Systematic evolution of temperature-dependent resistivity in $la_{2-x}sr_xcuo_4$. *Phys. Rev. Lett.*, 69:2975–2978, Nov 1992.

[98] Yoichi Ando, Seiki Komiya, Kouji Segawa, S. Ono, and Y. Kurita. Electronic phase diagram of high-T_c cuprate superconductors from a mapping of the in-plane resistivity curvature. *Phys. Rev. Lett.*, 93:267001, Dec 2004.

[99] T. R. Lemberger, I. Hetel, A. Tsukada, M. Naito, and M. Randeria. Superconductor-to-metal quantum phase transition in overdoped $la_{2-x}sr_xcuo_4$. *Phys. Rev. B*, 83:140507, Apr 2011.

[100] Andrea Damascelli, Zahid Hussain, and Zhi-Xun Shen. Angle-resolved photoemission studies of the cuprate superconductors. *Rev. Mod. Phys.*, 75:473–541, Apr 2003.

[101] Jonathan A. Sobota, Yu He, and Zhi-Xun Shen. Angle-resolved photoemission studies of quantum materials. *Rev. Mod. Phys.*, 93:025006, May 2021.

[102] I M Vishik. Photoemission perspective on pseudogap, superconducting fluctuations, and charge order in cuprates: a review of recent progress. *Reports on Progress in Physics*, 81(6):062501, apr 2018.

[103] María Luisa Medarde. Structural, magnetic and electronic properties of perovskites (r = rare earth). *Journal of Physics: Condensed Matter*, 9(8):1679, feb 1997.

[104] Yuxin Wang, Kun Jiang, Jianjun Ying, Tao Wu, Jinguang Cheng, Jiangping Hu, and Xianhui Chen. Recent progress in nickelate superconductors. *National Science Review*, 12(10):nwaf373, 09 2025.

[105] Pascal Puphal, Thomas Schäfer, Bernhard Keimer, and Matthias Hepting. Superconductivity in infinite-layer and ruddlesden–popper nickelates. *Nature Reviews Physics*, 8(2):70–85, Feb 2026.

[106] Sajedeh Manzeli, Dmitry Ovchinnikov, Diego Pasquier, Oleg V. Yazyev, and Andras Kis. 2d transition metal dichalcogenides. *Nature Reviews Materials*, 2(8):17033, Jun 2017.

[107] Saju Joseph, Jainy Mohan, Seetha Lakshmy, Simil Thomas, Brahmananda Chakraborty, Sabu Thomas, and Nandakumar Kalarikkal. A review of the synthesis, properties, and applications of 2d transition metal dichalcogenides and their heterostructures. *Materials Chemistry and Physics*, 297:127332, 2023.

[108] J. A. Wilson, F. J. Di Salvo, and S. Mahajan. Charge-density waves in metallic, layered, transition-metal dichalcogenides. *Phys. Rev. Lett.*, 32:882–885, Apr 1974.

[109] J. A. Wilson, F. J. Di Salvo, and S. Mahajan. Charge-density waves and superlattices in the metallic layered transition metal dichalcogenides. *Advances in Physics*, 50(8):1171–1248, 2001.

[110] P. Fazekas and E. Tosatti. Electrical, structural and magnetic properties of pure and doped 1t-tas$_2$. *Philosophical Magazine B*, 39:229–244, 1979.

[111] L. Perfetti, T. A. Gloor, F. Mila, H. Berger, and M. Grioni. Unexpected periodicity in the quasi-two-dimensional mott insulator $1t-\text{tas}_2$ revealed by angle-resolved photoemission. *Phys. Rev. B*, 71:153101, Apr 2005.

[112] B. Sipos, A. F. Kusmartseva, A. Akrap, H. Berger, L. Forró, and E. Tutiš. From mott state to superconductivity in 1t-tas2. *Nature Materials*, 7(12):960–965, Dec 2008.

[113] Doohee Cho, Sangmo Cheon, Ki-Seok Kim, Sung-Hoon Lee, Yong-Heum Cho, Sang-Wook Cheong, and Han Woong Yeom. Nanoscale manipulation of the mott insulating state coupled to charge order in 1t-tas2. *Nature Communications*, 7(1):10453, Jan 2016.

[114] S. V. Borisenko, A. A. Kordyuk, A. N. Yaresko, V. B. Zabolotnyy, D. S. Inosov, R. Schuster, B. Büchner, R. Weber, R. Follath, L. Patthey, and H. Berger. Pseudogap and charge density waves in two dimensions. *Phys. Rev. Lett.*, 100:196402, May 2008.

[115] S. V. Borisenko, A. A. Kordyuk, V. B. Zabolotnyy, D. S. Inosov, D. Evtushinsky, B. Büchner, A. N. Yaresko, A. Varykhalov, R. Follath, W. Eberhardt, L. Patthey, and H. Berger. Two energy gaps and fermi-surface "arcs" in nbse$_2$. *Phys. Rev. Lett.*, 102:166402, Apr 2009.

[116] V. Vescoli et al. Charge-density-wave correlations in the optical properties of layered transition-metal dichalcogenides. *Physical Review Letters*, 81:453–456, 1998.

[117] Lijun Li, Xiaoyu Deng, Zhen Wang, Yu Liu, Milinda Abeykoon, Eric Dooryhee, Aleksandra Tomic, Yanan Huang, John B. Warren, Emil S. Bozin, Simon J. L. Billinge, Yuping Sun, Yimei Zhu, Gabriel Kotliar, and Cedomir Petrovic. Superconducting order from disorder in 2h-tase2−xsx. *npj Quantum Materials*, 2(1):11, Feb 2017.

[118] Yoichi Kamihara, Takumi Watanabe, Masahiro Hirano, and Hideo Hosono. Iron-based layered superconductor la[o1-xfx]feas (x = 0.05−0.12) with tc = 26 k. *Journal of the American Chemical Society*, 130(11):3296–3297, 2008. PMID: 18293989.

[119] J. Paglione and R. L. Greene. High-temperature superconductivity in iron-based materials. *Nature Physics*, 6:645–658, 2010.

[120] P. J. Hirschfeld, M. M. Korshunov, and I. I. Mazin. Gap symmetry and structure of fe-based superconductors. *Reports on Progress in Physics*, 74:124508, 2011.

[121] G. R. Stewart. Superconductivity in iron compounds. *Rev. Mod. Phys.*, 83:1589–1652, Dec 2011.

[122] David C. Johnston. The puzzle of high temperature superconductivity in layered iron pnictides and chalcogenides. *Advances in Physics*, 59(6):803–1061, 2010.

[123] S. Kasahara, H. J. Shi, K. Hashimoto, S. Tonegawa, Y. Mizukami, T. Shibauchi, K. Sugimoto, T. Fukuda, T. Terashima, Andriy H. Nevidomskyy, and Y. Matsuda. Electronic nematicity above the structural and superconducting transition in bafe2(as1−xp x)2. *Nature*, 486(7403):382–385, Jun 2012.

[124] R. M. Fernandes, A. V. Chubukov, and J. Schmalian. What drives nematic order in iron-based superconductors? *Nature Physics*, 10(2):97–104, Feb 2014.

[125] James G. Analytis, H.-H. Kuo, Ross D. McDonald, Mark Wartenbe, P. M. C. Rourke, N. E. Hussey, and I. R. Fisher. Transport near a quantum critical point in bafe2(as1−xpx)2. *Nature Physics*, 10(3):194–197, Mar 2014.

[126] M. M. Qazilbash, J. J. Hamlin, R. E. Baumbach, Lijun Zhang, D. J. Singh, M. B. Maple, and D. N. Basov. Electronic correlations in the iron pnictides. *Nature Physics*, 5(9):647–650, Sep 2009.

[127] H. Shishido, A. F. Bangura, A. I. Coldea, S. Tonegawa, K. Hashimoto, S. Kasahara, P. M. C. Rourke, H. Ikeda, T. Terashima, R. Settai, Y. Ōnuki, D. Vignolles, C. Proust, B. Vignolle, A. McCollam, Y. Matsuda, T. Shibauchi, and A. Carrington. Evolution of the fermi surface

of bafe$_2$(as$_{1-x}$**p**$_x$)$_2$ on entering the superconducting dome. *Phys. Rev. Lett.*, 104:057008, Feb 2010.

[128] K. Terashima, Y. Sekiba, J. H. Bowen, K. Nakayama, T. Kawahara, T. Sato, P. Richard, Y.-M. Xu, L. J. Li, G. H. Cao, Z.-A. Xu, H. Ding, and T. Takahashi. Fermi surface nesting induced strong pairing in iron-based superconductors. *Proceedings of the National Academy of Sciences*, 106(18):7330–7333, 2009.

[129] J.-H. Chu, H.-H. Kuo, J. G. Analytis, and I. R. Fisher. Divergent nematic susceptibility in an iron arsenide superconductor. *Science*, 337:710–712, 2012.

[130] Hsueh-Hui Kuo, Jiun-Haw Chu, Johanna C. Palmstrom, Steven A. Kivelson, and Ian R. Fisher. Ubiquitous signatures of nematic quantum criticality in optimally doped fe-based superconductors. *Science*, 352(6288):958–962, 2016.

[131] D. S. Inosov, J. T. Park, P. Bourges, D. L. Sun, Y. Sidis, A. Schneidewind, K. Hradil, D. Haug, C. T. Lin, B. Keimer, and V. Hinkov. Normal-state spin dynamics and temperature-dependent spin-resonance energy in optimally doped $BaFe_{1.85}Co_{0.15}As_2$. *Nature Physics*, 6:178–181, 2010.

[132] Andrey Chubukov. Pairing mechanism in fe-based superconductors. *Annual Review of Condensed Matter Physics*, 3(Volume 3, 2012):57–92, 2012.

[133] G. R. Stewart. Heavy-fermion systems. *Reviews of Modern Physics*, 56:755–787, 1984.

[134] Steffen Wirth and Frank Steglich. Exploring heavy fermions from macroscopic to microscopic length scales. *Nature Reviews Materials*, 1(10):16051, Aug 2016.

[135] Hilbert v. Löhneysen, Achim Rosch, Matthias Vojta, and Peter Wölfle. Fermi-liquid instabilities at magnetic quantum phase transitions. *Rev. Mod. Phys.*, 79:1015–1075, Aug 2007.

[136] Philipp Gegenwart, Qimiao Si, and Frank Steglich. Quantum criticality in heavy-fermion metals. *Nature Physics*, 4(3):186–197, Mar 2008.

[137] J. Custers, P. Gegenwart, H. Wilhelm, K. Neumaier, Y. Tokiwa, O. Trovarelli, C. Geibel, F. Steglich, C. Pépin, and P. Coleman. The break-up of heavy electrons at a quantum critical point. *Nature*, 424(6948):524–527, Jul 2003.

[138] S. Paschen, T. Lühmann, S. Wirth, P. Gegenwart, O. Trovarelli, C. Geibel, F. Steglich, P. Coleman, and Q. Si. Hall-effect evolution across a heavy-fermion quantum critical point. *Nature*, 432(7019):881–885, Dec 2004.

[139] A. Schröder, G. Aeppli, R. Coldea, M. Adams, O. Stockert, H.v. Löhneysen, E. Bucher, R. Ramazashvili, and P. Coleman. Onset of antiferromagnetism in heavy-fermion metals. *Nature*, 407(6802):351–355, Sep 2000.

[140] O. Stockert, J. Arndt, E. Faulhaber, C. Geibel, H. S. Jeevan, S. Kirchner, M. Loewenhaupt, K. Schmalzl, W. Schmidt, Q. Si, and F. Steglich. Magnetically driven superconductivity in cecu2si2. *Nature Physics*, 7(2):119–124, Feb 2011.

[141] Hiroaki Shishido, Rikio Settai, Hisatomo Harima, and Yoshichika Ōnuki. A drastic change of the fermi surface at a critical pressure in cerhin5: dhva study under pressure. *Journal of the Physical Society of Japan*, 74(4):1103–1106, 2005.

[142] Qimiao Si and Frank Steglich. Heavy fermions and quantum phase transitions. *Science*, 329(5996):1161–1166, 2010.

[143] Hal Tasaki. The hubbard model - an introduction and selected rigorous results. *Journal of Physics: Condensed Matter*, 10(20):4353, may 1998.

[144] Daniel P. Arovas, Erez Berg, Steven A. Kivelson, and Srinivas Raghu. The hubbard model. *Annual Review of Condensed Matter Physics*, 13(Volume 13, 2022):239–274, 2022.

[145] Mingpu Qin, Thomas Schäfer, Sabine Andergassen, Philippe Corboz, and Emanuel Gull. The hubbard model: A computational perspective. *Annual Review of Condensed Matter Physics*, 13(Volume 13, 2022):275–302, 2022.

[146] Elliott H Lieb and F Yu Wu. Absence of mott transition in an exact solution of the short-range, one-band model in one dimension. *Physical Review Letters*, 20(25):1445, 1968.

[147] Antoine Georges and Gabriel Kotliar. Hubbard model in infinite dimensions. *Phys. Rev. B*, 45:6479–6483, Mar 1992.

[148] V. Janis and D. Vollhardt. Comprehensive mean field theory for the hubbard model. *International Journal of Modern Physics B*, 06(05n06):731–747, 1992.

[149] M. J. Rozenberg, X. Y. Zhang, and G. Kotliar. Mott-hubbard transition in infinite dimensions. *Phys. Rev. Lett.*, 69:1236–1239, Aug 1992.

[150] Marcelo J. Rozenberg, R. Chitra, and Gabriel Kotliar. Finite temperature mott transition in the hubbard model in infinite dimensions. *Phys. Rev. Lett.*, 83:3498–3501, Oct 1999.

[151] R. M. Noack and F. Gebhard. Mott-hubbard transition in infinite dimensions. *Phys. Rev. Lett.*, 82:1915–1918, Mar 1999.

[152] P. Werner and A. J. Millis. Doping-driven mott transition in the one-band hubbard model. *Phys. Rev. B*, 75:085108, 2007.

[153] Nozières, Ph. Some comments on kondo lattices and the mott transition. *Eur. Phys. J. B*, 6(4):"447–457", "" 1998.

[154] G. Kotliar, Sahana Murthy, and M. J. Rozenberg. Compressibility divergence and the finite temperature mott transition. *Phys. Rev. Lett.*, 89:046401, Jul 2002.

[155] Kotliar, G. Landau theory of the mott transition in the fully frustrated hubbard model in infinite dimensions. *Eur. Phys. J. B*, 11(1):27–39, 1999.

[156] Xiaoyu Deng, Jernej Mravlje, Rok Žitko, Michel Ferrero, Gabriel Kotliar, and Antoine Georges. How bad metals turn good: Spectroscopic signatures of resilient quasiparticles. *Phys. Rev. Lett.*, 110:086401, Feb 2013.

[157] R. Žitko, D. Hansen, E. Perepelitsky, J. Mravlje, A. Georges, and B. S. Shastry. Extremely correlated fermi liquid theory meets dynamical mean-field theory: Analytical insights into the doping-driven mott transition. *Phys. Rev. B*, 88:235132, Dec 2013.

[158] J. Vučičević, D. Tanasković, M. J. Rozenberg, and V. Dobrosavljević. Bad-metal behavior reveals mott quantum criticality in doped hubbard models. *Phys. Rev. Lett.*, 114:246402, Jun 2015.

[159] Nagamalleswararao Dasari, N. S. Vidhyadhiraja, Mark Jarrell, and Ross H. McKenzie. Quantum critical local spin dynamics near the mott metal-insulator transition in infinite dimensions. *Phys. Rev. B*, 95:165105, Apr 2017.

[160] Heike Eisenlohr, Seung-Sup B. Lee, and Matthias Vojta. Mott quantum criticality in the one-band hubbard model: Dynamical mean-field theory, power-law spectra, and scaling. *Phys. Rev. B*, 100:155152, Oct 2019.

[161] David E Logan and Martin R Galpin. Mott insulators and the doping-induced mott transition within DMFT: exact results for the one-band hubbard model. *Journal of Physics: Condensed Matter*, 28(2):025601, dec 2015.

[162] Y. Ōno, R. Bulla, and A. C. Hewson. Phase diagram of the mott transition in a two-band hubbard model in infinite dimensions. *The European Physical Journal B - Condensed Matter and Complex Systems*, 19(3):375–384, Feb 2001.

[163] Marcelo J Rozenberg. Integer-filling metal-insulator transitions in the degenerate hubbard model. *Physical Review B*, 55(8):R4855, 1997.

[164] FC Zhang and TM Rice. Effective hamiltonian for the superconducting cu oxides. *Physical Review B*, 37(7):3759, 1988.

[165] Motoharu Kitatani, Liang Si, Oleg Janson, Ryotaro Arita, Zhicheng Zhong, and Karsten Held. Nickelate superconductors - a renaissance of the one-band hubbard model. *npj Quantum Materials*, 5(1):59, Aug 2020.

[166] B J Powell and Ross H McKenzie. Strong electronic correlations in superconducting organic charge transfer salts. *Journal of Physics: Condensed Matter*, 18(45):R827, oct 2006.

[167] Philip W. Phillips, Nigel E. Hussey, and Peter Abbamonte. Stranger than metals. *Science*, 377:eabh4273, 2022.

[168] J. E. Hirsch. Two-dimensional hubbard model: Numerical simulation study. *Phys. Rev. B*, 31:4403–4419, Apr 1985.

[169] Steven R White, Douglas J Scalapino, Robert L Sugar, EY Loh, James E Gubernatis, and Richard T Scalettar. Numerical study of the two-dimensional hubbard model. *Physical Review B*, 40(1):506, 1989.

[170] T. Schäfer, F. Geles, D. Rost, G. Rohringer, E. Arrigoni, K. Held, N. Blümer, M. Aichhorn, and A. Toschi. Fate of the false mott-hubbard transition in two dimensions. *Phys. Rev. B*, 91:125109, Mar 2015.

[171] Ettore Vitali, Hao Shi, Mingpu Qin, and Shiwei Zhang. Computation of dynamical correlation functions for many-fermion systems with auxiliary-field quantum monte carlo. *Phys. Rev. B*, 94:085140, Aug 2016.

[172] Fedor Šimkovic, J. P. F. LeBlanc, Aaram J. Kim, Youjin Deng, N. V. Prokof'ev, B. V. Svistunov, and Evgeny Kozik. Extended crossover from a fermi liquid to a quasiantiferromagnet in the half-filled 2d hubbard model. *Phys. Rev. Lett.*, 124:017003, Jan 2020.

[173] K. Borejsza and N. Dupuis. Antiferromagnetism and single-particle properties in the two-dimensional half-filled hubbard model: A nonlinear sigma model approach. *Phys. Rev. B*, 69:085119, Feb 2004.

[174] Aaram J. Kim, Fedor Simkovic, and Evgeny Kozik. Spin and charge correlations across the metal-to-insulator crossover in the half-filled 2d hubbard model. *Phys. Rev. Lett.*, 124:117602, Mar 2020.

[175] Anirban Mukherjee and Siddhartha Lal. Scaling theory for mott–hubbard transitions: I. t = 0 phase diagram of the 1/2-filled hubbard model. *New Journal of Physics*, 22(6):063007, jun 2020.

[176] Marcel Klett, Nils Wentzell, Thomas Schäfer, Fedor Simkovic, Olivier Parcollet, Sabine Andergassen, and Philipp Hansmann. Real-space cluster dynamical mean-field theory: Center-focused extrapolation on the one- and two particle-levels. *Phys. Rev. Res.*, 2:033476, Sep 2020.

[177] HJ Schulz. Incommensurate antiferromagnetism in the two-dimensional hubbard model. *Physical review letters*, 64(12):1445, 1990.

[178] R. Frésard, M. Dzierzawa, and P. Wölfle. Slave-boson approach to spiral magnetic order in the hubbard model. *Europhysics Letters*, 15(3):325, jun 1991.

[179] Walter Metzner, Manfred Salmhofer, Carsten Honerkamp, Volker Meden, and Kurt Schönhammer. Functional renormalization group approach to correlated fermion systems. *Reviews of Modern Physics*, 84(1):299, 2012.

[180] Hiroyuki Yamase, Andreas Eberlein, and Walter Metzner. Coexistence of incommensurate magnetism and superconductivity in the two-dimensional hubbard model. *Physical review letters*, 116(9):096402, 2016.

[181] S Raghu, SA Kivelson, and DJ Scalapino. Superconductivity in the repulsive hubbard model: An asymptotically exact weak-coupling solution. *Physical Review B*, 81(22):224505, 2010.

[182] Fedor Šimkovic, Youjin Deng, and Evgeny Kozik. Superfluid ground state phase diagram of the two-dimensional hubbard model in the emergent bardeen-cooper-schrieffer regime. *Phys. Rev. B*, 104:L020507, Jul 2021.

[183] Jing Wang, Andreas Eberlein, and Walter Metzner. Competing order in correlated electron systems made simple: Consistent fusion of functional renormalization and mean-field theory. *Phys. Rev. B*, 89:121116, Mar 2014.

[184] Anirban Mukherjee and Siddhartha Lal. Scaling theory for mott–hubbard transitions-II: quantum criticality of the doped mott insulator. *New Journal of Physics*, 22(6):063008, jun 2020.

[185] M Zegrodnik, A Biborski, M Fidrysiak, and J Spałek. Superconductivity in the three-band model of cuprates: nodal direction characteristics and influence of intersite interactions. *Journal of Physics: Condensed Matter*, 33(41):415601, aug 2021.

[186] C. Weber, C. Yee, K. Haule, and G. Kotliar. Scaling of the transition temperature of hole-doped cuprate superconductors with the charge-transfer energy. *Europhysics Letters*, 100(3):37001, nov 2012.

[187] Steven R. White and D. J. Scalapino. Doping asymmetry and striping in a three-orbital cuo_2 hubbard model. *Phys. Rev. B*, 92:205112, Nov 2015.

[188] Bernhard Keimer, Steven A Kivelson, Michael R Norman, Shinichi Uchida, and J Zaanen. From quantum matter to high-temperature superconductivity in copper oxides. *Nature*, 518(7538):179, 2015.

[189] Cornelia Hille, Daniel Rohe, Carsten Honerkamp, and Sabine Andergassen. Pseudogap opening in the two-dimensional hubbard model: a functional renormalization group analysis. *arXiv preprint arXiv:2003.01447*, 2020.

[190] Wei Wu, Mathias S. Scheurer, Shubhayu Chatterjee, Subir Sachdev, Antoine Georges, and Michel Ferrero. Pseudogap and fermi-surface topology in the two-dimensional hubbard model. *Phys. Rev. X*, 8:021048, May 2018.

[191] Bo-Xiao Zheng, Chia-Min Chung, Philippe Corboz, Georg Ehlers, Ming-Pu Qin, Reinhard M. Noack, Hao Shi, Steven R. White, Shiwei Zhang, and Garnet Kin-Lic Chan. Stripe order in the underdoped region of the two-dimensional hubbard model. *Science*, 358(6367):1155–1160, 2017.

[192] Luca F. Tocchio, Arianna Montorsi, and Federico Becca. Metallic and insulating stripes and their relation with superconductivity in the doped Hubbard model. *SciPost Phys.*, 7:021, 2019.

[193] Yi-Fan Jiang, Jan Zaanen, Thomas P. Devereaux, and Hong-Chen Jiang. Ground state phase diagram of the doped hubbard model on the four-leg cylinder. *Phys. Rev. Res.*, 2:033073, Jul 2020.

[194] Mingpu Qin, Chia-Min Chung, Hao Shi, Ettore Vitali, Claudius Hubig, Ulrich Schollwöck, Steven R. White, and Shiwei Zhang. Absence of superconductivity in the pure two-dimensional hubbard model. *Phys. Rev. X*, 10:031016, Jul 2020.

[195] Th. Maier, M. Jarrell, Th. Pruschke, and J. Keller. A non-crossing approximation for the study of intersite correlations. *The European Physical Journal B - Condensed Matter and Complex Systems*, 13(4):613–624, Feb 2000.

[196] C. Huscroft, M. Jarrell, Th. Maier, S. Moukouri, and A. N. Tahvildarzadeh. Pseudogaps in the 2d hubbard model. *Phys. Rev. Lett.*, 86:139–142, Jan 2001.

[197] M. Civelli, M. Capone, S. S. Kancharla, O. Parcollet, and G. Kotliar. Dynamical breakup of the fermi surface in a doped mott insulator. *Phys. Rev. Lett.*, 95:106402, Sep 2005.

[198] O. Parcollet, G. Biroli, and G. Kotliar. Cluster dynamical mean field analysis of the mott transition. *Phys. Rev. Lett.*, 92:226402, Jun 2004.

[199] O. Gunnarsson, T. Schäfer, J. P. F. LeBlanc, E. Gull, J. Merino, G. Sangiovanni, G. Rohringer, and A. Toschi. Fluctuation diagnostics of the electron self-energy: Origin of the pseudogap physics. *Phys. Rev. Lett.*, 114:236402, Jun 2015.

[200] Ansgar Liebsch and Ning-Hua Tong. Finite-temperature exact diagonalization cluster dynamical mean-field study of the two-dimensional hubbard model: Pseudogap, non-fermi-liquid behavior, and particle-hole asymmetry. *Phys. Rev. B*, 80:165126, Oct 2009.

[201] Emanuel Gull, Olivier Parcollet, Philipp Werner, and Andrew J. Millis. Momentum-sector-selective metal-insulator transition in the eight-site dynamical mean-field approximation to the hubbard model in two dimensions. *Phys. Rev. B*, 80:245102, Dec 2009.

[202] Wei Wu, Mathias S. Scheurer, Michel Ferrero, and Antoine Georges. Effect of van hove singularities in the onset of pseudogap states in mott insulators. *Phys. Rev. Res.*, 2:033067, Jul 2020.

[203] Youjin Deng, Evgeny Kozik, Nikolay V. Prokof'ev, and Boris V. Svistunov. Emergent bcs regime of the two-dimensional fermionic hubbard model: Ground-state phase diagram. *Europhysics Letters*, 110(5):57001, jun 2015.

[204] Xi Chen, J. P. F. LeBlanc, and Emanuel Gull. Superconducting fluctuations in the normal state of the two-dimensional hubbard model. *Phys. Rev. Lett.*, 115:116402, Sep 2015.

[205] E. Gull and A. J. Millis. Pairing glue in the two-dimensional hubbard model. *Phys. Rev. B*, 90:041110, Jul 2014.

[206] Peter Cha, Aavishkar A. Patel, Emanuel Gull, and Eun-Ah Kim. Slope invariant t-linear resistivity from local self-energy. *Phys. Rev. Res.*, 2:033434, Sep 2020.

[207] Edwin W. Huang, Ryan Sheppard, Brian Moritz, and Thomas P. Devereaux. Strange metallicity in the doped hubbard model. *Science*, 366(6468):987–990, 2019.

[208] J. J. Vučičević, J. Kokalj, R. Žitko, N. Wentzell, D. Tanasković, and J. Mravlje. Conductivity in the square lattice hubbard model at high temperatures: Importance of vertex corrections. *Phys. Rev. Lett.*, 123:036601, Jul 2019.

[209] Hilbert v. Löhneysen, Achim Rosch, Matthias Vojta, and Peter Wölfle. Fermi-liquid instabilities at magnetic quantum phase transitions. *Rev. Mod. Phys.*, 79:1015–1075, Aug 2007.

[210] S. Doniach. The kondo lattice and weak antiferromagnetism. *Physica B+C*, 91:231–234, 1977.

[211] Qimiao Si and Silke Paschen. Quantum phase transitions in heavy fermion metals and kondo insulators. *physica status solidi (b)*, 250(3):425–438, 2013.

[212] Qimiao Si. Global magnetic phase diagram and local quantum criticality in heavy fermion metals. *Physica B: Condensed Matter*, 378-380:23–27, 2006. Proceedings of the International Conference on Strongly Correlated Electron Systems.

[213] D.M. Newns and N. Read. Mean-field theory of intermediate valence/heavy fermion systems. *Advances in Physics*, 36(6):799–849, 1987.

[214] A. Houghton, N. Read, and H. Won. Charge fluctuations, spin fluctuations, and superconductivity in the anderson lattice model of heavy-fermion systems. *Phys. Rev. B*, 37:3782–3785, Mar 1988.

[215] S. Burdin, A. Georges, and D. R. Grempel. Coherence scale of the kondo lattice. *Phys. Rev. Lett.*, 85:1048–1051, Jul 2000.

[216] Th. Pruschke, R. Bulla, and M. Jarrell. Low-energy scale of the periodic anderson model. *Phys. Rev. B*, 61:12799–12809, May 2000.

[217] Hirokazu Tsunetsugu, Manfred Sigrist, and Kazuo Ueda. The ground-state phase diagram of the one-dimensional kondo lattice model. *Rev. Mod. Phys.*, 69:809–864, Jul 1997.

[218] Kazuo Ueda, Hirokazu Tsunetsugu, and Manfred Sigrist. Singlet ground state of the periodic anderson model at half filling: A rigorous result. *Phys. Rev. Lett.*, 68:1030–1033, Feb 1992.

[219] Shun-Qing Shen. Total spin and antiferromagnetic correlation in the kondo model. *Phys. Rev. B*, 53:14252–14261, Jun 1996.

[220] Hirokazu Tsunetsugu. Rigorous results for half-filled kondo lattices. *Phys. Rev. B*, 55:3042–3045, Feb 1997.

[221] Qimiao Si and Frank Steglich. Heavy fermions and quantum phase transitions. *Science*, 329(5996):1161–1166, 2010.

[222] John A. Hertz. Quantum critical phenomena. *Phys. Rev. B*, 14:1165–1184, Aug 1976.

[223] Tôru Moriya. *Spin Fluctuations in Itinerant Electron Magnetism*. Springer Berlin, Heidelberg, 1985.

[224] A. J. Millis. Effect of a nonzero temperature on quantum critical points in itinerant fermion systems. *Phys. Rev. B*, 48:7183–7196, Sep 1993.

[225] P Coleman, C Pépin, Qimiao Si, and R Ramazashvili. How do fermi liquids get heavy and die? *Journal of Physics: Condensed Matter*, 13(35):R723, aug 2001.

[226] Qimiao Si, Silvio Rabello, Kevin Ingersent, and J. Lleweilun Smith. Local fluctuations in quantum critical metals. *Phys. Rev. B*, 68:115103, Sep 2003.

[227] O. Stockert and F. Steglich. Unconventional quantum criticality in heavy-fermion compounds. *Annual Review of Condensed Matter Physics*, 2(Volume 2, 2011):79–99, 2011.

[228] Peter Wölfle and Elihu Abrahams. Quasiparticles beyond the fermi liquid and heavy fermion criticality. *Phys. Rev. B*, 84:041101, Jul 2011.

[229] Qimiao Si. Quantum criticality and global phase diagram of magnetic heavy fermions. *physica status solidi (b)*, 247(3):476–484, 2010.

[230] O. Trovarelli, C. Geibel, S. Mederle, C. Langhammer, F. M. Grosche, P. Gegenwart, M. Lang, G. Sparn, and F. Steglich. $ybrh_2si_2$: Pronounced non-fermi-liquid effects above a low-lying magnetic phase transition. *Phys. Rev. Lett.*, 85:626–629, Jul 2000.

[231] H.v Löhneysen, M Sieck, O Stockert, and M Waffenschmidt. Investigation of non-fermi-liquid behavior in cecu6−xaux. *Physica B: Condensed Matter*, 223-224:471–474, 1996. Proceedings of the International Conference on Strongly Correlated Electron Systems.

[232] Sven Friedemann, Niels Oeschler, Steffen Wirth, Cornelius Krellner, Christoph Geibel, Frank Steglich, Silke Paschen, Stefan Kirchner, and Qimiao Si. Fermi-surface collapse and dynamical scaling near a quantum-critical point. *Proceedings of the National Academy of Sciences*, 107(33):14547–14551, 2010.

[233] L. Prochaska, X. Li, D. C. MacFarland, A. M. Andrews, M. Bonta, E. F. Bianco, S. Yazdi, W. Schrenk, H. Detz, A. Limbeck, Q. Si, E. Ringe, G. Strasser, J. Kono, and S. Paschen. Singular charge fluctuations at a magnetic quantum critical point. *Science*, 367(6475):285–288, 2020.

[234] S. Friedemann, T. Westerkamp, M. Brando, N. Oeschler, S. Wirth, P. Gegenwart, C. Krellner, C. Geibel, and F. Steglich. Detaching the antiferromagnetic quantum critical point from the fermi-surface reconstruction in ybrh2si2. *Nature Physics*, 5(7):465–469, Jul 2009.

[235] Nikola Maksimovic, Daniel H. Eilbott, Tessa Cookmeyer, Fanghui Wan, Jan Rusz, Vikram Nagarajan, Shannon C. Haley, Eran Maniv, Amanda Gong, Stefano Faubel, Ian M. Hayes, Ali Bangura, John Singleton, Johanna C. Palmstrom, Laurel Winter, Ross McDonald, Sooyoung Jang, Ping Ai, Yi Lin, Samuel Ciocys, Jacob Gobbo, Yochai Werman, Peter M. Oppeneer, Ehud Altman, Alessandra Lanzara, and James G. Analytis. Evidence for a delocalization quantum phase transition without symmetry breaking in cecoin₅. *Science*, 375(6576):76–81, 2022.

[236] Qimiao Si, Jedediah H. Pixley, Emilian Nica, Seiji J. Yamamoto, Pallab Goswami, Rong Yu, and Stefan Kirchner. Kondo destruction and quantum criticality in kondo lattice systems. *Journal of the Physical Society of Japan*, 83(6):061005, 2014.

[237] Stefan Kirchner, Silke Paschen, Qiuyun Chen, Steffen Wirth, Donglai Feng, Joe D. Thompson, and Qimiao Si. Colloquium: Heavy-electron quantum criticality and single-particle spectroscopy. *Rev. Mod. Phys.*, 92:011002, Mar 2020.

[238] Ping Sun and Gabriel Kotliar. Extended dynamical mean field theory study of the periodic anderson model. *Phys. Rev. Lett.*, 91:037209, Jul 2003.

[239] Marcin Raczkowski, Bimla Danu, and Fakher F. Assaad. Breakdown of heavy quasiparticles in a honeycomb kondo lattice: A quantum monte carlo study. *Phys. Rev. B*, 106:L161115, Oct 2022.

[240] Andreas Gleis, Jheng-Wei Li, and Jan von Delft. Controlled bond expansion for density matrix renormalization group ground state search at single-site costs. *Phys. Rev. Lett.*, 130:246402, Jun 2023.

[241] T. Senthil, Matthias Vojta, and Subir Sachdev. Weak magnetism and non-fermi liquids near heavy-fermion critical points. *Phys. Rev. B*, 69:035111, Jan 2004.

[242] P. Coleman, J. B. Marston, and A. J. Schofield. Transport anomalies in a simplified model for a heavy-electron quantum critical point. *Phys. Rev. B*, 72:245111, Dec 2005.

[243] Barbara M. Terhal, Michael M. Wolf, and Andrew C. Doherty. Quantum entanglement: A modern perspective. *Physics Today*, 56(4):46–52, 2003.

[244] Ryszard Horodecki, Paweł Horodecki, Michał Horodecki, and Karol Horodecki. Quantum entanglement. *Reviews of modern physics*, 81(2):865, 2009.

[245] J. Eisert, M. Cramer, and M. B. Plenio. Colloquium: Area laws for the entanglement entropy. *Rev. Mod. Phys.*, 82:277–306, Feb 2010.

[246] Nicolas Laflorencie. Quantum entanglement in condensed matter systems. *Physics Reports*, 646:1–59, 2016.

[247] Bei Zeng, Xie Chen, Duan-Lu Zhou, and Xiao-Gang Wen. *Quantum information meets quantum matter*. Springer, 2019.

[248] Manuel Erhard, Mario Krenn, and Anton Zeilinger. Advances in high-dimensional quantum entanglement. *Nature Reviews Physics*, 2(7):365–381, Jul 2020.

[249] X. G. Wen. Topological orders in rigid states. *International Journal of Modern Physics B*, 04(02):239–271, 1990.

[250] X. G. Wen and Q. Niu. Ground-state degeneracy of the fractional quantum hall states in the presence of a random potential and on high-genus riemann surfaces. *Phys. Rev. B*, 41:9377–9396, May 1990.

[251] X.G. Wen and A. Zee. Quantum statistics and superconductivity in two spatial dimensions. *Nuclear Physics B - Proceedings Supplements*, 15:135–156, 1990.

[252] Xiao-Gang Wen. Topological orders and chern-simons theory in strongly correlated quantum liquid. *International Journal of Modern Physics B*, 05(10):1641–1648, 1991.

[253] Xiao-Gang Wen. Topological orders and edge excitations in fractional quantum hall states. *Advances in Physics*, 44(5):405–473, 1995.

[254] Xiao-Gang Wen. Topological order: From long-range entangled quantum matter to a unified origin of light and electrons. *ISRN Condensed Matter Physics*, 2013:198710, Mar 2013.

[255] Xiao-Gang Wen. Colloquium: Zoo of quantum-topological phases of matter. *Reviews of Modern Physics*, 89(4):041004, 2017.

[256] R. Tao and Yong-Shi Wu. Gauge invariance and fractional quantum hall effect. *Phys. Rev. B*, 30:1097–1098, Jul 1984.

[257] Qian Niu, Ds J Thouless, and Yong-Shi Wu. Quantized hall conductance as a topological invariant. *Physical Review B*, 31(6):3372, 1985.

[258] X. G. Wen. Vacuum degeneracy of chiral spin states in compactified space. *Phys. Rev. B*, 40:7387–7390, Oct 1989.

[259] Hui Li and F Duncan M Haldane. Entanglement spectrum as a generalization of entanglement entropy: Identification of topological order in non-abelian fractional quantum hall effect states. *Physical review letters*, 101(1):010504, 2008.

[260] Xiao-Liang Qi, Hosho Katsura, and Andreas W. W. Ludwig. General relationship between the entanglement spectrum and the edge state spectrum of topological quantum states. *Phys. Rev. Lett.*, 108:196402, May 2012.

[261] Frank Pollmann, Ari M. Turner, Erez Berg, and Masaki Oshikawa. Entanglement spectrum of a topological phase in one dimension. *Phys. Rev. B*, 81:064439, Feb 2010.

[262] Hong Yao and Xiao-Liang Qi. Entanglement entropy and entanglement spectrum of the kitaev model. *Phys. Rev. Lett.*, 105:080501, Aug 2010.

[263] Zhao Liu, Hong-Li Guo, Vlatko Vedral, and Heng Fan. Entanglement spectrum: Identification of the transition from vortex-liquid to vortex-lattice state in a weakly interacting rotating bose-einstein condensate. *Phys. Rev. A*, 83:013620, Jan 2011.

[264] Pasquale Calabrese and Alexandre Lefevre. Entanglement spectrum in one-dimensional systems. *Phys. Rev. A*, 78:032329, Sep 2008.

[265] Andreas M. Läuchli, Emil J. Bergholtz, Juha Suorsa, and Masudul Haque. Disentangling entanglement spectra of fractional quantum hall states on torus geometries. *Phys. Rev. Lett.*, 104:156404, Apr 2010.

[266] John Schliemann. Entanglement spectrum and entanglement thermodynamics of quantum hall bilayers at $\nu = 1$. *Phys. Rev. B*, 83:115322, Mar 2011.

[267] B. I. Halperin. Quantized hall conductance, current-carrying edge states, and the existence of extended states in a two-dimensional disordered potential. *Phys. Rev. B*, 25:2185–2190, Feb 1982.

[268] Xiao-Liang Qi, Hosho Katsura, and Andreas W. W. Ludwig. General relationship between the entanglement spectrum and the edge state spectrum of topological quantum states. *Phys. Rev. Lett.*, 108:196402, May 2012.

[269] Nicolas Laflorencie. Quantum entanglement in condensed matter systems. *Physics Reports*, 646:1–59, 2016. Quantum entanglement in condensed matter systems.

[270] Saurya Das and S. Shankaranarayanan. How robust is the entanglement entropy-area relation? *Phys. Rev. D*, 73:121701, Jun 2006.

[271] M. Cramer, J. Eisert, M. B. Plenio, and J. Dreißig. Entanglement-area law for general bosonic harmonic lattice systems. *Phys. Rev. A*, 73:012309, Jan 2006.

[272] B. Blok and X. G. Wen. Effective theories of the fractional quantum hall effect: Hierarchy construction. *Phys. Rev. B*, 42:8145–8156, Nov 1990.

[273] N. Read. Excitation structure of the hierarchy scheme in the fractional quantum hall effect. *Phys. Rev. Lett.*, 65:1502–1505, Sep 1990.

[274] Daniel S. Rokhsar and Steven A. Kivelson. Superconductivity and the quantum hard-core dimer gas. *Phys. Rev. Lett.*, 61:2376–2379, Nov 1988.

[275] N. Read and B. Chakraborty. Statistics of the excitations of the resonating-valence-bond state. *Phys. Rev. B*, 40:7133–7140, Oct 1989.

[276] R. Moessner and S. L. Sondhi. Resonating valence bond phase in the triangular lattice quantum dimer model. *Phys. Rev. Lett.*, 86:1881–1884, Feb 2001.

[277] Eddy Ardonne, Paul Fendley, and Eduardo Fradkin. Topological order and conformal quantum critical points. *Annals of Physics*, 310(2):493–551, 2004.

[278] Michael A. Levin and Xiao-Gang Wen. String-net condensation: A physical mechanism for topological phases. *Phys. Rev. B*, 71:045110, Jan 2005.

[279] Alexei Kitaev and John Preskill. Topological entanglement entropy. *Physical review letters*, 96(11):110404, 2006.

[280] Hong-Chen Jiang, Zhenghan Wang, and Leon Balents. Identifying topological order by entanglement entropy. *Nature Physics*, 8(12):902–905, Dec 2012.

[281] Alioscia Hamma, Radu Ionicioiu, and Paolo Zanardi. Bipartite entanglement and entropic boundary law in lattice spin systems. *Phys. Rev. A*, 71:022315, Feb 2005.

[282] Michael Levin and Xiao-Gang Wen. Detecting topological order in a ground state wave function. *Phys. Rev. Lett.*, 96:110405, Mar 2006.

[283] Alexei Kitaev and John Preskill. Topological entanglement entropy. *Phys. Rev. Lett.*, 96:110404, Mar 2006.

[284] Yi Zhang, Tarun Grover, Ari Turner, Masaki Oshikawa, and Ashvin Vishwanath. Quasiparticle statistics and braiding from ground-state entanglement. *Phys. Rev. B*, 85:235151, Jun 2012.

[285] Tarun Grover, Ari M. Turner, and Ashvin Vishwanath. Entanglement entropy of gapped phases and topological order in three dimensions. *Phys. Rev. B*, 84:195120, Nov 2011.

[286] Alioscia Hamma and Daniel A. Lidar. Adiabatic preparation of topological order. *Phys. Rev. Lett.*, 100:030502, Jan 2008.

[287] Tian Lan and Xiao-Gang Wen. Topological quasiparticles and the holographic bulk-edge relation in (2 + 1)-dimensional string-net models. *Phys. Rev. B*, 90:115119, Sep 2014.

[288] Paul Fendley, Sergei V. Isakov, and Matthias Troyer. Fibonacci topological order from quantum nets. *Phys. Rev. Lett.*, 110:260408, Jun 2013.

[289] Zheng-Cheng Gu, Michael Levin, Brian Swingle, and Xiao-Gang Wen. Tensor-product representations for string-net condensed states. *Phys. Rev. B*, 79:085118, Feb 2009.

[290] Kevin Slagle, David Aasen, and Dominic Williamson. Foliated Field Theory and String-Membrane-Net Condensation Picture of Fracton Order. *SciPost Phys.*, 6:43, 2019.

[291] Xie Chen, Zheng-Cheng Gu, and Xiao-Gang Wen. Local unitary transformation, long-range quantum entanglement, wave function renormalization, and topological order. *Physical review b*, 82(15):155138, 2010.

[292] Zheng-Cheng Gu and Xiao-Gang Wen. Tensor-entanglement-filtering renormalization approach and symmetry-protected topological order. *Physical Review B*, 80(15):155131, 2009.

[293] Siddhartha Patra, Somnath Basu, and Siddhartha Lal. Unveiling topological order through multipartite entanglement. *Phys. Rev. A*, 105:052428, May 2022.

[294] Oskar Vafek and Ashvin Vishwanath. Dirac fermions in solids: From high-tc cuprates and graphene to topological insulators and weyl semimetals. *Annual Review of Condensed Matter Physics*, 5(1):83–112, 2014.

[295] B. Andrei Bernevig and Taylor L. Hughes. *Topological Insulators and Topological Superconductors*. Princeton University Press, 2013.

[296] Jérôme Cayssol. Introduction to dirac materials and topological insulators. *Comptes Rendus Physique*, 14(9):760–778, 2013. Topological insulators / Isolants topologiques.

[297] Roderich Moessner and Joel E. Moore. *Topological Phases of Matter*. Cambridge University Press, 2021.

[298] Stephan Rachel. Interacting topological insulators: a review. *Reports on Progress in Physics*, 81(11):116501, oct 2018.

[299] Jinying Wang, Shibin Deng, Zhongfan Liu, and Zhirong Liu. "The rare two-dimensional materials with Dirac cones". *National Science Review*, 2(1):22–39, 01 2015.

[300] Menghao Wu, Zhijun Wang, Junwei Liu, Wenbin Li, Huahua Fu, Lei Sun, Xin Liu, Minghu Pan, Hongming Weng, Mircea Dincă, Liang Fu, and Ju Li. Conetronics in 2d metal-organic frameworks: double/half dirac cones and quantum anomalous hall effect. *2D Materials*, 4(1):015015, nov 2016.

[301] Xiaojuan Ni, Huaqing Huang, and Jean-Luc Brédas. Emergence of a two-dimensional topological dirac semimetal phase in a phthalocyanine-based covalent organic framework. *Chemistry of Materials*, 34(7):3178–3184, 2022.

[302] Shi-Liang Zhu, Baigeng Wang, and L.-M. Duan. Simulation and detection of dirac fermions with cold atoms in an optical lattice. *Phys. Rev. Lett.*, 98:260402, Jun 2007.

[303] L. Lepori, G. Mussardo, and A. Trombettoni. (3+1) massive dirac fermions with ultracold atoms in frustrated cubic optical lattices. *EPL (Europhysics Letters)*, 92(5):50003, dec 2010.

[304] O Boada, A Celi, J I Latorre, and M Lewenstein. Dirac equation for cold atoms in artificial curved spacetimes. *New Journal of Physics*, 13(3):035002, mar 2011.

[305] Yoshihito Kuno, Ikuo Ichinose, and Yoshiro Takahashi. Generalized lattice wilson–dirac fermions in (1 + 1) dimensions for atomic quantum simulation and topological phases. *Scientific Reports*, 8(1):10699, Jul 2018.

[306] Kenjiro K. Gomes, Warren Mar, Wonhee Ko, Francisco Guinea, and Hari C. Manoharan. Designer dirac fermions and topological phases in molecular graphene. *Nature*, 483(7389):306–310, Mar 2012.

[307] Xiang Yuan, Cheng Zhang, Yanwen Liu, Awadhesh Narayan, Chaoyu Song, Shoudong Shen, Xing Sui, Jie Xu, Haochi Yu, Zhenghua An, Jun Zhao, Stefano Sanvito, Hugen Yan, and Faxian Xiu. Observation of quasi-two-dimensional dirac fermions in zrte5. *NPG Asia Materials*, 8(11):e325–e325, Nov 2016.

[308] Matthieu Bellec, Ulrich Kuhl, Gilles Montambaux, and Fabrice Mortessagne. Topological transition of dirac points in a microwave experiment. *Phys. Rev. Lett.*, 110:033902, Jan 2013.

[309] Guifre Vidal, José Ignacio Latorre, Enrique Rico, and Alexei Kitaev. Entanglement in quantum critical phenomena. *Physical review letters*, 90(22):227902, 2003.

[310] J. I. Latorre, E. Rico, and G. Vidal. Ground state entanglement in quantum spin chains, 2003.

[311] J. I. Latorre, C. A. Lütken, E. Rico, and G. Vidal. Fine-grained entanglement loss along renormalization-group flows. *Phys. Rev. A*, 71:034301, Mar 2005.

[312] B.-Q. Jin and V. E. Korepin. Quantum spin chain, toeplitz determinants and the fisher—hartwig conjecture. *Journal of Statistical Physics*, 116(1):79–95, Aug 2004.

[313] Neill Lambert, Clive Emary, and Tobias Brandes. Entanglement and the phase transition in single-mode superradiance. *Phys. Rev. Lett.*, 92:073602, Feb 2004.

[314] Christoph Holzhey, Finn Larsen, and Frank Wilczek. Geometric and renormalized entropy in conformal field theory. *Nuclear Physics B*, 424(3):443–467, 1994.

[315] H. Casini and M. Huerta. A finite entanglement entropy and the c-theorem. *Physics Letters B*, 600(1):142–150, 2004.

[316] Pasquale Calabrese and John Cardy. Entanglement entropy and quantum field theory. *Journal of Statistical Mechanics: Theory and Experiment*, 2004(06):P06002, 2004.

[317] Tobias J Osborne and Michael A Nielsen. Entanglement in a simple quantum phase transition. *Physical Review A*, 66(3):032110, 2002.

[318] Andreas Osterloh, Luigi Amico, Giuseppe Falci, and Rosario Fazio. Scaling of entanglement close to a quantum phase transition. *Nature*, 416(6881):608–610, 2002.

[319] H Casini, C D Fosco, and M Huerta. Entanglement and alpha entropies for a massive dirac field in two dimensions. *Journal of Statistical Mechanics: Theory and Experiment*, 2005(07):P07007–P07007, jul 2005.

[320] V. E. Korepin. Universality of entropy scaling in one dimensional gapless models. *Phys. Rev. Lett.*, 92:096402, Mar 2004.

[321] J. L. Cardy, O. A. Castro-Alvaredo, and B. Doyon. Form factors of branch-point twist fields in quantum integrable models and entanglement entropy. *Journal of Statistical Physics*, 130(1):129–168, Jan 2008.

[322] H Casini and M Huerta. Reduced density matrix and internal dynamics for multicomponent regions. *Classical and Quantum Gravity*, 26(18):185005, sep 2009.

[323] Benjamin Doyon. Bipartite entanglement entropy in massive two-dimensional quantum field theory. *Phys. Rev. Lett.*, 102:031602, Jan 2009.

[324] H Casini and M Huerta. Entanglement entropy in free quantum field theory. *Journal of Physics A: Mathematical and Theoretical*, 42(50):504007, dec 2009.

[325] Dimitri Gioev and Israel Klich. Entanglement entropy of fermions in any dimension and the widom conjecture. *Physical review letters*, 96(10):100503, 2006.

[326] Michael M. Wolf. Violation of the entropic area law for fermions. *Phys. Rev. Lett.*, 96:010404, Jan 2006.

[327] Weifei Li, Letian Ding, Rong Yu, Tommaso Roscilde, and Stephan Haas. Scaling behavior of entanglement in two- and three-dimensional free-fermion systems. *Phys. Rev. B*, 74:073103, Aug 2006.

[328] T. Barthel, M.-C. Chung, and U. Schollwöck. Entanglement scaling in critical two-dimensional fermionic and bosonic systems. *Phys. Rev. A*, 74:022329, Aug 2006.

[329] S. Farkas and Z. Zimborás. The von neumann entropy asymptotics in multidimensional fermionic systems. *Journal of Mathematical Physics*, 48(10):102110, 2007.

[330] Michael M Wolf, Frank Verstraete, Matthew B Hastings, and J Ignacio Cirac. Area laws in quantum systems: mutual information and correlations. *Physical review letters*, 100(7):070502, 2008.

[331] Olalla A Castro-Alvaredo and Benjamin Doyon. Bi-partite entanglement entropy in massive (1+1)-dimensional quantum field theories. *Journal of Physics A: Mathematical and Theoretical*, 42(50):504006, dec 2009.

[332] Brian Swingle. Entanglement entropy and the fermi surface. *Physical review letters*, 105(5):050502, 2010.

[333] Robert Helling, Hajo Leschke, and Wolfgang Spitzer. "A Special Case of a Conjecture by Widom with Implications to Fermionic Entanglement Entropy". *International Mathematics Research Notices*, 2011(7):1451–1482, 06 2010.

[334] P. Calabrese, M. Mintchev, and E. Vicari. Entanglement entropies in free-fermion gases for arbitrary dimension. *EPL (Europhysics Letters)*, 97(2):20009, jan 2012.

[335] Brian Swingle. Rényi entropy, mutual information, and fluctuation properties of fermi liquids. *Phys. Rev. B*, 86:045109, Jul 2012.

[336] Pasquale Calabrese, Mihail Mintchev, and Ettore Vicari. Exact relations between particle fluctuations and entanglement in fermi gases. *EPL (Europhysics Letters)*, 98(2):20003, apr 2012.

[337] Mao Tian Tan and Shinsei Ryu. Particle number fluctuations, renyi entropy, and symmetry-resolved entanglement entropy in a two-dimensional fermi gas from multidimensional bosonization. *Phys. Rev. B*, 101:235169, Jun 2020.

[338] Sara Murciano, Paola Ruggiero, and Pasquale Calabrese. Symmetry resolved entanglement in two-dimensional systems via dimensional reduction. *Journal of Statistical Mechanics: Theory and Experiment*, 2020(8):083102, aug 2020.

[339] Xiao Chen, William Witczak-Krempa, Thomas Faulkner, and Eduardo Fradkin. Two-cylinder entanglement entropy under a twist. *Journal of Statistical Mechanics: Theory and Experiment*, 2017(4):043104, apr 2017.

[340] Pablo Bueno and William Witczak-Krempa. Holographic torus entanglement and its renormalization group flow. *Phys. Rev. D*, 95:066007, Mar 2017.

[341] Max A. Metlitski, Carlos A. Fuertes, and Subir Sachdev. Entanglement entropy in the $o(n)$ model. *Phys. Rev. B*, 80:115122, Sep 2009.

[342] Raúl E Arias, David D Blanco, and Horacio Casini. Entanglement entropy as a witness of the aharonov–bohm effect in QFT. *Journal of Physics A: Mathematical and Theoretical*, 48(14):145401, mar 2015.

[343] Seth Whitsitt, William Witczak-Krempa, and Subir Sachdev. Entanglement entropy of large-n wilson-fisher conformal field theory. *Phys. Rev. B*, 95:045148, Jan 2017.

[344] Wei Zhu, Xiao Chen, Yin-Chen He, and William Witczak-Krempa. Entanglement signatures of emergent dirac fermions: Kagome spin liquid and quantum criticality. *Science Advances*, 4(11):eaat5535, 2018.

[345] Shijie Hu, W. Zhu, Sebastian Eggert, and Yin-Chen He. Dirac spin liquid on the spin-1/2 triangular heisenberg antiferromagnet. *Phys. Rev. Lett.*, 123:207203, Nov 2019.

[346] Valentin Crépel, Anna Hackenbroich, Nicolas Regnault, and Benoit Estienne. Universal signatures of dirac fermions in entanglement and charge fluctuations. *Phys. Rev. B*, 103:235108, Jun 2021.

[347] Joshuah T Heath and Kevin S Bedell. Necessary and sufficient conditions for the validity of luttinger's theorem. *New Journal of Physics*, 22(6):063011, jun 2020.

[348] Anirban Mukherjee and Siddhartha Lal. Holographic unitary renormalisation group for correlated electrons-i: a tensor network approach. *Nuclear Physics B*, 960:115170, 2020.

[349] Anirban Mukherjee and Siddhartha Lal. Holographic unitary renormalisation group for correlated electrons-ii: insights on fermionic criticality. *Nuclear Physics B*, 960:115163, 2020.

[350] G. 't Hooft. Dimensional reduction in quantum gravity. *arXiv:gr-qc/9310026*, 1993.

[351] Erik Verlinde. On the origin of gravity and the laws of newton. *Journal of High Energy Physics*, 2011(4):29, Apr 2011.

[352] Hsu-Wen Chiang, Yao-Chieh Hu, and Pisin Chen. Quantization of spacetime based on a spacetime interval operator. *Phys. Rev. D*, 93:084043, Apr 2016.

[353] Mark Van Raamsdonk. Building up spacetime with quantum entanglement. *General Relativity and Gravitation*, 42(10):2323–2329, 2010.

[354] Mark Van Raamsdonk. *Lectures on Gravity and Entanglement*, chapter Chapter 5, pages 297–351. World Scientific, 2017.

[355] Xiao-Liang Qi. Exact holographic mapping and emergent space-time geometry. *arXiv preprint arXiv:1309.6282*, 2013.

[356] Ching Hua Lee and Xiao-Liang Qi. Exact holographic mapping in free fermion systems. *Physical Review B*, 93(3):035112, 2016.

[357] Raphael Bousso. The holographic principle. *Rev. Mod. Phys.*, 74:825–874, Aug 2002.

[358] Joseph Katz and Jian Sheng. Applications of holography in fluid mechanics and particle dynamics. *Annual Review of Fluid Mechanics*, 42(1):531–555, 2010.

[359] A.G. Green. An introduction to gauge-gravity duality and its application in condensed matter. *Contemporary Physics*, 54(1):33–48, 2013.

[360] Sean A Hartnoll. Lectures on holographic methods for condensed matter physics. *Classical and Quantum Gravity*, 26(22):224002, oct 2009.

[361] Subir Sachdev. What can gauge-gravity duality teach us about condensed matter physics? *Annual Review of Condensed Matter Physics*, 3(1):9–33, 2012.

[362] Jan Zaanen, Yan Liu, Ya-Wen Sun, and Koenraad Schalm. *Holographic Duality in Condensed Matter Physics*. Cambridge University Press, 2015.

[363] Anosh Joseph. Review of lattice supersymmetry and gauge-gravity duality. *International Journal of Modern Physics A*, 30(27):1530054, 2015.

[364] Horaţiu Năstase. *Introduction to the AdS/CFT Correspondence*. Cambridge University Press, 2015.

[365] Johanna Erdmenger. Introduction to gauge/gravity duality (tasi lectures 2017), 2018.

[366] G.'t Hooft. A planar diagram theory for strong interactions. *Nuclear Physics B*, 72(3):461–473, 1974.

[367] A.M. Polyakov. Thermal properties of gauge fields and quark liberation. *Physics Letters B*, 72(4):477–480, 1978.

[368] A.M. Polyakov. *Gauge Fields and Strings (1st ed.)*. Routledge, 1987.

[369] David J. Gross and Washington Taylor. Two-dimensional qcd is a string theory. *Nuclear Physics B*, 400(1):181–208, 1993.

[370] E.T. Akhmedov. A remark on the ads/cft correspondence and the renormalization group flow. *Physics Letters B*, 442(1):152–158, 1998.

[371] Enrique Álvarez and César Gómez. Geometric holography, the renormalization group and the c-theorem. *Nuclear Physics B*, 541(1):441–460, 1999.

[372] D. Z. Freedman, S. S. Gubser, K. Pilch, and N. P. Warner. Renormalization group flows from holography–supersymmetry and a c-theorem. *Advances in Theoretical and Mathematical Physics*, 3(2):363–417, 1999.

[373] M. Porrati and A. Starinets. Rg fixed points in supergravity duals of 4-d field theory and asymptotically ads spaces. *Physics Letters B*, 454(1):77–83, 1999.

[374] Shamit Kachru, Michael Schulz, and Eva Silverstein. Self-tuning flat domain walls in 5d gravity and string theory. *Phys. Rev. D*, 62:045021, Jul 2000.

[375] L. Girardello, M. Petrini, M. Porrati, and A. Zaffaroni. The supergravity dual of n=1 super yang–mills theory. *Nuclear Physics B*, 569(1):451–469, 2000.

[376] Jan De Boer, Erik Verlinde, and Herman Verlinde. On the holographic renormalization group. *Journal of High Energy Physics*, 2000(08):003, 2000.

[377] Jan de Boer. The holographic renormalization group. *Fortschritte der Physik*, 49(4-6):339–358, 2001.

[378] Clifford V Johnson, Kenneth J Lovis, and David C Page. Probing some N = 1 AdS/CFT RG flows. *Journal of High Energy Physics*, 2001(05):036–036, may 2001.

[379] Satoshi Yamaguchi. AdS branes corresponding to superconformal defects. *Journal of High Energy Physics*, 2003(06):002–002, jun 2003.

[380] Juan Maldacena. The large-n limit of superconformal field theories and supergravity. *International journal of theoretical physics*, 38(4):1113–1133, 1999.

[381] S.S. Gubser, I.R. Klebanov, and A.M. Polyakov. Gauge theory correlators from non-critical string theory. *Physics Letters B*, 428(1):105–114, 1998.

[382] Edward Witten. Anti de sitter space and holography. *arXiv preprint hep-th/9802150*, 2:253–291, 1998.

[383] Jacob D. Bekenstein. Black holes and entropy. *Phys. Rev. D*, 7:2333–2346, Apr 1973.

[384] S. W. Hawking. Black hole explosions? *Nature*, 248(5443):30–31, Mar 1974.

[385] S. W. Hawking. Particle creation by black holes. *Communications in Mathematical Physics*, 43(3):199–220, Aug 1975.

[386] Shinsei Ryu and Tadashi Takayanagi. Holographic derivation of entanglement entropy from the anti–de sitter space/conformal field theory correspondence. *Physical review letters*, 96(18):181602, 2006.

[387] Shinsei Ryu and Tadashi Takayanagi. Aspects of holographic entanglement entropy. *Journal of High Energy Physics*, 2006(08):045, 2006.

[388] P. K. Kovtun, D. T. Son, and A. O. Starinets. Viscosity in strongly interacting quantum field theories from black hole physics. *Phys. Rev. Lett.*, 94:111601, Mar 2005.

[389] Kedar Damle and Subir Sachdev. Nonzero-temperature transport near quantum critical points. *Phys. Rev. B*, 56:8714–8733, Oct 1997.

[390] Sean A. Hartnoll, Pavel K. Kovtun, Markus Müller, and Subir Sachdev. Theory of the nernst effect near quantum phase transitions in condensed matter and in dyonic black holes. *Phys. Rev. B*, 76:144502, Oct 2007.

[391] Sung-Sik Lee. Non-fermi liquid from a charged black hole: A critical fermi ball. *Phys. Rev. D*, 79:086006, Apr 2009.

[392] Hong Liu, John McGreevy, and David Vegh. Non-fermi liquids from holography. *Phys. Rev. D*, 83:065029, Mar 2011.

[393] Thomas Faulkner, Hong Liu, John McGreevy, and David Vegh. Emergent quantum criticality, fermi surfaces, and ads$_2$. *Phys. Rev. D*, 83:125002, Jun 2011.

[394] Mihailo Čubrović, Jan Zaanen, and Koenraad Schalm. String theory, quantum phase transitions, and the emergent fermi liquid. *Science*, 325(5939):439–444, 2009.

[395] Steven S. Gubser, Silviu S. Pufu, and Fabio D. Rocha. Quantum critical superconductors in string theory and m-theory. *Physics Letters B*, 683(2):201–204, 2010.

[396] Jerome P. Gauntlett, Julian Sonner, and Toby Wiseman. Holographic superconductivity in m theory. *Phys. Rev. Lett.*, 103:151601, Oct 2009.

[397] Sean A. Hartnoll, Christopher P. Herzog, and Gary T. Horowitz. Building a holographic superconductor. *Phys. Rev. Lett.*, 101:031601, Jul 2008.

[398] Sean A Hartnoll, Christopher P Herzog, and Gary T Horowitz. Holographic superconductors. *Journal of High Energy Physics*, 2008(12):015–015, dec 2008.

[399] RongGen Cai, Li Li, LiFang Li, and RunQiu Yang. Introduction to holographic superconductor models. *Science China Physics, Mechanics & Astronomy*, 58(6):1–46, Jun 2015.

[400] Chunyan Wang, Dan Zhang, Guoyang Fu, and Jian-Pin Wu. Analytical study of the holographic superconductor from higher derivative theory. *Advances in High Energy Physics*, 2020:5902473, Jan 2020.

[401] Aristomenis Donos and Jerome P. Gauntlett. Holographic striped phases. *Journal of High Energy Physics*, 2011(8):140, Aug 2011.

[402] Aristomenis Donos. Striped phases from holography. *Journal of High Energy Physics*, 2013(5):59, May 2013.

[403] Sera Cremonini, Li Li, and Jie Ren. Holographic fermions in striped phases. *Journal of High Energy Physics*, 2018(12):80, Dec 2018.

[404] Shamit Kachru, Xiao Liu, and Michael Mulligan. Gravity duals of lifshitz-like fixed points. *Phys. Rev. D*, 78:106005, Nov 2008.

[405] Mihailo Čubrović, Yan Liu, Koenraad Schalm, Ya-Wen Sun, and Jan Zaanen. Spectral probes of the holographic fermi ground state: Dialing between the electron star and ads dirac hair. *Phys. Rev. D*, 84:086002, Oct 2011.

[406] T. Senthil, Subir Sachdev, and Matthias Vojta. Fractionalized fermi liquids. *Phys. Rev. Lett.*, 90:216403, May 2003.

[407] Subir Sachdev. Model of a fermi liquid using gauge-gravity duality. *Phys. Rev. D*, 84:066009, Sep 2011.

[408] Sean A. "Hartnoll, Diego M. Hofman, and David" Vegh. "Stellar spectroscopy: Fermions and holographic Lifshitz criticality". *"JHEP"*, "08":"096", "2011".

[409] Liza Huijse and Subir Sachdev. Fermi surfaces and gauge-gravity duality. *Phys. Rev. D*, 84:026001, Jul 2011.

[410] Francesco Aprile, Diederik Roest, and Jorge G. Russo. Holographic superconductors from gauged supergravity. *Journal of High Energy Physics*, 2011(6):40, Jun 2011.

[411] Aristomenis Donos and Jerome P. Gauntlett. Superfluid black branes in ads4 × s7. *Journal of High Energy Physics*, 2011(6):53, Jun 2011.

[412] Hiroaki Matsueda. Multiscale entanglement renormalization ansatz for kondo problem. *arXiv:1208.2872*, 2012.

[413] Hiroaki Matsueda, Masafumi Ishihara, and Yoichiro Hashizume. Tensor network and a black hole. *Phys. Rev. D*, 87:066002, Mar 2013.

[414] Hiroaki Matsueda. Emergent general relativity from fisher information metric. *arXiv:1310.1831*, 2013.

[415] Hiroaki Matsueda. Geometry and dynamics of emergent spacetime from entanglement spectrum, 2014.

[416] Bartłomiej Czech. Einstein equations from varying complexity. *Phys. Rev. Lett.*, 120:031601, Jan 2018.

[417] Thomas Faulkner, Felix M. Haehl, Eliot Hijano, Onkar Parrikar, Charles Rabideau, and Mark Van Raamsdonk. Nonlinear gravity from entanglement in conformal field theories. *Journal of High Energy Physics*, 2017(8):57, Aug 2017.

[418] Thomas Faulkner, Monica Guica, Thomas Hartman, Robert C. Myers, and Mark Van Raamsdonk. Gravitation from entanglement in holographic cfts. *Journal of High Energy Physics*, 2014(3):51, Mar 2014.

[419] Yingfei Gu, Ching Hua Lee, Xueda Wen, Gil Young Cho, Shinsei Ryu, and Xiao-Liang Qi. Holographic duality between $(2+1)$-dimensional quantum anomalous hall state and $(3+1)$-dimensional topological insulators. *Phys. Rev. B*, 94:125107, Sep 2016.

[420] Xueda Wen, Gil Young Cho, Pedro L. S. Lopes, Yingfei Gu, Xiao-Liang Qi, and Shinsei Ryu. Holographic entanglement renormalization of topological insulators. *Phys. Rev. B*, 94:075124, Aug 2016.

[421] Robert G. Leigh, Onkar Parrikar, and Alexander B. Weiss. Exact renormalization group and higher-spin holography. *Phys. Rev. D*, 91:026002, Jan 2015.

[422] Robert G. Leigh, Onkar Parrikar, and Alexander B. Weiss. Holographic geometry of the renormalization group and higher spin symmetries. *Phys. Rev. D*, 89:106012, May 2014.

[423] Michael R. Douglas, Luca Mazzucato, and Shlomo S. Razamat. Holographic dual of free field theory. *Phys. Rev. D*, 83:071701, Apr 2011.

[424] Robert de Mello Koch, Antal Jevicki, Kewang Jin, and João P. Rodrigues. ads_4/cft_3 construction from collective fields. *Phys. Rev. D*, 83:025006, Jan 2011.

[425] Sung-Sik Lee. Holographic description of quantum field theory. *Nuclear Physics B*, 832(3):567–585, 2010.

[426] Sung-Sik Lee. Tasi lectures on emergence of supersymmetry, gauge theory and string in condensed matter systems. *arXiv:1009.5127*, 2010.

[427] Sung-Sik Lee. Background independent holographic description: from matrix field theory to quantum gravity. *Journal of High Energy Physics*, 2012(10):160, Oct 2012.

[428] Sung-Sik Lee. Quantum renormalization group and holography. *Journal of High Energy Physics*, 2014(1):76, 2014.

[429] Guifre Vidal. Entanglement renormalization. *Physical review letters*, 99(22):220405, 2007.

[430] Guifré Vidal. Class of quantum many-body states that can be efficiently simulated. *Physical review letters*, 101(11):110501, 2008.

[431] Brian Swingle. Entanglement renormalization and holography. *Physical Review D*, 86(6):065007, 2012.

[432] G. Evenbly and G. Vidal. Scaling of entanglement entropy in the (branching) multiscale entanglement renormalization ansatz. *Phys. Rev. B*, 89:235113, Jun 2014.

[433] Ashley Milsted and Guifre Vidal. Geometric interpretation of the multi-scale entanglement renormalization ansatz, 2018.

[434] Glen Evenbly and Guifré Vidal. Tensor network states and geometry. *Journal of Statistical Physics*, 145(4):891–918, 2011.

[435] Justin Reyes and Miles Stoudenmire. A multi-scale tensor network architecture for classification and regression. *arXiv:2001.08286*, 2020.

[436] Nathan A. McMahon, Sukhbinder Singh, and Gavin K. Brennen. A holographic duality from lifted tensor networks. *npj Quantum Information*, 6(1):36, Apr 2020.

[437] Anirban Mukherjee and Siddhartha Lal. Superconductivity from repulsion in the doped 2d electronic hubbard model: an entanglement perspective. *Journal of Physics: Condensed Matter*, 34(27):275601, apr 2022.

[438] Ki-Seok Kim, Suk Bum Chung, Chanyong Park, and Jae-Ho Han. *Phys. Rev. D*, 99:105012, 2019.

[439] Ki-Seok Kim, Miok Park, Jaeyoon Cho, and Chanyong Park. Emergent geometric description for a topological phase transition in the kitaev superconductor model. *Phys. Rev. D*, 96:086015, Oct 2017.

[440] Ki-Seok Kim and Chanyong Park. Emergent geometry from field theory: Wilson's renormalization group revisited. *Phys. Rev. D*, 93:121702, Jun 2016.

[441] Ki-Seok Kim. Emergent dual holographic description for interacting dirac fermions in the large n limit. *Phys. Rev. D*, 102:086014, Oct 2020.

[442] Ki-Seok Kim. Geometric encoding of renormalization group β-functions in an emergent holographic dual description. *Phys. Rev. D*, 102:026022, Jul 2020.

[443] Ki-Seok Kim. Emergent geometry in recursive renormalization group transformations. *Nuclear Physics B*, 959:115144, 2020.

[444] Ki-Seok Kim. Emergent dual holographic description for interacting dirac fermions in the large n limit. *Phys. Rev. D*, 102:086014, Oct 2020.

[445] Ki-Seok Kim and Shinsei Ryu. Entanglement transfer from quantum matter to classical geometry in an emergent holographic dual description of a scalar field theory. *Journal of High Energy Physics*, 2021(5):260, May 2021.

[446] Kenneth G. Wilson. The renormalization group: Critical phenomena and the kondo problem. *Rev. Mod. Phys.*, 47:773–840, Oct 1975.

[447] Anirban Mukherjee and Siddhartha Lal. Superconductivity from repulsion in the doped 2d electronic hubbard model: an entanglement perspective. *Journal of Physics: Condensed Matter*, 34(27):275601, apr 2022.

[448] J L Calais, B T Pickup, M Deleuze, and J Delhalle. Translation symmetry for many-electron functions. *European Journal of Physics*, 16(4):179, jul 1995.

[449] Alexandrina Stoyanova. *Delocalized and correlated wave functions for excited states in extended systems*. PhD thesis, University of Groningen, 2006.

[450] Kenji Suzuki and Ryoji Okamoto. General structure of effective interaction in degenerate perturbation theory. *Progress of Theoretical Physics*, 71(6):1221–1238, 1984.

[451] PW Anderson. A poor man's derivation of scaling laws for the kondo problem. *Journal of Physics C: Solid State Physics*, 3(12):2436, 1970.

[452] FDM Haldane. Scaling theory of the asymmetric anderson model. *Physical Review Letters*, 40(6):416, 1978.

[453] PW Anderson. A poor man's derivation of scaling laws for the kondo problem. *Journal of Physics C: Solid State Physics*, 3(12):2436, 1970.

[454] Abhirup Mukherjee, N S Vidhyadhiraja, A Taraphder, and Siddhartha Lal. Kondo frustration via charge fluctuations: a route to mott localisation. *New Journal of Physics*, 25(11):113011, nov 2023.

[455] Abhirup Mukherjee, S R Hassan, Anamitra Mukherjee, N S Vidhyadhiraja, A Taraphder, and Siddhartha Lal. Mott criticality as the confinement transition of a pseudogap-mott metal. *New Journal of Physics*, 28(1):013503, jan 2026.

[456] Stefan Kehrein. *The flow equation approach to many-particle systems*, volume 217. Springer, 2007.

[457] Franz Wegner. Flow-equations for hamiltonians. *Annalen der physik*, 506(2):77–91, 1994.

[458] Steven R. White. Density matrix formulation for quantum renormalization groups. *Phys. Rev. Lett.*, 69:2863–2866, Nov 1992.

[459] U. Schollwöck. The density-matrix renormalization group. *Rev. Mod. Phys.*, 77:259–315, Apr 2005.

[460] Samuel L Braunstein and Carlton M Caves. Statistical distance and the geometry of quantum states. *Physical Review Letters*, 72(22):3439, 1994.

[461] Philipp Hauke, Markus Heyl, Luca Tagliacozzo, and Peter Zoller. Measuring multipartite entanglement through dynamic susceptibilities. *Nature Physics*, 12(8):778–782, Aug 2016.

[462] Siddhartha Patra, Anirban Mukherjee, and Siddhartha Lal. Universal entanglement signatures of quantum liquids as a guide to fermionic criticality. *New Journal of Physics*, 25(6):063002, jun 2023.

[463] Henrik Bruus and Karsten Flensberg. *Many-Body Quantum Theory in Condensed Matter Physics*. Oxford Graduate Texts, 2004.

[464] Y Kuramoto and T Watanabe. Theory of momentum-dependent magnetic response in heavy-fermion systems. In *Proceedings of the Yamada Conference XVIII on Superconductivity in Highly Correlated Fermion Systems*, pages 80–83. Elsevier, 1987.

[465] D. L. Cox and N. Grewe. Transport properties of the anderson lattice. *Zeitschrift für Physik B Condensed Matter*, 71(3):321–340, Sep 1988.

[466] X. Y. Zhang, M. J. Rozenberg, and G. Kotliar. Mott transition in the d=∞ hubbard model at zero temperature. *Phys. Rev. Lett.*, 70:1666–1669, Mar 1993.

[467] Thomas Maier, Mark Jarrell, Thomas Pruschke, and Matthias H. Hettler. Quantum cluster theories. *Rev. Mod. Phys.*, 77:1027–1080, Oct 2005.

[468] G. Kotliar, S. Y. Savrasov, K. Haule, V. S. Oudovenko, O. Parcollet, and C. A. Marianetti. Electronic structure calculations with dynamical mean-field theory. *Rev. Mod. Phys.*, 78:865–951, Aug 2006.

[469] Takuma Ohashi, Tsutomu Momoi, Hirokazu Tsunetsugu, and Norio Kawakami. Finite temperature mott transition in hubbard model on anisotropic triangular lattice. *Phys. Rev. Lett.*, 100:076402, Feb 2008.

[470] J. Vučičević, H. Terletska, D. Tanasković, and V. Dobrosavljević. Finite-temperature crossover and the quantum widom line near the mott transition. *Phys. Rev. B*, 88:075143, Aug 2013.

[471] Hyowon Park, Kristjan Haule, and Gabriel Kotliar. Cluster dynamical mean field theory of the mott transition. *Physical review letters*, 101(18):186403, 2008.

[472] G. Rohringer, H. Hafermann, A. Toschi, A. A. Katanin, A. E. Antipov, M. I. Katsnelson, A. I. Lichtenstein, A. N. Rubtsov, and K. Held. Diagrammatic routes to nonlocal correlations beyond dynamical mean field theory. *Rev. Mod. Phys.*, 90:025003, May 2018.

[473] A. I. Lichtenstein and M. I. Katsnelson. Ab initio calculations of quasiparticle band structure in correlated systems: Lda++ approach. *Phys. Rev. B*, 57:6884–6895, Mar 1998.

[474] K. Held. Electronic structure calculations using dynamical mean field theory. *Advances in Physics*, 56(6):829–926, 2007.

[475] Karsten Held, Andrey A Katanin, and Alessandro Toschi. Dynamical vertex approximationan introduction. *Progress of Theoretical Physics Supplement*, 176:117–133, 2008.

[476] Qimiao Si and Gabriel Kotliar. Metallic non-fermi-liquid phases of an extended hubbard model in infinite dimensions. *Phys. Rev. B*, 48:13881–13903, Nov 1993.

[477] Gabriel Kotliar and Qimiao Si. Quantum chemistry, anomalous dimensions, and the breakdown of fermi liquid theory in strongly correlated systems. *Physica Scripta*, T49:165, 1993.

[478] H. Terletska, J. Vučičević, D. Tanasković, and V. Dobrosavljević. Quantum critical transport near the mott transition. *Phys. Rev. Lett.*, 107:026401, Jul 2011.

[479] P. W. Anderson. Localized magnetic states in metals. *Phys. Rev.*, 124:41–53, Oct 1961.

[480] P. W. Anderson. Local moments and localized states. *Rev. Mod. Phys.*, 50:191–201, Apr 1978.

[481] Philip W Anderson and Gideon Yuval. Exact results in the kondo problem: equivalence to a classical one-dimensional coulomb gas. *Physical Review Letters*, 23(2):89, 1969.

[482] Philip W Anderson, G Yuval, and DR Hamann. Exact results in the kondo problem. ii. scaling theory, qualitatively correct solution, and some new results on one-dimensional classical statistical models. *Physical Review B*, 1(11):4464, 1970.

[483] J H Jefferson. a renormalisation group approach to the mixed valence problem. *Journal of Physics C: Solid State Physics*, 10(18):3589–3599, sep 1977.

[484] N Andrei, K Furuya, and J H Lowenstein. Solution of the kondo problem. *Rev. Mod. Phys.*, 55:331, 1983.

[485] A M Tsvelick and P B Wiegmann. Exact results in the theory of magnetic alloys. *Adv. in Phys.*, 32:453, 1983.

[486] Gabriel Kotliar and Qimiao Si. Toulouse points and non-fermi-liquid states in the mixed-valence regime of the generalized anderson model. *Phys. Rev. B*, 53:12373–12388, May 1996.

[487] Solomon F. Duki. Solvable limit for the su(n) kondo model. *Phys. Rev. B*, 83:134423, Apr 2011.

[488] L. Borda, A. Schiller, and A. Zawadowski. Applicability of bosonization and the anderson-yuval methods at the strong-coupling limit of quantum impurity problems. *Phys. Rev. B*, 78:201301, Nov 2008.

[489] Simon Streib, Aldo Isidori, and Peter Kopietz. Solution of the anderson impurity model via the functional renormalization group. *Phys. Rev. B*, 87:201107, May 2013.

[490] Erik S. Sørensen and Ian Affleck. Scaling theory of the kondo screening cloud. *Phys. Rev. B*, 53:9153–9167, Apr 1996.

[491] Ian Affleck and Pascal Simon. Detecting the kondo screening cloud around a quantum dot. *Phys. Rev. Lett.*, 86:2854–2857, Mar 2001.

[492] Pascal Simon and Ian Affleck. Kondo screening cloud effects in mesoscopic devices. *Phys. Rev. B*, 68:115304, Sep 2003.

[493] C. A. Busser, G. B. Martins, L. C. Ribeiro, E. Vernek, E. V. Anda, and E. Dagotto. *Phys. Rev. 9*, 81:045111, 2010.

[494] L. C. Ribeiro, G. B. Martins, G. Gomez-Silva, and E. V. Anda. *Phys. Rev. B*, 99:085139, 2019.

[495] D. Goldhaber-Gordon, Hadas Shtrikman, D. Mahalu, David Abusch-Magder, U. Meirav, and M. A. Kastner. Kondo effect in a single-electron transistor. *Nature*, 391(6663):156–159, Jan 1998.

[496] Sara M. Cronenwett, Tjerk H. Oosterkamp, and Leo P. Kouwenhoven. A tunable kondo effect in quantum dots. *Science*, 281(5376):540–544, July 1998.

[497] Jörg Schmid, Jürgen Weis, Karl Eberl, and Klaus v. Klitzing. A quantum dot in the limit of strong coupling to reservoirs. *Physica B: Condensed Matter*, 256-258:182–185, 1998.

[498] Michael Pustilnik and Leonid Glazman. Kondo effect in quantum dots. *Journal of Physics: Condensed Matter*, 16(16):R513, apr 2004.

[499] Ivan V. Borzenets, Jeongmin Shim, Jason C. H. Chen, Arne Ludwig, Andreas D. Wieck, Seigo Tarucha, H.-S. Sim, and Michihisa Yamamoto. Observation of the kondo screening cloud. *Nature*, 579(7798):210–213, Mar 2020.

[500] N. Néel, J. Kröger, R. Berndt, T. O. Wehling, A. I. Lichtenstein, and M. I. Katsnelson. Controlling the kondo effect in cocu$_n$ clusters atom by atom. *Phys. Rev. Lett.*, 101:266803, Dec 2008.

[501] Aidi Zhao, Qunxiang Li, Lan Chen, Hongjun Xiang, Weihua Wang, Shuan Pan, Bing Wang, Xudong Xiao, Jinlong Yang, J. G. Hou, and Qingshi Zhu. Controlling the kondo effect of an adsorbed magnetic ion through its chemical bonding. *Science*, 309(5740):1542–1544, sep 2005.

[502] Masahiro Nozaki, Shinsei Ryu, and Tadashi Takayanagi. Holographic geometry of entanglement renormalization in quantum field theories. *Journal of High Energy Physics*, 2012(10):193, 2012.

[503] Christophe Mora, Cătălin Paşcu Moca, Jan von Delft, and Gergely Zaránd. Fermi-liquid theory for the single-impurity anderson model. *Phys. Rev. B*, 92:075120, Aug 2015.

[504] Santanu Pal, Anirban Mukherjee, and Siddhartha Lal. Correlated spin liquids in the quantum kagome antiferromagnet at finite field: a renormalization group analysis. *New Journal of Physics*, 21(2):023019, feb 2019.

[505] Anirban Mukherjee, Siddhartha Patra, and Siddhartha Lal. Fermionic criticality is shaped by fermi surface topology: a case study of the tomonaga-luttinger liquid. *Journal of High Energy Physics*, 04:148, 2021.

[506] Siddhartha Patra and Siddhartha Lal. Origin of topological order in a cooper-pair insulator. *Phys. Rev. B*, 104:144514, Oct 2021.

[507] A. Taraphder and P. Coleman. Heavy-fermion behavior in a negative-u anderson model. *Phys. Rev. Lett.*, 66:2814–2817, May 1991.

[508] Daria Gazizova and J. P. F. LeBlanc. Emergent nearest-neighbor attraction in the fully renormalized interactions of the single-band repulsive hubbard model at weak coupling. *Phys. Rev. B*, 108:165149, Oct 2023.

[509] Abner Shimony. Degree of entanglement. *Annals of the New York Academy of Sciences*, 755(1):675–679, 1995.

[510] Tzu-Chieh Wei and Paul M Goldbart. Geometric measure of entanglement and applications to bipartite and multipartite quantum states. *Physical Review A*, 68(4):042307, 2003.

[511] Goetz Moeller, Qimiao Si, Gabriel Kotliar, Marcelo Rozenberg, and Daniel S. Fisher. Critical behavior near the mott transition in the hubbard model. *Phys. Rev. Lett.*, 74:2082–2085, Mar 1995.

[512] K. Held, R. Peters, and A. Toschi. Poor man's understanding of kinks originating from strong electronic correlations. *Phys. Rev. Lett.*, 110:246402, Jun 2013.

[513] R. Bulla. Zero temperature metal-insulator transition in the infinite-dimensional hubbard model. *Phys. Rev. Lett.*, 83:136–139, Jul 1999.

[514] Antoine Georges and Werner Krauth. Physical properties of the half-filled hubbard model in infinite dimensions. *Phys. Rev. B*, 48:7167–7182, Sep 1993.

[515] Marcelo J. Rozenberg, Goetz Moeller, and Gabriel Kotliar. The metal–insulator transition in the hubbard model at zero temperature ii. *Modern Physics Letters B*, 08(08n09):535–543, 1994.

[516] Walter Kohn. Theory of the insulating state. *Physical Review*, 133(1A):A171, 1964.

[517] C. Castellani, C. Di Castro, D. Feinberg, and J. Ranninger. New model hamiltonian for the metal-insulator transition. *Phys. Rev. Lett.*, 43:1957–1960, Dec 1979.

[518] H. R. Krishnamurthy, C. Jayaprakash, Sanjoy Sarker, and Wolfgang Wenzel. Mott-hubbard metal-insulator transition in nonbipartite lattices. *Phys. Rev. Lett.*, 64:950–953, Feb 1990.

[519] P. Limelette, A. Georges, D. Jérome, P. Wzietek, P. Metcalf, and J. M. Honig. Universality and critical behavior at the mott transition. *Science*, 302(5642):89–92, 2003.

[520] F. Kagawa, K. Miyagawa, and K. Kanoda. Unconventional critical behaviour in a quasi-two-dimensional organic conductor. *Nature*, 436(7050):534–537, Jul 2005.

[521] Tetsuya Furukawa, Kazuya Miyagawa, Hiromi Taniguchi, Reizo Kato, and Kazushi Kanoda. Quantum criticality of mott transition in organic materials. *Nature Physics*, 11(3):221–224, Mar 2015.

[522] Satyaki Kundu, Tapas Bar, Rajesh Kumble Nayak, and Bhavtosh Bansal. Critical slowing down at the abrupt mott transition: When the first-order phase transition becomes zeroth order and looks like second order. *Phys. Rev. Lett.*, 124:095703, Mar 2020.

[523] Piers Coleman. *Introduction to many-body physics*. Cambridge University Press, 2015. Chapter:18.

[524] A. C. Hewson. Renormalized perturbation expansions and fermi liquid theory. *Phys. Rev. Lett.*, 70:4007–4010, Jun 1993.

[525] CM Varma, Z Nussinov, and Wim Van Saarloos. Singular or non-fermi liquids. *Physics Reports*, 361(5-6):267–417, 2002.

[526] Gabriel Kotliar and Qimiao Si. Quantum chemistry, anomalous dimensions, and the breakdown of fermi liquid theory in strongly correlated systems. *Physica Scripta*, T49A:165–171, jan 1993.

[527] Jan von Delft, Gergely Zaránd, and Michele Fabrizio. Finite-size bosonization of 2-channel kondo model: A bridge between numerical renormalization group and conformal field theory. *Phys. Rev. Lett.*, 81:196–199, Jul 1998.

[528] P Coleman, C Pépin, Qimiao Si, and R Ramazashvili. How do fermi liquids get heavy and die? *Journal of Physics: Condensed Matter*, 13(35):R723, aug 2001.

[529] Philip W Anderson. Infrared catastrophe in fermi gases with local scattering potentials. *Physical Review Letters*, 18(24):1049, 1967.

[530] P. W. Anderson. "luttinger-liquid" behavior of the normal metallic state of the 2d hubbard model. *Phys. Rev. Lett.*, 64:1839–1841, Apr 1990.

[531] J. Friedel. On some electrical and magnetic properties of metallic solid solutions. *Canadian Journal of Physics*, 34(12A):1190–1211, 1956.

[532] JS Langer and V Ambegaokar. Friedel sum rule for a system of interacting electrons. *Physical Review*, 121(4):1090, 1961.

[533] Richard M Martin. Fermi-surface sum rule and its consequences for periodic kondo and mixed-valence systems. *Physical Review Letters*, 48(5):362, 1982.

[534] Joshuah T Heath and Kevin S Bedell. Necessary and sufficient conditions for the validity of luttinger's theorem. *New Journal of Physics*, 22(6):063011, jun 2020.

[535] Sudeshna Sen, Patrick J. Wong, and Andrew K. Mitchell. The mott transition as a topological phase transition. *Phys. Rev. B*, 102:081110, Aug 2020.

[536] A. J. Heeger, S. Kivelson, J. R. Schrieffer, and W. P. Su. Solitons in conducting polymers. *Rev. Mod. Phys.*, 60:781–850, Jul 1988.

[537] M. Stone. Elementary derivation of one-dimensional fermion-number fractionalization. *Phys. Rev. B*, 31:6112–6115, May 1985.

[538] János K. Asbóth, László Oroszlány, and András Pályi. *A Short Course on Topological Insulators*. Springer International Publishing, 2016.

[539] Z. Iftikhar, S. Jezouin, A. Anthore, U. Gennser, F. D. Parmentier, A. Cavanna, and F. Pierre. Two-channel kondo effect and renormalization flow with macroscopic quantum charge states. *Nature*, 526(7572):233–236, Oct 2015.

[540] Z. Iftikhar, A. Anthore, A. K. Mitchell, F. D. Parmentier, U. Gennser, A. Ouerghi, A. Cavanna, C. Mora, P. Simon, and F. Pierre. Tunable quantum criticality and super-ballistic transport in a "charge" kondo circuit. *Science*, 360(6395):1315–1320, 2018.

[541] T. Giamarchi, C. M. Varma, A. E. Ruckenstein, and P. Nozières. Singular low energy properties of an impurity model with finite range interactions. *Phys. Rev. Lett.*, 70:3967–3970, Jun 1993.

[542] Qimiao Si and G. Kotliar. Fermi-liquid and non-fermi-liquid phases of an extended hubbard model in infinite dimensions. *Phys. Rev. Lett.*, 70:3143–3146, May 1993.

[543] AE Ruckenstein and CM Varma. A theory of marginal fermi-liquids. *Physica C: Superconductivity*, 185:134–140, 1991.

[544] Michel Ferrero, Lorenzo De Leo, Philippe Lecheminant, and Michele Fabrizio. Strong correlations in a nutshell. *Journal of Physics: Condensed Matter*, 19(43):433201, oct 2007.

[545] Shiro Sakai, Yukitoshi Motome, and Masatoshi Imada. Evolution of electronic structure of doped mott insulators: Reconstruction of poles and zeros of green's function. *Phys. Rev. Lett.*, 102:056404, Feb 2009.

[546] Thierry Giamarchi. *Quantum physics in one dimension*. Clarendon Oxford, 2004.

[547] Matthew T Glossop and David E Logan. Single-particle dynamics of the anderson model: a local moment approach. *Journal of Physics: Condensed Matter*, 14(26):6737, jun 2002.

[548] David E. Logan, Adam P. Tucker, and Martin R. Galpin. Common non-fermi liquid phases in quantum impurity physics. *Phys. Rev. B*, 90:075150, Aug 2014.

[549] Angela Kopp, Xun Jia, and Sudip Chakravarty. Replacing energy by von neumann entropy in quantum phase transitions. *Annals of Physics*, 322(6):1466–1476, 2007.

[550] LD Landau. The theory of a fermi liquid. *Soviet Physics Jetp-Ussr*, 3(6):920–925, 1957.

[551] Philip W. Phillips, Brandon W. Langley, and Jimmy A. Hutasoit. Un-fermi liquids: Unparticles in strongly correlated electron matter. *Phys. Rev. B*, 88:115129, Sep 2013.

[552] A. G. Loeser, Z.-X. Shen, D. S. Dessau, D. S. Marshall, C. H. Park, P. Fournier, and A. Kapitulnik. Excitation gap in the normal state of underdoped bi₂sr₂cacu₂o₈₊_δ. *Science*, 273(5273):325–329, 1996.

[553] M. R. Norman, H. Ding, M. Randeria, J. C. Campuzano, T. Yokoya, T. Takeuchi, T. Takahashi, T. Mochiku, K. Kadowaki, P. Guptasarma, and D. G. Hinks. Destruction of the fermi surface in underdoped high-tc superconductors. *Nature*, 392(6672):157–160, Mar 1998.

[554] Makoto Hashimoto, Inna M. Vishik, Rui-Hua He, Thomas P. Devereaux, and Zhi-Xun Shen. Energy gaps in high-transition-temperature cuprate superconductors. *Nature Physics*, 10(7):483–495, Jul 2014.

[555] Louis Taillefer. Scattering and pairing in cuprate superconductors. *Annual Review of Condensed Matter Physics*, 1(Volume 1, 2010):51–70, 2010.

[556] Eduardo Fradkin, Steven A. Kivelson, and John M. Tranquada. Colloquium: Theory of intertwined orders in high temperature superconductors. *Rev. Mod. Phys.*, 87:457–482, May 2015.

[557] Y. Sato, S. Kasahara, H. Murayama, Y. Kasahara, E.-G. Moon, T. Nishizaki, T. Loew, J. Porras, B. Keimer, T. Shibauchi, and Y. Matsuda. Thermodynamic evidence for a nematic phase transition at the onset of the pseudogap in yba2cu3oy. *Nature Physics*, 13(11):1074–1078, Nov 2017.

[558] N. Doiron-Leyraud, O. Cyr-Choinière, S. Badoux, A. Ataei, C. Collignon, A. Gourgout, S. Dufour-Beauséjour, F. F. Tafti, F. Laliberté, M.-E. Boulanger, M. Matusiak, D. Graf, M. Kim, J.-S. Zhou, N. Momono, T. Kurosawa, H. Takagi, and Louis Taillefer. Pseudogap phase of cuprate superconductors confined by fermi surface topology. *Nature Communications*, 8(1):2044, Dec 2017.

[559] Sourin Mukhopadhyay, Rahul Sharma, Chung Koo Kim, Stephen D. Edkins, Mohammad H. Hamidian, Hiroshi Eisaki, Shin ichi Uchida, Eun-Ah Kim, Michael J. Lawler, Andrew P. Mackenzie, J. C. Séamus Davis, and Kazuhiro Fujita. Evidence for a vestigial nematic state in the cuprate pseudogap phase. *Proceedings of the National Academy of Sciences*, 116(27):13249–13254, 2019.

[560] Naman K. Gupta, Christopher McMahon, Ronny Sutarto, Tianyu Shi, Rantong Gong, Haofei I. Wei, Kyle M. Shen, Feizhou He, Qianli Ma, Mirela Dragomir, Bruce D. Gaulin, and David G. Hawthorn. Vanishing nematic order beyond the pseudogap phase in overdoped cuprate superconductors. *Proceedings of the National Academy of Sciences*, 118(34):e2106881118, 2021.

[561] Masafumi Horio, Shiro Sakai, Hakuto Suzuki, Yosuke Nonaka, Makoto Hashimoto, Donghui Lu, Zhi-Xun Shen, Taro Ohgi, Takuya Konno, Tadashi Adachi, Yoji Koike, Masatoshi Imada, and Atsushi Fujimori. Pseudogap in electron-doped cuprates: Strong correlation leading to band splitting. *Proceedings of the National Academy of Sciences*, 122(1):e2406624122, 2025.

[562] B. Kyung, S. S. Kancharla, D. Sénéchal, A.-M. S. Tremblay, M. Civelli, and G. Kotliar. Pseudogap induced by short-range spin correlations in a doped mott insulator. *Phys. Rev. B*, 73:165114, Apr 2006.

[563] Alexandru Macridin, M. Jarrell, Thomas Maier, P. R. C. Kent, and Eduardo D'Azevedo. Pseudogap and antiferromagnetic correlations in the hubbard model. *Phys. Rev. Lett.*, 97:036401, Jul 2006.

[564] Shiro Sakai, Yukitoshi Motome, and Masatoshi Imada. Evolution of electronic structure of doped mott insulators: Reconstruction of poles and zeros of green's function. *Physical review letters*, 102(5):056404, 2009.

[565] Philipp Werner, Emanuel Gull, Olivier Parcollet, and Andrew J Millis. Momentum-selective metal-insulator transition in the two-dimensional hubbard model: An 8-site dynamical cluster approximation study. *Physical Review B*, 80(4):045120, 2009.

[566] Shiro Sakai, Yukitoshi Motome, and Masatoshi Imada. Doped high-t c cuprate superconductors elucidated in the light of zeros and poles of the electronic green's function. *Physical Review B*, 82(13):134505, 2010.

[567] N. Lin, E. Gull, and A. J. Millis. Physics of the pseudogap in eight-site cluster dynamical mean-field theory: Photoemission, raman scattering, and in-plane and c-axs=is conductivity. *Phys. Rev. B*, 82:045104, 2010.

[568] Emanuel Gull, Michel Ferrero, Olivier Parcollet, Antoine Georges, and Andrew J Millis. Momentum-space anisotropy and pseudogaps: A comparative cluster dynamical mean-field analysis of the doping-driven metal-insulator transition in the two-dimensional hubbard model. *Physical Review B*, 82(15):155101, 2010.

[569] E. Gull and A. J. Millis. Energetics of superconductivity in the two-dimensional hubbard model. *Phys. Rev. B*, 86:241106, 2012.

[570] Seyed Iman Mirzaei, Damien Stricker, Jason N. Hancock, Christophe Berthod, Antoine Georges, Erik van Heumen, Mun K. Chan, Xudong Zhao, Yuan Li, Martin Greven, Neven Barišić, and Dirk van der Marel. Spectroscopic evidence for fermi liquid-like energy and temperature dependence of the relaxation rate in the pseudogap phase of the cuprates. *Proceedings of the National Academy of Sciences*, 110(15):5774–5778, 2013.

[571] Emanuel Gull, Olivier Parcollet, and Andrew J Millis. Superconductivity and the pseudogap in the two-dimensional hubbard model. *Physical review letters*, 110(21):216405, 2013.

[572] Cornelia Hille, Daniel Rohe, Carsten Honerkamp, and Sabine Andergassen. Pseudogap opening in the two-dimensional hubbard model: A functional renormalization group analysis. *Phys. Rev. Res.*, 2:033068, Jul 2020.

[573] Weilun Jiang, Yuzhi Liu, Avraham Klein, Yuxuan Wang, Kai Sun, Andrey V. Chubukov, and Zi Yang Meng. Monte carlo study of the pseudogap and superconductivity emerging from quantum magnetic fluctuations. *Nature Communications*, 13(1):2655, May 2022.

[574] Mathias S. Scheurer, Shubhayu Chatterjee, Wei Wu, Michel Ferrero, Antoine Georges, and Subir Sachdev. Topological order in the pseudogap metal. *Proceedings of the National Academy of Sciences*, 115(16):E3665–E3672, 2018.

[575] Friedrich Krien, Paul Worm, Patrick Chalupa-Gantner, Alessandro Toschi, and Karsten Held. Explaining the pseudogap through damping and antidamping on the fermi surface by imaginary spin scattering. *Communications Physics*, 5(1):336, Dec 2022.

[576] Motoharu Kitatani, Liang Si, Paul Worm, Jan M. Tomczak, Ryotaro Arita, and Karsten Held. Optimizing superconductivity: From cuprates via nickelates to palladates. *Phys. Rev. Lett.*, 130:166002, Apr 2023.

[577] Sandro Sorella. Systematically improvable mean-field variational ansatz for strongly correlated systems: Application to the hubbard model. *Phys. Rev. B*, 107:115133, Mar 2023.

[578] Thomas Schäfer, Nils Wentzell, Fedor Šimkovic, Yuan-Yao He, Cornelia Hille, Marcel Klett, Christian J. Eckhardt, Behnam Arzhang, Viktor Harkov, François-Marie Le Régent, Alfred Kirsch, Yan Wang, Aaram J. Kim, Evgeny Kozik, Evgeny A. Stepanov, Anna Kauch, Sabine Andergassen, Philipp Hansmann, Daniel Rohe, Yuri M. Vilk, James P. F. LeBlanc, Shiwei Zhang, A.-M. S. Tremblay, Michel Ferrero, Olivier Parcollet, and Antoine Georges. Tracking the footprints of spin fluctuations: A multimethod, multimessenger study of the two-dimensional hubbard model. *Phys. Rev. X*, 11:011058, Mar 2021.

[579] Steven R. White and D. J. Scalapino. Density matrix renormalization group study of the striped phase in the 2d $t - J$ model. *Phys. Rev. Lett.*, 80:1272–1275, Feb 1998.

[580] Kota Ido, Takahiro Ohgoe, and Masatoshi Imada. Competition among various charge-inhomogeneous states and d-wave superconducting state in hubbard models on square lattices. *Phys. Rev. B*, 97:045138, Jan 2018.

[581] Cyril Proust and Louis Taillefer. The remarkable underlying ground states of cuprate superconductors. *Annual Review of Condensed Matter Physics*, 10(Volume 10, 2019):409–429, 2019.

[582] Boris Ponsioen, Sangwoo S. Chung, and Philippe Corboz. Period 4 stripe in the extended two-dimensional hubbard model. *Phys. Rev. B*, 100:195141, Nov 2019.

[583] Hao Xu, Hao Shi, Ettore Vitali, Mingpu Qin, and Shiwei Zhang. Stripes and spin-density waves in the doped two-dimensional hubbard model: Ground state phase diagram. *Phys. Rev. Res.*, 4:013239, Mar 2022.

[584] Kiaran B. Dave, Philip W. Phillips, and Charles L. Kane. Absence of luttinger's theorem due to zeros in the single-particle green function. *Phys. Rev. Lett.*, 110:090403, Feb 2013.

[585] Philip W. Anderson and F. Duncan M. Haldane. The symmetries of fermion fluids at low dimensions. *Journal of Statistical Physics*, 103(3):425–428, May 2001.

[586] Edwin W. Huang, Gabriele La Nave, and Philip W. Phillips. Discrete symmetry breaking defines the mott quartic fixed point. *Nature Physics*, 18(5):511–516, May 2022.

[587] B. L. Altshuler, A. V. Chubukov, A. Dashevskii, A. M. Finkel'stein, and D. K. Morr. Luttinger theorem for a spin-density-wave state. *Europhysics Letters*, 41(4):401, feb 1998.

[588] Gabriele La Nave, Jinchao Zhao, and Philip W. Phillips, 2025.

[589] A. M. Tsvelick and P. B. Wiegmann. Exact solution of the multichannel kondo problem, scaling, and integrability. *Journal of Statistical Physics*, 38(1):125–147, Jan 1985.

[590] O. Gunnarsson, M. Calandra, and J. E. Han. Colloquium: Saturation of electrical resistivity. *Rev. Mod. Phys.*, 75:1085–1099, Oct 2003.

[591] N. E. Hussey, K. Takenaka, and H. Takagi. Universality of the mott–ioffe–regel limit in metals. *Philosophical Magazine*, 84(27):2847–2864, 2004.

[592] S. L. Herr, K. Kamarás, C. D. Porter, M. G. Doss, D. B. Tanner, D. A. Bonn, J. E. Greedan, C. V. Stager, and T. Timusk. Optical properties of $la_{1.85}sr_{0.15}cuo_4$: Evidence for strong electron-phonon and electron-electron interactions. *Phys. Rev. B*, 36:733–735, Jul 1987.

[593] Joseph Orenstein, G. A. Thomas, D. H. Rapkine, C. G. Bethea, B. F. Levine, R. J. Cava, E. A. Rietman, and D. W. Johnson. Normal-state gap transition in cu-o superconductors. *Phys. Rev. B*, 36:729–732, Jul 1987.

[594] S. Uchida, T. Ido, H. Takagi, T. Arima, Y. Tokura, and S. Tajima. Optical spectra of $la_{2-x}sr_xcuo_4$: Effect of carrier doping on the electronic structure of the cuo_2 plane. *Phys. Rev. B*, 43:7942–7954, Apr 1991.

[595] G. A. Thomas, D. H. Rapkine, S. L. Cooper, S-W. Cheong, A. S. Cooper, L. F. Schneemeyer, and J. V. Waszczak. Optical excitations of a few charges in cuprates. *Phys. Rev. B*, 45:2474–2479, Feb 1992.

[596] Elbio Dagotto. Correlated electrons in high-temperature superconductors. *Rev. Mod. Phys.*, 66:763–840, Jul 1994.

[597] David Bałut, Barry Bradlyn, and Peter Abbamonte. Quantum entanglement and quantum geometry measured with inelastic x-ray scattering. *Phys. Rev. B*, 111:125161, Mar 2025.

[598] Giacomo Mazza and Costantino Budroni. Entanglement detection in quantum materials with competing orders. *Phys. Rev. B*, 111:L100302, Mar 2025.

[599] T. Senthil. Critical fermi surfaces and non-fermi liquid metals. *Phys. Rev. B*, 78:035103, Jul 2008.

[600] Yasuhiro Sekino and L. Susskind. Fast scramblers. *Journal of High Energy Physics*, 2008(10):065, oct 2008.

[601] Patrick Hayden and John Preskill. Black holes as mirrors: quantum information in random subsystems. *Journal of High Energy Physics*, 2007(09):120, sep 2007.

[602] Gregory Bentsen, Tomohiro Hashizume, Anton S. Buyskikh, Emily J. Davis, Andrew J. Daley, Steven S. Gubser, and Monika Schleier-Smith. Treelike interactions and fast scrambling with cold atoms. *Phys. Rev. Lett.*, 123:130601, Sep 2019.

[603] Philip W. Phillips, Luke Yeo, and Edwin W. Huang. Exact theory for superconductivity in a doped mott insulator. *Nature Physics*, 16(12):1175–1180, Dec 2020.

[604] Oskar Vafek and Ashvin Vishwanath. Dirac fermions in solids: From high-tc cuprates and graphene to topological insulators and weyl semimetals. *Annual Review of Condensed Matter Physics*, 5(Volume 5, 2014):83–112, 2014.

[605] T. Morimoto and N. Nagaosa. Weyl mott insulator. *Sci. Rep.*, 6:19853, 2016.

[606] R. Flores-Calderón and Chris Hooley. Weyl-mott point: Topological and non-fermi liquid behavior from an isolated green's function zero. *Phys. Rev. B*, 111:235139, Jun 2025.

[607] Howard Georgi. Unparticle physics. *Phys. Rev. Lett.*, 98:221601, May 2007.

[608] Howard Georgi. Another odd thing about unparticle physics. *Physics Letters B*, 650(4):275–278, 2007.

[609] Philip W. Phillips. Beyond particles: Unparticles in strongly correlated electron matter. In J Jedrzejewski, editor, *Quantum Criticality in Condensed Matter*, pages 133–158. World Scientific, Singapore, 2014.

[610] Jan Zaanen. Planckian dissipation, minimal viscosity and the transport in cuprate strange metals. *SciPost Phys.*, 6:061, 2019.

[611] A Legros, S Benhabib, W Tabis, F Laliberté, M Dion, M Lizaire, B Vignolle, D Vignolles, H Raffy, Z Li, et al. Universal t-linear resistivity and planckian dissipation in overdoped cuprates. *Nature Physics*, 15(2):142–147, 2019.

[612] Sean A. Hartnoll and Andrew P. Mackenzie. Colloquium: Planckian dissipation in metals. *Rev. Mod. Phys.*, 94:041002, Nov 2022.

[613] John McGreevy. Generalized symmetries in condensed matter. *Annual Review of Condensed Matter Physics*, 14(Volume 14, 2023):57–82, 2023.

[614] Lei Su and Ivar Martin, 2025.

[615] Stephen L Adler. Axial-vector vertex in spinor electrodynamics. *Physical Review*, 177(5):2426, 1969.

[616] John S Bell and Roman Jackiw. A pcac puzzle: $\pi 0 \to \gamma\gamma$ in the σ-model. *Il Nuovo Cimento A*, 60(1):47–61, 1969.

[617] Horacio Casini and Javier M. Magán. On completeness and generalized symmetries in quantum field theory. *Modern Physics Letters A*, 36(36):2130025, 2021.

[618] M. Hashimoto, R.-H. He, I. M. Vishik, F. Schmitt, R. G. Moore, D. H. Lu, Y. Yoshida, H. Eisaki, Z. Hussain, T. P. Devereaux, and Z.-X. Shen. Superconductivity distorted by the coexisting pseudogap in the antinodal region of $bi_{1.5}pb_{0.55}sr_{1.6}la_{0.4}cuo_{6+\delta}$: A photon-energy-dependent angle-resolved photoemission study. *Phys. Rev. B*, 86:094504, Sep 2012.

[619] I. M. Vishik, E. A. Nowadnick, W. S. Lee, Z. X. Shen, B. Moritz, T. P. Devereaux, K. Tanaka, T. Sasagawa, and T. Fujii. A momentum-dependent perspective on quasiparticle interference in bi2sr2cacu2o8+δ. *Nature Physics*, 5(10):718–721, Oct 2009.

[620] Samuel Moukouri and Mark Jarrell. Absence of a slater transition in the two-dimensional hubbard model. *Physical review letters*, 87(16):167010, 2001.

[621] A C Hewson and D Meyer. Numerical renormalization group study of the anderson-holstein impurity model. *Journal of Physics: Condensed Matter*, 14(3):427, dec 2001.

[622] N. F. Mott. Rare-earth compounds with mixed valencies. *The Philosophical Magazine: A Journal of Theoretical Experimental and Applied Physics*, 30(2):403–416, 1974.

[623] Ming-Chiang Chung and Ingo Peschel. Density-matrix spectra for two-dimensional quantum systems. *Phys. Rev. B*, 62:4191–4193, Aug 2000.

[624] Hai-Zhou Lu, Wen-Yu Shan, Wang Yao, Qian Niu, and Shun-Qing Shen. Massive dirac fermions and spin physics in an ultrathin film of topological insulator. *Phys. Rev. B*, 81:115407, Mar 2010.

[625] Weiyao Zhao, Chi Xuan Trang, Qile Li, Lei Chen, Zengji Yue, Abuduliken Bake, Cheng Tan, Lan Wang, Mitchell Nancarrow, Mark Edmonds, David Cortie, and Xiaolin Wang. Massive dirac fermions and strong shubnikov–de haas oscillations in single crystals of the topological insulator Bi_2Se_3 doped with sm and fe. *Phys. Rev. B*, 104:085153, Aug 2021.

[626] B. Hunt, J. D. Sanchez-Yamagishi, A. F. Young, M. Yankowitz, B. J. LeRoy, K. Watanabe, T. Taniguchi, P. Moon, M. Koshino, P. Jarillo-Herrero, and R. C. Ashoori. Massive dirac fermions and hofstadter butterfly in a van der waals heterostructure. *Science*, 340(6139):1427–1430, 2013.

[627] A.G. Abanov and P.B. Wiegmann. Theta-terms in nonlinear sigma-models. *Nuclear Physics B*, 570(3):685–698, 2000.

[628] M. Blasone, F. Dell'Anno, S. De Siena, and F. Illuminati. Hierarchies of geometric entanglement. *Phys. Rev. A*, 77:062304, Jun 2008.

[629] Glen Evenbly and Guifré Vidal. Algorithms for entanglement renormalization. *Physical Review B*, 79(14):144108, 2009.

[630] Glen Evenbly and Steven R. White. Entanglement renormalization and wavelets. *Phys. Rev. Lett.*, 116:140403, Apr 2016.

[631] Patrick Hayden, Matthew Headrick, and Alexander Maloney. Holographic mutual information is monogamous. *Phys. Rev. D*, 87:046003, Feb 2013.

[632] Ning Bao, Sepehr Nezami, Hirosi Ooguri, Bogdan Stoica, James Sully, and Michael Walter. The holographic entropy cone. *Journal of High Energy Physics*, 2015(9):130, Sep 2015.

[633] Katharine Hyatt, James R Garrison, and Bela Bauer. Extracting entanglement geometry from quantum states. *Physical review letters*, 119(14):140502, 2017.

[634] Robert C. Myers and Aninda Sinha. Seeing a c-theorem with holography. *Phys. Rev. D*, 82:046006, Aug 2010.

[635] Robert C. Myers and Aninda Sinha. Holographic c-theorems in arbitrary dimensions. *Journal of High Energy Physics*, 2011(1):125, Jan 2011.

[636] Chong-Sun Chu and Dimitrios Giataganas. c-theorem for anisotropic rg flows from holographic entanglement entropy. *Phys. Rev. D*, 101:046007, Feb 2020.

[637] ChunJun Cao, Sean M. Carroll, and Spyridon Michalakis. Space from hilbert space: Recovering geometry from bulk entanglement. *Phys. Rev. D*, 95:024031, Jan 2017.

[638] Sudipto Singha Roy, Silvia N. Santalla, Javier Rodríguez-Laguna, and Germán Sierra. Entanglement as geometry and flow. *Phys. Rev. B*, 101:195134, May 2020.

[639] Sheng Bau and Alan F. Beardon. The metric dimension of metric spaces. *Computational Methods and Function Theory*, 13(2):295–305, Aug 2013.

[640] Joseph J. Bisognano and Eyvind H. Wichmann. "On the duality condition for a Hermitian scalar field". *Journal of Mathematical Physics*, 16(4):985–1007, 09 2008.

[641] Joseph J. Bisognano and Eyvind H. Wichmann. "On the duality condition for quantum fields". *Journal of Mathematical Physics*, 17(3):303–321, 08 2008.

[642] David D. Blanco, Horacio Casini, Ling-Yan Hung, and Robert C. Myers. Relative entropy and holography. *Journal of High Energy Physics*, 2013(8):60, Aug 2013.

[643] Sayan Kar. Geometry of renormalization group flows in theory space. *Phys. Rev. D*, 64:105017, Oct 2001.

[644] Sayan Kar and Soumitra Sengupta. The raychaudhuri equations: A brief review. *Pramana*, 69(1):49–76, 2007.

[645] Ingo Peschel. Calculation of reduced density matrices from correlation functions. *Journal of Physics A: Mathematical and General*, 36(14):L205, mar 2003.

[646] A. Alexandradinata, Taylor L. Hughes, and B. Andrei Bernevig. Trace index and spectral flow in the entanglement spectrum of topological insulators. *Phys. Rev. B*, 84:195103, Nov 2011.

[647] DJ Thouless, Mahito Kohmoto, MP Nightingale, and M Den Nijs. Quantized hall conductance in a two-dimensional periodic potential. *Physical Review Letters*, 49(6):405, 1982.

[648] Michael O. Flynn, Long-Hin Tang, Anushya Chandran, and Chris R. Laumann. Momentum space entanglement of interacting fermions, 2022.

[649] Vijay Balasubramanian, Michael B McDermott, and Mark Van Raamsdonk. Momentum-space entanglement and renormalization in quantum field theory. *Physical Review D*, 86(4):045014, 2012.

[650] TC.L. Hsu, M.B. McDermott, and M. Van Raamsdonk. Momentum-space entanglement for interacting fermions at finite density. *J. High Energ. Phys.*, 121 (2013), 2013.

[651] Matheus H. Martins Costa, Jeroen van den Brink, Flavio S. Nogueira, and Gastão I. Krein. Momentum space entanglement from the wilsonian effective action. *Phys. Rev. D*, 106:065024, Sep 2022.

[652] Vijay Balasubramanian and Per Kraus. Spacetime and the holographic renormalization group. *Physical Review Letters*, 83(18):3605, 1999.

[653] V. Balasubramanian, A. Bernamonti, N. Copland, B. Craps, and F. Galli. Thermalization of mutual and tripartite information in strongly coupled two dimensional conformal field theories. *Phys. Rev. D*, 84:105017, Nov 2011.

[654] M. Asadi and M. Ali-Akbari. Holographic mutual and tripartite information in a symmetry breaking quench. *Physics Letters B*, 785:409–418, 2018.

[655] M. Ali-Akbari, M. Rahimi, and M. Asadi. Holographic mutual and tripartite information in a non-conformal background. *Nuclear Physics B*, 964:115329, 2021.